Prototyping the next generation of versatile paleomagnetic laboratory

Thesis submitted in accordance with the requirements of the University of Liverpool for the degree of Doctor in Philosophy by

Joseph Michael Grappone, Jr.

30 September, 2020

DECLARATION OF AUTHORSHIP

I declare that this thesis titled, ***Prototyping the next generation of versatile paleomagnetic laboratory***. The material contained in the thesis has not been presented, nor is currently being presented, either wholly or in part, for any other degree or qualification.

Signed: *Joseph Michael Grappone, Jr.*

Joseph Michael Grappone Jr.
30th September, 2020

CONTENTS

GLOSSARY

WORD	DEFINITION	FIRST MENTION
AC	Alternating current	28
AF	Alternating field (demagnetization mechanism)	5
Aitken protocol	A variant of the Original Thellier method (in-field step then zero-field; IZ)	14
α	A measure of the reliability of a paleodirection in a paleointensity experiment	107
α_{95}	The 95% confidence interval from Fisher statistics	92
Arai plot	The standard paleointensity diagram	5
B	An external applied magnetic field (magnetic flux density)	14
BDS	Bulk domain stability	128
β	A measure of the scatter about the best fit line on an Arai plot	107
CIT	The file format used on the RAPID system	85
CMB	Core-mantle boundary	149
Coe protocol	A variant of the Original Thellier method (zero-field then in-field step; ZI)	13
COMSOL	A physics modelling program	198
CRM	Chemical remanent magnetization	11
CT	Coiled Tubing	199
DC	Direct current	4
Dec	Declination	70
Delrin	A type of plastic	41
ΔΘ	A measure of the perpendicularity of a Perpendicular paleointensity experiment	107
DP	Degradation parameter	203
DPDT	Double pole double throw (type of relay)	78
DRAT	A measure of thermochemical alteration derived from pTRM checks	107
DRM	Detrital remanent magnetization	11
f	Amount of NRM used in a paleointensity experiment	131
F.I.T.	Forschungsgesellschaft für Informationstechnik	42
FORC	First Order Reversal Curve	126
FRAC	A measure of the amount of natural remanent magnetization used in a paleointensity experiment	107
FTL	Fatigue life	203
Gyr	billions of years	102
H_{cr}/H_c	The ratio of coercivity of remanence to coercivity	129
HiTeCT	A high-temperature variant of the Coe variant of the Thellier-style protocols	174
HSDP	Hawai‘i Scientific Drilling Project	125
ID	Inner diameter	53
IEF	Intensity error fraction	117
Inc	Inclination	70
Inconel	Nominally non-magnetic stainless steel	64

IRM	Isothermal remanent magnetization	46
I-step	An in-field step	106
IZZI	A varient of the Original Thellier method (in-field/zero-field; zero-field/in-field; IZZI)	7
K	Fisher statistic for paleodirection data dispersion	92
Ka	Thousands of years ago	125
$\left\lvert \overrightarrow{K'} \right\rvert$	A measure of the amount of curvature on an Arai plot	107
KH	Kinghorn, Scotland	151
Lift-off distance	The distance from the surface (of Coiled Tubing) to the sensor	201
LTD	Low temperature demagnetization using liquid nitrogen	7
Ma	Millions of years ago	149
MAD	Maximum angular deviation	92
Magnon	Quantized spin wave packets	19
MD	Multi-domain (magnetic grains)	17
MFL	Magnetic flux leakage	198
MMTD	Magnetic Measurements Thermal Demagnetizer	81
M_{rs}/M_s	The ratio of magnetic remanence to saturation magnetization	128
μ_R	relative permeability	199
Mu-metal	A type of high magnetic coercivity metal used in paleomagnetic surveys	12
MW	Microwave demagnetization mechanism	105
Myr	Millions of years	125
NDE	Non-destructive evaluation	200
Nichrome	NiCr; a type of material used for heating wire	30
Non-SD	A catch all term for any non-single domain magnetic grain	5
NRM	Natural remanent magnetization	13
OD	Outer diameter	52
Orthogonal plot	The standard paleodirection diagram	71
OT	Original Thellier method; a paleointensity method using two antiparallel in-field steps (II)	12
Perp	A variant of the Original Thellier method using a single in-field step applied perpendicularly to the specimen's NRM	6
PI	Paleointensity	103
PID	Proportional-integral-derivative (type of control loop)	39
PINT	The absolute palaeointensity database	125
POOH	Pulling out of hole	203
PSD	Pseudo-single domain grains	17
P-step	A pTRM check (repeated I step)	106
pT_MRM	Partial microwave thermoremanent magnetization	105
pTRM	Partial thermoremanent magnetization	13
q	Quality of an Arai plot	107
Q	Defect severity	204

RAPID	Rock and Paleomagnetism Instrument Consortium (piece of equipment for paleomagnetic surveys)	4
RF	Radio frequency	27
SD	Single domain (magnetic grains)	12
SEM	Scanning Electron Microscope/Microscopy	104
Skelp	A flat sheet of metal than becomes folded in Coiled Tubing	199
SOH	Scientific Observation Hole (in Hawai‘i)	7
SPDT	Single pole double throw (type of relay)	79
SQUID	Superconducting Quantum Interference Device	4
SQUID jump	A sudden (quantized) step change in SQUID output (usually to the maximum possible voltage)	50
Tank circuit	An inductor - capacitor (LC) circuit used for tuning SQUIDs	63
TCRM	Thermochemical remanent magnetization	11
Th	Thermal demagnetization mechanism	130
Thermocouple, K-type	Nickel-Chromium/Nickel-Alumel thermocouple	32
Thermocouple, N-type	Nicrosil/Nisil thermocouple	45
Thermocouple, R-type	Platinum-Rhodium thermocouple	45
TRM	Thermoremanent magnetization	11
T-step	A tail check (repeated Z step)	181
VDM	Virtual dipole moment	161
VFTB	Variable field transition balance	30
VRM	Viscous remanent magnetization	17
Walton paleointensity technique	A stepwise paleointensity analogous to the Wilson paleointensity technique	15
Wilson paleointensity method	A continuous paleointensity technique consisting of a single heating and cooling step	5
WT	Wall thickness	215
Z-step	A zero-field step	106

ABSTRACT

English Abstract

Investigating the Earth's magnetic field provides a unique window into the history of Earth's outer core, where the field is generated. Rocks gain a magnetization that is in the direction of and proportional to the Earth's magnetic field at the time of their formation, such as when magma erupts from a volcano and cools below its Curie temperature. The gained magnetization has a relaxation time that is frequently longer than the age of the universe, but unfortunately, rocks are subject to the whims of the Earth over geologic time. Given the ages of rocks commonly studied (millions to billions of years old), some paleomagnetic data is noisy and complex. Paleomagnetic intensity data in particular have long been plagued by large and poorly quantified uncertainties. Extracting accurate magnetic measurements relies on having the most advanced equipment and best experimental techniques. This thesis approaches these goals from two directions: prototyping new equipment, which also introduces novel methodology, and fine-tuning existing methods. Contained herein is the development of the world's first automated high-temperature SQUID (Superconducting Quantum Interference Device) thermomagnetometer. This system can automatically measure the remanent magnetic field of a specimen at an elevated temperature without needing to cool the specimen to ambient temperature. Without repeated heating/cooling cycles, thermochemical alteration is minimized, and the rate of data collection is greatly increased. SQUID sensors improve the sensitivity of the magnetometer system, avoid low blocking temperature components, and provide precise temperature control and minimal alteration. While the original design called for an instrument that could provide continuous magnetization measurements, this proved to be untenable due to technical constraints with the SQUID sensors. Thus, a stepwise version was produced that measures each specimen in (up to) 10 °C increments, instead of continuously.

Introducing new equipment by itself is futile if the experiments performed on them are not well calibrated and optimized. To address this problem, this thesis investigates differences in paleomagnetic intensity results produced by different variants of Thellier-style paleointensity protocols using established instruments. The most modern protocol, the IZZI protocol, was found to be broadly accurate but sometimes imprecise. This thesis further attempts to ascertain the cause of differences observed in paleointensity data when the demagnetization mechanism or paleointensity protocol is changed, as nearly a dozen methods are in use throughout the world. Finally, a series of tests evaluates whether the addition of alternating field or liquid nitrogen demagnetization cleansing steps can improve data fidelity. The additional cleansing steps can, in some cases, improve the linearity of paleointensity data sufficiently to pass selection criteria, but cannot affect, for example, other complications like thermochemical alteration. With the ever-growing pressure to provide tangible impacts to the broader scientific community, expanding the versatility of magnetic techniques to new applications is paramount. This thesis broadly applies magnetic techniques to the energy sector, through Magnetic Flux Leakage experiments on Coiled Tubing, in conjunction with Schlumberger as an industrial partner.

The future paleomagnetic laboratory is a versatile one, capable of running large batches of specimens (both paleomagnetic and metallic) quickly and accurately, through a combination of improved methods and equipment. This thesis has successfully introduced a new prototype magnetometer design and found that for non-ideal (i.e. real) rocks, the interactions between the rocks and methods are complex. Going forward, the new magnetometer brings high temperature remanence measurements to more rock types and potentially further partnerships with external, industrial partners, like Schlumberger.

Abstrakti suomeksi

Maapallon magneettikentän tutkiminen sallii ainutlaatuisen katsauksen maan ulkoiseen ytimeen, jossa magneettikenttä syntyy, ja ulkoytimen historiaan. Kun laava puhkeaa tulivuoresta ja viilenee Curie-lämpötilan alle, maapallon magneettikenttä magnetisoi siinä syntyvät kivilaadut. Tämä magnetisointi säilyy kauemmin kuin maailmankaikkeus. Kivien erittäin pitkä ikä (ne voivat olla miljoonista miljardeihin vuosia vanhoja) tarkoittaa, että kivien mittaus voi olla epätarkkaa ja usein monimutkaista; tästä syystä paleointensitettikokeissa on usein suuria mittausvirheitä. Tarkat magneettiset mittaukset edellyttävät kehittyneimpiä laiteita ja parhaita tekniikkoja. Tässä tutkielmassa on seuraavat kaksi päämäärää: uusien laitteiden kehitys, joihin myös kehitetään ja sovelletaan uusia metodologeja; sekä nykyisten metodien hienosäätö. Tässä esitetään myös maapallon ensimmäisen SQUID-sensoreja käyttävän prototyyppilämpömagnetometrin kehitys. Laite voi mitata automaattisesti näytteen remanenssimagneettikentän korkeassa lämpötilassa jäähdyttämättä näytettä ympäröivään lämpötilaan. Välttämällä lämmitys-/jäähdytyssyklejä minimoidaan lämpökemiallinen muutos, ja tiedon keräämisen nopeutta lisätään. SQUID-sensorit lisäävät magnetometrin herkkyyttä, mikä mahdollistaa sovellukset, joissa pyritään välttämään alhaista Curie-lämpötilakomponenttia tai lämpökemiallisia muutoksia. Vaikka alkuperäiseen suunnitelmaan kuului jatkuvasti mittava mittari, tämä ei kuitenkaan osoittautunut toteutuskelpoiseksi SQUID-sensoreiden teknisten rajoitusten takia. Sen sijaan valmistui vaiheittainen versio, joka mittaa jokaisen näytteen 10 °C askelissa.

Uusien laitteiden käyttöönottaminen on turhaa, jos niillä tehdyt kokeet eivät ole hyvin kalibroituja ja optimoituja. Tästä syystä tutkielma käyttää nykyisiä laitteita tutkimaan paleomagneettisten intensiteettikoetuloksien eroavaisuuksia, jotka aiheutuvat erilaisista Thellier-typpisistä paleointensiteettiprotokollavarianteista. Nykyaikaisin protokolla, IZZI-protokolla, on yleisesti ottaen tarkka, mutta joskus epätäsmällinen. Tämä tutkielma yrittää lisäksi selittää paleo-intensiteettituloksissa nähtyjä eroja, jotka syntyvät, kun magnetointimekanismia tai paleo-intensiteettiprotokollaa vaihdetaan, sillä nykytutkijat käyttävät melkein tusinaa metodia. Lopuksi koesarja evaluoi, voivatko demagnetoimisaskeleet, jotka käyttävät vuorottelevaa kenttää tai nestemäistä typpeä, parantaa tuloslaatua. Lisäaskeleet voivat joissakin tapauksissa parantaa tarpeeksi paleo-intensiteettituloksien lineaarisuutta, jotta tulokset voivat läpäistä valitsemiskriteerit. Lisäaskeleet eivät kuitenkaan vaikuta muihin vaikeuttaviin tekijöihin kuten esimerkiksi lämpökemiallisiin muutoksiin. Ottaen huomioon kasvava paine tarjota konkreettisia vaikutuksia laajalle tiedeyhteisölle, magneettisten tekniikoiden laajentaminen ja soveltaminen uusiin käyttöihin on tärkeätä. Tämä tutkielma soveltaa magneettista tekniikkaa energiasektoriin, käyttämällä magneettivuovuodon kokeita kiemuraiseen putkistoon teollisuuskumppanin, Schlumbergerin, kanssa.

Tulevaisuuden paleomagneettinen laboratorio on monipuolinen ja voi testata isoja näytesarjoja nopeasti ja täsmällisesti, käyttämällä parannettuja metodeja ja laitteita. Tutkielma on menestyneesti ottanut käyttöön uuden prototyppimagnetometrilaiteen ja todennut, että kivien ja metodien välinen vuorovaikutus on monimutkaista, jos kivet ovat epäideaaleja (todellisia). Tulevaisuudessa, uusi magnetometrilaite tuo korkean lämpötilan remanenssimittaukset laajempaan kirjoon kivilajeja, mahdollisesti yhteistyössä ulkoisten teollisuuskumppaneiden, kuten Schlumbergerin, kanssa.

Abstraktet på dansk

Forskningen af jordklodens magnetfelt giver et enestående vindue ind i historie med Jordens ydre kerne, hvor magnetfeltet genereres. Bjergarter bliver magnetiseret i retning af jordens magnetfelt. Styrken i jordens magnetfelt er proportional med den, der magnetfelt havde, på dannelsestidspunkt; for eksempel da magma brød ud af en vulkan og derefter afkølede. Magnetiseringen har et relaksationstidspunkt, der normalt er længere end universets alder, men stener desværre påvirkes af Jorden i løbet af geologisk relevante tidspunkter. I betragtning af bjergarters aldre (fra millioner til milliarder år gammel), palæomagnetismedatene er støjende og komplekse. Datene om palæomagnetisk intensitet har især haft store og dårligt kvantificerede usikkerheder. Udvindingen af nøjagtige magnetiske målinger har brug for at have det mest avanceret udstyr og de bedste eksperimentteknikker. Denne afhandling bruger to tilgange: prototyperinget af ny udstyr, som også bringer ny metodologi, og finjustering af nuværende metoder. Afhandlingen har herind udviklingen af jordens første høj-temperatur termomagnetometer, der bruger SQUID-sensorer. Det automatisk system kan måle en prøves remanent magnetfelt ved høje temperaturer uden at afkøle prøven til omgivelsestemperatur. Uden disse gentagne opvarmnings- og afkølingscyklusser, den termokemiske ændring minimeres og datakollektionen øges. SQUID-sensorer øger magnetometersystemets følsomhed, som også øger sin nytte til applikationer, der må undgå magnetiske komponenter med lav blokeringstemperaturer og kræver temperaturkontrol og minimal ændring. Selvom det originale design ville et udstyr, der kunne give sammenhængende magnetiske målinger, SQUID-sensorerne kunne ikke virke pålideligt nok. I stedet, en trinvis version blev produceret, der kan måle hver prøve hver 10 °C.

Introduktionen af kun nyt udstyr er forgæves, hvis eksperimenterne er ikke godt kalibrerede og optimerede. Denne afhandling tackler dette ved at undersøge forskellene i palæomagnetiske intensitetsresultater, der produceres af de forskellige Thellier-type palæointensitetsprotokoller med etableret udstyr. Den mest moderne protokol, den IZZI-protokol, har opvist sig at være generelt nøjagtig men sommetider upræcis. Afhandlingen prøver at determinere causer af forskellene, der observeredes i palæointensitetsdataene når afmagnetiseringsmekanismen eller palæointensitetsprotokollen forandredes, fordi verdens videnskabsmænd bruger i dag næsten et dusin metoder. Finalt, en eksperimentrække tester om additionen af skiftende felt eller flydende nitrogen som afmagnetiseringstrin kan forbedre dataenes kvalitet. De ekstra afmagnetiseringstrin kan, i nogle tilfælde, forbedre palæointensitetsdataenes linearitet, så dataene kan bestå kriterierne. Hvordan end kan det ikke undvige andre komplikationer, som for eksempel, termokemisk ændring. Presset bliver at vokse for at udvise påvirkninger til det bredere videnskabsfællesskab, så derfor er ekspansionen af magnetiske teknikker til nye applikationer vigtig. Afhandlingen bredt anvender disse teknikker til energisektoren. Den rapporterer magnetfluxlækageeksperimenter, der blev fuldendt med en industripartner, Schlumberger.

Det fremtidige palæomagnetismelaboratorium er alsidigt og kan indsamle store (palæomagnetiske og metalliske) datasætter hurtigt og nøjagtigt ved hjælp af forbedrede metoder og udstyr. Afhandlingen har succesfuldt introduceret en ny magnetometerprototypedesign og fundet, at interaktioner mellem bjergarter og metoder er komplekse, hvis bjergarter har ikke-ideel magnetiske partikeller. I fremtiden bringer den nye magnetometer remanensmålinger med høj temperatur til flere bjergartstyper og til udvendige industripartnere; for eksempel, Schlumberger.

Le résumé en français

L'investigation du champ magnétique de la Terre fournit une opportunité unique pour étudier l'histoire du noyau externe, d'où vient le champ magnétique. Quand la lave jaillit d'un volcan et puis refroidit en dessous de sa température Curie dans le champ magnétique de la Terre, il se magnétise. Cette aimantation a un temps de relaxation qui dure plus que l'univers. Étant donné que les âges des rochers sont très vielles (ils a des millions jusqu'à milliards d'ans), les données magnétiques sont complexes, et pour cette raison, les expériences de paléointensité ont pendant beaucoup de temps des grandes erreurs. La détermination des données magnétiques compte sur les équipements les plus avancés et les meilleures techniques. Cette thèse s'approche ces objectifs de deux directions : un magnétomètre prototype, qui a sa propre méthodologie, et l'ajustement précis des méthodes actuel. Dans cette thèse est le développement du premier magnétomètre automatique qui utilise des capteurs SQUID pour mesurer le champ magnétique d'une roche. Cette pièce d'équipement peut mesurer le champ magnétique d'un spécimen à températures élevées sans la nécessité de le refroidir à la température ambiante. Sans ces cycles de chauffer et refroidir, l'altération thermochimique est minimisée et le taux de mesurer augmente considérablement. Les capteurs SQUID augmente la sensibilité du magnétomètre. Par conséquent, ils augmentent leur utilité pour beaucoup d'applications qui a besoin d'un contrôle de la température et d'éviter les components avec une température de déblocage basse et d'éviter l'altération thermochimique. La conception originale exigeait un équipement qui puisse mesurer continuellement, mais à cause des restrictions techniques, cela était intenable. À sa place, une version par étapes était produite qui mesure chaque spécimen par incréments de (jusqu'à) dix degrés.

L'introduction de nouvel équipement sera futile si les expériences réalisées ne sont pas bien calibrées et optimisées. Cette thèse s'adresse à ce problème par l'investigation des différences des résultats de paléointensité produites par variants de protocoles de paléointensité différents. Le protocole le plus moderne, le protocole IZZI, s'est avéré généralement exact mais parfois imprécis. Cette thèse tente de déterminer la cause des différences observées dans les données de paléointensité quand le mécanisme de démagnétisation ou le protocole de paléointensité est changé; au moment presqu'une douzaine de ces méthodes sont utilisées. Finalement, l'évaluation des techniques examine si l'addition d'une étape de démagnétisation à champ en alternance ou dans l'azote liquide peut améliorer la fidélité des données. Ces étapes additionnelles peuvent, dans certains cas, améliorer la linéarité des données de paléointensité suffisamment pour que les données dépassent les critères de sélection, mais elles ne peuvent pas améliorer certaines autres complications; par exemple, l'altération thermochimique. À cause de la pression de fournir des impacts tangibles pour la communauté scientifique plus large, il est important d'étendre la polyvalence des techniques magnétiques. Cette thèse applique les techniques magnétiques au secteur de l'énergie, à travers des expériences de la fuite de flux magnétique sur des tubes enroulés, dans le cadre d'un partenariat industriel avec Schlumberger.

Le laboratoire paléomagnétique de l'avenir est polyvalent. Il peut exécuter l'analyse de grands lots de spécimens rapidement et précisément, utilisant une combination des méthodes et équipements améliorés. Cette thèse a introduit un nouveau magnétomètre prototype et a trouvé que l'interaction entre les roches non-idéales et les méthodes est complexe. À l'avenir, le nouveau magnétomètre permettra à mesurer la rémanence magnétique aux températures élevées avec plus de types de roches, et possiblement en partenariat avec des partenaires industriels, tels que Schlumberger.

El resumen en español

La investigación del campo magnético de la Tierra provee una oportunidad singular para investigar la historia del núcleo externo de la Tierra, en el que se genera el campo magnético. Las rocas se imantan en la dirección de, y proporcionalmente al, campo magnético de la Tierra en el momento de su formación, por ejemplo, cuando el magma mana de un volcán y luego se enfría bajo su temperatura Curie. Esta imanación tiene un tiempo de relajación más largo que la edad del universo, pero desafortunadamente las rocas son afectadas por los caprichos de la Tierra. Las edades de las rocas comúnmente estudiadas (de millones a miles de millones de años) significan que los datos paleomagnéticos son ruidosos y complicados. Los datos de la intensidad del campo magnético (paleointensidad) han padecido particularmente de incertitudes grandes y mal cuantificadas. La extracción de medidas rigurosas requiere los equipamientos más avanzados y las mejores técnicas experimentales. Esta tesis se acerca a estos objetivos desde dos direcciones principales: la creación de prototipos de equipos nuevos (que también introducen algunas metodologías nuevas) y la afinación de métodos actuales. Esta tesis contiene el desarrollo del primero termomagnetómetro automático que utiliza sensores superconductores, SQUIDes. Este sistema puede medir automáticamente la remanencia magnética de un espécimen a temperaturas elevadas sin enfriarlo a la temperatura ambiental. Evitando así los ciclos de calentamiento y enfriamiento, la alteración química se minimiza y el ritmo de colección de datos aumenta. Los SQUIDes aumentan la sensibilidad del sistema, que en turno aumenta su utilidad en aplicaciones que requieren un control de temperatura preciso y una evasión de alteraciones químicas. Aunque el diseño original requirió un equipo que pudiera medir automáticamente, a causa de limitaciones técnicas con los SQUIDes, no fue posible. En su lugar, una versión escalonada, que mide cada espécimen en incrementos de 10 °C, fue construida.

La introducción de un equipamiento nuevo por sí solo es fútil, si los experimentos hechos no son bien calibrados u optimizados. Para abordar este problema, esta tesis investiga las diferencias entre los resultados de paleointensidad producidos por protocolos del estilo Thellier y con equipamientos actuales. El protocolo más moderno, IZZI, se ha demostrado ser largamente exacto, pero de vez en cuando impreciso. Esta tesis intenta, además, determinar la causa de las diferencias en los datos que resultan de cambios del mecanismo de desmagnetización o del protocolo, teniendo en cuento que al momento se usa casi una docena de métodos en el mundo. Finalmente, una serie de experimentos evalúa el efecto de la adición de una etapa de desmagnetización de campo alterno o de nitrógeno líquido para mejorar la fiabilidad de los datos. Las etapas pueden, en algunos casos, mejorar la linealidad de los datos suficientemente tal que los datos pasen los criterios de selección, pero no pueden afectar otras complicaciones, como, por ejemplo, la alteración química. A causa de la presión creciente para proporcionar impactos tangibles a la comunidad científica, la expansión de la versatilidad de técnicas magnéticas a aplicaciones nuevas es crucial. Esta tesis aplica en general las técnicas magnéticas al sector energético, por experimentos de fuga de flujo magnético aplicada a tubos en espiral, en conjunto con un socio, Schlumberger.

El laboratorio del paleomagnetismo del futuro es versátil y puede analizar especímenes (de roca y metálicos) rápida y exactamente en lotes grandes a través de una combinación de métodos y equipamientos mejorados. Esta tesis ha introducido exitosamente un prototipo de magnetómetro nuevo, y ha determinado además que las interacciones entre las rocas no ideales (reales) y los métodos son complejas. En el futuro, el magnetómetro nuevo permite medidas de la remanencia magnética a temperaturas altas sobre más tipos de rocas, quizás en colaboración con socios industriales, como Schlumberger.

在中文的摘要

地球磁场的研究让我们研究地球磁场产生的外核的历史。岩石形成的时候朝着地球磁场方向磁化。在这篇论文中，岩石噴發后在居里温度下冷却的同时磁化。岩石的磁场跟地球的磁场强度成正比。磁场的弛豫时间比宇宙的年龄长。然而噴發后，地球在地质时期继续影响岩石。古地磁学的数据很复杂可能会很多噪音因为研究的岩石非常古（百万到十亿年的历史）。古地磁强度 数据特别经常有未量化确定性。最准确磁测量的数据要求最高级的设备也最好实验室的方法。因此，这本论文有两个目标：新设备的原型制作（也有新方法），现有方法的微调。

在这篇论文有第一个自动高温超导量子干涉儀（SQUID）热磁强计的发展。这个磁强计可以在高温下自动测量一块岩石的磁场，而无需冷却样品至室温。加热和冷却周期的缺乏意味着热化学变化被最小化，和数据采集率被提高。SQUID 的传感器提高磁力设备的灵敏度。因此，如果一个实验需要精确温度的控制或者避免有低居里温度的剩磁元素，此设备很合适。原版的设计需要连续磁场的测量，但是 SQUID 传感器的无法进行连续的磁强测量。新的磁强计被发明。逐步地有条理地，磁强计会在每十度的温度变化自动测量样品的磁力。

如果实验没有被校准和优化，新设备未来的使用就没用了。因此论文研究地磁力结果的差异。不同 Thellier 程序的使用引起数据的差异。最现代的程序 IZZI 大致正确，但有时候不精确。此论文尝试测量出消磁机制和程序的差异，因为世界各地的古地磁学家用十多种不同的方法。最后， 一系列测试研究液氮或交变磁场消磁周期的加法。这两个加法有时可以提高数据的质量，使其通过选择标准。数据的线性度被提高，但是热化学变化不会被提高。磁技术应用的扩展很重要，因为科学家必须证明研究是相关的。论文的作者和他的工业伙伴斯伦贝谢用另一种磁技术：漏磁技术。

未来古地磁学的实验室会有很多的功能，有最好的方法和设备，可以很快地准确研究大批岩石和金属的样品。论文介绍一个新型磁强计的设计。论文演示方法学和岩石有复杂的方法学如何在岩石研究的应用。现在，新磁强计在高温下测量很多类型岩石的剩磁，允许更多不同的应用。

ACKNOWLEDGEMENTS

I'd like to first thank my partner, Krister Koskelo, who was the only person I knew in this time zone when I moved here and has remained supportive of me in everything throughout my entire PhD. I'd like to thank my mother, Blair Grappone, who (despite being 3000 miles away) was never more than a phone call away. I'd like to further thank my best friends from Caltech- Valerie Pietrasz, who provided both moral and magnetic theory support during my PhD; Alexandra Ilić, who has an answer for everything and the mathematical skills to boot; and Chris Cousté, off whom I can always bounce anything engineering.

Within the PhD program at large, I'd like to thank Julie Samson, whose support through the Earth, Atmosphere, and Ocean Doctoral Training Programme was invaluable. I'd also like to thank Lyn Hughes and the entire Duncan Norman board for their unwavering faith and support of my research projects. Within Liverpool's Geomagnetism Laboratory, I'd like to thank my supervisors, Andy Biggin, John Shaw, and Mimi Hill, without whom none of this would have been possible. I'd also like to thank my two closest friends (and sometimes officemates) in the laboratory, Dr. Louise Hawkins and Prof. Courtney Sprain, who have also occasionally been my co-authors. I'd finally like to thank my closest Liverpool friends, Niraj Shah, Claire Groves, Amy Hughes, Jordan Irving, and Shaun Rigby for always being nearby to commiserate or provide a laugh.

"It's good to know how the world works. It is not possible to be a scientist unless you believe that all the knowledge of the universe and all the power it bestows is of intrinsic value to everyone, and one must share that knowledge and allow it to be applied, and then be willing to live with the consequences." – Jetrel, Star Trek: Voyager

Section A

The prototype magnetometer

CHAPTER 1 INTRODUCTION

1.1 Motivation

Magnetism exists anywhere there is an electrical current. Electricity powers our world, and so magnetic fields are found everywhere, even deep inside the Earth, far from humanity's reach. Humans have been aware of magnetism since at least Ancient Greece and have been using magnetic compasses since at least Ancient China (Lowrie, 2007). Human society progressed and by the 19th century, scientists were working to relate electricity and magnetism. In 1861, Maxwell proposed his four equations describing electromagnetism (see, for example, Griffiths, 2017). These equations describe all magnetic fields as dipoles because there is, as far as we know now, never a magnetic source without a magnetic sink. The existence of magnetic monopoles has been postulated but remains to be verified). The equations further describe magnetic fields as a component of a time-varying electromagnetic field (usually from a time-varying current source).

The outer core's molten iron alloy creates a sea of electrons that churns and creates the geodynamo, which in turn powers the Earth's magnetic field (Butler, 1992). Earth's magnetic field gives animals a means of navigation (whether innate or by using a compass), and it protects the planet's atmosphere and surface from solar wind. Solar wind (which consists of charged particles) would otherwise react with and destroy the ozone layer, which would in turn allow ultraviolet radiation to reach the surface and irradiate all life on the planet (e.g. Gallet et al., 2005).

Modern satellites have provided extensive data on geomagnetic field variations for the last 30-40 years. Ground-based observatories (such as the Honolulu observatory or the French Bureau Central de Magnétisme Terrestre) provide records for up to an additional 100 years (Jackson et al., 2000). Navigational records can then extend the paleodirection (but not paleointensity) data for an additional few hundred years, or 0.001% of Earth's geologic history. Paleomagnetic techniques, on the other hand, let us extend these data to timescales of billions of years (e.g. Biggin et al., 2015; Courtillot and Olson, 2007; Landeau et al., 2017; and Smirnov et al., 2016). Paleomagnetic investigation of the rock record allows surface measurements that, given suitable rocks, can be used to provide insight into tectonic and deep Earth processes at any point in geologic time.

Rocks used for paleomagnetic surveys can range in age from recently erupted— such as the 1960 Kilauea lava flow studied here (e.g. Böhnel et al., 2011; Hill and Shaw, 2000; and Tanaka and Kono, 1991)— to over 3 billion years old (e.g. Biggin et al., 2011 or Bono et al.,

2019). Older rocks have longer histories and therefore more potential to have been reheated, metamorphosed, or at least rotated. Younger rocks are still prone to other sources of remagnetization, such as an isothermal remanent magnetization, which can be gained from a variety of natural and human processes. Determining the strength and original direction of the magnetic field in which a specimen formed is therefore not as simple as just measuring the rock once when it is taken back to the laboratory; specialized equipment is required.

Three primary pieces of paleomagnetic equipment are used in the University of Liverpool Geomagnetism Laboratory: an AGICO JR6 Spinner magnetometer (origins in Jelínek, 1966), a 2G Enterprises superconducting magnetometer with a Rock and Paleomagnetic Instrument Development (RAPID) sample changer attached (the RAPID system) (Kirschvink et al., 2008), and a Tristan Microwave magnetometer system (the microwave system) (Hill et al., 2008). This thesis uses the RAPID and the microwave system for the paleointensity studies in chapters 6 – 9.

The JR6 Spinner magnetometer is the cheapest, simplest, and most mass-produced magnetometer system currently available. It rapidly spins the sample inside of a multi-turn pickup coil. This motion causes the magnetic moment of a sample to induce an alternating voltage in the coil, from which the magnetization antiparallel to the spin axis can be determined. The magnetometer requires substantial user input to measure only a single specimen's full vector remanent magnetization at a time. Measuring a single specimen takes around 5 minutes per step and the sensitivity is limited to relatively strongly magnetized rock specimens. The JR6 is a great option when money is tight but plenty of researcher time is available. However, researcher time is usually at a premium.

Upgrading from a JR6 to a 2G superconducting magnetometer greatly increases the types of rocks that can be surveyed, due to its significantly higher sensitivity. Each 2G magnetometer contains 3 DC-biased Superconducting Quantum Interference Devices (SQUIDs), which means that each specimen can be measured more quickly but still requires manually inputting the specimen. Adding a RAPID sample changer (Kirschvink et al., 2008) removes the need to measure each specimen manually, greatly freeing up researcher time. However, both the 2G magnetometer and the RAPID sample changer are substantially more expensive than the JR6 magnetometer. The magnetometer and the RAPID sample changer, combined, cost an order of magnitude more than a JR6 and the combination is therefore not an option for most laboratories. Therefore, there exists a space and a need for a magnetometer that has capabilities between the two. Some other automated

magnetometers exist, but they use either fluxgate magnetometers or a spinner design like the JR6. Further, automated magnetometers like the Triaxe (Le Goff and Gallet, 2004) or ORION (Smirnov et al., 2019) magnetometers can measure a specimen's remanence at temperature. Measuring remanence at elevated temperatures avoids the repeated heating from/cooling to room temperature cycles that increase the chance for thermochemical alteration (Hodgson et al., 2018). This thesis sets out to fill this gap with a new solid-state (no spinning or vibrating of the specimen) magnetometer capable of measuring remanence at elevated temperatures using commercially available SQUID sensors. The goal is therefore a new magnetometer system that allows for measuring remanent magnetization at elevated temperatures and with higher speed and precision than a JR6, but at a significantly lower price point, compared to a full RAPID system.

In addition to the different types of equipment, there exist nearly a dozen methods for estimating the paleointensity of a rock. The most commonly used and longest-tested methods are the Thellier-style methods (Aitken et al., 1988; Coe, 1967; Kono and Ueno, 1977; Thellier and Thellier, 1959; Yu et al., 2004), which can be run on the time-intensive spinner magnetometers or expensive superconducting magnetometer systems. These techniques are time-intensive, requiring at least 2 heatings per temperature step. They have also long been known to have difficulties with rocks that contain non-Single Domain (non-SD) grains, which can cause high failure rates and can be a cause of curvilinear (two-slope) Arai plots (e.g. Levi, 1977).

In addition, there exists the Shaw (Shaw, 1974; Yamamoto and Shaw, 2008) methods, which combine alternating field (AF) demagnetization with as few as 1 thermal step. This family of techniques minimizes the number of heating steps, which reduces the opportunity for thermochemical alteration and can now be run quickly on the RAPID system. Another single heating step technique is the Wilson (1961) method, which requires a continuous magnetometer system to run. In this technique, only a single (demagnetization) heating step is used, and the magnetization is measured continuously throughout the experiment. During cooling, a magnetic field is applied and the new magnetization is measured continuously, yielding a paleointensity estimate.

The final family of paleointensity methods are (nearly) unique to the University of Liverpool geomagnetism laboratory, and these are the microwave paleointensity experiments. Using microwaves tuned near the excitation frequency of magnetite minimizes the bulk heating of the sample to minimize thermochemical alteration (e.g. Suttie et al., 2010

and Walton et al., 1992, 1993). Initially these experiments used a version of the Kono and Ueno (1977) modified (Perpendicular; Perp) Thellier-protocol adapted for the microwave system, but now microwave experiments are carried out using any of the Thellier-style double treatment protocols. The issue of how and why thermal Thellier experiments differ from each other and from microwave experiments has so far remained an open question.

Paleomagnetic laboratories need the best equipment and, just as importantly, the most precise and accurate methods. Chapter 2 contains further information on the paleointensity methods that are relevant for this thesis. This thesis uses the Wilson (1961) method in Chapter 3 and Chapter 4, as well as the various Thellier-style methods, the backbone of paleointensity studies, in Chapters 6 – 9.

1.2 Thesis structure and aims

As the name of this thesis suggests, the goal herein is to test new equipment in, validate new techniques for, and expand the utility of, the next generation of paleomagnetic laboratory. To accomplish these three goals, this thesis is structured into three parts. After this introduction comes Section 1, which contains chapters 2-5. This first section begins with a background overview in Chapter 2, and then details the development of a new magnetometer and its evolution from a single axis continuous controller to the full-vector automated system in Chapter 5. Specifically, Chapter 3 covers designing a non-magnetic oven for continuous heating and measuring with only a single SQUID magnetometer. Chapter 4 describes an attempt to expand the design from a single magnetometer to three dimensions, but the system failed to produce sufficiently stable measurements to allow for high temperature continuous experiments. Chapter 5 describes a redesign for the three-axis magnetometer in a different direction, converting it into an equally radical stepwise SQUID magnetometer. The timeline of the development of the magnetometer is important to note. This thesis was started in September 2016 and was submitted initially in July 2020. The development of the prototype single-axis continuous magnetometer occurred from September 2016 until March 2018. The three-axis prototype continuous magnetometer ran from April 2018 to February 2019. In March 2019, the three-axis continuous prototype was converted into the stepwise prototype. Development of this new prototype ran from March 2019 – May 2019 and then from September 2019 – March 2020, with the prototype being fully operational for the first time in February 2020. The testing of the prototype was therefore cut short by the complete shutdown of the university (and the world) in March 2020 because of the COVID-19 pandemic.

The second section is presented as a series of research articles. These chapters detail the work undertaken to understand how different paleointensity methods can affect the final paleointensity estimates. First, in Chapter 6, the 1960 Kilauea lava flow is investigated using the Tristan microwave system in order to explain previously observed discrepancies between microwave and thermal results. Previous microwave data had previously been considered too low, and it appeared to be a problem inherent with the microwave, but the data were derived from only a single machine and single protocol. Using the newest microwave system and newest protocol gives the correct estimate. This chapter therefore shows that the poor data were the result of using the perpendicular protocol instead of any inherent problem with the microwave system itself. From these results, the thesis then moves to a more complex dataset from the Hawaiian Scientific Observation Hole 1 (SOH1) borehole (Chapter 7). The SOH1 drill core is investigated using four different paleointensity techniques. 118 new specimens were tested, giving 73 new estimates, which showed that the discrepancy is not as simple as thermal vs microwave or Original Thellier vs Perpendicular. The original datasets were found to be biased away from (in different directions) the estimates gathered using the best practices techniques initially outlined in Chapter 6.

Third, in Chapter 8, instead of testing different paleointensity protocols, only a single protocol, IZZI+, is used. In place of different protocols, the addition of alternating field (AF) and liquid nitrogen demagnetization (LTD) steps to typical experiments was described and tested. These techniques are more involved than the conventional IZZI techniques and have previously been shown to potentially improve success rates and reliabilities by Biggin et al. (2007) and Smirnov et al. (2017), respectively. The subjects of these tests are the Kinghorn lava flows from Scotland UK, (studied in Hawkins, 2018), which already provided valuable insight into the Carboniferous, a time period previously missing the paleointensity data necessary for studying changes in the Earth's geodynamo. The addition of these steps had little impact on the success rates and paleointensity estimates. The highest quality data (as measured by the Arai plot quality), with the highest pass rates, were again found using the microwave. Aside from the methods work, this chapter also doubles the amount of paleointensity data available from the Kinghorn lava flows.

In Chapter 9, a short set of experiments was undertaken using rocks from the 1960 Kilauea lava flow, SOH drill core, and the Kinghorn lava flows, following the advice of Hodgson, Grappone et al. (2018) and using temperature steps only within 20 °C of the Curie temperature. Their data predicted that in this unblocking temperature region, non-single domain grains of magnetite behave the most linearly, likely because only in this region are

the blocking and unblocking temperatures of these grains comparable. Accurately finding the bulk Curie Temperatures of individual specimens can be challenging, which means obtaining quality results is equally challenging. This chapter shows that the technique has some potential, but the low pass rates and difficulties discussed therein preclude widespread application of the technique.

The third and final section (Chapter 10) extends magnetic techniques into the oil and gas sector through a collaboration with the author's industrial partner, Schlumberger Ltd, based at Schlumberger Cambridge Research. Magnetic survey techniques allow defects in stainless steel Coiled Tubing to be detected by their magnetic signature. This placement took place from May 2019 – August 2019. An initial setup is demonstrated for laboratory bench tests to mimic field conditions in a controlled setting.

Finally, Chapter 11, concludes this thesis and encompasses its aspirations for the future paleomagnetic laboratory.

1.3 References

Aitken, M. J., Allsop, A. L., Bussell, G. D., and Winter, M. B., 1988, Determination of the intensity of the earths magnetic-field during archaeological times - reliability of the thellier technique: Reviews of Geophysics, v. 26, no. 1, p. 3-12.

Biggin, A. J., de Wit, M. J., Langereis, C. G., Zegers, T. E., Voute, S., Dekkers, M. J., and Drost, K., 2011, Palaeomagnetism of Archaean rocks of the Onverwacht Group, Barberton Greenstone Belt (southern Africa): Evidence for a stable and potentially reversing geomagnetic field at ca. 3.5 Ga: Earth and Planetary Science Letters, v. 302, no. 3-4, p. 314-328.

Biggin, A. J., Perrin, M., and Shaw, J., 2007, A comparison of a quasi-perpendicular method of absolute palaeointensity determination with other thermal and microwave techniques: Earth and Planetary Science Letters, v. 257, no. 3-4, p. 564-581.

Biggin, A. J., Piispa, E. J., Pesonen, L. J., Holme, R., Paterson, G. A., Veikkolainen, T., and Tauxe, L., 2015, Palaeomagnetic field intensity variations suggest Mesoproterozoic inner-core nucleation: Nature, v. 526, no. 7572, p. 245-+.

Böhnel, H., Herrero-Bervera, E., and Dekkers, M. J., 2011, Paleointensities of the Hawaii 1955 and 1960 Lava Flows: Further Validation of the Multi-specimen Method, Dordrecht, Springer, Earth's Magnetic Interior, 195-211 p.:

Bono, R. K., Tarduno, J. A., and Cottrell, R. D., 2019, Primary pseudo-single and single-domain magnetite inclusions in quartzite cobbles of the Jack Hills (Western Australia): implications for the Hadean geodynamo: Geophysical Journal International, v. 216, no. 1, p. 598-608.

Butler, R. F., 1992, Paleomagnetism: Magnetic Domains to Geologic Terranes.

Coe, R. S., 1967, Determination of paleo-intensities of earths magnetic field with emphasis on mechanisms which could cause non-ideal behavior in thelliers method: Journal of Geomagnetism and Geoelectricity, v. 19, no. 3, p. 157-179.

Courtillot, V., and Olson, P., 2007, Mantle plumes link magnetic superchrons to phanerozoic mass depletion events: Earth and Planetary Science Letters, v. 260, no. 3-4, p. 495-504.

Griffiths, D. J., 2017, Introduction to Electrodynamics, Cambridge University Press.

Hawkins, L., 2018, A Mid-Paleozoic Dipole Low defined from new paleointensity estimates from Russia and the UK [Doctor in Philosophy: University of Liverpool.

Hill, M. J., Pan, Y. X., and Davies, C. J., 2008, An assessment of the reliability of palaeointensity results obtained from the Cretaceous aged Suhongtu section, Inner Mongolia, China: Physics of the Earth and Planetary Interiors, v. 169, no. 1-4, p. 76-88.

Hill, M. J., and Shaw, J., 2000, Magnetic field intensity study of the 1960 Kilauea lava flow, Hawaii, using the microwave palaeointensity technique: Geophysical Journal International, v. 142, no. 2, p. 487-504.

Hodgson, E., Grappone, J. M., Biggin, A. J., Hill, M. J., and Dekkers, M. J., 2018, Thermoremanent Behavior in Synthetic Samples Containing Natural Oxyexsolved Titanomagnetite: Geochemistry Geophysics Geosystems, v. 19, no. 6, p. 1751-1766.

Jackson, A., Jonkers, A. R. T., and Walker, M. R., 2000, Four centuries of geomagnetic secular variation from historical records: Philosophical Transactions of the Royal Society of London Series a-Mathematical Physical and Engineering Sciences, v. 358, no. 1768, p. 957-990.

Jelínek, V., 1966, A high sensitivity spinner magnetometer: Studia Geophysica et Geodaetica, v. 10, no. 1, p. 58-78.

Kirschvink, J. L., Kopp, R. E., Raub, T. D., Baumgartner, C. T., and Holt, J. W., 2008, Rapid, precise, and high-sensitivity acquisition of paleomagnetic and rock-magnetic data: Development of a low-noise automatic sample changing system for superconducting rock magnetometers: Geochemistry Geophysics Geosystems, v. 9.

Kono, M., and Ueno, N., 1977, Paleointensity determination by a modified thellier method: Physics of the Earth and Planetary Interiors, v. 13, no. 4, p. 305-314.

Landeau, M., Aubert, J., and Olson, P., 2017, The signature of inner-core nucleation on the geodynamo: Earth and Planetary Science Letters, v. 465, p. 193-204.

Le Goff, M., and Gallet, Y., 2004, A new three-axis vibrating sample magnetometer for continuous high-temperature magnetization measurements: applications to paleo- and archeo-intensity determinations: Earth and Planetary Science Letters, v. 229, no. 1-2, p. 31-43.

Levi, S., 1977, Effect of magnetite particle-size on paleointensity determinations of geomagnetic-field: Physics of the Earth and Planetary Interiors, v. 13, no. 4, p. 245-259.

Shaw, J., 1974, Method of determining magnitude of paleomagnetic field application to 5 historic lavas and 5 archeological samples: Geophysical Journal of the Royal Astronomical Society, v. 39, no. 1, p. 133-141.

Smirnov, A. V., Kulakov, E. V., Foucher, M. S., and Bristol, K. E., 2017, Intrinsic paleointensity bias and the long-term history of the geodynamo: Science Advances, v. 3, no. 2, e1602306.

Smirnov, A. V., Tarduno, J. A., Kulakov, E. V., McEnroe, S. A., and Bono, R. K., 2016, Palaeointensity, core thermal conductivity and the unknown age of the inner core: Geophysical Journal International, v. 205, no. 2, p. 1190-1195.

Smirnov, M., Sychev, A., Salnaia, N., Minaev, P., Powerman, V., and Veselovskiy, R. V., 2019, “ORION” – the versatile Full-vector Sample Magnetometer for Paleointensity, Rock Magnetic and Paleomagnetic Studies, European Geosciences Union General Assembly 2019, Volume 21: Vienna, Austria.

Suttie, N., Shaw, J., and Hill, M. J., 2010, Direct demonstration of microwave demagnetization of a whole rock sample with minimal heating: Earth and Planetary Science Letters, v. 292, no. 3-4, p. 357-362.

Tanaka, H., and Kono, M., 1991, Preliminary-results and reliability of paleointensity studies on historical and c-14 dated hawaiian lavas: Journal of Geomagnetism and Geoelectricity, v. 43, no. 5, p. 375-388.

Thellier, E., and Thellier, O., 1959, Sur l’intensité du champ magnétique terrestre dans le passé historique et géologique: Ann. Géophys., v. 15, p. 285-376.

Walton, D., Share, J., Rolph, T. C., and Shaw, J., 1993, Microwave magnetization: Geophysical Research Letters, v. 20, no. 2, p. 109-111.

Walton, D., Shaw, J., Share, J., and Hakes, J., 1992, Microwave demagnetization: Journal of Applied Physics, v. 71, no. 3, p. 1549-1551.

Wilson, R. L., 1961, Palaeomagnetism in northern ireland .1. The thermal demagnetization of natural magnetic moments in rocks: Geophysical Journal of the Royal Astronomical Society, v. 5, no. 1, p. 45-58.

Yamamoto, Y., and Shaw, J., 2008, Development of the microwave LTD-DHT Shaw method for absolute paleointensity determination: Physics of the Earth and Planetary Interiors, v. 170, no. 1-2, p. 15-23.

Yu, Y. J., Tauxe, L., and Genevey, A., 2004, Toward an optimal geomagnetic field intensity determination technique: Geochemistry Geophysics Geosystems, v. 5, p. 18.

CHAPTER 2 BACKGROUND

2.1 Paleomagnetism

Paleomagnetism as a field of research has existed since the 18th century, and paleointensity as one its subfields has existed for over 60 years (e.g. Nagata et al., 1963 and Thellier and Thellier, 1959). However, the methodology of paleomagnetic (and paleointensity, in particular) continues to evolve. Most paleomagnetic surveys are run on samples in the laboratory and attempt to extract the magnitude (paleointensity) or (paleo)direction of the Earth's magnetic field during the rock's formation. Paleodirection surveys have historically found their main application in the fields of plate tectonics and paleogeography (e.g. As and Zijderveld, 1958; Cox, 1957; and Irving et al., 1961). With improved data and techniques, paleomagnetic methods have also been applied to biology (e.g. Kobayashi et al., 2006) and to the Earth as a whole to better understand the evolution of its interior (e.g. Biggin et al., 2015; Landeau et al., 2017; Smirnov et al., 2016; and Courtillot and Olson, 2007).

Initial paleomagnetic studies proposed two mechanisms of isolating the characteristic magnetization of a specimen, using either alternating magnetic fields (AF) (As and Zijderveld, 1958) or heating steps (thermal) (Cox, 1957) to measure changes in its magnetic footprint. Irving et al. (1961) determined that, for sedimentary rocks, using AF steps was potentially insufficient to fully demagnetize the samples due the more complex history of such rocks, compared to their volcanic counterparts. Volcanic rocks gain their magnetization during cooling, which gives them a thermoremanent magnetization (TRM), which can be replicated in the lab to give an absolute paleointensity estimate (Thellier and Thellier, 1959). Metamorphic rocks are avoided for paleomagnetic surveys because of their complex history, which includes post-formational alteration and remagnetization, which can lead to chemical remanent magnetizations (CRM) or thermochemical remanent magnetizations (TCRM). Only relative intensities can be found for sedimentary rocks because the complex processes that lead to a detrital remanent magnetization (DRM) cannot be accurately recreated in a laboratory setting.

For thermal studies, a division exists between methods that heat specimens continuously (e.g. Stacey, 1959 and Chamalaun and Porath, 1968) and those that heat in discrete steps (e.g. Irving et al., 1961) until the samples' magnetization unblocks completely. Stepwise techniques require heating a specimen to a given temperature and then cooling it to room

temperature. These techniques have at least two clear advantages: they are technically simpler to run and can run large batches of samples, as is common in paleodirection studies (and more recently, in detailed paleointensity studies). The Rock and Paleomagnetic Instrument Development (RAPID) consortium's automatic sample changer has drastically reduced the labor required to run large batches of samples by coupling an automatic sample changer with a DC-biased Superconducting Quantum Interference Device (SQUID) magnetometer system (Kirschvink et al., 2008). Continuous heating techniques remove the need to cool to room temperature by measuring a specimen's magnetization at elevated temperatures and are therefore much faster to complete.

Paleodirection studies are relatively simple, being composed primarily of thermal steps. Low strength alternating field and low-temperature liquid nitrogen demagnetizations steps, which remove large (multi-domain) magnetic grains, can be added to improve data fidelity. The samples are heated as a batch to a given temperature, measured, and then taken to higher temperatures until the specimens unblock completely. Secondary magnetizations (magnetic overprints) gained after formation complicate data collection, especially for weak samples, but with large sample sets and high resolution equipment, accurate paleodirections can still be extracted (Grappone et al., 2017; Kirschvink et al., 2015). Present techniques are sufficient to study large numbers of samples quickly and obtain statistically significant results.

Paleointensity studies, by contrast, are more involved, as paleointensity data are much more sensitive to mineralogical changes and magnetic grain size effects than paleodirection studies are. As such, these studies are more prone to errors. Therefore, there is, as of yet, little consensus on the best technique; instead, numerous methods and protocols have been developed and tested over the years. One of the oldest protocols, the step-wise Original Thellier (OT) protocol, is the preferred protocol for many studies (e.g. Brown et al., 2006; Goguitchaichvili et al., 1999; Laj et al., 2011; Laj et al., 2014; and Teanby et al., 2002). This protocol is simpler to run, as it does not require expensive, modern technologies, such as Mu-metal (a type of high magnetic susceptibility iron alloy) shielding, and because all experiments are conducted in a non-zero (originally Earth's) magnetic field. Some paleointensity methods, like the Shaw method family, combine thermal and AF (and low-temperature liquid nitrogen) steps to extract a paleointensity estimate (Shaw, 1974; Yamamoto et al., 2003). The different methods each attempt to correct, in different ways, for errors in the majority of naturally occurring rocks. Most rocks do not fully obey Thellier's laws of thermoremanence; that is, they do not contain purely single domain (SD), non-interacting magnetic grains.

Succinctly, Thellier's laws of thermoremanence are: a single domain grain's magnetization is proportional to the Earth's field, any magnetization gained in a given temperature interval will also be removed in the same interval, and each magnetic component is independent and sums together as vectors (Thellier, 1938).

Additional stepwise techniques are described in the Stepwise Paleointensity Protocols section (below), which describes those used in this thesis. Some are designed to identify the effects of mineralogical changes or non-ideal magnetic grain effects. To avoid bulk mineralogical changes, which occur due to oxidation at high temperatures, microwave radiation can be used to heat (theoretically) only the magnetite grains in place of thermal radiation, while retaining the use of analogous power integral steps. More recently, studies have begun to use multiple protocols or demagnetization mechanisms, or have used different selection criteria, to try to extract the most accurate paleointensity estimates (e.g. Biggin et al., 2007a; Böhnel et al., 2009; Hawkins et al., 2019; and Yamamoto and Shaw 2008). Continuous paleointensity methods, the most common of which are the Wilson (Wilson, 1961) and Triaxe (Le Goff and Gallet, 2004) methods, have the advantage of saving time where precision measurements of a small set of specimens are paramount, as is needed for precision paleointensity studies (Heiniger and Heller, 1976; Schmidt and Clark, 1985). The Wilson method uses a single heating step in a zero-field and a single cooling step in a known field. The Triaxe uses a similar method, where the specimen is heated three times in zero-field, and cooled twice in-between, first in a zero-field and then in a known field. This method effectively replicates the Coe (1967)-style Thellier method but measures the specimen's magnetization continuously instead of stepwise. The Triaxe method requires no manual input and can detect changes caused by alteration, which would otherwise be undetected in the pure Wilson method.

Non-interacting SD grains only lose their natural remanent magnetization (NRM) during heating above their blocking temperature and then gain a new thermoremanent magnetization during cooling in a known field. Natural rocks contain grains with varying blocking temperatures, so after each heating and cooling in a known field, a natural specimen gains a partial thermoremanent magnetization (pTRM) (e.g. Hodgson et al. 2018). As long as the specimen's magnetization changes can be measured during both heating and cooling, only one large step to the Curie temperature is necessary. Although the continuous method is much faster, for non-ideal grains, the curvature of Arai plots derived from continuous data can be higher than for step-wise studies (Dunlop, 2008). The high temperature Thellier

experiments in Hodgson et al. (2018) somewhat disagree with the previous result, as they found specimens that were heated to a higher initial temperature had lower curvature.

2.2 Stepwise Paleointensity Protocols

One of the oldest protocols is the Original Thellier protocol (Thellier and Thellier, 1959), which requires two heat treatments for a given temperature step, T_N. Along with its derivates, the Thellier-style protocols are the most widely used techniques in paleointensity. The technique uses a non-zero intensity magnetic field for the first treatment, and then a magnetic field with the same magnitude but opposite polarity is applied for the second treatment. The advantage is that no Mu-metal shielding or Helmholtz coils are required. This protocol, used in Chapter 7, can therefore be referred to as "OT" (Original Thellier) or "II" (in-field, in-field). With the increasing availability of magnetic shielding, running experiments in a zero magnetic field became possible, which helps to simplify the experimental procedure and math required.

In the Coe modification to the Thellier and Thellier (1959) protocol (Coe, 1967a, b), samples are first taken to the desired T_N in a magnetic vacuum ($\boldsymbol{B} = \mathbf{0}$), then cooled to room temperature and measured. In the second treatment, the samples are again taken to the same T_N and cooled to room temperature, but in a known magnetic field $\boldsymbol{B}_{lab}$. The second measurement allows the laboratory TRM to be more directly calculated. This protocol can therefore be referred to as "Coe" or "ZI" (zero-field, in-field). This protocol is used in Chapter 9. The modification to Thellier-style paleointensities proposed by Aitken et al. (1988) takes advantage of the easier math in the Coe modification, but instead first heats the sample in $\boldsymbol{B}_{lab}$ and then heats the sample in a zero magnetic field (the reverse order) and is thus "Aitken" or "IZ". A third Thellier-style modification, named "IZZI", alternates between the Coe and Aitken modifications in an enclosed couplet (i.e. T_N: off/**Z**ero-field, on/**I**n-field; T_{N+1}: on/I, off/Z) (Yu et al., 2004). This protocol exaggerates non-ideal effects in the resulting dataset, which makes them more detectable during data analysis. The non-ideal effects present in IZZI experiments are discussed more extensively in Chapter 6 and Chapter 8, which use the IZZI protocol.

The perpendicular protocol is a modification of the Original Thellier protocol that only requires a single thermal (Kono and Ueno, 1977) or microwave treatment (Hill and Shaw, 2007). The protocol was once frequently used in microwave experiments but less frequently in thermal studies due to different equipment designs. Specimens are first stepwise demagnetized in a zero field to remove any soft magnetic overprints. Once the characteristic

component is identified (generally defined as when the magnetic direction stops changing), $\boldsymbol{B}_{lab}$ is applied in the direction perpendicular to the remaining NRM direction. This protocol, used in Chapter 6 and Chapter 7, can therefore be referred to as "Perp" or "I". Biggin et al. (2007b) showed that multi-domain effects can be also effectively removed using a quasi-perpendicular (greater than 45° angle) applied field with fewer technical difficulties.

In the Shaw (Shaw, 1974) and LTD-DHT Shaw method (Yamamoto et al., 2003), a sample is first demagnetized using AF steps, then given an anhysteric remanent magnetization (ARM) in the peak field, and then AF demagnetized. The sample is then heated above its Curie temperature and cooled in $\boldsymbol{B}_{lab}$, giving it a full TRM in one step. Next, the sample is given a second ARM, which serves to determine if the rock has undergone any alterations. Finally, the NRM is compared to the TRM to extract the paleointensity. If the LTD-DHT Shaw method is being used, a low-temperature liquid nitrogen (LTD) step and a second heating step (DHT) are added to correct for any thermochemical or non-SD effects in the specimen (Shaw, 1974; Yamamoto et al., 2003). Other full TRM stepwise methods that have been used historically are the AF-based van Zijl et al. (1962) and the thermally-based Walton (1977) methods. Of these alternative, non-Thellier methods, only (a variant of) the Walton (1977) method is used in this thesis, in Chapter 5.

2.3 Continuous Magnetometers

Companies such as Magnetic Measurements, AGICO, and 2G Enterprises currently build equipment that is well suited for use in paleodirection (i.e. stepwise thermal) studies: high-precision ovens and high-resolution SQUID magnetometers or lower-resolution but more robust fluxgate magnetometers. Their equipment is also frequently and successfully used for paleointensity studies using discrete steps. The ORION system (Smirnov et al., 2019) is a commercially available fluxgate-based system that can run Thellier-Coe or Wilson (1961)-style paleointensity experiments. Aside from the relatively new ORION system, equipment meant for continuous thermal measurements, however, has generally been built and used in-situ. Instruments currently in operation are detailed in Table 2-1.

Many magnetometers designed for continuous heating are spinners, which require rotation and translation of a sample about a central axis. Not only do moving parts complicate the engineering, but the rotation speed has to be selected properly for the application, complicating the underlying equations (Kono et al., 1981; Kono et al., 1991; Matzka, 2001). Another common design to overcome the challenges associated with having sensors near heating coils is to vibrate the samples in a controlled manner. The goal is similar

to that of spinner magnetometers: measure multiple magnetic directions using only a single sensor. One major problem with the vibrating magnetometer is the wear and tear it causes on the sample (Dunlop, 2008). Another, less common option is also an older design: an astatic magnetometer, which measures the change in magnetic gradient by comparing an unknown material with a known material of the same footprint (Johnson and Steiner, 1937). Due to the precision setup required, astatic magnetometers tended to have a lower sensitivity than spinner magnetometers, however (Nagata et al., 1957).

Table 2-1 Automated thermomagnetometer instrument designs around the world

Instrument name or location	Type	Sensitivity (Am^2)	Temperature range (°C)	Sample Size	Usage/References
Hotspin	Spinner	5×10^{-8}	Room - 600	$0.5\ cm^3$	Matzka (2001)
Hotspin 2	Spinner, hot air	2×10^{-7}	Room - 350	1 inch	Wack and Matzka (2007)
Geophysical Observatory Borok	Spinner	3×10^{-9}	Room - 600	$1\ cm^3$	Shcherbakova et al., (2000)
Institut de Physique du Globe de Paris (Triaxe)	Vibrating	1×10^{-8}	Room - 650	$0.75\ cm^3$	Coe et al. (2014); Gallet and Le Goff (2006); Le Goff and Gallet (2004)
Université de Montpellier	Vibrating	2×10^{-9}	-192 - 700	$12 \times 7\ mm$	Poidras et al. (2009)
Princeton Measurements Vibrating Sample Magnetometer	Vibrating	5×10^{-9}	-263 - 1025	$1\ cm^3$	Buz et al. (2015; Fukuma and Torii (2011)
ORION system	Vibrating	5×10^{-8}	Room - 800	$1\ cm^3$	Smirnov et al. (2019)

2.4 Continuous Thermomagnetometry

From an experimental perspective, using a continuous system allows the reduction of chemical alterations, saves time, and increases the detail of magnetic components. By avoiding the intermediate cooling steps, there are cooling rate effects have been shown experimentally to be manageable (e.g. Fox and Aitken, 1980 and Le Goff and Gallet, 2004), and the time spent cooling to room temperature and reheating is saved. The Wilson (1961) method uses only a single heating and cooling step and should, therefore, be domain-state independent, as asymmetry in pTRM blocking and unblocking temperatures does not exist for full TRMs without thermochemical alteration. The Triaxe system (Le Goff and Gallet, 2004) uses a modified Thellier-style technique that progressively demagnetizes and remagnetizes the specimen. Le Goff and Gallet (2004) showed a cooling rate correction was unnecessary, but recent work by Santos and Tauxe (2019) has shown that cooling rate corrections need to be considered on a case-by-case basis. Further, there is some evidence that continuous

demagnetization gives different results for pseudo-single domain (PSD) and multi-domain (MD) grains (Dunlop, 2009). Dunlop (2009) observed a non-single domain specimen's remanent magnetization drops more rapidly with increasing temperature in stepwise data than in continuous data, which is a result consistent with observations in Hodgson et al. (2018).

Continuous heating systems have allowed a great deal of research into the effects of high temperatures on the samples. Some examples of the types of experiments continuous magnetometers can run are given here. Coe et al. (2014) used the Triaxe to show that some inconsistent data can be explained by the reduction in sample alteration from the shorter heating time required. Coe et al. (2014) additionally showed the faster heating rate of continuous experiments, relative to stepwise experiments, prevents grains carrying (low unblocking temperature) Viscous Remanent Magnetization (VRM) components from thermochemically altering into grains with higher unblocking temperatures. Thermochemically alterations of this variety can interfere with the primary component. Krasa et al. (2005) used the Hotspin magnetometer to study self-reversal, the tendency of rocks to gain remanent magnetization in the direction opposite to the external field applied. The continuous magnetometer provided sufficient data to deconvolve two coupled magnetic phases with different blocking temperatures. Rahman and Parry (1975) used a continuous magnetometer to study magnetic self-shielding and associated self-reversal effects, which allowed an inclusion in a specimen to be given a pTRM above the host material's Curie Temperature. McClelland and Sugiura (1987) and Shcherbakov et al. (1993) took advantage of the single heating and cooling step of continuous magnetometers to study multi-domain structural changes and their effects on a sample's magnetization. Schmidt and Clark (1985) used a spinner magnetometer to compare stepwise and continuous treatment of multi-component magnetizations. For remanence components other than the most stable one, a correction for the temperature dependence of in-field induced (spontaneous) magnetization was needed to compare continuous magnetization data with stepwise data, which instead relies on measuring blocked magnetizations.

Draeger et al. (2006) used a vibrating sample thermomagnetometer to study chemical remanent magnetization (CRM) by heating and cooling 12 mm basalt samples to cause changes in their magnetic mineralogy. Coe et al. (2014) used the Triaxe vibrating sample magnetometer to restudy an apparent episode of fast field change. Cairanne et al. (2003) used a custom-built astatic magnetometer to study the hydrothermal production of magnetite. Their system was optimized for both high temperature and controlled pressure.

Gallet et al. (2008) used the Triaxe system for a more typical paleointensity survey. Their results were comparable to within ±5% of a stepwise survey done using the Original Thellier and Coe protocols, with a ~70% success rate.

2.5 Design Improvements

Two primary drawbacks exist for continuous heating systems. The first issue is unavoidable: the magnetic intensity of a sample decreases with temperature due to increasing instability of magnetic grains (Schmidt and Clark, 1985; Wack, 2006). Pauthenet and Bochirol (1951) determined a monotonically decreasing, concave down relationship between spontaneous magnetization and temperature, reproduced in Figure 2-1. For accurate measurements at high temperatures, clearly a high-resolution magnetometer is required, even for strong samples. By correcting for the thermomagnetic curve of each sample, this effect can be mitigated (Dunlop, 2008).

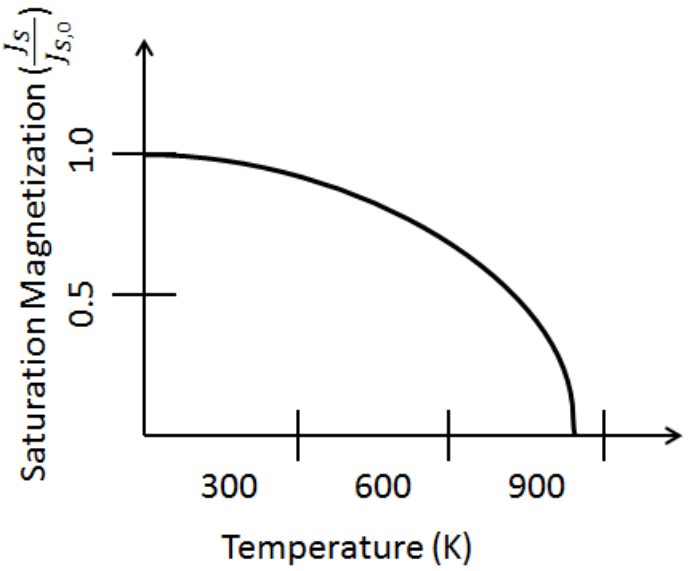

Figure 2-1 Saturation magnetization as a function of temperature for magnetite adapted from Pauthenet and Bochirol (1951) and Schmidt and Clark (1985).

One element common to current continuous magnetometer designs is the use of fluxgate magnetometers, which have a comparatively limited resolution. The sensitivity of each magnetometer system described in Table 2-1 is approximately the sensitivity of the sensor selected for their design. In order to increase a magnetometer system's resolution, the fluxgates must be upgraded. Several alternative magnetometers exist for various applications (e.g. a proton precession magnetometer, like that of Liu et al., 2019, for large-scale mineral or ground surveys), but the most frequently used magnetometers in paleomagnetism are SQUID magnetometers. SQUID magnetometers require the use of a liquid Helium or liquid Nitrogen reservoir to allow the superconductor to work but DC-biased

SQUIDs have sensitivities approaching 10^{-13} Am^2 (Grappone et al., 2017; Kirschvink et al., 2015). SQUID sensor sensitivities are dependent on the geometry and material of the superconducting loops. Sensitivities at these levels (4 orders of magnitudes better than those reported in Table 2-1) will allow weak samples, usually sediments, to potentially be studied more rigorously during continuous heating studies.

2.6 Microwave experiments

For samples that are highly susceptible to thermo-chemical alteration, the microwave demagnetization mechanism has proven to be a very successful technique (e.g. Hawkins et al., 2019; Hill et al., 2002; and Hill et al., 2008). The microwave works analogously to cooking a turkey in a microwave oven in a kitchen. In a microwave oven, instead of thermal radiation from heating coils cooking a turkey from the outside in, radiation in the microwave spectrum heats the water inside the turkey. A microwave oven uses a radiation frequency of 2.45 GHz (microwaves are defined as 1 – 1000 GHz), which is near the resonance frequency of water (but slightly below to increase penetration depth). The microwave system at the University of Liverpool operates on a similar principle but is tuned to be near the resonance frequency of magnetite, instead of that of water (Walton et al., 1993; Walton et al., 1992). The first generation of the microwave system (e.g. Gratton et al., 2005) used ~8.2 GHz and the later two models used ~14 GHz (e.g. Hill and Shaw, 2000 for the older model; e.g. Hill et al., 2008 and Chapters 6 – 8 for the newer model). Other research has shown that magnetite will readily absorb microwaves between 0.5 and 10 GHz (Kirschvink, 1996).

Operationally, the resonance frequency is controlled by means of sweeping through the spectrum (14 – 14.5 GHz) before an experiment and selecting the frequency with the lowest reflection (highest inferred absorption). During the sweeping process, the specimen is moved around by the system within the cavity to decrease reflection as much as possible. Some specimens have high reflection (> 50%) despite the tuning process. The lack of absorption is the result of differences in magnetic mineralogy (hematite and goethite, for example, have different resonance frequencies to magnetite) or grain size (smaller grains of magnetite require a higher frequency to be applied) (Suttie et al., 2010). Specimens displaying high reflection (which can damage the microwave system itself) are deemed unsuitable for paleointensity experiments using the microwave demagnetization mechanism.

The mechanism through which the microwave system demagnetizes magnetite grains is by bombarding the crystal lattice with magnons (quantized spin waves). Exciting (nominally) only the magnetite reduces the temperature that the matrix of the specimen reaches. The

electric field component of the magnetic field can cause some bulk dielectric heating of the sample, if the sample is poorly aligned inside the cavity (Suttie et al., 2010). With lower bulk temperatures, there is less thermochemical alteration in the specimen. The reduced alteration is similar to the effect observed with continuous magnetometers: having insufficient time to alter when the magnetic particles are at temperature. Suttie et al. (2010) contains a detailed look into the internal workings of the microwave system.

To facilitate a uniform energy absorption, microwave specimens are cut to be 5 mm in diameter (usually from standard 25 mm drill cores), with a length of 1 – 5 mm (instead of 10 – 25 mm). This means from a standard 25mm drill core, six or more microwave specimens can be produced, substantially increasing the number of potential paleointensity estimates. Each specimen is run individually in the microwave system, instead of in batches like thermal studies. The experiment can then be refined to each individual specimen because each power step (a combination of a given applied power and time) is individually input by the user after the previous step completes.

Individual microwave specimens (even those from the same 25 mm drill core) can behave differently in paleointensity experiments if the lava flow from which the specimens are taken has heterogeneities that can be observed at these scales. However, the increased number of specimens that can be analyzed allows heterogeneities at these scales to be averaged out. Specimens from the same site often behave similarly across both microwave and thermal experiments (e.g. Pan et al., 2004 and Pressling et al., 2007), but in other cases, they can vary widely in their paleointensity behavior (e.g. Biggin, 2010; Brown et al., 2006; Hill and Shaw, 2000; Hill et al., 2006; and Hill et al., 2005), which is investigated further in chapters 6 and 7, respectively.

The main disadvantage of the microwave system is that the theoretical basis of the technology is less well-understood than the equivalent thermally-based experimental technology. The original microwave system (the 8.2 GHz model) was substantially limited in its operation due to poor experimental reproducibility. The microwave system originally used the perpendicular protocol because reproducing the amount of energy absorbed from microwaves is more technically challenging than reproducing the same temperature (Hill and Shaw, 2007). Additionally, the magnetic mineralogy of each specimen has a more direct effect on the applicability of the equipment compared to thermal demagnetizers, as discussed above.

Improvements in both the theoretical basis for the microwave (Suttie et al., 2010) and technology have increased both the capabilities and reliability of the microwave system (Hill et al., 2008). The newest 14 GHz frequency Tristan magnetometer used in modern microwave studies is capable of running any paleointensity protocol successfully, which will be investigated further in Chapters 6 - 8.

2.7 References

Aitken, M. J., Allsop, A. L., Bussell, G. D., and Winter, M. B., 1988, Determination of the intensity of the earths magnetic-field during archaeological times - reliability of the thellier technique: Reviews of Geophysics, v. 26, no. 1, p. 3-12.

As, J. A., and Zijderveld, J. D. A., 1958, Magnetic cleaning of rocks in palaeomagnetic research: Geophysical Journal of the Royal Astronomical Society, v. 1, no. 4, p. 308-319.

Biggin, A. J., 2010, Are systematic differences between thermal and microwave Thellier-type palaeointensity estimates a consequence of multidomain bias in the thermal results? : Physics of the Earth and Planetary Interiors, v. 180, no. 1-2, p. 16-40.

Biggin, A. J., Perrin, M., and Dekkers, M. J., 2007a, A reliable absolute palaeointensity determination obtained from a non-ideal recorder: Earth and Planetary Science Letters, v. 257, no. 3-4, p. 545-563.

Biggin, A. J., Perrin, M., and Shaw, J., 2007b, A comparison of a quasi-perpendicular method of absolute palaeointensity determination with other thermal and microwave techniques: Earth and Planetary Science Letters, v. 257, no. 3-4, p. 564-581.

Biggin, A. J., Piispa, E. J., Pesonen, L. J., Holme, R., Paterson, G. A., Veikkolainen, T., and Tauxe, L., 2015, Palaeomagnetic field intensity variations suggest Mesoproterozoic inner-core nucleation: Nature, v. 526, no. 7572, p. 245-+.

Böhnel, H. N., Dekkers, M. J., Delgado-Argote, L. A., and Gratton, M. N., 2009, Comparison between the microwave and multispecimen parallel difference pTRM paleointensity methods: Geophysical Journal International, v. 177, no. 2, p. 383-394.

Brown, M. C., Shaw, J., and Goguitchaichvili, A. T., 2006, Microwave palaeointensity from the R3-N3 geomagnetic field reversal: Geophysical Journal International, v. 167, no. 1, p. 53-69.

Buz, J., Weiss, B. P., Tikoo, S. M., Shuster, D. L., Gattacceca, J., and Grove, T. L., 2015, Magnetism of a very young lunar glass: Journal of Geophysical Research-Planets, v. 120, no. 10, p. 1720-1735.

Cairanne, G., Brunet, F., Pozzi, J. P., Besson, P., and Aubourg, C., 2003, Magnetic monitoring of hydrothermal magnetite nucleation-and-growth: Record of magnetic reversals: American Mineralogist, v. 88, no. 8-9, p. 1385-1389.

Chamalaun, F. H., and Porath, H., 1968, A continuous thermal demagnetizer for rock magnetism: Pure and Applied Geophysics, v. 70, no. 2, p. 105-+.

Coe, R. S., 1967a, Determination of paleo-intensities of earths magnetic field with emphasis on mechanisms which could cause non-ideal behavior in thelliers method: Journal of Geomagnetism and Geoelectricity, v. 19, no. 3, p. 157-179.

-, 1967b, Paleo-intensities of earths magnetic field determined from tertiary and quaternary rocks: Journal of Geophysical Research, v. 72, no. 12, p. 3247-&.

Coe, R. S., Jarboe, N. A., Le Goff, M., and Petersen, N., 2014, Demise of the rapid-field-change hypothesis at Steens Mountain: The crucial role of continuous thermal demagnetization: Earth and Planetary Science Letters, v. 400, p. 302-312.

Courtillot, V., and Olson, P., 2007, Mantle plumes link magnetic superchrons to phanerozoic mass depletion events: Earth and Planetary Science Letters, v. 260, no. 3-4, p. 495-504.

Cox, A., 1957, Remanent magnetization of lower to middle eocene basalt flows from oregon: Nature, v. 179, no. 4561, p. 685-686.

Draeger, U., Prevot, M., Poidras, T., and Riisager, J., 2006, Single-domain chemical, thermochemical and thermal remanences in a basaltic rock: Geophysical Journal International, v. 166, no. 1, p. 12-32.

Dunlop, D. J., 2008, Paleointensity determination using continuous thermal measurements by a high-temperature vibrating thermomagnetometer: Geochemistry Geophysics Geosystems, v. 9.

-, 2009, Continuous and stepwise thermal demagnetization: are they equivalent?: Geophysical Journal International, v. 177, no. 3, p. 949-957.
Fox, J. M. W., and Aitken, M. J., 1980, Cooling-rate dependence of thermoremanent magnetization: Nature, v. 283, no. 5746, p. 462-463.
Fukuma, K., and Torii, M., 2011, Absolute calibration of low- and high-field magnetic susceptibilities using rare earth oxides: Geochemistry Geophysics Geosystems, v. 12.
Gallet, Y., and Le Goff, M., 2006, High-temperature archeointensity measurements from Mesopotamia: Earth and Planetary Science Letters, v. 241, no. 1-2, p. 159-173.
Gallet, Y., Le Goff, M., Genevey, A., Margueron, J., and Matthiae, P., 2008, Geomagnetic field intensity behavior in the Middle East between similar to 3000 BC and similar to 1500 BC: Geophysical Research Letters, v. 35, no. 2.
Goguitchaichvili, A. T., Prevot, M., and Camps, P., 1999, No evidence for strong fields during the R3-N3 Icelandic geomagnetic reversal: Earth and Planetary Science Letters, v. 167, no. 1-2, p. 15-34.
Grappone, J. M., Chaffee, T., Isozaki, Y., Bauert, H., and Kirschvink, J. L., 2017, Investigating the duration and termination of the Early Paleozoic Moyero Reversed Polarity Superchron: Middle Ordovician paleomagnetism from Estonia: Palaeogeography Palaeoclimatology Palaeoecology, v. TBD, no. TBD, p. TBD.
Hawkins, L. M. A., Anwar, T., Shcherbakova, V. V., Biggin, A. J., Kravchinsky, V. A., Shatsillo, A. V., and Pavlov, V. E., 2019, An exceptionally weak Devonian geomagnetic field recorded by the Viluy Traps, Siberia: Earth and Planetary Science Letters, v. 506, p. 134-145.
Heiniger, C., and Heller, F., 1976, High-temperature vector magnetometer: Geophysical Journal of the Royal Astronomical Society, v. 44, no. 1, p. 281-287.
Hill, M. J., Gratton, M. N., and Shaw, J., 2002, Palaeomagnetic investigation of Tertiary lava from Barrington Tops, NSW, Australia, using thermal and microwave techniques: Earth and Planetary Science Letters, v. 198, no. 3-4, p. 245-256.
Hill, M. J., Pan, Y. X., and Davies, C. J., 2008, An assessment of the reliability of palaeointensity results obtained from the Cretaceous aged Suhongtu section, Inner Mongolia, China: Physics of the Earth and Planetary Interiors, v. 169, no. 1-4, p. 76-88.
Hill, M. J., and Shaw, J., 2000, Magnetic field intensity study of the 1960 Kilauea lava flow, Hawaii, using the microwave palaeointensity technique: Geophysical Journal International, v. 142, no. 2, p. 487-504.
-, 2007, The use of the 'Kono perpendicular applied field method' in microwave palaeointensity experiments: Earth Planets and Space, v. 59, no. 7, p. 711-716.
Hill, M. J., Shaw, J., and Herrero-Bervera, E., 2006, Determining palaeointensity from the Gilbert Gauss reversal recorded in the Pu'u Heleakala lava section, Wai'anae Volcano, Oahu, Hawaii: Earth and Planetary Science Letters, v. 245, no. 1-2, p. 29-38.
Hill, M. J., Shaw, J., and Hettero-Bervera, E., 2005, Palaeointensity record through the lower mammoth reversal from the Waianae volcano, Hawaii: Earth and Planetary Science Letters, v. 230, no. 3-4, p. 255-272.
Hodgson, E., Grappone, J. M., Biggin, A. J., Hill, M. J., and Dekkers, M. J., 2018, Thermoremanent Behavior in Synthetic Samples Containing Natural Oxyexsolved Titanomagnetite: Geochemistry Geophysics Geosystems, v. 19, no. 6, p. 1751-1766.
Irving, E., Robertson, W. A. H., Ward, M. A., Tarling, D. H., and Stott, P. M., 1961, Treatment of partially stable sedimentary rocks showing planar distribution of directions of magnetization: Journal of Geophysical Research, v. 66, no. 6, p. 1927-&.
Johnson, E. A., and Steiner, W. F., 1937, An astatic magnetometer for measuring susceptibility: Review of Scientific Instruments, v. 8, p. 236-238.
Kirschvink, J. L., Isozaki, Y., Shibuya, H., Otofuji, Y., Raub, T. D., Hilburn, I. A., Kasuya, T., Yokoyama, M., and Bonifacie, M., 2015, Challenging the sensitivity limits of

Paleomagnetism: Magnetostratigraphy of weakly magnetized Guadalupian-Lopingian (Permian) Limestone from Kyushu, Japan: Palaeogeography Palaeoclimatology Palaeoecology, v. 418, p. 75-89.

Kirschvink, J. L., 1996, Microwave absorption by magnetite: A possible mechanism for coupling nonthermal levels of radiation to biological systems: Bioelectromagnetics, v. 17, no. 3, p. 187-194.

Kirschvink, J. L., Kopp, R. E., Raub, T. D., Baumgartner, C. T., and Holt, J. W., 2008, Rapid, precise, and high-sensitivity acquisition of paleomagnetic and rock-magnetic data: Development of a low-noise automatic sample changing system for superconducting rock magnetometers: Geochemistry Geophysics Geosystems, v. 9.

Kobayashi, A., Kirschvink, J. L., Nash, C. Z., Kopp, R. E., Sauer, D. A., Bertani, L. E., Voorhout, W. F., and Taguchi, T., 2006, Experimental observation of magnetosome chain collapse in magnetotactic bacteria: Sedimentological, paleomagnetic, and evolutionary implications: Earth and Planetary Science Letters, v. 245, no. 3-4, p. 538-550.

Kono, M., Hamano, Y., Nishitani, T., and Tosha, T., 1981, A new spinner magnetometer - principles and techniques: Geophysical Journal of the Royal Astronomical Society, v. 67, no. 1, p. 217-227.

Kono, M., Hoshi, M., Yamaguchi, K., and Nishi, Y., 1991, An automatic spinner magnetometer with thermal demagnetization equipment: Journal of Geomagnetism and Geoelectricity, v. 43, no. 5, p. 429-443.

Kono, M., and Ueno, N., 1977, Paleointensity determination by a modified thellier method: Physics of the Earth and Planetary Interiors, v. 13, no. 4, p. 305-314.

Krasa, D., Shcherbakov, V. P., Kunzmann, T., and Petersen, N., 2005, Self-reversal of remanent magnetization in basalts due to partially oxidized titanomagnetites: Geophysical Journal International, v. 162, no. 1, p. 115-136.

Laj, C., Guillou, H., and Kissel, C., 2014, Dynamics of the earth magnetic field in the 10-75 kyr period comprising the Laschamp and Mono Lake excursions: New results from the French Chaine des Puys in a global perspective: Earth and Planetary Science Letters, v. 387, p. 184-197.

Laj, C., Kissel, C., Davies, C., and Gubbins, D., 2011, Geomagnetic field intensity and inclination records from Hawaii and the Reunion Island: Geomagnetic implications: Physics of the Earth and Planetary Interiors, v. 187, no. 3-4, p. 170-187.

Landeau, M., Aubert, J., and Olson, P., 2017, The signature of inner-core nucleation on the geodynamo: Earth and Planetary Science Letters, v. 465, p. 193-204.

Le Goff, M., and Gallet, Y., 2004, A new three-axis vibrating sample magnetometer for continuous high-temperature magnetization measurements: applications to paleo- and archeo-intensity determinations: Earth and Planetary Science Letters, v. 229, no. 1-2, p. 31-43.

Liu, H., Dong, H., Ge, J., Liu, Z., Yuan, Z., Zhu, J., and Zhang, H., 2019, High-Precision Sensor Tuning of Proton Precession Magnetometer by Combining Principal Component Analysis and Singular Value Decomposition: IEEE Sensors Journal, v. 19, no. 21, p. 9688-9696.

Matzka, J., 2001, Besondere magnetische Eigenschaften der Ozeanbasalte im Altersbereich 10 bis 40 Ma [Ph.D.: Ludwig-Maximilians-Universität München.

McClelland, E., and Sugiura, N., 1987, A kinematic model of trm acquisition in multidomain magnetite: Physics of the Earth and Planetary Interiors, v. 46, no. 1-3, p. 9-23.

Nagata, T., Akimoto, S., Yueda, S., Shimizu, Y., Ozima, M., and Kobayashi, K., 1957, Palaeomagnetic study on a quaternary volcanic region in japan: Advances in Physics, v. 6, no. 23, p. 255-&.

Nagata, T., Momose, K., and Arai, Y., 1963, Secular variation of geomagnetic total force during last 5000 years: Journal of Geophysical Research, v. 68, no. 18, p. 5277-5281.

Pan, Y. X., Hill, M. J., Zhu, R. X., and Shaw, J., 2004, Further evidence for low intensity of the geomagnetic field during the early Cretaceous time: using the modified Shaw method and microwave technique: Geophysical Journal International, v. 157, no. 2, p. 553-564.

Pauthenet, R., and Bochirol, L., 1951, Aimantation spontanee des ferrites: Journal De Physique Et Le Radium, v. 12, no. 3, p. 249-251.

Poidras, T., Camps, P., and Nicol, P., 2009, Controlled atmosphere vibrating thermo-magnetometer (CatVTM): a new device to optimize the absolute paleointensity determinations: Earth Planets and Space, v. 61, no. 1, p. 101-110.

Pressling, N., Brown, M. C., Gratton, M. N., Shaw, J., and Gubbins, D., 2007, Microwave palaeointensities from Holocene age Hawaiian lavas: Investigation of magnetic properties and comparison with thermal palaeointensities: Physics of the Earth and Planetary Interiors, v. 162, no. 1-2, p. 99-118.

Rahman, A. A., and Parry, L. G., 1975, Self shielding of inclusions in titanomagnetite grains: Physics of the Earth and Planetary Interiors, v. 11, no. 2, p. 139-146.

Santos, C. N., and Tauxe, L., 2019, Investigating the Accuracy, Precision, and Cooling Rate Dependence of Laboratory-Acquired Thermal Remanences During Paleointensity Experiments: Geochemistry, Geophysics, Geosystems, v. 20, no. 1, p. 383-397.

Schmidt, P. W., and Clark, D. A., 1985, Step-wise and continuous thermal demagnetization and theories of thermoremanence: Geophysical Journal of the Royal Astronomical Society, v. 83, no. 3, p. 731-751.

Shaw, J., 1974, Method of determining magnitude of paleomagnetic field application to 5 historic lavas and 5 archeological samples: Geophysical Journal of the Royal Astronomical Society, v. 39, no. 1, p. 133-141.

Shcherbakov, V. P., McClelland, E., and Shcherbakova, V. V., 1993, A model of multidomain thermoremanent magnetization incorporating temperature-variable domain-structure: Journal of Geophysical Research-Solid Earth, v. 98, no. B4, p. 6201-6216.

Shcherbakova, V. V., Shcherbakov, V. P., and Heider, F., 2000, Properties of partial thermoremanent magnetization in pseudosingle domain and multidomain magnetite grains: Journal of Geophysical Research-Solid Earth, v. 105, no. B1, p. 767-781.

Smirnov, A. V., Tarduno, J. A., Kulakov, E. V., McEnroe, S. A., and Bono, R. K., 2016, Palaeointensity, core thermal conductivity and the unknown age of the inner core: Geophysical Journal International, v. 205, no. 2, p. 1190-1195.

Smirnov, M., Sychev, A., Salnaia, N., Minaev, P., Powerman, V., and Veselovskiy, R. V., 2019, "ORION" – the versatile Full-vector Sample Magnetometer for Paleointensity, Rock Magnetic and Paleomagnetic Studies, European Geosciences Union General Assembly 2019, Volume 21: Vienna, Austria.

Stacey, F. D., 1959, Spinner-magnetometer for thermal demagnetization experiments on rocks: Journal of Scientific Instruments, v. 36, no. 8, p. 355-359.

Suttie, N., Shaw, J., and Hill, M. J., 2010, Direct demonstration of microwave demagnetization of a whole rock sample with minimal heating: Earth and Planetary Science Letters, v. 292, no. 3-4, p. 357-362.

Teanby, N., Laj, C., Gubbins, D., and Pringle, M., 2002, A detailed palaeointensity and inclination record from drill core SOH1 on Hawaii: Physics of the Earth and Planetary Interiors, v. 131, no. 2, p. 101-140.

Thellier, E., 1938, Sur l'aimantation des terres cuites et ses applications géophysique: Annales de l'Institut de physique du globe de l'Université de Paris, v. 16, p. 157-302.

Thellier, E., and Thellier, O., 1959, Sur l'intensité du champ magnétique terrestre dans le passé historique et géologique: Ann. Géophys., v. 15, p. 285-376.

van Zijl, J. S. V., Graham, K. W. T., and Hales, A. L., 1962, The Palaeomagnetism of the Stormberg Lavas, II. The Behaviour of the Magnetic Field During a Reversal: Geophysical Journal of the Royal Astronomical Society, v. 7, no. 2, p. 169-182.

Wack, M., 2006, Aufbau eines Hochtemperatur-Spinnermagnetometers zur magnetischen Untersuchung von Ozeanbasalten [Diploma: Ludwig-Maximilians-Universität München.

Wack, M., and Matzka, J., 2007, A new type of a three-component spinner magnetometer to measure the remanence of rocks at elevated temperature: Earth Planets and Space, v. 59, no. 7, p. 853-862.

Walton, D., 1977, Archeomagnetic intensity measurements using a squid magnetometer: Archaeometry, v. 19, no. JUL, p. 192-200.

Walton, D., Share, J., Rolph, T. C., and Shaw, J., 1993, Microwave magnetization: Geophysical Research Letters, v. 20, no. 2, p. 109-111.

Walton, D., Shaw, J., Share, J., and Hakes, J., 1992, Microwave demagnetization: Journal of Applied Physics, v. 71, no. 3, p. 1549-1551.

Wilson, R. L., 1961, Palaeomagnetism in northern ireland .1. The thermal demagnetization of natural magnetic moments in rocks: Geophysical Journal of the Royal Astronomical Society, v. 5, no. 1, p. 45-58.

Yamamoto, Y., and Shaw, J., 2008, Development of the microwave LTD-DHT Shaw method for absolute paleointensity determination: Physics of the Earth and Planetary Interiors, v. 170, no. 1-2, p. 15-23.

Yamamoto, Y., Tsunakawa, H., and Shibuya, H., 2003, Palaeointensity study of the Hawaiian 1960 lava: implications for possible causes of erroneously high intensities: Geophysical Journal International, v. 153, no. 1, p. 263-276.

Yu, Y. J., Tauxe, L., and Genevey, A., 2004, Toward an optimal geomagnetic field intensity determination technique: Geochemistry Geophysics Geosystems, v. 5, p. 18.

CHAPTER 3 PROTOTYPING A NOVEL SINGLE-AXIS CONTINUOUS MAGNETOMETER SYSTEM

3.1 Overview

In this chapter, the work to design the prototype of a single-axis magnetometer work is presented. The design specifications for the prototype magnetometer system are detailed in Table 3-1. These specifications are the goals to which this and the following two chapters will be devoted. Building a new magnetometer system is an important next step for high-fidelity paleomagnetic surveys. The time spent waiting for the specimen to heat from and then cool to room temperature greatly increases the time required to complete the thermal steps, so specimens are usually heated and measured in batches. Decreasing the number of heating/cooling cycles a specimen undergoes also helps prevent the thermochemical alterations mentioned in the previous chapter. Thermochemical alteration mitigation strategies are noted further in Section B of this thesis. Using batches of specimens means that small variations in magnetic mineralogy cannot be accounted for. Currently, measuring paleomagnetic samples at high temperatures requires spinning or vibrating the specimen about a single axis magnetometer to attempt to measure all three vector directions. Spinning or vibrating the specimen complicates both the design and maintenance of the machine and the equations required to deconvolute the magnetic signal.

Superconducting Quantum Interference Devices (SQUIDs) are commercially available and have been used successfully in many paleomagnetic applications, as detailed in Chapter 2. The main focus of this section is on designing an oven that is compatible with the SQUIDs. The radio-frequency (RF) SQUIDs used in this project are highly sensitive to background electromagnetic interference in the RF wavelength range (< 1 MHz), which is a byproduct of all alternating current (AC) powered circuits. In addition, the single-axis prototype's design serves as a test-bed for the temperature control/data collection system and remagnetization coil. Once all the tests were completed, the best parts were collated to build the larger, more complete three-axis prototype (Chapter 4).

Table 3-1 Design specifications for the prototype magnetometer system

Design feature	Requirement
Temperature range	• Room – 600 °C (700 °C preferred)
Physical properties	• Operational outside of a shielded room • Solid-state (no moving of specimen) during measurement
Magnetic measurements	• Continuous three-axis acquisition of specimen magnetic moment
Measurement sensitivity	• SQUID magnetometer sensors • More sensitive than 5×10^{-8} Am^2
Control system	• Automated demagnetizations of rock specimens and paleointensity experiments
Total system cost	• Between a JR6 (€50 000) and a 2G RAPID system ($500 000)

3.2 High-Precision Oven

Before any part of the system could be tested, the oven needed to be designed and built. One of the simplest and fastest ways to heat a specimen is using resistive heating, where the resistance in a wire generates heat. The problem with this approach, however, is that electrical current creates a magnetic field, according to Faraday's Law, which can be seen in Equation 3-1. Normally the magnetic field is not a problem when using an oven (e.g. for cooking food), but any direct current (constant) magnetic field here will remagnetize the samples, destroying any useful data. A low-power alternating current (AC) oven avoids this problem but creates electromagnetic interference in the RF range (< 1 MHz). The specimens in the oven are cylindrical, as is the oven, so the wire is coiled around the outside of the quartz tube that constitutes the oven. As Equation 3-1 shows, coiled wire creates a magnetic field, as it would in any solenoid. By counter-coiling the wire, the net effect is of two solenoids of opposite polarity, and as a result, the magnetic field vectors cancel out to 0 inside the tube, for ideal solenoids.

$$\Phi_B = \iint_S \boldsymbol{B}(\boldsymbol{r},t) \cdot d\boldsymbol{S} = \iint_S \boldsymbol{B}(\boldsymbol{0},0) \cdot d\boldsymbol{S} = \sum_i \boldsymbol{B}_i = \boldsymbol{B}_{ccw} - \boldsymbol{B}_{cw} = \frac{\mu_0 NI}{l} + \frac{\mu_0 N(-I)}{l} = \boldsymbol{0}$$

Equation 3-1 Faraday's law for two opposite polarity, identical solenoids coiled together create a net 0 magnetic field. Φ_B is the magnetic flux, B(r,t) is the magnetic field vector, with B_{ccw} caused by the counter-clockwise rotations of wire and B_{cw} caused by the clockwise rotations.

The oven design selected was a tube with a diameter of 10 mm. The oven was designed to only heat a single specimen, while also minimizing the distance from the Superconducting Quantum Interference Device (SQUID) to the specimen. Therefore, to save space, the specimen was placed inside the solenoid as in the 'Sogo Fine-TD' oven from Zheng et al., (2010). Using a spring wire with toroidal curves at the edges might produce even less magnetic noise but would further increase the distance from the specimen to the sensor (Shaw, 2010). The downside to the Shaw (2010) design is that the wires need to be wound manually and as precisely as possible to ensure maximum negation of the internal magnetic field. In addition, the uninsulated side of the wire must be in direct contact with the quartz tube that holds the sample, which can potentially cause shorts at temperatures above 700-800 °C, due to the rapidly decreasing resistivity of quartz as its temperature increases (Enculescu and Iliescu, 1997).

The high-temperature SQUIDs (manufactured by Jülicher SQUID GmbH) must be housed separately from the oven, in a liquid nitrogen Dewar, because they have an operating temperature of 77 K. To reduce the electromagnetic interference from the AC oven, a copper tube was placed around the oven. The copper tube surrounding the oven needs to be cooled as much as possible to minimize the boil off from the liquid nitrogen surrounding the SQUID (see Figure 3-1). A few different designs were considered initially: heat sink and fan, liquid nitrogen cooling, and nitrogen vapor cooling (see Section 2.2). The cooling system is located as far from the specimen as possible to avoid large temperature gradients and/or boiling the liquid nitrogen near the SQUID. Although copper is one of the best conductors, it still has a finite thermal conductivity (which can change with temperature and oxidation), so the farther away the cooling system is from the heating coil and sample, the less efficient it is.

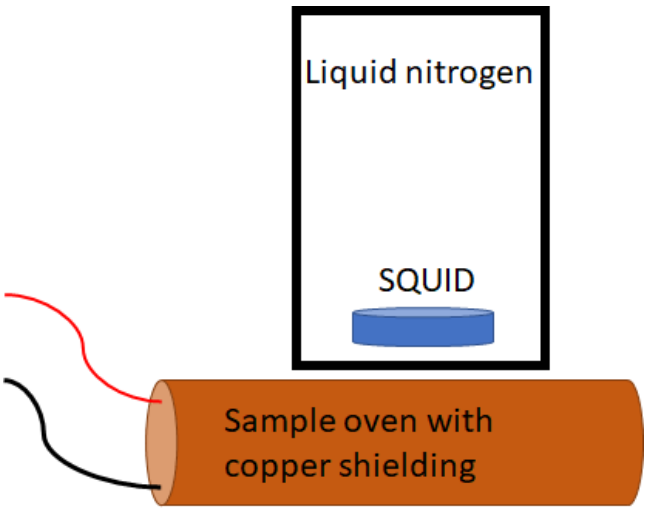

Figure 3-1 Cartoon showing SQUID and oven relationship (figure not to scale)

3.2.1 VFTB-style Oven

Following the Magnetic Measurements Variable Field Transition Balance (VFTB) as a guide, the initial oven was made from a nichrome (NiCr) wire counter-coiled around a quartz tube, with fire cement and insulation on the outside for structural support and to retain heat.

3.2.1.1 Constructing the oven

First, a small 1 cm diameter, 10 cm long oven was fabricated using a glass tube and nichrome wire, following the aforementioned oppositely wound, non-inductive coiling pattern used frequently in paleomagnetic oven designs (e.g. Zheng et al., 2010 and Draeger et al., 2006).

A 2 m piece of nichrome wire was folded in half and either side was threaded through a pulley onto a weight to provide tension for the wire. The folded point was then attached using superglue to the bottom of the quartz tube and then wrapped around the tube, with the weights ensuring the wire stayed tightly on the tube. RW80 nichrome wire with a resistance of 12.43 Ω/m and a diameter of 0.325 mm was selected. Once the wire was coiled around the entire tube, fire cement was added to hold the wire in place permanently (Figure 3-2). After the cement hardened, two leads were cemented to the end for the wires. Finally, thermal insulation was wrapped around the tube to minimize the heat transfer between the oven and the copper shielding.

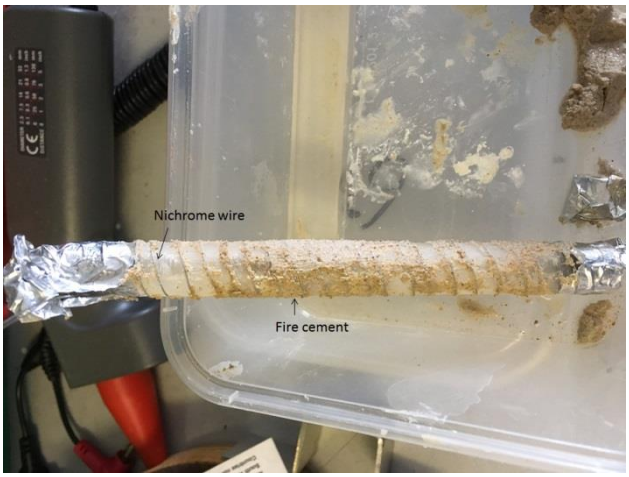

Figure 3-2 Partially completed 10 cm oven with fire cement holding the wire in place. The ends are foiled to better hold the nichrome wire during setting.

3.2.1.2 Shielding the Oven

The non-inductive coiling works well to negate the internal magnetic field of the quartz tube. However, the 2 solenoids still produce RF radiation on the outside of the coils as a result of the AC current. To combat the external radiation, the small-scale oven was fitted with a 1.8 mm thick copper tube, whose high conductivity makes it an ideal material to shield

against RF radiation. The tube is preferred over a simple metal plate between the SQUID and the oven because it gives more structure to the oven region. The formula for the skin depth, the depth into the material that $\frac{1}{e} \approx 37\%$ of the radiation is felt, is given in Equation 3-2.

$$\delta_{skin} = \sqrt{\frac{\rho}{\pi f \mu}}$$

Equation 3-2 Skin depth formula, used for RF radiation remediation δ is the skin depth, ρ is the resistivity, f is the radiation frequency, and μ is the permeability.

Substituting the values for copper- $\rho_{cu} = 1.678 \times 10^{-8}\Omega\text{m}$, $\mu_{cu} = 4\pi \times 10^{-7}\,\frac{H}{m}$ - and a given frequency show that the shield substantially reduces RF AC noise, as shown in Table 3-2. Copper is used because it has the highest conductivity of commonly available metals, except for silver. Since part of the goal is to create a cost-effective magnetometer, copper decreases the costs and a tube of silver would only reduce the skin depth by an additional 2-3%. Looking at the results for copper in Table 3-2, any improvements from silver would be minimal.

Table 3-2 Skin depths vs frequency for copper tube

Frequency (Hz)	Skin depth (μm)	# of skin depths in walls	% noise reduction
50 Hz	9220	0.2	18.13
10 kHz	652	2.8	93.92
50 kHz	293	6.1	99.78
60 kHz	267	6.7	99.88
65 kHz	257	7.0	99.91
75 kHz	239	7.5	99.94
100 kHz	206	8.7	99.98

For frequencies above 50 kHz, the additional noise reduction is minimal because of the inverse exponential nature of skin depths. To reduce the RF noise by 99% (2 orders of magnitude), 4.6 skin depths are required. For a frequency of 50 kHz, the walls must be 1.35 mm thick, and increasing the frequency to 100 kHz drops the wall thickness required to 0.95 mm. Selecting the appropriate frequency, however, required taking into consideration the power amplifier used. Amplifiers are not generally designed for frequencies above 20 kHz, which will be discussed further in the next section.

3.2.1.3 Powering the Oven

An old signal generator with variable voltage (0 - 10 V) and AC frequency (1 mHz - 100 kHz) was used as the power source (Figure 3-3). The maximum output frequency is 100 kHz. The output was confirmed by an oscilloscope. The output from the signal generator was then amplified using a W audio Zenith 2K5 audio amplifier to increase the voltage from 10V to 36-

66 V. A K-type (nickel-chromium/nickel-alumel) thermocouple rated up to 750 °C measured the temperature inside the oven. To get an approximation of the internal heating rate, data points were taken at 30s intervals to broadly characterize the ramping rate. The data from these initial tests are located in Table 3-3, which examined ramping rates for different voltages and frequencies.

Table 3-3 Small oven tests internal temperature (against amplification and Hz), plotted in Figure 3-4

Time (s)	½ amp, 50 Hz (°C)	½ amp, 10 kHz (°C)	½ amp, 100 kHz (°C)	¾ amp, 10 kHz (°C)	¾ amp, 60 kHz (°C)	¾ amp, 65 kHz (°C)	¾ amp, 75 kHz (°C)	¾ amp 100 kHz (°C)
0	13	20	16	18	19	19	15	15
30	72	87	57	214	170	158	124	69
60	161	187	119	500	389	350	278	156
90	234	263	170	661	538	489	388	222
120	286	314	207		618	574	458	269
150	328	352	233		665	624	504	302
180	360	378	253		694	655	536	324
210	381	398	268		712	676	559	341
240	397	413	280			690	577	355
270	409	425	290				592	367

Figure 3-3 Signal Generator set to 10 kHz

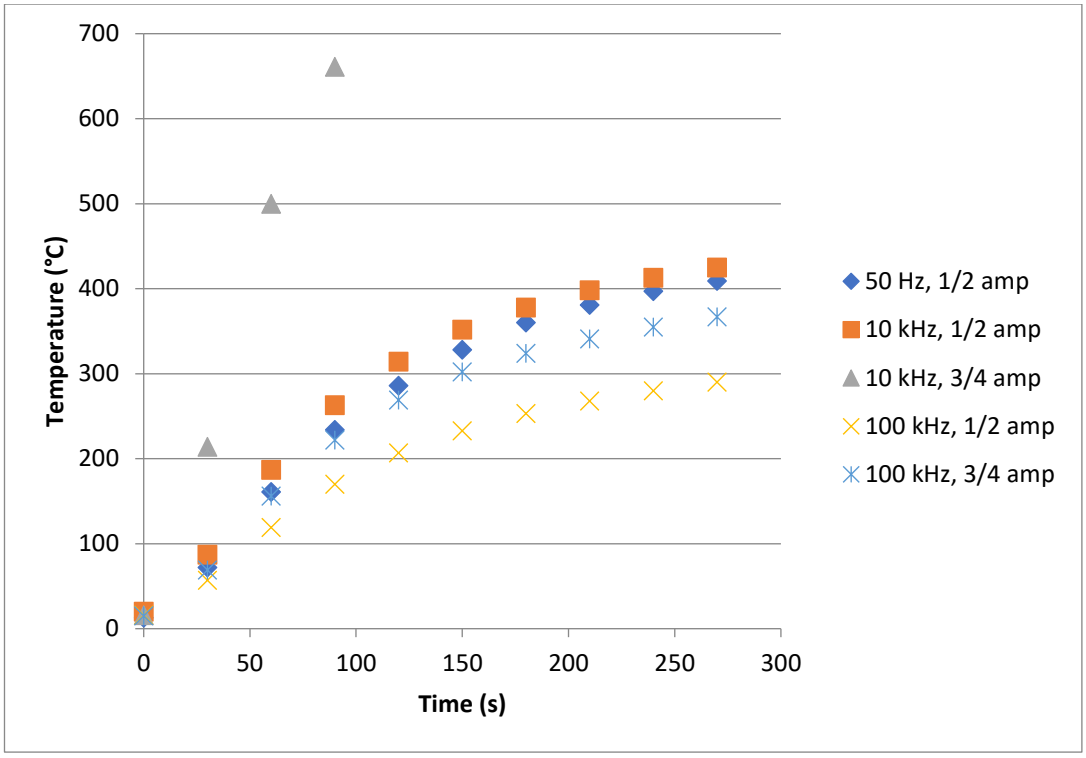

Figure 3-4 Internal temperature vs time curves for varying voltages and AC frequencies

The internal temperature data show that for similar voltages, the temperature inside the oven increases similarly for 50 Hz (wall outlet AC frequency in Europe) and 10 kHz, but the temperature increases much more slowly as the frequency approaches 100 kHz. At high AC frequencies like these, there is increased impedance, Z, in the system, as shown below in Equation 3-3.

$$Z = \sqrt{R^2 + X_L^2} = \sqrt{R^2 + 2\pi f L}$$

Equation 3-3 Impedance equation, showing how Z, impedance, increases as a function of f, frequency, and L, the length scale.

However, the more likely reason for the voltage drop-off is the audio amplifier, which is only calibrated for frequencies from 20 Hz to 20 kHz, the extent of human hearing. To check if the amplification decreases with increasing frequency, the tests were repeated with an oscilloscope attached to both the signal generator output (consistently 10 V) and the oven. The results from this test are in Table 3-4. The oscilloscope only measures voltage, not current, so the amplifier's power output is not directly known, but the decreased voltage output implied that less power was being output. It was decided to move forward with a 50 kHz frequency and revisit this selection as necessary.

Table 3-4 Output voltage at max amplification in the kHz range

Frequency	100 kHz	10 kHz	1 kHz
Amplifier voltage output	5 V	26 V	125 V

The next step was to check if the insulation was working properly, by determining the lag between the internal temperature of the oven and its external temperature. The test was carried out for only a few amplification and frequency combinations (Table 3-5) because a thermocouple is not designed for surface temperature measurements. Only a simple baseline was needed before carrying out the fan and heatsink tests, which are the more important tests.

Table 3-5 External oven temperatures (against V and Hz), plotted in Figure 3-5

Time (s)	¼ amp, 50 Hz	¼ amp, 10kHz	½ amp, 50 kHz
0	13	15	17
30	21	23	28
60	46	48	60
90	75	77	106
120	103	104	155
150	127	128	202
180	150	149	243
210	166	166	283
240	183	180	
270	194	192	

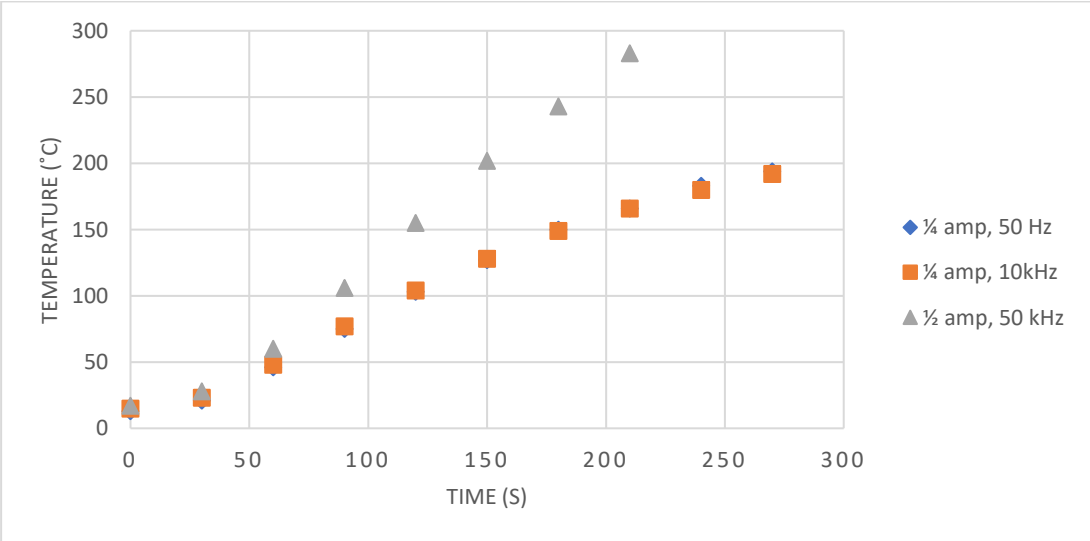

Figure 3-5 External oven temperature vs time for different frequencies

Upon confirmation of the oven working properly, the next step was to determine the viability of using a fan and heat sink to cool the copper tube. The tests were run at 50 kHz and ½ amplification, which corresponds to a voltage of approximately 18 V at this frequency. Baseline internal and external temperatures were taken first. The assumption for all the tests was that the internal oven temperature remained the same at each step for each test. The small size of the specimen means that the internal temperature immediately around the specimen needs to be equilibrated, which is handled by the internal thermocouple. Next, a fan was positioned at the far end of the tube (upper position in Figure 3-6) for a basic cooling system. The fourth test had the fan positioned right at the thermocouple (lower position) for maximum cooling. This is assumed to be the same position as the sample and SQUID for the sake of this experiment. The fifth test included a heat sink. The data are in Table 3-6 and plotted in Figure 3-7.

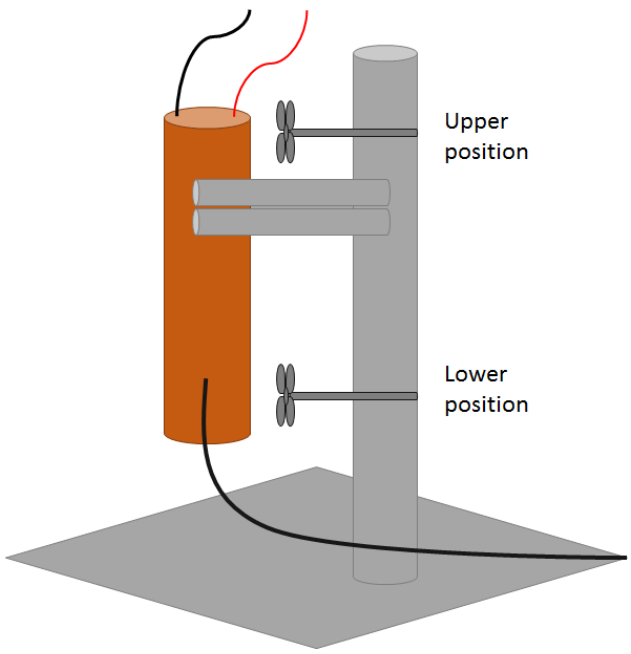

Figure 3-6 Cartoon of fan setup positioning, showing both locations during the external temperature tests (figure not to scale)

Table 3-6 Proof of concept test for fan + heat sink cooling. Temperatures given are internal temperatures

Time (s)	½ amp, 50 kHz (°C)	½ amp, 50 kHz (°C)	½ amp, 50 kHz, fan at far end (°C)	½ amp, 50 kHz, fan near sensor (°C)	½ amp, 50 kHz, fan + taped heatsink (°C)
0	14	17	15	14	17
30	146	28	26	23	27
60	345	60	57	47	57
90	474	106	99	78	98
120	537	155	146	110	142
150	568	202	187	137	181
180	590	243	224	158	215
210	607	283	256	174	245

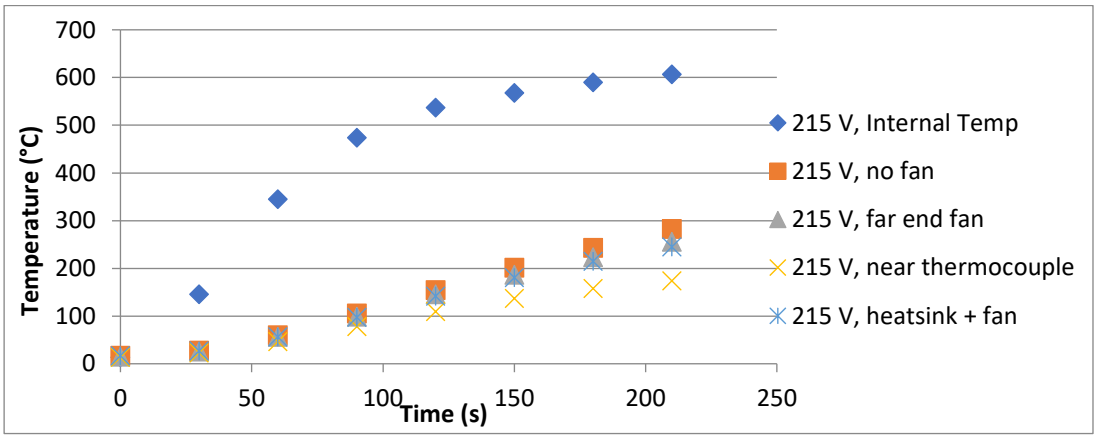

Figure 3-7 Oven cooling system design tests

Looking at the plot in Figure 3-7, the simple desk fan is better at reducing the temperature of the copper tube. The fan is more efficient when positioned directly opposite the thermocouple than when positioned at the far end of the tube. However, the latter configuration is the one required in order to minimize the distance between the oven and the SQUID sensor, once installed. The tests also showed that the cooling system's efficiency improves at higher temperatures, which makes sense due to the larger thermal gradients involved.

The basic heatsink made using tape worked better than no heatsink, as expected. Finding an appropriately sized heatsink for the copper pipe proved difficult, so instead a non-cylindrical heatsink was coupled with aluminum tape to the pipe. The heatsink was then attached to the external piece of copper, allowing much better contact and heat exchange with the pipe itself. The heatsink then was cooled by the same desk fan as before, before the oven/shielding system was fully integrated into the system.

3.2.1.4 Controlling the temperature

Having ascertained that the oven could reach the required temperatures using AC frequencies at or above 10 kHz, the next step was to control the oven. The desired design specification was a variable ramping rate of 10 - 30 °C/min to reach the target temperature within 0.5 °C. A Eurotherm 3216 temperature controller was selected for this purpose. The controller came with a logical output and a built-in relay, as well as a thermocouple input. The different output types allowed the creation and testing of multiple circuit designs for the oven system.

The controller was initially wired to a high-power, non-latching (only stays closed while a current is applied), solid-state relay, to control the current between the audio amplifier and the oven. During heating, the controller is programmed to output a logical value of 1 (heat on), which is represented electronically as a step function from a value of 0 to the maximum output allowed. The maximum is then maintained for a set duration, during which time the non-latching relay allows the main current to flow through. This circuit is shown in Figure 3-8A. The relay is designed to function with AC voltage from 110 – 250 V, but at 50-60 Hz frequency. The specifications are unclear if the relay will function with high frequencies, as high AC frequencies are rarely used. The Eurotherm controller's built-in solid-state relay's specifications also do not specify its usage at high frequencies. This circuit is shown in Figure 3-8B. Both pieces of equipment were tested at 50 Hz and then at 50 kHz at temperatures from 200°C to 500 °C. The pass requirement for the test was very simple: if the oven heated to the required temperature at the required rate, the test was passed. If the initial test at 200°C test was failed for a given AC frequency, no other test was run. The results of these tests are in Table 3-7 and Table 3-8, respectively.

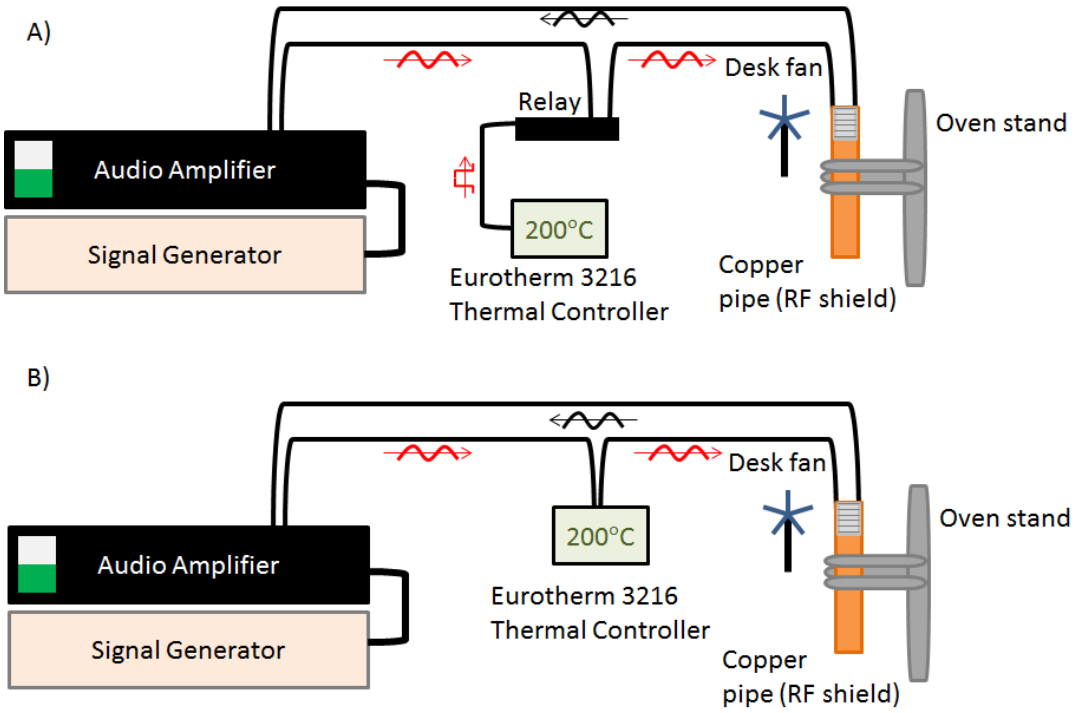

Figure 3-8 Cartoon of oven control circuits. A) external relay controlled by logical output, B) Internal relay. Figure not to scale.

Neither circuit shown in Figure 3-8 has a clear advantage from a complexity stand point. Circuit A has additional external wires, but the external relay allows for easier troubleshooting or repairing for any problems associated with it. The only difference between the two circuits is the relay used. During tests with the external relay, the relay became latching (the relay stayed closed even when the current was turned off) when AC frequencies above 5.3 kHz were used. Immediately upon lowering the frequency below this threshold, the relay immediately unlatched. Since the relay is not intended for use with high frequencies, its failure is reasonable. The relay built-in to the Eurotherm controller is non-latching at all tested frequencies (50 Hz – 100 kHz).

Table 3-7 Circuit A test results

Temperature (°C)	Pass at 50 Hz?	Pass at 50 kHz?
200	Pass	Not passed
250	Pass	Not tested
300	Pass	Not tested
400	Pass	Not tested
500	Pass	Not tested

Table 3-8 Circuit B test results

Temperature (°C)	Pass at 50 Hz?	Pass at 50 kHz?	Pass at 100 kHz?
200	Pass	Pass	Pass
250	Pass	Pass	Pass
300	Pass	Pass	Pass
400	Pass	Pass	Pass
500	Pass	Pass	Pass

The Eurotherm controller uses a proportional-integral-derivative (PID) control loop feedback mechanism. The control system requires continuous measurement of the oven temperature, which was accomplished using a thermocouple in direct contact with the specimen in a fixed position. The governing equation for the mechanism is given in Equation 3-4. The controller calculates the difference from the desired value (error as a function of time) and then calculates the heating time required for the next desired temperature. Selecting values for the control constants was an iterative process, which required balancing the speed at which the target temperature was reached with minimizing overshoot and thus overheating.

$$u(t) = Pe(t) + I\int_0^t e(\tau)d\tau + D\dot{e}(t)$$

Equation 3-4 PID control equation. P, I, and D are the proportional, integral, and derivative constants, respectively, and e(t) is the error as a function of time.

The initial design specifications called for a precision of ± 0.5 °C, which was attained using $< P, I, D > = < 9\ °C, 190\ s, 8\ s >$ in the Eurotherm proprietary iTools software.

The oven fits specimens with a small diameter, 10 – 12 mm, which decreases the magnitude of the difference in temperature between the interior and outer surfaces. The oven is enclosed and much larger than the specimen, so small variations in diameter do not substantially affect the heating of the specimen. The sensitivity of the instrument is unaffected, as magnetization grows as the cube of R and magnetic dipole moment falls off as the inverse cube of R. The downside is a loss of partial averaging that a larger sample provides.

3.2.1.5 Attempting to simplify the circuit

Another method for temperature control was explored: AC current ramping. The Eurotherm controller controls the temperature very well, but since it controls the temperature by turning the oven on and off, the noise increases by approximately 50% when the oven turns on because of the sudden change. In addition, the cycling of power into the wires potentially decreases their lifespan. Using AC current ramping, the oven's current is 0

only at the beginning and end of the test. Instead, the current into the oven can be steadily increased from 0 to the maximum required current over the course of the experiment by the computer.

As a result of the initial tests with different frequencies and amplifications, it was established that higher maximum temperatures are reached with higher currents. In order to have the desired 30 °C/min heating rate, the current needed to be increased at the proper rate. The Eurotherm controller uses PID control to determine when and for how long to turn the oven on. The selected program instead used PID control to determine what output current is required. Since the oven design is known, PID control is not strictly necessary. Instead, a look-up table that contains the desired temperatures and the corresponding output required by the program is also possible but would require better characterization of the conductive properties of the specimens to be studied.

The circuit could be significantly simplified, and the size of the apparatus significantly reduced because of the fewer components needed. The signal generator and the Eurotherm would be removed from the circuit, but nothing would be added, since the National Instruments USB-6211 controller could be used to output the desired waveform, as well as read the data. The problem with this design is comes from the USB-6211 controller, however. It can only output 250k samples/second. At a frequency of 40 kHz, each waveform only has 6 points that describe it. The copper shielding should help to mitigate this effect, but the sampling rate puts a fairly rigid upper limit on the useable frequency range. The program output the data successfully, but the high RAM requirements of the program potentially outweigh its benefits. The computer used for the tests was unable to keep the program stable for more than 30 seconds. The LabVIEW program was shelved pending either a stronger computer or a clear need for it.

3.2.1.6 Tuning the Oven

A significant issue with the coiled oven is that its inductance is not known theoretically. Since the system uses high AC frequencies, knowing the inductance of the oven is vital to the circuit working correctly without extreme power losses. The coiled oven sits inside a copper tube, which further changes its impedance at high frequencies. To determine the inductance of the oven, an RLC circuit was set up, as shown in Figure 3-9. The oven's resistance was directly measured to be 12 Ω (when turned off), and a capacitor with a capacitance of 100 (+/- 10%) nF was used. The oscilloscope was used to determine the AC frequency with the maximum voltage output. It was determined to be 9 kHz. A higher resolution was not possible with this setup.

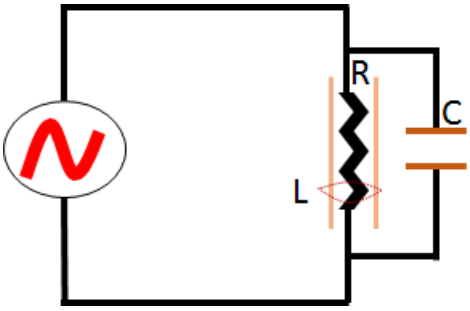

Figure 3-9 Diagram of RLC circuit used to calculate oven's induction due to its copper shielding

3.2.2 Cooling the RF shield design

With the control system functional, the interior of the oven was controllable up to 700°C. Initial tests (Table 3-6) showed that using a simple fan and heatsink gives an exterior temperature of 250°C after $210s$. The first test of the shielding using a SQUID sensor, detailed in the next section (SQUID Sensor), requires placing the oven inside of a Delrin (a type of plastic) tube that is pre-installed in the system shell used. The melting point of Delrin varies depending on the application but is approximately 175°C, which is substantially below 250°C. The next step up from an air-cooled system is a water-cooled system, which is more complicated but extracts heat more effectively.

For the initial water-cooling system, a biologically-inspired design was initially tested due to space constraints. The system is modelled after an amphibian's heart and is detailed in Figure 3-10.

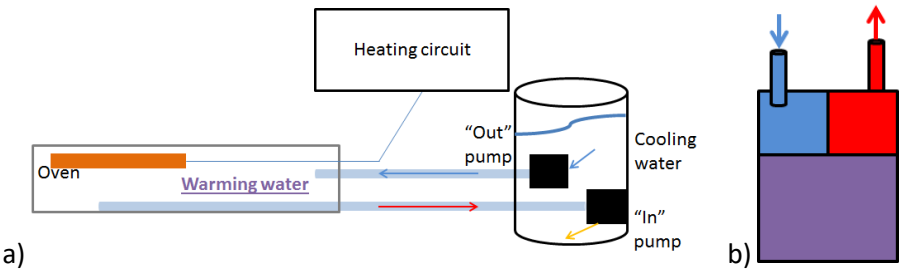

Figure 3-10 Water cooling system block diagram a) the system itself, b) amphibian heart model

The system was preliminarily tested to ensure there were no leaks but did not undergo extensive surface temperature testing before the first tests in the Delrin tubes. As a result of the broken Dewar (see Section 3.3 for details), the water-cooled system proved unnecessary. The broken Dewar meant there was poor insulation between the oven's shielding and the liquid nitrogen reservoir. All the heat from the shield was therefore extracted by the liquid nitrogen as it boiled off. After replacing the Dewar, the Delrin tube was upgraded to a 2 mm thick copper tube of the same diameter. Placing the oven and its shield inside the copper tube creates a 4mm thick RF shield between the oven and the SQUID sensor.

3.3 SQUID Sensor

To properly test the copper RF shielding, the oven was placed inside of a Delrin tube, which then went inside of an old piece of equipment, produced by Forschungsgesellschaft für Informationstechnik (F.I.T.), which housed a single SQUID magnetometer and kept it below 81K (its operating temperature). A picture of the container can be found in Figure 3-11.

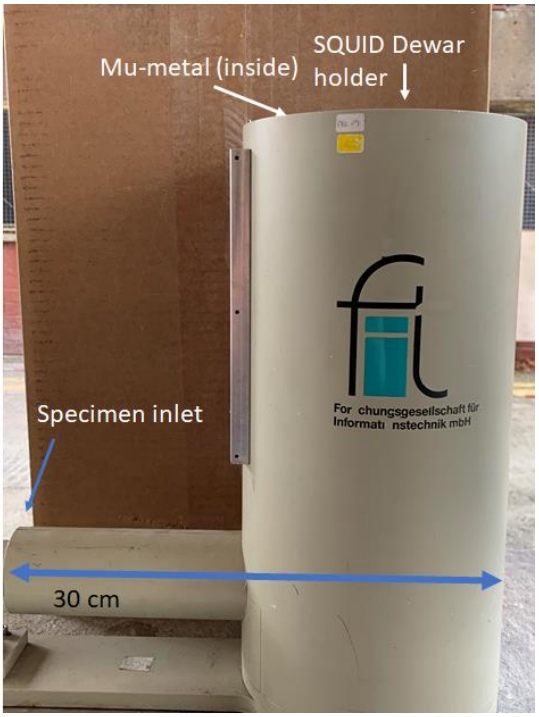

Figure 3-11 F.I.T housing for single axis magnetometer

Inside sat four layers of Mu-metal shielding and a vacuum Dewar flask (on top of the horizontal entry tube) for the liquid nitrogen (at 77K). The complete setup can be found in Figure 3-12.

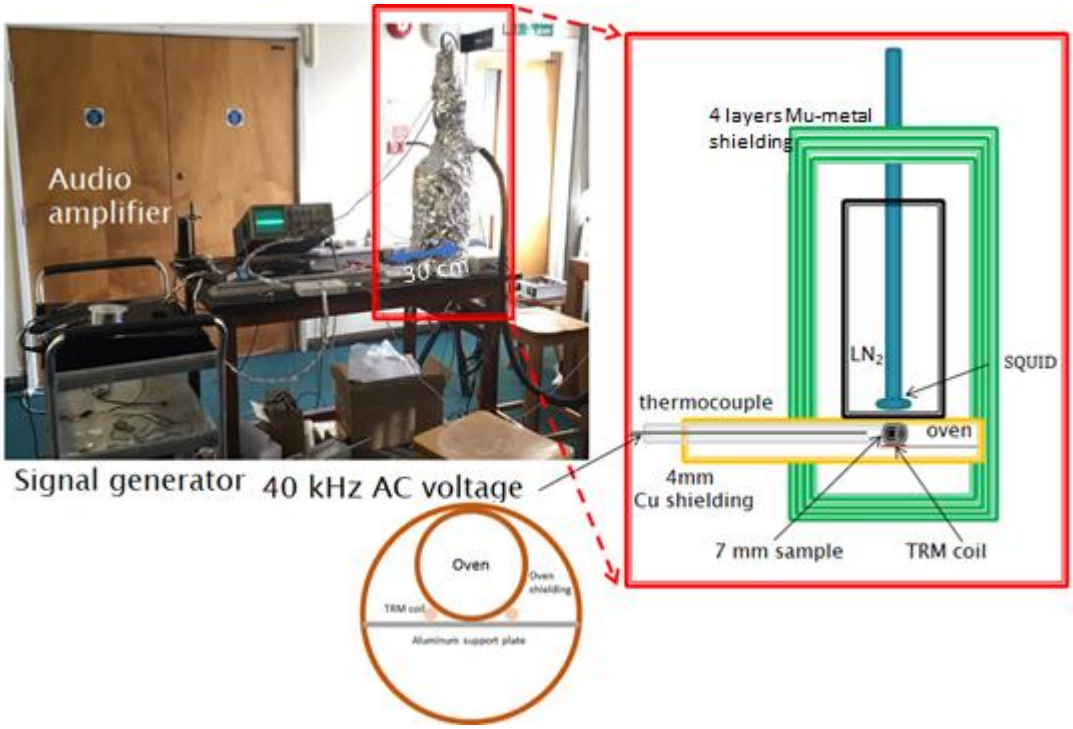

Figure 3-12 Initial single axis magnetometer design. Computer generated portion not to scale.

The first tests were a success, despite the aging SQUID. With the oven operating at 10kHz, a signal corresponding to a magnetic field of approximately 1.5 nT was displayed on the oscilloscope. The design specifications called for a 5 nT maximum, more than 3 times higher than the current noise level. The test was run with a distance from oven center to the SQUID sensor of approximately 14.4 mm (smaller distances are preferred because magnetic fields drop off as r^{-3}) due to space constraints in the Delrin tube. Since the magnetic noise from the oven is lower than required, the distance to the sample can be decreased in the future.

The test equipment had one major flaw, however. It had a nitrogen leak. During testing, the leak was useful because it meant that no cooling system was necessary, as ice frequently formed on interior surfaces. As a result, 120 L of liquid nitrogen were used up over the span of a week keeping the SQUID cool. Once the tank was emptied, it was found that the vacuum Dewar's bottom had ruptured. It appeared to be the result of water collecting in the bottom (also thinnest) part of the Dewar, which then caused the break when it flash froze upon the addition of the liquid nitrogen.

The broken Dewar was replaced with a cylindrical stainless-steel Dewar. The smaller diameter requires less liquid nitrogen to be used to keep the SQUID cold, but the bottom of the Dewar has a small lip on it, which increases the distance from the SQUID to the oven. The stainless-steel material of the Dewar is a lot more durable than the glass of the old Dewar. However, stainless steel is conductive. After installing and tuning the same SQUID, the

readout initially read 0. The SQUID was in contact with the Dewar and so became electrically grounded, which reduced the signal to 0. Once the SQUID was tuned and ungrounded, it had higher noise in the new Dewar and remained very sensitive to external RF noise, such as cell phones.

Since the system worked properly, a new RF SQUID was ordered from Jülicher SQUID GmbH, which is shown in Figure 3-13. A summary of its specifications is provided in Table 3-9. While the system was disassembled, the Delrin container was upgraded to a 2-mm thick copper tube of the same diameter. The addition of the copper tube effectively doubled the thickness of the copper shielding, further decreasing the oven's RF noise. To ensure the new copper tube would not have any unintended effect on the SQUID, it was grounded to the system's casing. Four layers of aluminum foil were then added to the exterior of the system and grounded to provide additional RF shielding. A no cell phone area was also set up at a radius of 3 m. The upgraded system has a liquid nitrogen boil-off rate of < 3L/day. This number is artificially inflated, as the large Dewar, which contains the liquid nitrogen reservoir is old and has its own boil-off rate as well.

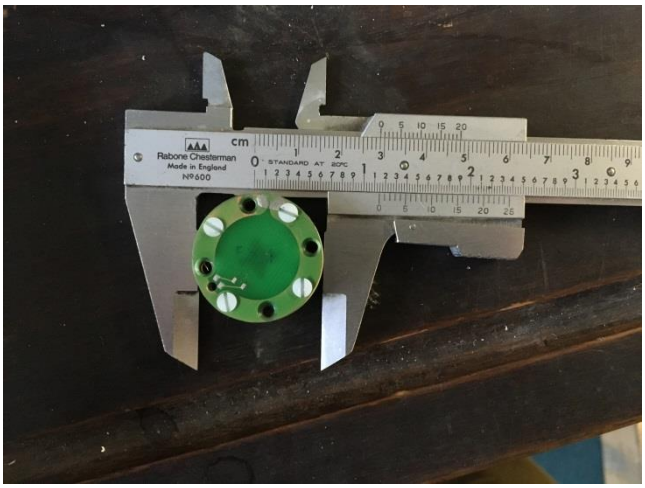

Figure 3-13 JSQ RF SQUID Magnetometer

Table 3-9 SQUID sensor and electronics specification summary

Parameter	Specification
SQUID loop size	100 x 100 μm^2
Maximum sensitivity	30 fT $Hz^{-1/2}$
Magnetic field to flux conversion constant	3.48 nT/Φ_0
Voltage per unit flux (adjustable range)	46.13 – 793.6 mV/ Φ_0
Output voltage range	± 10 V

The SQUID was tuned using triangle waves at 160 Hz with an amplitude of 3V to ensure stable operation, as recommended by Jülicher. The noise level in the oven was then measured to ensure that the residual noise level was sufficiently low. The minimum possible AC frequency for stable operation was 10 kHz. The signal generator was kept 1 m away from the SQUID under 3 layers of steel shielding to reduce its effect on the SQUID signal. Without the shielding, the signal generator caused noise levels on the order of 400 mV. The baseline (oven powered off) noise level also changed as a function of temperature, but not of time. The issue was the thermocouple used; inserting the thermocouple into the oven caused the SQUID to register a 100 mV ($\sim$1.5 nT) change in the SQUID measurements. K-type thermocouples use two nickel alloys, both of which have electromagnetic properties that change with temperature. An old R-type (platinum-rhodium) thermocouple complete with sample holder was tested to replace the other thermocouple. The noise levels were then remeasured for the oven and no visible change was observed in the SQUID output data on the oscilloscope. The R-type thermocouple was then replaced in later experiments with an N-type thermocouple, which has a lower Curie temperature than the K-type thermocouple but has a higher voltage output than the R-type. During neither test did the liquid nitrogen boil-off rate appear to increase, so no heat extraction system was needed for the oven inside of the holder.

After determining successfully that the noise level from the oven was low enough to allow operation of the SQUID, the initial tests began.

3.3.1 Keeping the SQUID cool

Inside the repurposed housing sits a vacuum flask that fits the liquid nitrogen level sensor, a single SQUID and a liquid nitrogen nebulizer. An auto-refill system keeps the SQUID cold between tests and overnight. It fills up the Dewar, approximately once per 7 hours. However, the stainless steel Dewar is not available in a large enough size to house more than a single SQUID and the required wiring. The only Dewar big enough was made of Styrofoam, instead of stainless steel with a vacuum between the layers. The hold time for the Styrofoam Dewar was only 3.5 hours from full to empty. To increase the hold time, 20 layers of thin (cryogenic) superinsulation were taped to the exterior of the Dewar. The hold time increased by 10% to almost 4 hours. However, this increased hold time was still far below the desired hold time of at least 8 hours (one workday). A glass Dewar was therefore necessary.

3.4 Single Axis Thermomagnetometry

Since the test system is repurposed from old equipment, the system is only capable of using a single SQUID. This system is designed to be solid state, so only magnetization in a

single direction can be measured. An initial test was run using a readily-available 7 mm-diameter pottery sample, given a uniaxial isothermal remanent magnetization (IRM) using a neodymium magnet in the laboratory. The sample was placed inside the oven (in contact with the thermocouple), and then the first test was run from room temperature to 600°C. The pottery was demagnetized from 45 mV to 20 mV (which corresponds to 0.66 nT to 0.293 nT, for this assuming the factory SQUID calibration of 67 mV/nT), but the SQUID's voltage change during the experiment was much higher (Figure 3-14).

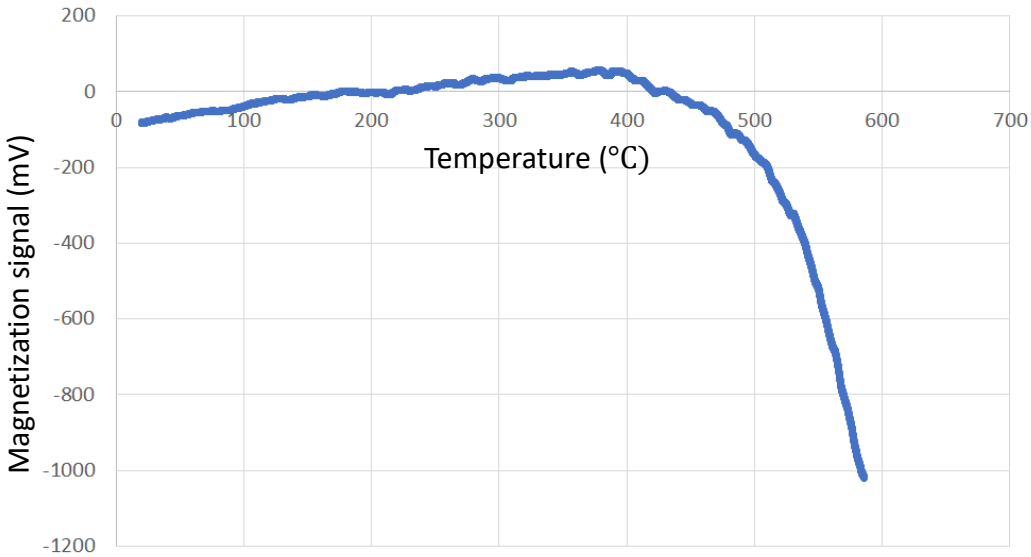

Figure 3-14 Raw pottery demagnetization curve.

The noise data (from the changing magnetic properties of the thermocouple) detailed in Figure 3-15 for the K-type (chromel) thermocouple were subtracted from the data in Figure 3-14. After this experiment, an R-type (platinum) and then an N-type (nicrosil) thermocouple were tested, and the noise experiments were repeated. The voltage output of an R-type thermocouple is quite low. Its output is approximately 6.7 mV at 700°C, significantly less than either the K-type thermocouple's output (approximately 29 mV at 700°C) or the N-type's output (approximately 24.5 mV at 700°C).

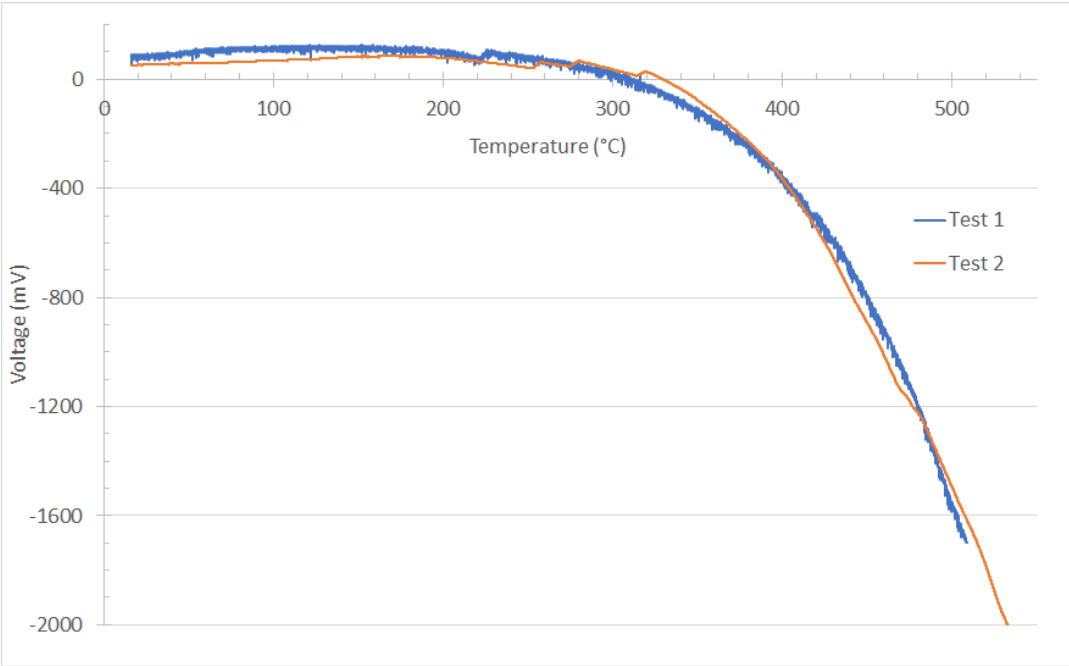

Figure 3-15 Two noise test examples

The signal drift was remeasured five times. An average noise curve was determined and then modelled Equation 3-5. Figure 3-16 shows the 95% confidence interval (3σ) of the noise.

$$y = \begin{bmatrix} -2 \times 10^{-8} & 1 \times 10^{-5} & -0.0029 & 0.4971 & -58.825 \end{bmatrix} \begin{bmatrix} T^4 \\ T^3 \\ T^2 \\ T \\ 1 \end{bmatrix}$$

Equation 3-5 Best fit curve for the signal drift, where T is the Temperature. The output (y) is in mV.

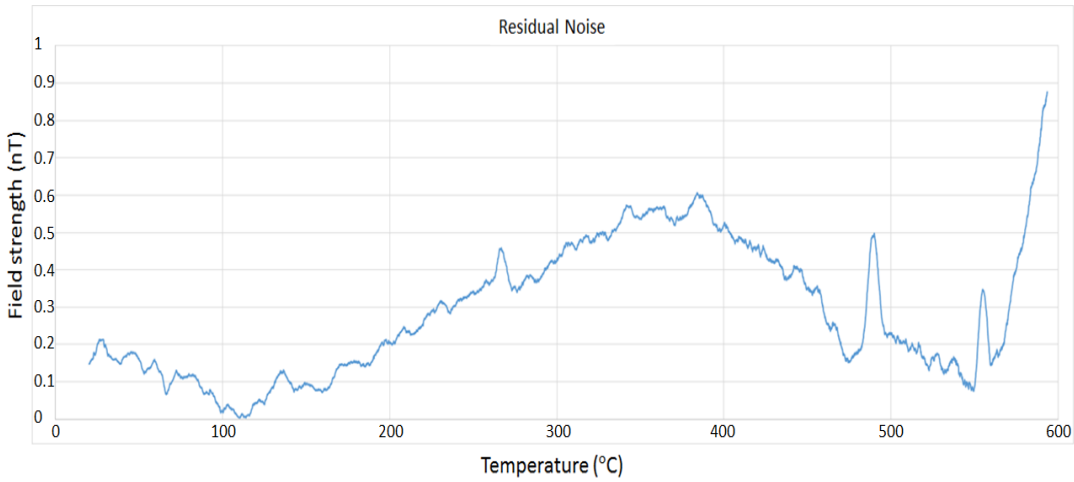

Figure 3-16 Residual noise after signal drift correction

To improve upon the signal to noise ratio, a 9-mm diameter basalt specimen was selected, heated to 600°C in a zero-field oven to fully demagnetize it, and then given a uniaxial isothermal remanent magnetization (IRM). To try to improve the precision of the temperature reading, and better hold the sample, a second quartz tube was used as a holder

for the basalt specimen. The basalt was then demagnetized from 1100 mV to 400 mV (SQUID raw output) in the test from room temperature to 600°C, as seen in Figure 3-17, with the thermal drift subtracted based on Equation 3-5. A second set of experiments with the same basalt given thermoremanent magnetizations (TRMs) was also performed.

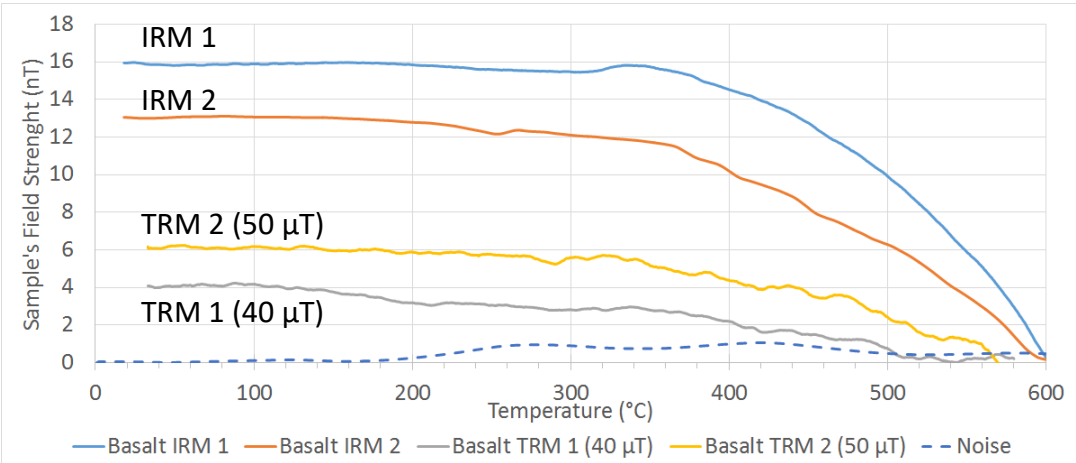

Figure 3-17 Basalt artificial TRM and IRM tests, corrected for thermal drift using Equation 3-5

The correction for the signal drift appeared to work sufficiently. A similar signal drift was observed with opposite polarity during a refill cycle of the Dewar. A likely cause of the drift is the formation of nitrogen bubbles in the reservoir, which cause the temperature of the SQUID to increase when they come into contact with it, as they rise to the top of the Dewar. Adding a layer of insulation between the oven and the Dewar decreased signal drift, but signal correction was still necessary.

The addition of the insulation layer changed the model, as the magnitude of the drift decreased. Since the prototype was undergoing continuous revisions, which changed the setup and required frequent SQUID recalibrations, it did not make sense to continuously create new noise models. Instead, a noise test was run before a given day's tests, if any changes had been made to the system. The principles behind the model stayed true and were helpful as a guide once the design reached later iterations.

3.5 Field Coil

3.5.1 Initial tests

Since demagnetization curves were now sufficiently measured, the next step was remagnetization curves. In order to do a paleointensity experiment, both demagnetization and remagnetization of a sample are required. To generate a known magnetic field, paleomagnetic ovens typically use a coil of wire to create a constant magnetic field at the location of the sample. Due to space constraints in the prototype, however, a typical

solenoid cannot fit around the specimen. Instead, a square coil of wire placed underneath the oven's shielding was used. The applied field is DC, so the oven's shielding does not affect the strength of the magnetic field. Owing to the small size of the sample used, having the coil only located below the oven gives an approximately (within 5%) constant field across the sample. The square coil also has an easily calculable field intensity and direction in the center. Figure 3-18 shows how the coil has been installed.

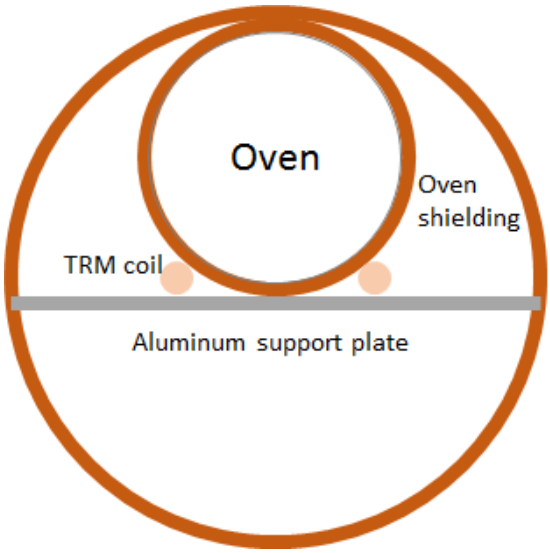

Figure 3-18 Oven housing cross-section with TRM coil installed. The oven's internal diameter is 10 mm.

The coil's remagnetization field also should not affect the measurements taken by the SQUID, as zeroing the SQUID removes any DC magnetic field effects. The drawback is that the SQUID must be reset any time the applied magnetic field is changed. The coil is simply set to the desired field, and then the SQUID is zeroed. The horizontal orientation of the coil means that the specimen can be inserted when the field is on or off. Initial tests showed background noise increasing from 20 mV (0.3 nT) to 200 mV (3 nT) with the field coil turned on, irrespective of the current passed through the coil. A choke was added to the circuit, designed to filter out any AC current that might be going through the system. The choke was large enough to remove 50 Hz mains AC current interference as well. The noise level, however, was unaffected. The wires leading from the power supply to the coil were then twined together and covered in aluminum RF shielding. The wiring changes reduced the background noise to 50 mV (0.7 nT), with the coil turned on. Shorting across the choke did not change the noise levels, so the choke was likely unnecessary and was removed to simplify the circuit.

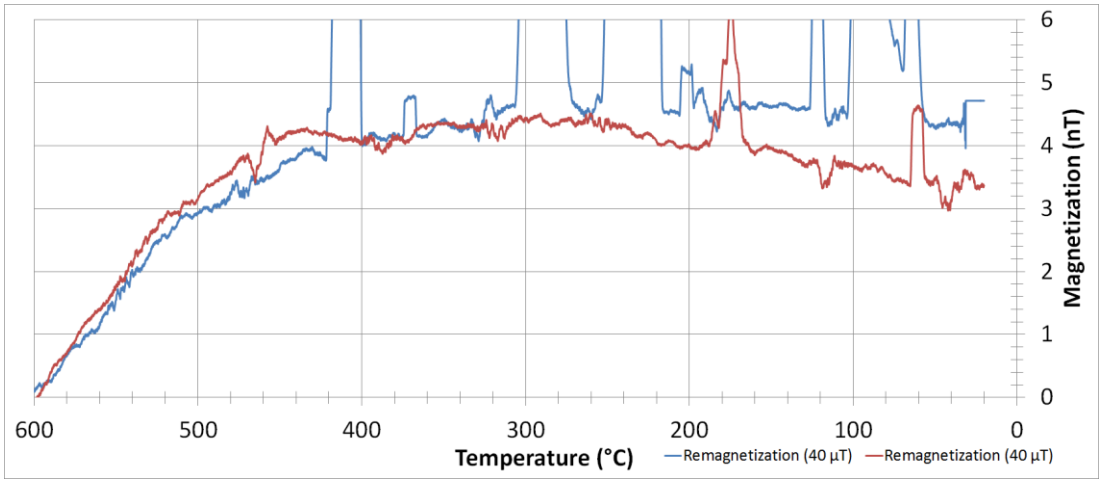

Figure 3-19 Remagnetization curves for 2 specimens. Both had a theoretical 40 µT field applied. The Y-scale is clipped to prevent the need for a logscale because the SQUID jump data are meaningless.

The initial remagnetization experiments, as observed in Figure 3-19, were run using the same 9 mm diameter basalt specimen as in Figure 3-17. These remagnetization experiments had significantly higher noise levels than the demagnetization experiments. The biggest source of error in the data were SQUID jumps, which appeared as sharp spikes in the measured magnetization (because the SQUID's output saturates). The SQUID then had to be manually reset, which in turn meant the data had to be manually moved to align with the pre-jump value. The magnetization values appear to be comparable to those of the 40 µT specimen in Figure 3-17. The 2 test specimens, however, both had very poor-quality data. One had at least 5 SQUID jumps and the other shows a decreasing magnetization after cooling below 200 °C. The most likely cause of the increased (non-SQUID jump) noise is from the DC current generator running the field coil. However, in principle, the specimen can be remagnetized, which was the goal.

3.5.2 Helmholtz coil

The initial coil design had high errors but largely were able to remagnetize the specimen. To improve the uniformity of the magnetic field across the specimen, it was decided to try to upgrade the coil to a full Helmholtz coil, placed around the sample and the SQUID sensor. Since the Helmholtz coil's field variation is much smaller in the desired area, it should cause less noise than the rectangular coil because of less variation over the volume of both the SQUID and the specimen. However, the radius of the coil was too small compared to the height required to get the oven and the SQUID inside the coil. Every time the coil was switched on, the SQUID was unable to stabilize, so it was decided to shelve the coil until a future design's geometry would allow it.

3.6 A more robust single magnetometer design

3.6.1 SQUID controller

After about 3 months of usage, the SQUID electronics pre-amplifier failed. The SQUID output dropped from ±5V to ±50 mV. The electronics, which had not been serviced in several years, were sent back to Jülicher SQUID GmbH for repair. The pre-amplifier was repaired, and the SQUID output increased to ±10V, as it should be. The data from before the repair appear to still be reliable, just with a lower clipping voltage, not systematically lower values.

To minimize the chance of potentially damaging the controller during the SQUID tuning process, the signal generator was upgraded to a GW Instek AFG-2005 Arbitary Function Generator. The signal generator has electronic, instead of analog, controls, which allow for more precise control of frequency (up to 5 MHz) and amplitude, limiting the potential for damaging the SQUID controller.

The National Instruments USB-6211 controller had a signal drift and noise level that appeared to be slowly increasing, until finally it stopped accepted analog inputs. A new 14-bit USB-6001 controller was purchased in its place. The controller has a comparable sensitivity (0.7 mV on a 10V scale) to the older model but is cheaper and smaller and has fewer inputs/outputs. With the new controller, the computer was also upgraded to a Windows 10 Core i3 computer to prevent any further RAM issues (as happened in Section 3.2.1.5).

3.6.2 Oven design 2: a robust failure

The initial oven design, while functional and proven to work, could be delicate, and its manufacture was time-consuming in order to get the counter-coils spaced properly. The other downside to the oven was that it was primarily handmade, instead of commercially available. Instead a 350W CoilHeater, made by Maxiwatt, was selected. The heating element uses a Nichrome heater wound back on itself, like the previous design, but is housed inside of stainless steel. The stainless-steel casing is slightly magnetic, so the goal of the initial tests is to determine if the effect is manageable. The heating element is also larger than the initial design, so the RF shielding also received a redesign because using only the outer shield, as seen in Figure 3-18, was insufficient shielding and caused SQUID jumps. However, the noise problem was rectified by moving the element at least 5 cm away from being directly below the SQUID sensor.

A thin-walled stainless steel vacuum flask (Dewar), with an outer diameter (OD) of 40.5 mm, was repurposed to function as the oven container. Figure 3-20 shows the updated oven container design. The quartz oven design was replaced with a brass oven, as a non-conductive oven is no longer required with the commercial heating coil. The opposite is now required, as the heating element is farther away from the sample and SQUID location. Between the brass oven and the RF shielding lies a piece of insulation and similarly between the RF shielding and the flask's interior wall. Due to the neck of the bottle being smaller than the bottle, this configuration gives the maximum amount of insulation and shielding possible to insert.

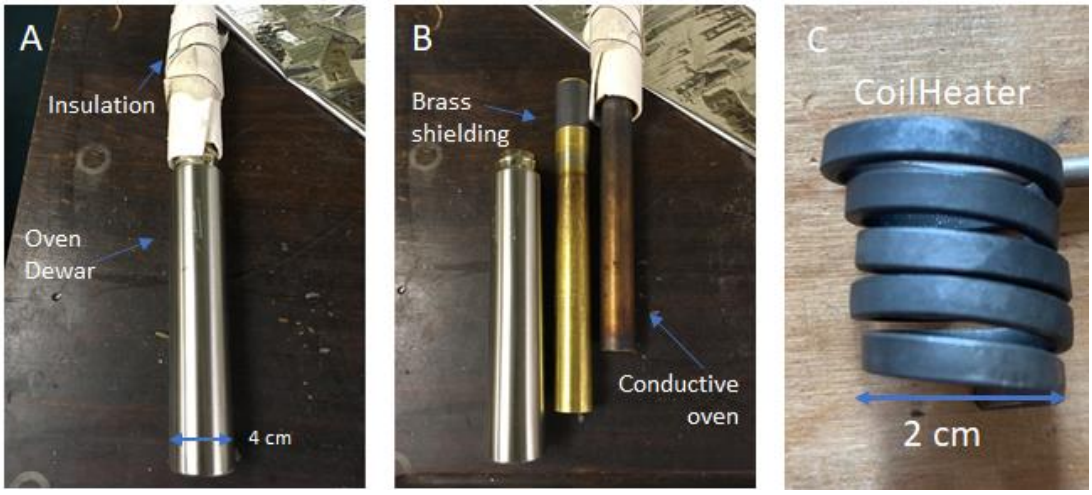

Figure 3-20 Shielded oven, inside a stainless steel Dewar flask. A: assembled. B: three part shielding. C: CoilHeater in isolation.

The heating element was coiled around a quartz tube and attached the same insulation as the previous oven to the outside of the oven. The heater is designed to work with a 220V power source, so a transformer was used to step up the voltage output of the audio amplifier by a factor of 3.3 for proper operation. The new heater successfully reaches 600°C at a frequency of 35 kHz and 700°C at a frequency of 28 kHz. These are lower than the previous oven's 40 kHz, but with insulation and transformer improvements, a more comparable frequency will be attainable. The new oven also shows less overshooting of set temperature in the initial tests.

With the higher wattage available from the new coil, the coil was moved farther from the SQUID and sample location (up the quartz tube) to try to minimize electrical noise (inside the visible insulation in Figure 3-20). This insulation was necessary because, upon moving the coil away from the specimen zone, a large temperature gradient formed, which can be seen in Table 3-10. The insulation improved the amount of heat penetrating down into the Dewar, but a large amount of heat still dissipated above the Dewar.

Table 3-10 CoilHeater temperature gradients

Distance from heating coil (cm)	Initial test- no added insulation Temperature (°C)	Second test- insulated design (Figure 3-20) Temperature (°C)
0	647	633
2	637	605
4	577	510
6	484	447
8	411	407
10	336	-
12	288	336
14	-	305
18	-	284
22	-	271

After a few tests with the CoilHeater, there were several problems- the biggest of which was associated with the transformer. The only transformers available with a high enough wattage rating (>800W) were designed to step down voltages- from 240V to 33V, for example. Thus, the transformer was running in the reverse direction. The transformer began to fail to step up the voltage as desired, and eventually the CoilHeater shorted. Once this happened, there was extensive feedback in the circuit and the audio amplifier was damaged.

3.6.3 Oven design 3: shedding light on the problem

Since the CoilHeater required both high voltages and high AC frequencies, the circuitry required was very non-standard, which was a main cause of the failure. Moving the heating element away from the specimen appeared to still be the favored method because the effect on the SQUIDs from the mere presence of the heating wire was still not fully understood. Two other options were proposed: using a non-electronic heat source or using infrared (IR or thermal) radiation. These options were explored while the 2 additional SQUIDs were being built.

One readily available non-electronic heat source was a blow torch, but the geometry of the system and the materials used did not lend themselves well to an open flame. Instead, IR radiation to heat the specimen was attempted.

Initial tests were run using (half of) an old 250W SpotIR heater. The full SpotIR heater has the bulb at one focus of a reflective ellipse and a specimen at the other focus. Only the half of the ellipse with the light bulb was used, so the light emitted was less focused than the original design (which can melt rocks). The heater was placed inside of a 1 cm inner diameter (ID) quartz tube, with aluminum foil wrapped around its outside. The high reflectivity of the

aluminum foil helped focus the radiation down the quartz tube (inner diameter of 12 mm). However, this initial test setup had no method to focus the radiation at the specimen. At a distance of 12 cm from the bulb, the maximum temperature the specimen reached consistently (before the rate of increase dropped below 10 ^{o}C/min) was 440 ^{o}C, well below the 580 ^{o}C required for magnetite, which is the minimum design specification. These initial tests were run without the Eurotherm controller included in the circuit. As a result, the sample heated up rapidly at first but then slowed exponentially, effectively following the inverse of Newton's Law of Cooling because the specimen heated by radiation, instead of cooling by radiation. These initial tests proved promising and the potential to move the heat source far from the SQUIDs was clear.

The 250W G4 Halogen lightbulb was then replaced with a 500W GY9 lightbulb to increase the power of the oven. The GY9 form factor is a much more common size, so the lightbulb is much cheaper but also much larger. In order to fit the lightbulb inside the oven tube, the tube's inner diameter was increased to 3 cm and switched from a quartz tube to a polished aluminum tube. Another advantage to this type of halogen bulb is that it is powered from the mains, so no signal generator or amplifier is required; however, the RF radiation resulting from the power supply might cause issues due to its relatively proximity to the SQUIDs.

The initial tests used an aluminum tube, which dulled easily, reducing the reflectivity of the interior of the tube, which causes the tube to heat up instead of the specimen. Using this set up, the 500W light bulb successful heated the test specimen to 480 ^{o}C. However, a cooling system was required for the lightbulb to function properly. As with the original oven (Section: Constructing the oven), a desk fan was used as the initial cooling system, and it proved to be sufficient to keep the lightbulb working for the duration of the test, even inside the tube. The lightbulb was then upgraded to a 650W GY9 lightbulb and a vacuum pump was installed (in reverse) to blow air across the higher power bulb. Because of the more powerful light bulb and the dulled aluminum tube, the heat from the bulb melted the aluminum tube, which can be seen in Figure 3-21. The design required the use of a non-magnetic Inconel (non-magnetic stainless steel) tube, which can be made with a high reflectivity, and has a melting point around 1400 °C, substantially higher than of aluminum (660 °C).

Figure 3-21 650W lightbulb heated the sample above 500 °C, but also heated the tube (locally) above 660 °C.

3.7 LabVIEW Control Software

LabVIEW was selected as the control system for the magnetometer, as it is designed for data collection and input/output control. Each control subsystem was designed and coded separately initially, but with the intent for them to be merged. The language is graphic, both on the user interface side and in the background, so combining each controller is simpler. The program design specifications are listed in Table 3-11.

Table 3-11 Control System Requirements

Requirement	Input	Output	Subsystem
Heat the oven up to 700 °C with ±0.5 °C precision	Temperature from thermocouple, desired temperature	Turning on/off current to heating coil	Oven; Eurotherm thermal controller
Cooling system – protect SQUID	None	Fan or water cooling, and vacuum /insulation	Oven
Cooling system – cool sample after measurements	Thermocouple	Fan or water cooling	Oven
Atmospheric flushing	User command	Argon flush	Oven
Single-axis magnetic field application	Desired field	Turn on magnetic coil	Magnetic coil
Triple-axis magnetic field measurement	SQUID data	Real-time graph and downloadable matrix of data	SQUID

3.7.1 Single-Axis Control Program

The initial LabVIEW program was designed only for data recording, so everything else had to be done manually. A 16-bit National Instruments USB-6211 data acquisition module was used to read the thermocouple and the SQUID's output data. The Eurotherm controller's temperature and heating rate were manually set, but the heating was otherwise done automatically. The control program version 1.1 was the first used for full range tests. It recorded the SQUID's output and the thermocouple and allowed exporting of the data into Excel. No active cooling system was implemented in the hardware, so no cooling was included in the software. The magnetic coil was controlled manually by the user.

Table 3-12 LabVIEW control program v1.1

Requirement	Method
Heat the oven up to 700 °C with ±0.5 °C precision	Eurotherm controller with temperature and rate set by user
Cooling system – protect SQUID	Not implemented; Vacuum Dewar + insulation
Cooling system – cool sample after measurements	Not implemented
Atmospheric flushing	Not implemented
Magnetic field application	Single-axis coil turned on manually by user and SQUID reset
Triple-axis magnetic field measurement	Single axis SQUID recorded by program, real time data and downloadable matrix

3.8 Conclusions and implications for the 3-axis design

Having tried several different oven designs, the most promising designs were those incorporating the lightbulb. The high-precision ovens, modelled after those from the VFTB, worked well, but the need to thermally control them and their inherent fragility made them less robust than the other designs tested. The lightbulb oven proved to be the most robust and required only minimal control systems and circuit design. A lightbulb oven was selected for implementation in the three-axis design. To separate the oven from the SQUIDs, the thin-walled stainless steel Dewar from section 6.2 was used, with internal insulation to heat in for the sample. The SQUIDs would need to sit as close to the wall as possible to maximize the signal from the sample. Using a Helmholtz coil for remagnetizing the sample is possible, but it depends heavily on the geometry of the oven and SQUIDS. The LabVIEW single-axis program, which worked well, was selected to be extended to accommodate three SQUID inputs and a temperature input. The heating curve for the specimen can be established using the lightbulb oven so that a direct PID controller would be unnecessary.

3.9 References

Draeger, U., Prevot, M., Poidras, T., and Riisager, J., 2006, Single-domain chemical, thermochemical and thermal remanences in a basaltic rock: Geophysical Journal International, v. 166, no. 1, p. 12-32.

Enculescu, I., and Iliescu, B., 1997, Electrical conductivity of quartz crystals: Crystal Research and Technology, v. 32, no. 7, p. 879-891.

Shaw, J., 2010, Comment on "A new high-precision furnace for paleomagnetic and paleointensity studies: Minimizing magnetic noise generated by heater currents inside traditional thermal demagnetizers" by Zhong Zheng, Xixi Zhao, and Chorng-Shern Horng: Geochemistry Geophysics Geosystems, v. 11.

Zheng, Z., Zhao, X. X., and Horng, C. S., 2010, A new high-precision furnace for paleomagnetic and paleointensity studies: Minimizing magnetic noise generated by heater currents inside traditional thermal demagnetizers: Geochemistry Geophysics Geosystems, v. 11.

CHAPTER 4 PROTOTYPING A NOVEL THREE-AXIS CONTINUOUS SQUID MAGNETOMETER SYSTEM

4.1 Overview

In this chapter, the prototype three-axis continuous magnetometer is presented. The three-axis magnetometer is an extension of the single-axis magnetometer. In order to get the full vector field of a specimen's magnetization without rotating or vibrating the sample, at least two SQUIDs must be used. By using three SQUIDs, the resolution of the directional data is increased; having three SQUIDs additionally avoids the explicit need for setting the SQUID sensors at an angle, as would be necessary with two SQUIDs. An angled SQUID design was eventually selected, however, as noted in Section 4.2.2, for compatibility with a solenoid remagnetization coil. The F.I.T. system shell described and used in the previous chapter was too small to fit three SQUIDs, and the horizontal loading made the SQUID geometry necessary for three-axis data more difficult. Therefore, this chapter focuses less on oven design and more on the electronics as well as the shielding. The three-axis prototype in this chapter lacks any remagnetization data, as the temperatures reached were insufficient for a full paleointensity experiment. The best parts from the design of the three-axis continuous magnetometer described in this chapter formed the basis for the design of the three-axis step-wise magnetometer described in Chapter 5.

4.2 Shielding and SQUIDs

4.2.1 Shielding design

The geometry for the F.I.T. system does not allow for multiple SQUIDs, so the entire system was redesigned. A two-layer Mu-metal shield with an outer diameter of 40 cm and height of 88 cm was supplied by Magnetic Measurements Ltd as the housing for the magnetometer, which can be seen in Figure 4-1. The inner shield has a diameter of 35 cm, which creates an overall shielding factor of ~45,000 in the radial direction. The ambient magnetic field of the magnetometer in the (least shielded) $\hat{z}$ direction (along the cylindrical axis) was measured and is plotted in Figure 4-2. Between the shields are foam spacers. The two shields are grounded to each other. Inside the inner shield sits a glass liquid nitrogen Dewar, with an inner diameter of 20 cm. This diameter was necessary to fit the inner, thin-walled stainless steel oven Dewar (4 cm outer diameter) and the SQUIDs. The SQUID's wires contain a waveguide, which could break if bent, and thus require a large radius of curvature.

The space between the Dewar and the inner shield is filled with non-magnetic expanding foam to ensure the glass Dewar is positioned correctly and damped against movements.

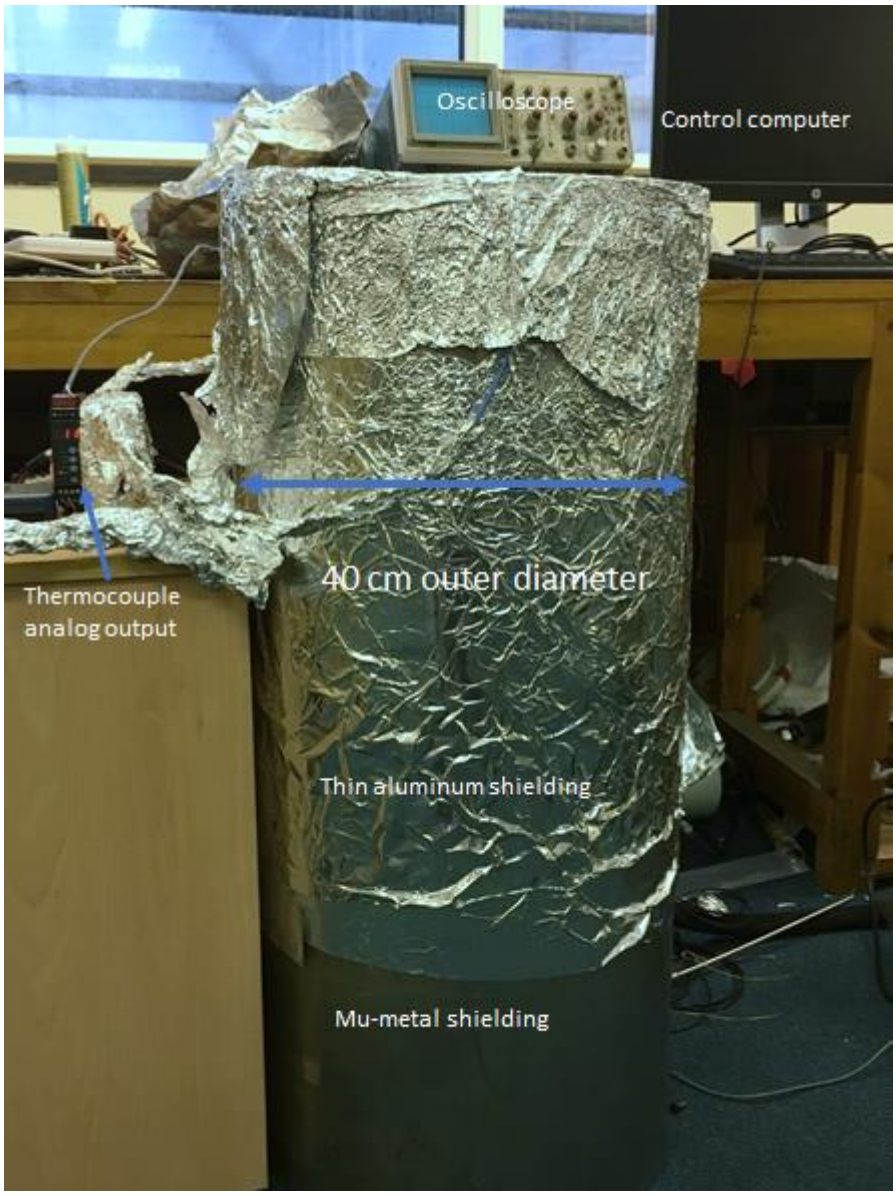

Figure 4-1 Exterior of magnetometer system.

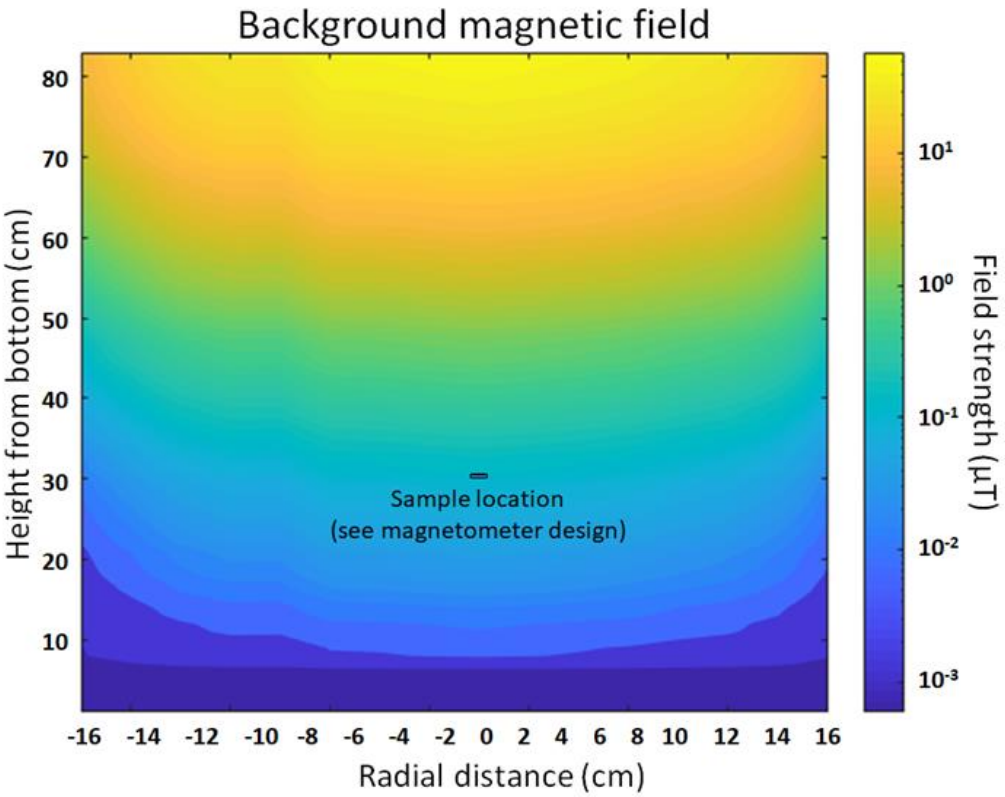

Figure 4-2 Ambient magnetic field in the $\hat{z}$ direction inside the mu metal shield.

On the outside of the shield is a layer of thin aluminum RF shielding. Just above the top of the glass Dewar, inside the inner magnetic shield, is a 4 mm thick aluminum plate, which is connected and grounded to the inner shield using 3 brass set screws at 120° to each other. An annotated photograph and schematic diagram of the aluminum top plate can be found in Figure 4-3. The aluminum plate also functions as a thick RF shield for the SQUIDs, but the holes required for the oven, the liquid nitrogen auto-fill system, and nitrogen gas vent create gaps in the RF shielding.

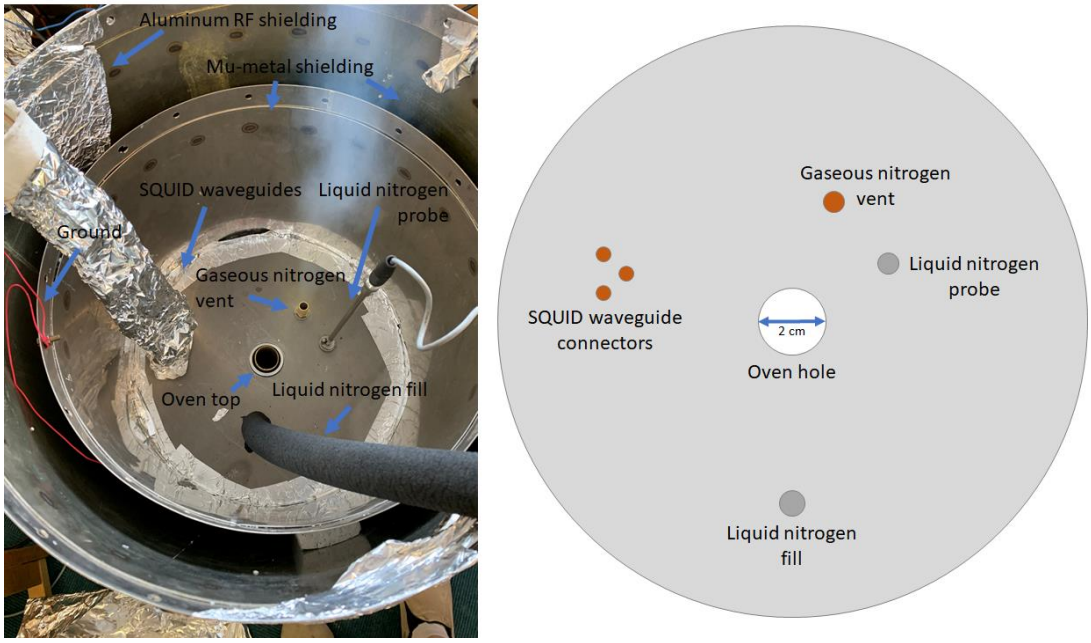

Figure 4-3 Aluminum top plate in-situ (left) and design (right)

The plate has seven transverse holes in it. The SQUID waveguide connectors, the liquid nitrogen probe, and the liquid nitrogen fill nebulizer are all metallic, so the holes in the top plate still block RF radiation. The gaseous nitrogen vent does not have a metallic plug, so the vent has the highest permittivity for RF radiation. A rubber O-ring separates the top of the oven Dewar from the aluminum top plate to prevent a grounding loop from forming, which would prevent SQUID operation.

Above the aluminum top plate sits a layer of thermal insulation to maintain a constant temperature for the SQUID waveguides. At the top of the outer shield sit an additional two layers of aluminum shielding (foil) that are connected to a single layer of cylindrical aluminum shielding (which can be seen in Figure 4-1). The top layer of aluminum shielding has a limited number of times it can be used (taken on and off) because when the shielding gets handled, small fractures form that disrupt the continuity of the shielding.

4.2.2 SQUIDs

Two additional RF SQUIDs were purchased from Jülicher SQUID, GmbH, with identical specifications to the SQUID described in the previous chapter. To control these SQUIDs, an old Jülicher two-axis computer-controlled SQUID controller available in the laboratory was used. The first channel on the controller is a standard magnetometer, but the second channel can also be used as a gradiometer. For this system, both channels are connected to SQUID magnetometers. The controller connects to the computer using an RS-232 port and was packaged with a proprietary control program that can tune the SQUID automatically. The computer generates the triangle waves required for tuning and then the parameters of

the voltage-controller amplifier and oscillator, which affects the tank (LC) circuit, are adjusted; example tuning curves can be found in Figure 4-4.

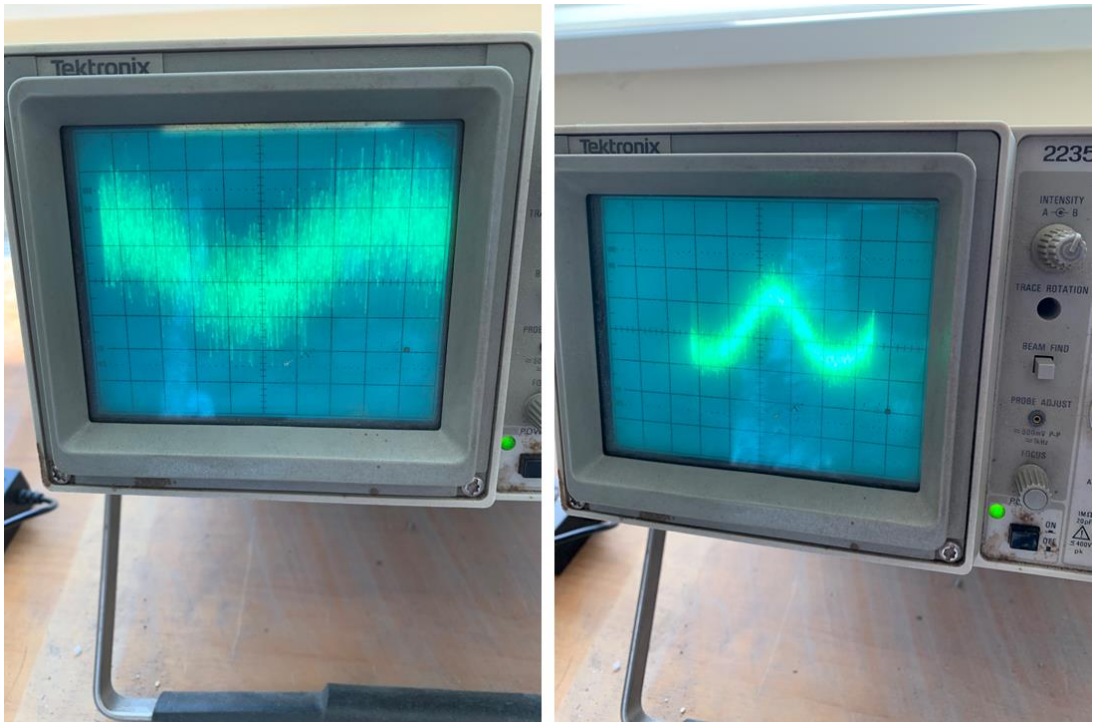

Figure 4-4 Tuning curves for two-axis computer-controlled system's gradiometer (left) and magnetometer (right). The scale is 0.5V; only the relative amplitude of the curves is relevant to the tuning process.

Channel 2, whose elections can also function with a SQUID gradiometer, is more sensitive to magnetic field gradients than channel 1. The SQUIDs thus need to be as low in the shield as possible, since the open top creates a magnetic field gradient in the Z-direction. The third SQUID continues to use the manual controller and behaves as before. The gradiometer feature of channel 2 is not used herein; the electronic box was inherited.

The SQUIDs are held in a 3D-printed onyx resin holder designed in AutoCAD that sits at the base of the glass Dewar (see Figure 4-5). The 3D-printed holder keeps the base of the oven Dewar 8 cm from the base of the glass liquid nitrogen Dewar and holds the SQUIDs 4 cm from the base of the oven Dewar. Spikes were placed at the top of the holder to create sites for the preferential nucleation of nitrogen gas bubbles to keep them away from the SQUID sensors. Inside it sits the oven Dewar, with the three SQUIDs equally spaced in a circle at a 30° angle to the horizontal. The mid-points of the SQUID sensors lie 3.14 cm from the center of the oven. The (design) minimum input on the USB-6001 National instruments data acquisition controller implemented in Chapter 3 is 0.7 mV, which means the minimum magnetic field that can be measured is ~3.48 pT, which is well within the sensitivity limit of the Jülicher SQUIDs (30 fT/√Hz). This arrangement means the minimum specimen moment

that is able be reliably measured is 1.08 nAm^2 (86 mA/m for the 8 mm specimen). The data from the three SQUIDs must then be deconvolved to extract the desired XYZ data. The SQUIDs are then connected to pass-through coaxial cable connectors in the aluminum top plate. A second set of coaxial cables runs from the top of the top plate to the SQUID controllers.

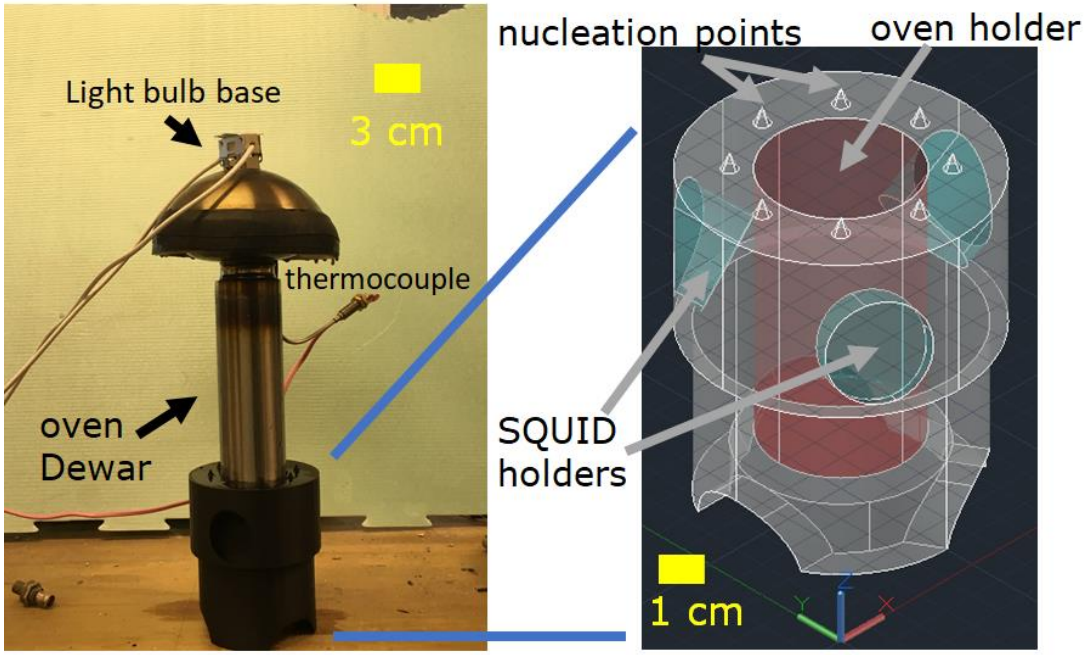

Figure 4-5 SQUIDs set up around oven

4.3 Oven

Of the three oven designs tested and described in the previous chapter, only one appeared viable: the lightbulb oven. The oven *in-situ* and a cartoon of its design can be found in Figure 4-6. A thin-walled 2.5 cm diameter Inconel tube sits inside the oven Dewar and extends 3 cm above the aluminum top plate. An 800 W lightbulb sits at the focal point of a polished hemispherical stainless-steel shell, just inside the top of the Inconel tube. Around the Inconel tube, at the top of the aluminum plate, sits a flat-bottomed, polished stainless-steel bowl. The two stainless steel bowls help redirect the light from the lightbulb down the Inconel to the sample inside the oven Dewar. The distance from the light bulb to the specimen is 8 cm. The lightbulb and stainless-steel pipe have diameters of 2 cm and 2.5 cm, respectively. The lightbulb sits 1 cm below the base of the stainless-steel cap, with the lightbulb defined as one focal point of the ellipse. With these dimensions, the eccentricity of the ellipse required for the specimen to sit properly at the other focal point was: $e \approx 0.95$. With an eccentricity this high, it was decided to forego trying to make an ellipse and instead

to opt for just the simple straight tube. The problem, however, with this approach is that nearly all light is absorbed by the top of the specimen. Therefore, the specimens used had to be thin disks (tested height: 5 mm) but could have a diameter up to 2 cm.

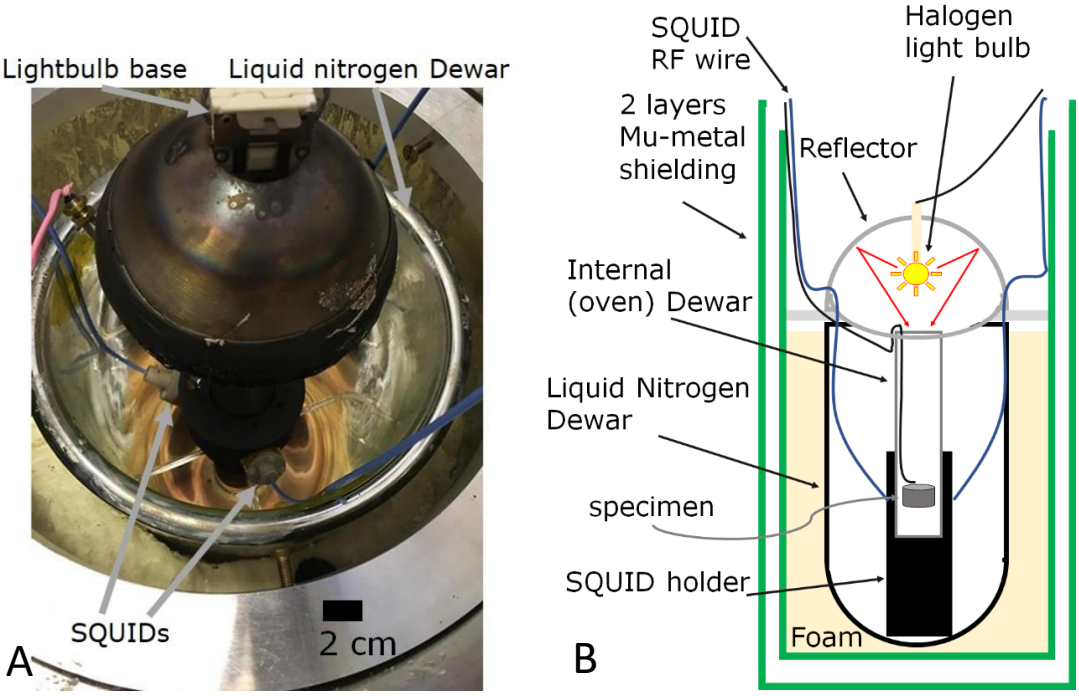

Figure 4-6 Lightbulb oven design. A: in-situ image. B: Cartoon of the interior (not to scale)

Temperatures were measured using a low Curie temperature N-type thermocouple, placed on the top of the specimen. For this type of heating, large thermal gradients can form if the specimen used is thicker than a few mm. The lightbulb set up was not capable of reaching the required 700 °C temperature. A maximum temperature of 600 °C was reached using the 800 W lightbulb at 85% voltage (nominally ~200V). This was experimentally determined to be the safest maximum operating voltage. At voltages above 90% of the maximum (nominally ~215 V), the lightbulbs would explode inside the system. Figure 4-7 contains a naturally s-shaped heating curve and decaying exponential cooling curve for the lightbulb oven system up to/from 530 °C.

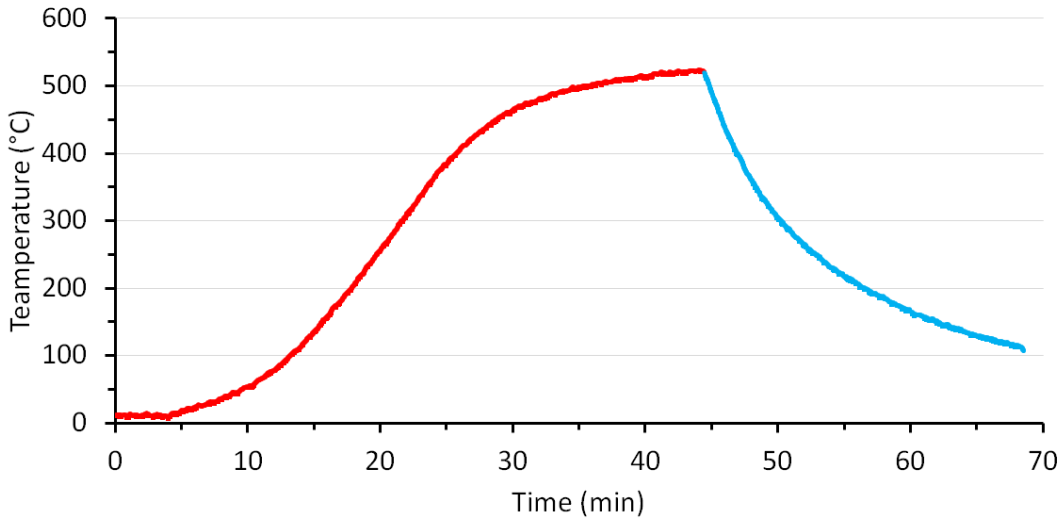

Figure 4-7 Lightbulb oven heating and cooling curve

The halogen lightbulb has an operating temperature above 400 °C, so heat leaks from the oven container out into the space above the top plate. The insulation around the SQUID wires protects them well; the insulation did not appear to heat up enough to oxidize the insulation during normal operation. The lightbulb runs off the mains power supply, using 50 Hz 240V, which creates a large amount of low frequency (long radio wave) electromagnetic radiation. The aluminum top plate filters out some of the RF radiation, but not all of it. As a result, a cyclical noise pattern was observed during SQUID operation, as shown in Figure 4-8. The 50 Hz frequency is out of phase with the sampling rate of the USB-6211. Three moving averages were tested (10, 50, and 100 data points) to filter out the noise.

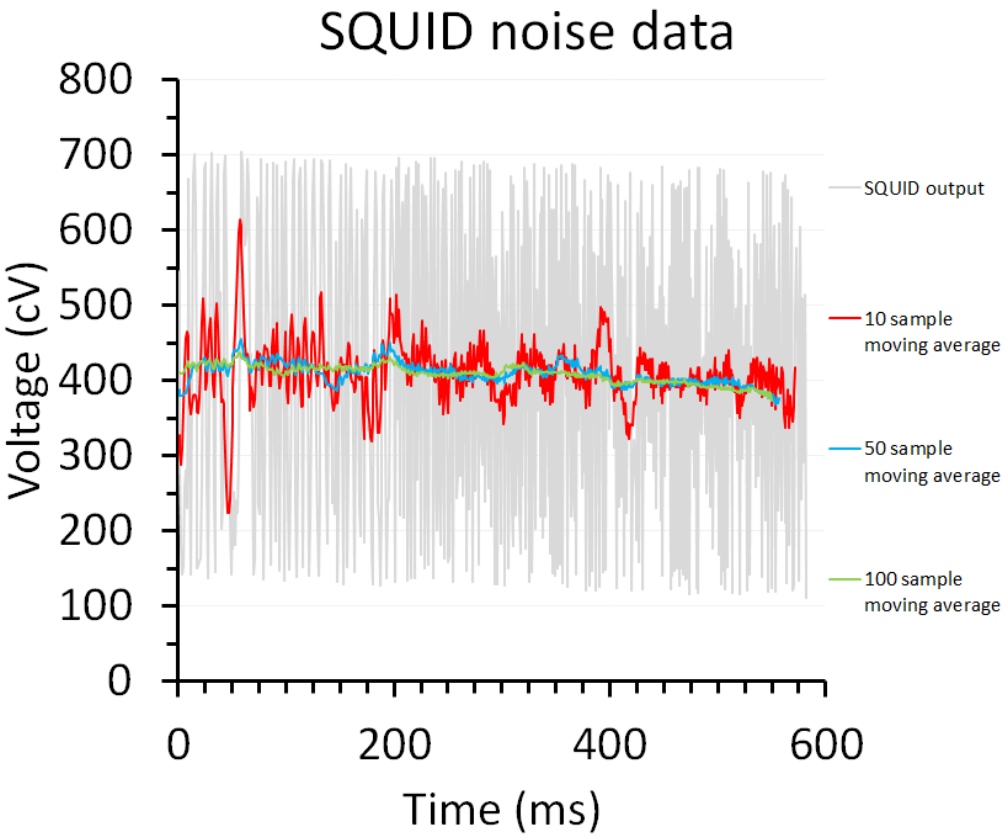

Figure 4-8 SQUID oven noise data for 240V, 650W light bulb. The signal to noise ratio is high, but the pattern and frequency mean it can be filtered out to provide useable data.

4.4 Control program

The three-axis continuous control program is based on the single-axis control program implemented for the single axis magnetometer described in the previous chapter. This program also requires that the SQUIDs be pre-tuned. The USB-6211 device has 4 Analog Input channels: one for each SQUID channel and one for thermocouple data. To maximize the data quality from the thermocouple, the data were first conditioned using an EYC analog output signal conditioner. The voltages were changed from 0 ~ 30 mV to 0 - 10 V, scaled linearly from -50 to 750 °C, such that 1 °C = 12.5 mV. The SQUID data was read directly from the SQUID controllers' outputs. Figure 4-9 contains the user control and the underlying LabVIEW code for the control program.

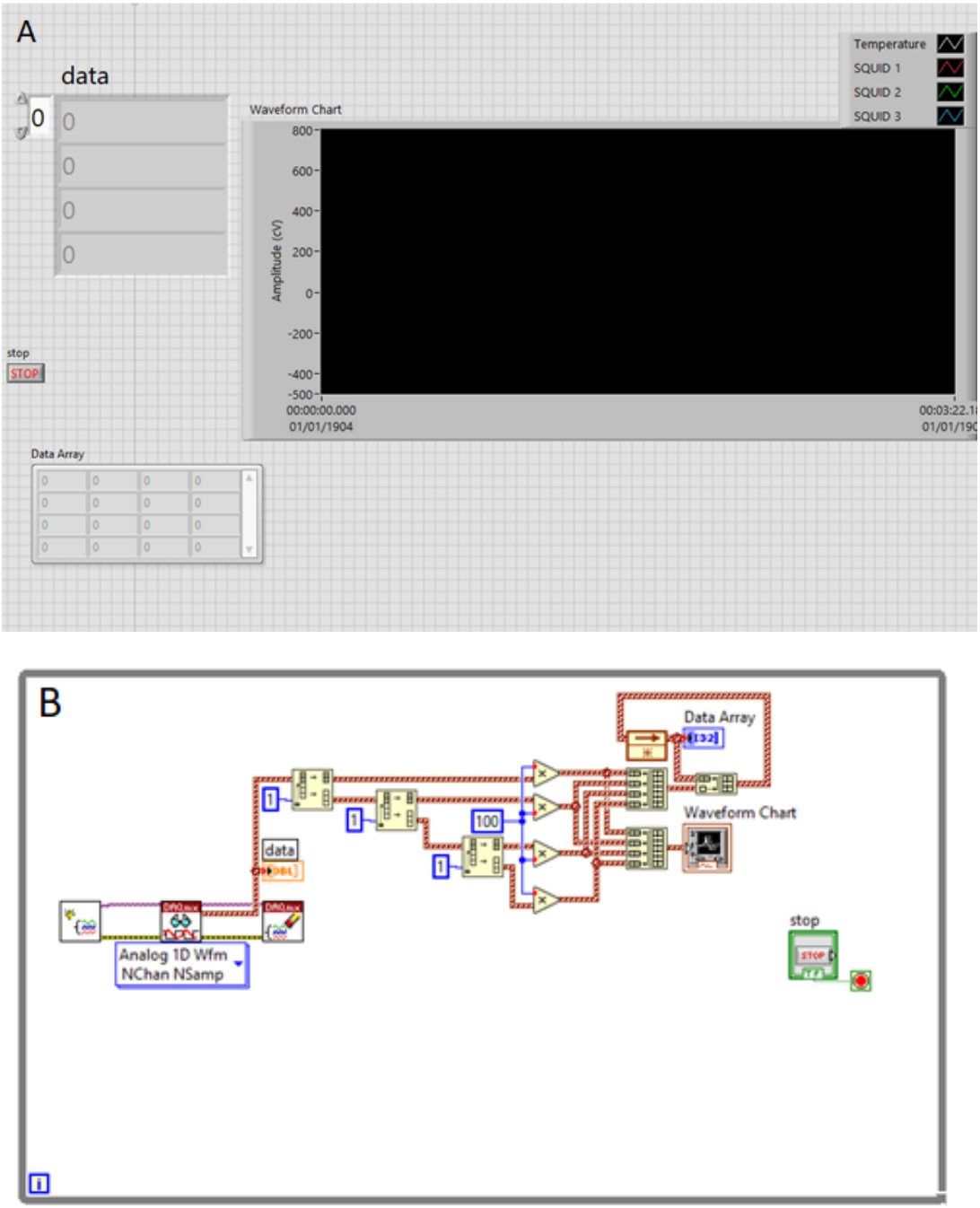

Figure 4-9 LabVIEW user interface (A) and underlying data collection code (B)

The incoming data are displayed to the user in the array on the left side of the interface screen. The data are then plotted as voltages on the waveform chart on the right side of the screen. The program saves the data in a 4-column (temperature, SQUID 1, SQUID 2, SQUID 3) comma separated values (csv) file format. The array of these data can be seen being populated on the lower part of the screen. Table 4-1 contains a summary of how this program implements the requirements outlined in the previous chapter.

Table 4-1 LabVIEW control program v1.1

Requirement	Method
Heat the oven up to 700 °C with ±0.5 °C precision	800W lightbulb heats up specimen in L-shaped curve to 600 °C without any input needed.
Cooling system – protect SQUID	Not implemented; Vacuum Dewar + insulation, manual air pump control
Cooling system – cool sample after measurements	Not implemented
Atmospheric flushing	Not implemented
Magnetic field application	Manually switched solenoid coil
Triple-axis magnetic field measurement	Three SQUIDs recorded by program, real time data and downloadable matrix

4.5 Operation

The prototype magnetometer described thus far in this chapter requires extensive manual operation, more than the original design plan calls for (see Table 3-1). The SQUIDs are tuned manually, the cooling is passive (following Newton's law of cooling), and the lightbulb is turned on/off manually.

Once the SQUIDs are tuned (either manually or using Jülicher's program), the program is initiated, and the oven is turned on at 85% voltage. Heating of the specimen begins immediately. As was seen in Figure 4-7, the heating begins slowly and then speeds up. After about 10 – 15 minutes of heating, the temperature reaches the vicinity of 200 °C. During this time period, the SQUIDs are consistently stable. Over the next 10 minutes, the SQUIDs' offset begins to drift away from the lowest energy state. The drift can initially be corrected for up to around 300 °C, but beyond this temperature, the SQUID retuning occurs too frequently to allow for sufficiently stable operation without losing significant amounts of data. As a result, the output data were unreliable.

The most readily apparent cause of the drift is the increased temperatures in the cavity above the aluminum plate, where the lightbulb is located. Thermal insulation was added around the SQUID waveguide wires to minimize temperature changes across them. The temperature of the waveguides initially varies from -196 °C inside the liquid nitrogen bath to room temperature (~20 °C) above the aluminum plate. The waveguides can, therefore, handle temperature gradients across them. A simple increase in temperature cannot be the only reason for drift at higher temperatures; but changing temperature gradients across the length of the wire above the aluminum plate have the potential to cause the observed drift.

When temperatures are kept constant, the SQUIDs can remain stable for around 10 minutes before they jump to a new energy state and have to be reset. The SQUIDs can then remain stable again if the temperature has not changed. The SQUIDs themselves can handle the oven's temperatures changing, which was shown in Chapter 3. However, after the SQUIDs jump, the optimal RF frequency can change as a result of changing inductance in the LC tank circuit. When the optimal frequency exits the local minimum (energy well), a full re-tuning is required for continued operation, which is not possible during heating operations with the current design. It is possible that a fully-computer controlled design could handle the retuning with minimal loss of data fidelity, but the scope of such a system is beyond that of this thesis.

Some data were able to be collected and are reported in Figure 4-10. The specimen was given an IRM and loaded such that the magnetic direction is expected to be declination (dec) = 270°, inclination (inc) = 80°. The data are presented as a function of time for the SQUID instability to be more apparent, as these instabilities generally occurred as a function of time, not of temperature. Since there exist XYZ cartesian data, an orthographic projection of the vector can be created. An example of one in the Zijderveld style can be found in Figure 4-11. After each SQUID jump (which appear as the dips in the data), the data have a tendency not to return to the same reading, and since the slope is changing continuously, any correction would be inherently inaccurate.

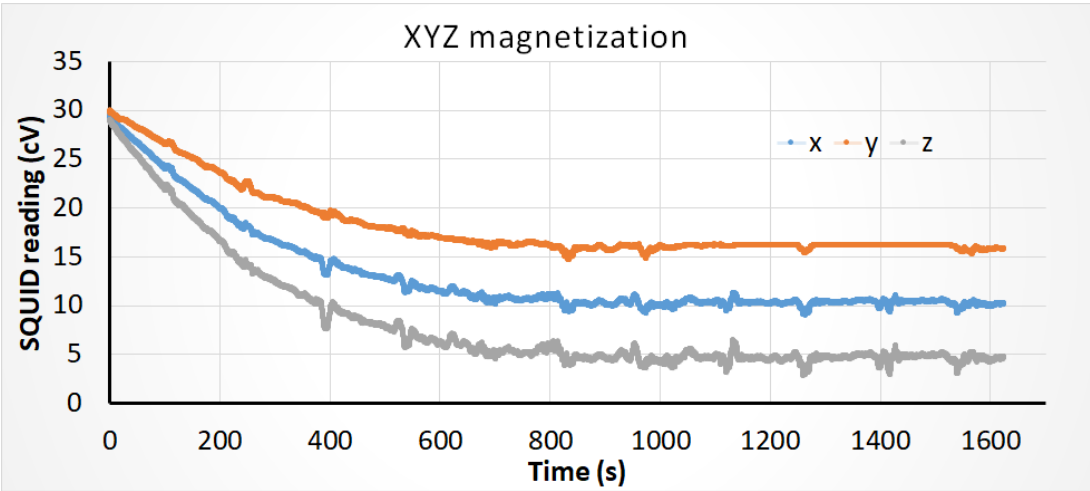

Figure 4-10 XYZ magnetization data example test as a function of time during heating of the specimen under a 800W halogen lightbulb.

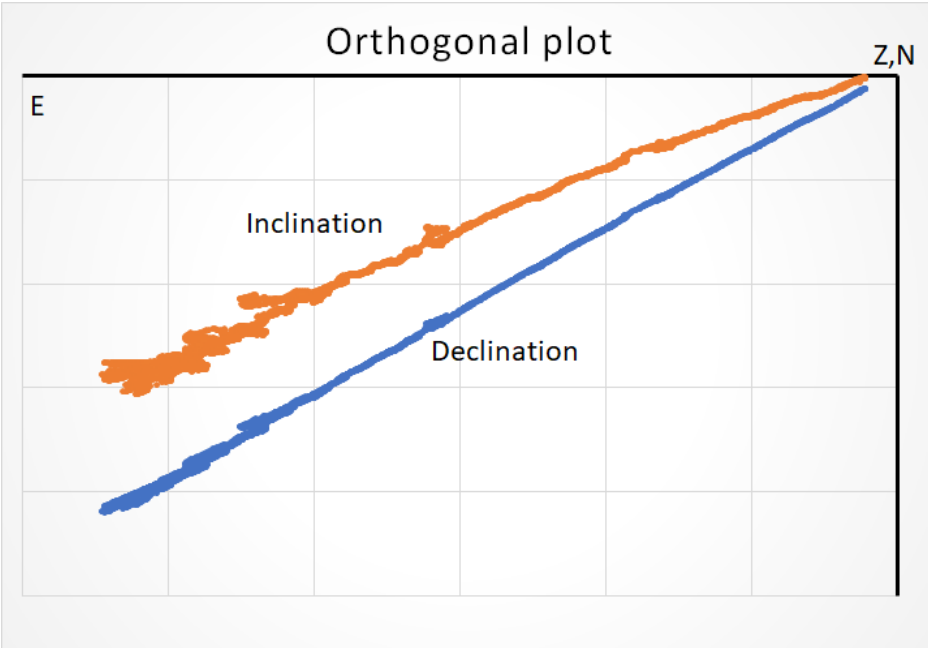

Figure 4-11 Orthogonal Plot in the Zijderveld-style based on XYZ data collected in previous figure (arbitrary units).

The data in Figure 4-11 are largely single component. The inclination data is extremely noisy at the lower temperature steps, and the loop at intermediate temperatures in the inclination line implies the possibility of a second magnetic component or a change in magnetic carrier mineralogy. However, since the rock was demagnetized and then given an IRM, the data should only show a single component, which is the case in the declination line. The resulting direction of the magnetic field is dec = 243°, inc = 70°, an error of 12°. The error is larger than desired, but it serves as an initial proof of concept.

4.6 Conclusions

The Mu-metal shield and oven behave as desired, keeping the background field below 100 nT at the specimen and SQUIDs' depth. The oven design works as desired, with a maximum temperature approaching 600 °C, and a noise profile that can be managed. Both the SQUID controllers work consistently, and the SQUIDs have sufficient RF shielding. The control program and USB-6211 have sufficient resolution and processing speed for all necessary data collection.

The issue herein, however, is the stable operation of the SQUID magnetometers. Other magnetometer systems using SQUIDs only require the SQUIDs to stabilize for the short period of time required to measure the specimen's magnetic field. SQUIDs are not designed to be used continuously for the long-term, continuous measurements required for paleomagnetic

surveys, in part due to their narrow superconducting temperature range. The only commercially available, cost-effective product capable of continuous magnetic recording at the sensitivities required for paleomagnetic surveys are fluxgate magnetometers. The system is therefore limited to running in continuous mode for specimens with a Curie Temperature below 300 °C. The design of the system is sound; however, to get the temperature to 600 °C or higher, the only option remaining is to limit SQUID usage to short periods of time by doing stepwise heatings.

CHAPTER 5 PROTOTYPING A NOVEL THREE-AXIS STEPWISE MAGNETOMETER SYSTEM

5.1 Overview

In this chapter, the process by which the prototype three-axis continuous magnetometer was transformed into a stepwise magnetometer is described. The previous two chapters have demonstrated that, although a SQUID-based continuous magnetometer can work at lower temperatures, the design is too unstable for paleointensity experiments performed on specimens containing mineral phases with higher Curie Temperatures. SQUIDs in other magnetometers are used for only short periods of time; their control systems therefore only have to maintain its stability for under a minute. The SQUIDs in the magnetometer described in the previous chapter were generally able to stay stable for time periods of this length, which was insufficient for continuous operation but is sufficient for stepwise operation. The design of the magnetometer was therefore changed to separate the heating zone (oven) and the measurement zone (SQUIDs). With this separation, the magnetometer described in this chapter functions the same way as any other commonly used magnetometer, like the JR6 or the 2G Enterprises RAPID system, but with a smaller (10 mm x 10 mm) cylindrical specimen. The main advantages here are that the heating occurs merely 30 cm away from where the specimens are measured, and the specimens do not have to cool to room temperature. Any cooling of the specimen between the oven and the SQUIDs is passive and the result of Newton's law of cooling, so the amount of cooling is calculable and can be confirmed using an independent (non-measuring) experiment.

The magnetometer presented in this chapter is the first to work consistently at high temperatures and to collect both paleodirection and paleointensity data. An automated thermomagnetometer system using SQUID sensors has never been done before. The advantages to this design are the ease of use (both paleodirection and paleointensity experiments can be automated) and higher sensitivity (because of the SQUID sensors), which increases its versatility compared to the magnetometers presented in Chapter 2. The main disadvantages to this system as it currently exists are that the control system cannot yet run Thellier-style paleointensity experiments (but there is the potential to be able to) and that the SQUID sensors remain sensitive to external disturbances (a problem all RF SQUID sensors have).

In this chapter, first, an overview of the design of the magnetometer is given, covering the parts retained from Chapter 4 and then the new additions to make the magnetometer function in a stepwise manner. Next the paleodirection and paleointensity methodologies used on the magnetometer are described. The paleodirection and paleointensity results section follows. The data for the results section were in the process of being collected when the laboratory shut down in March 2020 because of the COVID-19 pandemic. The results herein are therefore preliminary, and their problems will be addressed by completing the work detailed in Section 5.6.

5.2 Design

5.2.1 Carry-overs from continuous magnetometer design

Most of the parts from the continuous magnetometer were applicable to and usable for the stepwise magnetometer. The measurement region did not change in design or location, so the overall footprint of the magnetometer did not change. This design therefore uses the same two-layer Mu-metal shield with an open top. The same aluminum top plate was also used. The background magnetic field is reshown here in Figure 5-1, with both the measurement and the heating regions marked. The background magnetic field at the heating area is ~10 µT and around 300 nT at the measurement zone.

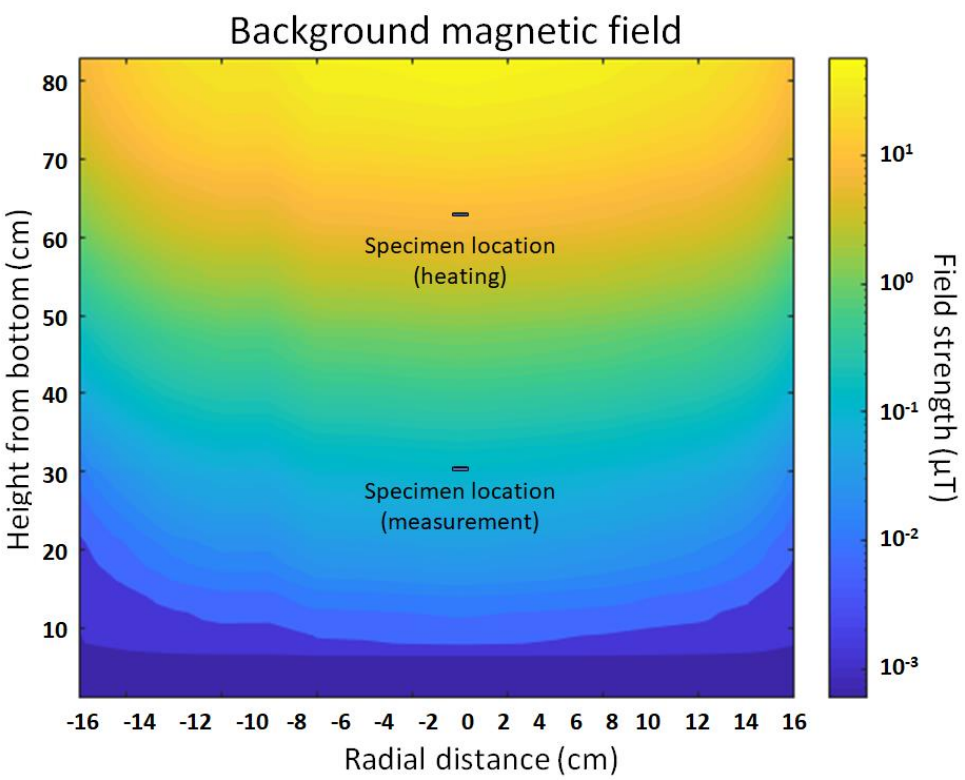

Figure 5-1 Background magnetic field in the $\hat{z}$ direction inside the Mu-metal shield. The specimen locations for heating and measurements are marked.

On the outside of the shielding is a single layer of thin aluminum RF shielding, except at the open end, where there are three layers of thin aluminum RF shielding around the edges but a central hole to allow access to the oven and for the actuator to move. The same liquid nitrogen auto-fill system is also used.

This design uses the same SQUID holder as in the previous chapter, with three SQUIDs in a circle, 120° offset and tilted 30° down from the horizontal. This magnetometer also used the same SQUID controllers as the magnetometer described in the previous chapter. The gradiometer (the controller's channel 2) remains sensitive to magnetic gradients, and so the SQUID plugged into channel 2 requires more fine-tuning and control to keep it stable.

5.2.2 New components

While the internals of the magnetometer have largely remained the same, the space outside the aluminum top plate has changed considerably, as has the magnetometer's vertical footprint in the lab. Figure 5-2 contains a picture of the interior of the magnetometer system, with the SQUIDs and their additional RF shielding. A brass guide was added to enable the SQUIDs and oven Dewar to sit lower within the glass Dewar, both to keep the SQUIDs away from the actuator motor and to decrease the background magnetic field. However, after initial testing, it was found that the brass tube was conducting heat and RF interference into the oven. As a result, the brass guide was removed before any of the experiments described in this chapter could be successfully conducted.

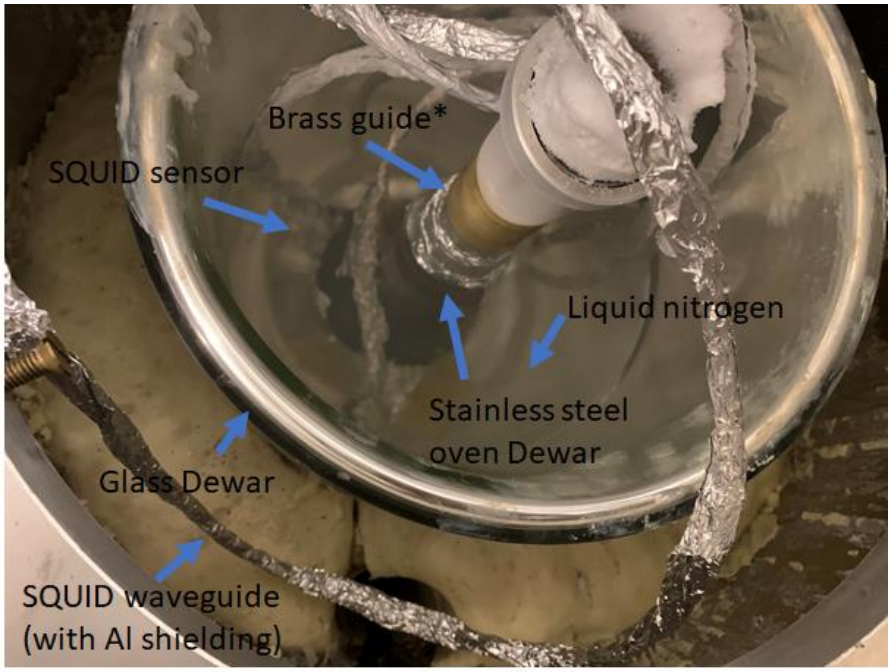

Figure 5-2 The magnetometer system under the aluminum plate. The internal workings are the same as described in Chapter 4. In this picture, a brass guide is present to move the SQUIDs farther from the top of the Mu-metal shield, but this brass guide was removed before any data were taken.

The main visual change is the addition of a quadpod, which holds the new linear actuator arm, described in the next section. The actuator has increased the overall height of the equipment, and the new electronics to power everything currently expands the magnetometer's footprint onto the lab bench. Figure 5-3 contains an external picture and an internal (not-to-scale) cartoon of the magnetometer system. The wooden quadpod, while a structural weak point, is also the backbone of the stepwise design. Its use has so far precluded the production of a proper schematic diagram. The quadpod is necessarily poorly coupled to the Mu-metal base, which means the quadpod can move independently and therefore requires careful alignment. Its height determined the sizing of the actuator arm, the quartz rod, and the location of the oven. Since the proportions of the system are a function of the quadpod, the oven needed to be suspended above the aluminum top plate.

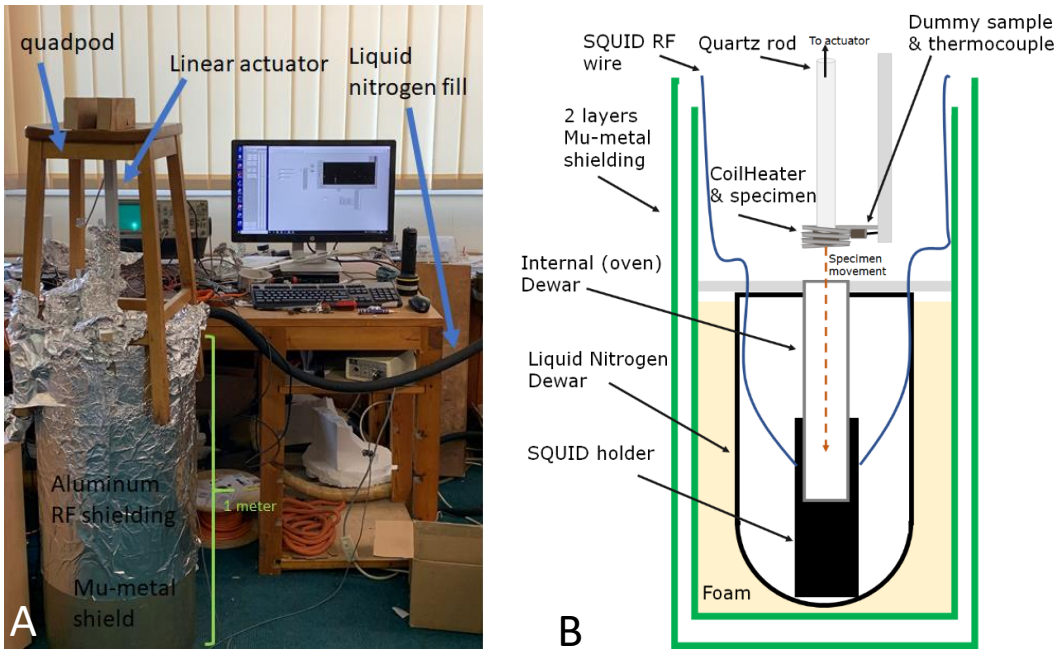

Figure 5-3 Stepwise prototype magnetometer system. A: laboratory picture. B: cartoon of the internals (cartoon not to scale). The main addition over the system described in Chapter 4 is the addition of the linear actuator and quadpod.

5.2.2.1 Linear actuator

The first major (and most obvious visual) change is the addition of a linear actuator with a 30 cm arm and a 20 cm quartz sample rod to move the specimen from the oven to the SQUIDs' measurement region and back (see Figure 5-3). The specimen is attached to the quartz rod using thermally-stable, non-magnetic fire cement. The addition of the actuator adds an additional degree of freedom in the design, as the specimen location is not permanently aligned like in the design described in Chapter 4. The actuator uses DC current, which means no RF interference is generated during operation, but the magnets in the motor create a magnetic field. The non-magnetic wooden quadpod keeps the actuator's motor 50

cm above the aluminum top plate to minimize the effect on the SQUIDs. At this distance, the SQUIDs have no apparent change in reading when the motor turns on or off. Since the SQUIDs do not need to continuously read the magnetization of the specimen, between each step, the SQUIDs can be reset— and if necessary, re-tuned to account for any natural drift— before taking the next measurement. Taking measurements over a short period of time is the operational environment for which SQUIDs are designed, which means they now behave as expected (and therefore as desired).

The additional factor to consider in the experimental setup, now that the measurement and heating zones are separate, is that of the specimen's temperature. A specimen's temperature can only be recorded by thermocouple while the specimen is in the oven and not while it is being measured. A thermocouple is made of two conductive pieces of metal (Nicrosil/Nisil in the case of the N-type thermocouples used herein), which means that it also conducts RF radiation, which must be kept far away from the SQUIDs (specifically above the aluminum top plate). Since specimens cool passively once moved away from the heat source, following Newton's law of cooling (Equation 5-1), the measurement temperature is always lower than the temperature read when movement begins. However, the measurement temperature will always be higher than room temperature, which is one of the key design ambitions of the new magnetometer designs presented in this thesis. The change in ambient temperature inside the internal Dewar is unknown during an experiment but ranges between -20 and 10 °C. Thus, with a premeasurement temperature of 500 °C and a post-measurement temperature of 450 °C, the measurement temperature would fall in the range of 472 – 475 °C.

$$T(t) = T_a + (T_0 - T_a)e^{-kt}$$

Equation 5-1 Newton's law of cooling. T_a is the ambient temperature, T_0 is the initial temperature, k is a constant, and t is time.

Attached to the end of the actuator arm is a thin-walled 10 mm outer diameter quartz rod that holds the 8 – 12 mm diameter paleomagnetic specimen on the far end using fire cement. The quartz rod is electrically and thermally resistive and prevents the aluminum actuator arm from approaching the SQUIDs and therefore keeps any associated RF interference above the aluminum top plate.

5.2.2.2 CoilHeater oven

The second design change, the various designs of which were also the focus of much of the previous two chapters, is that of the oven. Changing to stepwise heating removes some of the constraints on the oven because it will always operate independently of the SQUIDs.

The two main constraints removed are RF interference and heat exchange with the oven's surroundings. The design was therefore changed to use a 750W version of the Maxiwatt CoilHeater, whose theory and initial design were described in Chapter 3. The CoilHeater previously failed because the signal generator and amplifier setup was unable to generate a 240V signal at 10kHz+ AC frequencies. Since the CoilHeater now operates independently of the SQUIDs, it can run using a 50 Hz AC voltage.

The CoilHeater oven is designed for a 10 mm specimen because smaller sized specimens are more thermally uniform, but specimens need to be large enough to be oriented and have a sufficiently strong magnetic moment. With the appropriate CoilHeater, an oven for specimens up to 20 mm diameter is possible at the cost of thermal uniformity and experiment speed.

The CoilHeater was manually coiled to a 12 mm inner diameter and a height of 10 mm, which gives 1 mm of clearance around a 10 mm sized specimen. For the fastest and most uniform heating of the specimen, the coil should be in direct contact with the specimen. However, in order to smoothly move the specimen, there needs to be no friction and therefore no contact between the specimen and the oven. A fire-cement dummy specimen (analogous to the one in the laboratory's VFTB system) sits around the thermocouple so that the thermocouple measures an internal temperature instead of an external temperature. Figure 5-4 contains a 3D model of the CoilHeater, which can also be seen in the cartoon in Figure 5-3. Specimens of 8 mm can also be run; these specimens have lower thermal inertia and can be heated more uniformly, but the increased distance means the specimens may not heat as efficiently and may have difficulties reaching the peak temperature.

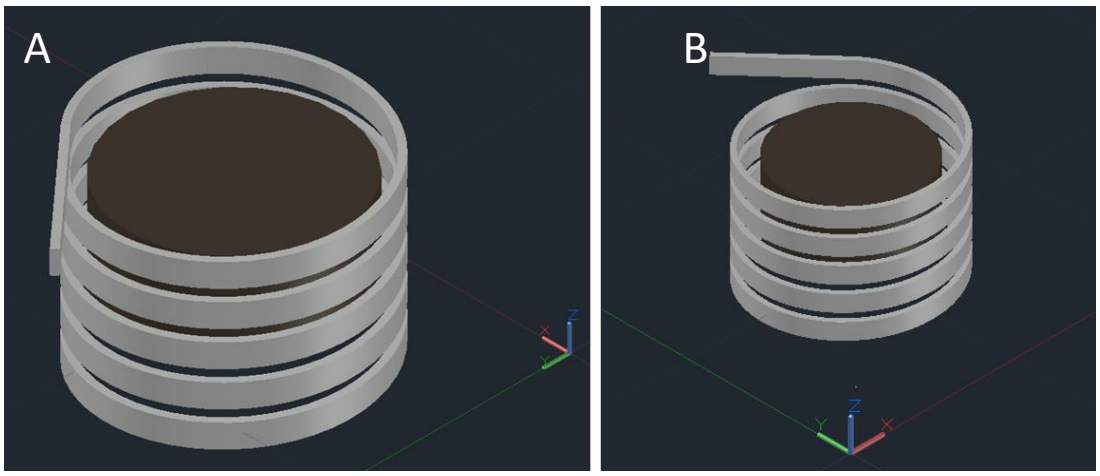

Figure 5-4 CoilHeater 3D model, containing A: 10 mm and B: 8 mm diameter cylindrical specimen. The main difference is the larger gap between the specimen and the coil in B, compared to A.

5.2.2.3 *Running the oven and actuator*

The addition of the actuator and the high power CoilHeater means that the new magnetometer design required the creation of a new power circuit design to both control the heating rate of CoilHeater and to run the actuator. Since the CoilHeater and the actuator are always run independently, the entire circuit is powered from a single 240V plug with a 5 W, 12V DC adaptor. A wiring diagram (during movement/measurement) is presented in Figure 5-5.

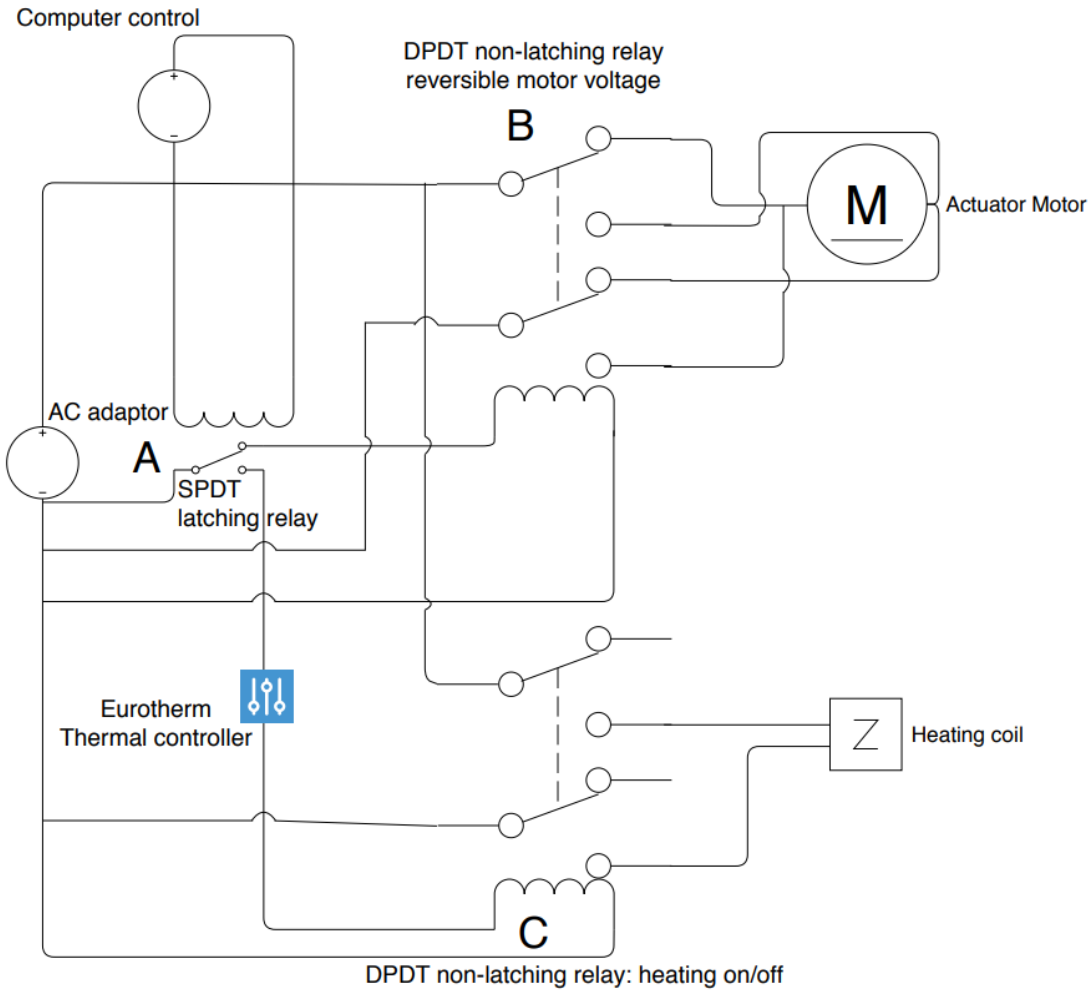

Figure 5-5 Wiring diagram for actuator, motor, and heating coil control. This configuration corresponds to specimen measurement. Relay A determines heating or measuring. Relay B controls the actuator motor. Relay C controls the heating coil.

The design of the actuator means that a positive DC voltage causes the arm to extend for 10s until fully extended and a negative DC voltage causes the reverse, a 10s retraction. Upon full extension or retraction, the actuator ceases to draw any current and the circuit breaks automatically. The change in polarity is handled by the computer. The computer outputs a short duration $\pm$5V DC current that changes the latching single pole double throw (SPDT) relay's orientation (A). A latching relay means that the computer does not need to output a

continuous voltage to maintain the relay's position. Switching relay A's lanes turns on/off the double pole double throw (DPDT) non-latching relay (B)'s coil, switching its poles. Relay B's 'off' is defined as 'reverse' such that when the actuator arm returns to the oven's position, the power is redirected to the CoilHeater.

When relay A is in the opposite position to that shown in Figure 5-5, which can be seen in Figure 5-6, the heating coil is active. A Eurotherm thermal controller controls the heating of the specimen by switching the poles of the second DPDT relay (C), using the power that would otherwise be used by the actuator, since the two are never used simultaneously. The default position is for the heating coil to be off to prevent any unwanted temperature increases in the oven. The DPDT relays in this design use a 12V coil voltage (powered by the Eurotherm controller) and are rated for a switching current of 10A for 240V AC, which gives a factor of safety of 3.2 for the 750W CoilHeater.

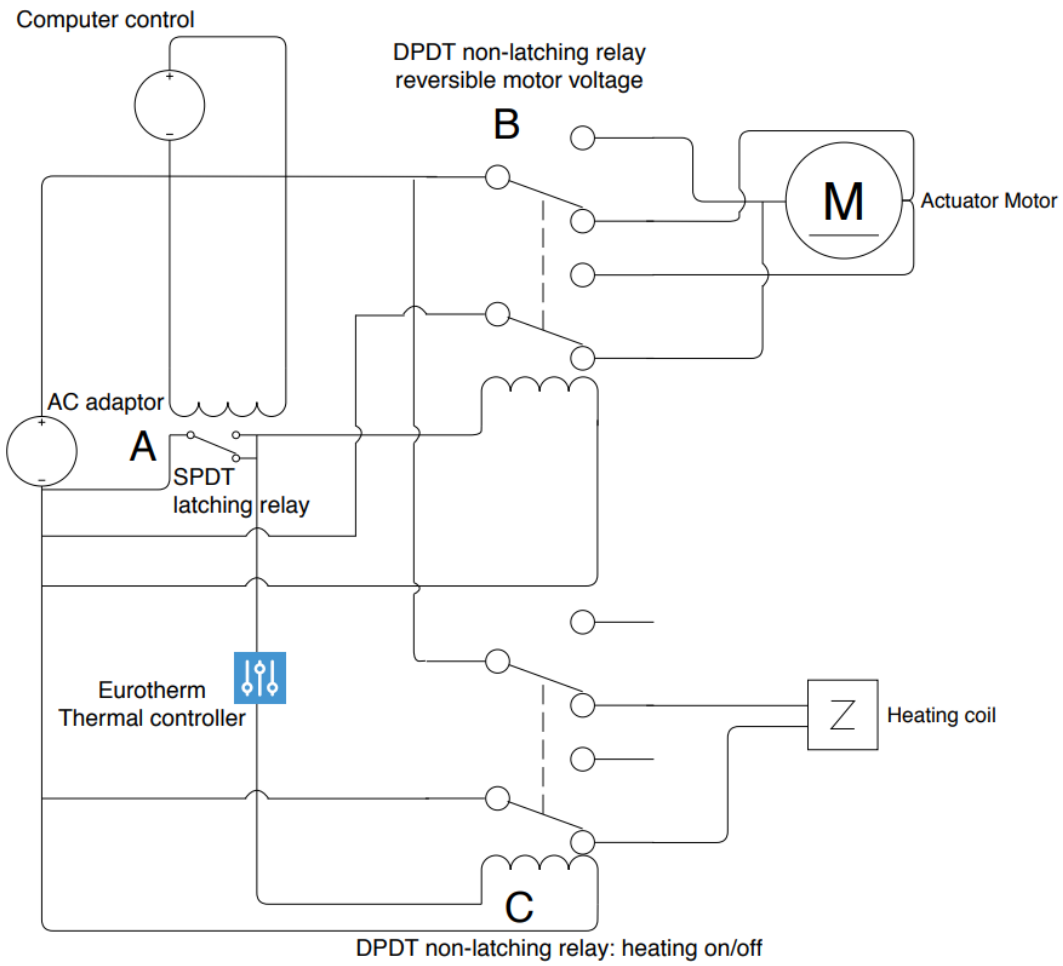

Figure 5-6 Wiring diagram for actuator, motor, and heating coil control. This configuration corresponds to specimen heating. Relay A determines heating or measuring. Relay B controls the actuator motor. Relay C controls the heating coil.

A new Eurotherm controller was purchased for this design. A model 3204 controller was selected, with a logic and a relay output (to control the CoilHeater), as well as RS232 comms and logic input (for computer control). The direct computer control is not implemented in the version of the control program used for the system described in this chapter. Instead the controller has a built-in proportional-integral-derivative (PID) control system, using the same principles outlined in Equation 3-4 for the control system described in previously, but with different control constants because of the different oven design.

5.2.2.4 Remagnetization coil

The last component required for a full paleointensity-ready thermomagnetometer is the remagnetization coil. The coil is necessary for fully independent experiments, but an alternative hybrid approach can make use of this instrument together with, for example, a Magnetic Measurements Thermal Demagnetizer (MMTD oven). This type of paleointensity experiment is described in the methods section below and applied herein. In the single-axis continuous magnetometer system presented in Chapter 3, a Helmholtz coil was selected to apply a magnetic field because of the design of the F.I.T. system. In the multi-axis continuous magnetometer system described in Chapter 4, a solenoid was designed but not fully implemented. Both coil designs would be applicable to this magnetometer system. A Helmholtz coil could be placed outside and around the oven or a solenoid could be placed inside the oven. Both coils would need to be able to tolerate the high temperatures of the oven area. However, there already is a coil present near the specimen: the CoilHeater. By applying a current across the skin of the CoilHeater, along the helix shape (see Figure 5-7), a magnetic field can be generated. The heating coils inside the helix are wound non-conductively, but the helical outer shell is not and is, in fact, the exact same shape as a coil of wire in a solenoid. The CoilHeater therefore acts like a solenoid, but with one important difference, which can be seen in Figure 5-4: there is no contact between turns of the CoilHeater because its skin is the electrical conductor. The space between turns means that the CoilHeater is both a finite and an imperfect solenoid. The field as a function of current was therefore determined experimentally. The results of this experiment are presented in Figure 5-8, along with the resulting best-fit equation.

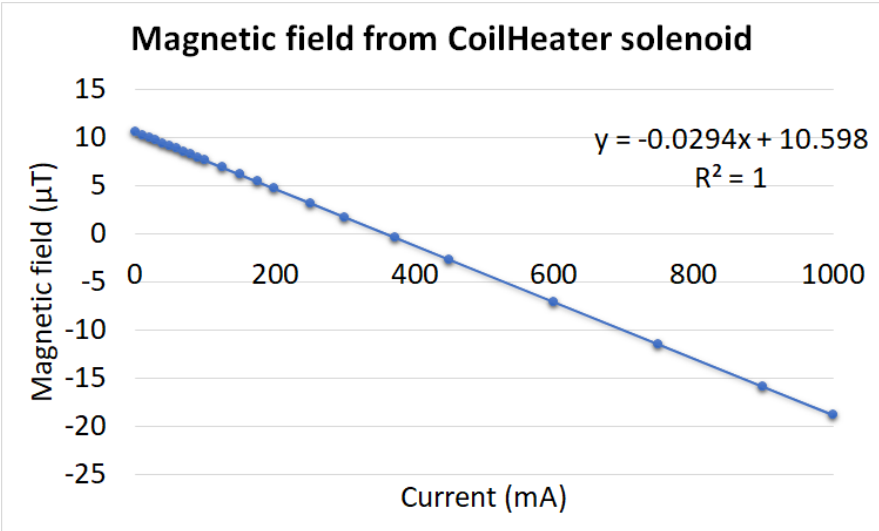

Figure 5-8 Magnetic field generated inside CoilHeater (at the center) by running a current along its casing.

The relationship is linear, as it should be for both a single coil of wire and a solenoid (the two theoretical end cases of the CoilHeater's design). Extrapolating beyond the testing range (1 A was the maximum output possible on the power supply), the upper limits of the necessary field strengths (± 50 µT in the $\hat{z}$ direction) would therefore be achievable with a current of 1.34 A (or 2.06A in the opposite direction). With the 1 A power supply, magnetic fields can be applied between +40 µT and -20 µT in the $\hat{z}$ direction. This means that this design is feasible and can be implemented and tested for compatibility.

These experiments were completed at room temperature with the CoilHeater turned off. During an experiment, the remagnetization coil will only operate (and can do so with 0 delay) while the CoilHeater is turned off and cooling, but the current loop wires remain attached even when the CoilHeater is in operation. This operating environment means that the resistance of the CoilHeater may change as a function of temperature, and it also means that the wires that carry the remagnetization current can also heat up. To avoid any problems with changing resistances, the remagnetization coil is powered by the same DC power supplies used by the MMTD ovens, which output a constant current (with a variable voltage). To minimize heat transfer, while still ensuring good electrical conductivity, a single terminal block was used to connect the terminus of the CoilHeater to the DC power supply. Terminal blocks use two screws connected by a metal body to provide the circuit connection. In terms of heat transfer, this increases the number of interfaces from two (wire -> solder -> wire) to four (wire -> screw -> body -> screw -> wire). A second wire was attached to the CoilHeater's grounding wire to complete the circuit. It was then experimentally determined that negligible heat was conducted from the CoilHeater out to the DC power supply.

5.2.3 Control program

The control program was still written in LabVIEW; however, it had to be completely redesigned and the block diagram rebuilt. The program requires the SQUIDs to be pre-tuned before use, but the Jülicher SQUID proprietary program's auto-reset feature can handle most SQUID jumps during the experiment. The same data acquisition controller and thermocouple voltage conditioner from the system presented in the previous chapter are used herein. The user loads the specimen onto the actuator arm and places it inside the oven inside the Mu-metal shielding. The user inputs a set of measurement temperatures for the experiments and then clicks 'start', which triggers the initial magnetization measurement. The oven is then turned on and controlled externally by the Eurotherm thermal controller's PID control system.

For a demagnetization experiment, the control program's protocol is straight-forward. When the thermocouple reads a given T_N, the program turns off the oven, moves the specimen to the measurement region, then collects 20 SQUID measurements and moves the specimen back to the oven. The program then waits for the thermocouple to read T_{N+1} and repeats the process until T_{max} is reached and the experiment ends. The raw data are saved automatically to an excel file with the (absolute) measurement time and three SQUID components. Temperature data are saved to a separate excel file as a function of absolute time. A separate MATLAB program converts these data into a useable format. For a remagnetization experiment, the protocol is the same except the temperature steps go from T_{max} down to T_{room}.

Table 5-1 LabVIEW control program v2

Requirement	Method
Heat the oven up to 700 °C with ±0.5 °C precision	CoilHeater heats specimen to 600 °C at 10 °C/min using a Eurotherm 3204 controller.
Cooling system – protect SQUID	Not necessary; Vacuum Dewar + insulation only
Cooling system – cool specimen after measurements	Not implemented; passive cooling only
Atmospheric flushing	Not implemented; spare channel available
Magnetic field application	Manually switched solenoid coil
Triple-axis magnetic field measurement	Up to three SQUIDs recorded by program, discrete sets of thermocouple and SQUID measurements are written into an Excel file.

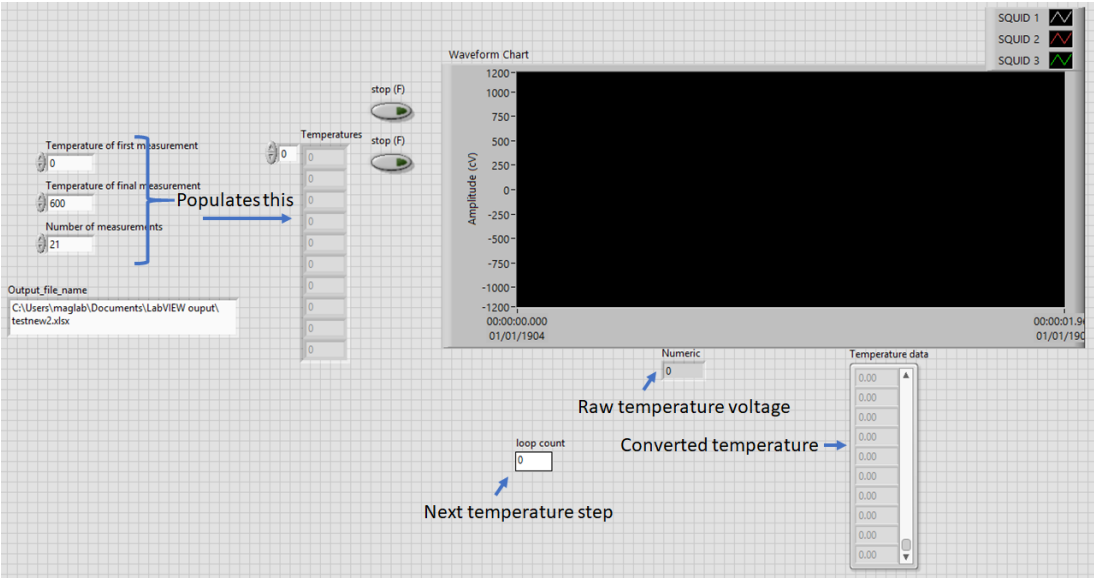

Figure 5-9 LabVIEW interface control panel for Control Program V2. The backend block diagram can be found in Supplementary Information Figure A1.

5.3 Methods

The specimens tested and presented in this section are basalts, drawn from the Scientific Observation Hole 1 (SOH1) drill core (see Chapter 7 and Chapter 9) archive of pre-used specimens. The SOH1 drill core specimens were selected because these cores have strong magnetization and well-described and stable magnetic properties. As noted above, the magnitude of the remaining background magnetic field at the CoilHeater is 10 µT. Therefore, a current of 360 mA was applied along the CoilHeater's casing to generate a 10 µT magnetic field in the $-\hat{z}$ direction to negate the background field.

The magnetometer system exists as a hybrid between the long-established stepwise (Cox, 1957) and continuous (Stacey, 1959) techniques described in Chapter 2. Measuring specimens stepwise at elevated temperatures using SQUID magnetometers is unique to this system. Specimens were not actively cooled before measuring, but once the oven is turned off, the specimens begin cooling. These changes can be tracked by the thermocouple, since the dummy specimen begins cooling at the same rate. The dummy specimen used is the same type as in the laboratory's Variable Field Transition Balance (VFTB; used in section B). The temperature change due to the measurement cycle is therefore recorded when the computer resumes logging temperature data. The amount of cooling increases as the temperature step increases (following Newton's law of cooling). The temperatures always remain substantially above room temperature, drastically reducing the chance for thermochemical alteration because of the reduced thermal cycling (Hodgson et al. 2018).

The two SQUIDs output voltages, which the LabVIEW control system then records into a csv file, along with a timestamp. A MATLAB script then converts the raw voltages into XYZ data and then into the file format (CIT), used on the RAPID. The SQUIDs have not been calibrated, so the output voltages are not converted into absolute values of magnetic field or sample (magnetic) moment.

5.3.1 Paleodirections

The most straightforward paleomagnetic technique to test the equipment is a thermal demagnetization experiment. Performed on a previously untreated natural specimen, this kind of experiment is designed to yield the specimen's paleodirection. In this case, the first set of specimens were given lab-induced single component (and then multi-component) TRMs in known directions up to 600°C. The specimens were then progressively heated from 20 °C to 540 °C, as measured in the middle of the dummy specimen, and measured automatically at 30 °C intervals.

Four specimens were used for the paleodirection survey. Specimen A was a 12 mm diameter (bigger than desired) specimen from the SOH1 drill core, whereas specimens B – E were 8 mm in diameter and from SOH1 flow 42, which is also investigated in Chapter 9. The lack of a 10 mm drill bit in the lab necessitated the use of 8 mm diameter specimens until the appropriately sized drill bit could be delivered. These specimens were given laboratory TRMs in MMTD ovens. Ten paleodirection experiments were run using these five specimens.

5.3.2 Paleointensities

The next set of experiments, the paleointensity experiments, are more technically complicated, a point that is made (and very thoroughly covered) in section B (Chapter 6 – Chapter 9) of this thesis. The first paleointensity method tested only requires the magnetometer to demagnetize a specimen. First a specimen was demagnetized as above (from a laboratory-induced TRM given in an MMTD oven) in the new magnetometer. Next, the specimen was given a new TRM in the same MMTD oven. Finally, the specimen was demagnetized in the new magnetometer a second time. By comparing the magnitude of the specimen's magnetization at each temperature step, a full-TRM paleointensity estimate can be determined. The resulting paleointensity method is a stepwise version of the continuous Wilson (1961) method, akin to the original Thellier (1938) method or a thermal application of the Shaw (1974) paleointensity method.

The second paleointensity method tested was completed entirely within the new magnetometer system. The method follows a second variant of the full-TRM Wilson (1961)

paleointensity method, similar to the stepwise, thermal protocol described in Walton (1977). Specimens were first fully demagnetized in a null magnetic field, being measured every 30 °C. Next, the oven was switched off and the magnetic field turned on (-19.8 µT in the $\hat{z}$ direction). The specimens then cooled passively in a known magnetic field. When the temperatures reached the same temperature as in the demagnetization experiment (every 30 °C in the opposite direction), the system measured the new magnetizations. Two specimens were used for each of these paleointensity methods.

5.4 Results

5.4.1 Paleodirections

Of the ten experiments, four failed (including both of the experiments using specimen B) as a result of the SQUID jumps not being managed successfully, rendering the data meaningless. Due to the small size of the B - E specimens (less than 1/3 of the diameter usually used in the MMTD ovens), the specimens sometimes fell over when the cooling fan turned on. As a result, the expected inclinations for some specimens is 0° for some and 90° for others, depending on the given experiment. Figure 5-10 contains two example raw SQUID output voltages as a function of temperature. From these figures, the demagnetization is apparent, but the resulting direction is not, so the data are processed through a MATLAB script.

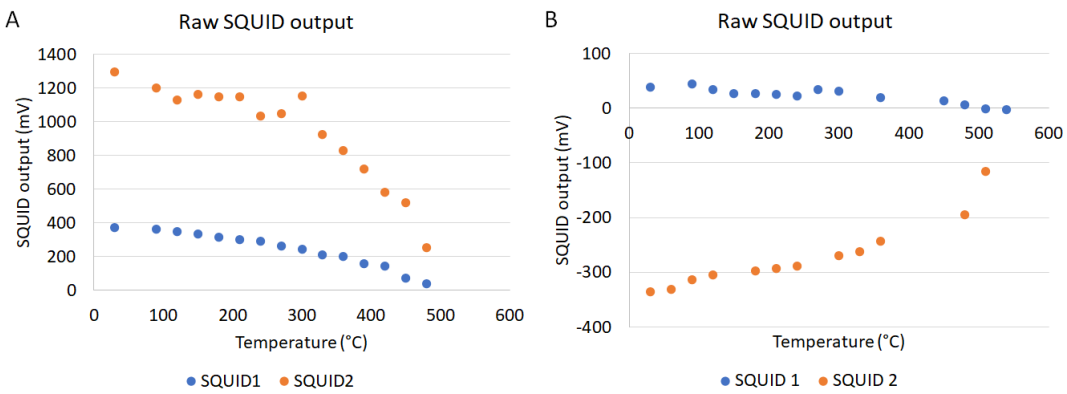

Figure 5-10 Raw SQUID voltage data for two paleodirection tests. A) Test specimen A. B) Test specimen E. These data show demagnetization occurring but require processing to extract paleodirection information. Data gaps are the result of SQUID jumps.

The data are processed in MATLAB to convert them to the CIT format for use in the PaleoMag 3.1 software (Jones, 2002), which then generates the orthogonal plots for the data. The six orthogonal plots generated from these experiments are presented in Figure 5-11. Despite inputting temperatures of 600 °C into the control program, the highest temperatures reached for these specimens was 540 °C. These temperatures are lower than the design

specification's maximum temperature of 600 °C, but the small sizes of these specimens meant the oven was unable to heat them as efficiently.

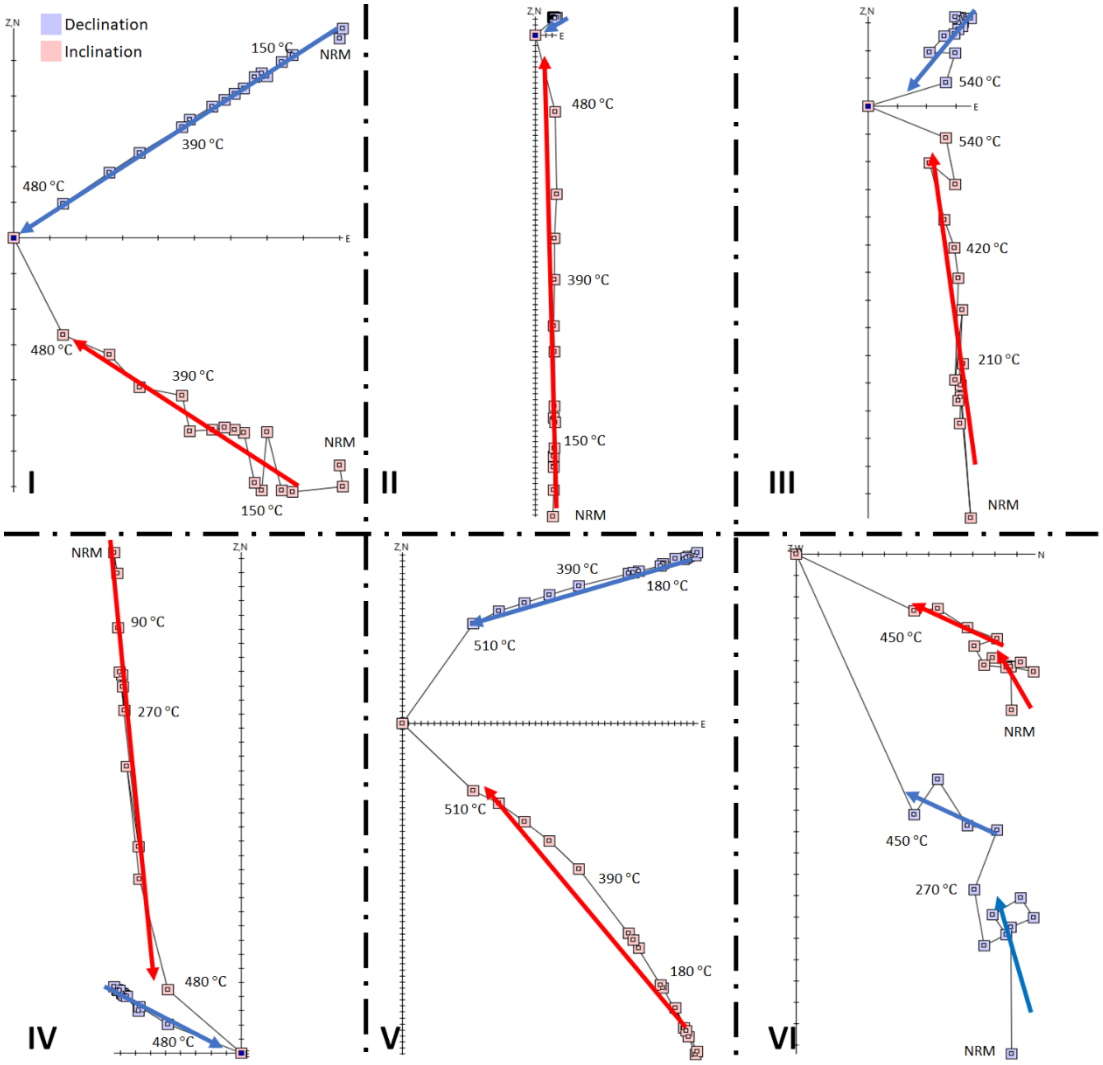

Figure 5-11 Orthogonal plots for paleodirection experiments attempted. I and II are from test specimen A. III and IV come from test specimens C and D, respectively. V and VI come from test specimen E, with it having been given two magnetic components in F. The arrows are hand-drawn as a guide for the magnetic components selected. Red directions represent inclinations; the blue arrow represents declination.

The behavior of the orthogonal plots in Figure 5-11 is varied, but all four plots have at least some non-linearity in their data, despite having been given well-defined laboratory magnetizations. Following the conversion of the data to XYZ coordinates, principal component analysis was completed using the methods outlined in Kirschvink (1980) using PaleoMag 3.1 (Jones, 2002). An equal area plot and a summary of the resulting direction are presented in Figure 5-12 and Table 5-2, respectively.

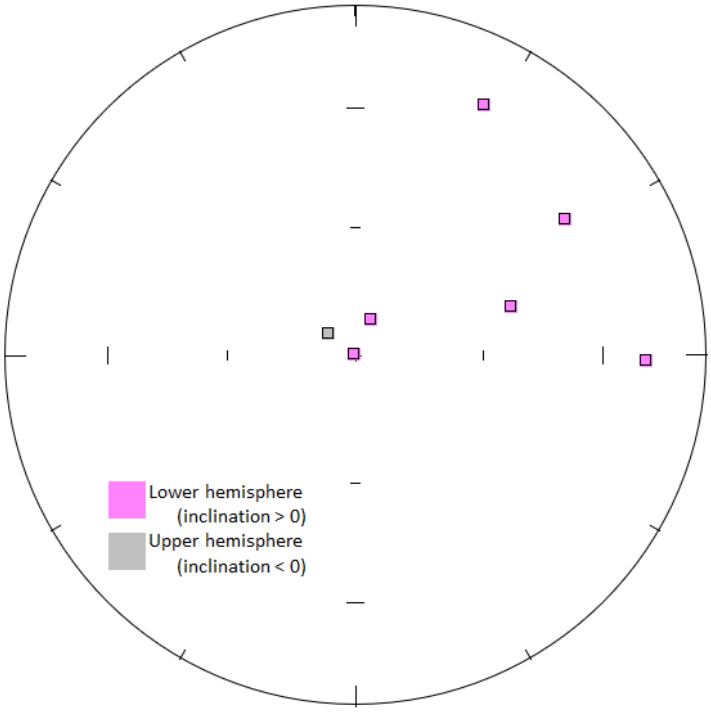

Figure 5-12 Equal area plot of results. The scatter of the results is a function both of experimental error and of the three applied field direction not being the desired inc. = 90° direction.

Table 5-2 Summary of paleodirection results by test specimen

	Measured			Expected		
Test specimen	Dec (°)	Inc (°)	MAD (°)	Dec (°)	Inc (°)	Error (°)
A*	57.1	29.2	9.2	90	0	42.9
A*	294.6	89.7	0.3	0	90	0.3
C	24.6	80.9	5.6	0	90	9.1
D	308.4	-82.2	2.4	0	-90	7.8
D	72.9	51.4	5.0	0	90	38.6
E (1)**	91.1	18.1	13.3	90	0	18.1
E (2)**	27.2	20.7	23.6	0	0	33.7

Note. Dec means declination and inc means inclination. MAD is the maximum angular deviation. Error is calculated as the angular difference between estimated and expected direction.

* The tests on specimen A were completed without an applied magnetic field to cancel out the 10 µT background field mentioned in Section 2.

** Test specimen E's first direction is its low-temperature component. Test specimen E's second direction is its high-temperature component.

5.4.2 Paleointensities

5.4.2.1 Magnetization Comparison

As a first step, two proof-of-concept paleointensity experiments were successfully run using this magnetometer system using the comparative paleointensity method (two heatings in an external oven). The data for these two experiments are the same as the data in Figure 5-11 A and B and Figure 5-11 D and E, respectively. Figure 5-13 presents the results of this demagnetization comparison. Each data point compares the magnetization of the specimen at the same temperature during the different experiments.

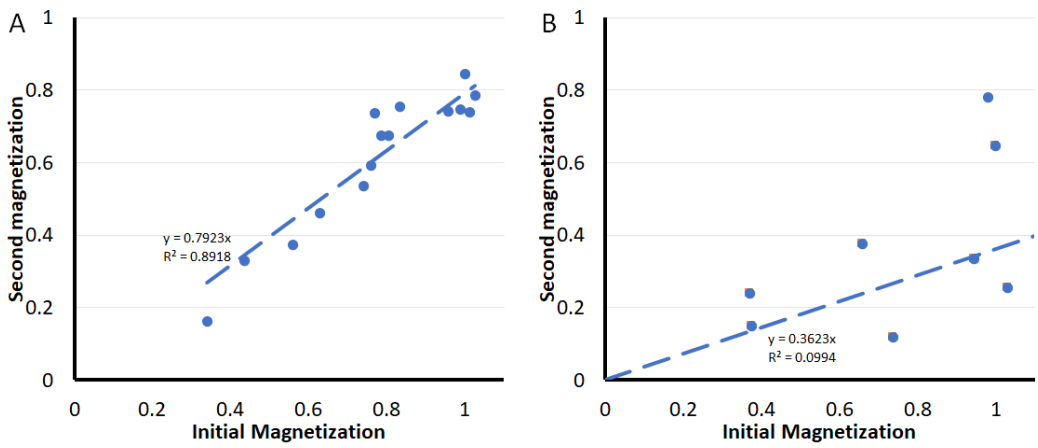

Figure 5-13 Paleointensity experiments using an external oven. A: test specimen A, giving an estimate of 50.5 µT against an expected value of 50 µT. B: test specimen D, giving an estimate of 55 µT against an expected value of 40 µT. The dotted line is the best fit lines, anchored to the origin.

In the case of specimen A, the initial magnetization (first heating) was given in a 50 µT field and the second magnetization (second heating) was given in a 40 µT field. The data give an R^2 value of 0.89 when anchored to the origin (because a demagnetized specimen given a second magnetization a field of $\mathbf{B} = \mathbf{0}$ remains demagnetized). The resulting slope of 0.79 in Figure 5-13 A gives a paleointensity estimate of 50.5 µT, an error of 1%.

In the case of test specimen D, which was less strongly magnetized but gave lower paleodirection errors in the previous section, the initial magnetization was given in a 40 µT field, and the second magnetization was given in a 20 µT field. The resulting R^2 value of .099 is extremely poor. The data in Figure 5-13 B visually look nearly random. The resulting slope when anchored to the origin is 0.36, which gives a paleointensity estimate of 55 µT, a 27% error.

5.4.2.2 In-situ remagnetization

Upon completion of the comparison experiments, two experiments were then completed using the remagnetization coil. This protocol is analogous to the protocol described in Walton (1977). These experiments are of particular note because they mark the

first two automated remagnetization experiments run by this magnetometer system. Both samples were initially magnetized in 20 µT fields in an MMTD oven. Net applied fields of 19.8 µT (the maximum possible after accounting for the 10 µT background field) were then used in the magnetometer to remagnetize them after the initial demagnetization. Figure 5-14 contains the results of these experiments. Magnetizations at given temperatures were compared as in the previous paleointensity experiments.

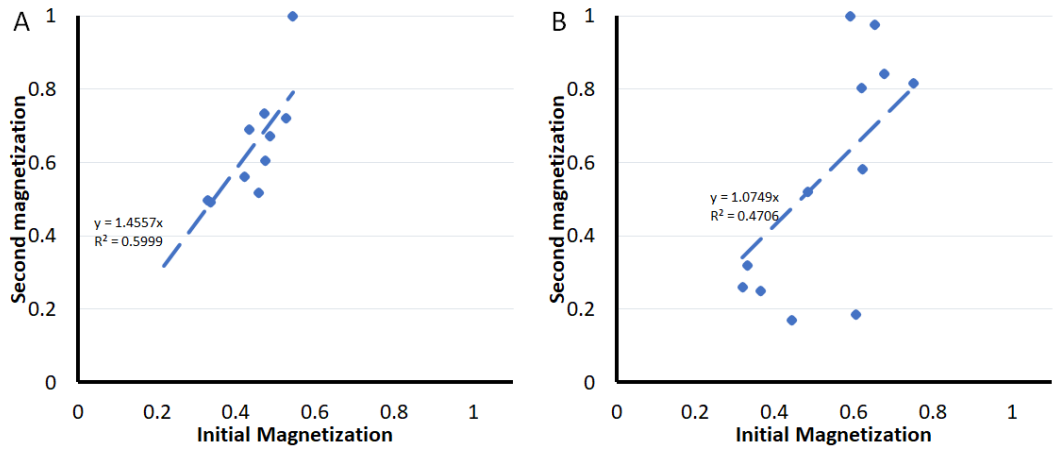

Figure 5-14 In-situ remagnetization paleointensity experiments. A: test specimen D. B: test specimen E. The dotted line is the best fit lines, anchored to the origin.

The data are again poor quality, with R^2 values of 0.6 and 0.47, respectively. The test with specimen D in Figure 5-14A yielded a paleointensity estimate of 28.9 µT, for an error of 45%. The test with specimen E in Figure 5-14B had a lower R^2 value of 0.47, but gave an estimate of 21.2 µT, which is an error of 6%. A summary of the paleointensity experiments from this chapter, using both methods, can be found in Table 5-3.

Table 5-3 Summary of Paleointensity experiments

Test specimen	Estimated PI (µT)	R^2	Expected PI (µT)	Error (%)
A	50.5	0.89	50	1
D	55	0.13	40	27
D	28.9	0.6	20	45
E	21.2	0.47	20	6

5.5 Discussion

5.5.1 Demagnetization behavior

Figure 5-15A provides the magnetization remaining as a function of temperature during these demagnetization experiments for two representative specimens of different diameters. Figure 5-15B provides an example thermomagnetic (Curie) curve for the SOH1 flow 42, reproduced using the raw data from Gratton et al. (2005). The specimens tested herein are

sister SOH1 specimens. The normalized SQUID output data (magnetic remanence) cannot completely replicate the linear trend of the thermoremanent magnetization curve because this thermoremanent curve measures induced magnetism. However, both have a generally linear demagnetization trend between 240 °C and 500 °C, which suggests a mixed single domain/non-single domain magnetic mineralogy. The new magnetometer's data further shows a demagnetization of at least 70% by 500 °C, which is comparable to the 70% demagnetization observed in Chapter 9 for these specimens but slightly lower than the 80% magnetization loss observed in the thermoremanent curve data presented in Figure 5-15B. The incomplete demagnetization around 500 °C is likely to manifest itself as non-converging orthogonal vector plots if the specimens are weakly magnetized due to either noisy data or remagnetization from the Earth's magnetic field. The demagnetization behavior, therefore, does not indicate any problems with the reliability of the data.

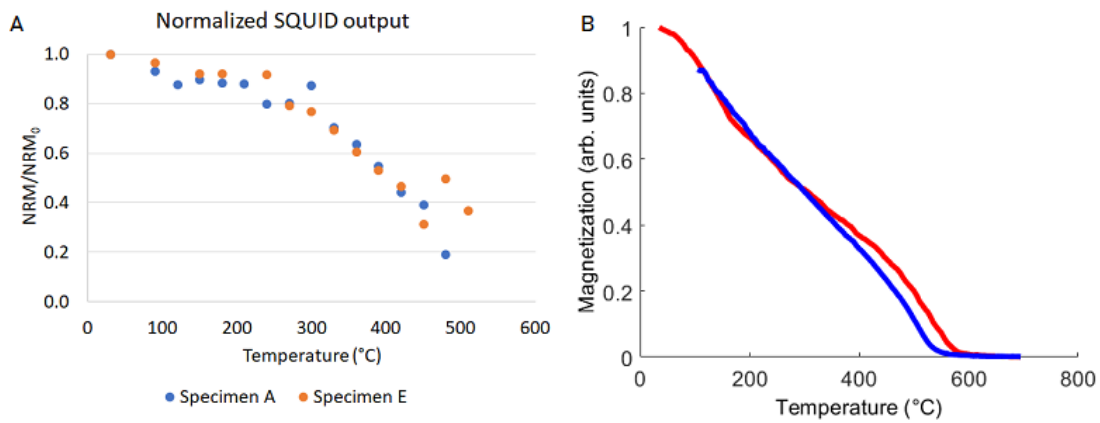

Figure 5-15 Natural Remanent Magnetization (NRM) remaining as a function of temperature. A: experimental results; B: Thermoremanent curve example from flow 42 (reproduced from the raw rock magnetic data from Gratton et al., 2005).

5.5.2 Paleodirections

In Figure 5-11, it was observed that the orthogonal vector plots generally trended to the origin but in some cases were non-convergent (Figure 5-11A, C, D). This non-convergence is likely the result of the incomplete demagnetizations observed in Figure 5-15A because grains with the highest unblocking temperatures were not unblocked. In addition, some orthogonal vector plot data (Figure 5-11A, C, F) were noisier (more non-linear and more scattered) than expected. In some cases, these data are the result of SQUID jumps during individual measurements that were unable to be corrected or were the result of the weak magnetization of certain specimens.

For the data that were expected to give a mean value of (Dec, Inc) = (0°, 90°), a mean direction of (72.1°, 78°) was obtained, with an α_{95} (95% confidence cone size) error of 21.5° (K = 31). The data therefore have an absolute angular difference of 12°, which falls within the α_{95} error bounds. Figure 5-16 contains an equal area plot of these direction data. The other expected directions have too few data points for analysis, but the overall average absolute angular distance from the expected direction is 21.5°.

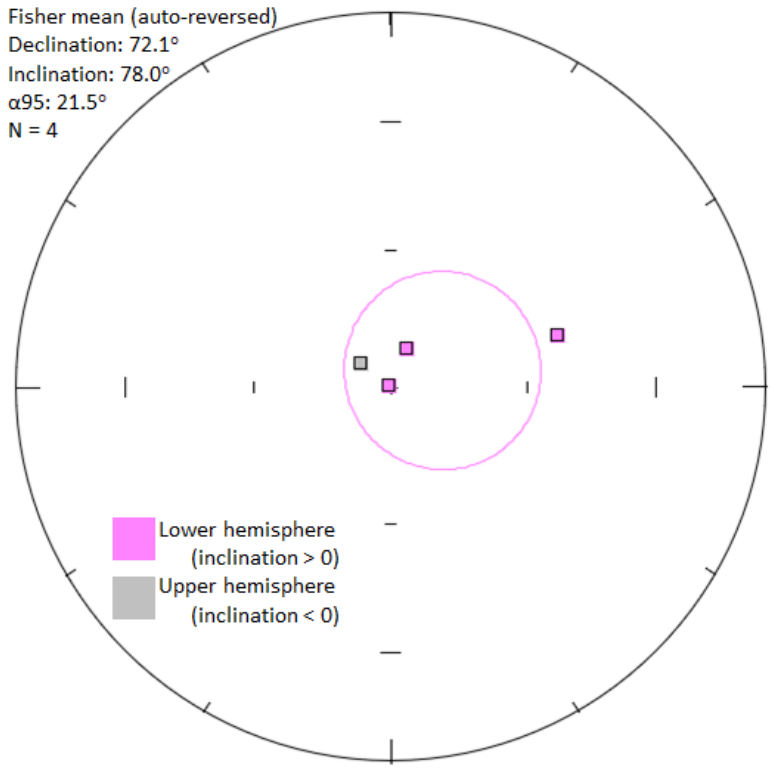

Figure 5-16 Paleodirection data for the directions expected have an inclination of 90°

The data collected from the paleodirection experiments are therefore poor. There are two obvious reasons for this non-ideal result. First, the 8 mm specimens used have 20% smaller diameters than the design specification, resulting in a magnetization 1/3 weaker than the larger specimens, which means their signal to noise ratio is inherently lower. The average maximum angular deviation (MAD) value for the 8 mm specimens is 10°, which is potentially acceptable by some paleodirection selection criteria. For the 12 mm specimen, however, the average MAD is less than half that, 4.8°. The 12 mm specimen used has a 20% larger diameter than the design specification, which in turn means the specimens have a magnetic moment 125% higher than the 8 mm specimens. During initial tests, magnetizations this large could cause the SQUIDs to saturate, making the data unreliable. Therefore, the 10 mm specimen is still the preferred specimen size because it provides a high signal to noise ratio without saturating the SQUIDs. Second, only two SQUID sensors are in use and their orientation is

carried over from the previous design, which means that the data deconvolution process is more complicated and has larger errors. A third possible reason for the poor data is that the linear actuator is misaligned, so the specimen is closer to one sensor than the other. The data processing script tries to correct for the error by assuming the $\hat{z}$ component should be the same for the two SQUIDs, but this assumption creates output data that are inherently less accurate.

5.5.3 Paleointensities

Of the four paleointensity estimates herein, none would pass even the loosest selection criteria (which require $R^2 > 0.9$), as used elsewhere in this thesis (such as in Chapter 6 and Chapter 9). These data are more preliminary than even the paleodirection data; they were collected in the week before the laboratory's closure. Given the poor quality of the preliminary paleodirection estimates, poor quality paleointensity data are generally expected; most paleointensity selection criteria require a suitable paleodirection. Further, none of the paleointensity experiments herein have checks for alteration. These experiments were run on specimens that had already undergone a paleointensity experiment in Chapter 9 and so were assumed to be thermally stable by the time of these experiments.

The external remagnetization experiment has the advantage of being a simple total TRM method, which means it, like the Shaw (1974) method before it, should be domain-state independent (assuming the non-ideal grains maintain their same domain-state, which is not a guarantee). In theory, it does not require checks for non-single domain behavior, but in practice, may require them. This experiment is also technically simpler to run but requires additional (albeit extremely commonly used) equipment. Specimen A again had the best data, likely because it had the strongest magnetic moment.

In the in-situ remagnetization experiment, specimen D's results were poor but gave an interesting result because the raw applied field was 30 µT (-30 µT applied + 10.2 µT background = -19.8 µT net remagnetizing field), which is 4% higher than the estimate of 28.9 µT. This result implies that there may have been a problem with the applied field during the demagnetization step. The other possibility is that too much cooling outside the applied magnetic field occurred during the remagnetization measurement cycles, so portions of the specimen's blocking spectrum were unable to be remagnetized, which gave a lower apparent net remagnetization. Specimen E was the most weakly magnetized specimen of the three used for paleointensity experiments. The poor quality of the data reflects this, but an accurate estimate was still obtained from this specimen's data which means that its magnetization was not outside the resolution of the SQUID sensors. The accuracy of this

estimate implies that the amount of cooling outside the applied magnetic field did not affect its remagnetization.

5.6 Future work

Overall, the system shows promise. Figure 5-4 contains the design specifications as reached during this work presented in this thesis. Three specimens— A, C, and E— consistently had paleomagnetically acceptable MAD values. One specimen (A) showed paleointensity experiments are technically possible, with proper stray-field minimization and temperature control. The data presented thus far are very preliminary but have shown the required paleodirection and paleointensity experiments are possible.

Table 5-4 Final magnetometer design specifications

Design feature	Requirement	Implementation
Temperature range	• Room – 600 °C (700 °C preferred)	• Room – 540 °C (reliably)
Physical properties	• Operational outside of a shielded room • Solid-state (no moving of specimen) during measurement	• Requirement met • Requirement met
Magnetic measurements	• Continuous three-axis acquisition of specimen magnetic moment	• Stepwise measurements at temperature
Measurement sensitivity	• SQUID magnetometer sensors • More sensitive than 5×10^{-8} Am²	• SQUID magnetometer sensors • Sensitivity of 1×10^{-9} Am²
Control system	• Automated demagnetizations of rock specimens and paleointensity experiments	• Requirement met
Total system cost	• Between a JR6 (€50 000) and a 2G RAPID system ($500 000)	• List price of components: ~£36 000 (+ work hours)

Some fine-tuning of the design is required before the magnetometer can be considered fully operational, however. There remain several inherited parts that were calibrated for the continuous magnetometer, but they are less appropriate for the stepwise magnetometer. These design improvements were intended to be completed once the magnetometer had been shown to be viable. However, the shutdown of the laboratory due to the COVID-19 coronavirus pandemic prevented these improvements from being implemented.

5.6.1 SQUID sensors

The instability of RF SQUIDs has been apparent since the first experiments in Chapter 3. This is easily remedied going forward, however, by simply doing a complete retuning each time. The instabilities that caused the failures in the paleodirection data were experimentally found to be the result of the SQUIDs' tank (LC) circuit using the wrong quantum energy well

(i.e. not at the lowest energy state). The SQUIDs can appear to operate correctly in a non-global minimum, but the unavoidable SQUID fluctuations have a higher chance of reaching the activation energy needed to escape the energy well, causing the SQUIDs to jump. Each time the SQUID electronics boxes and magnetometer equipment are turned on, the SQUIDs' tank circuit parameters (displayed as triangle/sine waves on an oscilloscope as in Chapter 4) must be adjusted, but usually by < 5%. These slight adjustments, if done each day for several days, can cause the SQUIDs to fall into a local minimum, instead of a global minimum. The additional time required for a complete (manual) tuning is less than five minutes.

Now that the heating and remagnetization take place far away from the SQUIDs, the SQUIDs can be realigned to a simpler XYZ arrangement, orthogonal to each other and at the base of the oven Dewar. The added benefit of this arrangement is that the SQUIDs will sit lower in the Mu-metal shield and therefore have a lower background magnetic field. The SQUIDs sensors and their orientation were inherited from Chapter 4, which had required a remagnetization coil to fit inside the oven Dewar. For that reason, the SQUIDs were moved up with respect to the base of the oven Dewar, which had necessitated that the three SQUIDs be positioned in a circle, 120° apart and at a 30° incline to get XYZ data. In the experiments presented in this chapter, only two SQUIDs were used because of the limitations of the two-channel SQUID controller available, With the addition of the one-channel, manually tuned SQUID controller from Chapter 3, this design can use all three SQUIDs to measure the data.

Arranging the sensors in an XYZ pattern will remove the need to de-convolute the output data because each channel records only a single vector. Further, the distance from the center of the oven to the SQUID sensors can be reduced from 3.14 cm to 2.6 cm, improving the resolution by a factor of 1.76. The minimum reliably-measurable specimen for the improved configuration is therefore 0.62 nAm^2 (49 mA/m for an 8 mm specimen).

5.6.2 CoilHeater & actuator

This chapter's CoilHeater was manually coiled and then later adjusted to be 12 mm in diameter, which was still too large for the specimen size used herein. Going forward, a new factory-coiled CoilHeater will need to replace the current oven, which will in turn improve both the heating and the magnetic uniformity in the oven.

The quadpod will need to be replaced with a purpose-built non-magnetic stand to minimize undesired 3D movement and maintain a constant stand-off distance for the actuator arm. Most of the problems associated with the quadpod are problems for the user and not for the data. The only symptoms of a slightly misaligned actuator are substantial

differences in SQUID output voltages. Since the distances are small and $B \propto r^{-3}$, small misalignments get amplified, reducing the overall signal to noise ratio of each measurement. The replacement quadpod would then cause the length of the quartz sample rod and/or location of the CoilHeater oven to each shift up to 2 cm in the $\pm \hat{z}$ direction to ensure proper alignment.

5.6.3 Experiments

The design improvements listed can be completed and tested in the span of one month each. Once the design updates are in place, a new set of paleodirection and paleointensity experiments can be undertaken. These next experiments will first replicate the demagnetization and remagnetization experiments undertaken in this chapter. The improved design features and larger specimens (10 mm diameter) are expected to substantially improve the data quality and resolution. The experiments will also have more clearly defined expected values. Following these experiments, specimens with natural remanent magnetizations are the next step.

The original aim was to run specimens from the 1960 Kilauea lava flow and SOH1 drill core, which are the subjects of Chapter 6 and Chapter 7, respectively. The data from these chapters, as well as the data presented in Chapter 9, suggest that the stability of the specimens would make them robust test cases for this magnetometer system. However, because of the COVID-19 outbreak, the laboratory was shut down in March 2020. As a result, it was not possible to run paleodirection or paleointensity experiments on naturally-magnetized specimens in time for the completion of this thesis.

The increased sensitivity from the improved SQUID arrangement will bring the magnetometer in line with other systems currently in operation, like the ORION system (Smirnov et al., 2019) (when used with a 10 mm diameter specimen) but without the need for vibrating the specimen (see table A1 in Supplementary Information A). The final addition to the magnetometer's experimental capabilities is the addition of checks for alteration, which will bring the magnetometer in line with the rest of the paleomagnetic community's expectations.

5.7 Conclusions

In this chapter, the development and initial testing of a novel three-axis stepwise SQUID magnetometer is described. This design presented herein used an oven design originally tested and described in Chapter 3 and the internals of the three-axis continuous magnetometer that were discussed in Chapter 4. The new prototype magnetometer can

automatically thermally demagnetize and measure a specimen from room temperature to 540 °C, with a theoretical maximum of 700 °C using the CoilHeater oven design. Specimens given single or multi-component laboratory TRMs were able to be demagnetized and analyzed using standard paleomagnetic principal component analysis software. Once the specimens have been demagnetized, the system can then remagnetize and measure the magnetization of the specimen as it cools back to room temperature. The system can therefore run a complete paleointensity experiment in-situ. The initial data in this chapter are noisy, incomplete, and imprecise, with errors sometimes greater than 30%. The biggest improvement in this system, and what makes it a break-through compared to the systems presented in the previous two chapters, is that the system consistently can collect magnetic data. The relatively minor problems that remain with this system have been identified and have a remediation plan going forward; there are no fundamental flaws identified herein. This stepwise magnetometer system therefore has immense potential for both its next generation and the next generation of paleomagnetic laboratory.

5.8 References

Cox, A., 1957, Remanent magnetization of lower to middle eocene basalt flows from oregon: Nature, v. 179, no. 4561, p. 685-686.

Gratton, M. N., Shaw, J., and Herrero-Bervera, E., 2005, An absolute palaeointensity record from SOH1 lava core, Hawaii using the microwave technique: Physics of the Earth and Planetary Interiors, v. 148, no. 2-4, p. 193-214.

Hodgson, E., Grappone, J. M., Biggin, A. J., Hill, M. J., and Dekkers, M. J., 2018, Thermoremanent Behavior in Synthetic Samples Containing Natural Oxyexsolved Titanomagnetite: Geochemistry Geophysics Geosystems, v. 19, no. 6, p. 1751-1766.

Jones, C. H., 2002, User-driven Integrated Software Lives: "PaleoMag" Paleomagnetics Analysis on the Macintosh: Computers and Geosciences, v. 28 (10), p. 1145-1151.

Kirschvink, J. L., 1980, The least-squares line and plane and the analysis of paleomagnetic data: Geophysical Journal of the Royal Astronomical Society, v. 62, no. 3, p. 699-718.

Shaw, J., 1974, Method of determining magnitude of paleomagnetic field application to 5 historic lavas and 5 archeological samples: Geophysical Journal of the Royal Astronomical Society, v. 39, no. 1, p. 133-141.

Stacey, F. D., 1959, Spinner-magnetometer for thermal demagnetization experiments on rocks: Journal of Scientific Instruments, v. 36, no. 8, p. 355-359.

Thellier, E., 1938, Sur l'aimantation des terres cuites et ses applications géophysique: Annales de l'Institut de physique du globe de l'Université de Paris, v. 16, p. 157-302.

Walton, D., 1977, Archeomagnetic intensity measurements using a squid magnetometer: Archaeometry, v. 19, no. JUL, p. 192-200.

Wilson, R. L., 1961, Palaeomagnetism in northern ireland .1. The thermal demagnetization of natural magnetic moments in rocks: Geophysical Journal of the Royal Astronomical Society, v. 5, no. 1, p. 45-58.

Section B

Paleointensity methodology

CHAPTER 6 SOLVING THE MYSTERY OF THE 1960 HAWAIIAN LAVA FLOW: IMPLICATIONS FOR ESTIMATING EARTH'S MAGNETIC FIELD

Foreword

This chapter was published in *Geophysical Journal International* on May 31st, 2019 under the title, "Solving the mystery of the 1960 Hawaiian lava flow: implications for estimating Earth's magnetic field". The authors are, in order, J Michael Grappone (also the author of this thesis), Andrew J Biggin, and Mimi J Hill. The co-authors have given permission to include this paper in my thesis. The author of this thesis completed all the paleointensity experiments and analyses, as well as the conception, conclusions, and writing of this paper. The co-authors provided feedback on the drafts and provided a forum for discussions of the larger implications of the data. The audience for this paper is a specific subset of paleomagnetists: those interested in method development.

The typeset, published version can be found in Supplementary Information F.

6.1 Abstract

Studying historic lava flows provides a rare comparison between direct measurements of the Earth's magnetic field and the field information recorded in the rock record. Connecting direct and indirect measurements provides a way to bridge the gap between historic data in the last 50-100 yr to geologic data over kyr to Gyr. The field strength in Hawaii in 1960 was directly measured at the Honolulu observatory to be 36.47 μT, so our paleointensity analysis of the 1960 flow is expected to give the same value. Two vertical sections of the 1960 flow (section 1 and section 2) were the focus of a previous microwave paleointensity study. The microwave experiments were run using the non-standard, perpendicular modified Thellier-type protocol and produced either apparently good quality data that were biased to low values (Section 1) or more scattered results averaging close to the expected value (Section 2). The cause of the non-ideal behavior observed in the data from the 1960 flow is a long-standing mystery that it is important to resolve to confirm the reliability of paleointensity measurements in general, and the microwave demagnetization mechanism in particular. Here, we test the hypothesis that higher quality, unbiased (only random noise) measurements are possible using an improved Thellier-type protocol coupled to an updated microwave system. New paleointensity experiments were performed primarily using the IZZI protocol (which allows alteration checks during the experiment) adapted for the microwave system. The specimens from section 1 produced more linear Arai plots and gave an estimate of 36.8 ± 3.4 μT, whereas those from section 2 gave an estimate of 39.1 ± 4.6 μT. Our new experiments demonstrate the microwave system's ability to produce accurate results and efficiently run any Thellier-style experiment. We investigate correcting Perpendicular data for undetected alteration and find that using too strict selection criteria can be counterproductive to obtaining accurate and precise microwave paleointensity results.

Key words: Paleointensity, paleomagnetism, remagnetization

6.2 Introduction

Understanding the Earth's magnetic field is key to understanding the behavior of the Earth's interior. Satellites give us extensive data on the geomagnetic field for the last 30-40 years and ground-based observatories (such as the Honolulu observatory or the French Bureau Central de Magnétisme Terrestre) provide data for up to an additional 100 years (Jackson et al., 2000). Paleomagnetic techniques let us extend these data to Gyr timescales. Paleomagnetic investigation of the rock record allows surface measurements that, given suitable rocks, can be used to provide insight into deep Earth processes at any point in geologic time.

Lavas contain magnetic field information stored in the magnetic grains, of which the most common is (titano)magnetite. Paleointensities cannot be directly measured in-situ, however. In order to extract paleointensity estimates, we must subject specimens to extensive experiments, whose accuracies are the subject of some debate (Biggin, 2010; Cromwell et al., 2018; Donadini et al., 2007). Data from historic lava flows, like those in Hawaii, therefore allow us to test various paleointensity methods on many rock types, since the answer is already known. In addition, the data allow geomagnetic models to connect the modern, continuous data records with the discrete datasets that volcanic eruptions provide.

One of the most important places for paleomagnetism are the Hawaiian Islands. The island of Hawai'i has active volcanoes and is located in the middle of the central Pacific, which covers 30% of the Earth's surface. In 1960, Kilauea's east rift zone erupted. The proximity of this site to the Honolulu Observatory (370 km away) provides a close approximation (36.47 μT) of the magnetic field intensity at the eruption site (Böhnel et al., 2011; Tanaka and Kono, 1991). Coe and Gromme (1973) suggested that the local magnetic field at the volcano could deviate from the observatory data by up to ±2 μT. The International Geomagnetic Reference Field: 12th Edition (IGRF-12)(Thebault et al., 2015) provides a second estimate of 36.2 μT, with the caveat that small scale magnetic anomalies can go undetected (Coe and Gromme, 1973).

Previous study-level average paleointensity (PI) estimates (e.g. Böhnel et al., 2011; Cromwell et al., 2015; Hill and Shaw, 2000; and Yamamoto et al., 2003) range from 33.9 μT using the microwave-perpendicular method (Hill and Shaw, 2000) to 49.0 μT using the Thellier-Coe method in Yamamoto et al. (2003). Detailed analyses of previous paleodirection studies, which show a recorded modern field direction, and paleointensity studies on the 1960 lava flow are given in Böhnel et al. (2011) and Cromwell et al. (2015). Herrero-Bervera and Valet (2009) extracted a highly accurate (< 2% error) PI estimate of 36.9 μT, using a

(relatively large) set of 36 specimens. Cromwell et al. (2015) similarly obtained an accurate estimate of 36.0 μT, using very strict selection criteria, which resulted in a success rate of 38% (7/18). The previous microwave study, Hill and Shaw (2000), used the non-standard perpendicular protocol out of necessity because the early 8.2 GHz microwave system had poor power absorption reproducibility precluding both double-treatments and alteration checks. For section 1, their data gave linear Arai plots, with a mean β (relative standard error) of 0.027, whose estimates were around 13% lower than expected, at 31.6 ± 3.6 μT. At section 2, the Arai plots showed considerable non-linear, two-slope behavior, but an (accurate) estimate of 37.1 ± 6.4 μT was extracted by fitting the entire Arai plot, regardless of linearity. This result is unexpected, as more linear (less noisy) data would be expected to be more accurate than less ideal (noisier) data.

These previous studies found significant variations in magnetic properties throughout the 1960 lava flow both vertically and laterally. Previously reported scanning electron microscopy (SEM) shows elongated primary low-Ti titanomagnetite, which form during cooling and thus retain a TRM (Böhnel et al., 2011; Dunlop and Ozdemir, 2001). Yamamoto et al. (2003) determined that alterations leading to a thermochemical remanent magnetization (TCRM) can explain why many thermal studies give high PI estimates. Generally, studies that used more specimens had estimates closer to the expected value, which suggests that either the flow has significant heterogeneities across it (a point noted in Hill and Shaw, 2000), or the PI methods used are inherently noisy. We note both of these explanations can be remedied by more extensive sampling of a given lava flow, since sparse sampling of heterogeneous flows can exaggerate the contribution of non-random (biased) noise in the data. Exaggerated non-Single Domain contributions can cause systematic differences in estimates for single and double treatment protocols (Biggin, 2010). The cause of the non-ideal behavior in these rocks, however, has been a mystery for over 20 years.

Hill and Shaw (2000) undertook extensive reflected-light microscopy and obtained hysteresis properties, isothermal remanent magnetization acquisitions, and thermoremanent curves for sister samples to those used herein. Hill and Shaw (2000) found, in both sections, predominantly titanomagnetite with a Curie temperature of approximately 520 °C. They further found predominately linear thermoremanent curves, which imply rapid cooling of the lava, preventing uniform iron oxide grain distribution. Figure 3 in Hill and Shaw (2000) shows moderately low (broadly between the single- and multi-domain ranges) hysteresis parameters, with section 2 having a larger range than section 1. Rapidly cooled pseudo Single-Domain grains typical of basalts have been shown to have negligible cooling

rate effects (Biggin et al., 2013; Ferk et al., 2014; Yu, 2011); however, this has become the subject of some debate (Santos and Tauxe, 2019). The previous microwave data set from Hill and Shaw (2000) gave underestimates, which is the opposite sense to that expected if a cooling rate correction were needed. Cooling rate correction has, therefore, not been investigated in this study.

Advances in the microwave technique now allow the use of the IZZI protocol (Yu et al., 2004), which allows $pT_{(M)}RM$ (partial (microwave-)thermoremanent magnetization) checks for alteration and contains a built-in check for multi-domain behavior, through the zigzagging of the Arai plots (Yu and Tauxe, 2005). We need to understand if using the more modern IZZI protocol helps resolve the unexpected outcome from Hill and Shaw (2000) to solidify the utility of not only the microwave system but also the IZZI protocol applied to the microwave. Our goal herein is, therefore, to extract high quality paleointensity data that yield an estimate of 36.2 – 36.5 μT using Liverpool's most sophisticated microwave system (Hill et al., 2008). We also aim, more generally, to determine the source of the non-ideal behavior to confirm the reliability of paleointensity measurements in general, and the microwave system as a demagnetization mechanism in particular.

6.3 Methods

The samples used are the archived samples remaining from Hill and Shaw (2000). In the original study, standard 25 mm diameter cores were taken from two sites, which were 16m apart. At section 1, the flow was 1 m in height. At section 2, the flow was 75 cm in height. For full details, readers are referred to Hill and Shaw (2000). Due to the scarcity of material available, microwave cores with a diameter of 5 mm and a height of 1-2 mm (instead of the more standard 5 mm height) were drilled from 21 individual 25 mm diameter cores to maximize the number of specimens.

The main protocol used in this study was the IZZI protocol (Yu et al., 2004), adapted for use on the microwave (MW) system, which we ran on 59 specimens. To compare our data to the previous study, we also used the MW Perpendicular (MW-Perp) method (Hill and Shaw, 2007) on 46 specimens, of which 21 also included pT_MRM (partial thermo-microwave remanent magnetization) checks. All MW tests were run on the 14 GHz Tristan Microwave system at the University of Liverpool's Geomagnetism Laboratory (Hill et al., 2008). We used MW powers starting at 5 W for 5s, up to the maximum of 40W, for a maximum time of 20s (normally 5-8s maximum), generally until specimens has lost at least 90% of their NRM. We used an applied laboratory field of 36 μT, approximately the expected strength. The field

was always applied perpendicular to the specimen's NRM. This can exaggerate Arai plot zigzagging (Yu and Tauxe, 2005) from specimens that contain non-SD magnetic grains, according to Shaar et al. (2011), but it allows a more direct comparison with Hill and Shaw (2000).

The IZZI protocol is a double treatment protocol that combines in-field (I) steps and zero-field (Z) steps in an enclosed couplet. At each MW power integral, both a Z and an I step are performed before being taken to a higher power integral and the treatments reversed. We used the variant ZIIZ, followed by a pT_MRM check step (P) with the same power integral as the last step in the previous couplet, which gives a complete pattern of 'ZIIZP'. The standard IZZI protocol includes pTRM checks (Yu et al., 2004), but it can, in theory, be run without them. Therefore, for consistency and clarity with the other protocols used, in this paper, we will refer to the MW version of IZZI with pT_MRM checks as MW-IZZI+.

The Perpendicular protocol (Kono and Ueno, 1977) uses only a single treatment at each temperature step, with the field applied perpendicular to the specimen's NRM. Variation from a perpendicularly applied field is represented by $\Delta\theta$ and is required to be small. For 21 specimens, we also included a Z step and a P step after every other I step. The Z step is necessary for the pT_MRM check to work. With the addition of the Z and P steps, this protocol can be written as 'IIZP'. We will refer to this protocol as MW-Perp++ to reflect the additional two steps. We note that Biggin (2010) predicted that the addition of Z and P steps to a perpendicular experiment would add considerable extra data point scatter on Arai plots if the remanence carriers do not behave as ideal Single-Domain grains.

In this paper, we use a primary, moderately strict, set of selection criteria, modelled after the MC-CRIT.C1 selection criteria (without tail checks) from Paterson et al. (2015). To test the influence of selection criteria on the PI estimates, we also tested two additional sets of selection criteria on the MW-IZZI+ data analysis: a loose set modelled after Bono et al. (2019) and a strict set modelled after Cromwell et al. (2015). These criteria can be found in Table 6-1. Paterson et al. (2015) details the statistics used and showed that the moderately strict selection criteria have a median accuracy of 95.3% in their experiments (with tail checks). In all cases, in order to try to minimize the impact of estimates made from lower power integral steps, we opted for the longest best-fit line that still passed the selection criteria.

Table 6-1 Selection criteria

Type	N	FRAC	R^2	β	q	$\lvert\vec{K}'\rvert$	MAD_{ANC}*	α*	DRAT**	Δθ***
Loose†	≥ 4	--	≥ 0.9	--	--	--	≤ 10	--	≤ 10%	--
Moderate	≥ 4	≥ 0.45	--	≤ 0.1	≥ 4	≤ 0.480	≤ 10	≤ 10	≤ 10%	≤ 0.25°
Strict†	≥ 4	≥ 0.78	--	≤ 0.1	≥ 4	≤ 0.164	≤ 5	≤ 10	≤ 10%	--

N is the number of data points, FRAC is a measure of the NRM used, β/R^2 are measures of scatter around the best-fit line, q is a measure of the data quality, $\lvert\vec{K}'\rvert$ is a measure of Arai plot curvature, MAD and α determine the scatter of the specimen's paleodirection. Δθ is the change in the θ1 + θ2 value, an indication of the perpendicularity between the NRM and TRM directions (Hill and Shaw, 2007) for the perpendicular experiment.

*for technical reasons, only IZZI+ data can use these criteria
** Perpendicular data lack pT_MRM checks, so DRAT cannot be used for these data
*** Used only for Perpendicular-style experiments
† These criteria were only tested on MW-IZZI+ data

First Order Reversal Curves (FORCs) were run on 2 specimens to assess their magnetic domain states. The data were gathered on a Princeton Instruments Vibrating Sample Magnetometer (VSM) at the Institute of Rock Magnetism (IRM) at the University of Minnesota. These data are available in supplementary information A.

We also were interested in correlating changes in hysteresis parameters with pT_MRM check failures. To do this, we ran hysteresis loops on a Magnetic Measurements Variable Field Transition Balance to compare changes in hysteresis parameters with the failure of pT_MRM checks. We used sister specimens of those used in the PI experiments. We ran an initial hysteresis loop, then simulated a MW-IZZI+ experiment, completing the ZIIZP pattern at the same powers used on sister PI experiment specimens. Another hysteresis loop was measured, and then the specimen underwent another ZIIZP at the next power integral steps.

6.4 Results

6.4.1 Paleointensity estimates

We ran 70 specimens from 13 samples from section 1 and 35 specimens from 8 samples from section 2. Using our preferred selection criteria, the moderately strict set, 68 new PI estimates were accepted, for an overall success rate of 65%. All new paleointensity estimates and raw data will be available on the MagIC database. Arai plot fit data can be found in Supplementary Information B. Some specimens showed an overprint removed at low power integrals, but the additional component generally disappeared by power integral applications of approximately 40-60 Ws. No systematic variation was observed over the available sampling of the section. We therefore report an arithmetic mean and one standard deviation of the successful specimens' paleointensity estimates, in Table 6-2. Most specimens lost the

majority of their magnetization by 1600 Ws. It was necessary, however, to treat some (usually in one or two large steps) to ~2400 Ws.

Table 6-2 New Paleointensity estimates

Method	Section 1 PI estimate (μT ± 1σ)	Median β (passed ± 1σ)	Success rate	N	Section 2 PI estimate (μT)	Median β (passed ± 1σ)	Success rate	N
MW-Perp	31.2 ± 5.0	0.0354 ± 0.015	88%	15	37.7 ± 5.4	0.0395 ± 0.028	63%	5
MW-Perp++	33.5 ± 1.9	0.0394 ± 0.0068	50%	6	36.8 ± 5.7	0.0295 ± 0.016	89%	8
MW-IZZI+ (loose)	37.3 ± 3.3	0.0615 ± 0.024	70%	29	41.7 ± 6.5	0.0628 ± 0.028	78%	14
MW-IZZI+ (moderate)	36.8 ± 3.4	0.0571 ± 0.022	54%	22	39.1 ± 4.6	0.0692 ± 0.027	61%	11
MW-IZZI+ (strict)	--	--	--	0	43.9 ± 8.9	0.0490 ± 0.036	17%	3

6.4.1.1 Section 1

Of the 41 specimens that underwent a MW-IZZI+ treatment, 70% passed the loose selection criteria and averaged 37.3 ± 3.3 μT, 54% passed the moderately strict selection criteria and averaged 36.8 ± 3.4 μT and 0% passed the strict selection criteria. The loose and moderately strict estimates are not statistically distinct from the IGRF field estimate of 36.2 μT, with p = 0.20 and p = 0.68, respectively. The most common reason for failure for the MW-IZZI+ experiments were pT_MRM check failures. A set of 4 example Arai plots (Nagata et al., 1963) from these experiments that show the range of behavior observed can be found in the top row of Figure 6-1. Approximately half of the specimens that passed our selection criteria had a pT_MRM failure in the highest (not accepted) power integral ranges. Zigzag was visually observed in 14/41 (34%) specimens (Figure 6-1 top row), with the zigzag often increasing after a pT_MRM failure. In no case was the zigzag alone sufficient for the Arai plot data to have unacceptably high scatter (β).

We ran 17 specimens from Section 1 using MW-Perp with an 88% success rate. The 2 failures for the MW-Perp experiments were the result of the angle ($\theta_1 + \theta_2$) between the total vector and NRM (θ_1) and total vector and B_{lab} (θ_2) (Hill and Shaw, 2007) exceeding the tolerance allowed. This kind of failure can be attributed to anisotropy, alteration, or imperfect removal of any overprints (which results in a non-perpendicular field direction). We found an average PI of 31.2 ± 5.0 μT. Figure 6-1's middle row demonstrates that although the plots are often very straight, the estimates are still biased to lower values.

As an intermediate between MW-IZZI+ and MW-Perp, we ran 12 specimens using MW-Perp++, with a below average success rate of 50%. Like the MW-IZZI+ specimens, the most

common reason for failure was pT_MRM check failures. Like this section's MW-IZZI+ specimens, half of the specimens that passed the selection criteria had a pT_MRM failure in the highest (not accepted) power integrals. These specimens gave an estimate falling between that of the MW-IZZI+ and MW-Perp, at 33.5 ± 1.9 µT. The bottom row of Figure 6-1 demonstrates that the MW-Perp++ also has Arai plots with data characteristics between those of MW-IZZI+ and MW-Perp.

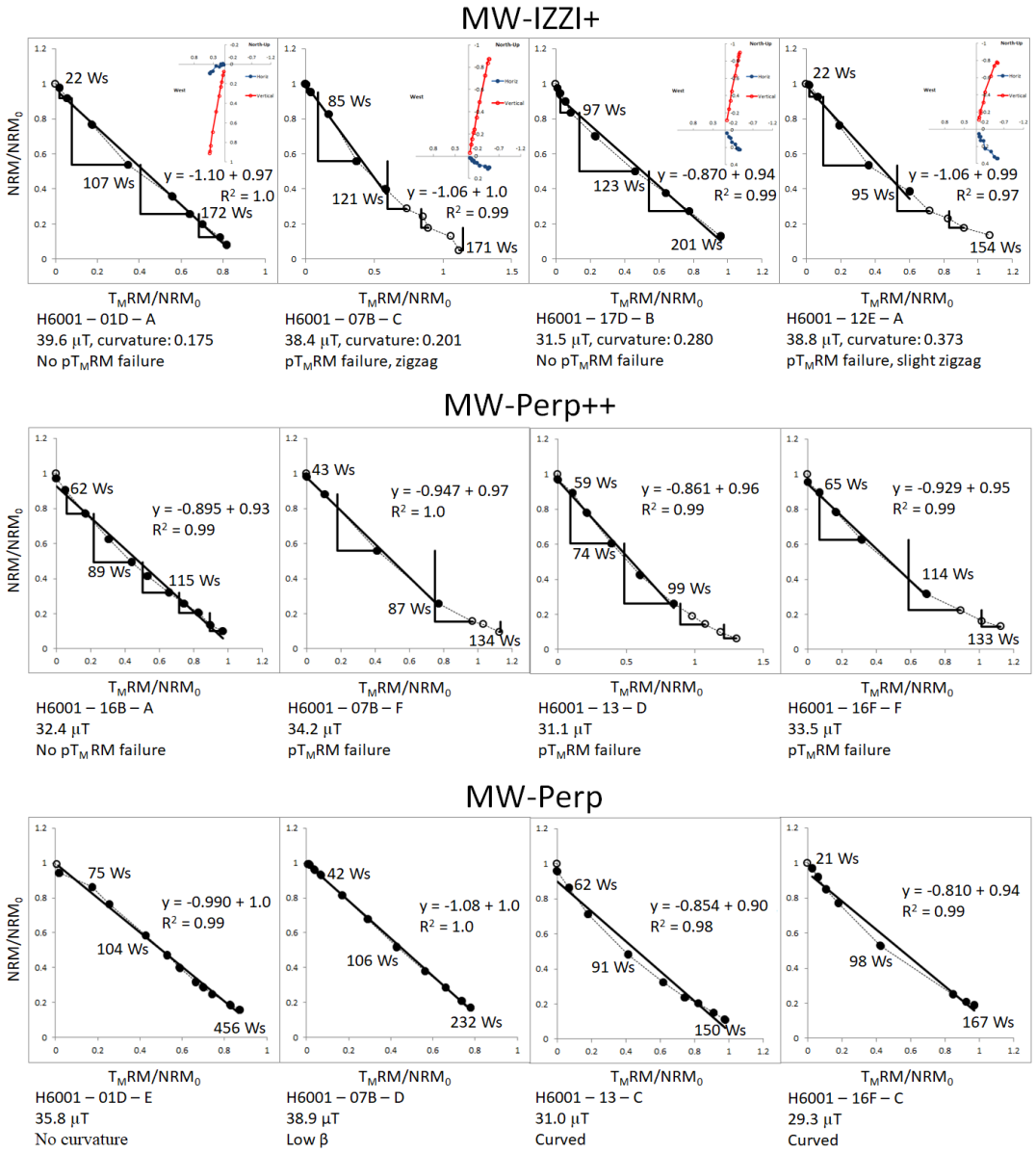

Figure 6-1. Section 1 Arai Plot examples. Orthogonal projections are provided for MW-IZZI+ data. Black circles are accepted data points (with their line of best fit in black), open circles are rejected data points (using the moderately strict selection criteria). The black right-angled lines are pT_MRM checks, and β is a measure of data scatter around the best fit line. Evidence of alteration was found in approximately half of specimens that had pT_MRM checks. The MW-Perp specimens have some of the most linear Arai plots but on average also gave the lowest PI estimate.

6.4.1.2 Section 2

Section 2 gave higher estimates than section 1 and showed relatively consistent results from all three protocols. 18 specimens received a MW-IZZI+ treatment. 14 specimens (78%) passed the loose selection criteria, 11 specimens (61%) passed the moderately strict selection criteria, and 3 specimens (17%) passed the strict selection criteria. These gave the highest average PI estimates, at $41.7 \pm 6.5\ \mu\mathrm{T}$, $39.8 \pm 4.6\ \mu\mathrm{T}$, and $43.9 \pm 8.9\ \mu\mathrm{T}$, respectively. The loose selection criteria's estimate is statistically distinct from the expected 36.2 µT expected value (p = 0.010), but the moderately strict (p = 0.090) and strict estimates are not (p = 0.29). All the specimens that failed did so because of pT_MRM check failures. Half of the specimens that passed had pT_MRM failures at higher (not-accepted) power integrals. The top row of Figure 6-2 contains representative Arai plots from these data. Slight zigzag was observed in 5/18 (36%) Arai plots, with minimal observed change after pT_MRM failures.

Of the 8 specimens that received a MW-Perp treatment, 5 passed. The 3 failures were, like for specimens from section 1, the result of the $\theta_1 + \theta_2$ angle exceeding tolerance. The successful experiments gave an average PI estimate of $37.7 \pm 5.4\ \mu\mathrm{T}$. The bottom row of Figure 6-2 shows half of the accepted Arai plots from section 2's MW-Perp data set.

Like with section 1, the MW-Perp++ PI estimates for section 2 falls between that of the MW-IZZI+ and the MW-Perp. Only 1 specimen out of 9 failed, as a result of its pT_MRM checks failing. Of the specimens that passed, 2 had pT_MRM failure at the highest (not accepted) power integrals. The successful specimens gave an average of $36.8 \pm 5.7\ \mu\mathrm{T}$. Representative Arai plots can be found in Figure 6-2's middle row.

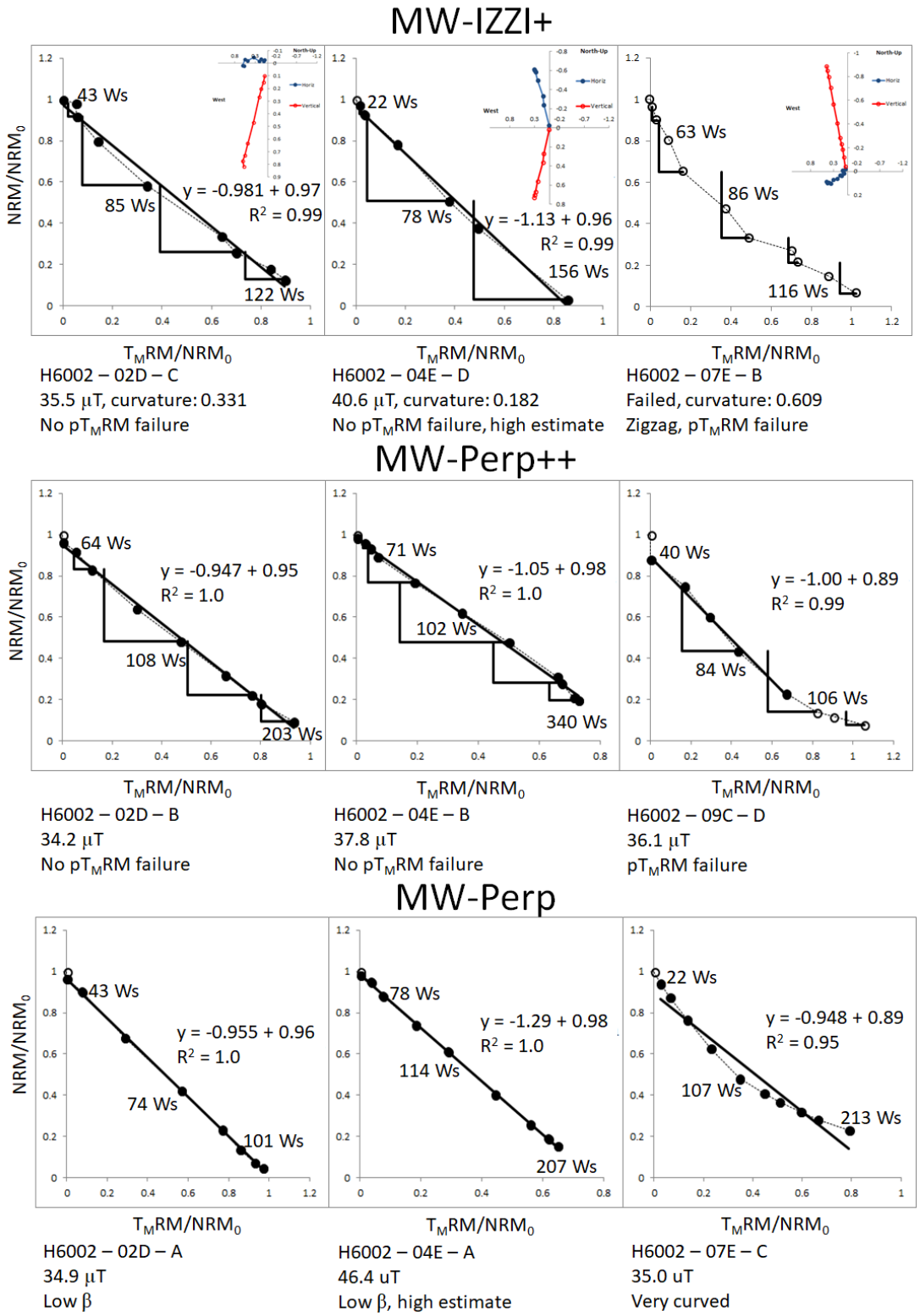

Figure 6-2 Section 2 Arai Plot examples. Orthogonal projections are provided for MW-IZZI+ data. Black circles are accepted data points (with their line of best fit in black), open circles are rejected data points (using the moderately strict selection criteria). The black right-angled lines are pT_MRM checks, and β is a measure of data scatter around the best fit line. The Arai plots for specimens in section 2 had similar behavior to those in section 1 in terms of pT_MRM failures and zigzagging MW-IZZI+ Arai plots.

6.4.2 Interpreting MW-IZZI+ as MW-Perp and MW-Perp++

The MW-IZZI+ experiments were run perpendicular to each specimen's NRM direction. For the derived MW-Perp++ (MW-derPerp++) test, we removed the first Z step data from each ZIIZP couplet and treated the rest of the data as normal for MW-Perp++. For the derived MW-Perp (MW-derPerp) test, we removed all the Z and P steps from the raw data file. We then processed these data through the same plotting routine as the MW-Perp and MW-Perp++ data. Many specimens failed due to the angle changing, which was also observed in our real MW-Perp experiments.

From the MW-derPerp++ Arai plots (examples in Figure 6-3), we found an average PI estimate of 33.2 ± 5.8 μT (28/41 passed) for section 1 and 39.9 ± 8.2 μT (10/18 passed) for section 2. These estimates are not statistically distinct from the (direct) MW-Perp++ estimates and are on average 10% lower and 2% higher than the respective MW-IZZI+ estimates. The MW-IZZI+ estimate for section 1 is statistically distinct from the section 1 MW-derPerp++ estimate; the section 2 estimates are not statistically distinct. Figure 6-3 compares the specimen-level MW-derPerp++ PI estimates with the MW-IZZI+ data from which the MW-derPerp++ data are derived. Table 6-3 contains a comparison of the MW-derPerp++ mean with the MW-IZZI+ and MW-Perp++ means.

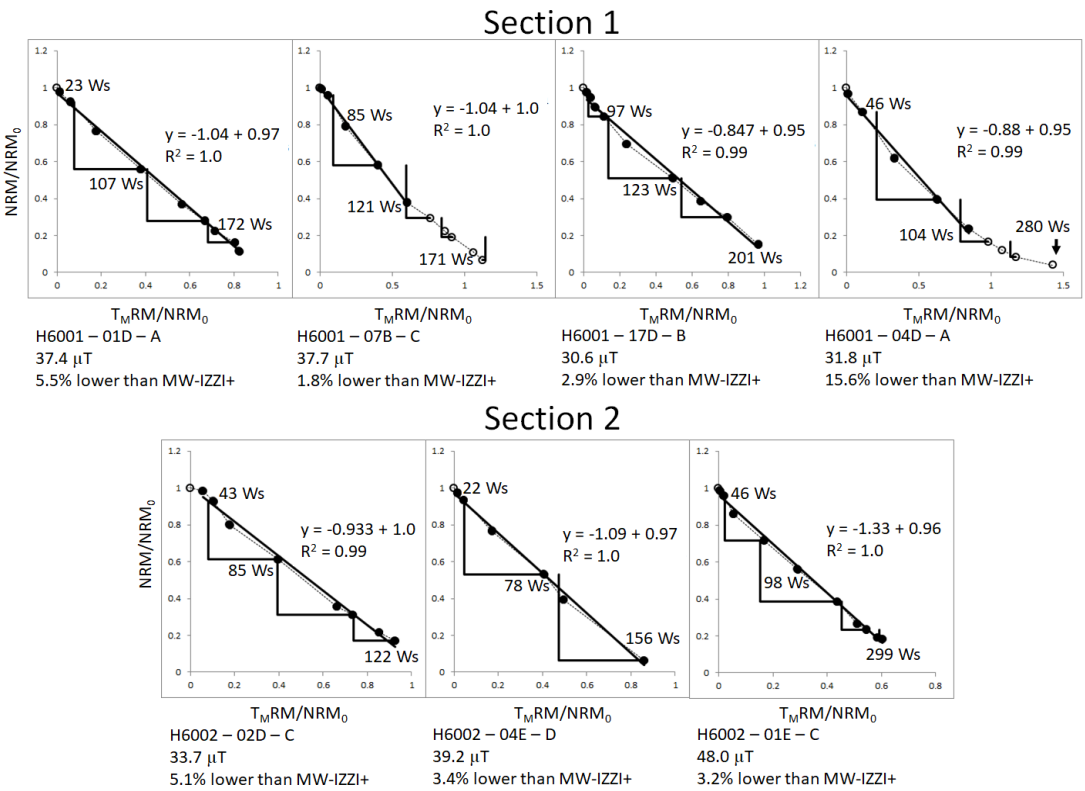

Figure 6-3 MW-IZZI+ data interpreted as MW-Perp++ (MW-derPerp++) data; appropriate Z steps were removed and then the raw data were replotted. Black circles are accepted data points (with their line of best fit in black), open circles are rejected data points. The black right-angled lines are pT_MRM checks. Top: Section 1 (section average with this treatment: 33.2 ± 5.8 µT). Bottom: Section 2 (section average with this treatment: 39.9 ± 8.2 µT)

From the MW-derPerp Arai plots (examples in Figure 6-4), we extracted an average PI estimate of 31.3 ± 4.6 µT (32/41 passed) for section 1 and 37.1 ± 9.9 µT (13/18 passed) for section 2. Using the MW-IZZI+ data without pT_MRM checks or Z steps gave PI estimates that are not statistically distinct from and are within 4% our MW-Perp estimates of 31.2 µT and 37.7 µT, respectively (but are from each other). The estimates are 15% and 8.7% lower than the respective MW-IZZI+ site-level estimates. Figure 6-4 compares the specimen-level MW-derPerp PI estimates with the MW-IZZI+ data from which the MW-derPerp data are derived. Table 6-3 contains a comparison of the MW-derPerp mean with the MW-IZZI+ and MW-Perp means.

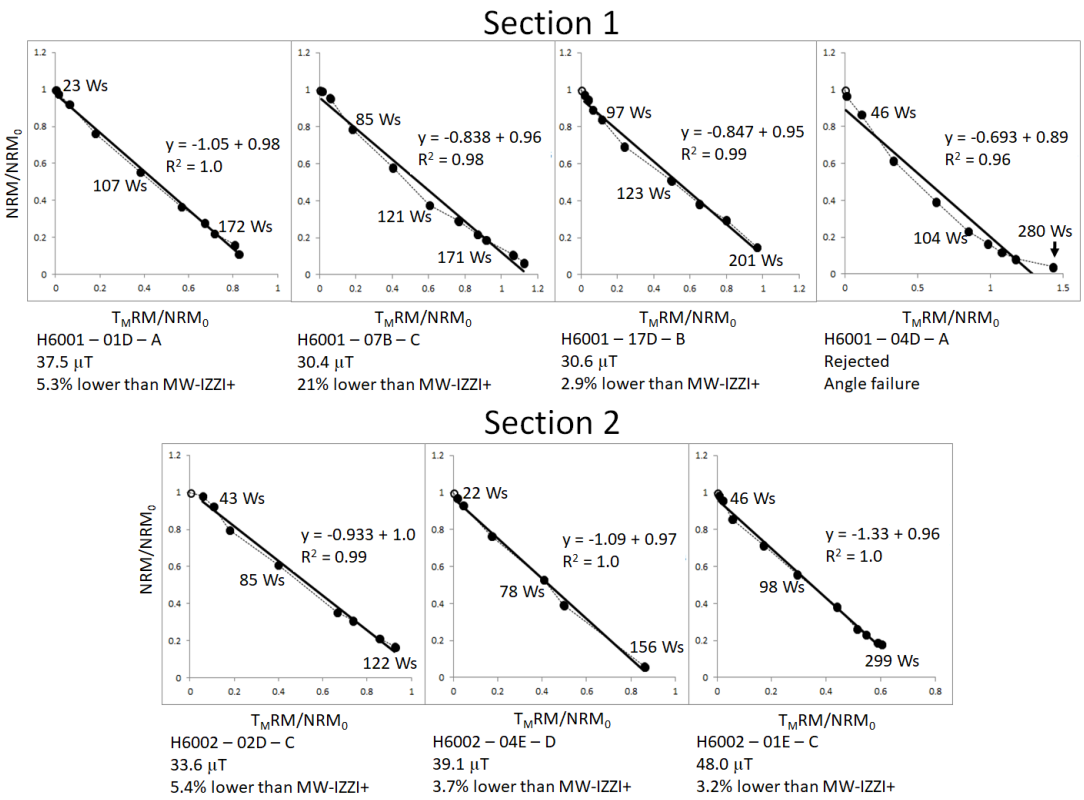

Figure 6-4 MW-IZZI+ data interpreted as derived MW-Perp (MW-derPerp) data; Z and P steps were removed and then the raw data were replotted. Black circles are accepted data points (with their line of best fit in black), open circles are rejected data points. The black right-angled lines are pT_MRM checks. Top: Section 1 (section average with this treatment: 31.3 ± 4.6 µT). Bottom: Section 2 (section average with this treatment: 37.1 ± 9.9 µT)

6.4.3 Using the MW-IZZI+ data to interpret the MW-Perp data

To try to remove the effects of alteration on the PI estimates, we repeated the analysis of the MW-Perp with the additional constraint that we only allowed data from power integrals below which pT_MRM checks in MW-IZZI+ sister specimens did not fail. We extracted PI estimates of 34.6 ± 4.7 µT (14/17 passed) for section 1 and 41.0 ± 7.0 (6/8 passed) for section 2. These estimates are not statistically different from their respective MW-IZZI+, MW-Perp++, or MW-Perp estimates. Assuming sister specimens had alterations occur at similar power integrals, this observation implies that undetected alterations caused a shallowing of the Arai plot, which caused PI estimates to be lower than expected.

6.4.4 pT_MRM checks vs hysteresis parameters

This experiment aims to test if changes observing hysteresis parameters is sufficient to identify alterations when pT_MRM checks are not present (Hill and Shaw, 2000). We ran 6 specimens, 3 from section 1 and 3 from section 2 to compare the changes in the hysteresis parameters of the specimens with the results of pT_MRM checks measured during a series of

treatments that mimicked a paleointensity experiment. Figure 6-5 contains the results of this experiment (the reader is referred to supplementary information B.2 for further discussion). All specimens exhibited a trend to move towards the Single Domain region as the applied power increased. The dotted lines correspond to failed pT_MRM checks and the solid lines correspond to positive pT_MRM checks for sister specimens. The largest changes in hysteresis parameters generally corresponded to pT_MRM check failures. The correlation, however, is insufficiently quantified to be used in place of pT_MRM checks.

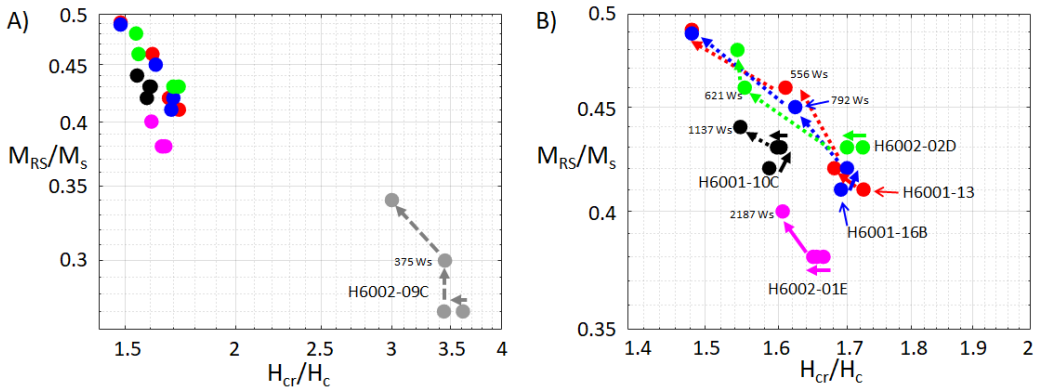

Figure 6-5 Hysteresis parameter plot showing movement over a simulated MW-IZZI+ experiment. A) all data taken and B) zoomed in near the S.D. section. Solid colored arrows correspond to a passed pT_MRM check on sister specimens, whereas dotted colored arrows correspond to a failed pT_MRM check on sister specimens. Power integrals are noted at the first failed pT_MRM check or highest power integral step.

6.5 Discussion

6.5.1 Non-SD behavior

The overall goal was to find estimates as close to 36.2 – 36.5 μT as possible, while minimizing the unnecessary rejection of measurement-level Arai plot data. Our closest estimate from section 1 was produced by MW-IZZI+ experiments and the closest estimate from section 2 came from its MW-Perp++ experiments (all estimates can be found in Table 6-3). Section 2 was previously shown in Hill and Shaw (2000) to exhibit two-slope behavior in its Arai plots. We have found the inflection point for their two-sloped Arai plots to be correlated with pT_MRM check failures when present. The mean curvatures, $\left|\overrightarrow{K'}\right|$, for sections 1 and 2 are 0.283 and 0.261, respectively, which are relatively high. Curved Arai plots are characteristic of specimens containing non-SD grains (Biggin, 2010; Hodgson et al., 2018; Levi, 1977; Shcherbakov and Shcherbakova, 2001). The pT_MRM check failures in the MW-Perp++ data are consistent with the findings in Biggin (2010), who found that pT_MRM checks can exaggerate non-SD behavior. The MW-derPerp++ data have pT_MRM check failures at similar power integrals and NRM remaining to the MW-IZZI+ data. We interpret the pT_MRM check

failures to be the result of irreversible thermochemical alteration, but the data also indicate non-SD behavior as a potential source of error. Zigzagging Arai plots were found in more than 1/3 of all new specimens given an IZZI+ treatment; this is also characteristic of non-SD grains.

6.5.2 Comparison with previous microwave results

Our new MW-Perp estimates agree very closely with those from Hill and Shaw (2000). For section 1, we extracted an estimate of 31.2 ± 5.0 μT, compared to their overall estimate of 31.6 ± 3.6 μT. For section 2, we extracted an estimate of 37.7 ± 5.4, compared to their overall estimate of 37.1 ± 6.4. If we look only at estimates from the exact same core samples, Hill and Shaw (2000) extracted estimates of 31.2 ± 3.4 μT and 36.6 ± 7.1 μT, differences of <1% and 3%, respectively. Like Hill and Shaw (2000), we found that specimens from section 1, on average, had straighter Arai plots than section 2. Even though we used a different MW system, the 14 GHz Tristan system, instead of the original 8 GHz system Hill and Shaw (2000) used, we still recovered the same MW-Perp estimates, so equipment effects appear to be negligible.

In section 6.3.3, we used our MW-IZZI+ power integrals and pT_MRM checks to select MW-Perp Arai plot points. Here we reanalyze the Hill and Shaw (2000) data to independently verify the results. Hill and Shaw (2000) used a different resonant cavity, so we cannot use the power integrals directly like in section 6.3.3. Instead, we can estimate the power integrals of the pT_MRM check failures on the Arai plots using the NRM remaining as a rough analog. For example, if MW-IZZI+ specimen had a failed pT_MRM check when 40% of the NRM remained, then we only accept MW-Perp data points from Hill and Shaw (2000) that have at least 40% NRM remaining. Following this method, we extracted estimates of 33.4 ± 5.8 μT and 36.3 ± 6.4 μT for sections 1 and 2, respectively, which are < 2% different from our new MW-Perp++ estimates of 33.5 ± 1.9 μT and 36.8 ± 5.7 μT, respectively. The lower estimates observed in MW-Perp compared to MW-Perp++ are, therefore, likely the result of undetected alterations in the MW-Perp data. In the original study of Hill and Shaw (2000), it appears that non-SD and alteration effects were cancelling one another out to a degree such that Section 2 fortuitously recovered the palaeointensity accurately when the entire (curved) Arai plot was used.

Table 6-3 Estimates extracted by section and protocol

Method	Section 1 PI estimate (μT)	IEF	N	Section 2 PI estimate (μT)	IEF	N
MW-Perp (new)	31.2 ± 5.0	0.16	15	37.7 ± 5.4	0.031	5
MW-Perp++ (new)	33.5 ± 1.9	0.081	6	36.8 ± 5.7	0.016	8
MW-IZZI+ (new, loose)	37.3 ± 3.3	0.030	29	41.7 ± 6.5	0.15	14
MW-IZZI+ (new, moderate)	36.8 ± 3.4	0.016	22	39.1 ± 4.6	0.074	11
MW-IZZI+ (new, strict)	–	-	0	43.9 ± 8.9	0.21	3
MW-IZZI+ (treated as MW-Perp in section 6.3.2)	31.3 ± 4.6	0.016	32	37.1 ± 9.9	0.024	13
MW-IZZI+ (treated as MW- Perp++ in section 6.3.2)	33.2 ± 5.8	0.090	28	39.9 ± 8.2	0.093	10
MW-Perp (treated as in section 6.3.3)	34.6 ± 4.7	0.046	14	41.0 ± 7.0	0.12	6
MW-Perp (Hill and Shaw, 2000)	$31.6 \pm 3.6\ (all)$ $31.2 \pm 3.4\ (sister)$	0.15 0.16	40 22	$37.1 \pm 6.4\ (all)$ $35.9 \pm 5.5\ (sister)$	0.024 0.008	30 14
MW-Perp (treated as in section 6.4.2)	33.4 ± 5.8	0.084	21	36.3 ± 6.4	0.003	14

Note. N is the number of specimens across all samples from the section. IEF is the intensity error fraction (Biggin et al., 2007)

MW-IZZI+ data, with moderately strict selection criteria, for both sections 1 and 2 produce paleointensity estimates that are not statistically distinct (p_1 = 0.417; p_2 = 0.063) from the 36.2 μT value given by the IGRF (Thebault et al., 2015). The data with loose selection criteria give overestimates, which is broadly consistent with the findings of Herrero-Bervera and Valet (2009). The data with strict selection criteria give the smallest data set, which means the data likely do not sample the flow sufficiently (Biggin et al., 2003). The high scatter, with inaccurate values both above and below the expected value, is consistent with the findings of Paterson et al. (2012) that overly strict selection criteria can, in some cases, overly reject accurate data.

Both the new MW-Perp and MW-Perp++ data also give PI estimates that are not statistically different from 36.2 μT (p_{perp} = 0.85; p_{perp++} = 0.77). All new data have intensity error fractions (IEFs) of less than 0.1, except for the new MW-Perp data from section 1, which was expected to have the highest IEF. The new MW-Perp data have IEFs within 0.01 of the data from Hill and Shaw (2000).

The addition of alteration checks in the MW-Perp++ and the data treatment in section 6.3.3 decrease the IEF of the MW-Perp data in section 1 by 0.08 and 0.11, respectively. These same techniques increase the IEF of the MW-Perp data in section 2 by 0.01 and 0.08, respectively but the new estimates are within uncertainties of the former ones. The low estimates produced by the MW-Perp experiments appears, therefore, to be the result of undetected alterations in the MW-Perp data, rather than a systematic error caused by the MW radiation.

The MW-Perp++ data lack the zigzagging (Yu and Tauxe, 2005) of the MW-IZZI+ data, which sometimes allowed more Arai plot data points to be selected. In the case of section 1, selecting additional Arai plot data produced a lower average PI estimate, which mirrors the behavior seen in the MW-Perp data. For the generally less linear Arai plots in section 2, the different data caused a large increase of dispersion in the PI estimates because different specimens passed the selection criteria.

6.5.3 Implications for similar experiments

When compared to other, thermal studies on this lava flow (e.g. Böhnel et al., 2011), some of the MW data in Hill and Shaw (2000) appeared to be biased low. The large differences in properties between sections 1 and 2 further obfuscated their results. Cromwell et al. (2018) notes this pattern to hold true for all non-thermal Thellier PI experiments for the 0 – 2 ka age range. We also note, however, that thermal studies from different, often sparsely-sampled, sections of the 1960 Kilauea lava flow generally gave PI estimates higher than the 36.5 µT field strength observed at the Honolulu Observatory, which probably indicates that the data were affected by exaggerated non-Single Domain behavior.

We have demonstrated that MW-IZZI+ experiments can produce results that are highly distinctive from those produced by MW-Perp experiments. With the newest microwave system's ability to run any Thellier-style experiment, and the protocol-dependent PI estimates extracted in this paper, microwave data should not be combined into a single 'Microwave method' data set. The new Microwave Thellier-style results are still lower than those reported in Böhnel et al. (2011) and Cromwell et al. (2018), but they are not statistically different from the expected values for this lava flow. A direct thermal – microwave comparison is therefore needed in the future on sister specimens.

The lower estimates observed herein for specimens receiving a MW-Perp treatment, compared to MW Thellier-style experiments is broadly in agreement with Biggin (2010). Biggin (2010) found the largest discrepancies between MW and thermal studies where the

MW demagnetization mechanism was coupled with the perpendicular protocol, but the thermal demagnetization mechanism was coupled with a double heating Thellier-style protocol (see Table 2 in Biggin, 2010). We have expanded on these results and shown here that low MW-Perp estimates can potentially be the result of both undetected alterations because the Perp protocol lacks pT_MRM checks as well as the enhanced non-SD behavior that can be observed in double-heating protocols (Biggin, 2010; Hodgson et al., 2018).

Whenever relevant rock magnetic data are sparse, our data suggest that the IZZI+ protocol is preferred, as it contains a built-in check for non-SD behavior and uses pT_MRM checks. However, as demonstrated in section 2, IZZI+ data can be prone to slight overestimations, so IZZI+, by itself (without any rock magnetism or other independent data), may not always be sufficient for high accuracy paleointensity surveys on older, less well-behaved specimens. Using the MW-IZZI+ data to reinterpret the MW-Perp data gave a PI estimate that was not statistically different from the expected value. The Perp protocol only requires a single treatment at each step, which increases experimental speed and reduces chances for alteration. If the Perpendicular protocol is used, the data set can then be corrected using sister IZZI+ experiments.

A multi-technique approach is favored when selection criteria have to be more relaxed, due to, for example, the age of the specimens and resulting poorer quality of the Arai plot data. The data herein have showed that running IZZI+ with a perpendicular applied magnetic field allows the data to be interpreted as Perp or Perp++ to have an implicit second protocol to check robustness.

If a multi-technique approach is not possible for technical reasons, then maximizing the number of paleointensity estimates another way is paramount. Multiple sampling sites- to maximize flow coverage, as suggested by Biggin et al. (2007)- and reduced-size cores (5 mm diameter x 1-2 mm height, in our case for microwave specimens), if possible, increases the amount of heterogeneity between specimens. We have seen with these specimens that averaging all these helps approach the correct mean strength of the Earth's magnetic field if previously unrecognized heterogeneities exist.

6.6 Conclusions

The modern, 14 GHz Tristan microwave system, using the IZZI+ protocol, has yielded PI estimates that are not statistically distinct from the expected values. With the addition of pT_MRM checks, we have shown that undetected alterations are a primary cause of the lower

estimates observed in the Microwave-Perpendicular data, not a bias resulting from microwave radiation or the older system. The Microwave-IZZI+ protocol has also showed that there is some non-Single Domain behavior present in the data. Since the observed alteration mandates using lower 'temperature' (power integral) portions of (subtly) concave Arai Plots, some of the paleointensity data appear to be overestimated and often created large Arai plot data point scatter in the Microwave-Perpendicular and Microwave-IZZI+ estimates. In addition, we have found that Microwave-IZZI+ and Microwave-Perpendicular (with pT_MRM checks) are reliable protocols in samples with thermochemical alterations because their pT_MRM checks detect and therefore help mitigate the resulting effect on PI estimates. This non-ideal behavior appears to be the primary cause of the high estimates and alterations appear to be the primary cause of the lower estimates. Our data herein, therefore, confirm the ability of the MW system to extract accurate PI estimates from samplings that exhibit thermochemical alterations and non-ideal behavior. The data further demonstrate the utility of both a flexible IZZI protocol and a multi-protocol approach that can be applied to gather large and accurate data sets quickly from basalts that yield fewer ideal data.

6.7 Acknowledgments and data availability

This study was led by J Michael Grappone as a portion of a University of Liverpool match-funded studentship, supported by the Duncan Norman Research Scholarship. J Michael Grappone further acknowledges support from the NERC EAO Doctoral Training Partnership, grant NE/L002469/1 and NERC studentship 1793213. Andrew J Biggin acknowledges support from NERC standard grant NE/P00170X/1 and Leverhulme Research Leadership Award RL-2016-080. J Michael Grappone thanks Louise Hawkins and the Institute for Rock Magnetism at the University of Minnesota for the use of their facilities to gather FORC data. Mimi J Hill acknowledges the assistance of John Shaw, Emilio Herrero-Bevera, and Don Tarling with the original collection of the examined lava samples. New raw data collected as part of this study will be available on MagIC at earthref.org/MagIC/16586.

6.8 References

Biggin, A. J., 2010, Are systematic differences between thermal and microwave Thellier-type palaeointensity estimates a consequence of multidomain bias in the thermal results? : Physics of the Earth and Planetary Interiors, v. 180, no. 1-2, p. 16-40.

Biggin, A. J., Badejo, S., Hodgson, E., Muxworthy, A. R., Shaw, J., and Dekkers, M. J., 2013, The effect of cooling rate on the intensity of thermoremanent magnetization (TRM) acquired by assemblages of pseudo-single domain, multidomain and interacting single-domain grains: Geophysical Journal International, v. 193, no. 3, p. 1239-1249.

Biggin, A. J., Bohnel, H. N., and Zuniga, F. R., 2003, How many paleointensity determinations are required from a single lava flow to constitute a reliable average?: Geophysical Research Letters, v. 30, no. 11.

Biggin, A. J., Perrin, M., and Dekkers, M. J., 2007, A reliable absolute palaeointensity determination obtained from a non-ideal recorder: Earth and Planetary Science Letters, v. 257, no. 3-4, p. 545-563.

Böhnel, H., Herrero-Bervera, E., and Dekkers, M. J., 2011, Paleointensities of the Hawaii 1955 and 1960 Lava Flows: Further Validation of the Multi-specimen Method, Dordrecht, Springer, Earth's Magnetic Interior, 195-211 p.:

Bono, R. K., Tarduno, J. A., Nimmo, F., and Cottrell, R. D., 2019, Young inner core inferred from Ediacaran ultra-low geomagnetic field intensity: Nature Geoscience, v. 12, no. 2, p. 143-147.

Coe, R. S., and Gromme, C. S., 1973, Comparison of 3 methods of determining geomagnetic paleointensities: Journal of Geomagnetism and Geoelectricity, v. 25, no. 4, p. 415-435.

Cromwell, G., Tauxe, L., Staudigel, H., and Ron, H., 2015, Paleointensity estimates from historic and modern Hawaiian lava flows using glassy basalt as a primary source material: Physics of the Earth and Planetary Interiors, v. 241, p. 44-56.

Cromwell, G., Trusdell, F., Tauxe, L., Staudigel, H., and Ron, H., 2018, Holocene Paleointensity of the Island of Hawai'i From Glassy Volcanics: Geochemistry, Geophysics, Geosystems, p. 3224-3245.

Donadini, F., Riisager, P., Korhonen, K., Kahma, K., Pesonen, L., and Snowball, I., 2007, Holocene geomagnetic paleointensities: A blind test of absolute paleointensity techniques and materials: Physics of the Earth and Planetary Interiors, v. 161, no. 1-2, p. 19-35.

Dunlop, D. J., and Ozdemir, O., 2001, Beyond Neel's theories: thermal demagnetization of narrow-band partial thermoremanent magnetizations: Physics of the Earth and Planetary Interiors, v. 126, no. 1-2, p. 43-57.

Ferk, A., Leonhardt, R., Hess, K. U., Koch, S., Egli, R., Krasa, D., and Dingwell, D. B., 2014, Influence of cooling rate on thermoremanence of magnetite grains: Identifying the role of different magnetic domain states: Journal of Geophysical Research-Solid Earth, v. 119, no. 3, p. 1599-1606.

Herrero-Bervera, E., and Valet, J. P., 2009, Testing determinations of absolute paleointensity from the 1955 and 1960 Hawaiian flows: Earth and Planetary Science Letters, v. 287, no. 3-4, p. 420-433.

Hill, M. J., Pan, Y. X., and Davies, C. J., 2008, An assessment of the reliability of palaeointensity results obtained from the Cretaceous aged Suhongtu section, Inner Mongolia, China: Physics of the Earth and Planetary Interiors, v. 169, no. 1-4, p. 76-88.

Hill, M. J., and Shaw, J., 2000, Magnetic field intensity study of the 1960 Kilauea lava flow, Hawaii, using the microwave palaeointensity technique: Geophysical Journal International, v. 142, no. 2, p. 487-504.

-, 2007, The use of the 'Kono perpendicular applied field method' in microwave palaeointensity experiments: Earth Planets and Space, v. 59, no. 7, p. 711-716.

Hodgson, E., Grappone, J. M., Biggin, A. J., Hill, M. J., and Dekkers, M. J., 2018, Thermoremanent Behavior in Synthetic Samples Containing Natural Oxyexsolved Titanomagnetite: Geochemistry Geophysics Geosystems, v. 19, no. 6, p. 1751-1766.

Jackson, A., Jonkers, A. R. T., and Walker, M. R., 2000, Four centuries of geomagnetic secular variation from historical records: Philosophical Transactions of the Royal Society of London Series a-Mathematical Physical and Engineering Sciences, v. 358, no. 1768, p. 957-990.

Kono, M., and Ueno, N., 1977, Paleointensity determination by a modified thellier method: Physics of the Earth and Planetary Interiors, v. 13, no. 4, p. 305-314.

Levi, S., 1977, Effect of magnetite particle-size on paleointensity determinations of geomagnetic-field: Physics of the Earth and Planetary Interiors, v. 13, no. 4, p. 245-259.

Nagata, T., Momose, K., and Arai, Y., 1963, Secular variation of geomagnetic total force during last 5000 years: Journal of Geophysical Research, v. 68, no. 18, p. 5277-5281.

Paterson, G. A., Biggin, A. J., Hodgson, E., and Hill, M. J., 2015, Thellier-type paleointensity data from multidomain specimens: Physics of the Earth and Planetary Interiors, v. 245, p. 117-133.

Paterson, G. A., Biggin, A. J., Yamamoto, Y., and Pan, Y., 2012, Towards the robust selection of Thellier-type paleointensity data: The influence of experimental noise: Geochemistry, Geophysics, Geosystems, v. 13, no. 5.

Santos, C. N., and Tauxe, L., 2019, Investigating the Accuracy, Precision, and Cooling Rate Dependence of Laboratory-Acquired Thermal Remanences During Paleointensity Experiments: Geochemistry, Geophysics, Geosystems, v. 20, no. 1, p. 383-397.

Shaar, R., Ron, N., Tauxe, L., Kessel, R., and Agnon, A., 2011, Paleomagnetic field intensity derived from non-SD: Testing the Thellier IZZI technique on MD slag and a new bootstrap procedure: Earth and Planetary Science Letters, v. 310, no. 3-4, p. 213-224.

Shcherbakov, V. P., and Shcherbakova, V. V., 2001, On the suitability of the Thellier method of palaeointensity determinations on pseudo-single-domain and multidomain grains: Geophysical Journal International, v. 146, no. 1, p. 20-30.

Tanaka, H., and Kono, M., 1991, Preliminary-results and reliability of paleointensity studies on historical and c-14 dated hawaiian lavas: Journal of Geomagnetism and Geoelectricity, v. 43, no. 5, p. 375-388.

Thebault, E., Finlay, C. C., Beggan, C. D., Alken, P., Aubert, J., Barrois, O., Bertrand, F., Bondar, T., Boness, A., Brocco, L., Canet, E., Chambodut, A., Chulliat, A., Coisson, P., Civet, F., Du, A., Fournier, A., Fratter, I., Gillet, N., Hamilton, B., Hamoudi, M., Hulot, G., Jager, T., Korte, M., Kuang, W., Lalanne, X., Langlais, B., Leger, J. M., Lesur, V., Lowes, F. J., Macmillan, S., Mandea, M., Manoj, C., Maus, S., Olsen, N., Petrov, V., Ridley, V., Rother, M., Sabaka, T. J., Saturnino, D., Schachtschneider, R., Sirol, O., Tangborn, A., Thomson, A., Toffner-Clausen, L., Vigneron, P., Wardinski, I., and Zvereva, T., 2015, International Geomagnetic Reference Field: the 12th generation: Earth Planets and Space, v. 67, p. 19.

Yamamoto, Y., Tsunakawa, H., and Shibuya, H., 2003, Palaeointensity study of the Hawaiian 1960 lava: implications for possible causes of erroneously high intensities: Geophysical Journal International, v. 153, no. 1, p. 263-276.

Yu, Y., 2011, Importance of cooling rate dependence of thermoremanence in paleointensity determination: Journal of Geophysical Research-Solid Earth, v. 116.

Yu, Y. J., and Tauxe, L., 2005, Testing the IZZI protocol of geomagnetic field intensity determination: Geochemistry Geophysics Geosystems, v. 6.

Yu, Y. J., Tauxe, L., and Genevey, A., 2004, Toward an optimal geomagnetic field intensity determination technique: Geochemistry Geophysics Geosystems, v. 5, p. 18.

CHAPTER 7 COMPARISON OF THERMAL AND MICROWAVE PALEOINTENSITY ESTIMATES IN SPECIMENS DISPLAYING NON-IDEAL BEHAVIOR IN THELLIER-STYLE PALEOINTENSITY EXPERIMENTS

Foreword

This chapter was accepted by the *Journal of Geophysical Research – Solid Earth* in July 2020 under the title, "Comparison of thermal and microwave paleointensity estimates in specimens displaying non-ideal behavior in Thellier-style paleointensity experiments". The authors are, in order, J Michael Grappone (also the author of this thesis), Andrew J Biggin, Thomas J Barrett, Mimi J Hill, and Courtney J Sprain. The co-authors have given permission to include this paper in my thesis.

The author of this thesis completed the writing of and data analysis in this paper, as well as the scanning electron microscopy analysis and all paleointensity experiments, except for the majority of the Microwave-Perpendicular dataset. The co-authors provided a forum for discussion and gave advice for statistical tests to run. Additionally, most MW-Perp data were collected by TJB and FORCs were collected by CJS.

The typeset version can be found in Supplementary Information F.

7.1 Abstract

Determining the strength of the ancient geomagnetic field is vital to our understanding of the core and geodynamo but obtaining reliable measurements of the paleointensity is fraught with difficulties. Over a quarter of magnetic field strength estimates within the global paleointensity database from 0-5 Ma come from Hawai'i. Two previous studies on the SOH1 drill core gave inconsistent, apparently method-dependent paleointensity estimates, with an average difference of 30%. The paleointensity methods employed in the two studies differed both in demagnetization mechanism (thermal or microwave radiation) and Thellier-style protocol (perpendicular and Original Thellier protocols) – both variables that could cause the strong differences in the estimates obtained. Paleointensity experiments have therefore been conducted on 79 specimens using the previously untested combinations of Thermal-Perpendicular and Microwave-Original Thellier methods to analyze the effects of demagnetization mechanism and protocol in isolation. We find that, individually, neither demagnetization mechanism nor protocol entirely explains the differences in paleointensity estimates. Specifically, we found that non-ideal multi-domain-like effects are enhanced using the Original Thellier protocol (independent of demagnetization mechanism), often resulting in paleointensity overestimation. However, we also find evidence, supporting recent findings from the 1960 Kilauea lava flow, that Microwave-Perpendicular experiments performed without pTRM checks can produce underestimates of the paleointensity due to unaccounted-for sample alteration at higher microwave powers. Together, these findings support that the true paleointensities fall between the estimates previously published and emphasize the need for future studies (thermal or microwave) to use protocols with both pTRM checks and a means of detecting non-ideal grain effects.

7.2 Motivation

The Pacific Ocean covers 30% of the Earth's surface but has few islands, with the Hawaiian Islands being some of the most easily accessed. Volcanic islands, like Hawaiʻi, contain some of the best records of the temporal variation in Earth's magnetic field over the last few Myr. Paleosecular variation timescales of this length are necessary to better understand long-term variations in geomagnetic behavior, as well as crust, mantle, and core interactions (e.g. McElhinny and Merrill, 1975). Accurate paleointensity data in the 0 – 5 Ma period is crucial because only in this interval is there enough spatial and temporal global coverage of data to characterize long term (Myr) variations. In order to obtain accurate paleointensity data, an appropriate paleointensity method for the mineral magnetic characteristics of any particular site must be used.

Many paleomagnetic studies over the last 60 years (e.g. Coe et al., 1978; Cromwell et al., 2018; de Groot et al., 2013; Doell and Cox, 1963; Doell and Cox, 1965; and Teanby et al., 2002) have found the Hawaiian Islands ideal for studying magnetic field variations in the central Pacific Ocean over the past hundred to few million years. Hawaiian absolute paleointensities (PI) have substantial temporal coverage and comprise 28% of the global paleointensity (PINT) database in this interval (Biggin et al., 2015) and are therefore important to study to understand long-term field behavior over this time interval. Numerous studies have taken advantage of the drill core from the Scientific Observation Hole (SOH) and Hawaiʻi Scientific Drilling Project (HSDP) projects to extract the required paleointensity data over the last 45 kyr (e.g. Cai et al., 2017; Gratton et al., 2005; and Teanby et al., 2002), but the data have proven to be inconsistent and thus of potentially limited use.

The paleomagnetism of the SOH1 core was studied twice previously- once by Teanby et al. (2002) using thermal PI experiments and again by Gratton et al. (2005) using microwave PI experiments and a different PI protocol. Teanby et al. (2002) and Gratton et al. (2005) each sampled the core independently and extracted paleointensities from 83 common flows. Teanby et al. (2002) additionally reported a new inclination record and dated the flows from 0 - 45 ka. The mean paleointensities reported by the two studies, 33.5 µT (Teanby et al., 2002) and 25.1 µT (Gratton et al., 2005), differ by approximately 33%. Both studies reported mean uncertainty estimates of approximately 10%, which implies the possibility for a resolvable difference between them.

At this stage it is useful to introduce our nomenclature that a given paleointensity "method" is composed of a combination of a specific "demagnetization mechanism" and a

specific "protocol". Teanby et al. (2002) used the conventional thermal demagnetization mechanism paired with the Original Thellier protocol (Thellier and Thellier, 1959), while Gratton et al. (2005) used the microwave demagnetization mechanism paired (predominantly) with the Perpendicular protocol (Kono and Ueno, 1977). A third study, Laj et al. (2011), used the raw data from Teanby et al. (2002) (reanalyzed with their updated selection criteria to give an SOH1 average of 29.7 μT) combined with additional (non-SOH1) data (acquired using the same method) from the SOH4 and HSDP1 drill cores, which cover additional flows, to create a more complete and statistically rigorous Hawaiian paleointensity record. Even after the Laj et al. (2011) reassessment, there remains nearly a 20% discrepancy between the thermal mechanism Original Thellier protocol and the microwave mechanism Perpendicular protocol results.

To investigate discrepancies between paleointensity results obtained using different demagnetization mechanisms (i.e. thermal and microwave), a meta-analysis of 13 paired studies (including that of the SOH1 drill core) was undertaken by Biggin (2010). It is important to note that the studies assessed in the Biggin (2010) analysis differed not only in demagnetization mechanism but also in protocol. Biggin (2010) concluded, firstly, that systematic differences existed between paleointensity estimates derived from thermal and microwave experiments performed on the same rocks, with the former tending to be significantly higher than the latter (at the 95% confidence level). We carried out a further analysis (available in Supporting Information C.1), which showed this as well at the flow level. Secondly, Biggin (2010) suggested that the most plausible explanation for the bulk of these discrepancies resided in unrecognized biasing from multi-domain-like effects being more prevalent in the thermal results. Importantly it was suggested that the discrepancies were more or less entirely due to the difference in the *protocols* used rather than in the *demagnetization mechanism*. With respect to the SOH1 case, Biggin (2010) hypothesized that the thermal results being higher than the microwave results was likely unrelated to the choice of thermal or microwave energy for demagnetization. Rather, the discrepancy was due to Teanby et al. (2002) employing the Original Thellier protocol while Gratton et al. (2005) employed the Perpendicular protocol.

Since our initial flow level analysis of the SOH1 data confirmed the results of Biggin (2010), the aim of the present study is to test the hypothesis that the differences found in paleointensity results from the SOH1 core are entirely due to protocol and not due to demagnetization mechanism. We hypothesize that if the demagnetization mechanism-protocol pairs are reversed, such that microwave demagnetization is paired with the Original

Thellier protocol and thermal demagnetization is paired with the Perpendicular protocol, then the sense of the discrepancy between the microwave and thermal results should reverse such that the former should give higher estimates than the latter. This study will explicitly test this hypothesis using new experiments performed on 24 of the same SOH1 flows as studied originally by both Teanby et al. (2002) and Gratton et al. (2005).

The results of this study are important on several levels. First, they provide improved insight into the strength of the magnetic field at the time of emplacement of the 241 flows sampled by the SOH1 drill core dataset. Second, they have implications for how the swathes of paleointensity estimates obtained by similar methods from rocks elsewhere in the world should be interpreted. As such, they expand the results of a recent restudy of the 1960 Kilauea lava flow by Grappone et al. (2019) to more Hawaiian lava flows. Lastly, they can provide guidance on how future paleointensity experiments should be performed and analyzed in order to maximize their reliability.

7.3 Geology and sampling

The samples used in this study are from the SOH1 drill core, which was drilled from the Kilauea volcano on Hawaiʻi Island between 1989 and 1991 at 19°29'N, 154°54'W, to a total depth of 1685 m. The Hawaiʻi Institute of Geophysics and Planetology and the Hawaiʻi Natural Energy Institute drilled the borehole to assess the viability of using geothermal energy in the area (Quane et al., 2000). The core consists primarily of a'a (~ 66%) and pahoehoe (~ 22%) lavas from 241 aerial, subaerial, and submarine flows with thicknesses varying from 0.3 m to 17.4 m (Gratton et al., 2005; Teanby et al., 2002). The remaining ~11% of the core consists of dyke intrusions. Samples were taken from 196 lava flows from the upper 779 m of the core to avoid the increasing number of dyke intrusions and apparent alteration at greater depths (Gratton et al., 2005). This portion of the core has been modelled with an age range of 0 – 45 ka (Teanby et al., 2002).

The portions of each drilled 2.5 cm diameter core that were saved by Gratton et al. (2005) from their SOH1 study were retrieved from the University of Liverpool archive and subsequently used in this study. We cut 120 new specimens for the restudy from the material remaining from 24 flows that span the range of flows sampled in Gratton et al. (2005). Although the specimens used in this study are sister specimens from Gratton et al. (2005), we cannot rule out the possibility that the flows may be inhomogeneous even on a cm scale. Flows were selected based on the degree of disagreement in paleointensity (PI) estimates

between the Gratton et al. (2005) and Teanby et al. (2002) studies, number of samples previously studied, and the availability of specimens. For the flows selected for this study, the Teanby et al. (2002) PI estimates, at the flow level, ranged from 21% lower to 53% higher (with a mean of 27% higher) than the Gratton et al. (2005) estimates.

7.4 Rock magnetism

Gratton et al. (2005) undertook an extensive survey of the hysteresis loop parameters of the SOH1 borehole. The raw data from their rock magnetic survey were reanalyzed here using *Hystlab's* automatic hysteresis loop processing program (Paterson et al., 2018) and are replotted in Figure 7-1, with the flows investigated herein highlighted. The bulk domain stability (BDS) trendline from Paterson et al. (2017) lies below the main sequence of hysteresis loop parameters for SOH1 flows, which indicates the data have a mixture of magnetic domain types, potentially also including superparamagnetic grains. The specimens used in this study sample the main sequence of SOH1 data observed in Figure 7-1. The ratio of magnetic remanence to saturation magnetization (Mrs/Ms) values of the main sequence of SOH1 data lie consistently above the values that would be expected for multi-domain grains of magnetite (Mrs/Ms > 0.1), which implies the presence of single domain and non-single domain grains. Gratton et al. (2005) also determined thermomagnetic behavior for all the flows in their study. They found highly reversible thermomagnetic curves with 98% of Curie temperatures falling in the range from 520 – 600 °C, with a mean of 561 °C and median of 570 °C. 22% of flows also contained a secondary ferrimagnetic phase with Curie temperatures below 340 °C.

The hysteresis and thermomagnetic parameters are typical of low-Ti magnetite-rich basaltic lavas found on Hawai'i and which have been the focus of other Hawaiian paleointensity surveys (e.g. Cai et al., 2017; Cromwell et al., 2018; and Hill and Shaw, 2000). Additional, new rock magnetic information (FORC and SEM analysis) from the main sequence can be found in Supporting Information C.2.

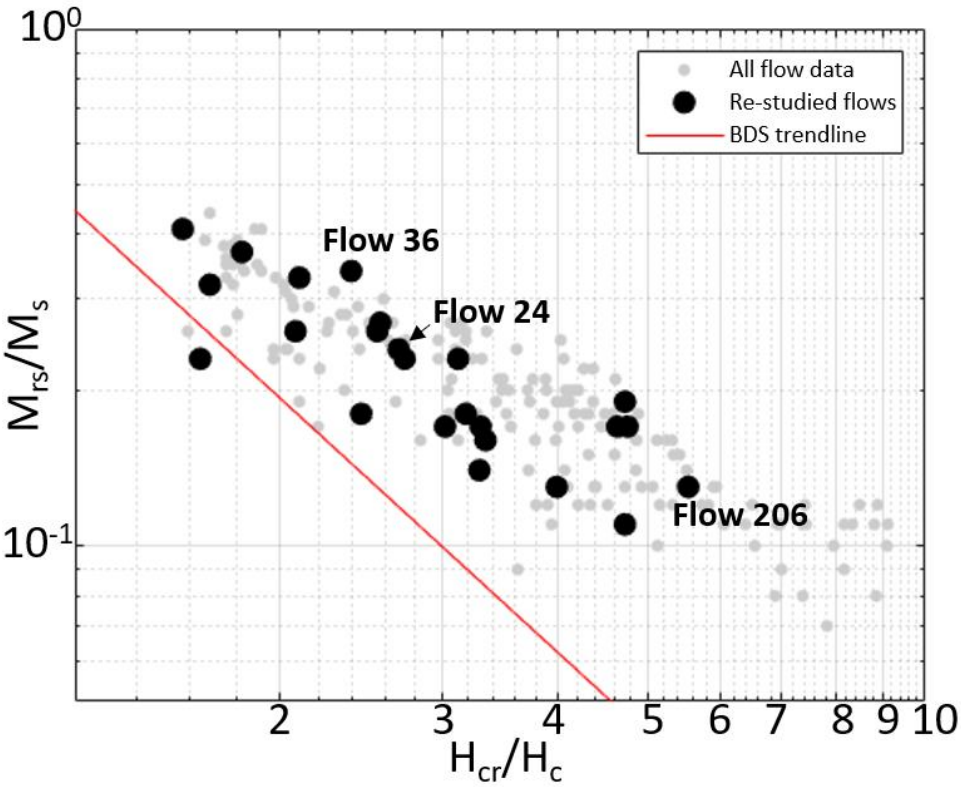

Figure 7-1 Hysteresis parameters plot for all the flows in the SOH1 borehole (as studied by Gratton et al., 2005), highlighting which flows were studied herein for new PI estimates. M_{rs}/M_s refers to the ratio of remanent saturation magnetization to the saturation magnetization and H_{CR}/H_C refers to the ratio of coercivity of remanence to coercivity. The BDS trendline derives from the results of Paterson et al. (2017). The three named flows have new PI estimates, as well as FORC and SEM analysis in Supplementary Information C.2.

7.5 Methods

All new thermal tests were carried out in air using a Magnetic Measurements MMTD-80 thermal demagnetizer, and specimens were cooled quickly using a built-in cooling fan. The specimens were then measured on the University of Liverpool Geomagnetism Laboratory's 2G SQUID Magnetometer and RAPID system. All microwave tests were run on the 14 GHz Tristan Microwave System (Hill et al., 2008), also at the University of Liverpool. The goal of this study was to replicate the experimental conditions of the previous studies as closely as possible to properly isolate each variable of interest.

In the Original Thellier (OT) protocol (Thellier and Thellier, 1959), each specimen is heated to a given temperature, T_N, in a known, non-zero intensity magnetic field and then cooled to room temperature and measured. The polarity of the magnetic field is then reversed, and the sample is taken to T_N again. The protocol can also be referred to as infield-infield, or 'II'. The process is then repeated at T_{N+1}. Partial thermal remanent magnetization (pTRM) checks were included after every 2nd step (i.e. from T_{N+1} to T_{N-1}). For consistency with the

PINT database (Biggin et al., 2009), when used with thermal energy, this protocol (with pTRM checks) will be referred to as Th-OT+, to acknowledge the pTRM check addition. The microwave (MW) variant of the OT protocol simply replaces the heat with microwave power integrals and will be referred to as MW-OT+. We used powers ranging from 5 to 40 W in 3 to 5 W steps, applied for 5 to 15 s and assumed that any power not reflected was absorbed by the specimen-cavity coupled system. For MW-OT+, we used a steady magnetic field applied parallel/anti-parallel to the natural remanent magnetization (NRM), which Biggin (2010) predicted to be the least affected by non-ideal Arai plot behavior. For Th-OT+, we used an applied field with an inclination of $\pm 90°$ in specimen coordinates.

The Perpendicular (Perp) protocol is a modification of the Original Thellier protocol that only requires a single thermal or microwave treatment (Kono and Ueno, 1977). Samples first get stepwise demagnetized in a zero field to remove any soft magnetic overprints. Once the primary component of magnetization is identified as beginning at some T_P, the sample is then heated to T_{P+1} in a magnetic field applied in the direction perpendicular to the characteristic component (the remaining NRM). The process is then repeated for T_{P+2} and higher. Gratton et al. (2005) determined that many samples had a second ferrimagnetic phase with an unblocking temperature around 300 °C, which they interpreted to be the result of oxyexsolution into Ti-rich and Ti-poor lamellae during extrusion. Therefore, samples undergoing Thermal Perpendicular (Th-Perp) were first step-wise demagnetized in 40-50 °C steps from 100 °C to 300-340 °C to ensure that the perpendicular field was applied only to the high temperature ferrimagnetic phase. After successfully finding the characteristic direction, the field in the oven was switched on. The steps continued to 590 °C in 10-30 °C increments. The process is the same using the microwave system (MW-Perp), but with power integral steps instead of temperature steps until a consistent magnetic direction is obtained (Hill and Shaw, 2007). We did not include any pTRM checks in our new perpendicular experiments in order to replicate the methods used by Gratton et al. (2005). All data were analyzed using the methods described in Hill and Shaw (2007).

Laboratory field strengths were selected that were as close to the original analyses as possible. All experiments in Teanby et al. (2002) were carried out using an applied field of 40 µT, as were the new MW-OT+ experiments completed herein. Microwave studies are carried out one sample at a time, so the field strength often varied specimen to specimen within a flow in Gratton et al. (2005). For the specimens we selected, the mean applied field used in Gratton et al. (2005) for microwave treatments was 31 ± 1.3 µT, so we used a field of 31 µT in our Th-Perp experiments.

A summary of the experiments carried out in this study is given in Table 7-1. We ran 79 specimens using either MW-OT+ or Th-Perp. Additionally, 19 specimens were tested using Th-OT+ and 22 were tested using MW-Perp, replicating the original studies in order to confirm the previous results. The median number of specimens tested from each of the 24 flows we examined was 3, with a range of 1-11.

Table 7-1 Summary information of new experiments carried out in this study

Method	Number of specimens	Number of accepted estimates	Success rate	Lab field (μT)
Microwave-OT+	48	33	69%	40
Microwave-Perp	22	13	59%	25-50
Thermal-OT+	19	10	52%	40
Thermal-Perp	31	17	55%	31
Total	120	73	61%	25-50

Number of specimens run for each method is given along with the number of specimens that gave acceptable results (number of passes) and the associated success rate. The final column gives the applied Lab fields used during the experiment for each method.

Our selection criteria are based on the MC-CRIT.C1 selection criteria, without tail checks, from Paterson et al. (2015). These were also used successfully by Grappone et al. (2019) to study the 1960 Kilauea lava flow. We relaxed the FRAC/f criterion (Shaar and Tauxe, 2013) (a measure of the proportion of the NRM used to determine the result) from 0.45 (used in Grappone et al., 2019) to 0.35 because of extensive alteration observed at higher temperatures/power integrals and because of difficulties in demagnetizing the specimens using microwaves. Relaxing this criterion yielded seven additional specimen-level estimates most notably from MW-Perp experiments, without changing any flow-level estimates in a statistically significant manner. The selection criteria are detailed in Table 6-1.

Table 7-2 Selection criteria

N	FRAC/f*	β	q	$\lvert\vec{K}'\rvert$	MAD_{ANC}**	α**	DRAT**	Δθ***
≥ 4	≥ 0.35	≤ 0.1	≥ 1	≤ 0.480	≤ 10	≤ 10	≤ 10%	≤ 1°

N is the number of data points, FRAC/f are measures of the NRM used, β is a measure of scatter around the best-fit line, q is a measure of the data quality, $\lvert\vec{K}'\rvert$ is a measure of Arai plot curvature, MAD and α determine the scatter of the specimen's paleodirection. Δθ is the change in the $\theta_1 + \theta_2$ value, an indication of the perpendicularity between the NRM and TRM directions (Hill and Shaw, 2007) for the perpendicular experiment. For further details the reader is referred to Paterson et al. (2015).
*FRAC is used for OT+ experiments and f for Perp experiments.
**OT+ techniques use these criteria, but Perp does not, for technical reasons
*** Used only for Perpendicular experiments

For our analysis, we use two statistical tests: the T-test and the Wilcoxon signed rank test (see for example, Klugh, 1986). For the study-level data, which are normally distributed (see the failure to reject the null hypothesis in Kolmogorov-Smirnov test in Supporting Information C.1), we use a two-sample, unpaired T-test to test if the method-level means are equal. A paired difference test is more appropriate for the flow-level data, which have flow-level data pairings. The paired data do not visually appear to be normally distributed (a weak assumption required for a paired T-test), so we should choose a nonparametric test. Biggin (2010) used the Wilcoxon signed rank test in their analysis of the SOH1 dataset so for consistency we also use that for flow level data.

7.6 Paleomagnetic results and analysis

7.6.1 New data

A summary of all experiments run herein is given in Supporting Information C.3, and these new experiments are described in this subsection. Paleointensity estimates that passed the selection criteria were obtained from experiments performed on 73 specimens from 20 flows. A pass rate of >50% at the specimen-level was achieved for every experimental method tested. The most common reason for failure of the new MW-Perp and MW-OT+ experiments was low FRAC/f, as the microwave often could not fully demagnetize each specimen. The most common reason for failure for the new Th-OT+ experiments was high DRAT (i.e. pTRM check failures), and for Th-Perp, it was high scatter around the best fit line (β). The only clear difference in Arai plot shape observed between the different methods is that the new Th-OT+ data often show two slopes where for some specimens both slopes passed the selection criteria. In these cases, the low temperature slope was selected, as they had the higher FRAC. These new Th-OT+ data additionally show the highest mean curvature values (as defined by $|\vec{K}'|$) at 0.30, compared to those of the Th-Perp (0.22), MW-OT+ (0.21), or MW-Perp (0.093). All new measurement data can be found on the MagIC database. Examples of passed MW-OT+ and Th-Perp data can be found in Figure 7-2 (Aii, Aiii, Bii, Biii, Cii, Ciii). Examples of passed Th-OT+ and MW-Perp data can be found in Supporting Information C.3.

Flow mean results are detailed by paleointensity method in Supporting Information C.3. The new Th-OT+ and MW-OT+ flow-level mean PI estimates tend to yield higher values with 44.0 ± 16 μT across 5 flows and 29.5 ± 9.2 μT, across 19 flows, respectively. New Th-Perp and MW-Perp experiments tend to yield lower mean PI estimates with estimates of 27.8 ± 8.1 μT, across 11 flows, and 18.5 ± 10 μT, across 5 flows, respectively. If we assume our new

PI estimates are normally distributed, which is noted (see Supporting Information C.1), we can use a two-sample T-test to determine whether observed differences between experiments are statistically significant. From the new data, the Th-OT+ mean estimate (44.0 µT) is higher than the MW-OT+ mean (29.5 µT), the Th-Perp mean (27.8 µT), and the MW-Perp mean (18.5 µT), at the 95% confidence level, with p-values of 0.0147, 0.0176, and 0.0001, respectively. The new data's Th-Perp mean estimate is not statistically distinct from the new data's MW-OT+ mean estimate at the 95% confidence level ($p = 0.62$). The new data's MW-Perp flow-level mean PI estimate of 18.5 µT is lower than the new data's MW-OT+ mean estimate at the 95% confidence level, with a p-value of 0.0015. The new data's Th-Perp and MW-Perp estimates are not statistically different at the 95% confidence interval, with a p-value of 0.0676.

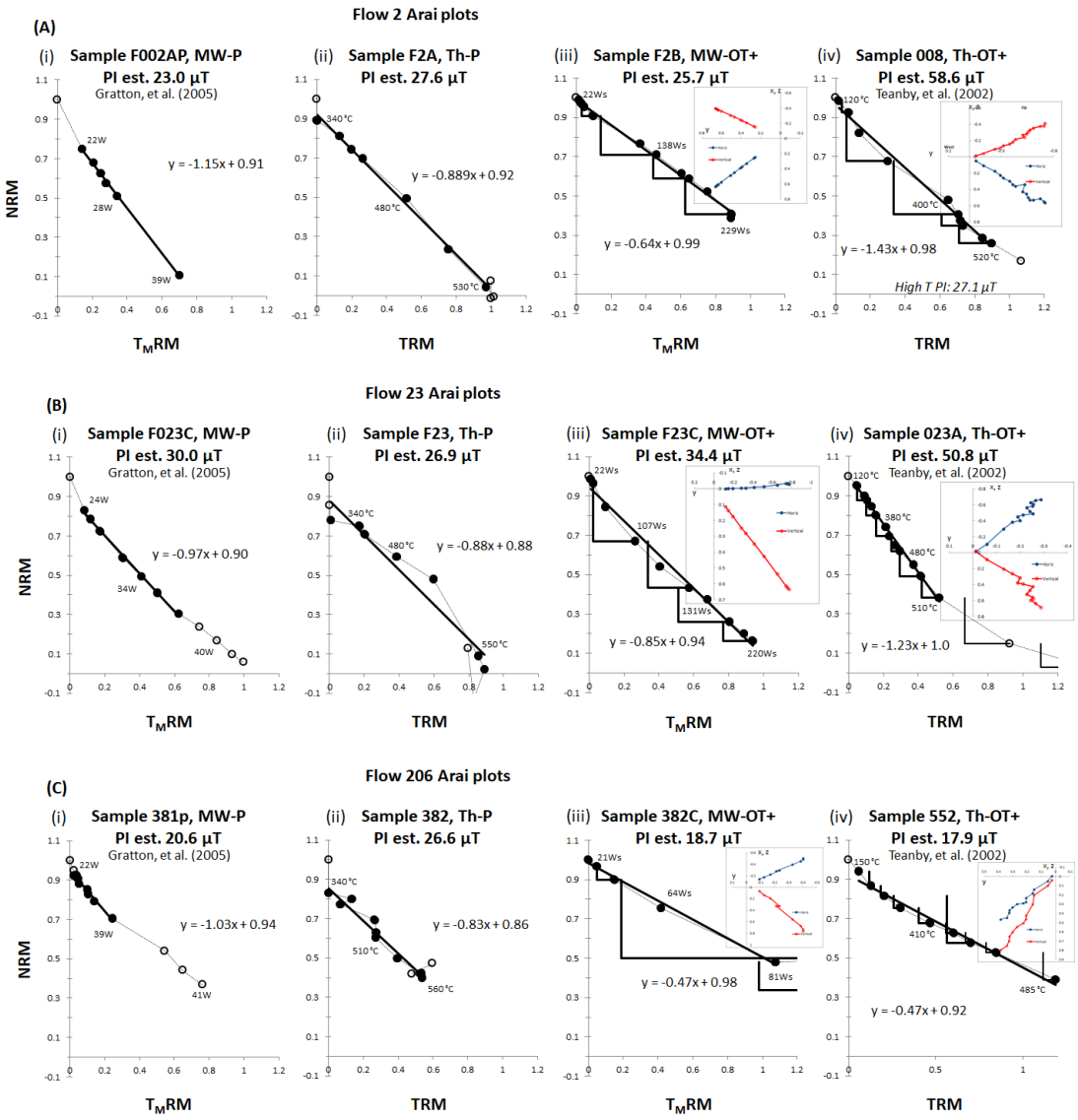

Figure 7-2 Normalized Arai plot examples comparing the different methods used. A) Flow 2 (503 cm thickness), B) Flow 23 (137 cm thickness), and C) Flow 206 (290 cm thickness). The data are normalized by NRM_0. The filled circles are accepted data points, with the solid black line being the best-fit line. Open circles are rejected data points. The black right-angles lines are $pT_{(M)}RM$ checks, which are only present in OT+ data. Orthogonal vector plots are provided in core coordinates for the OT+ data. All specimens presented pass their original study's selection criteria. The microwave data are visually more linear than the thermal data, and the OT+ data are often two-sloped. The powers given for the Gratton et al. (2005) MW data are power applied and the power integrals given in the new data are (inferred) energy absorbed.

7.6.2 Incorporation of existing datasets

The new Th-OT+ results reported here are broadly consistent with their original counterparts reported by Teanby et al. (2002) and Laj et al. (2011). Both have the same two-slope (concave-up) behavior (see Figure 7-2 for Teanby et al. (2002) results and Supporting Information C.3 for a direct comparison). When considering only the four flows tested in both the present study and by Teanby et al. (2002), the mean PI values (43.5 ± 19 µT and 30.8 ±

14 μT) have overlapping uncertainty bounds and are not statistically distinct from each other at the 95% confidence level (p = 0.3232).

The new MW-Perp data reported here also broadly replicate the lower estimates reported by Gratton et al. (2005). The Arai plots appear single-sloped (see Figure 7-2 for Gratton et al. (2005) results and Supporting Information C.3 for a direct comparison) and the mean PI values for the nine flows tested here and in Gratton et al. (2005) are 18.2 ± 10 μT and 18.6 ± 9.8 μT, respectively. These mean values are not statistically distinct at the 95% confidence level (p = 0.9462). This result supports Grappone et al. (2019)'s finding that the different generations of the microwave systems give equivalent results.

The consistency of our newly obtained results with those from the previous studies enables us to conclude that we may reasonably combine our new Th-OT+ data with the Teanby et al. (2002) data and our new MW-Perp data with the Gratton et al. (2005) data. All the data is therefore combined to create one dataset which forms the basis for discussion in the following section. The combined SOH1 dataset, consisting of data from this study, Teanby et al. (2002), and Gratton et al. (2005) is summarized in Table 7-3.

Table 7-3 Paleointensity results, broken down by flow and method for the combined dataset, consisting of new data, data from Teanby et al. (2002) and data from Gratton et al. (2005).

Flow	Th-OT+ (μT)	N_{pass}/ N_{tested}	MW-OT+ (μT)	N_{pass}/ N_{tested}	Th-Perp (μT)	N_{pass}/ N_{tested}	MW-Perp (μT)	N_{pass}/ N_{tested}
2	58.6	1/2	22.5 ± 4.7	2/2	29.4 ± 5.1	3/3	21.3 ± 2.0	4/4
6	50.4 ± 4.5	2/3	45.1 ± 2.8	2/2			36.5 ± 0.6	3/3
7		0/1			39.2	1/1	35.8 ± 1.6	4/4
8	59.0 ± 3.2	3/3	43.7 ± 4.9	2/2		0/1	36.5 ± 5.9	8/10
22		0/1	37.2 ± 2.6	3/3	26.3	1/2	21.3 ± 9.5	2/2
23	51.4 ± 0.9	2/2	36.7 ± 2.2	3/5	27.7 ± 0.1	2/2	28.8 ± 1.0	2/2
24			25.9	1/2		0/2	18.5 ± 4.1	2/4
26		0/1	32.5	1/2	21.2	1/3	33.1 ± 2.0	5/5
36		0/1	32.7	1/1		0/1	34.8 ± 2.8	2/2
37	54.2 ± 6.0	4/5	33.4 ± 1.6	2/2			24.8 ± 6.0	3/4
48			29.4 ± 3.4	2/2	26.4 ± 4.1	3/3	28.0 ± 0.5	2/2
87	32.2 ± 2.3	2/4		0/1			14.6 ± 1.9	4/4
91	23.8 ± 0.8	2/3		0/1			11.8 ± 0.9	4/4
163	45.9 ± 11	3/3	25.7 ± 1.5	2/3			18.6	1/3
176	26.3 ± 13	3/4				0/1		
186	25.1 ± 4.0	2/6				0/1	18.2 ± 2.6	2/2
189	27.7 ± 0.2	2/3	22.1	1/1	25.6	1/1	19.8 ± 1.0	2/2
193	31.7	1/2	18.5	1/1		0/1	15.0 ± 0.1	2/3
196	24.7 ± 1.3	2/2	15	1/1			12.6	1/3
206	40.1 ± 29	2/5	18.7	1/3	26.2	1/1		0/3
220	46.4 ± 7.9	4/6	37.2 ± 6.1	2/3	33.8	1/1	27.5 ± 2.8	7/12
221	40.9 ± 2.1	3/3	36.7	1/4	39.5 ± 2.8	2/4	31.4 ± 2.8	4/5
222	39.8 ± 3.3	3/3	33.7	1/2		0/1	37.8 ± 1.6	3/3
237	25.5 ± 8.2	3/9	14.3 ± 8.5	4/5	10.4	1/2	19.1 ± 0.2	2/4
Mean	39.0 ± 12	18/22	29.5 ± 9.2	19/21	27.8 ± 8.1	11/18	24.8 ± 8.5	22/23

Note: N_{pass} is the combined number of specimens that passed the PI selection criteria. N_{tested} is the combined number of specimens that were tested from a given flow with a given method. Empty cells indicate no experiments were attempted because of a lack of material. For the mean row, N_{pass} and N_{tested} reference the number of flows.

7.6.3 Analysis of combined dataset

Figure 7-2, Figure 7-3, and Figure 7-4 display a series of one-to-one comparisons of the PI data produced by different methods at the flow level, utilizing data from the combined dataset, which allows the influence of demagnetization technique and PI protocol to be scrutinized. From visual inspection, the data do not appear to be symmetrically random about the 1:1 line nor cluster close to it. Thus, the PI estimate data pairs do not visually appear to be consistently normally distributed about the 1:1 line, which indicates that a two-sample T-test may be insufficient. We instead use the Wilcoxon signed rank test (see Biggin, 2010) to examine if the respective deviation of the datasets from the 1:1 line is significant at the 95% ($\alpha = 0.05$) confidence interval. The null hypothesis is that the data scatter about the 1:1 line is random.

In keeping with Biggin (2010), we first confirm that the Th-OT+ data are consistently higher than the MW-Perp data (Figure 7-3A). The Wilcoxon signed rank test gives W = 1, which corresponds to a p-value of 0.0008 for 15 data points, so we can reject the null hypothesis that the deviation from the 1:1 line and hence the data scatter is random.

Next we test the hypothesis of Biggin (2010) that the primary cause for the Th-OT+ data being consistently higher than the MW-Perp data is due to the differing PI protocol (OT+ vs Perp) and not demagnetization mechanism (MW vs. thermal). We do this by comparing the MW-OT+ and Th-Perp data (i.e. the inverse combination) to see if the OT+ protocol continues to yield systematically higher values than the Perp protocol. It can be seen in Figure 7-3B that in fact, MW-OT+ data are not consistently higher than Th-Perp data; the paired results are significantly closer to and fall on either side of the 1:1 line. The Wilcoxon signed rank test gives W = 18, which corresponds to a p-value of 0.33 for 10 data points, so we cannot reject the null hypothesis that the deviation from the 1:1 line is random. Having failed to support the simple hypothesis that the protocols are entirely responsible for the differences in PI results, we now examine demagnetization mechanisms and protocols in isolation to probe deeper into these specimens' behavior.

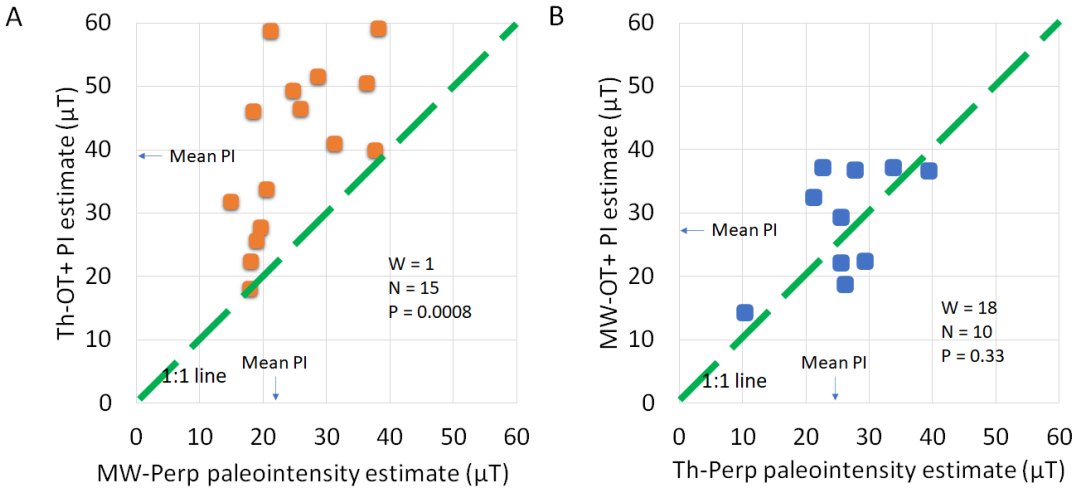

Figure 7-3 Testing Biggin (2010)'s hypothesis that only paleointensity protocol affects PI estimate. Flow-level paleointensity estimates are plotted against each other for completely distinct PI methods (no shared protocol or demagnetization mechanism). A: Confirming that the Th-OT+ data are higher than the MW-Perp data. B: Checking if MW-OT+ data are higher than Th-Perp. The mean PIs listed are for the flows the methods have in common. N is the number of data points, W and p are the statistics from the Wilcoxon signed rank test.

If the cause of the discrepancy between the Th-OT+ and MW-Perp data were purely due to demagnetization mechanism, then we would expect that estimates from MW-OT+ and MW-Perp would be similar and would cluster around the 1:1 line. Similarly, estimates from

Th-OT+ and Th-Perp, would also be similar, clustering around their 1:1 line. These cases are plotted in Figure 7-4. For the flows they have in common (Figure 7-4A), the mean PI estimate for the MW-OT+ data is 30 ± 8.8 µT and for the MW-Perp data is 26.1 ± 7.7 µT. The Wilcoxon signed rank test gives W = 23, which corresponds to a p-value of 0.0065 for 18 data points, so we can reject the null hypothesis that the deviation from the 1:1 line is random. Next, we investigate the Th-OT+ and Th-Perp data (Figure 7-4B). For the flows they have in common, the mean PI estimate for the Th-OT+ data is 38.3 ± 14 µT and 27.5 ± 8.3 µT for the Th-Perp data. The Wilcoxon signed rank test for Th-OT+ vs Th-Perp gives W = 3, which gives a p-value of 0.05 for 7 data points, therefore also rejecting the null hypothesis that the deviation from the 1:1 line is random. Therefore, changing the protocol to OT+ from Perp does indeed cause higher paleointensities to be measured, but this is not the entire explanation for the discrepancy illustrated in Figure 7-3A.

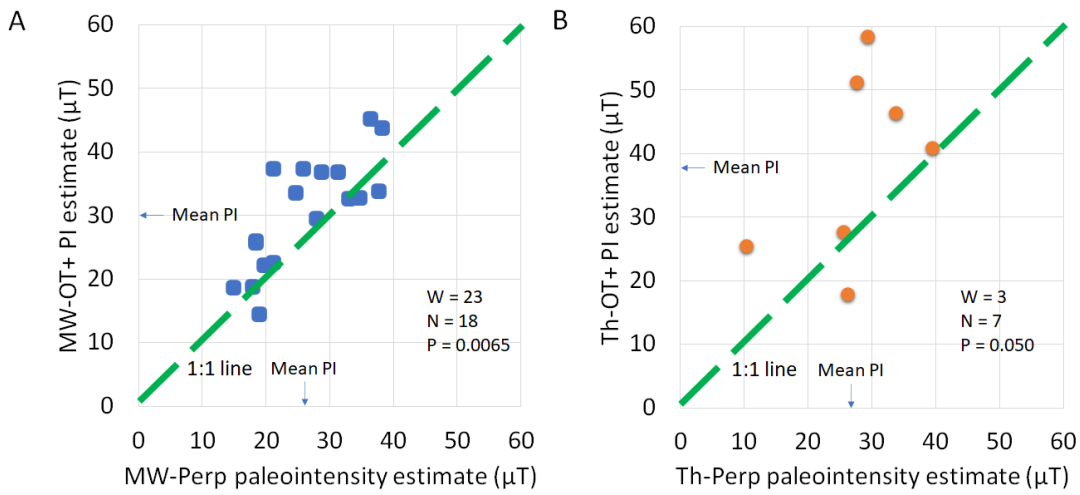

Figure 7-4 Testing the hypothesis that only paleointensity protocol affects PI estimate, control. Flow-level paleointensity estimates are plotted against each other for different PI protocols, separated by demagnetization mechanism. A: Microwave data; B: Thermal data. The mean PIs listed are for the flows the methods have in common. N is the number of data points, W and p are the statistics from the Wilcoxon signed rank test.

For the flows that have both Th-OT+ and MW-OT+ data (Figure 7-5A), we observe mean PI estimates of 40.7 ± 13 µT and 28.8 ± 10 µT, respectively. The Th-Perp and MW-Perp data give more similar estimates (Figure 7-5B). For the flows they have in common, the mean PI estimates are 28 ± 8.6 and 26.6 ± 5.9, respectively. For Th-OT+ vs MW-OT+, the Wilcoxon signed rank test gives W = 1, which corresponds to a p-value of 0.0012 for 14 data points. We can therefore reject the null hypothesis that the deviation from the 1:1 line is random, which indicates Th-OT+ data are higher than the MW-OT+ data. For the Th-Perp and MW-Perp data, the Wilcoxon signed rank test gives W = 25, which corresponds to a p-value of 0.24 for 11 data points. Thus, we cannot reject the null hypothesis that the Th-Perp and MW-Perp data's

deviation is random, which suggests that the Th-Perp data are not higher than the MW-Perp data. This result agrees with the T-test in section 7.6.1.

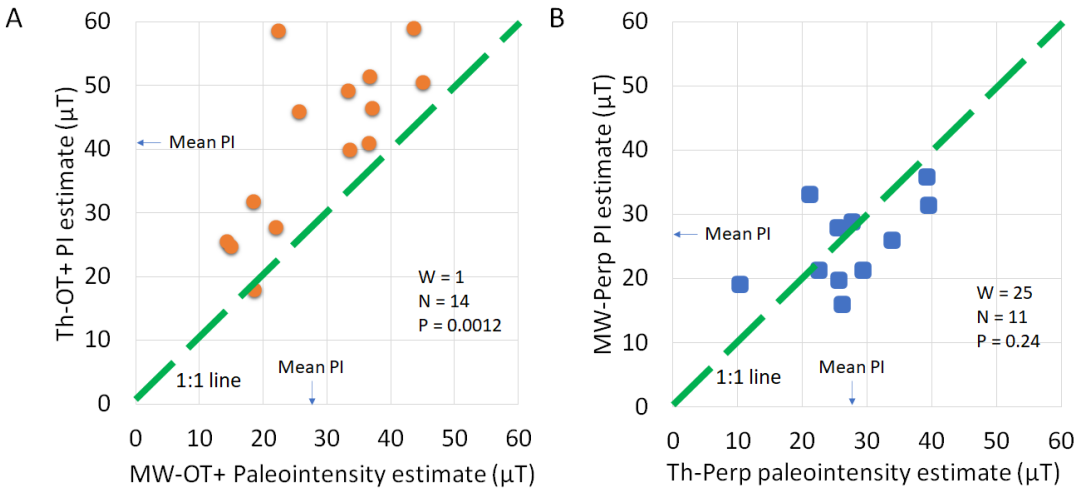

Figure 7-5 Testing the hypothesis that only demagnetization mechanism matters. Flow-level paleointensity estimates are plotted against each other for different PI methods, separated by protocol. A: Original Thellier data; B: perpendicular data. The mean PIs listed are for the flows the methods have in common. N is the number of data points, W and p are the statistics from the Wilcoxon signed rank test.

We therefore observe that neither the demagnetization mechanism nor the protocol used can, in isolation, fully explain the differences in paleointensity estimates observed. We additionally find that the Th-OT+ method yields results that are consistently (and statistically) higher than the other three methods used.

7.7 Discussion

7.7.1 Paleointensity methodology differences

Double-heating Thellier protocols have long been known to have problems with multi-domain components causing non-linear Arai plots (Levi, 1977). Hodgson et al. (2018) showed that this can apply to non-single domain oxyexsolved titanomagnetite grains as well, which are common in basaltic lavas such as the Hawaiian lavas of the SOH1 drill core. These non-single domain components can lead to concave up (two-slope) Arai plots. If the low blocking temperature (power integral) portion is used, the data give PI overestimates and conversely, underestimates are obtained if the high blocking temperature (power integral) portion is used (Levi, 1977; Smirnov et al., 2017; Thomas, 1993; Xu and Dunlop, 2004). Grappone et al. (2019) studied samples from the 1960 Kilauea lava flow, another Hawaiian lava flow. They showed that the high estimates often found using thermal double treatment methods (of which Thermal-Original Thellier is one) (e.g. Yamamoto et al., 2003) are not replicated when

using the microwave demagnetization mechanism. Our data here confirm this conclusion, as the Thermal-Original Thellier method yields the highest estimates, but the Microwave-Original Thellier data align much more closely with the Perpendicular datasets obtained using either demagnetization mechanism.

A recent study by Cromwell et al. (2018) (using the Thermal-IZZI method and strict selection criteria) reports PI estimates from 22 surface lava flows across the island of Hawaiʻi. They found estimates consistent with geomagnetic field models in the 270 – 10,000 yr range. However, the study was unable to reproduce the high estimates found in Teanby et al. (2002) and Laj et al. (2011). Cai et al. (2017) additionally found systematically lower estimates than Laj et al. (2011) using subaerial glassy basaltic margins on older flows from the HSDP2 core, using the same techniques as Cromwell et al. (2018). Based on the data herein and the other studies, the thermal Original Thellier method appears to give higher PI estimates than other PI methods and is likely an overestimate of the true palaeointensity due to exaggerated multi-domain-like effects and the lack (in these experiments) of any mechanism to detect these.

The original microwave study for the 1960 Kilauea lava flow, Hill and Shaw (2000), gave site-level estimates up to 20% lower than the expected value of 36.5 µT. In both the Hill and Shaw (2000) and the Gratton et al. (2005) studies, an older MW system was used with the Perpendicular protocol (Kono and Ueno, 1977), which uses only a single treatment per step and no pTRM checks. Grappone et al. (2019) showed that changing the microwave experimental protocol to a more common double-treatment technique including alteration (pTRM) checks (in their case the IZZI protocol; Yu et al., 2004) gave the correct answer of 36.5 µT for the 1960 Kilauea lava flow. Although the Original Thellier protocol's additional treatments cause more thermochemical alteration than the perpendicular protocol, it is likely that the SOH1 samples behave in a similar way to the 1960 Kilauea flow and that the Perpendicular datasets give low estimates due to undetected alteration.

The Microwave-Perpendicular and the Thermal-Perpendicular datasets are not statistically distinct implying that it is not something inherent to the microwave causing the differences between the original Teanby et al. (2002) and Gratton et al. (2005) datasets. It has been shown that for well-behaved (single domain; SD) grain-containing ceramics, there is a detectable difference in paleointensity estimates due to differences in cooling rate (Poletti et al., 2013). Since the Microwave-Perpendicular and the Thermal-Perpendicular datasets are not statistically distinguishable, any cooling rate effect would be relatively

minimal. Further, the Microwave-Original Thellier data have a faster cooling rate but give lower estimates than the Thermal-Original Thellier data, which is the opposite of the expected cooling rate effect (Poletti et al., 2013).

Additionally, the perpendicular protocol having less than half the number of treatments as in the Original-Thellier protocol introduces another complication if these specimens undergo stress relaxation during the experiment. If even mild stress relaxation affects the specimens, the perpendicular data will appear too low because pTRMs would be gained more efficiently than NRM would be lost (Kosterov and Prevot, 1998).

That the Microwave-Original Thellier results are lower than their Thermal-Original Thellier counterparts suggests that something inherent to the microwave demagnetization mechanism dampens the effects on the data from non-ideal vortex-state grains. If this finding were the result of the microwave not causing the same magnitude of stress relaxation as in thermal experiments, the Microwave-Perpendicular data would be expected to be even lower than the Thermal-Perpendicular data (Kosterov and Prevot, 1998). This does appear to be the case here (Figure 7-5B), as the differences are not statistically significant.

Based on the above discussion, explanations therefore exist both for why the thermal original Thellier experiments overestimate the true value (multi-domain-like effects) and for why perpendicular experiments (both thermal and microwave) underestimate it (unrecognized alteration), which implies that the best estimate should fall between these two extremes.

The inherent uncertainty in the data and techniques used to obtain paleointensity estimates can and should be expressed in the stated uncertainties associated with a flow-level mean (for example, averaging the Th-OT+ and MW-Perp and providing the resulting large std. deviation). Until new, high-quality data exist for all the flows studied here from the SOH1 drill core, the authors propose that for each flow, the available flow-level Th-OT+ and MW-Perp datasets, which are the largest two, be averaged. Supporting Information C.4 provides an example of this averaging for the flows containing at least two specimens in each Th-OT+ and MW-Perp dataset (i.e. the flows studied in the meta-analysis described in Supporting Information C.1). This method gives a mean paleointensity estimate of 29.2 ± 12 μT. This mean value is virtually identical to the mean MW-OT+ estimate of our newly collected data, 29.5 ± 9.2 μT, but higher than the equivalents measured by Gratton et al. (2005) and lower than those in Teanby et al. (2002). Flows characterized by data produced

from only a single method (more than half; 97/181) across these studies (and the Laj et al. (2011) reanalysis) should not be considered accurate to within stated uncertainties.

7.7.2 Implications for future experiments

The perpendicular protocol has largely fallen out of use due to the lack of pTRM checks, but the Original Thellier protocol lives on as do the IZZI (Yu et al., 2004), Coe (ZI) (Coe, 1967), and Aitken (IZ) (Aitken et al., 1988) protocols. Modeling done in Biggin (2010) carries the implication that the Original Thellier protocol has the potential to exaggerate multi-domain behavior compared to other Thellier-style double treatment experiments, which is largely consistent with the study carried out here. We therefore suggest that any future experiments performed with the Original-Thellier protocol (or indeed the Coe or Aitken protocols), should incorporate pTRM tail checks alongside pTRM checks such that multi-domain-like effects may be detected. The IZZI protocol has the built-in advantage of allowing detection of non-ideal behavior via zig-zags in the Arai plot.

This study is consistent with previous studies (e.g. Grappone et al., 2019) that have shown that while different methods can give seemingly reliable data, non-ideal effects (multidomain behavior, stress relaxation, undetected alteration) can be a biasing influence. We therefore concur with the finding in Grappone et al. (2019) that at least pilot specimens should be run using at least 2 Thellier-style protocols (or the IZZI protocol) as a 1st order check for non-ideal paleointensity behavior. Better still, different methods (e.g. Thermal Thellier, Microwave Thellier, or Multi-Specimen) should be employed to produce reliable multi-method paleointensity estimates (de Groot et al., 2013), which, ideally, should be internally consistent. Biggin and Paterson (2014) provided a set of quantitative criteria for evaluating the reliability of paleointensity estimates. Such paleointensity estimates are required to satisfy the TECH QPI criterion of Biggin and Paterson (2014), which requires paleointensity estimates to come from multiple techniques.

7.8 Conclusions

In this paper, we have sought to identify the cause for systematic discrepancies between previously published paleointensity studies on the SOH1 drill core. New paleointensity data confirm the systematic offset observed from previous studies when using the same methods; namely, Thermal-Original Thellier estimates were ~30% higher than Microwave-perpendicular estimates. For the first time, Thermal-Perpendicular experiments and

Microwave-Original Thellier experiments were undertaken on these rocks. Our results confirm that Thermal-Original Thellier data can be too high in the presence of magnetic carriers that do not behave as non-interacting SD grains. We further confirm that perpendicular data, which lack pTRM checks for alteration, can be too low due to undetected thermochemical alteration.

Until new measurements are made using reliable methods, results previously obtained from the SOH1 drill core using different methods should be combined at the flow level. The resulting enhanced standard deviation will accurately reflect the intrinsic uncertainty associated with the mean. The potential for biasing in those flows only represented by estimates produced by only one of the previously applied methods should be recognized.

Future studies undertaken using the thermal and/or microwave demagnetization mechanisms should avoid any protocols which do not contain within them checks for both lab-induced alteration and non-ideal multi-domain- like behavior. The IZZI protocol with pTRM checks satisfies both of these criteria.

7.9 Acknowledgments and data availability

This study was carried out by J. Michael Grappone as part of a University of Liverpool match-funded studentship, with support from the Duncan Norman Research Scholarship. J Michael Grappone acknowledges support from the NERC EAO Doctoral Training Partnership, grant NE/L002469/1 and NERC studentship 1793213. Andrew J Biggin and Courtney J Sprain acknowledge support from NERC standard grant NE/P00170X/1. Mimi J Hill acknowledges NERC grant NE/I013873/1. Courtney J Sprain thanks the Institute for Rock Magnetism at the University of Minnesota for use of their facilities to gather FORC data. The authors thank Nick Teanby for supplying the raw data from Teanby et al. (2002) and Martin Gratton for his systematic data archiving, from which we obtained the raw data from Gratton et al. (2005). All new raw data collected in this study can be found on MagIC at earthref.org/MagIC/16664. The authors also acknowledge the extensive, helpful comments of the reviewers, associate editor, and editors of JGR – Solid Earth.

7.10 References

Aitken, M. J., Allsop, A. L., Bussell, G. D., and Winter, M. B., 1988, Determination of the intensity of the earths magnetic-field during archaeological times - reliability of the thellier technique: Reviews of Geophysics, v. 26, no. 1, p. 3-12.

Biggin, A. J., 2010, Are systematic differences between thermal and microwave Thellier-type palaeointensity estimates a consequence of multidomain bias in the thermal results? : Physics of the Earth and Planetary Interiors, v. 180, no. 1-2, p. 16-40.

Biggin, A. J., and Paterson, G. A., 2014, A new set of qualitative reliability criteria to aid inferences on palaeomagnetic dipole moment variations through geological time: Frontiers in Earth Science, v. 2, no. 24.

Biggin, A. J., Piispa, E. J., Pesonen, L. J., Holme, R., Paterson, G. A., Veikkolainen, T., and Tauxe, L., 2015, Palaeomagnetic field intensity variations suggest Mesoproterozoic inner-core nucleation: Nature, v. 526, no. 7572, p. 245-248.

Biggin, A. J., Strik, G., and Langereis, C. G., 2009, The intensity of the geomagnetic field in the late-Archaean: new measurements and an analysis of the updated IAGA palaeointensity database: Earth Planets and Space, v. 61, no. 1, p. 9-22.

Cai, S., Tauxe, L., and Cromwell, G., 2017, Paleointensity From Subaerial Basaltic Glasses From the Second Hawaii Scientific Drilling Project (HSDP2) Core and Implications for Possible Bias in Data From Lava Flow Interiors: Journal of Geophysical Research: Solid Earth, v. 122, no. 11, p. 8664-8674.

Coe, R. S., 1967, Determination of paleo-intensities of earths magnetic field with emphasis on mechanisms which could cause non-ideal behavior in thelliers method: Journal of Geomagnetism and Geoelectricity, v. 19, no. 3, p. 157-179.

Coe, R. S., Gromme, S., and Mankinen, E. A., 1978, Geomagnetic paleointensities from radiocarbon-dated lava flows on hawaii and question of pacific nondipole low: Journal of Geophysical Research, v. 83, no. NB4, p. 1740-1756.

Cromwell, G., Trusdell, F., Tauxe, L., Staudigel, H., and Ron, H., 2018, Holocene Paleointensity of the Island of Hawai'i From Glassy Volcanics: Geochemistry, Geophysics, Geosystems, p. 3224-3245.

de Groot, L. V., Biggin, A. J., Dekkers, M. J., Langereis, C. G., and Herrero-Bervera, E., 2013, Rapid regional perturbations to the recent global geomagnetic decay revealed by a new Hawaiian record: Nature Communications, v. 4 Article No. 2727.

Doell, R. R., and Cox, A., 1963, The accuracy of paleomagnetic method as evaluated from historic Hawaiian lava flows: Journal of Geophysical Research, v. 68, no. 7, p. 1997-2009.

-, 1965, Paleomagnetism of Hawaiian lava flows: Journal of Geophysical Research, v. 70, no. 14, p. 3377-3405.

Grappone, J. M., Biggin, A. J., and Hill, M. J., 2019, Solving the mystery of the 1960 Hawaiian lava flow: implications for estimating Earth's magnetic field: Geophysical Journal International, v. 218, no. 3, p. 1796-1806.

Gratton, M. N., Shaw, J., and Herrero-Bervera, E., 2005, An absolute palaeointensity record from SOH1 lava core, Hawaii using the microwave technique: Physics of the Earth and Planetary Interiors, v. 148, no. 2-4, p. 193-214.

Hill, M. J., Pan, Y. X., and Davies, C. J., 2008, An assessment of the reliability of palaeointensity results obtained from the Cretaceous aged Suhongtu section, Inner Mongolia, China: Physics of the Earth and Planetary Interiors, v. 169, no. 1-4, p. 76-88.

Hill, M. J., and Shaw, J., 2000, Magnetic field intensity study of the 1960 Kilauea lava flow, Hawaii, using the microwave palaeointensity technique: Geophysical Journal International, v. 142, no. 2, p. 487-504.

-, 2007, The use of the 'Kono perpendicular applied field method' in microwave palaeointensity experiments: Earth Planets and Space, v. 59, no. 7, p. 711-716.

Hodgson, E., Grappone, J. M., Biggin, A. J., Hill, M. J., and Dekkers, M. J., 2018, Thermoremanent Behavior in Synthetic Samples Containing Natural Oxyexsolved Titanomagnetite: Geochemistry Geophysics Geosystems, v. 19, no. 6, p. 1751-1766.

Klugh, H. E., 1986, Statistics : The Essentials for Research, London, United Kingdom, Taylor & Francis Group.

Kono, M., and Ueno, N., 1977, Paleointensity determination by a modified thellier method: Physics of the Earth and Planetary Interiors, v. 13, no. 4, p. 305-314.

Kosterov, A. A., and Prevot, M., 1998, Possible mechanisms causing failure of Thellier palaeointensity experiments in some basalts: Geophysical Journal International, v. 134, no. 2, p. 554-572.

Laj, C., Kissel, C., Davies, C., and Gubbins, D., 2011, Geomagnetic field intensity and inclination records from Hawaii and the Reunion Island: Geomagnetic implications: Physics of the Earth and Planetary Interiors, v. 187, no. 3-4, p. 170-187.

Levi, S., 1977, Effect of magnetite particle-size on paleointensity determinations of geomagnetic-field: Physics of the Earth and Planetary Interiors, v. 13, no. 4, p. 245-259.

McElhinny, M. W., and Merrill, R. T., 1975, Geomagnetic secular variation over the past 5 m.y: Reviews of Geophysics, v. 13, no. 5, p. 687-708.

Paterson, G. A., Biggin, A. J., Hodgson, E., and Hill, M. J., 2015, Thellier-type paleointensity data from multidomain specimens: Physics of the Earth and Planetary Interiors, v. 245, p. 117-133.

Paterson, G. A., Muxworthy, A. R., Yamamoto, Y., and Pan, Y. X., 2017, Bulk magnetic domain stability controls paleointensity fidelity: Proceedings of the National Academy of Sciences of the United States of America, v. 114, no. 50, p. 13120-13125.

Paterson, G. A., Zhao, X., Jackson, M., and Heslop, D., 2018, Measuring, Processing, and Analyzing Hysteresis Data: Geochemistry Geophysics Geosystems, v. 19, no. 7, p. 1925-1945.

Poletti, W., Hartmann, G. A., Hill, M. J., Biggin, A. J., and Trindade, R. I. F., 2013, The cooling-rate effect on microwave archeointensity estimates: Geophysical Research Letters, v. 40, no. 15, p. 3847-3852.

Quane, S. L., Garcia, M. O., Guillou, H., and Hulsebosch, T. P., 2000, Magmatic history of the East Rift Zone of Kilauea Volcano, Hawaii based on drill core from SOH 1: Journal of Volcanology and Geothermal Research, v. 102, no. 3-4, p. 319-338.

Shaar, R., and Tauxe, L., 2013, Thellier GUI: An integrated tool for analyzing paleointensity data from Thellier-type experiments: Geochemistry Geophysics Geosystems, v. 14, no. 3, p. 677-692.

Smirnov, A. V., Kulakov, E. V., Foucher, M. S., and Bristol, K. E., 2017, Intrinsic paleointensity bias and the long-term history of the geodynamo: Science Advances, v. 3, no. 2, e1602306.

Teanby, N., Laj, C., Gubbins, D., and Pringle, M., 2002, A detailed palaeointensity and inclination record from drill core SOH1 on Hawaii: Physics of the Earth and Planetary Interiors, v. 131, no. 2, p. 101-140.

Thellier, E., and Thellier, O., 1959, Sur l'intensité du champ magnétique terrestre dans le passé historique et géologique: Ann. Géophys., v. 15, p. 285-376.

Thomas, N., 1993, An integrated rock magnetic approach to the selection or rejection of ancient basalt samples for paleointensity experiments: Physics of the Earth and Planetary Interiors, v. 75, no. 4, p. 329-342.

Xu, S., and Dunlop, D. J., 2004, Thellier paleointensity theory and experiments for multidomain grains: Journal of Geophysical Research-Solid Earth, v. 109, B07103.

Yamamoto, Y., Tsunakawa, H., and Shibuya, H., 2003, Palaeointensity study of the Hawaiian 1960 lava: implications for possible causes of erroneously high intensities: Geophysical Journal International, v. 153, no. 1, p. 263-276.

Yu, Y. J., Tauxe, L., and Genevey, A., 2004, Toward an optimal geomagnetic field intensity determination technique: Geochemistry Geophysics Geosystems, v. 5, Q02H07.

References from Supporting Information

Cisowski, S., 1981, Interacting vs non-interacting single domain behavior in natural and synthetic samples: Physics of the Earth and Planetary Interiors, v. 26, no. 1-2, p. 56-62.

Harrison, R. J., and Feinberg, J. M., 2008, FORCinel: An improved algorithm for calculating first-order reversal curve distributions using locally weighted regression smoothing: Geochemistry Geophysics Geosystems, v. 9.

Paterson, G. A., Muxworthy, A. R., Roberts, A. P., and Mac Niocaill, C., 2010, Assessment of the usefulness of lithic clasts from pyroclastic deposits for paleointensity determination: Journal of Geophysical Research-Solid Earth, v. 115.

Pike, C. R., Roberts, A. P., and Verosub, K. L., 2001, First-order reversal curve diagrams and thermal relaxation effects in magnetic particles: Geophysical Journal International, v. 145, no. 3, p. 721-730.

Roberts, A. P., Pike, C. R., and Verosub, K. L., 2000, First-order reversal curve diagrams: A new tool for characterizing the magnetic properties of natural samples: Journal of Geophysical Research-Solid Earth, v. 105, no. B12, p. 28461-28475.

CHAPTER 8 IMPROVING THE QUALITY OF ANOMALOUSLY LOW PALEOINTENSITY ESTIMATES OBTAINED FROM CARBONIFEROUS-AGE ROCKS

Foreword

The work from this chapter will contribute to two papers. This chapter therefore follows the publication format of Chapter 6 and Chapter 7 for consistency. The title of the first paper is *A Mid-Paleozoic Dipole Low*. Some of the data for this paper is provided in this chapter (the KHA/KHB data and some MW-IZZI+ data from the other sites). The authors of this paper are, in order, Louise MA Hawkins, J Michael Grappone (the author of this thesis), Courtney J Sprain, Patipan Saengduan, Edward Sage, Sheikerra T Cunningham, Banusha Kugabalan, and Andy J Biggin. The paper was submitted to the journal *Proceedings of the National Academy of Science* in August 2020. It is in revision as of September 2020.

The second paper will be based on the methods work in this chapter and submitted immediately after the former paper is accepted. The authors are, in order, J Michael Grappone (the author of this thesis), Courtney J Sprain, Louise MA Hawkins, Said Al Abdali, Nathaniel J Topie, and Andrew J Biggin. The co-authors have given permission to include this paper in my thesis. The difficulties of balancing the goals of these two papers is apparent in this chapter.

The format of this chapter partially reflects the co-mingling of these two papers. All Th-IZZI+, Th-LTD-IZZI+, and low temperature susceptibility data were collected by the author of this thesis. All Th-AF-IZZI+ and high temperature susceptibility data from lettered (KHA, KHB, etc.) were collected by the author of this thesis. The conception and analysis of the combined dataset, as well as the second draft manuscript, were completed by the author of this thesis. The co-authors collected most of the MW-(LTD-)IZZI+ data herein and provided a forum for the discussion of the data and analyses.

While putting together this study, it was determined that three of the new sites collected for this thesis, KHC/KHD/KHE, are likely not of Carboniferous age. These data are presented separately to reflect this development but are kept in for the methodology discussions. The methodology is valid for these rocks, even if their magnetizations are not clearly comparable to those from the other sites. The data from KHC/KHD/KHE will not be going into either of the papers.

8.1 Abstract

Understanding changes in the strength of the Earth's magnetic field over geologic history is a fundamental endeavor for studying the Earth's deep interior. Changes in conditions in the Earth's deep interior, such as core-mantle heat flux, result in forcing of the geodynamo, which can be observed as long-term (millions of years) changes in the magnetic field. Snapshots of the geodynamo are recorded in rocks during their formation, which means the geologic record contains billions of years of geodynamo changes. One of the major time periods of interest in this regard is the Carboniferous Period (from 360 Ma– 299 Ma), which includes the transition into, and the first part of, the Kiaman Reverse Superchron. Older time periods present numerous challenges, however, which are related to finding suitable rocks of suitable age, type and geologic history. Parsing the most accurate data from non-ideal recorders is therefore a top priority for paleointensity surveys.

A set of Carboniferous-age lava flows from the Kinghorn beaches, north of Edinburgh, Scotland, has been investigated. Previous studies of these rocks gave high quality directions and intensities using thermal and microwave Thellier techniques, but the intensities showed signs of non-SD magnetic grain influences. To try to mitigate the impact of these gains, the addition of alternating field (AF) and liquid nitrogen demagnetization (LTD) steps to typical IZZI thermal experiments was tested. The addition of these steps improved the Arai Plot data quality but had little impact on the success rates and paleointensity estimates. The highest quality data (as measured by the linearity of the generated Arai plot), and the highest pass rates, were found using the microwave paleointensity technique without LTD.

8.2 Introduction

Paleomagnetism provides one of the few tools to study the evolution of the Earth's deep interior. Studying changes in the strength of the Earth's magnetic field over long (>1 Myr) timescales yields information on changes in the Earth's deep interior; specifically, in the geodynamo and at the Core-Mantle Boundary (CMB). Data on these timescales are necessary to determine changes in CMB heat flux.

Research in the last decade has suggested the presence of a 200 Myr cycle during which rising plumes and sinking crustal slabs through the Earth's mantle link long-term variations in the planet's magnetic field with geological processes that affect the surface (Amit and Olson, 2015; Biggin et al., 2012; Hounslow et al., 2018; Olson and Amit, 2015). The most recent of these hypothesized cycles covers the Cretaceous Normal Superchron (no magnetic reversals) and Middle Jurassic hyper-reversal (frequent reversals). The second most recent of these cycles should therefore exist in the preceding time period. This time period contains the Permian, which is largely characterized by the Kiaman Reverse Superchron (Irving and Parry, 1963); the Carboniferous; and the Devonian time periods. To know if these cycles exist, high quality paleointensity and reversal frequency data are necessary.

The Devonian and Carboniferous (~420 Ma - ~300 Ma) have therefore been identified as key time periods that require additional and more robust data (Hawkins, 2018). Older rocks have more complex histories and therefore more complex data from which paleointensities must be estimated. Recent studies, such as Shcherbakova et al. (2017) and Hawkins et al. (2019) have filled in some of the data gaps, but fewer than 20 references exist in the global absolute paleointensity (PINT) database for these time periods (Biggin et al., 2009). The paleointensity (PI) values (mean values < 10 μT) obtained in these studies are substantially lower than the modern field at low latitudes (~34 μT) and are of a comparable magnitude to the low estimates found in Bono et al. (2019) from the Ediacaran, over 200 Myr prior to the Carboniferous. Such anomalously low PI values indicate substantial changes in the geodynamo (which generates the magnetic field) and CMB heat flux (which is one of the drivers of the geodynamo) during this time period, but the reliability of low PI values has historically been the subject of some debate (see Hawkins, 2018), impeding efforts to use these data to study deep Earth processes (e.g. Biggin et al., 2012; Hounslow et al., 2018; and Olson et al., 2013).

A common source for anomalous PI estimates can be the presence of large, non-ideal (non-single domain/multi-domain or magnetically interacting, closely-spaced) magnetic

grains. Non-ideal grains fail to follow Thellier's laws of thermoremanence and are generally too big or too closely packed (interacting) to have single, independent magnetic domains controlling their net magnetization. Large (non-single domain or multi-domain) grains of magnetite are common in volcanic rocks and can be problematic if not appropriately accounted for (e.g. Biedermann et al., 2019 and Roberts et al., 2019). These grains can cause a shallowing of Arai plots and are often associated with concave-up (two-slope) Arai plot (Nagata et al., 1963) data. It has been shown that selecting the low (high) temperature portion of these data give PI estimates that are higher (lower) than the actual paleofield (e.g. Biggin and Thomas, 2003; Hodgson et al., 2018; Levi, 1977; Smirnov et al., 2017). The previous studies from the Devonian and Carboniferous periods (Hawkins, 2018, Hawkins et al., 2019, and Shcherbakova et al., 2017) primarily used volcanic basalts that produced concave-up Arai plot data. The age of these rocks means that low-temperature magnetic overprints are common, which can cause a change in both direction on an orthogonal plot and a change in slope on an Arai plot. These studies selected the high temperature portion of their respective Arai plots, which means that there exists the possibility that the low paleointensities observed during the Carboniferous are biased low to some degree by these non-ideal grains.

Hawkins (2018) sampled Carboniferous outcrops throughout the north of the United Kingdom. Two locations were selected for paleointensity experiments: outcrops near Strathmore and near Kinghorn, Scotland. The data from the Kinghorn outcrops (just north of Edinburgh, Scotland) are of particular note because all the paleointensity data from these sites are low, ranging from 4 - 11 µT. Torsvik et al. (1989) dated the magnetization of the Kinghorn lava flows to be Lower Carboniferous in origin, which agrees with Fitch et al. (1970)'s K-Ar dating of 338 $\pm$ 4 Ma (Monaghan and Browne, 2010).

During the Carboniferous time period, Scotland was near the equator, where, for reference, the modern field strength is around 35 µT. The Arai plots generated from the Kinghorn data are of particular interest because they have zigzagging data (Shaar et al., 2011) and are largely concave up (two-sloped), instead of linear. Many specimens have low temperature overprints, but a change in Arai plot slope is not always correlated with a change in direction on the associated orthogonal plot. The behavior of these data point to the presence of non-ideal grains in these specimens.

Various techniques (with varying amounts of specialty equipment required) have been proposed to improve data quality. The first fix is to add a low alternating field (AF) step after

each heating step (Biggin et al., 2007; Dunlop et al., 2005) to suppress multi-domain behavior. The AF cleanse is expected to demagnetize any low coercivity (soft) magnetic components, which will remove their influence from the paleointensity data. In an IZZI experiment, if the AF cleanse is successful at removing MD effects, the curvature (which is measured by |K'|) and zigzag (which can be inferred from the scatter of the Arai plot, β) of the plot should decrease (Biggin et al., 2007). A second, and more time-consuming, corrective step is the addition of a cyclical liquid nitrogen demagnetization step (Smirnov et al., 2017). Cooling a specimen in liquid nitrogen below its Verwey transition (-148 °C) and then warming it causes magnetite's crystal lattice to undergo a phase transition from monoclinic to cubic inverse spinel (stable at room temperature). This cooling/heating cycle in a zero-magnetic field causes multi-domain (MD) grains to demagnetize but single-domain grains retain their previous magnetization (Smirnov et al., 2017; Verwey, 1939). A Verwey transition is characteristic of, and therefore requires the presence of, stoichiometric MD magnetite (Fe_3O_4), which means the liquid nitrogen cycling is potentially less widely applicable.

A third option to improve data quality is to use microwave radiation, a demagnetization mechanism pioneered at the University of Liverpool (e.g. Hill et al., 2008). The microwave system exists to minimize the bulk heating of a specimen, by using microwave radiation tuned near the resonance frequency of magnetite to excite only the magnetite and not the rest of the matrix (Suttie et al., 2010). At lower temperatures, the specimen is less susceptible to thermochemical alteration and should therefore produce more reliable data (Suttie et al., 2010).

To assess the cause of the two-slope behavior and therefore determine the reliability of the Carboniferous data, additional rocks from the Kinghorn sites studied in Hawkins (2018) were collected. In addition, three sites to the north of their study area were sampled to add to the Carboniferous paleointensity dataset. These new sites were studied in Torsvik et al. (1989) and gave predominately reversed polarity directions. This chapter presents and compares results from each studied site and from each of these techniques to determine the best Carboniferous paleointensity estimates possible.

8.3 Materials and Methods

The Kinghorn Volcanic Formation consists of 30 mapped flows that range in thickness from 2.5 – 12 m and dip moderately (20 – 30 °) to the NE (Geikie, 1900). During the 2018 field season, samples from eight sites were collected. Five sites (KH1, 2, 6, A, B) were sampled to supplement the sampling performed previously in Hawkins (2018). Three new sites were

collected North of Kinghorn Harbour (KHC, KHD, and KHE), with KHE outcropping directly above the first Abden Limestone. Sites were collected along the coast, where the outcrops are most easily accessible. A Google Earth image of the Kinghorn collection sites can be found in Figure 8-1. Numbered sites were previously studied in Hawkins (2018). Lettered sites were newly acquired in the 2018 field season.

Figure 8-1 Google Earth image of the Kinghorn region, north of Edinburgh, Scotland.

Before paleointensity experimentation, high and low temperature susceptibility experiments on representative specimens from each site were run. In order to successfully use LTD to remove the MD grains' component, the magnetite (in theory) needs to be stochiometric (i.e. no Ti inclusions). In practice, its low temperature susceptibility data must contain a clear Verwey transition in the low temperature susceptibility data.

The IZZI protocol (Yu et al., 2004) was used for all paleointensity experiments. The IZZI protocol combines In-field (I) and Zero-field (Z) treatment steps in an enclosed couplet, ZIIZ, and in this study is followed by a pTRM check (P step) (IZZI+ protocol). For the treatment steps, both thermal (Th) and microwave (MW) radiation were used as demagnetization mechanisms. The heating steps were performed in a rapid-cooling Magnetic Measurements thermal demagnetizer and measured on the University of Liverpool's 2G RAPID magnetometer system (Kirschvink et al., 2008). These specimens were standard 25 mm diameter cores with heights ranging from 5 – 15 mm. The field used in these thermal experiments was 10 µT, applied at inc = 90°, in core coordinates. Th-IZZI+ is the most common experiment type of those tested herein and ample studies (e.g. Chapter 6; Paterson

et al., 2015; and Shaar et al., 2011) have shown that IZZI+ data do not have inherent problems. These data will therefore serve as the baseline for comparison with the modified techniques. Arai plots of specimens containing non-ideal grains are expected to have zigzagging and curvilinear (two-slope) data. This non-linear behavior can, however, also arise from a change in magnetic vector component, which is seen on many specimens' orthogonal plots.

A subset of 68 specimens received an additional 5 mT cleanse after heating but before measurement. These experiments will be referred to as "Th-AF-IZZI+". Adding the AF step on the RAPID (Kirschvink et al., 2008) increased the measurement time for each specimen by one minute per temperature step. A separate, additional set of 49 specimens received 2 null-field LTD bath cycles of 30 minutes after each heating step (Th-LTD-IZZI+), before being measured. Adding the LTD steps doubled the length of each temperature step.

The microwave experiments were run on the University of Liverpool's Tristan microwave system (Hill et al., 2008). These specimens were 5 mm diameter cores with heights of 2 – 5 mm. For these microwave experiments, applied fields from 5 – 20 μT were used, applied perpendicular to the specimen's NRM direction in core coordinates, as utilized in Chapter 6. The MW-IZZI+ experiments were also extended to see if the addition of an LTD step to the MW data would have the same effect as in the thermal experiments. 17 specimens received an additional 5-minute LTD null-field step after each microwave treatment (MW-LTD-IZZI+), which increased the length of each experiment from 1 hour to 5 hours. Adding the LTD step to the microwave protocol required manually pulling out the specimen from the microwave system. After the LTD treatment, the specimen was replaced on the glass holder and returned to the measurement region. Markings were added to system as a guide to maintain the specimen's orientation within the system, but the small (5 mm) size of the specimens means this process of reorienting the cores introduced a new source of error into an already complex paleointensity experiment. Hawkins (2018) used MW-IZZI+ and Th-AF-IZZI+ for the original paleointensity study.

The same selection criteria were used as in the methods work done in Chapter 6 and Chapter 7, which are based on the MC.CRIT-C1 developed by Paterson et al. (2015) to extract accurate PI estimates from specimens with data characteristic of non-SD grains. The statistics were used to classify the results into "A quality" data (passed all the selection criteria) and "B quality" data (passed all the selection criteria except 1). The selection criteria for A and B quality data are detailed in Table 8-1.

Table 8-1 Selection criteria used in this chapter

	N	beta	FRAC	q	DRAT	alpha	|K'|
A quality	4	0.1	0.35	1	10%	10	0.48
B quality	4	0.12	0.25	1	15%	15	0.48

Note. Only a maximum of one of the A selection criteria can be failed for the B selection criteria to be used.

For rock magnetic work, one untreated specimen was selected from each site and manually crushed. The Liverpool Variable Field Transition Balance (VFTB) was used to determine thermomagnetic curves and hysteresis parameters. An Agico MFK1-FA Kappabridge was used for low temperature susceptibility curves.

8.4 Rock magnetism

First, the low temperature susceptibility data and thermoremanent curves are presented. If multi-domain stoichiometric magnetite is present is present in the specimens, these grains will have a susceptibility peak around -148 °C, which is characteristic of a low-temperature phase transition (from monoclinic to cubic inverse spinel crystal lattices), named the Verwey transition (Verwey, 1939). Data from each site are presented in Figure 8-2. Verwey transitions were observed in specimens from six sites (KH2, 4, 7, 8, C, and E), identified as peaks in the susceptibility data around -150 °C.

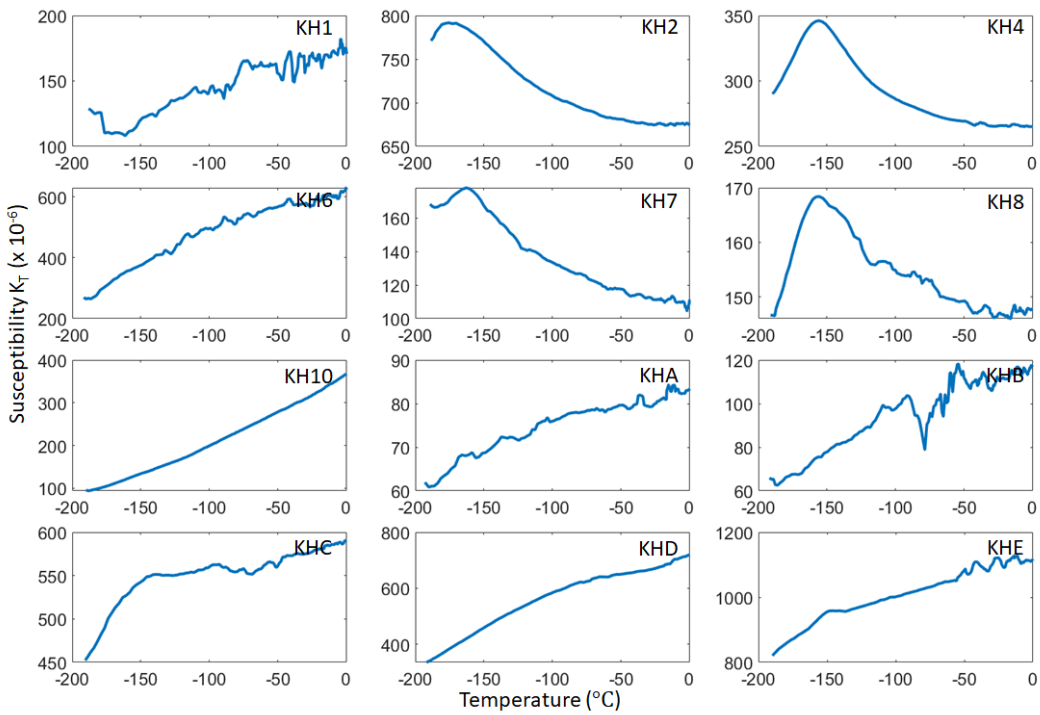

Figure 8-2 Low temperature susceptibility experiments for all sites, seeking to locate a Verwey transition at -148 °C. Peaks corresponding to Verwey transitions were found for six sites – KH2, KH4, KH7, KH8, KHC, and KHE.

The magnetization of single-domain magnetite is unaffected by the Verwey transition, but multi-domain magnetite remains unblocked upon warming past the transition in a zero magnetic field. Visibly clear peaks in the low temperature susceptibility data were observed for the representative specimens from KH2, KH4, KH7, KH8, KHC, and KHE. The lack of Verwey peaks in some sites and the presence of high Ti-titanomagnetite and potentially minor secondary maghemite phases in other sites, such as KHB (Hawkins, 2018), implies the addition of the LTD step will be overall less efficient at removing any non-SD components compared to the AF cleanse in these samples.

In addition to low temperature susceptibility, high temperature thermomagnetic experiments were undertaken. These results are presented in Figure 8-3. The thermomagnetic curves are largely reversible, but some sites (e.g. KH6 and KHB) show the potential presence of minor secondary magnetite phases, such as maghemite. Specimens generally show low-Ti titanomagnetite, with Curie Temperatures above 500 °C, but a few sites (e.g. KHC and KHE) show have larger amounts of Ti, giving Curie Temperatures closer to 400 °C.

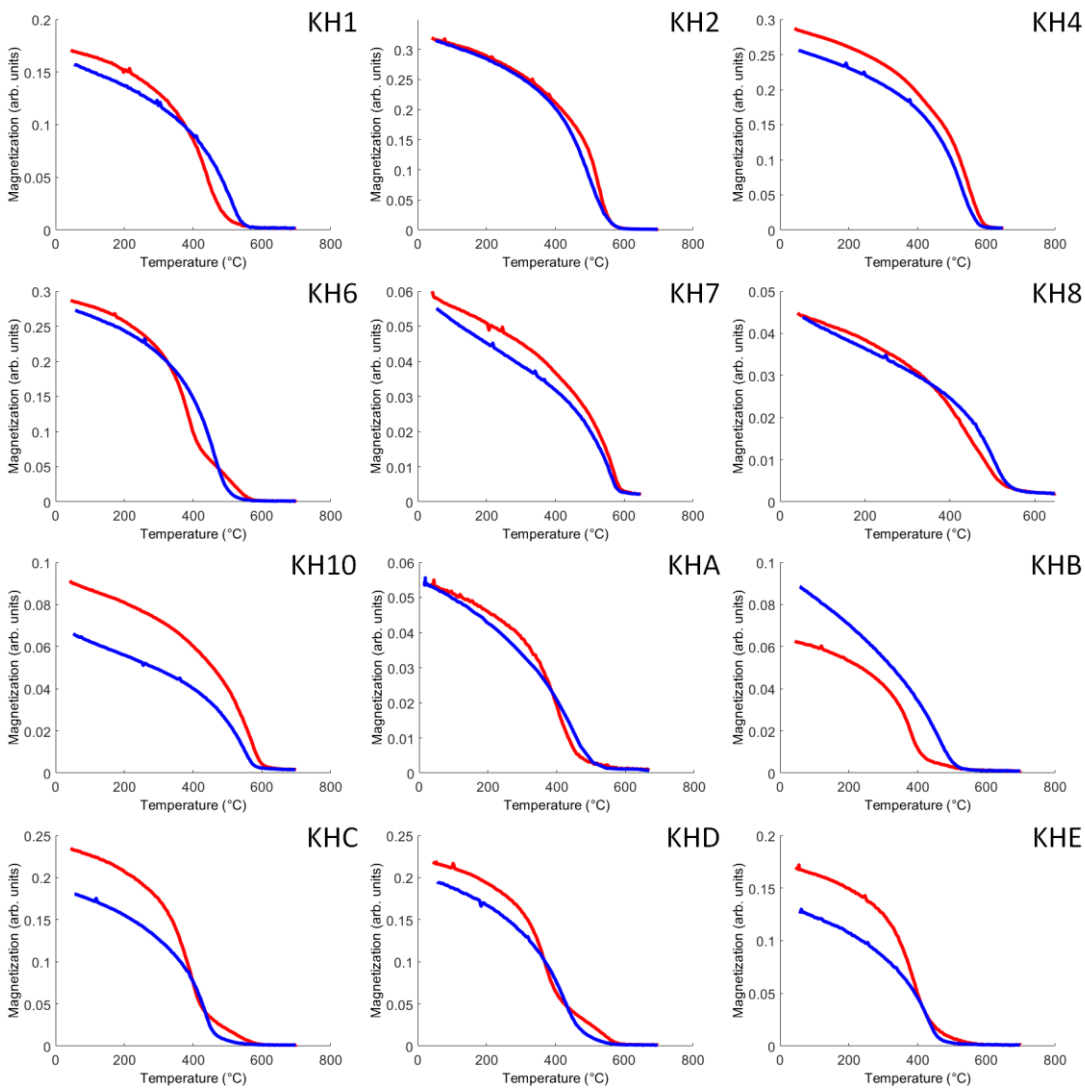

Figure 8-3 High temperature thermomagnetic curves for all the sites studied herein

A summary of the hysteresis parameters for the Kinghorn data is provided in Figure 8-4. The KH sites generally sit above the bulk domain stability (BDS) trendline from Paterson et al. (2015), which means they are largely stable but likely have some superparamagnetic or hematite grains present in addition to (titano-)magnetite. The new sites fall in the middle of the range of behavior previously observed in the Kinghorn site data provided in Hawkins (2018).

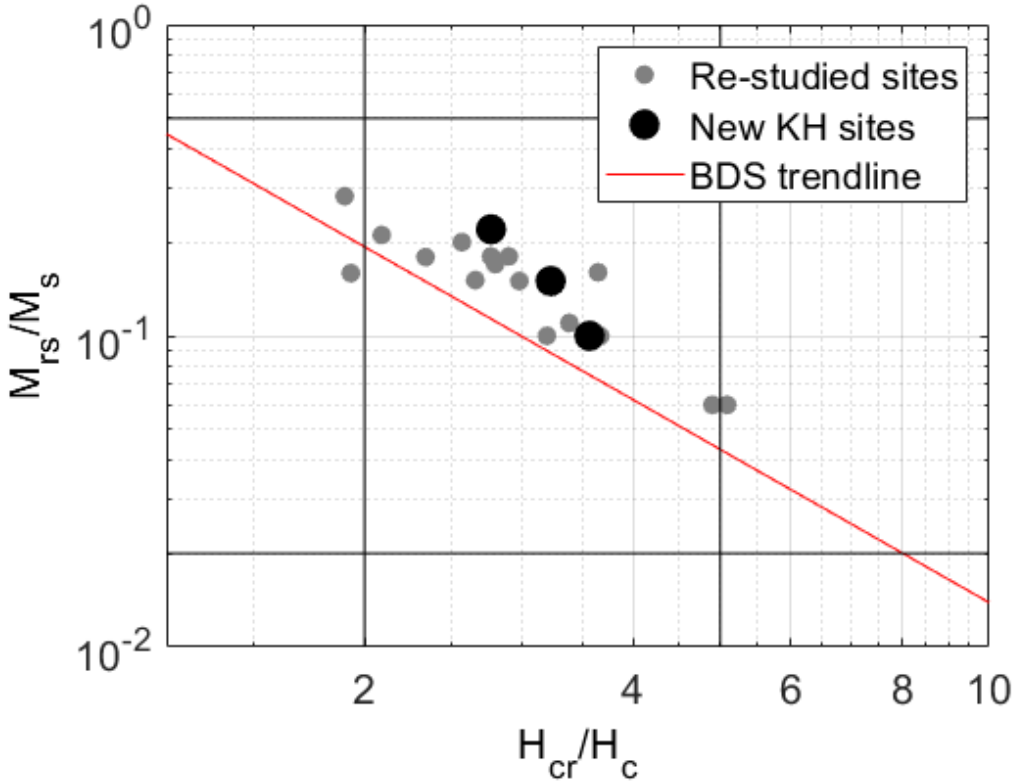

Figure 8-4 Summary hysteresis parameter figure, including both old and new sites and bulk domain stability (BDS) trendline (Paterson et al., 2015). M_{rs}/M_s refers to the ratio of remanent saturation magnetization to the saturation magnetization and H_{CR}/H_C refers to the ratio of coercivity of remanence to coercivity.

A second test for the utility of the addition of corrective LTD or AF steps is identifying the percent of NRM that is lost from a two-cycle LTD step or a 5mT AF demagnetization before any heating has occurred. The results of these tests are provided in Table 8-2, organized by site and technique.

Table 8-2 NRM lost by site, by data correction mechanism (AF and LTD)

Site	KH1	KH2	KH4	KH6	KH7	KH8	KH10	KHA	KHB	KHC	KHD	KHE
% NRM lost (2x LTD)	1.0	40.4	2.2	27.1	2.6	8.1	25.8	4.2	4.7	3.5	5.9	8.7
% NRM lost (5 mT AF)	12.7	25.9	5.0	35.4	4.8	19.4	18.8	13.0	3.0	2.8	4.7	23.1

In Figure 8-2, sites KH2, KH4, KH7, KH8, KHC, and KHE were identified as being the most likely candidates for improvements from the addition of an LTD step. From Table 8-2, KH2, KH6, KH8, KH10, KHD, and KHE had the largest (> 5%) NRM lost as a result of cyclic LTD steps. Despite the lack of Verwey transitions in the susceptibility data for KH6, KH10, and KHD, it appears these sites would respond to an LTD treatment, given that the low temperatures are able to unblock (what is presumably) a multi-domain component. Given 9/12 sites should

respond to the LTD treatments by at least 5%, this study applies LTD treatments to all sites for completeness.

As can be seen in Table 8-2, 8/12 sites show an NRM loss of at least 5% after an initial 5 mT AF demagnetization before the first heating step. Since adding an AF demagnetization step before each measurement adds < 30 s per measurement per specimen (and is automated), this study applies AF treatments to all sites.

8.5 Questionably Carboniferous sites: KHC, KHD, KHE

8.5.1 Paleodirections

Paleodirections were not a goal of this chapter but were obtained directly from the Th-IZZI+ experiments that were performed on oriented samples. Presented here are the tilt-corrected directions for the new sites, KHA, KHB, KHC and KHD. Paleodirections for restudied sites were calculated from oriented Th-IZZI experiments and were consistent with the results in Hawkins (2018). Reliable paleodirections were unable to be determined for KHE, due to only having one unoriented hand sample, so the age of the magnetization data cannot be confirmed as Carboniferous. Therefore, the data are excluded from any discussion about Carboniferous PI.

The directions found in KHC and KHD are not consistent with the accepted Reverse/Normal directions determined by Torsvik et al. (1989) and Hawkins (2018) for the more southerly Kinghorn sites (see Figure 8-5). Most of their sites gave Normal polarity directions, but some sites instead had antipolar Reverse polarity directions. The most southern sites (KH1, KH2, KHA, and KHB) are the least antipolar to the Kinghorn normal pole, but within α_{95} error range. The new site, KHC has a direction that corresponds to a rejected direction in Torsvik et al. (1989). The most northern site with directions, KHD has a direction that falls within error of the great circle between the Reverse directions of the KH1, KH2, KHA, KHB sites and Hawkins (2018)'s Kinghorn Normal, which means that the KHD site potentially formed during an intermediate magnetic field, possibly during a reversal. An in-depth rock magnetic study, including Scanning Electron Microscopy to help constrain the origin of the magnetite, and more directional data would be required to properly determine the robustness of the data from KHD.

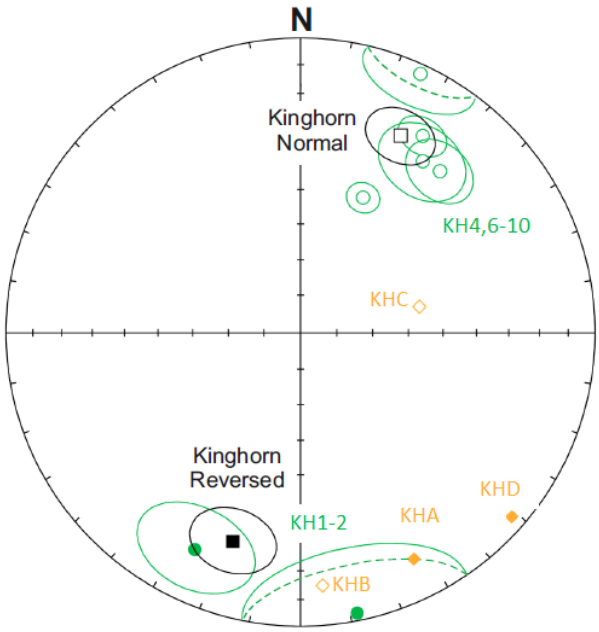

Figure 8-5 Kinghorn paleodirections, compared to expected Kinghorn Reversed and Kinghorn Normal directions (Torsvik et al., 1989), in black. Green data come from Hawkins (2018), from multiple, independently oriented drill cores. Orange data come from a single hand sample. Unfilled symbols have a negative inclination; filled symbols have a positive inclination.

Given the uncertainty surrounding the paleodirections of KHC, KHD, and KHE, these new sites are excluded from any discussion referring specifically to magnetic field during the Carboniferous. They will, however, still be included in the methods discussion.

8.5.2 Paleointensity results

A total of 76 specimens were run from the 3 newly investigated (non-Carboniferous) Kinghorn sites— KHC, KHD, and KHE—located to the north of the restudied sites. The 3 new northern sites had pass rates across all methods that ranged from 4% to 37%.

The low temperature susceptibility data for KHC indicate the presence of a Verwey transition, so the AF and LTD demagnetization steps were expected to improve the data. However, the weathering and mineralogy of the site resulted in a failure to obtain meaningful paleointensity estimates using conventional Th-IZZI+, which means data improvements from the LTD or AF steps were unlikely. In fact, the additional steps were unable to correct the data sufficiently to allow them to pass either set of selection criteria because the most common reasons for failure were high alteration (DRAT) and a lack of demagnetization to the origin (high α; indicative of a non-characteristic remanent magnetization). Switching to using the MW system allowed one specimen to pass the A selection criteria and one additional specimen to pass the B selection criteria out of 17 total specimens.

The Arai plot behavior of the KHD specimens is also anomalous. The Arai plot data in Figure 8-6 have a similar two-slope shape to the other sites studied here and previously, but the associated orthogonal plots, compared to the other sites, are substantially different, as they are generally single component. From 30 tested specimens, KHD had at least 1 B quality pass from every tested PI technique. Of the 9 A quality passes, 8 (100% pass rate) came from MW-IZZI+ data. These specimens overall give a mean A quality PI estimate of 16.6 µT. This PI estimate is substantially higher (55% higher) than the next highest site (KH7; 10.7 µT).

From the northern-most site, KHE, 31 specimens were tested and yielded an A quality pass rate of 13%. They gave some of the lowest PI estimates (2.5 – 3.0 µT) of any of the sites tested and have a very sharp slope change around 300 °C. The large change in slope, which is correlated with a change in direction on the orthogonal plot, meant that this second, convergent component generally covered less than 40% of the NRM of a specimen. As a result, many specimens failed the FRAC criterion (which is largely dependent on the amount of NRM used), especially in the MW, which often cannot fully demagnetize a specimen.

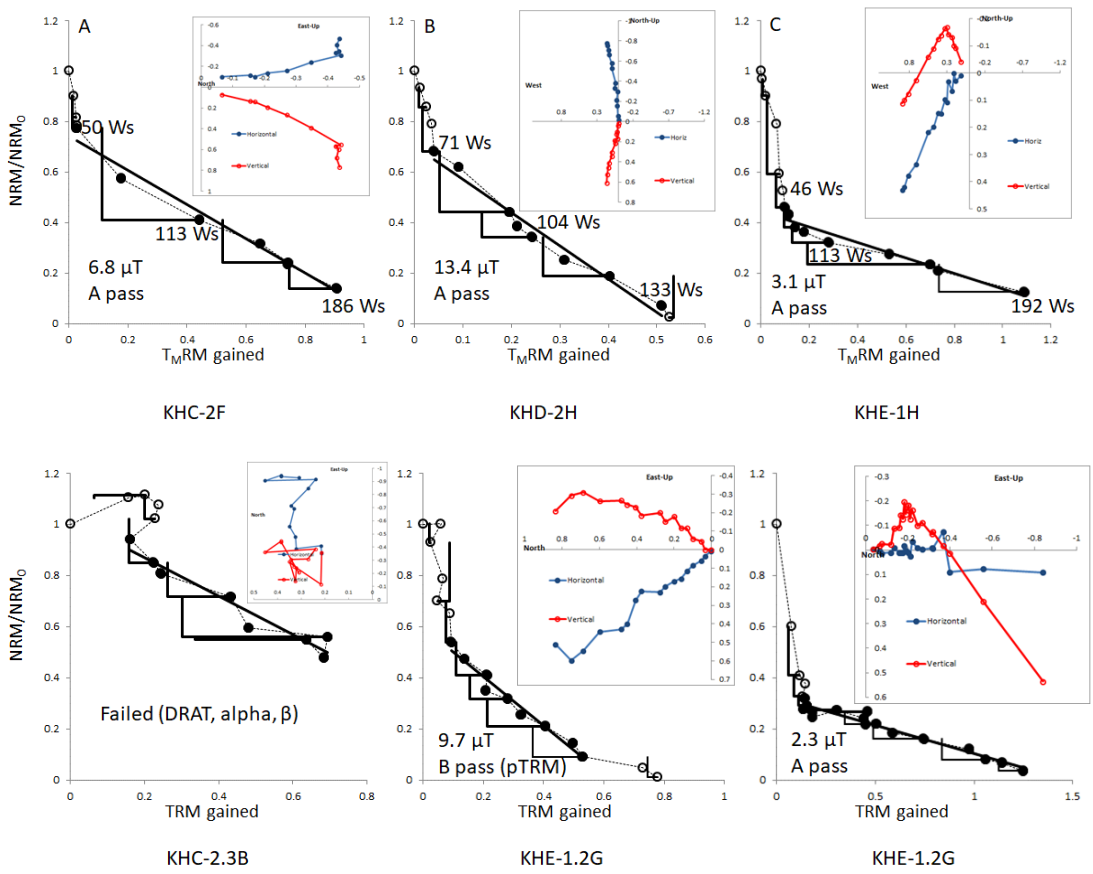

Figure 8-6 New sites' (KHC, D, E) paleointensity data. Top: Microwave-IZZI+; bottom: Thermal-IZZI+.

8.6 New paleointensity results (KH1 – KHE)

8.6.1 Summary

A total of 211 new specimens were run in this chapter from 12 sites across the 29 Kinghorn lava flows, including the 76 from 3 newly investigated Kinghorn sites (see Section 8.5.2). The new sites (KHC, KHD, and KHE) are the only sites that received Th-AF-IZZI+ treatments. A breakdown by method for all the new data can be found in Table 8-3, along with the respective pass rates. The overall A and B quality pass rates were 12% and 18%, respectively. For the A quality data, 12 site-level PI estimates were extracted, ranging from 2.3 to 16.9 µT, which correspond to a virtual dipole moments (VDM) of 5.2 – 39 ZAm^2. The experiments newly run on these rocks are Th-IZZI+, Th-LTD-IZZI+, and MW-LTD-IZZI+, which will be investigated further in this section. The Arai plot data for each individual specimen can be found in Supplementary Information C. Figure 8-6 contains representative Arai plots from the new sites, and Figure 8-7 contains representative Arai plots from the restudied sites.

Table 8-3 Summary of experiments and pass rate broken down by method for new results from this study.

Method	A passes	Pass rate	A + B passes	Pass rate	N total
Th-IZZI+	8	7.6%	21	20%	105
Th-AF-IZZI+	0	0%	1	6.7%	15
Th-LTD-IZZI+	3	6.7%	5	11%	45
MW-IZZI+	11	42%	13	50%	26
MW-LTD-IZZI+	0	0%	2	12%	17
Total	16	12%	24	18%	211

8.6.2 Carboniferous-age sites (KH1, KH2, KHA, KHB, KH4, KH6, KH7, KH8, and KH10)

A total of 130 specimens were run from the previously studied Kinghorn sites. Paleointensity data were collected from these sites and are reported in Hawkins (2018) and reported in a manuscript currently being written with this thesis's author as a second author. To test the efficacy of the LTD step addition (and the AF step used in Hawkins, 2018), these sites were therefore tested using Th-IZZI+ and Th-LTD-IZZI+. Specimens from three sites— KH1, KH2, and KH6— also received MW-LTD-IZZI+ treatments. A summary of the new experiments by method and site can be found in Table 8-4.

Table 8-4 Experiments broken down by site and method

Method	KH1	KH2	KHA	KHB	KH4	KH6	KH7	KH8	KH10
Th-IZZI	2/3/10	0/1/10	1/1/12	1/2/6	0/1/7	0/2/9	0/1/6	1/4/9	1/3/8
Th-LTD-IZZI+	1/1/4	0/0/2	0/0/4	1/1/3	1/1/4	0/0/4	0/0/4	0/1/6	0/0/5
MW-LTD-IZZI+	0/2/7	0/0/5	0/0/0	0/0/0	0/0/0	0/0/5	0/0/0	0/0/0	0/0/0
Total	3/6/21	0/1/17	0/1/16	2/3/9	1/2/11	0/2/18	0/1/10	1/5/15	1/3/13

Note. The first number listed is number of specimens that passed the A selection criteria. The second number is the number of specimens that passed the B selection criteria. The third number is the total number of specimens tested.

Of the 130 total specimens run from these sites, 9 passed the A criteria (6.9%) and a further 15 passed only the B criteria (18% total). The Th-IZZI+ data's A quality pass rate of 7.8% was comparable to the Th-LTD-IZZI+ pass rate of 8.3%. The Th-IZZI+ data had a substantially higher B quality pass rate of 23%, compared to the Th-LTD-IZZI+'s pass rate of 11%. The MW-LTD-IZZI+ data's A and B quality pass rates 0% and 12%, respectively, were substantially lower than the respective Th-IZZI+ pass rates.

The mean Th-IZZI+ A quality estimate of 4.7 ± 1.9 µT is lower than the Th-LTD-IZZI+ estimate of 8.7 ± 2.8 µT, with p = 0.0124 in a two-sample T-test. The B quality estimates (5.6 ± 2.8 µT and 7.8 ± 3.7 µT, respectively) are not statistically distinct, with p = 0.141. The mean MW-LTD-IZZI+ B quality estimate of 7.4 ± 0.57 µT is not distinct from the Th-LTD-IZZI+ estimates (p = 0.38, and 0.89, respectively). Arai plots representative of the (Th-IZZI+) characteristics of the ten Carboniferous age sites are given in Figure 8-7.

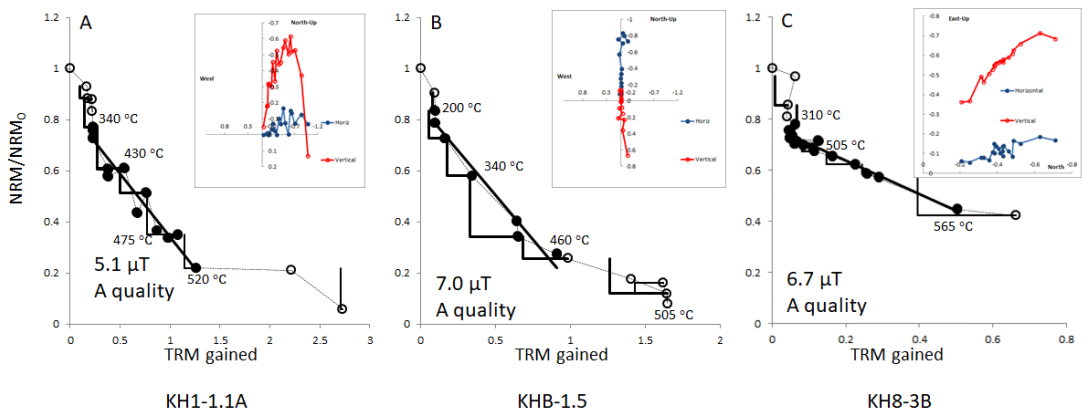

Figure 8-7 Arai plots representative of the characteristics of the Kinghorn dataset for the ten Carboniferous-age sites. Insets are orthogonal paleodirection plots. All three specimens gave A quality data and low PI estimates. All plots use the Th-IZZI+ method.

All the Arai plot data show characteristic multi-slope (non-linear) Arai plots. The changes in slope do not necessarily correlate one-to-one with changes in direction on the associated orthogonal plots, which may be the result of weathering, given these specimens' ages. The most likely alternative answers are alternation (observed via pTRM checks) or non-single domain behavior (observed via Arai plot zigzag). The middle- (to high-) temperature slopes trend to the origin and may pass the selection criteria. The highest temperature components have directions that trend to the origin but suffer associated pTRM check failure, which suggests that the change in slope is the result of thermochemical alteration. The zigzag observed in some of the Arai plots point to the presence of non-single domain grains which is what the LTD treatment steps aimed to remedy.

8.6.3 LTD-IZZI+

The addition of LTD was only expected to impact the data of specimens from KH10, 2, 4, 8, C, 7, and E because these are the sites whose low temperature susceptibility plots showed a Verwey transition. Adding the 2-cycle liquid nitrogen cooling step after each heating step doubled the time required for the experiment. In Table 8-3, the overall pass rates for Th-IZZI+ and Th-LTD-IZZI+ are not substantially (< 1%) different. In the top row of Figure 8-8, the results from these experiments are presented.

The addition of the LTD steps after each MW treatment increased the time required for each experiment from 1 hour to 5 hours. Of the 17 specimens run, only 2 specimens passed the B selection criteria, for a 12% pass rate, compared to the Th-IZZI+ pass rate of 20%. In the bottom row of Figure 8-8, 4 Arai plots are reported from the 3 sites tested, including the two specimens that passed the B selection criteria. The main reasons for failure were high Arai plot scatter and high DRAT. The MW-LTD-IZZI+ experiments also suffered from errors that stacked each time the 5 mm diameter core was removed from the cavity for the LTD step and then reoriented. The small size means that movements on the order of 50 µm correspond to a 1° orientation error.

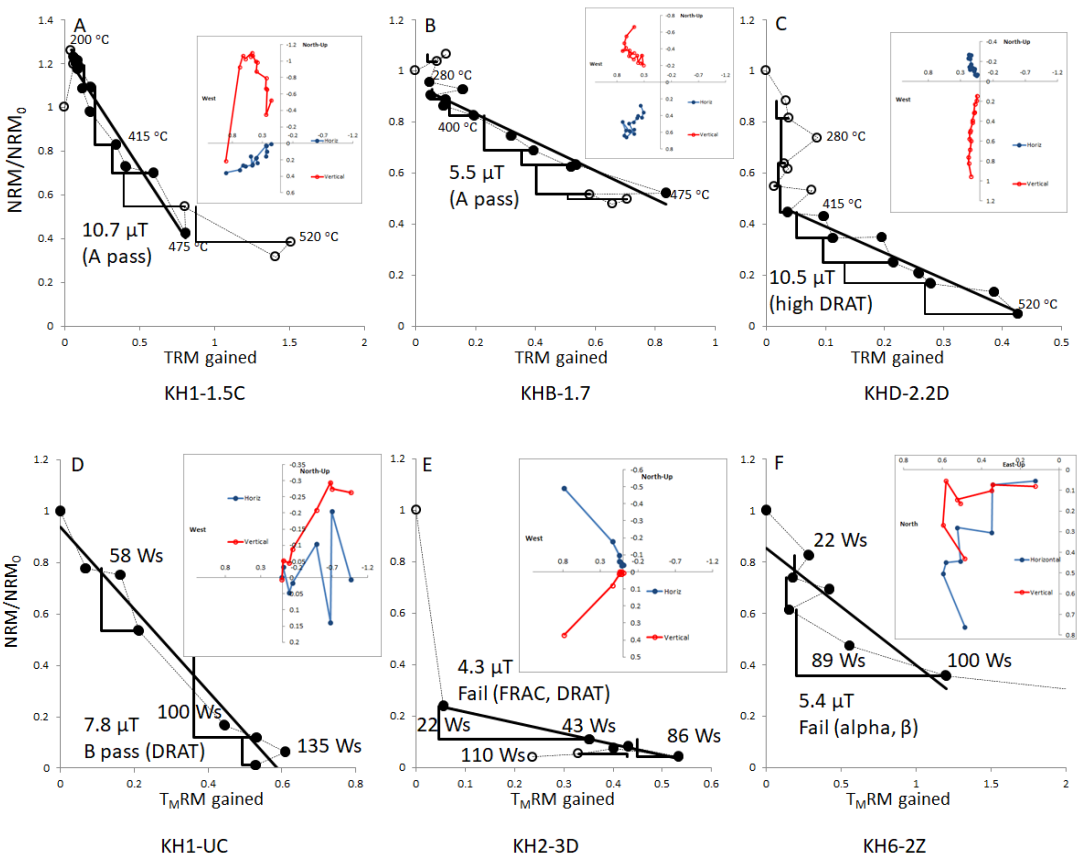

Figure 8-8 LTD-IZZI+ Arai plot data. Top: thermal examples; bottom: microwave examples.

8.7 Synthesis

Experiments were run on sister specimens (and three new sites) and on the same equipment as those in Hawkins (2018), who reported Th-AF-IZZI+ and MW-IZZI+ results. Both datasets showed two-slope behavior and zigzag in their Arai plots. Since the techniques and baseline results are comparable, the new site-level data can be compared directly with their results.

The overall mean PI estimates (across all re-tested and new sites) are 9.5 µT and 8.2 µT, which are not substantially different from the estimate of 7.4 µT previously found in Hawkins (2018). To combine the two datasets for the purpose of this study, the raw data from Hawkins (2018) were reanalyzed using this chapter's A and B quality selection criteria. Statistics regarding the pass rates resulting from this dataset compilation can be found in Table 8-5. A summary of Arai Plot fits by site can be found in Supplementary Information B.

Table 8-5 Experiments and pass rate broken down by method for the combined dataset (this study and Hawkins, 2018).

Method	A passes	Pass rate	A + B passes	Pass rate	N total
Th-IZZI+	8	7.6%	21	20%	105
Th-AF-IZZI+	7	10%	12	18%	67
Th-LTD-IZZI+	3	6.3%	5	10%	48
MW-IZZI+	50	44%	67	59%	113
MW-LTD-IZZI+	0	0%	2	12%	17
Total	68	19%	107	31%	350

Table 8-6 Mean PI estimate by site and technique

Site	Th-IZZI+		Th-AF-IZZI+		Th-LTD-IZZI+		MW-IZZI+		MW-LTD-IZZI+		Mean	
	A	B	A	B	A	B	A	B	A	B	A	B
1	4.7	4.7		6.4	11	11	6.2	6.2		7.4	6.3	6.2
2		7.8					5.9	6.0			5.9	6.1
6		6.0					9.8	9.9			9.8	9.0
A	2.3	2.3					3.2	3.6	-	-	2.7	3.1
B	7.0	4.9	13	13	5.5	5.5	5.6	5.9	-	-	6.7	6.3
C*							6.8	6.0	-	-	6.8	6.0
D*		9.7	14	14		11	17	17	-	-	17	15
E*	2.5	2.5					3.0	2.9	-	-	2.8	2.8
4		6.4	4.7	4.7	10	10	5.7	5.7	-	-	5.9	5.9
7		14	8.5	6.5			12	12	-	-	11	10
8	6.7	4.9		4.1		2.4	9.9	8.3	-	-	9.5	6.5
10	3.0	3.4					4.7	5.2	-	-	4.3	4.4
Mean	4.4	6.0	10	8.1	8.7	7.8	7.6	7.4		7.4	7.1	6.8

Note: all paleointensity data in this table are given in µT. Blank cells indicate no experiments were successful. Cells with a dash indicate no experiments were run.
* New sites; excluded from Carboniferous data discussion (see Section 8.5)

Table 8-7 Arai plot statistics by method

Method	Pass rate		Scatter (β)		Curvature (|K'|)	
Th-IZZI+	7.6%	20%	0.070	0.070	0.235	0.234
Th-AF-IZZI+	10%	18%	0.084	0.088	0.247	0.283
Th-LTD-IZZI+	6.3%	10%	0.063	0.076	0.356	0.322
MW-IZZI+	44%	59%	0.055	0.055	0.197	0.196
MW-LTD-IZZI+	0%	12%	n/a	0.073	n/a	0.042

Note. The first column derives from A quality data; the second column derives from B quality data

8.7.1 Th-IZZI+

The Th-IZZI+ data give some of the lowest PI estimates for both the A and B quality datasets. Further, this is the only technique where the B dataset gives a higher estimate than the A dataset. Recent research on young basaltic glass, such as Cromwell et al. (2018)'s study,

has shown that high-quality and reliable estimates can be extracted using strict selection criteria, but overly strict selection criteria have the possibility of over-rejecting otherwise accurate data (e.g. Paterson et al., 2015). However, with only moderately strict selection criteria and an A-quality pass rate below 10%, the quality of these estimates can reasonably be questioned, which leads to the need for the modified methods to increase the reliability of these estimates.

8.7.2 Th-AF-IZZI+

The pass rate for A and B quality data changed by +2.8% and -2%, respectively. For the specimens that passed the A quality selection criteria, the mean |K'| remained virtually unchanged at 0.23, and the mean β increased from 0.071 to 0.084, with the addition of the AF cleanse. For those that passed at least the B selection criteria, the mean |K'| increased substantially from 0.25 to 0.45, and the average β increased from 0.070 to 0.085.

8.7.3 Th-LTD-IZZI+

The pass rate for A and B quality data decreased by 1.3% and 10%, respectively. For the specimens that met the A quality selection criteria, the mean |K'| increased substantially from 0.23 to 0.36, but the mean β decreased from 0.071 to 0.063, with the addition of the LTD steps. For those that passed at least the B selection criteria, the mean |K'| increased less substantially, from 0.25 to 0.32, and the average β increased from 0.070 to 0.077.

8.7.4 MW-IZZI+

Using the Tristan microwave system and replacing the thermal steps with microwave steps completely changed the experimental behavior and the resulting data. Most notably, the pass rate substantially increased for both the A and B quality data to 44% and 59%, respectively. For the specimens that met A selection criteria, the mean |K'| decreased from 0.23 to 0.21, and the mean β decreased from 0.071 to 0.056. For those that passed at least the B selection criteria, the mean |K'| decreased from 0.25 to 0.20, and the average β decreased from 0.070 to 0.057. The mean DRAT decreased from 7.7% to 5.7% and from 10.5% to 7.2% for the A and B passes, respectively.

8.7.5 MW-LTD-IZZI+

The low pass rate and difficulty of the experiment limit the data available to just a single site from which two samples passed the B quality selection criteria. These two data points from KH1 can be compared with the B quality MW-IZZI+ data from KH1. The mean |K'| decreased from 0.23 to 0.21, and the mean β decreased from 0.071 to 0.056, with the

addition of the LTD steps, which implies that the Arai Plot data quality is slightly but not substantially improved.

8.8 Discussion

8.8.1 Paleointensities

To determine if the addition of AF or LTD steps improved the data, there are three important metrics used herein: pass rate, Arai plot scatter (β), and curvature (|K'|). A summary of the changes in these metrics for the A quality data is provided in Table 8-7.

For the addition of the AF step, the pass rate increased for the A quality data (7.6% to 10%), but the mean Arai scatter and curvature also increased marginally (0.070 to 0.084 and 0.235 to 0.247, respectively). These results imply that the AF cleanse likely improved the data that were already close to passing the selection criteria sufficiently to allow the specimens to just pass the selection criteria. For the B quality data, the pass rate decreased, and the mean Arai plot scatter and curvature increased. From this result, the AF cleanse cannot correct for cases where non-ideal grain effects dominate. This finding is largely in agreement with Biggin et al. (2007), who also found that while the AF steps can provide some smoothing to the Arai Plot data, it is not a cure-all.

In contrast with the addition of the AF step, the addition of the LTD step caused an overall decrease in both the A and the B quality pass rates (7.6% to 6.7% and 20% to 11%, respectively). On the surface, the lower pass rate would seem to imply that the addition of the LTD step has been a failure; however, the extra rejections might be the result of poor-quality, highly non-SD results being removed. For the A-quality LTD data, the Arai plot scatter decreased marginally (0.070 to 0.063) but the curvature increased substantially (0.235 to 0.356). For the B-quality data, both the curvature and the scatter increased (0.234 to 0.322 and (0.070 to 0.076). The lower quality of Arai plots, coupled with the decreased pass rates, means that the addition of the LTD step did not improve the data quality. However, the resulting paleointensity estimates are more in-line with the (higher quality) microwave data, which implies that the estimates themselves are better (just sparser).

Although Smirnov et al. (2017) showed that LTD steps can substantially improve data in sufficiently homogenous rocks, this study has not found that to be the case in the more complex specimens studied herein. The natural specimens studied in this study had M_{rs}/M_s values between 0.1 and 0.3. These hysteresis parameter values corresponded to mean grain sizes $< \sim 5$ µm in Smirnov et al. (2017). The quantity of titanium impurity in, and at least a partial quantification of the grain size distribution of the magnetite in, the tested Kinghorn

specimens constitute the remaining factors of interest that were not addressed in this study. These can, in subsequent research, be determined from Scanning Electron Microscopy. In the immediate term, however, the data herein can be compared with the 'MIX' series data from Smirnov et al. (2017), which showed a ~6-7% increase in PI estimates from the addition of the LTD corrective steps, which is drastically different from the result in Table 8-6, which found changes ranging from a 63% decrease to a 128% increase. Given the substantial increase in experimental time, this study has found that the addition of the LTD step is not necessary if the specimens' rock magnetic data cannot be shown to be close to the well-behaved examples in Smirnov et al. (2017).

The MW-IZZI+ data exhibit the highest pass rates and the lowest Arai plot scatter and curvature for both A-quality and B-quality data. The mean A and B quality MW-IZZI+ paleointensity estimates, 7.6 µT and 7.4 µT, respectively) do not differ significantly from the mean A and B quality Thermal paleointensity estimates of 7.3 µT and 6.9 µT, respectively ($p = 0.73$ and 0.42, respectively). It is also worth noting that the MW-IZZI+ mean paleointensity estimates are slightly higher than the thermal estimates, which further implies the MW-IZZI+ data are less affected by any concave-up Arai plot component (high vs low temperatures/power integrals) selection bias. Santos and Tauxe (2019) recently showed that for basalts containing non-SD grains, a cooling rate effect can still be of concern. However, given that the microwave data has a substantially faster cooling time than the thermal data (< 1 min, compared to 1 hour), the lack of significant difference between the microwave and thermal data means a cooling rate correction is likely unnecessary. Any cooling rate correction would only lower the already low PIs reported in Hawkins (2018) and herein even further.

The MW-IZZI+ data here are higher than the Th-IZZI+ data, which is the opposite of what was observed in Chapter 6 and Chapter 7. The most immediate explanation is that the high-temperature Arai plot components were used in this chapter (instead of the low-temperature components used in the previous chapter). The low-temperature components could not have been used, since they gave a non-convergent direction and were too poor quality to pass any selection criteria. This behavior of overestimates from low-temperature Arai plot components and underestimates from high-temperature components is broadly characteristic of the presence of non-single domain effects in the Arai plot data.

Given that every technique used gave consistently low PI estimates (overall mean A quality: 7.1 µT/ B quality: 6.8 µT), it can therefore be concluded that these low Carboniferous paleointensity values were (Hawkins, 2018), and continue to be, reliable.

8.8.2 Implications for the evolution of Earth's geodynamo

The Carboniferous and Devonian time periods sit in the middle of the second most recent 200 Myr cycle of paleomagnetic field behavior, which is likely linked to mantle dynamics. The positioning of these time periods means this time period is expected to show reversal activity and to have lower field strengths. When the full Kinghorn dataset (these new data and those from Hawkins, 2018) is combined with the recent low results from Shcherbakova et al. (2017) and Hawkins et al. (2019), a clear dipole low is established during the inter-superchron period. The low dipole moment indicates substantial changes in the geodynamo during this time period and further predicts high and heterogeneous heat flux at the Core-Mantle Boundary (Hounslow et al., 2018; Olson and Amit, 2015).

8.9 Conclusions

In this chapter, different variants of a standard Thermal-IZZI experiment were tested to determine the viability of removing non-SD behavior by introducing changes to the experimental procedures. The addition of a 5 mT AF cleanse, the addition of a low temperature demagnetization step, and the replacement of thermal energy with microwave energy were tested. The addition of a cyclic liquid nitrogen demagnetization step was found to not substantially improve any of the data. Adding a low (5 mT) alternating field step can improve the pass rate for the best data without necessarily requiring any substantial changes to the experimental setup. Finally, using microwave energy in place of thermal energy gave the best overall improvement to the data but requires very specialized equipment and is therefore of less general use at this time.

The amount of paleointensity data available for nine Kinghorn sites increased substantially and three new sites were added to the total dataset. An overall mean paleointensity of 7.1 µT for the best (A) quality data, compared to 6.8 µT for the B quality data (V(A)DM: 16 – 17 ZAm^2), was found. These paleointensity estimates are not substantially different from those previously reported during this time period in Scotland. The persistently low paleointensity estimates demonstrate the presence of a dipole low during the Carboniferous time period, which in turn correlates with a substantial change in the Earth's paleomagnetic field behavior likely linked to variable mantle forcing of the geodynamo.

8.10 References

Amit, H., and Olson, P., 2015, Lower mantle superplume growth excites geomagnetic reversals: Earth and Planetary Science Letters, v. 414, p. 68-76.

Biedermann, A. R., Bilardella, D., Jackson, M., Tauxe, L., and Feinberg, J. M., 2019, Grain-size-dependent remanence anisotropy and its implications for paleodirections and paleointensities - Proposing a new approach to anisotropy corrections: Earth and Planetary Science Letters, v. 512, p. 111-123.

Biggin, A. J., Perrin, M., and Shaw, J., 2007, A comparison of a quasi-perpendicular method of absolute palaeointensity determination with other thermal and microwave techniques: Earth and Planetary Science Letters, v. 257, no. 3-4, p. 564-581.

Biggin, A. J., Steinberger, B., Aubert, J., Suttie, N., Holme, R., Torsvik, T. H., van der Meer, D. G., and van Hinsbergen, D. J. J., 2012, Possible links between long-term geomagnetic variations and whole-mantle convection processes: Nature Geoscience, v. 5, no. 8, p. 526-533.

Biggin, A. J., Strik, G., and Langereis, C. G., 2009, The intensity of the geomagnetic field in the late-Archaean: new measurements and an analysis of the updated IAGA palaeointensity database: Earth Planets and Space, v. 61, no. 1, p. 9-22.

Biggin, A. J., and Thomas, D. N., 2003, Analysis of long-term variations in the geomagnetic poloidal field intensity and evaluation of their relationship with global geodynamics: Geophysical Journal International, v. 152, no. 2, p. 392-415.

Bono, R. K., Tarduno, J. A., Nimmo, F., and Cottrell, R. D., 2019, Young inner core inferred from Ediacaran ultra-low geomagnetic field intensity: Nature Geoscience, v. 12, no. 2, p. 143-147.

Cromwell, G., Trusdell, F., Tauxe, L., Staudigel, H., and Ron, H., 2018, Holocene Paleointensity of the Island of Hawai'i From Glassy Volcanics: Geochemistry, Geophysics, Geosystems, p. 3224-3245.

Dunlop, D. J., Zhang, B. X., and Ozdemir, O., 2005, Linear and nonlinear Thellier paleointensity behavior of natural minerals: Journal of Geophysical Research-Solid Earth, v. 110, no. B1.

Fitch, F. J., Miller, J. A., and Williams, S. C., 1970, Isotopic ages of British Carboniferous rocks, Compte Rendu 6e Congrès International de Stratigraphie et de Géologie du Carbonifère, Volume 2: Sheffield, UK, p. 771-790.

Geikie, A., 1900, The Geology of Central and Western Fife and Kinross, Memoirs of the Geological Survey of Great Britain (Scotland), 248 p.:

Hawkins, L., 2018, A Mid-Paleozoic Dipole Low defined from new paleointensity estimates from Russia and the UK [Doctor in Philosophy: University of Liverpool.

Hawkins, L. M. A., Anwar, T., Shcherbakova, V. V., Biggin, A. J., Kravchinsky, V. A., Shatsillo, A. V., and Pavlov, V. E., 2019, An exceptionally weak Devonian geomagnetic field recorded by the Viluy Traps, Siberia: Earth and Planetary Science Letters, v. 506, p. 134-145.

Hill, M. J., Pan, Y. X., and Davies, C. J., 2008, An assessment of the reliability of palaeointensity results obtained from the Cretaceous aged Suhongtu section, Inner Mongolia, China: Physics of the Earth and Planetary Interiors, v. 169, no. 1-4, p. 76-88.

Hodgson, E., Grappone, J. M., Biggin, A. J., Hill, M. J., and Dekkers, M. J., 2018, Thermoremanent Behavior in Synthetic Samples Containing Natural Oxyexsolved Titanomagnetite: Geochemistry Geophysics Geosystems, v. 19, no. 6, p. 1751-1766.

Hounslow, M. W., Domeier, M., and Biggin, A. J., 2018, Subduction flux modulates the geomagnetic polarity reversal rate: Tectonophysics, v. 742, p. 34-49.

Irving, E., and Parry, L. G., 1963, The magnetism of some permian rocks from new-south-wales: Geophysical Journal of the Royal Astronomical Society, v. 7, no. 4, p. 395-411.

Kirschvink, J. L., Kopp, R. E., Raub, T. D., Baumgartner, C. T., and Holt, J. W., 2008, Rapid, precise, and high-sensitivity acquisition of paleomagnetic and rock-magnetic data: Development of a low-noise automatic sample changing system for superconducting rock magnetometers: Geochemistry Geophysics Geosystems, v. 9.

Levi, S., 1977, Effect of magnetite particle-size on paleointensity determinations of geomagnetic-field: Physics of the Earth and Planetary Interiors, v. 13, no. 4, p. 245-259.

Monaghan, A. A., and Browne, M. A. E., 2010, Nine 40Ar/39Ar dates from Carboniferous igneous rocks of the Midland Valley of Scotland: British Geological Survey Open Report, v. OR/10/065, p. 46pp.

Nagata, T., Momose, K., and Arai, Y., 1963, Secular variation of geomagnetic total force during last 5000 years: Journal of Geophysical Research, v. 68, no. 18, p. 5277-5281.

Olson, P., and Amit, H., 2015, Mantle superplumes induce geomagnetic superchrons: Frontiers in Earth Science, v. 3.

Olson, P., Deguen, R., Hinnov, L. A., and Zhong, S. J., 2013, Controls on geomagnetic reversals and core evolution by mantle convection in the Phanerozoic: Physics of the Earth and Planetary Interiors, v. 214, p. 87-103.

Paterson, G. A., Biggin, A. J., Hodgson, E., and Hill, M. J., 2015, Thellier-type paleointensity data from multidomain specimens: Physics of the Earth and Planetary Interiors, v. 245, p. 117-133.

Roberts, A. P., Hu, P. X., Harrison, R. J., Heslop, D., Muxworthy, A. R., Oda, H., Sato, T., Tauxe, L., and Zhao, X., 2019, Domain State Diagnosis in Rock Magnetism: Evaluation of Potential Alternatives to the Day Diagram: Journal of Geophysical Research-Solid Earth, v. 124, no. 6, p. 5286-5314.

Santos, C. N., and Tauxe, L., 2019, Investigating the Accuracy, Precision, and Cooling Rate Dependence of Laboratory-Acquired Thermal Remanences During Paleointensity Experiments: Geochemistry, Geophysics, Geosystems, v. 20, no. 1, p. 383-397.

Shaar, R., Ron, N., Tauxe, L., Kessel, R., and Agnon, A., 2011, Paleomagnetic field intensity derived from non-SD: Testing the Thellier IZZI technique on MD slag and a new bootstrap procedure: Earth and Planetary Science Letters, v. 310, no. 3-4, p. 213-224.

Shcherbakova, V. V., Biggin, A. J., Veselovskiy, R. V., Shatsillo, A. V., Hawkins, L. M. A., Shcherbakov, V. P., and Zhidkov, G. V., 2017, Was the Devonian geomagnetic field dipolar or multipolar? Palaeointensity studies of Devonian igneous rocks from the Minusa Basin (Siberia) and the Kola Peninsula dykes, Russia: Geophysical Journal International, v. 209, no. 2, p. 1265-1286.

Smirnov, A. V., Kulakov, E. V., Foucher, M. S., and Bristol, K. E., 2017, Intrinsic paleointensity bias and the long-term history of the geodynamo: Science Advances, v. 3, no. 2, e1602306.

Suttie, N., Shaw, J., and Hill, M. J., 2010, Direct demonstration of microwave demagnetization of a whole rock sample with minimal heating: Earth and Planetary Science Letters, v. 292, no. 3-4, p. 357-362.

Torsvik, T. H., Lyse, O., Atteras, G., and Bluck, B. J., 1989, Paleozoic paleomagnetic results from scotland and their bearing on the british apparent polar wander path: Physics of the Earth and Planetary Interiors, v. 55, no. 1-2, p. 93-105.

Verwey, E. J. W., 1939, Electronic conduction of magnetite (Fe3O4) and its transition point at low temperatures: Nature, v. 144, p. 327-328.

Yu, Y. J., Tauxe, L., and Genevey, A., 2004, Toward an optimal geomagnetic field intensity determination technique: Geochemistry Geophysics Geosystems, v. 5, Q02H07.

CHAPTER 9 INVESTIGATING THE UTILITY OF A HIGH TEMPERATURE THELLIER EXPERIMENT

Foreword

This chapter follows up on the work done in Hodgson, Grappone et al. (2018). This chapter was completed in parallel with Chapters 6 – 8, as the rocks used in this chapter are their sister specimens, but stands alone.

This chapter has been written up in the style of a paper for consistency with the methodology work in Chapters 6 – 8. The HiTeCT method herein is thus far, at best, inconclusive; however, the less extreme version, with a lower initial temperature, is worth investigating further.

As it stands, the data are not yet publishable but are nonetheless important in their current state as the documentation of a negative result.

9.1 Abstract

High quality data are vital to the research field of paleointensity, which has long suffered from poor quality and/or sparse data. Recent work has shown that repeatedly heating specimens in paleointensity experiments can exaggerate the effects of non-ideal, non-single domain grains. Arai plots resulting from paleointensity experiments containing such grains are often curvilinear (two-slope) across most of the specimen's unblocking temperature spectrum, except in the temperature range nearest to the specimen's Curie Temperature. Two possible remedies exist: fewer treatments or a smaller temperature range. This chapter focuses primarily on the latter.

The paleointensity protocol proposed herein utilizes an initial step with a large (on the order of hundreds of °C; e.g. 500 °C) temperature increase, followed by closely-spaced steps with small (e.g. 3 °C) temperature increments. Specimens with well-constrained rock magnetic data from the 1960 Kilauea lava flow, Scientific Observation Hole 1 (SOH1), and Kinghorn lava flows were selected for this study to capture a range of ages, magnetic mineralogy, and unblocking spectra. The experiments that focused in on the portion of the unblocking temperature spectrum near the Curie Temperature of the specimen (HiTeCT) had an exceptionally low success rate, and thus focusing in on the highest temperature range is not feasible for real rocks. Experiments with a more moderate initial temperature, however, deserve further study.

9.2 Motivation

Every paleointensity chapter of this thesis so far has been concerned with understanding the differences caused by different paleointensity methods. A paleointensity method consists of a demagnetization mechanism (thermal vs microwave) and a paleointensity protocol (OT+ vs IZZI+ vs Perp vs Perp++). Previously, inconsistent results have been reported between each of these (e.g. Biggin, 2010; Böhnel et al., 2011; Coe et al., 2004; Donadini et al., 2007; Hill and Shaw, 2000; and Paterson et al., 2014 and 2015). In this chapter, rather than trying to parse which method gives the most accurate or most precise results, a new method is attempted, which is based on the Coe (1967) paleointensity method.

Over fifty years ago, just a single step was used to replace the specimen's magnetic field with a field of known strength. Then the method was expanded to include multiple steps and a best-fit line for a more precise estimate (Thellier and Thellier, 1959). Next, checks for thermochemical alteration (pTRM checks) were added because alteration can cause a sharp change in the slope of the Arai plot data, but not always (e.g. Coe, 1967). Thereafter, checks for non-Single Domain behavior (pTRM tail checks) were added because non-SD behavior can cause sagging (concave up) Arai plots (Riisager and Riisager, 2001). The addition of each of these steps increases the required amount of time to complete but aimed to improve the fidelity of the data.

Hodgson et al. (2018) showed that repeatedly heating a specimen containing interacting single domain (SD) or multi-domain (MD) grains can cause increased deviation from ideal SD behavior, which in turn causes an Arai plot to become curvilinear over the course of a paleointensity experiment, a point previously predicted in Biggin and Bohnel (2003) for MD grains. Hodgson et al. (2018) used the Coe (1967) variant of the Thellier protocol, which gives downward sloping, concave up Arai plots when non-SD effects are strong. The result can be a paleointensity overestimate if the low temperature portion of an Arai plot (Nagata et al., 1963) is used (Coe et al., 2004; Dunlop and Ozdemir, 2001; Xu and Dunlop, 2004) and an underestimate if the high temperature portion of an Arai plot is used (Biggin and Thomas, 2003; Dunlop et al., 2005).

One of the findings in Hodgson et al. (2018) was that the Arai plot straightens out in the temperature region approximately 20 °C below a given specimen's Curie Temperature. In addition, Hodgson et al. (2018) showed non-SD effects can be reduced by minimizing the number of heatings and restricting the experiment to only temperatures near the Curie temperature (T_C) of the specimens. The specimens in Hodgson et al. (2018) were artificially

created from naturally occurring magnetite and oxyexsolved titanomagnetite. As a result, these specimens had well-defined Curie temperatures, which made doing high temperature paleointensity experiments relatively straightforward. This chapter develops and tests the method proposed by Hodgson et al. (2018) using natural specimens left over (and as yet unused) from the previous studies that are presented in this thesis.

In the purest form of Hodgson et al. (2018)'s method, only temperatures in the range $T \in [T_C - 20, T_C]$ are used, and alteration checks were omitted to minimize the number of heatings. However, the lack of systematic pTRM checks means that alteration is not accounted for during the experiments, which would limit the reliability— as expressed by, for example, the QPI score (Biggin and Paterson, 2014) of these experiments. This technique will be developped further herein by testing the effects of systematic alteration tests on the experimental protocol. The Coe (1967) protocol lacks a check for MD grains, so tail checks can be included to check for their presence (Riisager and Riisager, 2001). In addition to checking for MD behavior, if the TRM capacity of the specimen increases because of alteration that occurred at any temperature (even before the first in-field step), some magnetization will remain after the check, giving a magnetization 'tail'. If the TRM capacity decreases as a result of the alteration, the pTRM tail check will not provide useful information.

This study therefore investigated three types of experiments. First, the experiment as proposed by Hodgson et al. (2018), a Coe (1967) experiment limited to the range $T \in [T_C - 20, T_C]$, was tested. Next, the same type of experiment was tested but with the inclusion of pTRM checks (Prevot et al., 1981), which increases the number of heating cycles but checks for thermochemical alteration. Finally, a third iteration of the same type of experiment was tested but with the addition of both pTRM and tail checks to mitigate both alteration and non-SD behavior. From these tests, reliable paleointensity estimates were expected to be obtained from only the characteristic component of the specimen's magnetic field.

9.3 Sampling

For this study, 81 specimens were used from three localities. A summary of the lava flows supplying the specimens is given in Table 9-1. They were spare samples from the studies presented in Chapters 6, 7, and 8. All the rocks used are drab-colored iron-rich basalts. The ages range extremely non-uniformly from 60 years to 340 million years. All specimens used have had rock magnetic studies completed on them by previous work, and each

specimen's Curie Temperature (range) and hysteresis properties are therefore well-established. Specimens were selected primarily on the basis of their Curie Temperatures so that a range of temperatures could be tested and so that batches of samples could be made for oven heatings. The goal was to test the viability of this technique as a paleointensity method by itself, so the behavior of the specimens in other paleointensity experiments was not taken into account to give a more randomized selection.

The primary source of specimens (63) for this study is the SOH1 drill core from the island of Hawaii (see Chapter 7). None of the samples used were from flows studied and presented in Chapter 7 because of the limited material available for a given flow. The SOH1 drill core covers 240 flows and the flows selected were ones with sufficiently similar Curie Temperatures to allow batch sizes of at least 8 specimens. Flows with Curie Temperatures above 500 °C were favored, on the basis that Ti-poor titanomagnetite grains are expected to behave the most similarly to those in Hodgson et al. (2018) in these experiments.

In addition, 12 specimens were used from Kinghorn sites KH4 and KH10, which have been studied at length and are described in Chapter 8. Samples from KH10 had the lowest Curie Temperatures (around 370 °C) and samples from KH4 had the highest (around 570 °C). Finally, 6 specimens from the 1960 Hawaiian Kilauea lava flow, studied in Chapter 6, were selected. The 1960 lava flow's characteristics have been extremely well documented (see Chapter 6 for more details), but they have a broader range of Curie Temperatures than many of the SOH1 cores.

9.4 Rock magnetism

Hodgson et al. (2018) worked with artificial samples made from naturally occurring magnetite of known magnetic grain size. In order to eventually compare these new results with theirs, the rock magnetic properties of the natural samples need to be well-defined. Specifically, the Curie Temperature, the demagnetization curve shape, and the hysteresis parameters are required. The Curie temperature provides the basis for calculating the temperature range for the experiment. The demagnetization curve provides information on the unblocking temperature spectrum. The hysteresis parameters provide a proxy for magnetic domain states contained in the samples. A summary of the magnetic properties of the samples studied is provided in Table 9-1. Example demagnetization curves can be found in Figure 9-1. The two predominant types of thermoremanent curves observed are in Figure 9-1A and B (17/21 flows). Thermoremanent curves of the types observed in Figure 9-1 A and

Figure 9-1B are typical for specimens that have a narrow and a broad range of grain unblocking temperatures, respectively. The thermoremanent curve observed in Figure 9-1C is of particular note because the specimen becomes more magnetic and has a higher temperature on cooling, which implies that the alteration created a more Fe-rich magnetite end-member. For specimens containing a distinct second and lower Curie temperature magnetic phase, thermoremanent curves of the type presented in Figure 9-1D were observed. At the high temperatures used for these experiments, lower temperature phases are removed during the initial heating step and therefore of little importance. However, the substantial thermochemical alteration in Figure 9-1D (and to a lesser extent in C) would be sufficient grounds to reject the specimen a traditional paleointensity experiment. That rejection would likely apply here as well, but, given the apparent reversibility near the Curie temperature (but with relatively low magnetizations), the low temperature phase may be irrelevant.

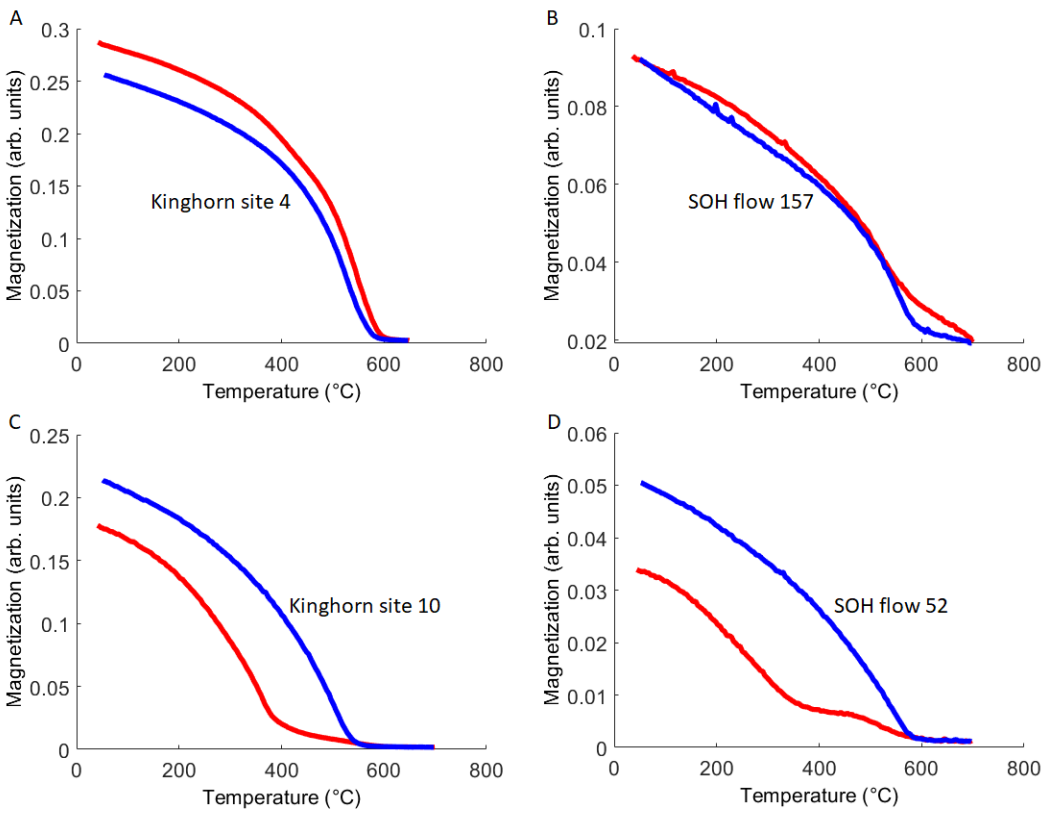

Figure 9-1 Example demagnetization curves characteristic of the flows studied herein. A and B are the most common types. A shows a single magnetic phase with a more narrow unblocking temperature range. B shows an example of a broad unblocking temperature range. C and D show examples of sites with more than one distinct magnetic phases.

Table 9-1 Rock magnetic parameters for samples tested herein

Sample	Curie Temp (°C)	$\frac{Mrs}{Ms}$	$\frac{Hcr}{Hc}$	Experiment Range (°C)	Curve type	Source
SOH flow 42	580	0.16	3.98	560-590	B	Gratton et al. (2005)
SOH flow 43	580	0.12	5.73	560-590	A	Gratton et al. (2005)
SOH flow 52	510	0.36	1.77	480-510	D	Russell (2018)
SOH flow 120	515	0.17	2.77	498-528	A	Russell (2018)
SOH flow 123	510	0.15	5.34	480-510	C	Russell (2018)
SOH flow 126	500	0.13	5.9	480-510	A	Russell (2018)
SOH flow 147	510	0.18	2.82	490-520	B	Russell (2018)
SOH flow 148	520	0.37	1.82	490-520	B	Gratton et al. (2005)
SOH flow 150	530	0.19	3.99	490-520	A	Gratton et al. (2005)
SOH flow 152	570	0.47	1.46	558-578	A	Russell (2018)
SOH flow 157	550	0.28	2.27	530-554	B	Russell (2018)
SOH flow 225	580	0.11	8.17	560-590	A	Gratton et al. (2005)
SOH flow 226	580	0.12	5.82	560-590	A	Gratton et al. (2005)
SOH flow 232	520	0.17	3.3	490-520	D	Gratton et al. (2005)
Kinghorn Site 4	570	0.28	1.9	550 - 580	A	Hawkins (2018)
Kinghorn Site 10	370	0.18	2.9	350 - 380	C	Hawkins (2018)
1960 (1-9,15,16)	510	0.37	1.47	490 - 520	B	Hill et al. (2000)
1960 (1-4)	523	0.37	1.91	500 - 530	B	Hill et al. (2000)
1960 (2-4,5)	520	0.39	1.39	500 - 530	B	Hill et al. (2000)
LM6 <5*	569	0.18	2.13	n/a	A	Hodgson et al. (2018)
LM6 25 - 30*	567	0.076	3.44	n/a	A	Hodgson et al. (2018)

9.5 Methods

The Thellier experiments reported herein are a modified version of the Coe (1967) protocol, which has historically been one of the most used Thellier protocols and was the protocol used in (Hodgson et al., 2018). In this variant, each temperature step is first run in a zero-field (Z-step), followed by an in-field step (I-step). As the purpose of this study is to further develop this method, this chapter will present the development of the method and explain how some pitfalls were overcome. Due to the requisite temperature precision of the technique, individual initial Curie temperature measurements for each specimen were necessary.

During the second year of my PhD, I supervised a final-year undergraduate student named James Russell. The first set of experiments were run using SOH1 specimens (Gratton et al., 2005; Teanby et al., 2002) and completed as part of his bachelor's thesis project at the University of Liverpool. His paleointensity and supporting rock magnetic experiments are detailed extensively in his bachelor thesis (Russell, 2018). The high temperature Thellier-Coe experiments began at an initial temperature 20 °C below the specimen's Curie Temperature. Steps of 3 °C were then used to approach (and pass) the specimen's Curie Temperature with as many data points as possible. These initial experiments had only two partial thermal remanent magnetization (pTRM) checks (P-step), which is a repeated lower temperature in-field step to check for alteration, as suggested by Hodgson et al. (2018) to minimize the number of heatings. Instead, the susceptibility of each specimen was measured after each heating step using an AGICO MFK1-FA Kappabridge. Russell (2018) failed to find any meaningful alteration information from the bulk susceptibility data, so these data are not detailed herein. For these first tests, this chapter additionally presents parallel results, which were performed as a part of this study, from specimens from the same flows that underwent two less radical experiments. The first experiment, which is a true control experiment, was a full Thellier-Coe experiment that began at an initial temperature of 200 °C in a field of 40 μT and used temperature steps of 20-50°C. Next, a second experiment was run to try to bridge the gap between the full Thellier-Coe experiment and the Hodgson et al. (2018) method. The 'abridged' Thellier-Coe experiments began at an elevated temperature, with an initial temperature of 100 °C below the specimen's Curie Temperature, which is approximately 250 °C higher than that of the full experiment. An applied field of 40 μT and temperature steps of 20°C were used, which are typical values for paleointensity experiments. For all experiments herein, laboratory fields were applied in the same direction in specimen coordinates: inclination = 90 °. Some SOH1 samples may have overprints up to 300 °C (see

Chapter 7), which will be completely bypassed using the Hodgson et al. (2018) method and the abridged Thellier-Coe experiment.

The next set of experiments also used SOH1 specimens. These high temperature experiments used pTRM checks after every other Z step, for the pattern of ZIZPI in steps of 3 °C. The experiments ran from T_C – 20 °C to T_C + 10 °C, outside of the range proposed by Hodgson et al. (2018) to ensure complete demagnetization in the event of any thermochemical alteration. The addition of pTRM checks mitigates the effects of alteration during the experiment but cannot rule out the possibility of alteration occurring during the first (large) temperature step. All the specimens in this section were selected because thermoremanent curves determined their Curie Temperatures to be 580 °C.

The final set of experiments adds tail checks (a repeated lower temperature Z step; referred to as a T-step) to the experimental protocol, giving a final pattern of ZITZPI in steps of 3 °C. The experiments ran from T_C – 20 °C to T_C + 10 °C. The addition of the tail checks mitigates the risk of chemical remanent magnetizations affecting the final result. Tail checks are also used in Thellier-Coe experiments to detect potential non-SD grain effects, but this application should be minimal to these experiments because, according to Hodgson et al. (2018), there should be no non-SD grain effects in the temperature ranges tested. These tests were run using SOH1 specimens, Kinghorn specimens (Hawkins, 2018), and 1960 Kilauea lava flow specimens (Hill and Shaw, 2000).

The set of experiments that focus on only the highest temperatures are collectively called the T_C – 20 experiments. The experiments without pTRM checks are referred to as "HiTeCT" (pronounced like high-tech) for "high temperature Coe-Thellier". Following the naming scheme of the Absolute Palaeointensity (PINT) Database (Biggin et al., 2009), the addition of pTRM checks creates HiTeCT+, and the further addition of tail checks creates HiTeCT++. A summary of the types of experiments can be found in Table 9-2.

Table 9-2 Summary of experiments run in this chapter

Experiment	Temperatures (°C)	Pattern
Full Coe-Thellier	$T \in [200, Tc]$	ZI
Abridged Coe-Thellier	$T \in [T_C - 100, Tc]$	ZIZPI
HiTeCT	$T \in [Tc - 20, Tc + 10]$	ZI
HiTeCT+	$T \in [Tc - 20, Tc + 10]$	ZIZPI
HiTeCT++	$T \in [Tc - 20, Tc + 10]$	ZITZPI

Note: T_C is the specimen's Curie Temperature. Z are zero-field steps. I are in-field steps. P are pTRM checks (repeated I step). T are tail checks (repeated Z step).

The selection criteria used for this chapter are outlined in Table 6-1. The standard set of selection criteria are based on 'SELCRIT-2 (modified)' from Paterson et al. (2015), and the loose set are based on the selection criteria successfully used in Bono et al. (2019), which also formed the basis of the loose selection criteria used in the study of the 1960 Kilauea lava flow presented in Chapter 6.

Table 9-3 Selection criteria

Type	N	F	R^2	β	q	MAD_{ANC}	α	DRAT*	pTRM* error
Loose	≥ 4	--	≥ 0.9	--	--	≤ 10	--	--	<10%
Standard	≥ 4	≥ 0.3	--	≤ 0.1	≥ 4	≤ 10	≤ 10	≤ 10%	--

Note. N is the number of data points on the Arai plot. F is the fraction of NRM used. R is the linear regression coefficient. β is a measure of the Arai plot data scatter. Q is the quality factor. MAD_{ANC} and α are measures of how well a specimen's direction is demagnetizing to the origin. DRAT and pTRM error check for alteration by comparing the error to the length of the best-fit line and to the origin NRM, respectively.
*Only applicable for experiments that include pTRM checks

9.6 Results

9.6.1 Initial experiments

Very different success rates were found for each experiment. The full, typical Coe experiment had a success rate of 8/16 (50%), whereas the abridged experiment had a success rate of 5/9 (56%). None of the specimens from the HiTeCT experiments passed either set of selection criteria. Most of them additionally had atypical backwards sloping behavior, where both TRM and NRM were lost as the temperatures increased past the initial heating steps (see Figure 9-2A and B). Specimens displaying this behavior also had non-convergent orthogonal plots. Not all specimens fully demagnetized by the end of the experiments, as experiments were abandoned when a visible change in slope occurred. A possible cause for the atypical behavior is that the specimens were not sometimes measured until a few days after being heated instead of immediately thereafter and therefore gained spurious viscous magnetizations. The limited data from these experiments does not yet provide sufficient insight into this behavior. If this behavior is present in future results, this behavior can be investigated further.

The results by flow and method are detailed in

Table 9-4. Individual specimens' Arai Plot data can be found in the supplementary information. Included in the table are some estimates from the failed HiTeCT experiments.

These estimates were generated by fitting the NRM point on the Arai plot and the initial temperature step, at a temperature of T_C – 20 °C for each specimen. This estimation method is not statistically rigorous and is given for reference only in

Table 9-4 under the column "High temperature single step". Only those flows which had estimates that passed the standard selection criteria in either the full or abridged test are included.

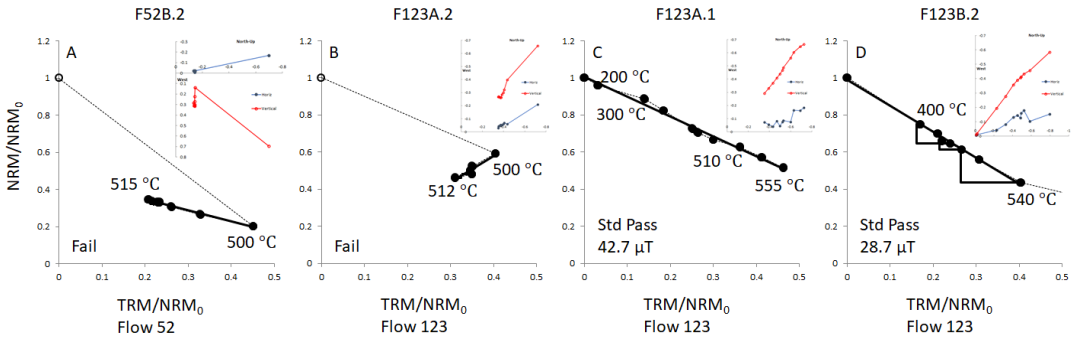

Figure 9-2 Initial experimental results using SOH1 specimens. A and B are the high temperature Thellier experiments and have substantially atypical behavior. C is the full Thellier-Coe experiment, and D is the abridged Thellier-Coe experiment. In this and all subsequent figures containing Arai plots, filled circles are accepted data points, with the solid black line being their best-fit line. Unfilled circles are rejected data points.

Table 9-4 Initial experimental results by method

Flow	Full Th-Coe (µT)	N_{passed} /N_{tested}	Abridged Th-Coe (µT)	N_{passed} /N_{tested}	High temperature single step (µT)*	N_{passed} /N_{tested}
52	–	0/2	–	–	–	0/1
120	56.5	½	–	0/2	49.6	0/2
123	47.1 ± 6.3	2/2	29.1 ± 0.35	3/3	47.3	0/3
126	36 ± 18	2/2	–	–	–	0/1
147	–	0/2	16.6	1/1	–	0/1
152	44.8	½	–	0/2	–	0/2
157	30.6 ± 1.1	2/2	27.1	1/1	27.1	0/1

*** These data are not statistically rigorous and are included for reference only.**

From these results, it is apparent that there is a problem with the HiTeCT experiments because the data do not lose NRM and gain TRM in a manner consistent with Thellier experiments. The Arai plot data have a generally linear trend (even in the wrong direction). A clear change in slope in the abridged Thellier-Coe experiment is correlated with a failed pTRM check; an example of this behavior is provided in Figure 9-2D. The lack of pTRM checks anywhere in the HiTeCT experiments means that it is impossible to know if the changes in slopes result from thermochemical alteration. It therefore follows that the next set of should include regular pTRM checks to improve the experiment rigor, but it will increase the number

of heatings by 25% and therefore likely increase the non-SD effects in the data because the non-SD grains will not return to identical domain states.

9.6.2 Regularly spaced pTRM checks

The next set of experiments, HiTeCT+, uses 12 specimens from the SOH1 drill core that were taken from different flows (because of insufficient remaining material), with higher (and therefore a sharper range of) Curie Temperatures. Measurements were completed immediately after heating steps to mitigate any unexpected effects that may have occurred, as described in the previous section. Using the standard set of selection criteria gives 2 passes (Figure 9-2B and C) for a pass rate of 17%. Using the relaxed set of selection criteria doubles the number of passes, giving a pass rate of 33%.

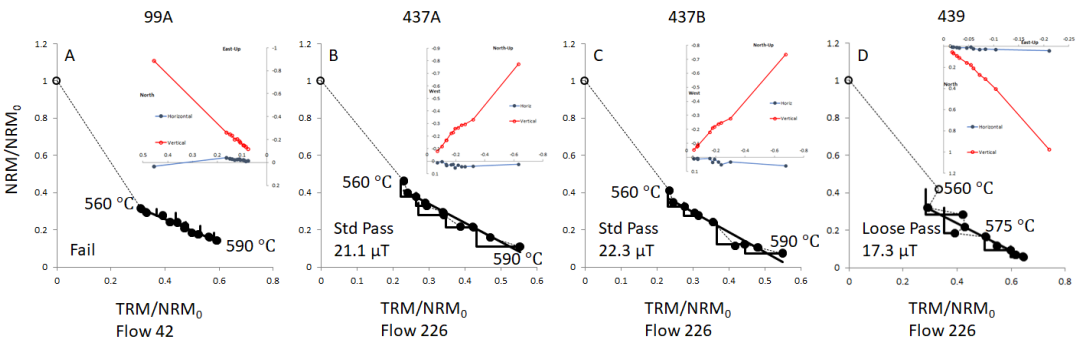

Figure 9-3 Follow-up SOH1 experiments adding pTRM checks for alteration. The temperature step size for all HiTeCT experiments is 3°C.

Table 9-5 Results from high temperature Thellier experiments including pTRM checks

Flow	Standard selection criteria	N_{passed}/N_{tested} (typical)	Loose selection criteria	N_{passed}/N_{tested} (relaxed)	Single step (µT)*
42	–	0/1	–	0/1	29.0
43	–	0/2	21.5	½	37.8 ± 15.6
225	–	0/4	–	0/4	30.8 ± 13.4
226	21.7 ± 0.89	2/5	20.2 ± 2.6	3/5	25.1 ± 9.2

*** These data are not statistically rigorous and are included for reference only.**

Despite the improved rigor of these experiments, the addition of pTRM checks can only detect and mitigate any alteration that occurs after the first temperature step, which for these samples was 560 °C, a temperature by which thermochemical alteration would not be unreasonably expected.

9.6.3 Adding tail checks

The final set of experiments, HiTeCT++, uses 26 specimens from the SOH1 drill core, the Kinghorn lava flows, and the 1960 Kilauea lava flow. These data further improve the reliability of the previous experiments by adding in pTRM tail checks to better capture the

full range of temperatures over which alteration may have occurred. Using the standard set of selection criteria, all specimens are rejected. Using the relaxed set of selection criteria gives three passes, a pass rate of 12%.

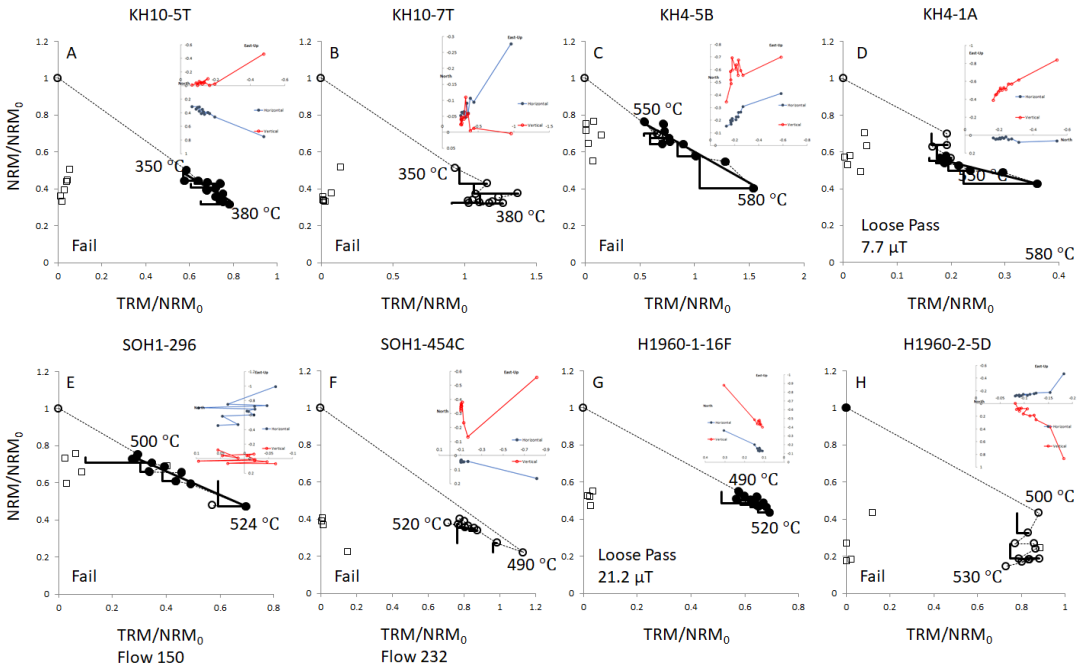

Figure 9-4 Final set of experiments using both pTRM and tail checks for samples from two Kinghorn sites, SOH1 flows, and the 1960 lava flow. The temperature step size for all HiTeCT experiments is 3°C.

Table 9-6 Results from high temperature Thellier experiments including pTRM and tail checks, with three rock sources

Flow	Loose selection criteria	N_{passed}/N_{tested} (relaxed)	Single step (µT)*
$KH4$	7.7	1/5	7.0 ± 5.0
$KH10$	–	0/7	5.8 ± 2.2
1960 ($site$ 1)	21.2	1/4	32.7 ± 4.2
1960 ($site$ 2)	–	0/2	34.7 ± 16
$SOH1 - 147$	–	0/2	27.7 ± 0.85
$SOH1 - 148$	–	0/2	25.1 ± 0.2
$SOH1 - 150$	30.2	1/1	30.2
$SOH1 - 232$	–	0/3	20.2 ± 1.0

*** These data are not statistically rigorous and are included for reference only.**

For this sections data, the decreased pass rate is due to increased Arai Plot scatter, as measured by β or R^2, rather than having failed pTRM tail checks. Adding the pTRM tail checks did not improve the pass rate and does not provide any additional rigor for assessing the quality of the produced data.

9.6.4 Reverse Arai plot behavior

In the Arai plot data in Figure 9-2 and Figure 9-4, it was observed that some tested specimens had abnormal data slope directions. The tail checks in the HiTeCT++ experiments provide a set of data that can be used to investigate this phenomenon. Tails can cause an apparent loss of laboratory-gained pTRM because the tail left after the Z step becomes subtracted from the pTRM added at the next I step. The effect on the apparent NRM remaining would therefore be determined by the direction of the resulting tail. This effect can be seen in Figure 9-4, where the Arai plot data trend appears correlated with the size. By comparing the results (size and sign) of the first tail check with the direction of the data, a distinct pattern emerges (see the supplementary information for the relevant table). Tail checks with magnitudes greater than 8% consistently yielded erroneous slopes, with negative values causing the slopes to trend to the origin and positive values causing the slopes to trend backwards (NRM >> TRM). These results clearly show that an initial tail check can predict if the specimen's data are likely to fail the HiTeCT experiment.

9.7 Discussion

9.7.1 SOH1 drill core

Combining all these new data provided a fuller picture of the viability of the High Temperature Thellier experiment and which protocols might be useful to the greater paleomagnetic community. One primary limiting factor of these experiments is how well-defined a given specimen's Curie temperature is. A specimen with a mixture of magnetic grains has a broader demagnetization spectrum, which in turn means that focusing on a small temperature range is less effective and potentially problematic if the wrong temperature range is selected.

The dataset for the SOH1 drill core is presented in Table 9-7, which also contains the values for the relevant flows as determined by Teanby et al. (2002) and Gratton et al. (2005). No data from Chapter 7 is reported because all of the flows in this chapter are different. The overall pass rate for the SOH1 data using the T_c – 20 (all HiTeCT variants) experiments was 6.5% and 16% for the standard and relaxed criteria, respectively, which is substantially less than the pass rates for the previous studies (see Chapter 7). The pass rates for the regular (50%) and abridged Coe experiments (56%) are comparable to the pass rates observed in Chapter 7 for the SOH1 flow's new Th-OT+ experiments (52%). The sparseness and scatter of the SOH1 data herein are similar to that observed therein for the SOH1, as well.

Table 9-7 SOH1 results from this chapter compared with results from previous work

Flow	Teanby et al. (2002) (μT)	N_{passed} /N_{tested}	Gratton et al. (2005) (μT)	N_{passed} /N_{tested}	$T_C - 20$ (μT) (standard)	N_{passed} /N_{tested}	$T_C - 20$ (μT) (relaxed)	N_{passed} /N_{tested}
42	–	0/1	24.1 ± 0.6	2/3	–	0/1	–	0/1
43	–	0/0	33.7 ± 6.8	2/2	–	0/2	21.5	1/2
52	–	0/1	13.7 ± 1.6	2/3	–	0/1	–	0/1
120	37.5 ± 3.3	2/3	–	0/4	–	0/2	–	0/2
123	19.5	1/2	12.5 ± 1.2	2/2	–	0/3	–	0/3
126	–	0/1	–	0/3	–	0/1	–	0/1
147	–	0/1	11.7 ± 1.7	2/2	–	0/3	–	0/3
148	19.1 ± 1.6	3/3	12.7	1/2	–	0/2	–	0/2
150	22.1 ± 3.8	3/3	17.3 ± 0.1	2/3	–	0/1	30.2	1/1
152	–	0/0	–	0/0	–	0/2	–	0/2
157	27.3 ± 1.4	2/2	12.6 ± 1.3	3/3	–	0/1	–	0/1
225	–	0/2	10.8 ± 6.8	2/3	–	0/4	–	0/4
226	22.2 ± 4.5	2/3	16.3 ± 1.2	3/3	21.7 ± 0.89	2/5	20.2 ± 2.6	3/5
232	–	0/0	13.5 ± 0.2	2/2	–	0/3		0/3

Note. N_{tested} and N_{passed} refer to the number of specimens that were tested and passed selection criteria, respectively.

The only flow that gave passes using the standard set of selection criteria, flow 226, gives an estimate that falls between that of Teanby et al. (2002) and Gratton et al. (2005). The estimate is statistically distinct from that of Gratton et al. (2005) (p = 0.013) but is not statistically distinct from Teanby et al. (2002)'s estimate of 22.2 μT (p = 0.89). This result is largely in agreement with Chapter 7's result that thermal double heating techniques give higher PI estimates than Microwave Perpendicular. The reader is referred to Chapter 7 for any additional insights into the SOH1 drill core.

Looking at the relaxed selection criteria yields three flow-level estimates. The estimate for flow 43, 21.5 μT, is substantially lower than the 33.7 μT estimate from Gratton et al. (2005), which is unusual for the SOH1 drill core. The estimate for flow 150 is substantially higher than both the 22.1 μT estimate from Teanby et al. (2002) and the 17.3 μT estimate from Gratton et al. (2005). For flow 226, the updated estimate of 20.2 μT is not statistically distinct from either Gratton et al. (2005) (p = 0.078) or Teanby et al. (2002) (p = 0.56). These estimates are largely inconsistent with the results from Chapter 7, but not impossible. The relaxed selection criteria do not appear, however, to be a particularly suitable set of selection criteria for the SOH1 drill core's experiments.

The result that the experiments with pTRM tail checks have higher Arai Plot scatter (0.181 without tail checks and 0.294 with tail checks for specimens with N > 6) carries the implication that the addition of the tail checks (which increased the number of heating cycles) may have

caused the Arai Plot data quality to decrease. An increase in scatter from additional heating cycles, which was predicted by Hodgson et al. (2018), is the *raison d'être* of this technique and why minimal pTRM checks were carried out initially.

9.7.2 Kinghorn and 1960 Kilauea lava flow

Results from the additional sites (Kinghorn and 1960 Kilauea) can be found in Table 9-8. None of these experiments passed using the standard selection criteria and only 2 passed the relaxed selection criteria. The most likely reason is the age of, and the generally poor quality of, the thermal Kinghorn data (see Chapter 8 for further discussion) and the more continuous Curie Temperature spectrum of the 1960 Kilauea lava flow samples (see e.g. Hill and Shaw (2000), as Chapter 6 contains no thermal experiments).

Table 9-8 Kinghorn and 1960 Kilauea lava flow results from this chapter compared with results from previous chapters

Flow	Previous chapter*	N_{passed} /N_{tested}	$T_C - 20$ (µT) (standard)	N_{passed} /N_{tested}	$T_C - 20$ (µT) (relaxed)	N_{passed} /N_{tested}	Single step (µT)*
$KH4$	5.9 ± 1.8	$8/21$	$-$	$0/5$	7.7	$1/5$	7.0 ± 5.0
$KH10$	4.3 ± 1.3	$4/30$	$-$	$0/7$	$-$	$0/7$	5.8 ± 2.2
1960 ($site$ 1)	36.8 ± 3.4	$22/41$	$-$	$0/4$	21.2	¼	32.7 ± 4.2
1960 ($site$ 2)	39.1 ± 4.6	$11/18$	$-$	$0/2$	$-$	$0/2$	34.7 ± 16

*In the case of the 1960 Kilauea lava flow, the previous chapter is Chapter 6 (the MW-IZZI+ data are reported here), and in the case of the Kinghorn data, the previous chapter is Chapter 8 (the full, combined A pass dataset is reported here).

There are two studies with which the Kinghorn data are comparable: Hawkins (2018) and Chapter 8. The new data collected in Chapter 8 gave a B-quality pass rate of 18% for KH4 and 23% for KH10 and estimates of 8.2 µT and 3.4 µT, respectively. The KH4 relaxed criteria pass rate is comparable at 20%. The one relaxed criteria pass from KH4 gave a comparable estimate of 7.7 µT. The estimates from the unreliable single step estimation method, 7.0 µT and 5.8 µT, respectively are similar to the other available estimates but imprecise. Having no passes from KH10 was unexpected given Chapter 8's higher pass rate for KH10, compared to KH4. KH10 specimens have the lowest Curie Temperatures in this study (around 370 °C), compared to those of the KH4 and SOH1 specimens (all above 500 °C), which likely affected the data. Hodgson et al. (2018) used specimens with Curie Temperatures near or above 570 °C, so the complete failure of the KH10 specimens indicates this method is inappropriate for specimens containing moderate-Ti titanomagnetite. The most apparent explanation relies on Figure 9-1C, where the thermoremanent curves suggest that, upon cooling from high temperatures, the titanomagnetite in KH10 is decomposing into a more Fe-rich magnetite, and the small temperature steps in this experiment are unable to unblock it properly.

The 1960 Kilauea lava flow results are not directly comparable with the results from Chapter 6 because of the lack of thermal data from that chapter. Instead, these results can be compared with those of Böhnel et al. (2011), which contains an extensive list of paleointensity experiments run on this lava flow. The one sample that passed the relaxed selection criteria gives an estimate of 21.2 µT, which is 43% lower than the expected value of 36.5 µT and is also lower than every other estimate on the list provided in Böhnel et al. (2011). Notably, the unreliable single step estimation method gives substantially more accurate estimates that are similar to those obtained in Hill and Shaw (2000). Site 1 here gives an estimate of 32.7 µT, compared to 31.6 µT, and site 2 here gives an estimate of 34.7 µT, compared to 37.1 µT. The error bars in the single step data are larger, however (substantially so in the case of site 2). The poor result from the 1960 Kilauea lava flow is not unreasonable given that Hill and Shaw (2000) showed that these data generally have the thermoremanent curves with the most linear curve of the specimens investigated herein.

9.7.3 Implications for future experiments

Most of the samples that passed have thermoremanent curves like those in Figure 9-1A, which is consistent with needing a small unblocking temperature range for this type of experiment to work. Figure 9-5 contains a plot of the hysteresis parameters of the various flows investigated in this study. No flows have characteristics entirely consistent with those of SD or MD grains. The flows that have at least one pass using the loose selection criteria are well-distributed over the main sequence of hysteresis parameters. The most apparent takeaway from Figure 9-5 is that these real samples have substantially less MD character than the rocks tested in Hodgson et al. (2018)'s experiments, which provides some evidence that the results in Hodgson et al. (2018) may not be broadly generalizable for natural basalts.

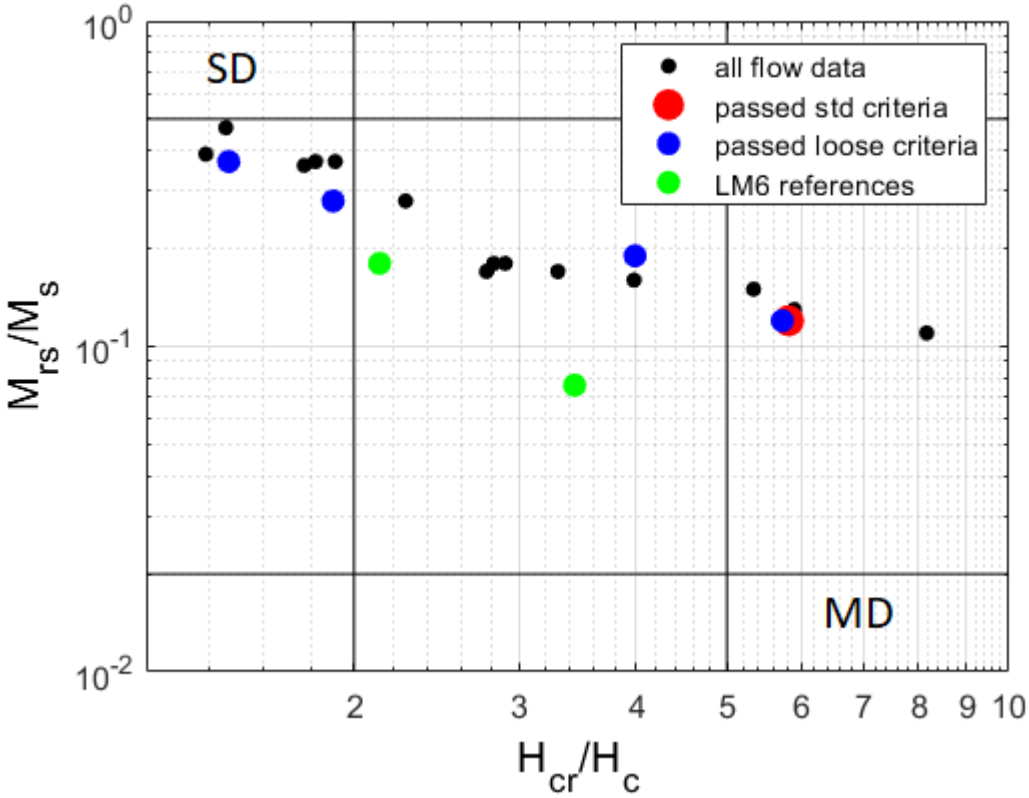

Figure 9-5 Hysteresis parameter plot for the flows studied herein, highlighting which flows passed the two types of selection criteria. M_{rs}/M_s refers to the ratio of remanent saturation magnetization to the saturation magnetization and H_{CR}/H_C refers to the ratio of coercivity of remanence to coercivity

The data herein extend the finding in Hodgson et al. (2018) that isolating the highest temperature portions of a PI experiment can produce paleointensity estimates, but the failure rate is substantially higher that a normal paleointensity experiment. The reliability of some of the data can be questioned because of the lack of pTRM checks for up to 550 °C of heating. One possibility would be to have an intermediate heating step to a lower temperature, for example 200 °C, where thermochemical alteration is less likely. This intermediate temperature would become the point of comparison for pTRM checks and would add fewer steps than the systematic tail checks in section 9.6.3. Skipping over the lowest temperature ranges, like in the abridged experiments, but still starting the experiment substantially below the Curie Temperature is therefore the most widely applicable method and the recommendation of this study.

The data in this study provide an example of the application of concentrated temperature steps. In the case of this study, the temperature steps were likely over-concentrated around the Curie Temperature, but the data are applicable to the general case of a restricted blocking temperature interval for the component of relevance. This aspect of the HiTeCT method can be applied to other rocks, such as plutons, which cool slowly enough

that different temperature ranges can hold different magnetizations and thus can record several paleointensities. Isolating a non-characteristic magnetic component is more difficult, but, having shown that it is possible with small temperature steps to produce a paleointensity estimate, the potential exists in the general case of this method.

9.8 Conclusions

In this chapter, an abridged Thellier-style protocol was tested that limits the experiment to temperatures near a specimen's Curie Temperature. The behavior of the specimens in these experiments is strongly tied to a given specimen's Curie Temperature distribution and thus its mineralogy. Not including pTRM checks reduced the data's statistical rigor too substantially, but adding tail checks decreased the data quality. The recommendation of this chapter for this high temperature technique is to only include pTRM checks, as their inclusion justifies the additional heating cycles. The results show that this technique can give paleointensity estimates that are largely comparable to previous studies, but the pass rate was substantially lower. This technique only gives useful results for specimens with narrow, high, and reversible Curie temperature ranges, which means it is likely to not be commonly applicable and potentially may be of limited use. The technique does, however, show that a better understanding of what constitutes an ideal recorder for paleointensities is needed. Using this technique with such a narrow temperature range is, therefore, unlikely to provide substantial, meaningful results. Nonetheless, a less extreme version, more along the lines of the abridged Coe-Thellier experiment can address some of the pitfalls of two-slope paleointensity data. The unusually low success rate for these experiments, however, means that this technique is likely not worth pursuing further for paleointensity estimates.

9.9 References

Biggin, A. J., 2010, Are systematic differences between thermal and microwave Thellier-type palaeointensity estimates a consequence of multidomain bias in the thermal results? : Physics of the Earth and Planetary Interiors, v. 180, no. 1-2, p. 16-40.

Biggin, A. J., and Bohnel, H. N., 2003, A method to reduce the curvature of Arai plots produced during Thellier palaeointensity experiments performed on multidomain grains: Geophysical Journal International, v. 155, no. 3, p. F13-F19.

Biggin, A. J., and Paterson, G. A., 2014, A new set of qualitative reliability criteria to aid inferences on palaeomagnetic dipole moment variations through geological time: Frontiers in Earth Science, v. 2, no. 24.

Biggin, A. J., Strik, G., and Langereis, C. G., 2009, The intensity of the geomagnetic field in the late-Archaean: new measurements and an analysis of the updated IAGA palaeointensity database: Earth Planets and Space, v. 61, no. 1, p. 9-22.

Biggin, A. J., and Thomas, D. N., 2003, Analysis of long-term variations in the geomagnetic poloidal field intensity and evaluation of their relationship with global geodynamics: Geophysical Journal International, v. 152, no. 2, p. 392-415.

Böhnel, H., Herrero-Bervera, E., and Dekkers, M. J., 2011, Paleointensities of the Hawaii 1955 and 1960 Lava Flows: Further Validation of the Multi-specimen Method, Dordrecht, Springer, Earth's Magnetic Interior, 195-211 p.:

Bono, R. K., Tarduno, J. A., Nimmo, F., and Cottrell, R. D., 2019, Young inner core inferred from Ediacaran ultra-low geomagnetic field intensity: Nature Geoscience, v. 12, no. 2, p. 143-147.

Coe, R. S., 1967, Determination of paleo-intensities of earths magnetic field with emphasis on mechanisms which could cause non-ideal behavior in thelliers method: Journal of Geomagnetism and Geoelectricity, v. 19, no. 3, p. 157-179.

Coe, R. S., Riisager, J., Plenier, G., Leonhardt, R., and Krasa, D., 2004, Multidomain behavior during Thellier paleointensity experiments: results from the 1915 Mt. Lassen flow: Physics of the Earth and Planetary Interiors, v. 147, no. 2-3, p. 141-153.

Donadini, F., Riisager, P., Korhonen, K., Kahma, K., Pesonen, L., and Snowball, I., 2007, Holocene geomagnetic paleointensities: A blind test of absolute paleointensity techniques and materials: Physics of the Earth and Planetary Interiors, v. 161, no. 1-2, p. 19-35.

Dunlop, D. J., and Ozdemir, O., 2001, Beyond Neel's theories: thermal demagnetization of narrow-band partial thermoremanent magnetizations: Physics of the Earth and Planetary Interiors, v. 126, no. 1-2, p. 43-57.

Dunlop, D. J., Zhang, B. X., and Ozdemir, O., 2005, Linear and nonlinear Thellier paleointensity behavior of natural minerals: Journal of Geophysical Research-Solid Earth, v. 110, no. B1.

Gratton, M. N., Shaw, J., and Herrero-Bervera, E., 2005, An absolute palaeointensity record from SOH1 lava core, Hawaii using the microwave technique: Physics of the Earth and Planetary Interiors, v. 148, no. 2-4, p. 193-214.

Hawkins, L., 2018, A Mid-Paleozoic Dipole Low defined from new paleointensity estimates from Russia and the UK [Doctor in Philosophy: University of Liverpool.

Hill, M. J., and Shaw, J., 2000, Magnetic field intensity study of the 1960 Kilauea lava flow, Hawaii, using the microwave palaeointensity technique: Geophysical Journal International, v. 142, no. 2, p. 487-504.

Hodgson, E., Grappone, J. M., Biggin, A. J., Hill, M. J., and Dekkers, M. J., 2018, Thermoremanent Behavior in Synthetic Samples Containing Natural Oxyexsolved Titanomagnetite: Geochemistry Geophysics Geosystems, v. 19, no. 6, p. 1751-1766.

Nagata, T., Momose, K., and Arai, Y., 1963, Secular variation of geomagnetic total force during last 5000 years: Journal of Geophysical Research, v. 68, no. 18, p. 5277-5281.

Paterson, G. A., Biggin, A. J., Hodgson, E., and Hill, M. J., 2015, Thellier-type paleointensity data from multidomain specimens: Physics of the Earth and Planetary Interiors, v. 245, p. 117-133.

Paterson, G. A., Tauxe, L., Biggin, A. J., Shaar, R., and Jonestrask, L. C., 2014, On improving the selection of Thellier-type paleointensity data: Geochemistry Geophysics Geosystems, v. 15, no. 4, p. 1180-1192.

Prevot, M., Lecaille, A., and Mankinen, E. A., 1981, Magnetic effects of maghemitization of oceanic-crust: Journal of Geophysical Research, v. 86, no. NB5, p. 4009-4020.

Riisager, P., and Riisager, J., 2001, Detecting multidomain magnetic grains in Thellier palaeointensity experiments: Physics of the Earth and Planetary Interiors, v. 125, no. 1-4, p. 111-117.

Russell, J., 2018, Thermoremanent behaviour in natural samples [B.Sc.: University of Liverpool.

Teanby, N., Laj, C., Gubbins, D., and Pringle, M., 2002, A detailed palaeointensity and inclination record from drill core SOH1 on Hawaii: Physics of the Earth and Planetary Interiors, v. 131, no. 2, p. 101-140.

Thellier, E., and Thellier, O., 1959, Sur l'intensité du champ magnétique terrestre dans le passé historique et géologique: Ann. Géophys., v. 15, p. 285-376.

Xu, S., and Dunlop, D. J., 2004, Thellier paleointensity theory and experiments for multidomain grains: Journal of Geophysical Research-Solid Earth, v. 109, no. B7.

Section C

Beyond the paleomagnetism laboratory

CHAPTER 10 MAGNETIC FLUX LEAKAGE IN PITTED COILED TUBING

Foreword

From May 2019 to August 2019, the author completed a research placement with Schlumberger Gould Laboratory in Cambridge, England (Schlumberger Cambridge Research; SCR). The funding for this industrial placement was provided by the Duncan Norman Research Scholarship, the University of Liverpool School of Environmental Sciences, and the NERC EAO DTP.

This chapter is conceived as an example of how magnetic methods can be applied to open questions outside academia. Its connection to the previous chapters is by means of an example of the impact magnetic methods can have when they are applied at the opposite extreme: very magnetic applications. The author had intended to return during the second half of 2020 to complete a six-month post-PhD internship (paid for by Schlumberger). However, the COVID-19 pandemic prevented this.

10.1 Introduction

Quantifying the changes that a material undergoes during its lifetime determines its future utility. Finding defects in metallic objects has been of interest since the transition from the Stone Age to the Bronze Age. As technology improved, the defects decreased in volume and finding them became more difficult. Locating them, however, never decreased in importance. If the defects in a metallic object are too large, the object will fail when under routine stress from its expected working conditions (e.g. Stayer et al., 2013)

For ferromagnetic materials, like carbon steel or some types of stainless steel, the magnetic field of the material can be used to find these defects (Stayer et al., 2013). Non-ferromagnetic partitions in the material- for example, copper/bronze, coal, or air- will cause strong, localized changes in the magnetic properties (especially susceptibility), which can be detected using powerful magnets and magnetic probes (Kopp and Willems, 2013; Liu et al., 2014). A localized decrease in susceptibility causes the magnetic field to reflect into free space, a phenomenon called magnetic flux leakage (MFL).

Finding defects in stainless steel pipes is extremely important for pipe operating in high-pressure or corrosive environments, the conditions in which coiled tubing often operates in the oil and gas sector (e.g. Brondel et al., 1994). The high pressures can cause mechanical damage, which has been the subject of much previous MFL work (see section 10.2.1). Corrosion-induced damage in coiled tubing, however, has had minimal research.

The goal herein is to design and test a lab-based technique for studying MFL caused by the acid pits in stainless steel. Schlumberger Cambridge Research (SCR) studies all facets of oil-well technologies. During this placement, the author worked with SCR to develop a laboratory setup capable of replicating a single channel of data from CoilSCAN™, a piece of equipment that detects coiled tubing defects using MFL (Christie et al., 2015; sections 10.2.2 and 10.2.3). First, COMSOL (a physics modelling program) magnetic flux density models were completed to confirm the theory of the setup (section 10.4). Next, the simple, well-studied single-defect tests were completed to confirm the application of the setup and determine the lower bound of sensitivity (section 10.5.1 and section 10.5.2). The final sets of experiments expand the data from one dimension to two dimensions, with a full XY scan of the test plate (section 10.5.3). The laboratory tests herein are predominantly qualitative in nature and use. A single hall probe (1/64th of what is found in a full CoilSCAN™ unit) was used to probe finer features in more depth than the complete CoilSCAN™ unit currently can.

Refining the measurements and detecting the finest scale defects is an important next step for this equipment but is also the most challenging next step.

10.2 Background magnetic flux leakage in coiled tubing

Magnetic field lines begin at the N pole of a magnet and follow the path of least resistance to the nearest S pole. The relative permeability (μ_r) of a material measures, in a broad sense, how easily magnetic field lines can penetrate a material, relative to free space. Metals have a μ_r anywhere from 1 ('non-magnetic' materials, like wood, brass, Inconel, or aluminum) up to 10^6 (Mu-metal). Being made of carbon steel, Coiled Tubing has a μ_r on the order of 10^2.

10.2.1 Coiled tubing background

Coiled Tubing (CT) has historically been used primarily for well service in oil and gas operations. However, with increased tapping of unconventional resources and horizontal wells, the market for coiled tubing has continued to grow (Jackson et al., 2014). Currently, Coiled Tubing is used for well remediation (acid stimulation, or cleaning out solids or scales), non-rotational drilling, or offshore support (Avery et al., 2019; Liu et al., 2017; Ottolina et al., 2016; Rahman et al., 2012). The pipe is made of a deformable type of carbon steel, consisting of layers of pearlite and ferrite extruded as sheets that are welded together using a 45° bias weld (Torregrossa et al., 2014) (to distribute the weld over more of the pipe) and then in turn seam-welded into skelps (the flat sheets that become tubing). Coiled Tubing generally has a diameter in the range of 2.5 – 13 cm (1 – 5 in), with wall thicknesses of 2 – 7.6 mm (0.080 – 0.300 in) (Figure 10-1 contains a Coiled Tubing cartoon). Pipes of these sizes are flexible on large scales (strings can be up to 36 000 ft long) and can fit down live wells, saving time and money for the operator (Afghoul et al., 2004; Boumali et al., 2005). The setup required for Coiled Tubing consists of 4 main parts: the tubing reel, injector head, control cabin, and power pack. These can be mounted on a multi-purpose support vehicle for offshore operations, such as closing off wellbores (Ottolina et al., 2016).

CT is often used to carry acid downhole for focused acid injection to enlarge pore space (Crabtree and Gavin, 2005) or it can be fitted with a jet to clean out scale build-up (Afghoul et al., 2004). However, just as the acid dissolves the rock downhole, it also damages the pipes (Crabtree and Gavin, 2005), which can also be corroded by oxygen, water/brine, carbon dioxide (CO_2; sweet well), and hydrogen sulfide (H_2S; sour well) (Brondel et al., 1994; Crabtree and Gavin, 2005; Ottolina et al., 2016; Usman and Ali, 2018). Including inhibitors in the injection fluid is therefore essential to minimize damage to the pipe and extend its lifetime (Finsgar and Jackson, 2014; Ho et al., 2018; Padron et al., 2007; Usman and Ali, 2018).

Inhibitors work by forming a film on the surface of the pipe to physically separate the pipe from the pumped solution and prevent acid corrosion (Ho et al., 2018). The intactness of the film, however, is strongly affected by the concentration of the inhibitor in the pumped solution and the flow regime (laminar or turbulent) of the fluid (Barmatov et al., 2016; Barmatov et al., 2015). Selecting the correct inhibitor is therefore the subject of much current chemical engineering research. The optimal inhibitor for a given well depends on its temperature, the concentration and type of acid used, environmental considerations, and microbial concentrations (Finsgar and Jackson, 2014; Kahrilas et al., 2015; Sherman et al., 2014; Usman and Ali, 2018). When microbes are present, usually when brine has entered the well, they anaerobically respire H_2S, which causes unexpected, local corrosion of the Coiled Tubing (Kahrilas et al., 2015; Sherman et al., 2014). The pipe can, additionally, be damaged electrochemically (as an anode) or mechanically (Brondel et al., 1994).

CT generally operates below its maximum yield strength (with a factor of safety of 1.25), so any damage needs to be found promptly (Boumali et al., 2005; Sherman et al., 2014). Coiled Tubing's flexibility is its main asset; but bending the string causes plastic deformation on entry and exit (a form of low-cycle fatigue), which leads to the formation of microcracks (Boumali et al., 2005; Christie et al., 2015; Crabtree and Gavin, 2005). The tubing can also fail under compression, if it arches too substantially (Ottolina et al., 2016) or under tension from the weight of the downhole tubing, usually as a result of the presence of a severe defect (such as a large crack) (Liu et al., 2017). Mechanical damage is one of the most important causes, potentially the leading cause, of Coiled Tubing failure, as any damage will concentrate stress and increase its severity under normal loads (Christie et al., 2015; Liu et al., 2015; Padron et al., 2007). The correct grade (and tapering) of tubing is therefore needed for each application, to ensure pipe can withstand any potential hydrogen embrittlement and high-cycle fatigue in the elastic regime (below the yield strength) (Crabtree and Gavin, 2005; Liu et al., 2017; Ottolina et al., 2016; Sherman et al., 2014). The damage needs to be characterized and quantified accurately to reduce the probability of a premature retirement of the string (Gallagher et al., 2015).

10.2.2 Magnetic flux leakage testing background

One of the best methods of non-destructive evaluation (NDE) available for Coiled Tubing is a Magnetic flux leakage (MFL) survey, which can be run over the entire length of the Coiled Tubing string (Stayer et al., 2013). MFL is a volumetric, non-contact technique that can detect both internal and external defects (Kopp and Willems, 2013; Liu et al., 2014). MFL surveys of Coiled Tubing use strong magnetic fields to locally magnetically saturate the pipe in either

the axial or radial direction (see Figure 10-1), using either permanent magnets or, less commonly, Helmholtz coils (Liu et al., 2015; Wu et al., 2017). The optimal saturation field (for maximum signal to noise ratio) sits at the inflection point (knee point) of the material's B-H (external, internal magnetic fields, respectively) curve, where the B-H curve changes from linear to asymptotic (Amineh et al., 2008) (*Figure 10-2*). The Hall probes are very sensitive to the lift-off distance from the pipe, so lift-off distance is tracked closely (Dutta, 2008). The corollary to this problem is that deeper external defects have a correspondingly larger lift-off distance since the depth of a defect adds to the lift-off distance (Kopp and Willems, 2013), but it was shown in (Dutta et al., 2009a) that this effect can be scale-invariant; a larger defect has a larger lift-off distance (distance from the surface to the sensor) but also a larger MFL signal.

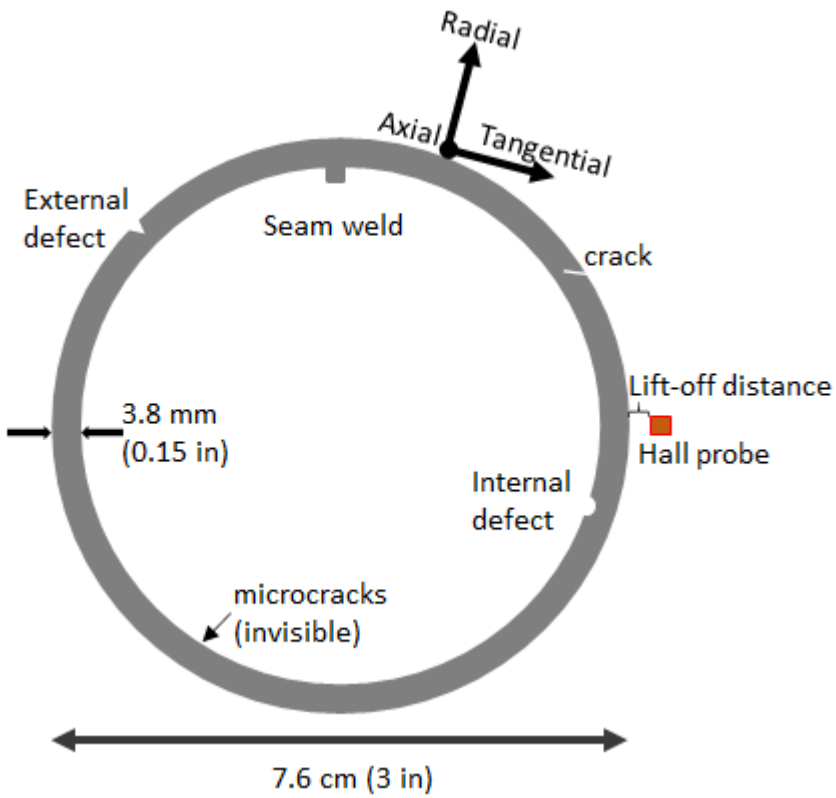

Figure 10-1 Example Coiled Tubing cross-section, showing relevant components and examples of defects.

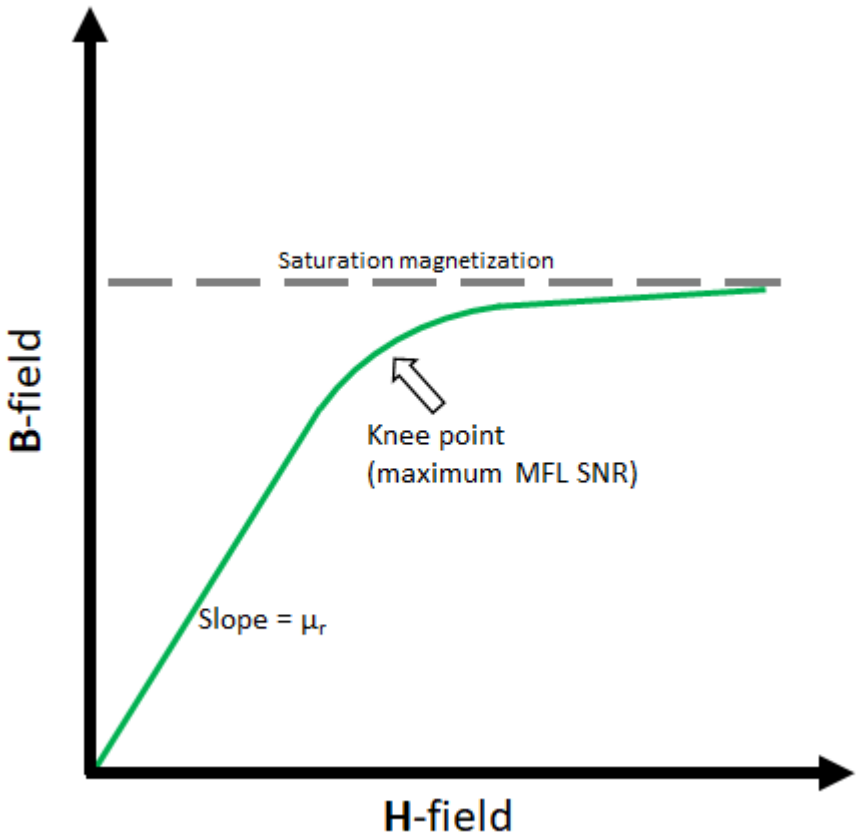

Figure 10-2 Generic magnetic saturation curve for a steel pipe. MFL SNR means magnetic flux leakage signal to noise ratio. The variable μ_r refers to the relative permeability of the material. B is the magnetic flux density and H is the resulting magnetic field vector.

Carbon steel has μ_r around 100; the exact value is dependent on the alloying of the steel. Any defects in the steel will cause the local permeability to decrease, increasing the local magnetic reluctance (Stayer et al., 2013) and causing the magnetic field to refract or 'leak' into free space (Liu et al., 2015). Figure 10-3 contains a cartoon of a generalized MFL experimental setup. At a defect, the magnetic field refracts into the free space surrounding the pipe, which can then be picked up using a Hall probe (Sun and Kang, 2013). Both bumps (extra material, lower leakage) and damage (less material, higher leakage) can be detected using MFL, but damage has a higher signal to noise ratio (SNR) since increased magnetic fields are easier to measure than decreased magnetic fields by the Hall probe (Liu et al., 2017; Sun and Kang, 2013). Both the seam and the bias welds can be observed using MFL, which helps orient the string and track the location of any defects (Liu et al., 2017; Stayer et al., 2013; Torregrossa et al., 2014).

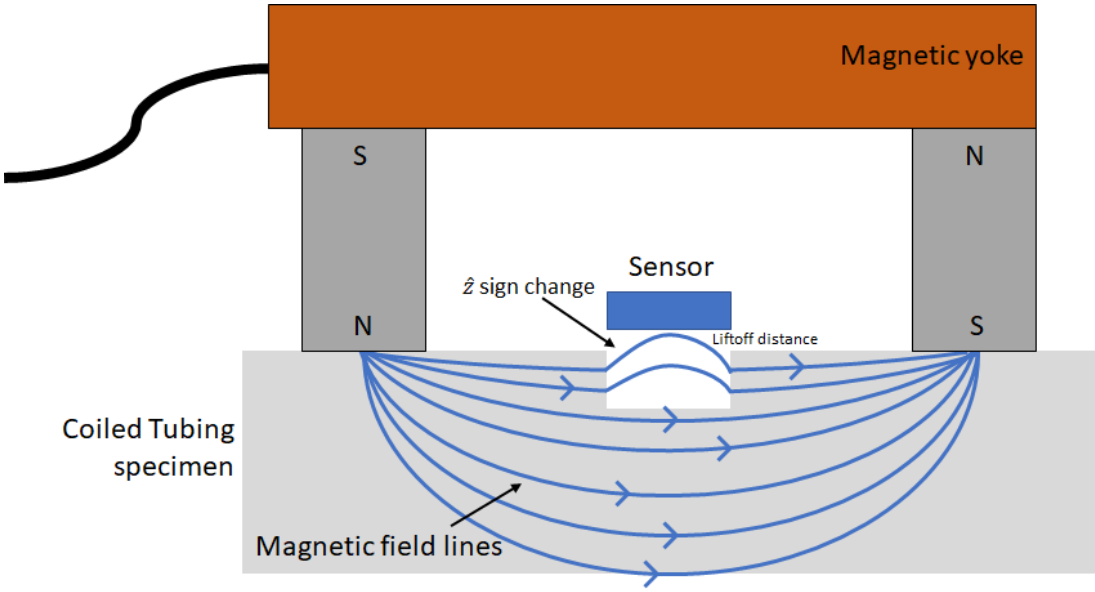

Figure 10-3 Generalized MFL experiment setup

MFL tests can be run off-line (in the maintenance yard) or well-site at the Coiled Tubing's regular working speeds- up to 0.76 m/s (150 ft/min) (Stayer et al., 2013), using CoilSCAN™, for example. Moving a conductor through a magnetic field creates eddy currents, but these currents are usually neglected in models for these speeds (Liu et al., 2014). MFL data are usually measured (either internally or externally) in the axial and radial directions, with the azimuthal/tangential component typically ignored (Dutta et al., 2009a; Kopp and Willems, 2013). Liu et al. (2014) showed that the axial and azimuthal/tangential components can be modelled from 1D axial data. In the case of more complex defect geometries, all 3 components can be used to refine the model (Li et al., 2007). The measurements can be done while the tubing is pressurized (under hoop stress) (Liu et al., 2016; Reichert et al., 2016). However, increased stress changes the magnetic properties of the steel (its magnetic easy direction) (Mandal and Atherton, 1998) and decreases the MFL signal (Liu et al., 2016; Reichert et al., 2016).

Well-site tests are usually performed during Pulling Out Of Hole (POOH) operations and therefore cannot real-time measurements (Stayer et al., 2013). Initially, alarm thresholds are set for MFL signal magnitudes, but the thresholds are optimal only for new pipes and require operator training for recognizing which threshold alarms are significant on older strings (Liu et al., 2015). These data are collected and analyzed using the methods described above to determine changes in the string's fatigue life (FTL; how many cycles until failure) and its degradation parameter (DP) (Stayer et al., 2013). Bumps (either bending or additional material), and damage can be detected (Deffo et al., 2019; Sun and Kang, 2013). This principle applies inside a defect with a complex geometry: the 'valleys' of the defects can be

measured better than the 'hills'. The valleys, however, are the thinner points of the pipe's wall and therefore more important in the analysis (Sun and Kang, 2013). Accurate defect sizing and severity (Q) are required for accurate fatigue life and degradation parameter determination (Liu et al., 2014; Liu et al., 2015). As long as Q is within safety limits, the pipe can continue to be used (Gallagher et al., 2015). Seemingly counterintuitively, defects decrease the remaining fatigue life percentage more severely for low pressure operations than for high pressure operations. During high pressure operations, microcracks form after fewer cycles than during low pressure operations, so an early forming crack has a much higher Q in low pressure operations (Christian and Tipton, 2009). The location (depth along the string) of the defect also affects its severity and its effect on fatigue li (Liu et al., 2016).

Two main defect characterization methods are commonly used: semi-empirical defect mapping (Liu et al., 2015; Reichert et al., 2016; Torregrossa et al., 2014) and modelling (Amineh et al., 2008; Dutta et al., 2009a; Han et al., 2017; Khodayari-Rostamabad et al., 2009; Kopp and Willems, 2013; Liu et al., 2014; McJunkin et al., 2006; Ravan et al., 2010; Wang et al., 2018; Xu et al., 2012). Using a defect library, an unknown defect signal is compared using a defect identification algorithm to the library of known defects, which contains pictures and signals (Liu et al., 2015; Reichert et al., 2016). The library, however, must contain information about signals from mechanical damage, corrosion, abrasion, erosion, and cavitation (Liu et al., 2015). The shape and speed of the Hall probe eliminate sharp variations in the MFL signal, which can cause the defect to appear larger in the data. This effect is called data blooming (Kopp and Willems, 2013; Liu et al., 2014; Ravan et al., 2010). Analyzing the data from multiple sensors and monitoring the location of the defects (cracks usually form near welds) can help differentiate a pit from a crack (Khodayari-Rostamabad et al., 2009; McJunkin et al., 2006).

Modelling the data to determine defect type is complex: the defects need to be classified as injurious or benign, the size of the Hall probes limits data resolution, and the data are very sensitive to lift-off distance (deeper defects have larger lift-off) (Dutta et al., 2009a; Khodayari-Rostamabad et al., 2009; Liu et al., 2014). The models can estimate volume change well, but (micro)cracks, which are the most injurious defects, often have the least volume loss (Liu et al., 2014; McJunkin et al., 2006; Padron et al., 2007). The choice of model for a given set of MFL data is largely determined by computational constraints and available time. Analytic models are much faster but significantly less accurate because of the assumptions required for the governing equations, but can still include other variables, such as the aforementioned stress effects (Dutta et al., 2009b; Wang et al., 2018). Many different

types of numerical models have been proposed and are currently used: Finite Element Models (Kopp and Willems, 2013), Space Mapping between coarse and fine models (which also helps to ensure global minima are found) (Amineh et al., 2008; Ravan et al., 2010), Finite Element Neural Networks (without training) (Xu et al., 2012), Machine learning (which works well with real defects) (Khodayari-Rostamabad et al., 2009), and Particle Swarm Optimization (Han et al., 2017).

Recent work by Sun et al. (2019) and Wu et al. (2017) have shown that with external design modifications, lift-off distance can be increased, which increases the versatility of the machine. Sun et al. (2019) and Wu et al. (2017) placed a second magnet and a ferrite core, respectively, above (further from the pipe) the Hall probe and demonstrated a stronger MFL signal at a greater lift-off distance than in the conventional design.

10.2.3 CoilSCAN™ device background

This chapter's partner, Schlumberger Ltd uses a well-site MFL scanning device named CoilSCAN™. CoilSCAN™ and its associated data are property of Schlumberger. As such, this section reports briefly on the publicly-available information about the device. The device uses stainless steel guide rollers to maintain a constant 3 mm distance from the pipe to the MFL sensors and odometer wheels to track position along the pipe (Christie et al., 2015). Strong (proprietary) permanent magnets and magnetic yokes provide the saturation magnetic field for the MFL measurements (Christie et al., 2015). CoilSCAN™ operates at Pulling Out Of Hole velocities, up to 0.66 m/s (130 ft/min). Eddy current sensors and 64 Hall effect sensors line the guide rollers, and together they measure outer diameter, ovality, defects, and wall thickness (Christie et al., 2015). CoilSCAN™ measures both the axial and radial MFL signal to determine wall thickness and air gap, respectively. Figure 10-4 contains a picture of CoilSCAN™. Figure 10-5 (taken from Stayer et al., 2015) contains example output data from CoilSCAN™. These data are high-quality and quantitative and cover 360° of the pipe's circumference. The setup described in this chapter cannot reproduce this level of data with a single hall probe. Additional publicly-available details of the design of CoilSCAN™ can be found in Christie et al. (2015). Despite being a well-established device, a current issue with CoilSCAN™ is its inability to detect finer features of Coiled Tubing defects, like those caused from long-term acid pitting. The experiments and analyses in this chapter aim to simulate the data collection process in CoilSCAN™ but with only a single Hall effect sensor.

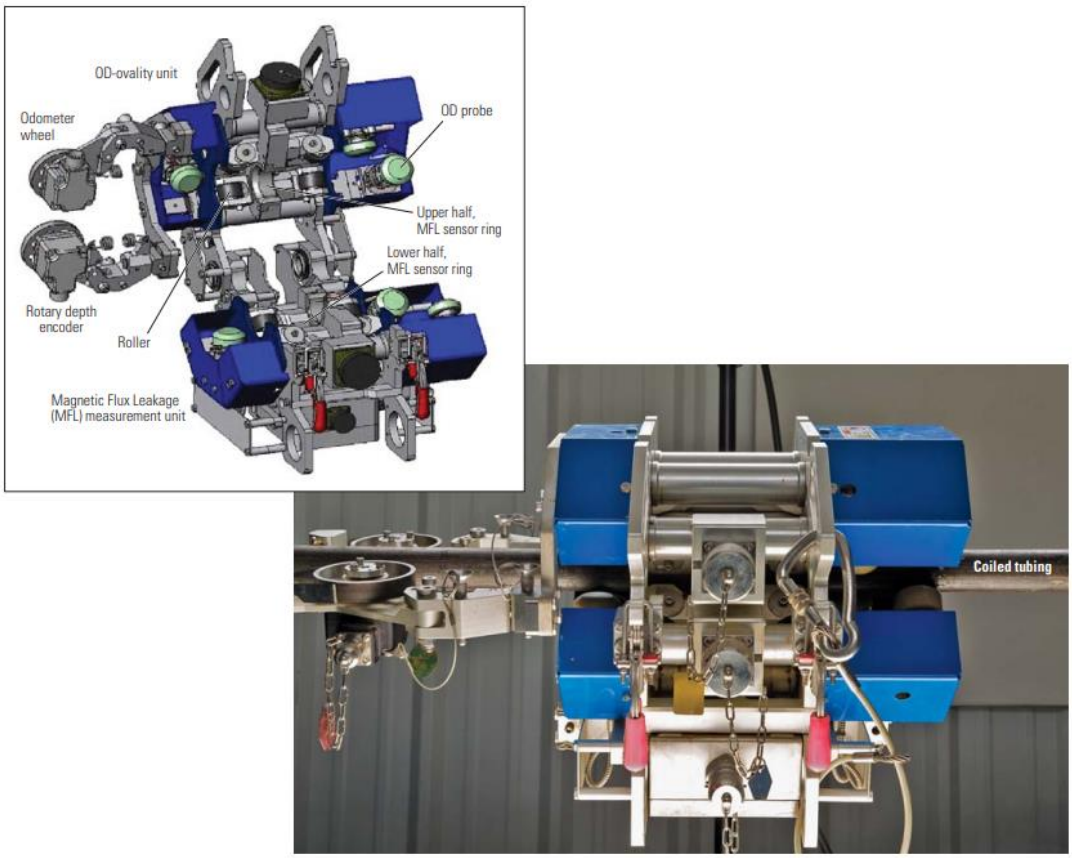

Figure 10-4 CoilSCAN^{TM} technical sketch and in-situ image, showing individual parts. Image reproduced from Christie et al. (2015).

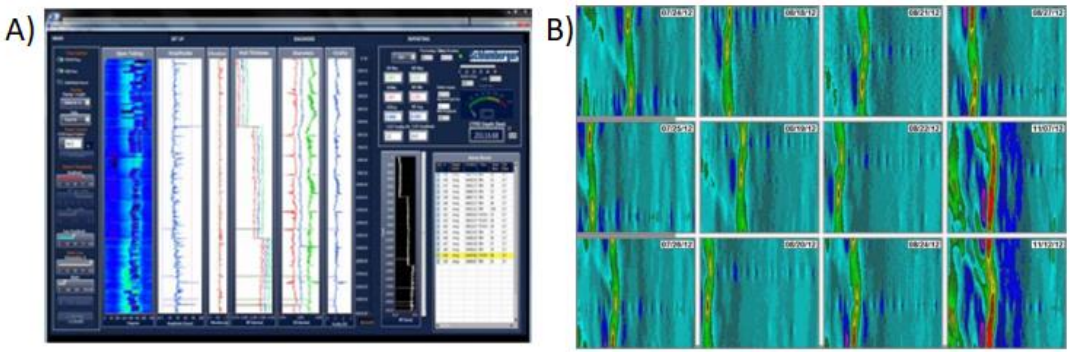

Figure 10-5 CoilSCAN^{TM} output data. A) the control panel and data as a function of length along the pipe. B) the MFL signal for a weld. The color coding for the MFL signal is rainbow, with dark blue being the lowest leakage and red being the highest leakage. Both figures are reproduced from Stayer et al. (2015).

10.3 Methods

10.3.1 COMSOL modelling

COMSOL Multiphysics is a physics modelling program that lets any subset of physical properties be used to calculate a static or dynamic system. The only physics relevant herein is magnetism, so in setting up the physics for the models, the main material parameter of interest is each material's susceptibility. The simplicity of the setup means only three materials are important: stainless steel, neodymium (or a similar material) magnets, and air (free space). These models were run to validate the MFL setup of interest before running the experiments.

10.3.2 Magnetic flux leakage

Two MFL setups were used to simulate (1/64th of) CoilSCAN™ in the laboratory. The initial tests used a Senis 3MH3A Teslameter (0.1% accuracy on 200 mT scale), on a moveable platform. The saturation magnetic field was provided by 12 N42 grade 25 x 5 x 5 mm rectangular magnets, on the surface of the tube, 15° from the sensor. The platform was moved continuously along the pipe sample at a speed of 18 mm/s with a lift-off distance of 3 mm. MFL data were recorded by a custom LabVIEW program and analyzed in MATLAB. A cartoon of the experiment and the in-situ setup can be found in Figure 10-6.

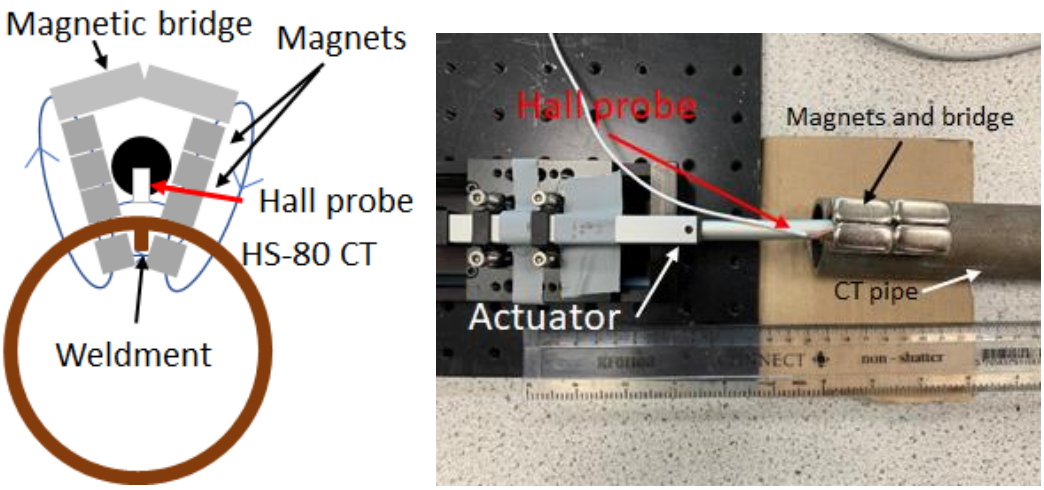

Figure 10-6 MFL experiment setup. Left: experiment cartoon. Only the experiments to locate the weldment used the internal magnets. Right: real experiment. These initial MFL experiments used a minimalist setup to test largescale features.

After the success of the first set of experiments, which confirmed the validity of this setup based on previous work, (see Section 10.2), a second, more complex setup was designed. A Hirst GM-08 computer controlled gaussmeter was used, with a range of 20 mT and an error of 0.1%, with a sampling rate of 5 samples/s. The gaussmeter was mounted using a 3D printed holder to a computer controlled XY stage, capable of moving in a 2D grids at speeds from 0.1 – 10 mm/s. To ensure a smooth transition from the previous design to the new design, each part was changed individually. First, the gaussmeter was changed, then the pipe specimen was exchanged for an artificially pitted steel plate, and then finally the permanent magnets were exchanged for a magnetic yoke. An intermediate design can be found in Figure 10-7 (top) and the final design in Figure 10-7 (bottom).

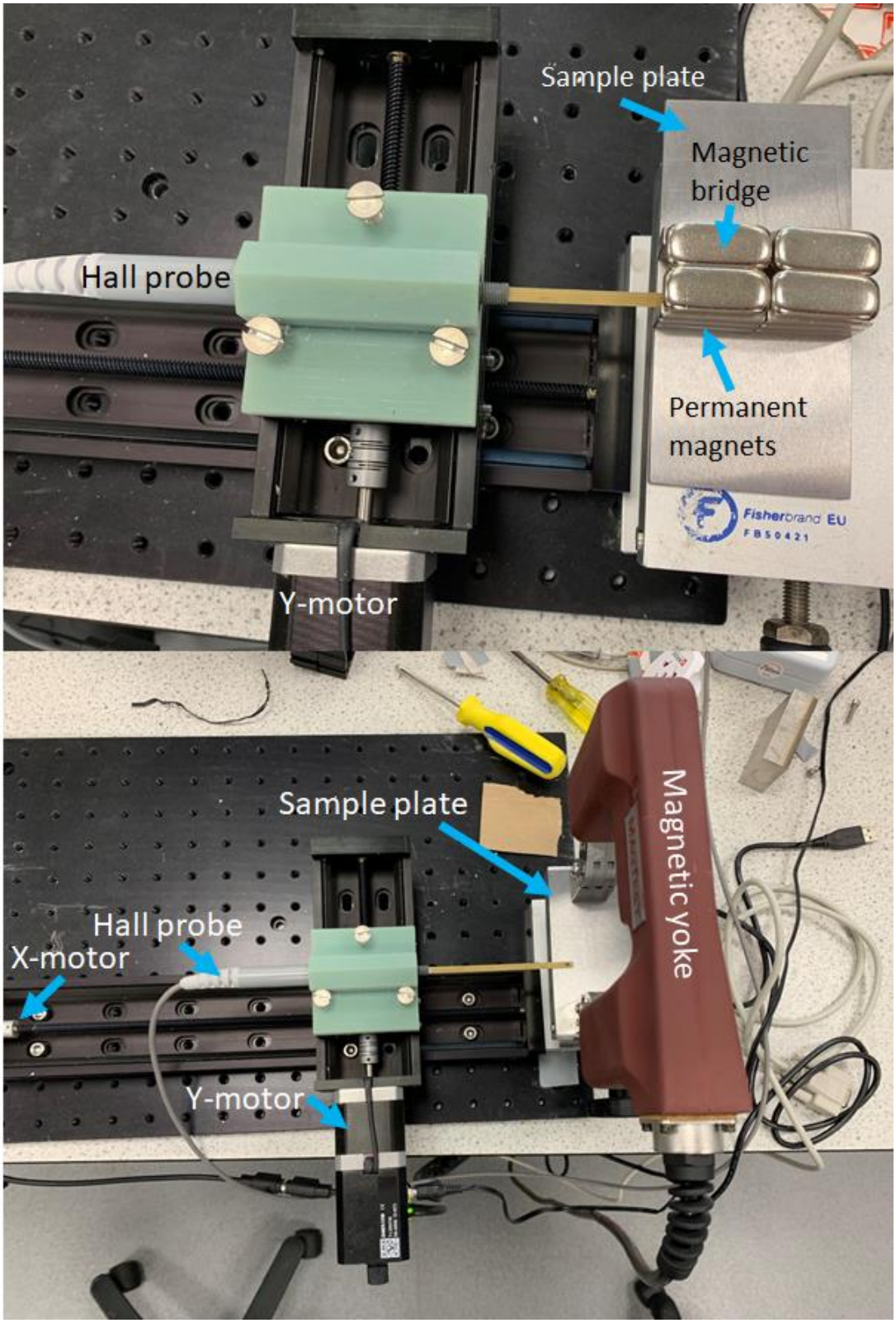

Figure 10-7 Updated MFL setup. Top: new gaussmeter and steel plate. Bottom: new magnetic yoke.

10.3.3 Contact profilometry

To assess the surface roughness of the investigated sample, contact profilometry was performed on a subset of the steel plate sample's defects. The Mitutoyo Surftest SJ-400 contact profilometer had a scanning width of 2 µm and a scanning length of 13 mm, with a stylus velocity of 0.05 mm/s. Data were recorded automatically by the Surftest's program and analyzed in MATLAB.

10.3.4 Scanning Electron Microscopy

To supplement the contact profilometry survey, a coarse Scanning Electron Microscopy study of a subset of the acid pitting observed in the regions near the survey lines was completed. The Zeiss EVO HD15 Scanning Electron Microscope (10 keV accelerating voltage) in-house at Schlumberger was used to create the defect images. One representative defect of each of the four types was imaged and analyzed.

10.4 COMSOL modelling

10.4.1 Initial geometry

To better understand the physics and limitations of the MFL setups, a few simple COMSOL models were designed for an initial check on the suitability of the proposed experimental setup. The first model uses the same geometry as the initial experiments run in the following MFL tests section. A simplified geometry was used that assumes the 6 magnets on either side behave as a single large magnet. Figure 10-8 shows the expected magnetic flux in the region of the pipe both in the absence and presence of a small pass-through defect. To visualize the data with the weldment but no defects, a YZ planar slice was taken through the middle of the pipe, since the pipe is homogeneous in the $\hat{x}$-direction, far from the edges. The weldment was simulated by adding an internal channel with a rectangular cross-section with the same permeability as the rest of the pipe. For the defect data, two planar slices were taken: YZ and XZ, since the pipe is no longer homogeneous in the $\hat{x}$-direction. The data are plotted on a log scale, as most of the magnetic flux remains in the magnet, the pipe, and the steel top plate.

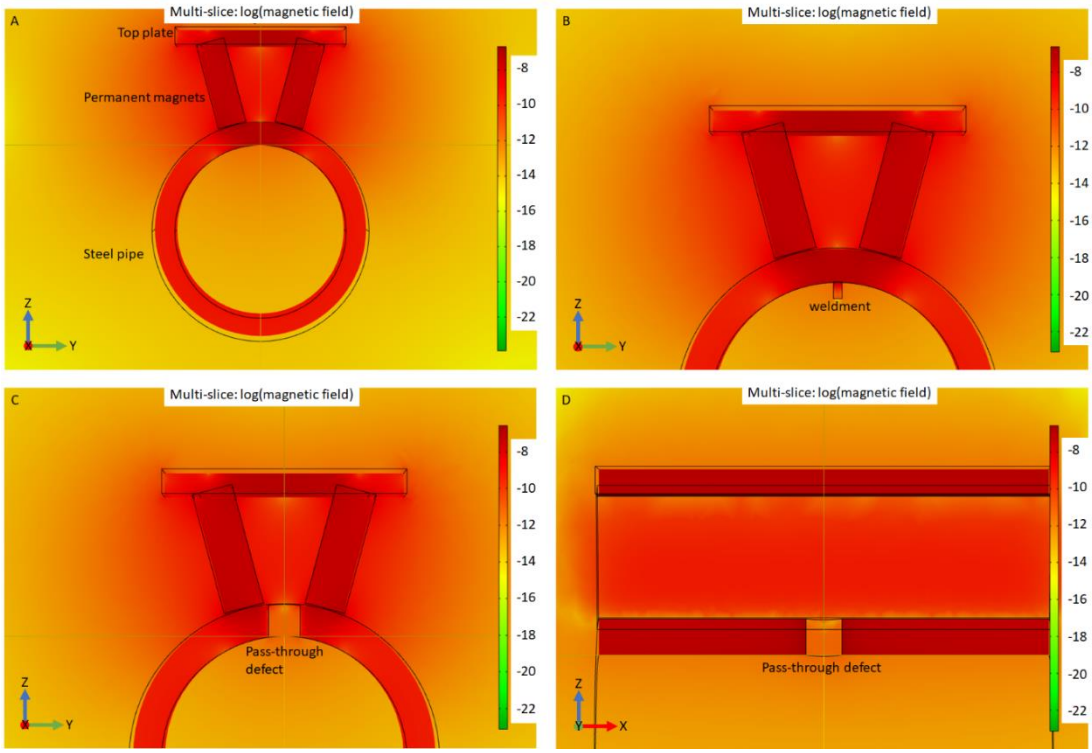

Figure 10-8 COMSOL models for initial test geometry, (A) without a defect, (B) with the weldment (C&D) with a pass-through defect. An arbitrary magnetization (within one order of magnitude of that expected for the magnets used) was given to the magnets, so the scale is an arbitrary log scale.

It is apparent that the weldment and the defect in the pipe cause localized changes in the magnetic field both inside and outside the pipe. The weldment's lack of magnetic saturation in Figure 10-8B means that these magnets are potentially too weak by themselves for the seam weld to be picked up by the gaussmeter. The defect data in Figure 10-8C and D show that the magnetic field changes continuously through the defect, with the center plane of the defect having the most distinct behavior. The sinusoidal pattern of the flux density in Figure 10-8D should also appear in the gaussmeter data. In the background section, it was noted that changes in lift-off distance strongly affect the MFL signal, and the model shows this to be the case as well, as the field quickly becomes the same as the background field as the distance to the pipe increases. These models suggest that the initial setup (Figure 10-7, top) produces a signal 1 – 2 orders of magnitude higher than the surrounding data and will therefore be sufficient to find bulk features, but the model neglects the interfaces between the six magnets on either side, which will affect the laboratory signal.

10.4.2 Plate model

10.4.2.1 Simple defect geometry

The second model's geometry investigates the feasibility of the plate MFL model used for the second part of the study. As noted in the background section, most MFL studies start with a plate, so this geometry is expected to be relatively straight-forward. This model uses

a simplified geometry for the magnetic yoke that assumes the magnetization is permanent, instead of being generated by a current. The setup is stationary, and the magnetic yoke is rated for 30s of on-time, so the model is valid in the middle of the plate, where the yoke has been on for a short while.

Figure 10-9 contains the first 2 models run using this geometry: no defect and a single spherical defect. The defect has been placed on the top of the plate, which is equivalent to the defect being an external defect. Aside from the difference in geometry, an air gap has been included between the plate and the magnets to represent the geometry that is used in CoilSCAN™. The bulk data are again plotted on a log scale, as most of the magnetic flux remains inside the magnetic circuit, but the plate slice's data are plotted on a linear scale. The tessellation observed in the slice is a remanent of taking a slice along the top surface of the plate. The change in magnetic flux is concentrated near the defect, as expected, but as the spacing between the magnets is larger, compared to the spacing in the previous geometry, the model's bulk minimization has more flexibility. As a result, the scaling can change between runs. These models show that the bulk of the flux is located in the plate, between the two magnets. The defect's effect on the magnetic field is still localized near the defect, which was expected.

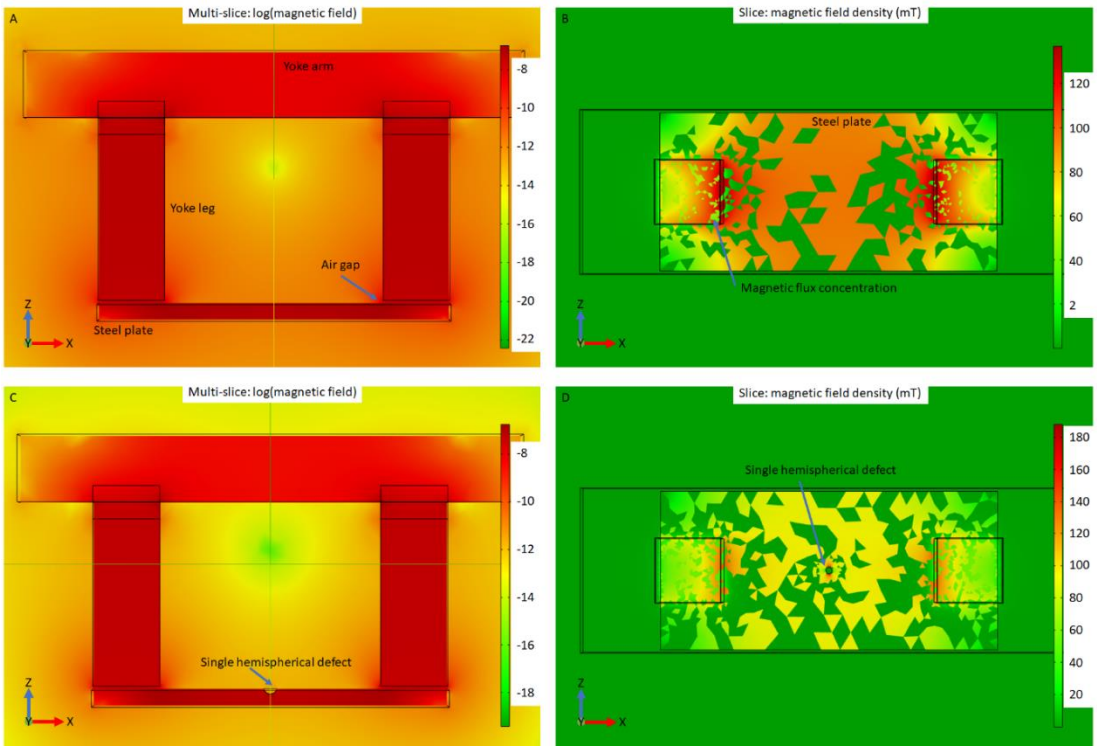

Figure 10-9 Plate geometry COMSOL models measuring magnetic flux density. No defect is present in A) and B) and a single spherical defect is present in C) and D). The differences are localized near the defect. The tessellation observed in B) and D) is an artifact of slicing the model at the top surface of the plate.

Now that the large-scale features of this geometry are known, the next stage is to introduce more complex defects.

10.4.2.2 Complex defect geometry

The first test is to determine the relationship between the defects and the MFL signal. Two multi-defect geometries were therefore tested: five spherical defects loosely (3 mm separation) and closely packed (1 mm separation). Figure 10-10 contains these results from two different angles, with the same plotting as before.

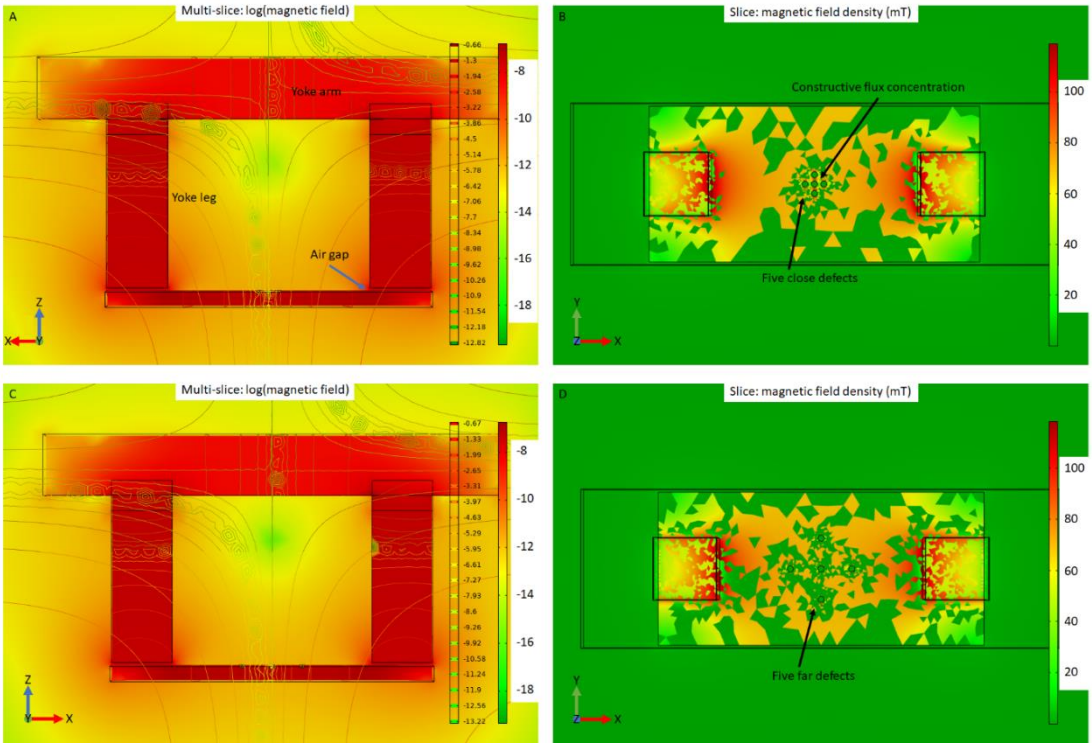

Figure 10-10 Complex defect geometries for plate tests measuring magnetic flux density. A & B) Five spherical defects closely packed, C & D) five spherical defects loosely packed. The different angles provide complementary information about magnetic flux density in 3D. The XY planes in B and D are taken at the surface of the plate. The tessellations are an artifact of taking a slice along the top surface of the plate.

The most immediate result from these models is the flux concentration observed in the XY slices in Figure 10-10B and Figure 10-10D. Both defect geometries have zones of lower flux concentration surrounding the defects and their individual flux leakage signals. The tightly packed defects' signals build constructively, such that the total high flux area around the defects is larger than in the case of the loosely packed defects. This is expected to translate into larger peaks as described in the next section.

The next test is to investigate different types of defects: two additional defect geometries were used: a spherical defect on the bottom of the plate and a conical defect on the top of the plate. The latter defect can be considered analogous to an internal defect, since the magnets and area of interest are on the opposite side of the plate. These results are located

in the bottom row of Figure 10-11. Contour lines are included in these data to help distinguish more subtle differences caused by the differences in defects, but the differences in defect shape observed in Figure 10-11 are nonetheless minimal.

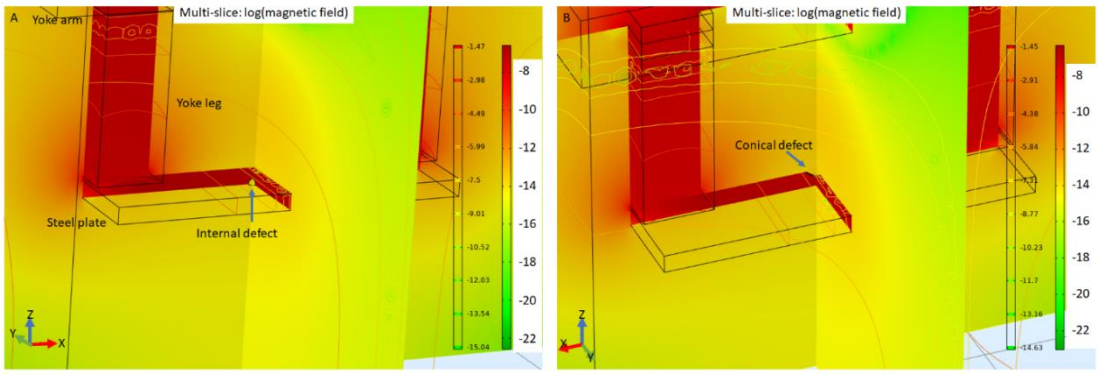

Figure 10-11 COMSOL models for different defect types' magnetic flux densities: A) internal defect and B) conical defect

The internal and external defects do not have noticeably different magnitudes of magnetic flux around them. The contour lines on the surface of the plate show similar spikes in magnetic flux near the defects and their pattern does not change substantially with the defect's location, so an internal and external defect should be detected equally as well during the MFL tests.

From these results, all the defects should be detectable when the lift-off distance is small; the defects only change the background magnetic flux near the edges of the defect. The "internal" and "external" defects should have symmetric signals along the measurement line, with a decrease in signal expected in the center of the defect, compared to the edges. The pass-through defect should behave similarly, except with a sign-change due to the change in flux direction. This setup has a flaw, however. The simulated magnets fail to completely saturate the weldment, so detecting its presence may prove difficult in the real experiments.

10.5 Magnetic flux leakage experiments

Now that the theoretical basis for the experimental setup has been confirmed using the COMSOL models, the tests can be run.

10.5.1 Initial MFL tests

The initial (proof of concept) tests were run with a simplified setup: a single 3-axis Teslameter (Senis 3MH3A with Hall probe type C) that ran between 12 N42 Neodymium magnets. The magnets were 5 x 5 x 25 mm in dimension and arranged into two 5 mm thick walls with heights of 15 mm and lengths of 50 mm. This set up was easy to produce quickly and cheaply but with the consequence of a complicated internal field.

This setup was for validation purposes and was aimed at answering three questions:

1. Can a large defect in the wall be located?
2. Can differences in wall thickness be determined?
3. Can the weldment be located?

The first two questions were tested on pieces of scrap steel from the machine shop, with a single 4 mm hole drilled through the wall. Test pipe 1 had an outer diameter of 45 mm and a wall thickness (WT) of 3.9 mm. Test pipe 2 had an outer diameter of 38 mm and a wall thickness of 10 mm. The best geometry used had a curved magnetic bridge at the top of the magnets to complete the magnetic circuit.

The easiest test is finding the large defect. The signal is expected to be strong enough to be apparent even with the complex magnetic geometry herein. The axial and radial directions of the probe were used to locate the defect, with the axial data giving a very clear signal: a sharp change in signal followed by a sign change of comparable magnitude, as seen in Figure 10-12. The edge effects from the pipe sample cause changes in signals with magnitudes comparable to those caused by the defect. This edge effect would not be observed if the defect was part of a Coiled Tubing string.

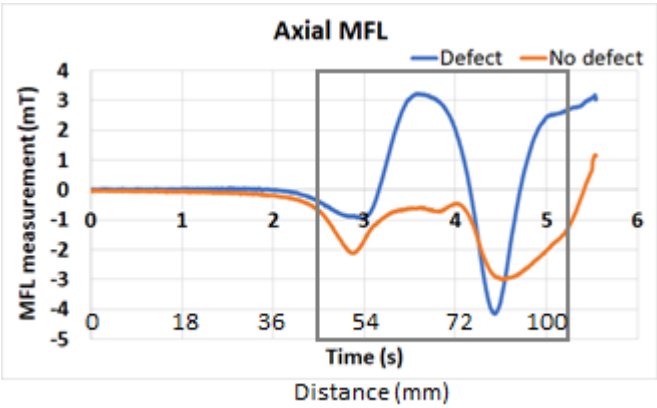

Figure 10-12 MFL data for single pass-through defect. The gray box represents the specimen location. The sharp increase followed by a sign change in the data is characteristic of a hole in the wall. The probe moves at 18 mm/s across the specimen.

The next test attempted was to determine differences in wall thickness. Based on the findings of previous work described in Section 10.4, finding absolute changes in wall thickness was not expected to be possible with this setup alone. It requires the data to be analyzed using a modelling program, but the work presented in this section aims to find broadly if the signal changes with different wall thicknesses. Thicker walls mean more material is present to trap magnetic flux, which in turn means less magnetic flux will leak out. The axial and radial data can be found in Figure 10-13. The MFL data generally have lower magnitudes and lower peaks when the walls are thicker, as expected.

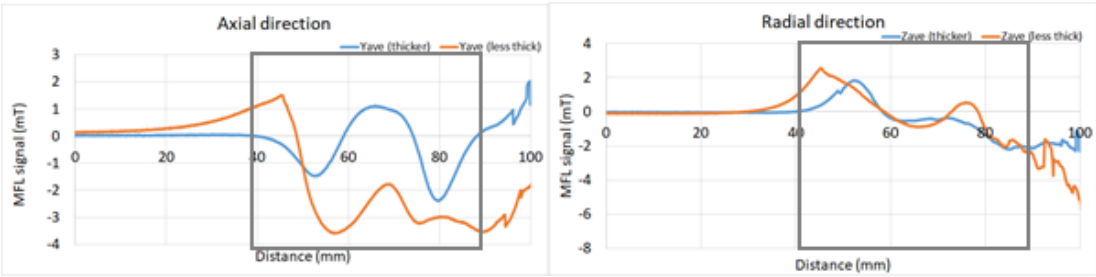

Figure 10-13 Axial and radial MFL data for different wall thicknesses. The gray box represents the specimen location. Generally thicker walls have a more damped MFL profile.

The final test using this setup is locating the weldment in the HS-90™ Tenaris Coiled Tubing (OD: 38 mm, WT: 3.8 mm). These tests had the most subtle and complex changes of those in this section. The weldment should cause a small, localized decrease in signal magnitude, which should also smooth out the peak observed in the middle of the magnetized section, where the magnet changes. In order to get a strong enough signal to detect the weld, 4 additional magnets of the same type (2 on each side) were added inside the pipe to ensure that both the pipe's outer surface and the weldment were saturated. The most apparent result was a more complex field geometry. Figure 10-14 shows the normalized axial and radial data for this set of experiments. The weldment smooths out the magnet interface as expected. The data are normalized by each set's most negative MFL signal. Doing this makes the initial peak larger for the data taken near the weldment, which makes sense because the weldment's presence will cause a larger decrease in the magnetic field observed within the measurement region, as compared to outside the pipe. As with the defect, the dimensions of the weldment are not discernable without significant processing of the raw data.

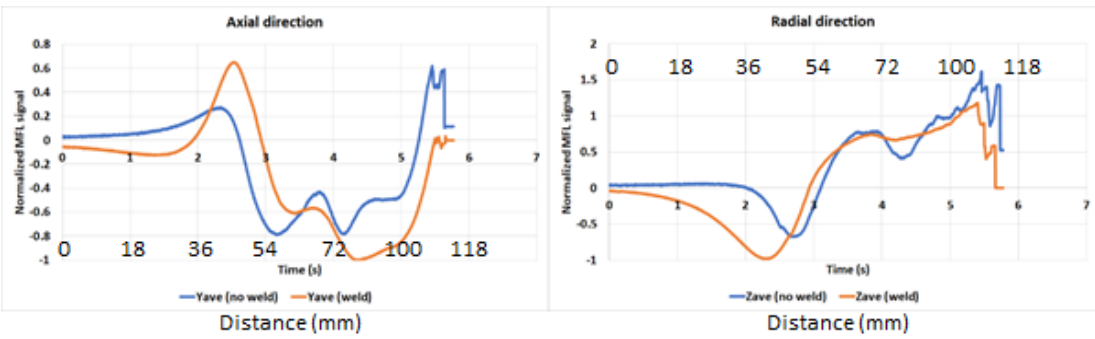

Figure 10-14 MFL data for locating the weldment. The data are normalized individually by experiment's most negative MFL signal. The anomalies observed are the result of edge effects from the pipes and the magnet – magnetic bridge geometry. The probe moves at 18 mm/s across the specimen.

These experiments demonstrate that, in principle, this setup can detect MFL in Coiled Tubing (which was expected). The complex field geometries underscore the need for larger, stronger magnets that can saturate the pipe on their own. Given the need to move the probe quickly through zones of high magnetization, a more robust sensor is also required. The fact that the weldment can be found is an important next step, but the signal is much more subtle than the signal observed in CoilSCAN™, which shows up for the entire length of the weldment, even as it travels rotationally down the Coiled Tubing.

10.5.2 Intermediate tests

10.5.2.1 Internal pipe defects

In order to move from the initial design to the CoilSCAN™ analog, a few intermediate tests were run with internal defects of various depths. These experiments use the new gaussmeter and XY scanning stage (1 mm/s movement speed) but the same permanent magnetic design as in the defect tests described in the previous section. No internal magnets were used. These defects have a cylindrical shape with a half circle cross section. The defect geometry can be found in Figure 10-15.

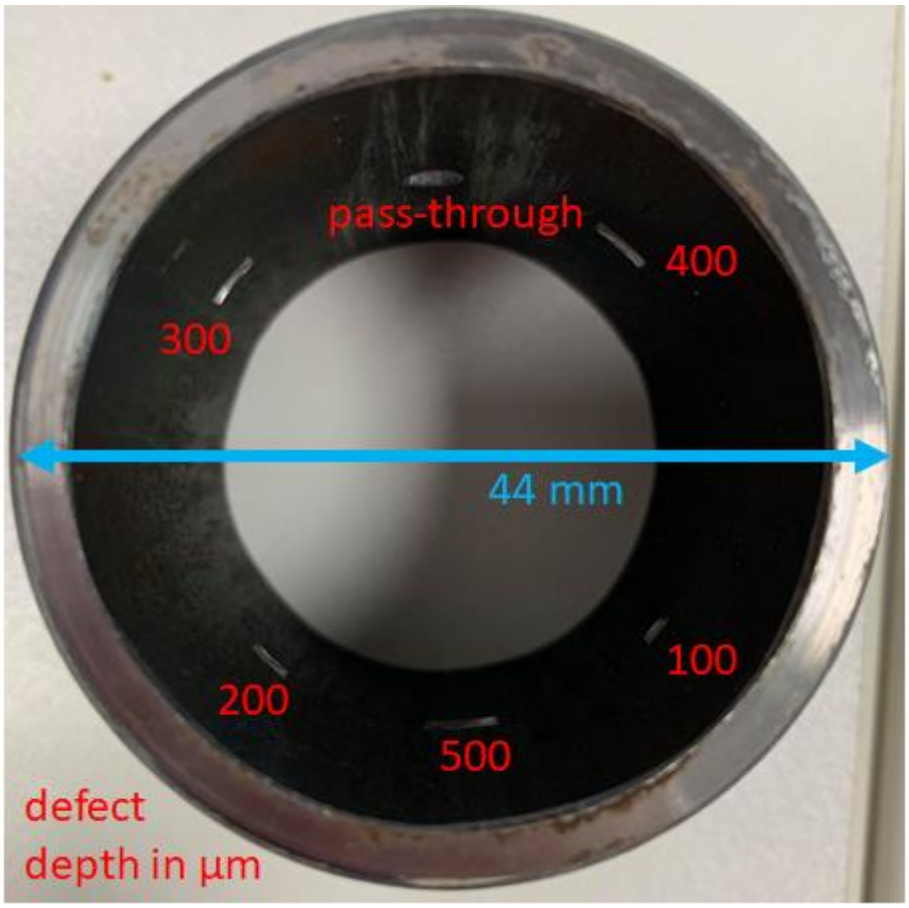

Figure 10-15 Machined internal pipe defects

Figure 10-16 contains the MFL signal as a function of depth (at the deepest point) from 0.1 – 0.5 mm. The most noticeable MFL characteristic of these defects is the symmetric local maxima about a local minimum, located at the approximate location of the defect. The difference between the local maxima and the local minimum increases as the defect's depth increases.

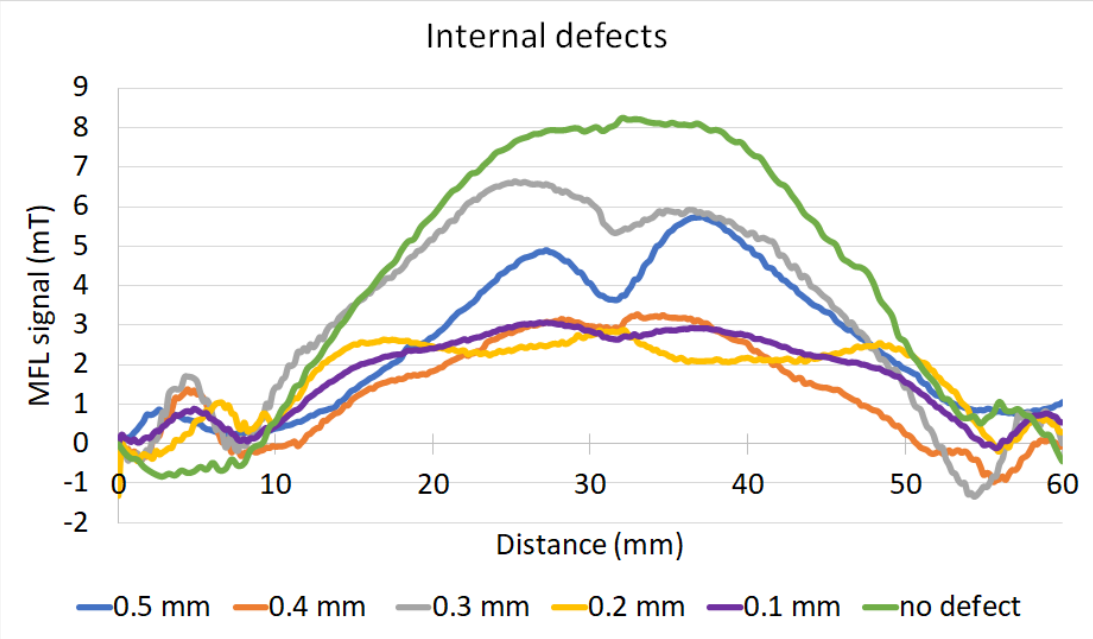

Figure 10-16 Intermediate test with different internal defect depths (at a location of approximately 30 mm). Each line is the average of 4 runs. The pipe sits between 10 and 50 mm on the figure.

The defect's depth and shape cannot be accurately ascertained directly from these data; a computer model would be required, as the background section noted. The differently shaped data is consistent with the defect not being transverse; a sign change in the MFL data would not be expected at these interfaces. The next set of tests was run at double speed (2 mm/s). These data are plotted in Figure 10-17.

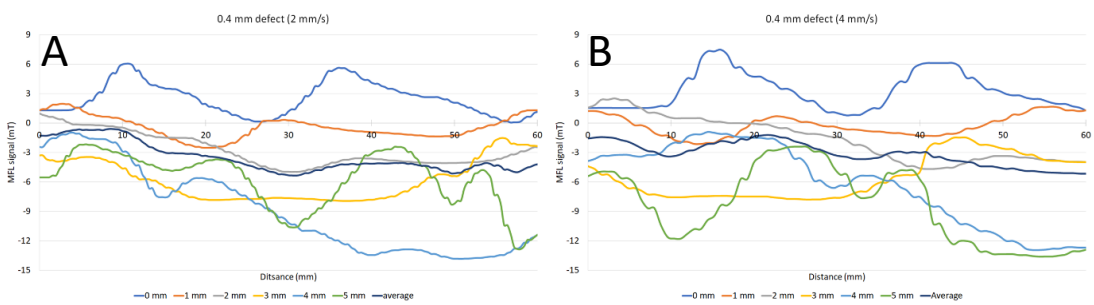

Figure 10-17 Internal defects tests at increased speed. Both are investigating the 0.4 mm defect at speeds of A: 2mm/s and B: 4 mm/s, respectively. The pipe sits between 10 and 50 mm on the figure.

The same shape of signal is observed as in Figure 10-16, with similar magnitudes. These data did not have the background fields removed, as it did not enhance the defect signal. The increased speed leads to more small-scale variations and thus less precise MFL measurements. However, the observed MFL signal from the features (i.e. the difference between the local minimum and local maxima) is significantly larger than the reduced resolution.

Identifying the smallest pit (with a depth of 0.1 mm) is the most important but also the most challenging identification. Therefore, several additional tests were run to determine the limits of locating this defect. The arc length of the defect is smaller than the arc length of the magnetized zone, so six lines were run (which covered the entire arc length of the magnetized zone). These data are plotted in Figure 10-18. As noted in the figure, finding the initial defect required subtracting out the background magnetic field.

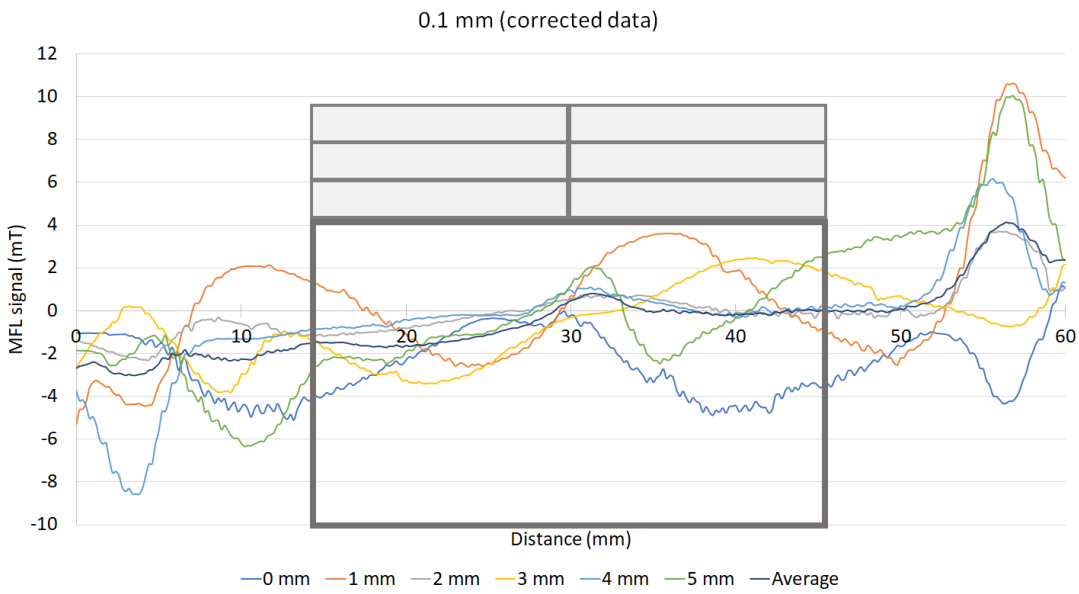

Figure 10-18 The 0.1 mm internal defect has a subtle signal peak located around 30 mm, when corrected for the background magnetic field. The pipe sits between 10 and 50 mm on this figure.

10.5.2.2 External plate defects

The next series of tests run use a flat steel plate with 100 total defects in a 2 cm x 2 cm area. The plate can be seen in Figure 10-19 and Figure 10-20, and it has 4 types of defects (25 each): 0.4 mm diameter x 0.3 mm depth, 0.4 mm diameter x 0.1 mm depth, 0.2 mm diameter x 0.3 mm depth, and 0.2 mm diameter x 0.1 mm depth. These defect sizes were selected based on proprietary acid pitting data from field tests that showed these sizes of defects to be among the largest observed and the smallest that the machine shop could reliably drill. These are therefore the natural first step to try to detect. Figure 10-21 contains an overlay of the defects for more information on their ordering.

The first tests quantified the reproducibility of the raw data in the zone of interest. These data can be found in Figure 10-19. The data are reproducible within <1% in the zone of interest. The largest anomalies in the data are found at the far end of the plate, where the probe exits the magnetized zone.

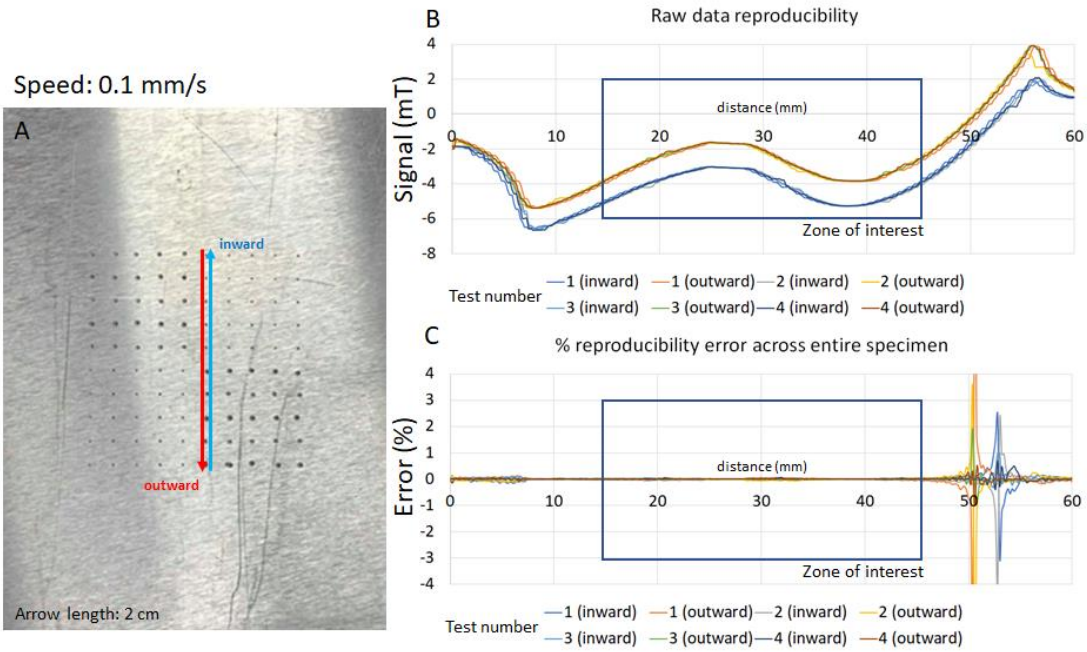

Figure 10-19 Data reproducibility. For all the following figures, blue lines are inward; red lines are outward.

The data were then filtered using a second order Butterworth filter (which minimizes oscillatory artifacts) to extract the signal from the defects on the plate's top surface. The normalized frequency used for the filter were defined using the sampling rate (5 Hz) and speed (0.1 – 2 mm/s). From these tests, Figure 10-20 was obtained.

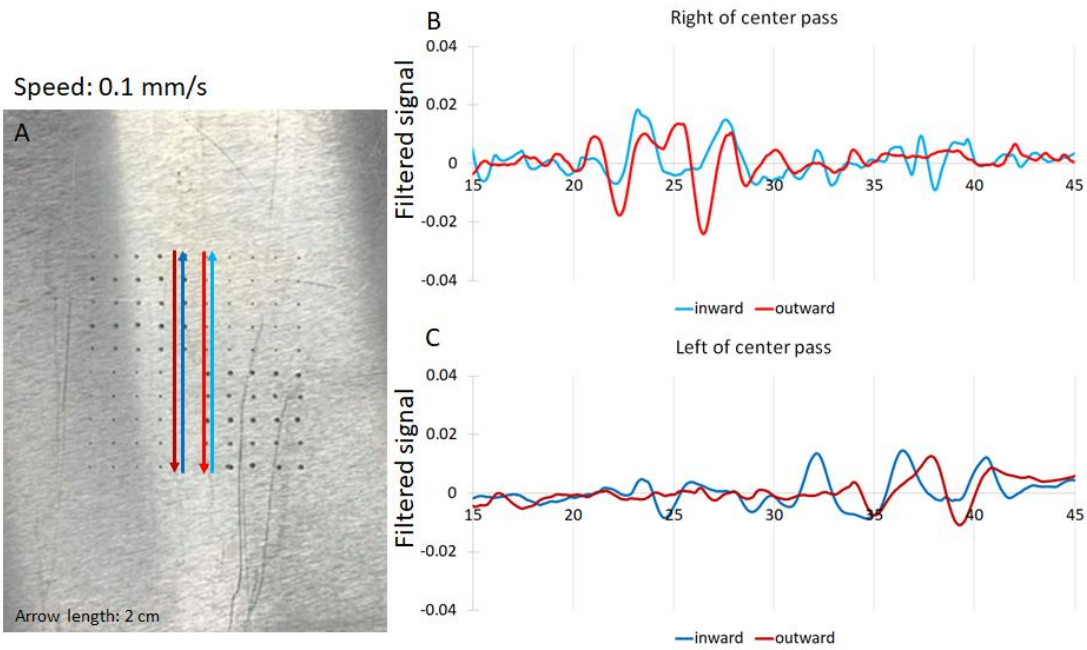

Figure 10-20 Initial defect location tests.

The setup allows for an XY raster between the two sets of magnets, so running the same test as before but over 7 sets of lines, for 14 total lines, gives a 2D profile of the defects' MFL magnitude in the 'radial' direction. The data from these tests can be found in Figure 10-21, both with and without defects, respectively.

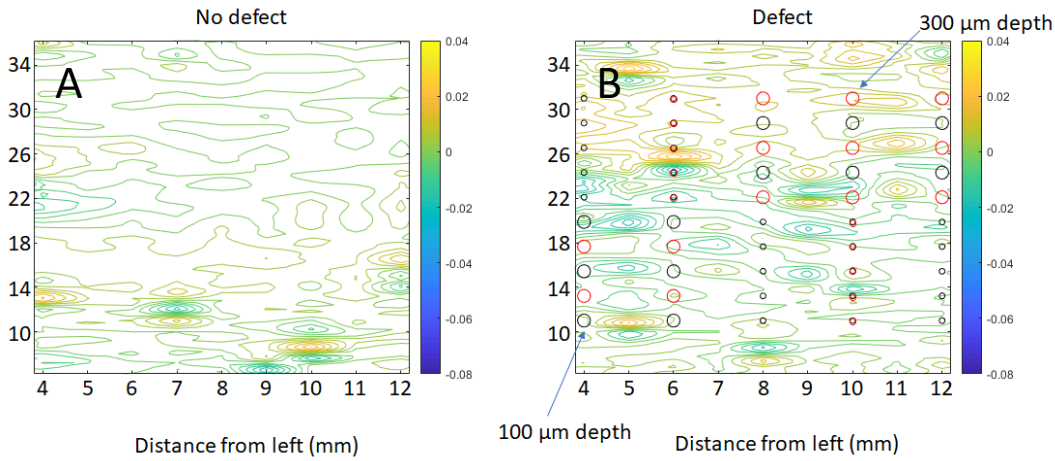

Figure 10-21 XY raster using permanent magnets. A: without defects. B: with defects. Black defects have 100 µm depth and red defects have 300 µm depth. Large defects have a diameter of 400 µm and small defects have a diameter of 200 µm.

These tests show that patches of defects can be located but individual defects cannot be located. It therefore appears that the sensitivity limit of this setup has been reached. The next section exchanges the permanent magnets from this section for an electromagnetic yoke to try to increase the sensitivity again.

10.5.3 CoilSCAN™ analog

With the completion of the proof of concept and transition design tests, the CoilSCAN™ analog setup was built. The permanent magnets described in the previous section were replaced with a mains-powered MY-2 electromagnetic yoke. The yoke has an operation time of 30s, so each scan segment must be completed in this timeframe. The magnetic field of the yoke will be both stronger and simpler than the previous design, given the geometry of the yoke. These tests use a plate with machined defects instead of a steel pipe specimen. The yoke is not directly in contact with the sample, which means that more magnetic flux leaks into the air at the yoke's base than with the permanent magnets, but the increased distance from the measurement zone means that the measurements are less sensitive to variations in lift-off distance.

The tests run and described herein investigated a 30 x 30 mm zone that completely contained the 20 x 20 mm defect zone. Two tests were run: one with the defects on the same side of the plate as the gaussmeter and the yoke and one with the defects on the opposite side. The results from the first set of tests, with the defects on the same side as the magnets and the gaussmeter can be found in Figure 10-22. The results from the second set of tests, with the defects on the opposite side, can be found in Figure 10-23.

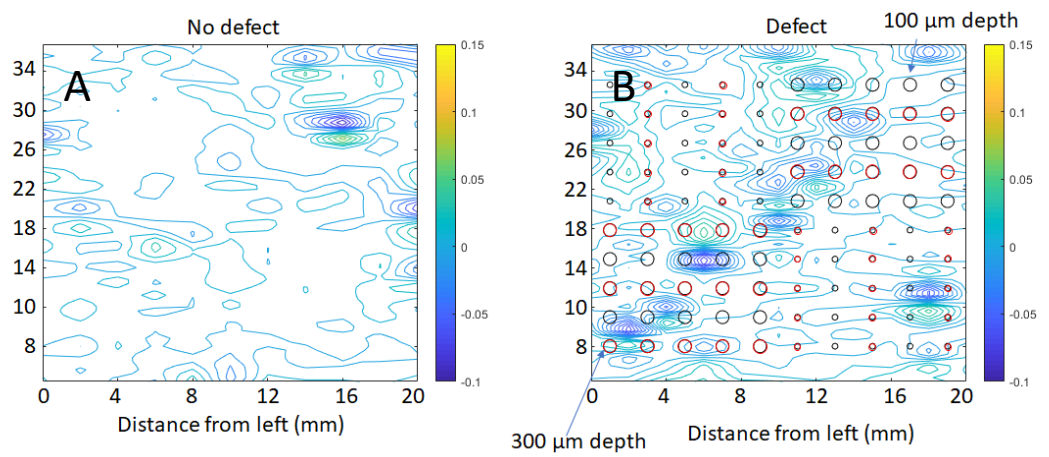

Figure 10-22 3D raster of sample plate, with defects and gaussmeter on the same side. A: when no defects are present, few peaks in the magnetic field are observed. B: more peaks appear when defects are present, but the peaks are relatively generalized, compared to the scale of the area and the defects.

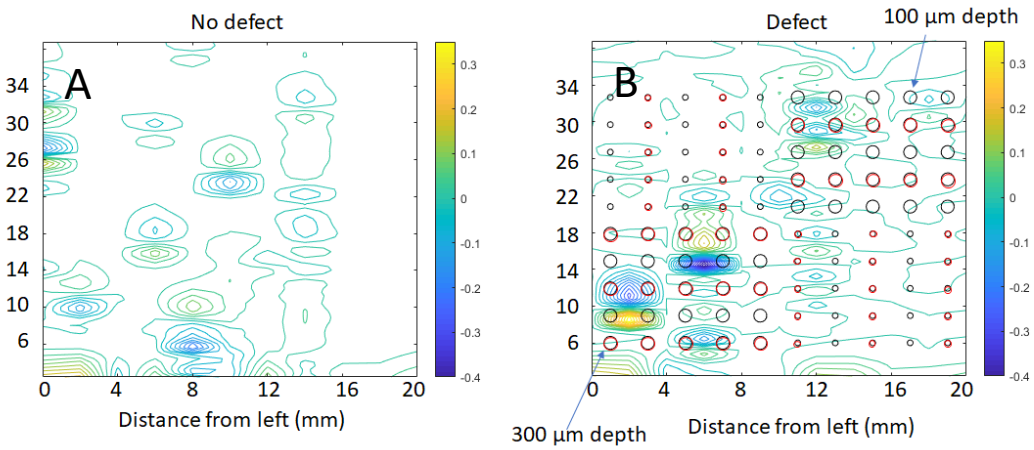

Figure 10-23 3D raster of sample plate, with defects and gaussmeter on opposite sides. A: when no defects are present, few peaks in the magnetic field are observed. B: more peaks appear when defects are present, but the peaks are relatively generalized, compared to the scale of the area and the defects.

The MFL data in this section demonstrate that large concentrations of small defects (in the upper range of acid pitting observed in the field) can be qualitatively detected. A clear difference can be observed in both the number of peaks and the magnitude of the peaks in MFL signal for defects both on the (relative) inside and outside of the pipe simulation. Individual defects of these sizes, or the density of defects cannot, reliably be detected with the MFL setup herein.

10.6 Non-magnetic defect characterization

The machined plate standard has known defect diameters and depths, but given the small sizes of the defects, the internals of the defect can potentially affect the defect's MFL signal. The bottom of the defect has an uncharacterized shape, defined by that of the drill bit used, and potentially metallic debris left in the holes from drilling. The effects cannot be directly deconvolved from the MFL signals generated, so instead contact profilometry and 3D microscopy were used to investigate the true size and shape of the defects.

10.6.1 Contact profilometry

The first characterization method used is also the simpler technique, as the computer simply records the position of the stylus head. Lines were taken to the left and the right of the line of defects to create a 2D depth map of a subset of the defects. The subset used was a line of deep, wide defects. The results of this investigation are given in Figure 10-24.

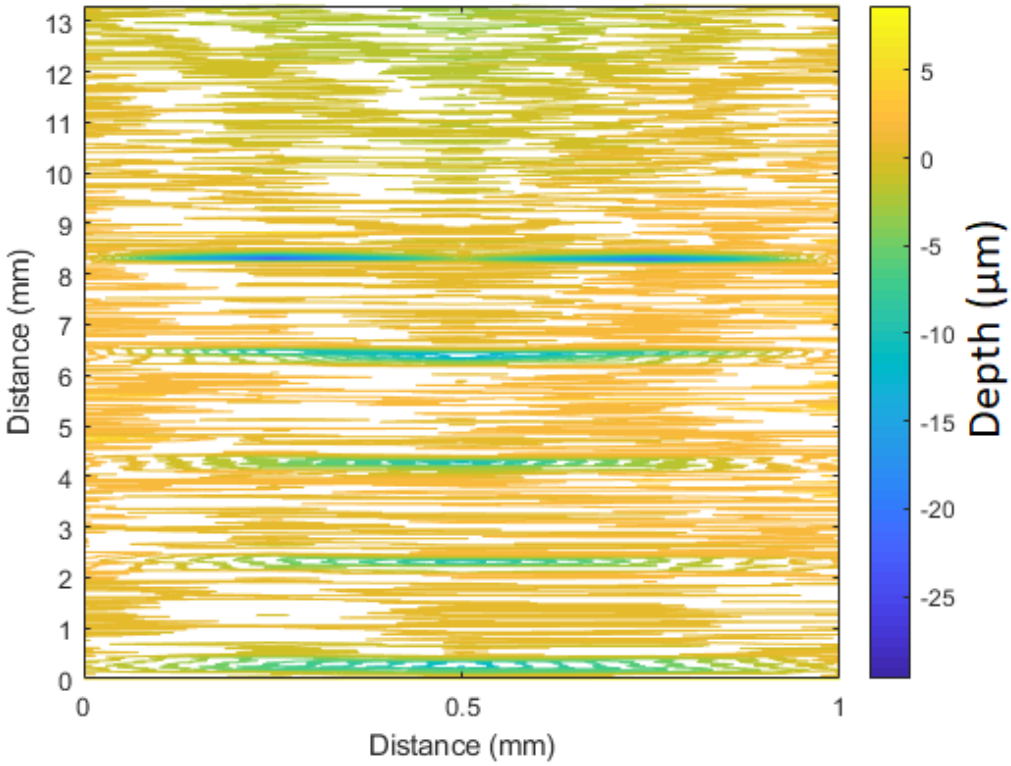

Figure 10-24 Contact profilometry of the plate. The data show the presence of defects, but the probe was unable to correctly size the pits.

It is apparent from the depth data that there is a problem, as the depths measured are 10 – 30 µm, instead of the 100 or 300 µm depths expected and one of the defects appears bifurcated. The defects either have large errors or the profilometer could not measure these types of defects correctly. To determine the more likely explanation, a non-contact technique is necessary.

10.6.2 Scanning Electron Microscopy

A Scanning Electron Microscope (SEM) was used to examine the defects individually to investigate the extent to which each defect was contaminated with debris from drilling. Using the SEM's focusing mechanism, the shallower defects were determined (to 1 significant figure) to be 0.1 mm in depth and the deeper defects were determined to be 0.3 mm in depth. Debris is observed in all the defects, ranging in size from approximately 0.02 to 0.05 mm. Figure 10-25A contains a shallower, wider defect. This defect type has a non-circular cross-section, which is a result of the shallow depth relative to the size of the drill bit used. Figure 10-25B contains a deeper, wider defect. This defect has the correct cross-section and a relatively small amount of internal debris. Figure 10-25C is an image of a shallower, narrower defect. These types of defects have the most internal debris, which cover more than 2/3 of the internal surface. This defect does not show the same type of non-circular cross-section

as in Figure 10-25A because the depth is larger relative to the drill bit size. Figure 10-25D contains an example of a deeper, narrow defect. This defect has the largest depth to width ratio and correspondingly has the least amount of debris with a properly circular cross-section.

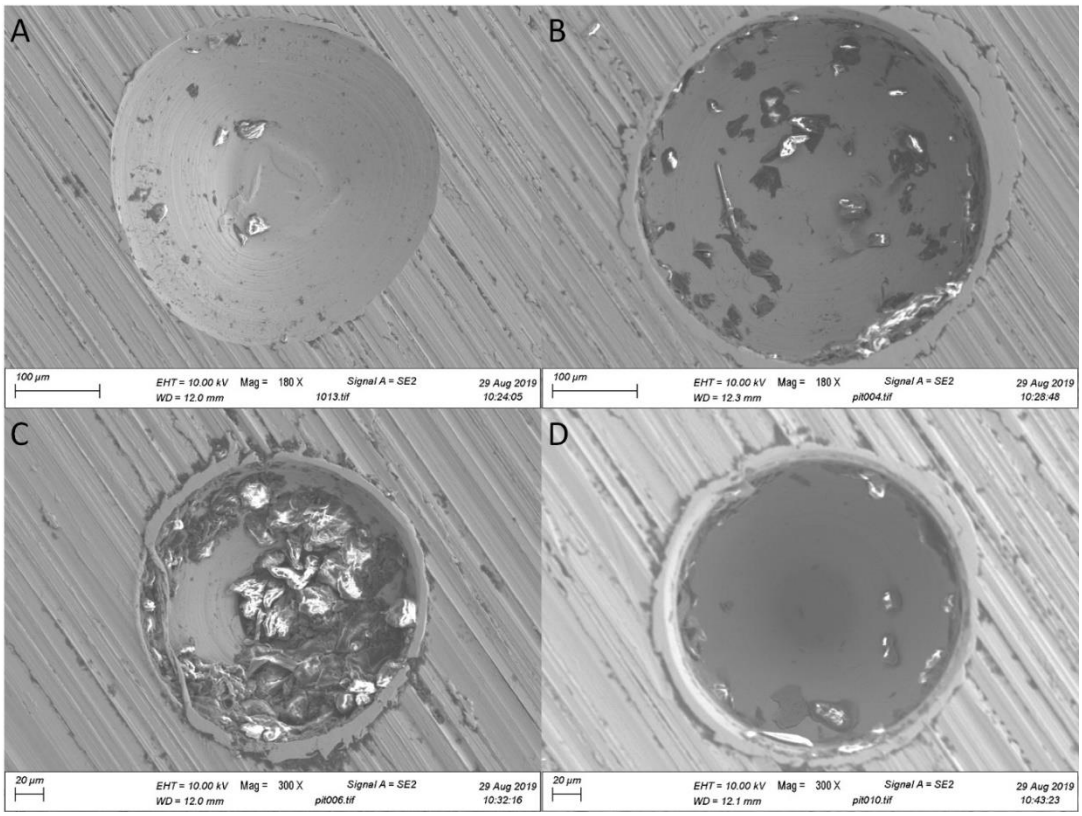

Figure 10-25 SEM images of machined defects. A) shallow and wide, B) deep and wide, C) shallow and narrow, and D) deep and narrow

The SEM confirmed that all the defects are the correct shape within <10% and have the correct depth to within 1 significant figure, which is a substantial improvement over the data from contact profilometry.

10.7 Conclusions

In this section, magnetic survey techniques were applied to an open question in the oil and gas industry: how sensitive can CoilSCAN^{TM} become? The COMSOL simulations run for this setup showed that large-scale features and closely packed small-scale features could be detected. The initial tests run using permanent magnets confirmed the models and showed that differences in the width of holes and depth of internal defects in the walls of stainless-steel tubing can be detected using the laboratory magnetic flux leakage setup.

With the more powerful electromagnet, dense patches of smaller defects can be detected as a scattered series of peaks. The data quality is currently insufficient to detect the defects individually. The debris in the smallest defects also decreases the magnitude of the magnetic flux leakage signal. These tests have preliminarily shown that severe acid pitting can be detected using magnetic flux leakage. Currently, CoilSCAN™ primarily finds single, large defects; these tests have further expanded MFL surveys into the second dimension and shown that large densities of smaller defects can be also located.

The questions now become centered around defect density and a further extension to in-field acid pitted specimens of coiled tubing. Currently, the single hall probe system has not tested the effect of lift-off distance on the data and cannot determine the size of individual defects or their number density (directly or from dimensional analysis in a computer program). More sensors or even a full CoilSCAN™ setup, however, might be capable of doing so.

10.8 References

Afghoul, A. C., Amaravadi, S., Boumali, A., Neves Calmeto, J. C., Lima, J., Lovell, J., Tinkham, S., Zemlak, K., and Staal, T., 2004, Coiled Tubing: The Next Generation: Oilfield Review, v. Spring 2004, p. 38-57.

Amineh, R. K., Koziel, S., Nikolova, N. K., Bandler, J. W., and Reilly, J. P., 2008, A Space Mapping Methodology for Defect Characterization From Magnetic Flux Leakage Measurements: Ieee Transactions on Magnetics, v. 44, no. 8, p. 2058-2065.

Avery, M., Large, R., Azhar, H., Wong, K. S., and Yusoff, M. F. B., 2019, Asia's First Rigless Subsea Stimultion Using Patented Well Access Technology and a Fully Integrated Service Model, SPE Subsea Well Intervention Symposium: Galveston, Texas, USA, Society of Petroleum Engineers.

Barmatov, E., Hughes, T., and Eskin, D., 2016, Effect of surface roughness on corrosion behaviour of low carbon steel in inhibited 4 M hydrochloric acid under laminar and turbulent flow conditions: Corrosion Science, v. 103, p. 196-205.

Barmatov, E., Hughes, T., and Nagl, M., 2015, Efficiency of film-forming corrosion inhibitors in strong hydrochloric acid under laminar and turbulent flow conditions: Corrosion Science, v. 92, p. 85-94.

Boumali, A., Brady, M. E., Ferdiansyah, E., Kumar, S., van Gisbergen, S., Kavanagh, T., Ortiz, A. Z., Ortiz, R. A., Pandey, A., Pipchuk, D., and Wilson, S., 2005, Coiled Tubing: Inovative rigless interventions: Oilfield Review, v. December.

Brondel, D., Edwards, R., Hayman, A., Hill, D., Mehta, S., and Semerad, T., 1994, Corrosion in the oil industry: Oilfield Review, v. 6, no. 2, p. 4-18.

Christian, A., and Tipton, S. M., 2009, Statistical Analysis of Coiled Tubing Fatigue Data, SPE/ICoTA Coiled Tubing and Well Intervention Conference and Exhibition: The Woodlands, Texas, USA, Society of Petroleum Engineers.

Christie, R., Liu, Z., Stanley, R., Torregrossa, M., Zheng, A., and Zsolt, L., 2015, Monitoring and Managing Coiled Tubing Integrity: Oilfield Review, v. 27, no. 1.

Crabtree, A. R., and Gavin, W., 2005, Coiled tubing in sour environments: Theory and practice: Spe Drilling & Completion, v. 20, no. 1, p. 71-80.

Deffo, Y., Tsafack, P., Ducharne, B., Le, M., and Cottinet, P., 2019, Effect of bending stress on the magnetic properties of electrical steel using needle probe method: COMPUMAG, v. Jul 2019.

Dutta, S. A., Ghorbel, F. H., and Stanley, R. K., 2009a, Simulation and Analysis of 3-D Magnetic Flux Leakage: Ieee Transactions on Magnetics, v. 45, no. 4, p. 1966-1972.

Dutta, S. M., 2008, Magnetic flux leakage sensing: The forward and inverse problems [Doctor of Philosophy: Rice University.

Dutta, S. M., Ghorbel, F. H., and Stanley, R. K., 2009b, Dipole Modeling of Magnetic Flux Leakage: Ieee Transactions on Magnetics, v. 45, no. 4, p. 1959-1965.

Finsgar, M., and Jackson, J., 2014, Application of corrosion inhibitors for steels in acidic media for the oil and gas industry: A review: Corrosion Science, v. 86, p. 17-41.

Gallagher, P., Kemp, C., Hudson, L., Liu, Z., and Rivas Diaz, O. O., 2015, Extending Coiled Tubing String Utilization by Real-Time Field Inspections, Abu Dhabi International Petroleum Exhibition and Conference: Abu Dhabi, UAE.

Han, W., Wu, Z., Zhou, M., Hou, E., Su, X., Wang, P., and Tian, G., 2017, Magnetic Flux Leakage Signal Inversion Based on Improved Efficient Population Utilization Strategy for Particle Swarm Optimization: Russian Journal of Nondestructive Testing, v. 53, no. 12, p. 862-873.

Ho, M. Y., Geddes, J., Barmatov, E., Crawford, L., and Hughes, T., 2018, Effect of composition and microstructure of duplex stainless steel on adsorption behaviour and efficiency of corrosion inhibitors in 4 molar hydrochloric acid. Part I: Standard DSS 2205: Corrosion Science, v. 137, p. 43-52.

Jackson, R. B., Vengosh, A., Carey, J. W., Davies, R. J., Darrah, T. H., O'Sullivan, F., and Petron, G., 2014, The Environmental Costs and Benefits of Fracking, *in* Gadgil, A., and Liverman, D. M., eds., Annual Review of Environment and Resources, Vol 39, Volume 39: Palo Alto, Annual Reviews, p. 327-362.

Kahrilas, G. A., Blotevogel, J., Stewart, P. S., and Borch, T., 2015, Biocides in Hydraulic Fracturing Fluids: A Critical Review of Their Usage, Mobility, Degradation, and Toxicity: Environmental Science & Technology, v. 49, no. 1, p. 16-32.

Khodayari-Rostamabad, A., Reilly, J. P., Nikolova, N. K., Hare, J. R., and Pasha, S., 2009, Machine Learning for the Analysis of Magnetic Flux Leakage Images in Pipeline Inspection: IEEE Transactions on Magnetics, v. 45, no. 8, p. 3073-3084.

Kopp, G., and Willems, H., 2013, Sizing limits of metal loss anomalies using tri-axial MFL measurements: A model study: Ndt & E International, v. 55, p. 75-81.

Li, Y., Wilson, J., and Tian, G. Y., 2007, Experiment and simulation study of 3D magnetic field sensing for magnetic flux leakage defect characterisation: Ndt & E International, v. 40, no. 2, p. 179-184.

Liu, Z., Kenison, M., and Campbell, G., 2016, A Hybrid Approach of Coiled Tubing Fatigue Assessment Considering Effects of Localized Damage Based on Magnetic Flux Leakage Measurements, SPE/ICoTA Coiled Tubing and Well Intervention Conference and Exhibition: Houston, Texas, USA.

Liu, Z., Minerbo, G., and Zheng, A., 2014, Steel Coiled Tubing Defect Evaluation Using Magnetic Flux Leakage Signals, SPE/ICoTA Coiled Tubing and Well Intervention Conference and Exhibition: The Woodlands, Texas, USA.

Liu, Z., Wiranata, K., Ridene, A., Wortmann, H., Bucher, R., Campbell, G., Bulloch, S., and Chaari, Y., 2017, Utilization of Monitoring Inspection and Evaluation Technology in Safeguarding Pipe Integrity for Coiled Tubing Drilling Operations, SPE Europec featured at 79th EAGE Conference and Exhibition: Paris, France.

Liu, Z., Zheng, A., Rivas Diaz, O. O., and Hauglund, L., 2015, A Novel Fatigue Assessment of Coiled Tubing with Defects Based on Magnetic Flux Leakage, SPE/ICoTA Coiled Tubing and Well Intervention Conference and Exhibition: The Woodlands, Texas, USA.

Mandal, K., and Atherton, D. L., 1998, A study of magnetic flux-leakage signals: Journal of Physics D-Applied Physics, v. 31, no. 22, p. 3211-3217.

McJunkin, T. R., Miller, K. S., and Tolle, C. R., 2006, Observations on Characterization of Defects in Coiled Tubing from Magnetic-Flux-Leakage Data, SPE/ICoTA Coiled Tubing Conference and Exhibition: The Woodlands, Texas, USA.

Ottolina, R., Torres, C., and Rudnik, A., 2016, Deepwater Riserless Operations with Coiled Tubing in the Gulf of Mexico: An Innovative, Safe, and Efficient Plug-and-Abandonment Technique, SPE/ICoTA Coiled Tubing and Well Intervention Conference and Exhibition: The Woodlands, Texas, USA.

Padron, T., Luft, B. H., Kee, E., and Tipton, S. M., 2007, Fatigue Life of Coiled Tubing with External Mechanical Damage, SPE/ICoTA Coiled Tubing and Well Intervention Conference and Exhibition: The Woodlands, Texas, USA, Society of Petroleum Engineers.

Rahman, A. A. A., Hamzah, N. E., Ahmed Fauzi, N. B., El-hariry, H. F., Jenie, J. R., and Chaari, Y., 2012, Drilling Performance Optimization on Malaysia's first Coiled Tubing Drilling Project: A Case Study, IADC/SPE Asia Pacific Drilling Technology Conference and Exhibition: Tianjin, China, Society of Petroleum Engineers.

Ravan, M., Amineh, R. K., Koziel, S., Nikolova, N. K., and Reilly, J. P., 2010, Sizing of 3-D Arbitrary Defects Using Magnetic Flux Leakage Measurements: Ieee Transactions on Magnetics, v. 46, no. 4, p. 1024-1033.

Reichert, B., Nguyen, T., Rolovic, R., and Newman, K., 2016, Advancements in Fatigue Testing and Analysis, SPE/ICoTA Coiled Tubing and Well Intervention Conference and Exhibition: The Woodlands, Texas, USA, Society of Petroleum Engineers.

Sherman, S., Brownlee, D., Kakadjian, S., and Luft, B., 2014, Microbial Influenced Corrosion of Coil Tubing Milling Strings in the Eagle Ford Shale, International Petroleum Technology Conference.

Stayer, A., Zwanenburg, M., Scuadroni, N., Zheng, A., Liu, Z., and Burgos, R., 2013, State-of-the-Art Portable Measurement and Defect Detection Technology for Coiled-Tubing String, Society of Petroleum Engineers: The Woodlands, Texas, USA.

Sun, Y. H., and Kang, Y. H., 2013, Magnetic mechanisms of magnetic flux leakage nondestructive testing: Applied Physics Letters, v. 103, no. 18.

Sun, Y. H., Liu, S. W., Jiang, X. Y., He, L. S., Gu, M., Liu, C. D., Kang, Y. H., Luo, X., and Xu, J., 2019, A Novel Electromagnetic Testing Method Based on the Magnetic Field Interaction: Ieee Transactions on Magnetics, v. 55, no. 8.

Torregrossa, M., Zsolt, L., and Zwanenburg, M., 2014, Optimizing Pipe Management with a New Approach of Coiled Tubing Integrity Monitoring., SPE/ICoTA Coiled Tubing and Well Intervention Conference and Exhibition: The Woodlands, Texas, USA, Society of Petroleum Engineers.

Usman, B. J., and Ali, S. A., 2018, Carbon Dioxide Corrosion Inhibitors: A review: Arabian Journal for Science and Engineering, v. 43, no. 1, p. 1-22.

Wang, Y., Liu, X., Wu, B., Xiao, J., Wu, D., and He, C., 2018, Dipole modeling of stress-dependent magnetic flux leakage: Ndt & E International, v. 95, p. 1-8.

Wu, J. B., Fang, H., Li, L., Wang, J., Huang, X. M., Kang, Y. H., Sun, Y. H., and Tang, C. Q., 2017, A Lift-Off-Tolerant Magnetic Flux Leakage Testing Method for Drill Pipes at Wellhead: Sensors, v. 17, no. 1.

Xu, C., Wang, C. L., Ji, F. Z., and Yuan, X. C., 2012, Finite-Element Neural Network-Based Solving 3-D Differential Equations in MFL: Ieee Transactions on Magnetics, v. 48, no. 12, p. 4747-4756.

CHAPTER 11 CONCLUSIONS AND FUTURE WORK

In Chapter 1, the goals of this thesis were set out: to test new equipment in, validate new techniques for, and expand the utility of, the next generation of paleomagnetic laboratory. The success of the continuous magnetometer for limited, low temperature applications and the success of the stepwise magnetometer for two types of paleointensity protocols mean that a new, versatile instrument has entered the field of paleomagnetism. The first section, the magnetometer, cataloged the design and construction of the prototype from its beginning stages (just an oven and a single SQUID sensor) to a three-axis prototype continuous magnetometer and then to a fully operational three-axis prototype stepwise magnetometer, capable of both demagnetizing and remagnetizing specimens in-situ.

The second goal, to validate paleointensity techniques, was accomplished over four chapters using eleven well-tested and three new techniques. The second section presented four research projects that investigated the intricacies and optimizations of existing paleointensity methods. The first experiments examined the magnetic behavior of young, well-studied lava flows before being expanded to older lava flows from the Carboniferous time period, whose data is of paramount importance. This section further aided in the selection of the rock samples best suited for testing the new magnetometer system's capabilities.

The third goal, to expand the utility of a paleomagnetic laboratory was completed in Chapter 10. This third section expanded the magnetics work in the first two sections with an application to work done with an external, industrial partner, Schlumberger. The work therein introduced, literally and figuratively, a new dimension to magnetic surveys of steel piping for use in the energy sector.

11.1 Magnetometer (Chapters 2 – 5)

The single-axis and three-axis continuous prototypes showed that a continuous SQUID magnetometer system is possible up to temperatures around 300 °C, which is comparable to some of the other continuous magnetometers currently in operation. In the time it takes to reach these temperatures, the SQUIDs' offset began to drift and subsequently required on-the-fly retuning. Every time the SQUIDs were reset and retuned, the data collection process was interrupted, which limited the ability of the SQUIDs to correctly collect the data in a continuous manner. SQUIDs are not generally used in applications that require continuous operation, and as such they are not designed for this type of operational environment. A

continuous magnetometer with a maximum temperature of 300 °C does, however, have some applications, such as studying multi-domain structural changes or self-reversal in grains with low blocking temperatures. These applications can benefit from the improved resolution provided by the SQUIDs.

The three-axis stepwise prototype showed that by separating the SQUID components from the oven, the maximum temperature of the specimen can increase to at least 540 °C, without causing the SQUIDs to drift uncontrollably. This oven temperature was sufficient to demagnetize the tested specimens by at least 70%. The oven's maximum temperature of 700 °C means that the maximum operational specimen temperature can be pushed higher, once the geometric issues noted in Chapter 5 can be remedied. This thesis describes paleomagnetic surveys using specimens given artificial NRMs from laboratory TRMs and then de-/remagnetizing them in the magnetometer. Accurate paleodirection and paleointensity data were able to be obtained from these experiments, but the large errors in some results mean that the data are, as of yet, merely preliminary. Experiments going forward will also need to be done taking into account everything learned about the most common Thellier methods in Chapters 6 – 9 because, despite the magnetometer currently using a full-TRM method, thermochemical alteration and non-SD grain effects can still affect the recorded data.

11.2 Paleointensity methods (Chapters 6 – 9)

In these chapters, the reliability and versatility of eleven existing paleointensity methods and three new methods were examined. In Chapter 6, MW-IZZI+, MW-Perp++, and MW-Perp were investigated, with MW-IZZI+ giving the best results. In Chapter 7, Th-OT+, Th-Perp, MW-OT+, and MW-Perp were tested, with MW-OT+ giving the best data (but not without its pitfalls). In Chapter 8, Th-IZZI+, Th-AF-IZZI+, Th-LTD-IZZI+, MW-IZZI+, and MW-LTD-IZZI+ were examined, with the MW-IZZI+ data proving the most reliable. In Chapter 9, Th-Coe+ and HiTeCT(+/++) were tested, with HiTeCT failing to provide new, meaningful data. Further, the studies in this thesis have shown that Th-OT+ and MW-Perp experiments should largely be avoided due to the unacceptably high probability of erroneous estimates (Chapters 6 and 7). In addition, although Th-LTD-IZZI+ and MW-LTD-IZZI+ as techniques are not inherently problematic, both require significantly more time than their non-LTD variants, without providing substantially better data (Chapter 8). Avoiding the lowest temperature components, while still providing a full paleointensity experiment, substantially improves data consistency and reliability (Chapter 7 and 9).

Each chapter, however, has left a few unanswered questions. In the 1960 Kilauea lava flow data in Chapter 6, can the findings from the different MW protocols be applied to the respective thermal protocols? Chapter 7 seems to suggest they cannot be, but the result is unclear. In the SOH1 data from Chapter 7, how would MW-IZZI+ data fit into the structure? Would its data be comparable to the MW-OT+ data? In the Kinghorn data in Chapter 8, do the three new sites actually give Carboniferous paleointensities? New, oriented cores are required. In Chapter 9, if the abridged Thellier-Coe experiments work better than either the full Thellier-Coe experiments or the HiTeCT experiments, where is the inflection point? That is, what is the optimal starting temperature for these experiments? Would chemical analyses and SEM imaging help constrain which specimens are suitable for HiTeCT experiments?

Taking all these remaining questions into account, the methods broadly recommended going forward (when technical considerations allow) are: Th-AF-IZZI+ (Chapter 8) and MW-IZZI+ (chapter 6).

11.3 Magnetic flux leakage (Chapter 10)

The work done with Schlumberger for this thesis expanded laboratory-based MFL surveys from simple line measurements to two-dimensional surface measurements using a single Hall probe. Dense patches of smaller defects were able to be detected as a scattered series of peaks along the surface of the test plate. Although the data quality was thus far insufficient to detect individual peaks, the tests showed that severe acid pitting can be detected using the magnetic flux leakage technique. Further experiments with different test plates and additional Hall probes can potentially bridge the gap between the setup described in Chapter 10 (1 sensor) and the CoilSCAN™ equipment supplied by Schlumberger (64 sensors). Despite all the progress made to find the smallest defects, two major questions remain, however, which also keeps the potential for additional collaboration open. What is the effect of the number density of the defects on the MFL dataset? How does the lift-off distance affect the MFL data for this type of defect structure?

11.4 Outputs

This thesis has already yielded three external outputs, and three more are planned in the immediate future. The entirety of Chapter 6 was published as an article, titled "Solving the mystery of the 1960 Hawaiian lava flow: implications for estimating Earth's magnetic field" in *Geophysical Journal International* (https://doi.org/10.1093/gji/ggz252). The entirety of Chapter 7, under the title, "Comparison of thermal and microwave paleointensity estimates in specimens displaying non-ideal behavior in Thellier-style paleointensity experiments," was accepted for publication in July 2020 in the *Journal of Geophysical Research – Solid Earth*

(https://doi.org/10.1029/2020JB019802). Chapter 10 also became an internal Schlumberger report on both magnetic flux leakage and CoilSCAN™. The typeset, published versions of Chapter 6 and Chapter 7 are available in Supplementary Information F.

Material from Chapter 5 will be adapted into a paper on the design and operation of the magnetometer– once the modifications, noted in Chapter 5, have been completed– and I intend to continue the use and development of it as an important aspect of my research in the future. The Th-AF-IZZI+ data from Chapter 8 is to be included in a paper on the Mid-Paleozoic Dipole Low, which will soon be submitted to the *Proceedings of the National Academy of Sciences*. Finally, the remaining Chapter 8 data, which substantially builds upon the previous dataset by including additional paleointensity methods (e.g. the LTD data), will be worked into a publication (of the same title as Chapter 8). These data provide key insights into the behavior of specimens in paleointensity experiments but are extraneous to the Mid-Paleozoic Dipole Low.

11.5 Future work

The logical next step for the magnetometer, once the testing and calibration described in Chapter 5 is complete, is to do paleomagnetic surveys on specimens with true, non-laboratory-induced NRMs. The SOH1, 1960 Kilauea, and Kinghorn specimens from Chapter 6, Chapter 7 and Chapter 8, respectively, are the obvious candidates. These specimens provide a range of well-quantified, commonly-found magnetic properties and paleointensity estimates (2 – 60 µT). These paleointensity experiments can be run immediately using either the demagnetization comparison experiments or in-situ remagnetization experiments and, in the future, with Thellier-style experiments, adapted for use in the new magnetometer system.

Many of the remaining questions from each chapter can be investigated going forward with meta-analyses across multiple datasets and cross-analyses through different rock formations or lava flows. For example, the logical next step with the SOH1 drill core dataset is to restudy each lava flow using the MW-IZZI+ method. It would likely make a straightforward master's thesis project. On the other hand, the introduction of the new magnetometer and its two proprietary paleointensity techniques means that the new data it will provide will still require independent validation against other datasets from the same formations. Thus, the validation of paleointensity techniques is still an on-going process. The logical next step will be to compare its new data with the existing datasets, mirroring the process for the HiTeCT experiments in Chapter 9.

The magnetic flux leakage project (in collaboration with Schlumberger) showed that, through flexible utilizations of existing research methods, magnetic techniques have important applications not just to the oil and gas industry but also to the non-destructive testing field at large. A continued academic-industrial partnership in collaboration with Schlumberger remains feasible, pending a global economic recovery in the near future.

11.6 Afterword: the next generation

From this thesis, it can now be confirmed that the next generation of versatile paleomagnetic laboratory has the best equipment and is capable of both running large quantities of any paleomagnetic test and handling magnetic surveys of ferromagnetic materials. Paleomagnetism should not remain as a primarily academic endeavor. The data magnetic techniques provide are extremely valuable for any metallic application; magnetic flux leakage data are not limited to pipes; anything containing steel, such as rebar-reinforced concrete, is a potential utilization of the techniques presented herein.

As for my next generation, I plan to use the new magnetometer and lessons learned about the pitfalls of paleointensity data as a springboard for my postdoctoral research. My time period of interest is older than the oldest period, the Carboniferous, discussed herein. I intend to study the time period from 500 – 400 Ma. This period contains the end of the Cambrian, the Ordovician, and the Silurian time periods. My focus is on the extremely important Ordovician time period, which contains the oldest superchron on record, which was also the topic of my master's thesis. The paleointensity record from the time period of and surrounding the Ordovician superchron is extremely sparse; only four data points are available across this 100-million-year time period. My plan is to, at a minimum, double the data set; obtain the best estimates, using the new magnetometer system and all the technical information that my thesis offers; and to investigate the existence of a 200 Myr global magnetic superchron/hyper-reversal cycle.

There is one more matter going forward, however. The new magnetometer needs a name: SQUID Magnetometer for Automatic Recording of Thermoremanence (SMARTr).

Supplementary Information

TABLE OF FIGURES

The last component required for a full paleointensity-ready thermomagnetometer is the remagnetization coil. The coil is necessary for fully independent experiments, but an alternative hybrid approach can make use of this instrument together with, for example, a Magnetic Measurements Thermal Demagnetizer (MMTD oven). This type of paleointensity experiment is described in the methods section below and applied herein. In the single-axis continuous magnetometer system presented in Chapter 3, a Helmholtz coil was selected to apply a magnetic field because of the design of the F.I.T. system. In the multi-axis continuous magnetometer system described in Chapter 4, a solenoid was designed but not fully implemented. Both coil designs would be applicable to this magnetometer system. A Helmholtz coil could be placed outside and around the oven or a solenoid could be placed inside the oven. Both coils would need to be able to tolerate the high temperatures of the oven area. However, there already is a coil present near the specimen: the CoilHeater. By applying a current across the skin of the CoilHeater, along the helix shape (see Figure 5-7), a magnetic field can be generated. The heating coils inside the helix are wound non-conductively, but the helical outer shell is not and is, in fact, the exact same shape as a coil of wire in a solenoid. The CoilHeater therefore acts like a solenoid, but with one important difference, which can be seen in Figure 5-4: there is no contact between turns of the

TABLE OF TABLES

TABLE OF EQUATIONS

SUPPLEMENTARY INFORMATION A: CHAPTER 5

Table A1 Automated thermal instrument designs around the world

Instrument name or location	Type	Sensitivity (Am^2)	Temperature range (°C)	Sample Size	Usage/References
Hotspin	Spinner	5×10^{-8}	Room – 600	$0.5\ \mathrm{cm}^3$	(Matzka, 2001)
Hotspin 2	Spinner, hot air	2×10^{-7}	Room – 350	$1\ \mathrm{inch}$	(Wack and Matzka, 2007)
Geophysical Observatory Borok	Spinner	3×10^{-9}	Room – 600	$1\ \mathrm{cm}^3$	(Shcherbakova et al., 2000)
Institut de Physique du Globe de Paris (Triaxe)	Vibrating	1×10^{-8}	Room – 650	$0.75\ \mathrm{cm}^3$	(Coe et al., 2014; Gallet and Le Goff, 2006; Le Goff and Gallet, 2004)
Université de Montpellier	Vibrating	2×10^{-9}	-192 – 700	$12 \times 7\ \mathrm{mm}$	(Poidras et al., 2009)
Princeton Measurements Vibrating Sample Magnetometer	Vibrating	5×10^{-9}	-263 – 1025	$1\ \mathrm{cm}^3$	(Buz et al., 2015; Fukuma and Torii, 2011)
ORION system	Vibrating	5×10^{-8}	Room – 800	$1\ \mathrm{cm}^3$	(Smirnov et al., 2019)
SMARTr	Solid state	1×10^{-9}	Room – 600	8 – 12 mm diameter cylinders	This thesis

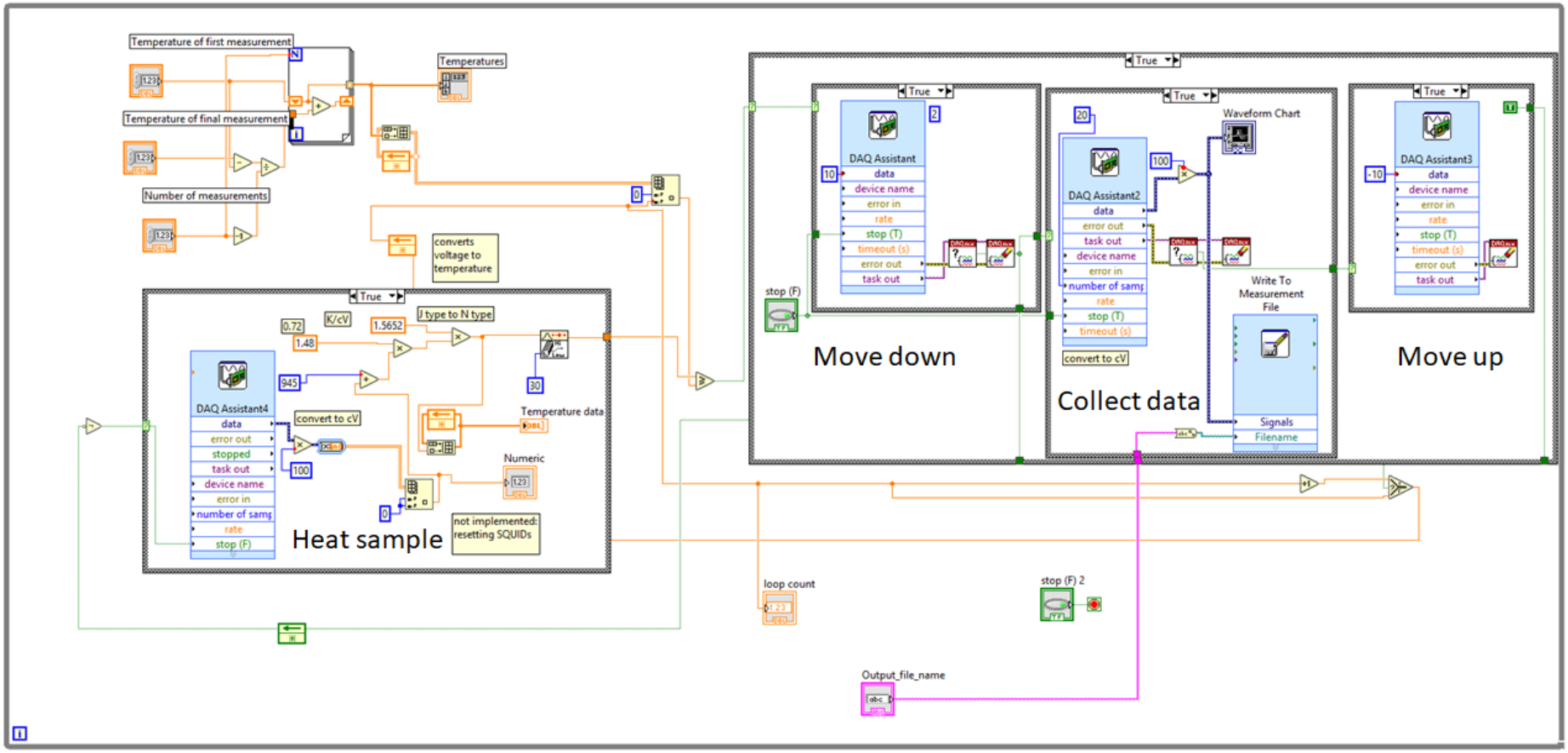

Figure A1. Backend LabVIEW diagram for Figure 5-9.

SUPPLEMENTARY INFORMATION B: CHAPTER 6

Permissions from co-authors

The two co-authors are my supervisors, Andrew J Biggin and Mimi J Hill, who have provided assistance in the preparation of this manuscript for inclusion here.

B.1 FORCs

The two FORCs run can be found in Figure B1. Sister specimens from these FORCs tended to give lower PI estimates, in the range of 30 – 33 µT for MW-IZZI+, with pT_MRM check failures in 50% of cases. We therefore expect these to be generally representative of the less well-behaved specimens. The strong peaks surrounded by closed contours are characteristic of single domain grains and appear to be more abundant in H6001-09D (Fig. B1B), compared to H6001-04A (Fig. B1A). The open contours in H6001-04A are characteristic of the additional presence of non-SD grains. The Arai plots for H6001-04A generally had more zigzagging, but the Arai plots for H6001-09D had more pT_MRM check failures.

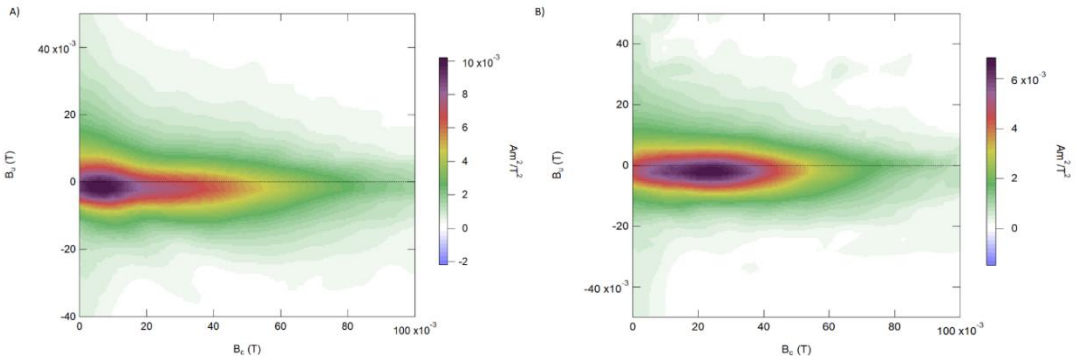

Figure B1. FORC diagrams for 2 specimens from section 1. A) H6001-04A and B) H6001-09D. Sister specimens of these gave lower than expected PI estimates from Arai plots with some pT_MRM check failures, so they appear to be characteristic of the specimens tested.

B.2 Hysteresis loops without heating

We ran four of the samples from Section 3.4 through repeated hysteresis loops without heating. The changes in hysteresis parameters for steps after a failed pTRM check (loop 3 or 4) were always higher than the changes in hysteresis parameters for loop 3 or 4 respectively without heating. The repeated hysteresis loops therefore do not appear to be the cause of the largest changes observed in hysteresis loop parameters.

B.3 Arai Plot statistics – Real data

In this section, the PI estimate is provided in µT. H_{lab} is the applied laboratory field (in µT). N is the number of data points on the Arai plot selected. B, or β, is a measure of scatter around the best-fit line. FRAC is a measure of the amount of NRM used for the fit. G is the gap factor. Q is the quality factor. DelCK refers to the individual pTRM checks' errors. DRAT is a normalized measure of alteration as defined by pTRM checks. CDRAT is a measure

of the cumulative alteration. Alpha, or α, and MAD are measures of the goodness of the orthogonal vector plot fit. |K'| is the curvature criterion.

Table B1. MW-IZZI+

Sample	Low T	High T	PI	H_{lab}	N	β	FRAC	g	q	delCK	DRAT	CDRAT	Alpha	MAD (fixed)	$\lvert\overline{K'}\rvert$
H601DA	1	9	39.6	36	9	0.025	0.895	0.835	30.8	6.8%	5.0%	3.0%	1.7	1.6	0.175
H601DB	1	9	39.5	36	9	0.031	0.914	0.783	24.1	7.5%	5.2%	8.8%	0.18	0.5	0.249
H601DC	1	9	37.5	36	9	0.056	0.902	0.823	14.7	12.3%	8.5%	14.2%	3.6	5.4	0.368
H601DD	1	9	37.4	36	9	0.045	0.950	0.831	18.9	3.7%	2.5%	6.4%	0.65	1.2	0.314
H614DA	0	3	35.7	36	4	0.042	0.483	0.307	3.6	0.0%	0.0%	0.0%	4.6	1.5	0.588
H614DB	0	3	39.9	36	4	0.077	0.345	0.454	2.0	0.1%	0.3%	-0.3%	9.7	1.8	0.626
H604DA	0	5	32.8	36	6	0.031	0.775	0.744	18.7	7.6%	7.3%	7.8%	10	6.3	0.126
H604DB	4	9	24.3	36	6	0.028	0.518	0.646	15.6	17.9%	22.3%	30.3%	0.54	1.3	-0.764
H609DA	2	5	31.0	36	4	0.102	0.421	0.610	2.9	1.2%	1.9%	1.9%	17	5.1	0.547
H609DB	2	5	20.8	36	4	0.105	0.392	0.665	4.5	30.2%	36.9%	-11.6%	9.8	7.5	0.765
H609DD	2	5	30.3	36	4	0.063	0.377	0.606	4.1	1.4%	2.4%	2.0%	6.0	2.0	0.401
H611CA	0	3	30.5	36	4	0.084	0.504	0.377	2.0	0.3%	0.6%	0.6%	8.1	4.3	0.314
H611CB	1	4	42.7	36	4	0.053	0.725	0.583	8.2	9.6%	8.3%	8.5%	2.2	1.2	0.201
H611CC	0	3	36.7	36	4	0.119	0.388	0.502	1.7	2.7%	4.8%	4.8%	5.4	1.2	0.512
H611CD	0	3	40.3	36	4	0.095	0.514	0.499	2.8	0.7%	0.9%	0.9%	0.6	0.8	0.568
H611CE	1	5	42.4	36	5	0.086	0.651	0.717	5.8	5.5%	5.1%	5.1%	2.7	1.9	0.381
H611CG	0	3	38.1	36	4	0.050	0.739	0.367	5.5	0.3%	0.3%	0.3%	1.3	1.0	0.548
H612EA	1	5	38.8	36	5	0.093	0.587	0.714	4.8	3.4%	3.7%	3.7%	4.7	2.3	0.373
H612EB	0	5	40.4	36	6	0.103	0.738	0.733	5.4	2.3%	2.0%	1.9%	23.6	11.3	0.632
H612EC	1	5	38.8	36	5	0.073	0.600	0.673	6.0	2.3%	2.4%	4.1%	2.9	1.5	0.277
H612ED	1	9	38.3	36	9	0.039	0.424	0.852	9.2	6.0%	9.7%	15.1%	5.8	1.3	0.182
H617DA	1	9	31.4	36	8	0.040	0.914	0.740	17.7	4.1%	3.2%	9.1%	2.0	2.3	0.185
H617DB	1	9	31.5	36	9	0.036	0.845	0.835	20.5	7.4%	6.3%	10.0%	1.0	0.9	0.279
H617FA	1	9	35.9	36	9	0.051	0.710	0.819	12.4	6.8%	6.3%	13.9%	0.5	0.4	0.355
H617FB	1	9	36.4	36	9	0.036	0.830	0.806	19.9	3.7%	2.9%	5.2%	1.5	1.8	0.276
H708EA	0	5	33.7	36	6	0.089	0.921	0.753	8.3	8.5%	6.3%	7.2%	3.3	5.3	-0.027
H708EB	0	5	36.1	36	6	0.091	0.887	0.763	8.0	10.5%	7.8%	8.2%	2.9	4.0	0.462
H712FA	1	10	48.5	36	10	0.035	0.712	0.820	17.1	8.1%	6.7%	14.9%	3.6	2.0	0.032
H712FB	1	6	56.8	36	6	0.087	0.675	0.769	6.9	9.6%	6.6%	8.1%	2.5	1.6	0.626
H712FC	1	10	40.4	36	10	0.038	0.866	0.855	21.3	9.2%	6.4%	8.7%	3.1	3.1	0.231
H616FA	1	4	35.4	36	4	0.078	0.735	0.497	4.8	10.2%	9.5%	9.1%	3.8	1.7	0.370
H616FB	1	5	34.7	36	5	0.069	0.673	0.722	7.7	8.9%	8.7%	8.8%	2.2	1.4	0.306
H616FD	0	4	37.2	36	5	0.067	0.631	0.609	5.9	26.4%	28.4%	28.7%	2.0	1.2	0.633
H610CA	1	8	29.3	36	8	0.062	0.842	0.790	11.2	27.9%	24.7%	44.5%	0.3	0.6	0.249
H610CE	0	10	36.1	36	11	0.065	0.538	0.880	7.3	10.6%	14.1%	39.9%	4.5	1.4	0.577
H610CF	0	3	37.6	36	4	0.085	0.552	0.364	2.4	0.1%	0.1%	0.1%	1.0	0.6	0.623
H615DA	0	7	35.2	36	8	0.203	0.654	0.666	1.7	17.3%	24.0%	-25.3%	50.1	12.7	0.406
H615DB	0	8	36.0	36	9	0.065	0.794	0.790	10.0	28.2%	24.2%	27.5%	5.1	4.2	0.538
H615DD	1	10	30.0	36	10	0.064	0.960	0.841	13.5	41.2%	30.7%	45.2%	1.4	1.3	0.697
H615DF	2	11	27.8	36	10	0.069	0.800	0.870	11.5	13.3%	11.5%	28.2%	2.8	1.9	0.506
H707EA	0	10	31.1	36	11	0.095	0.867	0.876	9.1	20.1%	15.5%	28.6%	2.8	2.1	0.820
H707EB	0	10	33.0	36	11	0.075	0.939	0.875	12.0	21.3%	15.1%	43.6%	1.6	1.7	0.609
H707ED	0	8	37.5	36	9	0.082	0.898	0.835	9.9	30.5%	21.6%	35.4%	1.8	1.6	0.590
H707EE	0	8	33.5	36	9	0.090	0.879	0.841	9.1	26.1%	19.6%	37.7%	3.1	2.4	0.699
H607BA	0	7	38.2	36	8	0.089	0.151	0.680	1.1	0.1%	0.6%	0.8%	3.9	0.4	0.212
H607BB	0	9	39.4	36	10	0.033	0.777	0.841	20.5	10.9%	9.2%	14.0%	1.9	1.1	0.246
H607BC	0	5	38.4	36	6	0.046	0.600	0.695	9.3	5.6%	6.2%	6.3%	2.4	0.9	0.201
H705DA	0	7	36.3	36	8	0.100	0.771	0.813	6.8	4.3%	3.6%	4.4%	4.6	2.6	0.147
H705DC	2	7	38.8	36	6	0.093	0.467	0.786	4.1	2.6%	3.6%	4.3%	2.3	1.1	0.410
H705DD	0	7	42.8	36	8	0.070	0.535	0.820	6.5	4.9%	5.6%	6.7%	5.8	1.7	0.462
H705DE	1	7	39.5	36	7	0.082	0.490	0.809	5.1	4.9%	6.4%	7.4%	5.6	1.5	0.459
H701EB	1	10	46.0	36	10	0.025	0.510	0.839	16.9	6.0%	7.3%	-4.8%	2.0	0.8	0.086
H701EC	1	10	49.6	36	10	0.022	0.823	0.829	31.5	6.1%	4.2%	4.0%	0.5	0.7	0.130
H702DC	0	8	35.5	36	9	0.041	0.880	0.808	17.6	5.6%	4.4%	7.0%	2.6	2.4	0.331
H616BB	1	7	43.6	36	7	0.044	0.581	0.769	10.4	5.5%	5.9%	5.9%	5.3	1.8	0.268
H704ED	1	6	40.6	36	6	0.038	0.941	0.721	18.5	11.9%	8.0%	9.1%	0.9	1.0	0.182
H709CA	0	6	38.7	36	7	0.075	0.926	0.719	9.0	11.6%	8.4%	7.0%	5.5	5.1	0.169
H613A	0	5	37.4	36	6	0.088	0.577	0.725	5.0	2.1%	2.4%	2.1%	4.5	1.9	0.407
H613G	0	5	34.1	36	6	0.055	0.828	0.739	11.6	11.8%	9.9%	9.8%	1.6	1.7	0.317

Table B2. MW-Perp++

Sample	Low T	High T	PI	H_{lab}	N	β	FRAC	g	q	delCK	DRAT	CDRAT	Alpha	MAD (fixed)	$\overline{K'}$
H601DG	3	6	33.7	36	4	0.052	0.410	0.558	4.4	4.3%	7.6%	7.6%	#N/A	#N/A	0.002
H607BF	0	4	34.7	36	5	0.034	0.755	0.619	13.8	7.0%	6.7%	6.7%	#N/A	#N/A	0.164
H609DE	0	11	29.2	36	10	0.035	1.008	0.829	23.7	25.1%	19.3%	30.1%	#N/A	#N/A	0.279
H611CF	4	8	22.8	36	5	0.121	0.591	0.640	3.1	11.3%	16.2%	17.9%	#N/A	#N/A	-0.401
H613B	2	5	27.2	36	4	0.015	0.577	0.625	23.4	9.5%	13.1%	13.1%	#N/A	#N/A	-0.013
H613D	1	6	31.1	36	6	0.038	0.744	0.783	15.2	8.2%	8.4%	6.9%	#N/A	#N/A	0.174
H613F	0	4	32.5	36	5	0.057	0.653	0.656	7.5	10.4%	11.8%	11.8%	#N/A	#N/A	0.283
H615DE	0	11	22.1	36	11	0.057	0.632	0.683	7.6	34.4%	46.3%	79.1%	#N/A	#N/A	0.659
H616BA	0	11	33.3	36	12	0.033	0.947	0.892	25.5	6.3%	4.9%	18.4%	#N/A	#N/A	0.287
H616BD	1	10	35.9	36	10	0.046	0.609	0.862	11.5	6.8%	7.9%	15.4%	#N/A	#N/A	0.375
H616FF	2	6	33.5	36	5	0.042	0.678	0.646	10.5	0.2%	0.3%	-0.3%	#N/A	#N/A	0.185
H616FG	0	4	30.7	36	5	0.067	0.965	0.603	8.6	36.2%	28.5%	28.5%	#N/A	#N/A	0.408
H701EA	2	10	42.6	36	9	0.021	0.611	0.859	25.4	3.4%	3.6%	-1.0%	#N/A	#N/A	0.008
H701EE	1	9	43.2	36	9	0.029	0.812	0.835	23.1	7.8%	6.2%	-4.9%	#N/A	#N/A	0.149
H702DB	0	8	35.6	36	9	0.022	0.832	0.828	30.9	5.5%	4.7%	6.6%	#N/A	#N/A	0.153
H702DE	0	7	33.8	36	8	0.026	0.932	0.792	28.0	8.9%	7.0%	6.1%	#N/A	#N/A	0.181
H704EB	1	11	37.8	36	11	0.016	0.790	0.839	40.5	5.3%	4.6%	-14.0%	#N/A	#N/A	-0.060
H704EF	1	9	40.6	36	9	0.013	0.881	0.816	55.3	6.8%	5.1%	-3.5%	#N/A	#N/A	-0.055
H709CB	3	7	33.6	36	5	0.072	0.346	0.736	3.6	5.8%	12.3%	6.1%	#N/A	#N/A	0.547
H709CD	1	6	36.1	36	5	0.042	0.740	0.739	13.0	1.2%	1.2%	-1.2%	#N/A	#N/A	0.013
H709CF	2	9	24.3	36	8	0.066	0.862	0.837	10.9	5.0%	4.8%	6.8%	#N/A	#N/A	0.292

Table B3. MW-Perp

Sample	Low T	High T	PI	H_{lab}	N	β	FRAC	g	q	delCK	DRAT	CDRAT	Alpha	MAD (fixed)	$\overline{K'}$
H601DE	2	12	35.8	36	11	0.027	0.818	0.874	26.2	0.0%	0.0%	0.0%	#N/A	#N/A	-0.007
H601DF	2	10	34.5	36	9	0.026	0.922	0.814	28.7	0.0%	0.0%	0.0%	#N/A	#N/A	0.162
H604DC	2	8	31.2	36	7	0.030	0.898	0.812	24.4	0.0%	0.0%	0.0%	#N/A	#N/A	0.001
H604DD	5	11	24.8	36	7	0.055	0.399	0.814	5.9	0.0%	0.0%	0.0%	#N/A	#N/A	0.467
H607BD	0	10	38.9	36	11	0.009	0.830	0.863	76.3	0.0%	0.0%	0.0%	#N/A	#N/A	0.279
H607BE	0	10	27.2	36	11	0.049	0.042	0.808	0.7	0.0%	0.0%	0.0%	#N/A	#N/A	0.279
H609DC	3	12	19.6	36	10	0.051	0.950	0.832	15.4	0.0%	0.0%	0.0%	#N/A	#N/A	-0.401
H610CB	0	11	24.2	36	12	0.049	0.520	0.867	9.1	0.0%	0.0%	0.0%	#N/A	#N/A	0.092
H610CC	0	10	28.3	36	11	0.042	0.893	0.844	18.0	0.0%	0.0%	0.0%	#N/A	#N/A	-0.072
H610CD	0	8	31.6	36	9	0.045	0.849	0.848	16.1	0.0%	0.0%	0.0%	#N/A	#N/A	0.111
H613C	1	9	31.0	36	9	0.051	0.936	0.840	15.3	0.0%	0.0%	0.0%	#N/A	#N/A	-0.041
H615DC	2	12	37.3	36	11	0.034	0.541	0.879	14.1	0.0%	0.0%	0.0%	#N/A	#N/A	0.431
H616FC	1	8	29.3	36	8	0.046	0.820	0.736	13.2	0.0%	0.0%	0.0%	#N/A	#N/A	0.393
H617DC	3	11	29.5	36	9	0.057	1.066	0.856	15.9	0.0%	0.0%	0.0%	#N/A	#N/A	0.427
H617DD	3	9	28.6	36	7	0.033	0.982	0.772	23.1	0.0%	0.0%	0.0%	#N/A	#N/A	0.364
H617FC	3	10	37.4	36	8	0.015	0.845	0.826	45.4	0.0%	0.0%	0.0%	#N/A	#N/A	0.287
H617FD	3	11	31.0	36	9	0.019	0.789	0.863	35.6	0.0%	0.0%	0.0%	#N/A	#N/A	0.645
H702DA	0	8	34.9	36	9	0.012	0.970	0.808	64.2	0.0%	0.0%	0.0%	#N/A	#N/A	0.079
H702DD	0	8	35.2	36	9	0.016	0.926	0.816	46.5	0.0%	0.0%	0.0%	#N/A	#N/A	-0.039
H704EA	1	9	46.4	36	9	0.008	0.846	0.838	86.6	0.0%	0.0%	0.0%	#N/A	#N/A	0.381
H705DB	1	9	39.0	36	9	0.055	0.645	0.857	10.0	0.0%	0.0%	0.0%	#N/A	#N/A	0.059
H707EC	0	10	36.8	36	11	0.074	0.851	0.887	10.2	0.0%	0.0%	0.0%	#N/A	#N/A	0.107
H708EC	0	10	23.0	36	8	0.134	1.141	0.799	6.8	0.0%	0.0%	0.0%	#N/A	#N/A	0.407
H708ED	0	13	23.2	36	10	0.137	1.073	0.819	6.4	0.0%	0.0%	0.0%	#N/A	#N/A	0.485
H709CE	3	9	32.9	36	7	0.057	0.967	0.816	13.9	0.0%	0.0%	0.0%	#N/A	#N/A	0.413

B.4 Arai Plot statistics – Derived/re-analyzed

Table B4. MW-Perp (using MW-IZZI+ pT_MRM data)

Sample	Low T	High T	PI	H_{lab}	N	β	FRAC	g	q	delCK	DRAT	CDRAT	Alpha	MAD (fixed)	$\overline{\lvert K' \rvert}$
H601DE	0	10	36.6	36	10	0.026	0.745	0.856	24.5	0.0%	0.0%	0.0%	#N/A	#N/A	#N/A
H601DF	2	10	34.5	36	9	0.026	0.922	0.814	28.7	0.0%	0.0%	0.0%	#N/A	#N/A	#N/A
H604DC	2	6	31.5	36	5	0.047	0.720	0.746	11.5	0.0%	0.0%	0.0%	#N/A	#N/A	#N/A
H604DD	5	8	29.9	36	4	0.024	0.226	0.652	6.1	0.0%	0.0%	0.0%	#N/A	#N/A	#N/A
H607BD	0	8	39.7	36	9	0.009	0.714	0.828	66.9	0.0%	0.0%	0.0%	#N/A	#N/A	#N/A
H607BE	0	10	27.2	36	11	0.049	0.042	0.808	0.7	0.0%	0.0%	0.0%	#N/A	#N/A	#N/A
H609DC	4	7	24.0	36	4	0.030	0.409	0.596	8.3	0.0%	0.0%	0.0%	#N/A	#N/A	#N/A
H610CB	1	5	30.7	36	5	0.051	0.354	0.723	5.1	0.0%	0.0%	0.0%	#N/A	#N/A	#N/A
H610CC	0	4	38.6	36	5	0.016	0.408	0.606	15.3	0.0%	0.0%	0.0%	#N/A	#N/A	#N/A
H610CD	1	5	38.1	36	5	0.042	0.479	0.706	8.1	0.0%	0.0%	0.0%	#N/A	#N/A	#N/A
H613C	1	5	37.0	36	5	0.062	0.682	0.718	7.9	0.0%	0.0%	0.0%	#N/A	#N/A	#N/A
H615DC	0	12	38.0	36	12	0.034	0.553	0.882	14.4	0.0%	0.0%	0.0%	#N/A	#N/A	#N/A
H616FC	0	5	40.0	36	6	0.043	0.478	0.645	7.2	0.0%	0.0%	0.0%	#N/A	#N/A	#N/A
H617DC	3	11	29.5	36	9	0.057	1.066	0.856	15.9	0.0%	0.0%	0.0%	#N/A	#N/A	#N/A
H617DD	3	9	28.6	36	7	0.033	0.982	0.772	23.1	0.0%	0.0%	0.0%	#N/A	#N/A	#N/A
H617FC	3	10	37.4	36	8	0.015	0.845	0.826	45.4	0.0%	0.0%	0.0%	#N/A	#N/A	#N/A
H617FD	3	10	31.1	36	8	0.024	0.700	0.842	24.3	0.0%	0.0%	0.0%	#N/A	#N/A	#N/A
H702DA	1	8	34.4	36	8	0.008	0.956	0.801	91.5	0.0%	0.0%	0.0%	#N/A	#N/A	#N/A
H702DD	1	8	34.6	36	8	0.011	0.908	0.807	63.9	0.0%	0.0%	0.0%	#N/A	#N/A	#N/A
H704EA	1	6	47.2	36	6	0.015	0.587	0.745	28.6	0.0%	0.0%	0.0%	#N/A	#N/A	#N/A
H705DB	0	6	49.0	36	7	0.018	0.369	0.794	16.2	0.0%	0.0%	0.0%	#N/A	#N/A	#N/A
H707EC	0	7	45.5	36	8	0.058	0.663	0.835	9.5	0.0%	0.0%	0.0%	#N/A	#N/A	#N/A
H708EC	5	9	20.5	36	5	0.080	0.474	0.698	4.1	0.0%	0.0%	0.0%	#N/A	#N/A	#N/A
H708ED	6	9	24.0	36	4	0.054	0.324	0.637	3.8	0.0%	0.0%	0.0%	#N/A	#N/A	#N/A
H709CE	3	8	35.2	36	6	0.048	0.890	0.786	14.7	0.0%	0.0%	0.0%	#N/A	#N/A	#N/A

Table B5. MW-derPerp

Sample	Low T	High T	PI	H_{lab}	N	β	FRAC	g	q	delCK	DRAT	CDRAT	Alpha	MAD (fixed)	$\overline{K^r}$
H601DA	0	9	37.9	36	10	0.019	0.895	0.839	40.3	0.0%	0.0%	0.0%	#N/A	#N/A	#N/A
H601DB	0	9	40.1	36	10	0.028	0.985	0.791	27.7	0.0%	0.0%	0.0%	#N/A	#N/A	#N/A
H601DC	0	9	36.8	36	10	0.043	0.885	0.833	17.0	0.0%	0.0%	0.0%	#N/A	#N/A	#N/A
H601DD	0	9	37.5	36	10	0.040	1.033	0.829	21.4	0.0%	0.0%	0.0%	#N/A	#N/A	#N/A
H604DA	0	9	26.5	36	10	0.070	1.077	0.850	13.1	0.0%	0.0%	0.0%	#N/A	#N/A	#N/A
H604DB	0	8	17.5	36	9	0.111	0.658	0.637	3.8	0.0%	0.0%	0.0%	#N/A	#N/A	#N/A
H607BA	0	9	58.4	36	10	0.110	0.235	0.734	1.6	0.0%	0.0%	0.0%	#N/A	#N/A	#N/A
H607BB	0	10	38.1	36	11	0.033	0.972	0.862	25.6	0.0%	0.0%	0.0%	#N/A	#N/A	#N/A
H607BC	0	10	30.8	36	11	0.038	0.974	0.857	21.8	0.0%	0.0%	0.0%	#N/A	#N/A	#N/A
H609DA	0	9	23.3	36	10	0.073	1.006	0.839	11.6	0.0%	0.0%	0.0%	#N/A	#N/A	#N/A
H609DB	0	7	39.1	36	8	0.160	1.712	0.798	8.6	0.0%	0.0%	0.0%	#N/A	#N/A	#N/A
H609DD	0	7	22.2	36	8	0.101	0.526	0.753	3.9	0.0%	0.0%	0.0%	#N/A	#N/A	#N/A
H610CA	0	8	30.8	36	9	0.052	0.900	0.777	13.5	0.0%	0.0%	0.0%	#N/A	#N/A	#N/A
H610CE	0	11	30.9	36	12	0.056	0.614	0.884	9.6	0.0%	0.0%	0.0%	#N/A	#N/A	#N/A
H610CF	0	7	30.2	36	8	0.075	0.975	0.750	9.8	0.0%	0.0%	0.0%	#N/A	#N/A	#N/A
H611CA	0	8	33.7	36	9	0.074	1.113	0.755	11.4	0.0%	0.0%	0.0%	#N/A	#N/A	#N/A
H611CB	0	6	31.9	36	7	0.083	1.010	0.768	9.4	0.0%	0.0%	0.0%	#N/A	#N/A	#N/A
H611CC	0	8	27.3	36	9	0.068	0.854	0.828	10.3	0.0%	0.0%	0.0%	#N/A	#N/A	#N/A
H611CD	0	8	27.3	36	9	0.078	0.868	0.818	9.1	0.0%	0.0%	0.0%	#N/A	#N/A	#N/A
H611CE	0	8	33.2	36	9	0.066	1.011	0.841	12.9	0.0%	0.0%	0.0%	#N/A	#N/A	#N/A
H611CG	0	5	30.8	36	6	0.082	1.045	0.643	8.2	0.0%	0.0%	0.0%	#N/A	#N/A	#N/A
H612EA	0	9	29.8	36	10	0.056	0.874	0.853	13.4	0.0%	0.0%	0.0%	#N/A	#N/A	#N/A
H612EB	0	9	32.6	36	10	0.106	1.118	0.852	9.0	0.0%	0.0%	0.0%	#N/A	#N/A	#N/A
H612EC	0	7	33.5	36	8	0.074	1.102	0.799	11.9	0.0%	0.0%	0.0%	#N/A	#N/A	#N/A
H612ED	0	13	26.8	36	14	0.044	0.804	0.880	15.9	0.0%	0.0%	0.0%	#N/A	#N/A	#N/A
H613A	0	8	27.2	36	9	0.047	0.808	0.850	14.5	0.0%	0.0%	0.0%	#N/A	#N/A	#N/A
H613G	0	6	29.5	36	7	0.062	0.896	0.795	11.6	0.0%	0.0%	0.0%	#N/A	#N/A	#N/A
H614DA	0	9	24.0	36	10	0.079	1.033	0.815	10.6	0.0%	0.0%	0.0%	#N/A	#N/A	#N/A
H614DB	0	9	22.9	36	10	0.084	1.012	0.838	10.1	0.0%	0.0%	0.0%	#N/A	#N/A	#N/A
H615DA	0	10	49.3	36	11	0.205	1.185	0.807	4.7	0.0%	0.0%	0.0%	#N/A	#N/A	#N/A
H615DB	0	8	35.1	36	9	0.060	0.779	0.803	10.5	0.0%	0.0%	0.0%	#N/A	#N/A	#N/A
H615DD	0	10	30.2	36	11	0.053	0.978	0.845	15.7	0.0%	0.0%	0.0%	#N/A	#N/A	#N/A
H615DF	0	11	28.2	36	12	0.057	0.872	0.885	13.5	0.0%	0.0%	0.0%	#N/A	#N/A	#N/A
H616BB	0	7	41.8	36	8	0.030	0.619	0.793	16.2	0.0%	0.0%	0.0%	#N/A	#N/A	#N/A
H616FA	0	6	27.3	36	7	0.066	0.957	0.716	10.4	0.0%	0.0%	0.0%	#N/A	#N/A	#N/A
H616FB	0	8	28.0	36	9	0.069	0.950	0.838	11.6	0.0%	0.0%	0.0%	#N/A	#N/A	#N/A
H616FD	0	8	28.1	36	9	0.075	0.862	0.786	9.1	0.0%	0.0%	0.0%	#N/A	#N/A	#N/A
H617DA	0	9	30.4	36	10	0.022	0.922	0.794	33.6	0.0%	0.0%	0.0%	#N/A	#N/A	#N/A
H617DB	0	9	31.2	36	10	0.036	0.875	0.842	20.4	0.0%	0.0%	0.0%	#N/A	#N/A	#N/A
H617FA	0	10	41.7	36	11	0.036	0.782	0.844	18.2	0.0%	0.0%	0.0%	#N/A	#N/A	#N/A
H617FB	0	9	36.5	36	10	0.022	0.850	0.822	32.1	0.0%	0.0%	0.0%	#N/A	#N/A	#N/A
H701EB	0	10	44.8	36	11	0.025	0.499	0.854	17.0	0.0%	0.0%	0.0%	#N/A	#N/A	#N/A
H701EC	0	10	48.6	36	11	0.022	0.839	0.842	32.1	0.0%	0.0%	0.0%	#N/A	#N/A	#N/A
H702DC	0	8	33.7	36	9	0.029	0.845	0.815	24.1	0.0%	0.0%	0.0%	#N/A	#N/A	#N/A
H704ED	0	6	39.7	36	7	0.031	0.962	0.736	22.8	0.0%	0.0%	0.0%	#N/A	#N/A	#N/A
H705DA	0	7	33.0	36	8	0.081	0.756	0.827	7.7	0.0%	0.0%	0.0%	#N/A	#N/A	#N/A
H705DC	0	11	24.7	36	12	0.088	1.119	0.868	11.0	0.0%	0.0%	0.0%	#N/A	#N/A	#N/A
H705DD	0	10	28.2	36	11	0.077	0.892	0.869	10.1	0.0%	0.0%	0.0%	#N/A	#N/A	#N/A
H705DE	0	10	26.7	36	11	0.074	0.804	0.878	9.6	0.0%	0.0%	0.0%	#N/A	#N/A	#N/A
H707EA	0	10	28.5	36	11	0.096	0.901	0.878	8.2	0.0%	0.0%	0.0%	#N/A	#N/A	#N/A
H707EB	0	10	33.6	36	11	0.077	1.105	0.865	12.4	0.0%	0.0%	0.0%	#N/A	#N/A	#N/A
H707ED	0	8	35.5	36	9	0.085	0.978	0.833	9.5	0.0%	0.0%	0.0%	#N/A	#N/A	#N/A
H707EE	0	8	56.4	36	9	0.163	0.827	0.815	4.1	0.0%	0.0%	0.0%	#N/A	#N/A	#N/A
H708EA	0	6	34.4	36	7	0.131	1.238	0.776	7.3	0.0%	0.0%	0.0%	#N/A	#N/A	#N/A
H708EB	0	6	33.2	36	7	0.133	1.071	0.785	6.3	0.0%	0.0%	0.0%	#N/A	#N/A	#N/A
H709CA	0	6	18.8	36	7	0.190	0.457	0.622	1.5	0.0%	0.0%	0.0%	#N/A	#N/A	#N/A
H712FA	0	10	45.7	36	11	0.024	0.697	0.845	24.3	0.0%	0.0%	0.0%	#N/A	#N/A	#N/A
H712FB	0	8	60.1	36	8	0.064	0.738	0.788	9.0	0.0%	0.0%	0.0%	#N/A	#N/A	#N/A
H712FC	0	10	43.0	36	11	0.116	1.051	0.845	7.7	0.0%	0.0%	0.0%	#N/A	#N/A	#N/A

Table B6. MW-derPerp++

Sample	Low T	High T	PI	H_{lab}	N	β	FRAC	g	q	delCK	DRAT	CDRAT	Alpha	MAD (fixed)	$\overline{\lvert K' \rvert}$
H601DA	1	9	37.5	36	9	0.020	0.880	0.833	36.5	3.0%	2.3%	4.8%	#N/A	#N/A	#N/A
H601DB	1	9	39.6	36	9	0.030	0.966	0.783	25.4	6.7%	4.7%	7.4%	#N/A	#N/A	#N/A
H601DC	1	9	38.1	36	9	0.047	0.848	0.822	14.7	10.6%	8.6%	-11.8%	#N/A	#N/A	#N/A
H601DD	1	9	36.7	36	9	0.045	1.016	0.822	18.8	2.7%	1.9%	3.6%	#N/A	#N/A	#N/A
H614DA	1	9	23.0	36	9	0.092	1.022	0.807	8.9	12.0%	9.9%	23.9%	#N/A	#N/A	#N/A
H614DB	1	9	21.9	36	9	0.095	0.997	0.830	8.7	11.5%	9.8%	24.9%	#N/A	#N/A	#N/A
H604DA	1	9	25.5	36	9	0.079	1.067	0.844	11.4	12.5%	9.6%	24.4%	#N/A	#N/A	#N/A
H604DB	3	9	21.5	36	7	0.040	0.650	0.665	10.8	11.6%	15.3%	15.7%	#N/A	#N/A	#N/A
H609DA	1	9	23.0	36	9	0.083	1.034	0.847	10.5	13.5%	11.0%	23.7%	#N/A	#N/A	#N/A
H609DB	2	7	26.9	36	6	0.068	1.891	0.737	20.4	77.0%	32.6%	60.0%	#N/A	#N/A	#N/A
H609DD	2	6	25.6	36	5	0.040	0.483	0.719	8.8	5.9%	10.0%	3.4%	#N/A	#N/A	#N/A
H611CA	2	4	34.9	36	3	0.125	0.743	0.476	2.8	38.7%	37.4%	37.4%	#N/A	#N/A	#N/A
H611CB	0	5	34.9	36	6	0.085	0.942	0.727	8.0	6.2%	4.7%	4.7%	#N/A	#N/A	#N/A
H611CC	1	8	26.2	36	8	0.080	0.833	0.818	8.6	10.1%	9.8%	26.4%	#N/A	#N/A	#N/A
H611CD	1	5	31.9	36	5	0.089	0.663	0.691	5.1	18.7%	21.1%	21.1%	#N/A	#N/A	#N/A
H611CE	1	5	41.2	36	5	0.060	0.699	0.716	8.3	5.3%	5.0%	5.0%	#N/A	#N/A	#N/A
H611CG	1	4	32.4	36	4	0.111	0.983	0.573	5.1	17.6%	13.3%	-13.3%	#N/A	#N/A	#N/A
H612EA	1	9	29.4	36	9	0.066	0.861	0.849	11.1	7.6%	6.9%	11.9%	#N/A	#N/A	#N/A
H612EB	1	9	30.3	36	9	0.114	1.066	0.835	7.8	20.9%	15.0%	24.0%	#N/A	#N/A	#N/A
H612EC	2	5	39.0	36	4	0.038	0.638	0.590	10.0	5.9%	6.3%	6.3%	#N/A	#N/A	#N/A
H612ED	1	11	31.6	36	11	0.039	0.520	0.887	11.9	2.4%	3.5%	6.8%	#N/A	#N/A	#N/A
H617DA	1	9	30.0	36	9	0.022	0.899	0.784	31.6	2.9%	2.4%	-3.2%	#N/A	#N/A	#N/A
H617DB	1	9	30.6	36	9	0.037	0.856	0.835	19.4	4.4%	3.9%	4.7%	#N/A	#N/A	#N/A
H617FA	1	4	49.6	36	4	0.029	0.373	0.531	6.8	3.7%	5.9%	-5.9%	#N/A	#N/A	#N/A
H617FB	1	9	36.8	36	9	0.024	0.822	0.811	27.3	4.4%	3.7%	-9.6%	#N/A	#N/A	#N/A
H708EA	1	6	32.7	36	6	0.159	1.196	0.753	5.7	40.1%	24.8%	39.9%	#N/A	#N/A	#N/A
H708EB	1	6	30.9	36	6	0.154	1.028	0.761	5.1	33.1%	24.5%	39.7%	#N/A	#N/A	#N/A
H712FA	1	10	45.3	36	10	0.027	0.654	0.828	19.8	4.2%	4.0%	-8.3%	#N/A	#N/A	#N/A
H712FB	1	6	54.7	36	6	0.073	0.685	0.778	7.3	6.1%	4.9%	-4.2%	#N/A	#N/A	#N/A
H712FC	1	8	57.6	36	5	0.295	0.573	0.991	1.9	24.4%	22.6%	29.4%	#N/A	#N/A	#N/A
H616FA	1	5	28.3	36	5	0.086	0.891	0.660	6.8	6.1%	5.4%	5.4%	#N/A	#N/A	#N/A
H616FB	1	8	26.8	36	8	0.077	0.925	0.828	10.0	10.1%	8.8%	21.7%	#N/A	#N/A	#N/A
H616FD	1	4	35.8	36	4	0.075	0.599	0.563	4.5	22.1%	26.1%	26.1%	#N/A	#N/A	#N/A
H610CA	1	5	34.8	36	5	0.069	0.730	0.653	6.9	4.1%	4.0%	4.0%	#N/A	#N/A	#N/A
H610CE	1	11	29.9	36	11	0.057	0.598	0.880	9.2	6.8%	8.8%	23.6%	#N/A	#N/A	#N/A
H610CF	1	7	29.3	36	6	0.082	0.953	0.603	7.0	18.3%	14.9%	26.9%	#N/A	#N/A	#N/A
H615DA	1	3	19.5	36	3	0.547	0.066	0.303	0.0	0.0%	0.0%	0.0%	#N/A	#N/A	#N/A
H615DB	1	7	38.8	36	7	0.054	0.698	0.752	9.7	3.5%	3.4%	-4.4%	#N/A	#N/A	#N/A
H615DD	1	7	40.0	36	7	0.038	0.530	0.719	10.1	3.2%	4.1%	-7.8%	#N/A	#N/A	#N/A
H615DF	1	11	27.7	36	11	0.063	0.854	0.881	11.9	7.9%	7.3%	12.8%	#N/A	#N/A	#N/A
H707EA	1	5	51.2	36	5	0.054	0.455	0.689	5.8	1.8%	2.2%	-2.2%	#N/A	#N/A	#N/A
H707EB	1	5	53.0	36	5	0.097	0.576	0.633	3.7	4.4%	4.2%	4.2%	#N/A	#N/A	#N/A
H707ED	1	5	51.5	36	5	0.074	0.564	0.664	5.1	4.2%	4.3%	4.3%	#N/A	#N/A	#N/A
H707EE	1	8	73.0	36	8	0.151	0.535	0.800	2.8	42.3%	34.9%	17.9%	#N/A	#N/A	#N/A
H607BA	1	9	59.4	36	9	0.123	0.228	0.716	1.3	2.6%	6.0%	0.0%	#N/A	#N/A	#N/A
H607BB	1	9	40.2	36	9	0.025	0.823	0.839	27.5	7.3%	5.9%	8.4%	#N/A	#N/A	#N/A
H607BC	1	5	37.7	36	5	0.035	0.616	0.698	12.4	3.7%	4.1%	4.1%	#N/A	#N/A	#N/A
H705DA	1	7	32.3	36	7	0.097	0.726	0.814	6.1	2.9%	3.0%	-5.7%	#N/A	#N/A	#N/A
H705DC	1	7	40.3	36	7	0.068	0.549	0.803	6.4	3.1%	3.8%	7.2%	#N/A	#N/A	#N/A
H705DD	1	9	31.9	36	9	0.070	0.705	0.863	8.7	7.9%	8.4%	7.5%	#N/A	#N/A	#N/A
H705DE	1	9	29.5	36	9	0.073	0.655	0.863	7.8	6.8%	8.1%	5.6%	#N/A	#N/A	#N/A
H701EB	1	9	44.7	36	9	0.031	0.462	0.834	12.5	3.8%	5.2%	-13.3%	#N/A	#N/A	#N/A
H701EC	1	10	48.0	36	10	0.023	0.829	0.838	30.6	6.6%	4.7%	5.4%	#N/A	#N/A	#N/A
H702DC	1	8	33.7	36	8	0.034	0.810	0.801	18.8	2.4%	2.2%	-2.2%	#N/A	#N/A	#N/A
H616BB	1	7	41.1	36	7	0.030	0.595	0.778	15.6	3.4%	3.8%	2.9%	#N/A	#N/A	#N/A
H704ED	1	6	39.2	36	6	0.035	0.942	0.724	19.7	7.7%	5.5%	5.8%	#N/A	#N/A	#N/A
H709CA	1	6	8.7	36	4	0.094	0.147	0.835	1.3	2.3%	15.4%	2.7%	#N/A	#N/A	#N/A
H613A	1	5	33.2	36	5	0.065	0.512	0.712	5.6	3.1%	4.5%	-4.5%	#N/A	#N/A	#N/A
H613G	1	6	28.9	36	6	0.076	0.865	0.780	8.9	11.0%	9.9%	15.0%	#N/A	#N/A	#N/A

SUPPLEMENTARY INFORMATION C: CHAPTER 7

Permissions from co-authors

I, Dr. Thomas James Barrett, do formally grant permission to you include the article entitled, “Comparison of thermal and microwave paleointensity estimates in specimens displaying non-deal behavior in Thellier-style paleointensity experiments” in your thesis.

You have my, Courtney J Sprain, permission to include “Comparison of thermal and microwave paleointensity estimates in specimens displaying non-deal behavior in Thellier-style paleointensity experiments” in your thesis.

The remaining two co-authors are my supervisors, Andrew J Biggin and Mimi J Hill, who have provided assistance in the preparation of this manuscript for inclusion here.

Introduction

The supporting information herein is separated into four parts. Part C.1 contains a short meta-analysis, justifying the need for more data. Part C.2 contains rock magnetic data, which are useful for putting the paleointensity results of the main text into context for other rocks. Part C.3 contains the Arai plot fits for the new data presented in the main text. Finally, Part C.4 contains a new flow averaged dataset providing a best estimate of the true paleointensity.

C.1 Flow-level meta-analysis

Before undertaking any additional paleointensity experiments, confirmation of Biggin (2010)'s meta-analysis at the flow level was necessary. We use a Kolmogorov-Smirnov test on the datasets to be analyzed (Table C1) to check if the flow-level datasets are not normally-distributed over the 0 – 45ka age range. We fail to reject the null hypothesis that the data are normally-distributed for both the Teanby et al. (2002) and the Gratton et al. (2005) datasets at the 95% confidence level, with p-values of 0.126 and 0.054, respectively. This allows us to use two-sample T-tests on collections of flow means from the same studies (see Section 7.5).

In order to test for differences between specific flows measured in different studies (Table C1), we also use two-sample T-tests because we assume that the differences are simply caused by random error, the estimates obtained from specimens within a given flow should be normally distributed. The results of this series of T-tests are given in Table C1. For 28/56 flows with at least 2 PI estimates from each of Teanby et al. (2002) and Gratton et al. (2005), the difference is significant at the 95% confidence level. The mean PI estimates for these flows are 33.5 μT and 24.8 μT, respectively (35% difference). An additional 152 flows were studied by Gratton et al. (2005) but had insufficient flow-level data for this test, which means up to 180 flows have discrepancies that cannot be said to be within the possibility of random error.

Table C1. Two-sample T-test statistics for flow-level meta-analysis of Teanby et al. (2002) and Gratton et al. (2005) paleointensity estimates.

Flow	Teanby et al. (2002) estimate (μT)	SD	N	Gratton et al. (2005) Estimate (μT)	SD	N	Significance level
1	57.4	9.7	4	39.9	1.6	3	0.0293
4	56.6	3	2	38.9	2.2	3	0.0044
6	50.4	4.5	2	36.5	0.6	3	0.0104
8	59.0	3.2	3	38.3	1	6	<0.0001
9	58.0	19.5	2	40.0	8.4	2	0.3533*
10	60.1	7.1	2	56.3	7.6	2	0.6568*
18	51.2	9.1	5	39.6	0.1	2	0.0464
23	51.4	0.9	2	28.8	1	2	0.0018
33	48.7	4.5	3	57.4	2.1	4	0.0178
34	49.4	7	3	64.7	4.9	2	0.0785*
37	49.2	3.4	2	24.8	6	3	0.0149
39	36.3	3	2	20.1	1.3	2	0.0198
40	48.9	3.3	2	35.2	6	2	0.1055*
46	32.4	1	2	25.1	8.6	2	0.3554*

49	62.8	0.5	3	29.4	7.4	3	0.0015
50	42.2	0.1	2	39.4	1.4	3	0.0751*
51	24.7	5.9	2	20.1	1.9	2	0.4041*
56	38.3	3.5	3	28.3	0.8	2	0.0324
63	30.2	3.3	2	24.9	5.3	2	0.3528*
64	18.0	2.6	2	15.1	5.8	2	0.5849*
76	37.9	0.1	2	26.5	1.9	3	0.0040
77	32.3	9.2	3	21.6	15.6	2	0.3912*
87	27.7	4.2	2	14.6	1.9	2	0.0420
91	23.8	0.8	2	12.1	0.8	3	0.0005
103	21.1	2.4	3	18.2	1.1	2	0.2207*
105	20.6	1.9	3	19.4	1.5	3	0.4390*
106	17.9	1.5	2	16.5	0.3	3	0.1869*
108	16.4	1.8	3	9.9	0.8	2	0.0191
114	18.0	0	2	18.4	1.3	4	0.7026*
116	20.8	0.2	2	22.7	2	3	0.2932*
140	25.6	1.2	2	19.7	3.2	2	0.1347*
149	22.1	3.8	3	16.7	0.1	2	0.1527*
150	21.2	0.5	3	17.3	0.1	2	0.0019
157	27.3	1.4	2	12.6	1.3	3	0.0012
159	34.3	1.7	2	24.9	5.9	2	0.1628*
160	27.1	2	3	15.2	5.5	2	0.0355
164	36.7	3.3	2	22.6	1	4	0.0009
165	27.6	1.5	2	17.8	1.9	2	0.0292
166	22.3	4.2	2	14.5	0.7	2	0.1223*
167	25.6	2.9	3	31.0	0.5	2	0.0464
171	32.1	0.5	2	19.2	1.5	3	0.0015
174	33.6	2.8	3	20.7	1.1	2	0.0095
187	18.7	6.2	2	16.7	0.7	2	0.6948*
189	27.7	0.2	2	19.8	1	2	0.0082
200	32.0	3.2	3	19.3	1.9	2	0.0162
202	28.2	4.7	2	18.7	11.8	3	0.3621*
221	40.9	2.1	3	31.4	2.8	4	0.0045
222	39.8	3.3	3	37.8	1.6	3	0.3984*
223	36.3	3.2	3	22.6	6.7	2	0.0488
226	22.2	4.5	2	16.3	1.2	3	0.1024*
227	22.1	5.9	2	15.2	1.4	2	0.2488*
229	20.5	4.1	2	16.3	3.7	3	0.3167*
230	19.9	2.2	2	16.4	0.3	2	0.1556*
236	21.8	1.6	3	12.5	1.7	2	0.0083
237	25.5	8.2	3	19.1	0.2	2	0.3720*
240	18.8	6.4	2	13.7	0.9	2	0.3805*
Mean	33.5	13		24.8	12		n/a

*Indicates these flows have estimates that are not statistically distinct at the 95% confidence level.

This next section investigates the possibility of reanalyzing the Teanby et al. (2002) data, to remove some confounding variables: selection criteria and temperature ranges. First, the Teanby et al. (2002) data were reanalyzed using the selection criteria from Gratton et al. (2005), which includes accepting only single slope Arai plots. The results of these tests are in Table C2. The reanalysis left 57 PI estimates across 43 flows, with 9 flows having enough data for a two-sample T-test to compare the reanalyzed Teanby et al. (2002) data with the data from Gratton et al. (2005). The resulting mean PI estimates from the relevant flows were 32.8 µT and 27.1 µT, respectively (21% difference). Of these 9 flows, 5 flows remained statistically distinct, a proportion virtually unchanged from the original selection criteria, but the Teanby et al. (2002) pass rate drops from 54% to 16%. We note that the gain from rejecting 138 PI estimates is just a 5% improvement in agreement.

Table C2. Reanalyzed Teanby et al. (2002) data, using the selection criteria of Gratton et al. (2005) that accepts only single-slope Arai plots, with appropriate Gratton et al. (2005) data for reference.

Flow	Teanby et al. (2002) original (μT)	Teanby et al. (2002) updated (μT)	Gratton et al. (2005) (μT)	T-Test significance level (old / new)
3	56.9	57.6	44.8 ± 5.7	$-/-$
6	50.4 ± 4.5	41.8 ± 4.9	36.5 ± 0.6	0.010/0.138*
10	60.1 ± 7.1	57	56.3 ± 7.6	$0.657/-$
12	$-$	25.1	30.1 ± 4.4	$-/-$
13	46.4	52.5	45.2 ± 3.3	$-/-$
18	51.2 ± 9.1	50.4 ± 7.5	39.6 ± 0.1	0.046/0.268*
25	48.2	41.5	39.9 ± 3.4	$-/-$
33	48.7 ± 4.5	43.8	57.4 ± 2.1	$0.018/-$
34	49.4 ± 7	$46.1 \pm 4.3(3)$	64.7 ± 4.9	0.079/0.020
35	53.8	57.7	32.9 ± 0.5	$-/-$
37	49.2 ± 3.4	$44.7 \pm 13(3)$	24.8 ± 6.0	0.015/0.074*
39	36.3 ± 3.0	$33.2 \pm 7.4(3)$	20.1 ± 1.3	0.020/0.100
40	48.9 ± 3.3	$39.3 \pm 3.8(3)$	35.2 ± 6.0	0.106/0.548*
41	$-$	34.1	21.9 ± 0.3	$-/-$
46	32.4 ± 1.0	31.9	25.1 ± 8.6	$0.355/-$
50	42.2 ± 0.1	41.1	39.4 ± 1.4	$0.075/-$
55	$-$	44.4	33.4 ± 5.0	$-/-$
56	38.3 ± 3.5	38.8	28.3 ± 0.8	$0.032/-$
63	30.2 ± 3.3	37.6	24.9 ± 5.3	$0.353/-$
67	24.7 ± 1.5	24.6	$-$	$-/-$
75	28.8	30.1	20.4 ± 11	$-/-$
77	32.2 ± 9.2	32.4 ± 8.6	21.6 ± 16	0.391/0.549
82	42.7	41.8 ± 0.1	$-$	$-/-$
91	23.8 ± 0.8	14.9	12.1 ± 0.8	$0.001/-$
100	$-$	15.5	13.1 ± 0.8	$-/-$
103	21.1 ± 2.4	22.8	18.2 ± 1.1	$0.221/-$
105	20.6 ± 1.9	20.1 ± 1.4	19.4 ± 1.5	0.439/0.648
106	17.9 ± 1.5	19.2	16.5 ± 0.3	$0.187/-$
114	18 ± 0.0	19.0	18.4 ± 1.3	$0.703/-$
116	20.8 ± 0.2	22.6	22.7 ± 2.0	$0.293/-$
118	21.4 ± 1.2	17.8	$-$	$-/-$
120	37.5 ± 3.3	29.6	$-$	$-/-$
132	20.4	13.2	14.5 ± 0.3	$-/-$
146	15.8	18.4	14.5 ± 1.9	$-/-$
149	22.1 ± 3.8	21.9	16.7 ± 0.1	$0.153/-$
150	21.2 ± 0.5	21.5	17.3 ± 0.1	$0.002/-$
155	12.4	15.3	10.8 ± 0.6	$-/-$
157	27.3 ± 1.4	24.2 ± 1.3	12.6 ± 1.3	0.001/0.035

171	32.1 ± 0.5	26.2	19.2 ± 1.5	$0.002/-$
174	33.6 ± 2.8	30.7	20.7 ± 1.1	$0.010/-$
181	45.8	46.8	–	$-/-$
186	22.3	17.4	18.2 ± 2.6	$-/-$
195	20.0 ± 0.2	46.3	22.4	$-/-$
Mean	34.0 ± 13	32.8 ± 13	27.1 ± 13	n/a

*Indicates these flows have estimates that are not statistically distinct at the 95% confidence level.

– Indicates a one-sample T-test was unable to be run as a result of insufficient data (at least 2 estimates per flow-level dataset are needed)

Note. Uncertainties are only listed when more than 1 estimate is available. Teanby et al. (2002) used the Th-OT+ method. Gratton et al. (2005) used the MW-Perp method. The Old T-test significance level is that from Table B1.

The Teanby et al. (2002) data were then reanalyzed a second time by only selecting data from temperature steps above 300 °C, which is a requirement of the Perpendicular protocol to ensure only the higher temperature ferrimagnetic phase is being studied. The results of these tests are in Table C3. The reanalysis left 58 PI estimates across 45 flows, again with 9 flows having enough data for a two-sample T-test to compare the reanalyzed Teanby et al. (2002) results with the data from Gratton et al. (2005). The resulting mean PI estimates from the relevant flows were 33.6 µT and 27.6 µT, respectively (22% difference). Of these 9 flows, 4 flows remained statistically distinct, a proportion again virtually unchanged from previously, but the Teanby et al. (2002) pass rate again drops from 54% to 16%. We note that the effect of rejecting 137 PI estimates is just a 15% improvement in agreement.

Table C3. Reanalyzed Teanby et al. (2002) data, rejecting all steps below 300 °C

Flow	Teanby et al. (2002) estimate (µT)	Teanby et al. (2002) estimate updated (µT)	Gratton et al. (2005) estimate (µT)	Difference (old/new) (%)	T-Test significance level (old/new)
2	58.6	52.0	21.3 ± 2.0	$175/144$	$-/-$
3	56.9	55.0	44.8 ± 5.7	$27/23$	$-/-$
6	50.4 ± 4.5	44.6	36.5 ± 0.6	$38/22$	$0.010/-$
8	59.0 ± 3.2	50.2 ± 11	38.3 ± 1.0	$54/31$	$< 0.001/0.021$
9	58.0 ± 19.5	48.6	40 ± 8.4	$45/22$	$0.353/-$
10	60.1 ± 7.1	55.1	56.3 ± 7.6	$7/-2$	$0.657/-$
18	51.2 ± 9.1	51.8	39.6 ± 0.1	$29/31$	$0.046/-$
23	51.4 ± 0.9	48.7 ± 1.9	28.8 ± 1.0	$78/69$	$0.002/0.006$
33	48.7 ± 4.5	44.5	57.4 ± 2.1	$-15/-23$	$0.018/-$
34	49.4 ± 7.0	41.9 ± 0.5	64.7 ± 4.9	$-24/-35$	$0.079/0.023$
35	53.8	56.1	–	$-/-$	$-/-$
37	49.2 ± 3.4	42.5 ± 11	24.8 ± 6.0	$98/71$	$0.015/0.072$*
39	36.3 ± 3.0	35.5 ± 1.7	20.1 ± 1.3	$81/77$	$0.020/0.010$
40	38.9 ± 3.3	36.1 ± 3.2	35.2 ± 6.0	$11/3$	$0.106/0.835$*
41	–	32.6	21.9 ± 0.3	$123/49$	$-/-$
46	32.4 ± 0.5	28.8	25.1 ± 8.6	$29/15$	$0.355/-$
50	42.2 ± 0.1	40.6	39.4 ± 1.4	$7/3$	$0.075/-$
53	–	33.8	14.4 ± 0.7	$-/$	$-/-$
54	–	23.7 ± 16	–	$-/-$	$-/-$

55	–	42.2	–	−/−	−/−
56	38.3 ± 3.5	35.6	28.3 ± 0.8	35/26	0.032/−
64	18 ± 2.6	23.3 ± 1.8	15.1 ± 5.8	19/54	0.585/0.196*
75	28.8	27.8	20.4 ± 11	41/36	−/−
82	42.7	41.2 ± 1.0	–	−/−	−/−
100	–	14.5	–	−/−	−/−
105	20.6 ± 1.9	19.8 ± 1.4	19.4 ± 1.5	6/2	0.439/0.785*
106	17.9 ± 1.5	28.1 ± 13	16.5 ± 0.3	8/70	0.187/0.189*
114	18.0 ± 0.0	18.5	18.4 ± 1.3	−2/1	0.703/−
116	20.8 ± 0.2	21.4	22.7 ± 2.0	−8/−6	0.293/−
117	31.4 ± 2.8	33.8	–	−/−	−/−
120	37.5 ± 3.3	39.4	–	−/−	−/−
133	–	29.6	–	−/−	−/−
146	15.8	16.4	14.5 ± 1.9	9/13	−/−
149	22.1 ± 3.8	19.7	16.7 ± 0.1	32/18	0.153/−
150	21.2 ± 0.5	20.7	17.3 ± 0.1	23/20	0.002/−
157	27.3 ± 1.4	24.1	12.6 ± 1.3	117/92	0.001/−
164	36.7 ± 3.3	18.4	22.6 ± 1.0	62/−18	0.001/−
171	32.1 ± 0.5	24.3	19.2 ± 1.5	67/26	0.002/−
181	45.8	41.8	–	−/−	−/−
186	22.3	17.5	18.2 ± 2.6	−/−	−/−
191	–	34.0	–	−/−	−/−
200	32.0 ± 3.2	30.4	19.3 ± 1.9	66/58	0.016/−
208	19.4	12.3	–	−/−	−/−
221	40.9 ± 2.1	41.4	31.4 ± 2.8	30/32	0.005/−
229	20.5 ± 4.1	12.4	16.3 ± 3.7	26/−24	0.317/−
Mean	37.7 ± 14	33.6 ± 13	27.6 ± 13	37/22	n/a

Note. Uncertainties are only listed when more than 1 estimate is available. Teanby et al. (2002) used the Th-OT+ method. Gratton et al. (2005) used the MW-Perp method. The Old T-test significance level is that from Table C1.

*Indicates these flows have estimates that are not statistically distinct at the 95% confidence level.

−Indicates a one-sample T-test was unable to be run as a result of insufficient data (at least 2 estimates per flow-level dataset are needed)

Since simple re-analyses of the data failed to provide meaningful, consistent improvements in the data agreement without throwing out so much data as to make the results nearly meaningless, the only remaining option is to collect more data to analyze the demagnetization mechanisms and protocols in isolation.

C.2 Rock magnetic data

In this section, we report additional rock magnetic information that the reader might find helpful to put the SOH1 samples studied in the main text into context for other studies.

We ran First Order Reversal Curves (FORCs), at the Institute for Rock Magnetism at the University of Minnesota, to assess magnetic domain states. The data were gathered on a Princeton Instruments Vibrating Sample Magnetometer. We had thin sections prepared by Hands on Thin Sections in Birmingham, UK. We scanned them using a Hitachi TM2000 table-top Scanning Electron Microscope (15 kV accelerating voltage) at the University of Liverpool to identify mineralogy and estimate magnetic grain sizes.

The focus of this study is on comparative PI estimates, but we also endeavored to put the new data in a larger context with a broad rock magnetic survey, beyond the hysteresis properties reported in Gratton et al. (2005). From the flows investigated, we then selected five representative specimens for FORC analysis, and five for scanning electron microscopy, which had various rates of success in PI experiments from 0 to 100%.

We present five SEM images and five FORC diagrams that, from their flow-level hysteresis properties, we expect to be broadly representative of the primary rock magnetic properties of the investigated flows.

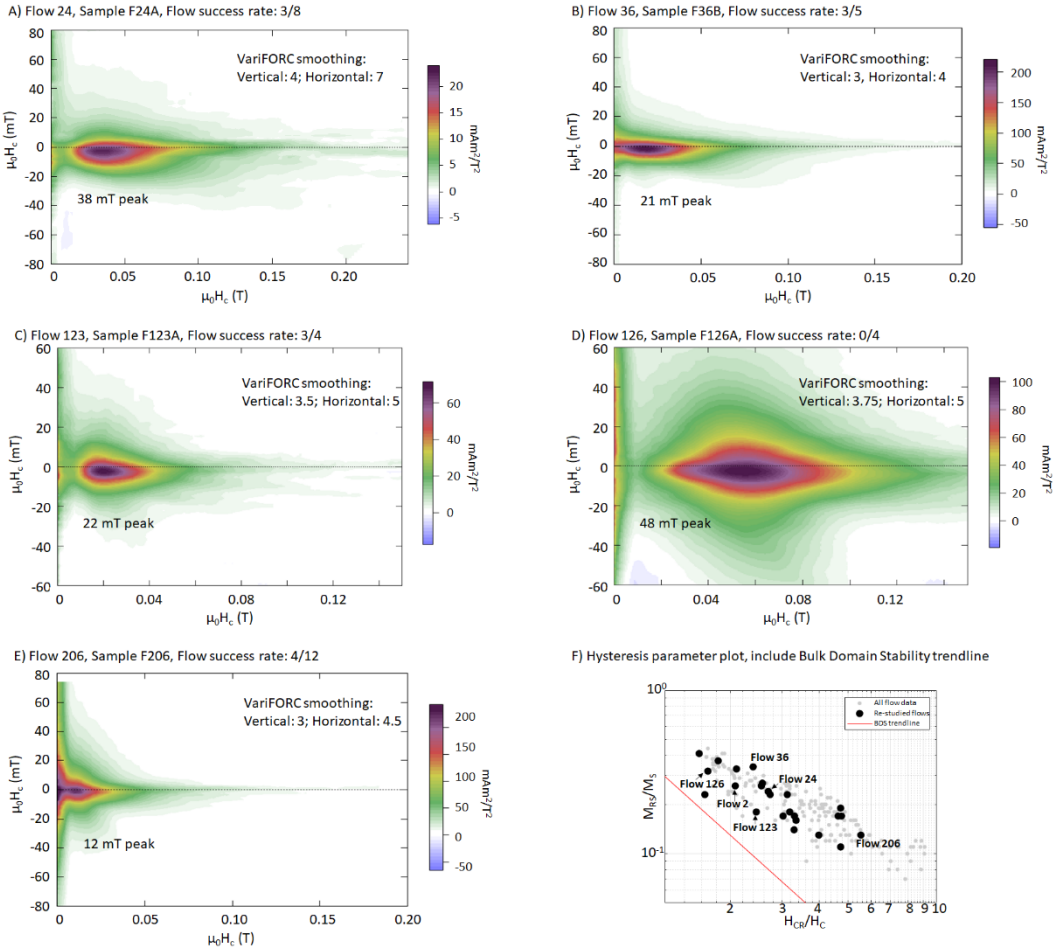

Figure C1. First Order Reversal Curves for 3 flows, analyzed using VariFORC in the FORCinel program. The smoothing factors increased at a rate, $\lambda = 0.1$, as H_C increases (Harrison and Feinberg, 2008). The flow success rate is the aggregate rate of successful PI estimates (regardless of method) across Teanby et al. (2002), Gratton et al. (2005) and this study. The horizontal axis is a measure of coercive force and the vertical axis is a measure of interactivity between grains. A) Flow 24 has predominately single domain magnetite. B) Flow 36 has more interacting grains. C) Flow 123 has a clear single domain magnetite peak, combined with a mildly interacting component. D) Flow 126 has a predominately single domain magnetite. E) Flow 206 has the most interacting grains of the flows studied by FORC analysis. F) Hysteresis parameters plot, showing which flows were studied herein for new PI estimates, FORC data, and SEM images.

The five specimens show coercivity peaks ranging from 12 mT to 48 mT. Strong, circular peaks surrounded by closed contours were found in some specimens and are characteristic

of single domain magnetite (Pike et al., 2001; Roberts et al., 2000). However, many specimens also display non-closed contours that diverge as they approach the origin, which is characteristic of larger-sized and/or interacting grains (Pike et al., 2001; Roberts et al., 2000). We note that all the measured FORCs have at least some interacting characteristics, given the spreading observed along the $\mu_0 H_C$ axis and non-closed contours. We therefore interpret the main sequence of the Gratton et al. (2005) data in Figure F to be primarily that of mixed stability magnetic carriers. Our data do not have an apparent correlation between the aggregation of successful PI estimates and the interacting characteristics of the FORCs, an outcome which is broadly consistent with that reported by Paterson et al. (2010). For example, Flow 36 (Fig. C1B) had the most consistent PI estimates between methods, but other flows, like Flow 24 (Fig. C1A), displayed more single-domain behavior.

After examining the five thin sections made, we found two primary populations of opaque minerals. The first (Fig. C2A, B, D, and E), contains abundant quantities of cruciform magnetite, including some examples of magnetite twinning. Elemental analysis was completed using Electron-Dispersive X-ray Spectroscopy (EDS) with a time period of 10 minutes. The predominant elements found in point analysis were iron, silicon, and titanium, which is consistent with titanomagnetite grains surrounded by plagioclase and clinopyroxene. The second type (Fig. C2C), contains large grains of ilmenite- with near stoichiometric ratios of iron and titanium (making them non-magnetic at or above room temperature) but no visible cruciform structures.

The darkest grains (with respect to the SEM backscatter electron image grayscale) in each example have elemental ratios consistent with plagioclase, and the second darkest are consistent with clinopyroxene. The large brighter areas have ratios consistent with ilmenite, and the small brightest particles have ratios consistent with magnetite. The specimens in Figure C2B and C2C both show elongated ilmenite structures.

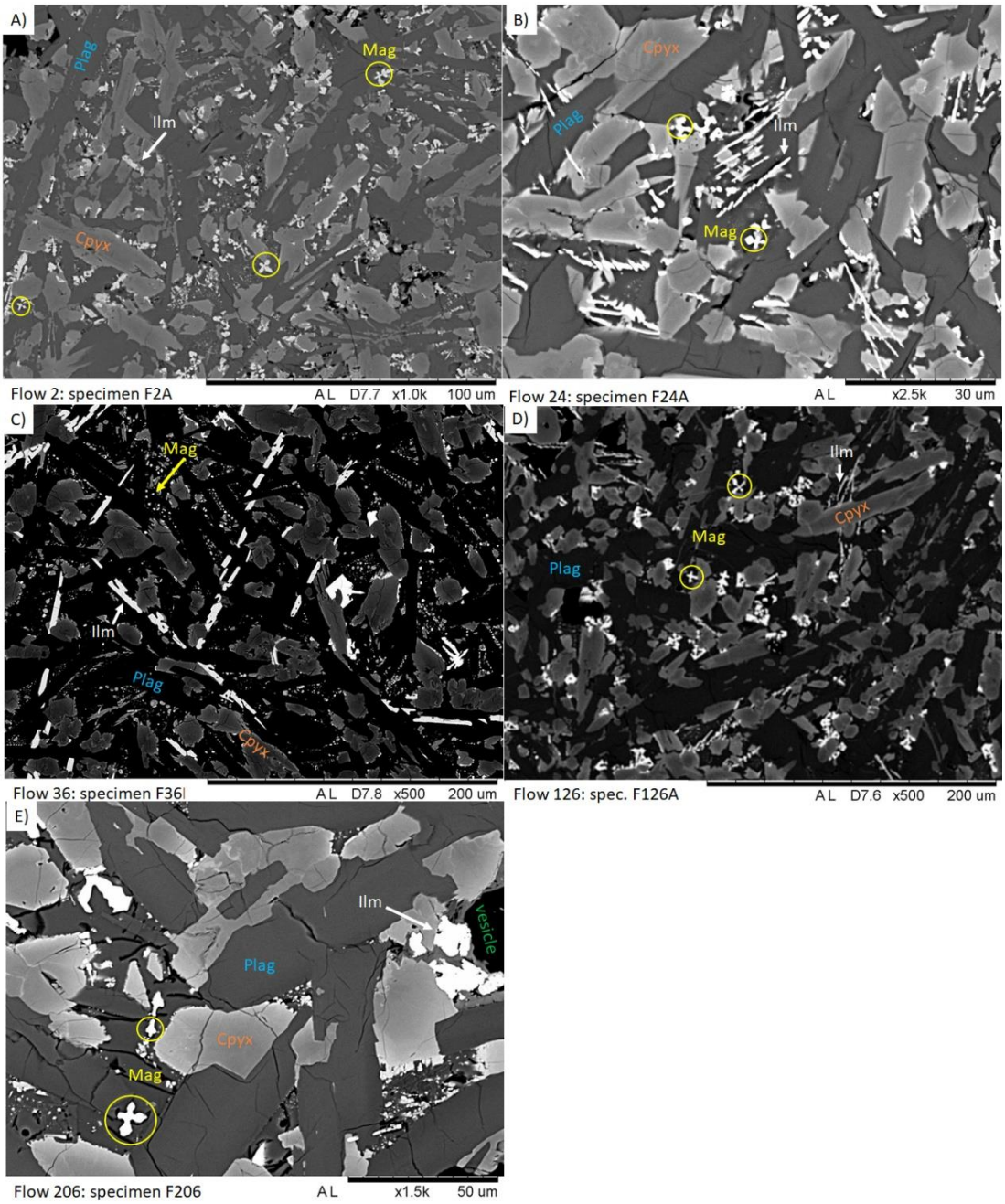

Figure C2 Representative examples of specimens observed. A) Flow 2 example, showing magnetite cruciform structures (some examples circled). B) Flow 24 example, showing elongated ilmenite grains with magnetite cruciform structures. C) Flow 36 example, showing larger grains of ilmenite and scattered, smaller quantities of magnetite. D) Flow 126 example, showing both closely packed and sparse cruciform magnetite but relatively little ilmenite. E) Flow 206 example, with relatively large grains of (titano-)magnetite, compared to others. Plag = plagioclase, Cpyx = clinopyroxene, Mag = magnetite, Ilm = ilmenite.

The specimens show a clear plagioclase and clinopyroxene groundmass, consistent with these rocks being basalt. Varying amounts of large-grained ilmenite and smaller grains of magnetite (1 – 10 µm in size), with some displaying cruciform structures (3 – 10 µm in size), imply the presence of a mixture of magnetic carriers. The magnetite grains' shapes do not imply secondary growth, so we see no immediate reason to reject the small grains as TRM carriers. There was no apparent cracking, zonation, or exsolution lamellae observed in the

SEM images, so we do not expect the magnetic grains to be strongly maghematized or interacting (Cisowski, 1981). These results are broadly consistent with the hysteresis parameters in Figure B1.

Gratton et al. (2005) found that most specimens had thermomagnetic curves characteristic of low-Ti magnetite accompanied by a fraction of high-Ti titanomagnetite grains present. Their data are consistent with the data herein. From the rock magnetic data, we do not have a strong case for pre-rejecting any of the main sequence of SOH1 rocks from paleointensity study. All rock magnetic results are consistent with these rocks being reliable paleointensity recorders.

C.3 New paleointensity results

Here we present the per specimen details of our new paleointensity results and associated flow level summaries. In addition, representative Arai plots are presented in Figures C3 and C4 comparing the newly obtained MW-PERP and TH-OT+ results to the original study results.

In Tables C4, C6, C8, and C10, Low T and High T refer to the temperature range of the fit for the thermal data and the treatment number for the microwave data. The PI estimate is provided in μT. H_{lab} is the applied laboratory field (in μT). N is the number of data points on the Arai plot selected. B, or β, is a measure of scatter around the best-fit line. FRAC is a measure of the amount of NRM used for the fit. G is the gap factor. Q is the quality factor. DRAT is a measure of alteration as defined by pTRM checks. CDRAT is a measure of the cumulative alteration. Alpha, or α, and MAD are measures of the goodness of the orthogonal vector plot fit. K, or |K'|, is the curvature criterion.

Table C4. MW-OT+ Arai plot fits

Flow	Sample	Low T	High T	PI estimate	H_{lab}	N	B	FRAC	G	Q	DRAT	CDRAT	Alpha	MAD (fixed)	K
2	SOHR F2B	1	12	25.8	40	12	0.022	0.600	0.839	22.9	4.2%	0.4%	0.1	0.1	0.143135
2	SOHR F2C	2	5	19.1	40	4	0.072	0.390	0.359	2.1	0.1%	0.0%	5.4	1.1	0.476885
6	SOHR 14A	3	10	43.1	40	8	0.026	0.647	0.830	22.3	2.7%	2.2%	1.9	0.8	0.167882
6	SOHR 14B	0	4	47.1	40	4	0.046	0.629	0.604	8.4	4.7%	4.7%	2.9	2.2	0.071234
8	SOHR 16 01	1	10	47.1	40	10	0.030	0.768	0.847	23.6	6.9%	0.7%	5.1	2.3	0.158106
8	SOHR 17 03	1	8	40.2	40	8	0.043	0.574	0.772	11.3	8.1%	14.3%	3.9	2.0	0.275337
22	SOHR 65A	1	5	35.4	40	5	0.028	0.625	0.737	17.0	0.8%	1.6%	1.2	0.7	0.124408
22	SOHR 65B	1	8	36.0	40	8	0.032	0.611	0.853	18.1	5.8%	9.0%	1.0	0.7	0.218719
22	SOHR 65C	1	5	40.2	40	5	0.035	0.687	0.730	15.4	1.5%	2.2%	2.8	2.0	0.170379
23	SOHR 23B	1	14	47.4	40	14	0.069	0.365	0.895	4.3	5.5%	6.8%	5.6	1.9	0.522952
23	SOHR F23A	1	11	38.8	40	11	0.067	0.405	0.892	4.8	0.8%	-1.4%	7.2	1.7	0.421406
23	SOHR F23C	1	10	34.4	40	10	0.041	0.821	0.864	18.2	5.8%	-2.1%	1.4	0.8	0.289715
23	SOHR F23AB	1	5	37.0	40	5	0.053	0.354	0.707	4.8	2.5%	2.8%	0.8	0.2	0.221352
23	SOHR F23ca	0	9	32.5	40	10	0.092	0.464	0.831	4.5	7.3%	9.2%	4.7	1.1	0.529529
24	SOHR F24B	1	9	25.9	40	9	0.032	0.683	0.869	18.5	5.3%	13.3%	1.9	1.1	0.226316
24	SOHR F24AA	0	3	35.9	40	4	0.047	0.367	0.577	4.5	1.1%	1.1%	1.3	0.3	0.153833
26	SOHR F26A	2	11	32.5	40	10	0.041	0.656	0.839	13.0	11.6%	26.6%	39.7	21.4	0.202608
26	SOHR F26B	1	5	29.3	40	5	0.017	0.592	0.744	24.2	4.1%	5.7%	4.6	2.6	0.086275
36	SOHR F36B	1	12	32.7	40	12	0.027	0.698	0.896	25.8	2.3%	0.2%	0.8	0.5	0.233222
37	SOHR F37BA	2	5	34.5	40	4	0.091	0.395	0.629	3.1	0.3%	-0.3%	2.3	0.6	0.340031
37	SOHR F37BB	1	10	32.3	40	10	0.037	0.744	0.812	16.2	8.3%	6.4%	5.5	4.5	0.18682
48	SOHR F48CA	1	12	31.8	40	12	0.022	0.611	0.902	28.1	1.5%	-1.0%	0.4	0.3	0.16611
48	SOHR F48CB	1	10	27.0	40	10	0.033	0.764	0.872	20.8	1.9%	3.5%	1.1	0.9	0.248351
87	SOHR 202 02	1	14	14.2	40	14	0.062	0.680	0.876	10.4	4.5%	1.5%	12.3	3.9	0.585295
91	SOHR F91 03	2	11	17.0	40	10	0.062	0.395	0.826	5.7	7.1%	8.0%	16.6	2.9	0.443615
163	SOHR F163CC	1	8	24.6	40	8	0.032	0.711	0.833	18.9	3.0%	0.6%	1.4	0.6	0.14166
163	SOHR F163CB	1	7	20.9	40	7	0.194	0.739	0.774	3.0	2.2%	-3.3%	5.1	2.7	0.703786
163	SOHR F163CA	3	10	26.7	40	8	0.047	0.563	0.840	13.0	2.9%	-1.1%	4.4	2.0	0.273176
189	SOHR 351	1	8	22.1	40	8	0.011	0.684	0.792	51.6	1.6%	-1.3%	7.1	3.6	0.050073
193	SOHR 358 01	1	11	18.5	40	11	0.019	0.715	0.868	30.8	6.8%	2.7%	4.1	3.7	0.069762
196	SOHR 363 04	1	10	15.0	40	10	0.018	0.666	0.775	28.7	5.3%	2.4%	11.1	5.0	0.107566
206	SOHR 382A	1	4	22.1	40	4	0.047	0.335	0.520	3.7	2.2%	2.5%	3.7	0.6	
206	SOHR 382B	1	7	8.5	40	7	0.082	0.505	0.761	4.6	2.6%	-2.1%	31.2	10.8	0.555083
206	SOHR 382C	1	4	18.7	40	4	0.058	0.460	0.545	4.7	0.1%	0.1%	7.7	1.9	0.250291
220	SOHR 414 02	1	14	42.1	40	14	0.064	0.516	0.847	7.1	2.0%	-2.4%	9.0	1.9	0.551979
220	SOHR 416 02	1	14	32.9	40	14	0.038	0.377	0.878	8.8	2.7%	-4.4%	2.5	0.7	0.276792
220	SOHR 417 05	0	15	41.5	40	16	0.050	0.381	0.913	7.1	2.0%	-8.2%	3.2	0.8	0.389452
221	SOHR 424	7	14	94.8	40	8	0.038	0.295	0.835	10.0	7.6%	-22.9%	1.8	0.5	0.078151
221	SOHR 426	2	5	105.0	40	4	0.073	0.341	0.628	4.3	0.9%	1.6%	29.7	10.4	0.063553
221	SOHR 425	1	5	36.7	40	5	0.017	0.465	0.629	17.8	0.0%	0.0%	5.1	1.2	0.092437
221	SOHR 423	3	10	39.6	40	8	0.084	0.366	0.810	5.5	8.1%	-10.3%	17.3	5.7	0.249594
222	SOHR 428	1	2	23.8	40	2	#DIV/0!	0.000	#DIV/0!	#DIV/0!	#DIV/0!	#DIV/0!	#NUM!	15.3	'NA'
222	SOHR 428B	1	7	33.7	40	7	0.038	0.496	0.725	9.7	2.0%	-2.2%	0.9	0.4	0.214608
237	SOHR 464A	1	7	16.5	40	7	0.079	0.451	0.815	5.9	4.7%	-3.0%	6.1	2.5	0.360104
237	SOHR 464B	3	12	9.0	40	10	0.096	0.460	0.870	8.3	1.5%	0.6%	9.6	5.6	0.636266
237	SOHR F2A	2	5	25.4	40	4	0.039	0.422	0.327	4.0	0.7%	0.4%	5.3	2.7	0.283881
237	SOHR 464B	0	7	8.2	40	8	0.054	0.739	0.811	10.9	6.3%	-5.2%	10.2	5.0	0.158627
237	SOHR 464A	1	11	7.2	40	11	0.030	0.758	0.878	21.4	3.0%	0.5%	10.6	5.6	0.090579

Table C5. MW-OT+ Flow-level summary

Flow	MW-OT+ (μT)	N_{pass}/ N_{tested}		Flow	MW-OT+ (μT)	N_{pass}/ N_{tested}
2	22.5 ± 4.7	2/2		91		0/1
6	45.1 ± 2.8	2/2		163	25.7 ± 1.5	2/3
8	43.7 ± 4.9	2/2		189	22.1	1/1
22	37.2 ± 2.6	3/3		193	18.5	1/1
23	36.7 ± 2.2	3/5		196	15	1/1
24	25.9	½		206	18.7	1/3
26	32.5	½		220	37.2 ± 6.1	2/3
36	32.7	1/1		221	36.7	¼
37	33.4 ± 1.6	2/2		222	33.7	½
48	29.4 ± 3.4	2/2		237	14.3 ± 8.5	4/5
87		0/1		Mean	29.5 ± 9.2	19/21

Note: N_{pass} is the total number of specimens that passed the PI selection criteria. N_{tested} is the total number of specimens that were tested from a given flow with a given method. Empty cells indicate no experiments succeeded. For the mean row, N_{pass} and N_{tested} reference the number of flows.

Table C6. Th-OT+ Arai plot fits

Flow	Sample	Low T	High T	PI estimate	H_{lab}	N	B	FRAC	G	Q	DRAT	CDRAT	Alpha	MAD (fixed)	K
37	SOHR F37A	120	585	61.6	40	13	0.038	0.914	0.885	21.5	6.4%	-14.4%	0.7	1.6	0.05833
37	SOHR F37B	120	580	56.8	40	12	0.058	0.921	0.863	13.9	4.5%	1.6%	1.2	2.9	0.275685
162	SOHR F162A	120	585	16.0	40	13	0.097	0.804	0.835	8.5	9.3%	1.3%	4.1	12.7	0.6215
162	SOHR F162B	120	585	17.5	40	13	0.077	0.948	0.812	9.4	10.7%	-31.9%	1.7	14.1	0.41538
162	SOHR F162C	120	585	16.5	40	13	0.087	0.911	0.801	8.7	13.5%	-24.1%	4.3	16.6	0.071128
163	SOHR F163A	120	500	58.3	40	7	0.037	0.547	0.815	13.0	0.3%	-0.4%	5.4	1.9	0.198068
163	SOHR F163B	120	555	41.3	40	10	0.052	0.871	0.870	16.2	5.9%	-1.7%	1.9	2.8	0.327762
163	SOHR F163C	120	540	38.0	40	9	0.070	0.790	0.860	11.4	8.3%	11.0%	3.4	2.3	0.441504
176	SOHR F176A	480	555	41.1	40	5	0.077	0.653	0.653	7.3	2.5%	5.2%	2.4	2.2	0.46756
176	SOHR 335A	220	555	22.2	40	9	0.063	0.594	0.816	10.2	6.7%	-11.3%	6.8	3.2	0.271212
176	SOHR 335B	120	570	15.7	40	11	0.038	0.821	0.833	18.9	4.1%	-3.2%	2.8	3.1	0.211754
185	SOHR F185A	380	540	13.4	40	6	0.066	0.427	0.720	5.7	19.0%	-38.0%	13.9	14.5	0.3963
186	SOHR 347A	120	480	33.1	40	6	0.085	0.422	0.793	5.4	10.4%	-14.6%	34.4	14.8	0.285628
186	SOHR 347B	120	520	22.3	40	8	0.073	0.533	0.846	8.9	7.2%	-14.1%	32.3	15.6	0.417826
186	SOHR F186A	220	520	27.9	40	7	0.076	0.430	0.827	6.8	5.3%	8.4%	11.4	4.3	0.474033
186	SOHR F186B	220	520	34.3	40	7	0.080	0.505	0.823	6.7	5.4%	11.1%	8.1	3.2	0.502473
186	SOHR 348	120	440	34.2	40	5	0.072	0.313	0.659	3.2	1.8%	-1.7%	10.5	2.2	0.278479
206	SOHR F206	120	585	22.9	40	2	#DIV/0!	0.308	0.000	#DIV/0!	51.2%	-141.5%	#NUM!	1.4	'NA'
206	SOHR 381	300	500	60.7	40	5	0.080	0.456	0.712	4.9	1.4%	1.2%	12.1	4.8	0.239357

Table C7. Th-OT+ Flow-level summary

Flow	New Th-OT+ (μT)	N_{pass}/ N_{tested}	Teanby et al. (2002) Th-OT+ (μT)	N_{pass}/ N_{tested}
37	59.2 ± 3.4	2/2	49.2 ± 3.4	2/3
162		0/3		-/-
163	45.9 ± 11	3/3		-/-
174	26.3 ± 13	3/3	33.6 ± 2.8	3/3
185		0/1		-/-
186	27.9	1/1	22.3	1/2
206	60.7	1/2	17.9	1/2
Mean	44.0 ± 16	5/7	30.8 ± 14	4/4

Note: N_{pass} is the total number of specimens that passed the PI selection criteria. N_{tested} is the total number of specimens that were tested from a given flow with a given method. Empty cells indicate no experiments succeeded. For the mean row, N_{pass} and N_{tested} reference the number of flows.

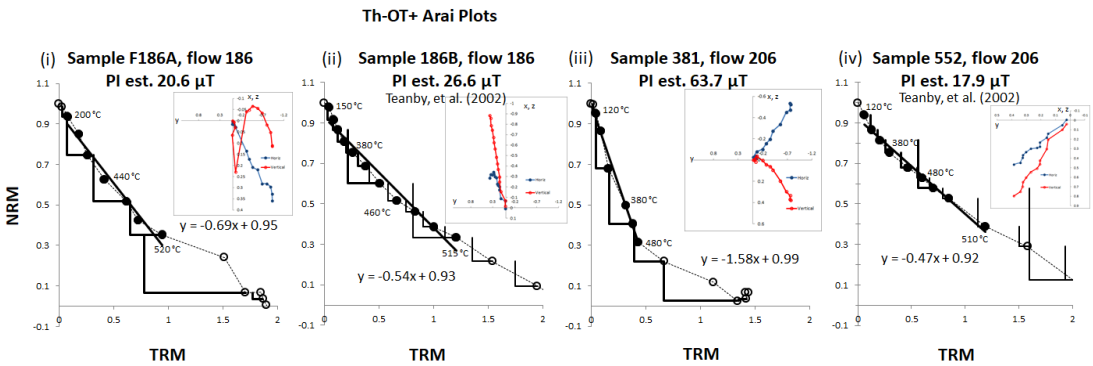

Figure C3 Normalized Arai plot examples for Th-OT+ data. The data in (i) and (ii) are for flow 186. The data in (iii) and (iv) are for flow 206. The data in (i) and (iii) are newly obtained in this study and (ii) and (iv) are from Teanby et al (2002). The data are normalized by NRM_0. The filled circles are accepted data points, with the solid black line being the best-fit line. Open circles are rejected data points. The black right-angles lines are pTRM checks. Orthogonal vector plots are provided in core coordinates. All specimens presented pass their original study's selection criteria.

Table C8. Th-Perp Arai plot fits

Flow	Sample	Low T	High T	PI estimate	H_{lab}	N	B	FRAC	G	Q	DRAT	CDRAT	Alpha	MAD (fixed)	K
2	SOHR F2A	340	530	27.6	31	7	0.029	0.930	0.789	25.4	0.0%	0.0%	#N/A	#N/A	0.145994
2	SOHR F2B	340	560	35.2	31	9	0.098	0.960	0.843	8.3	0.0%	0.0%	#N/A	#N/A	0.388224
2	SOHR 5	340	550	25.4	31	8	0.089	0.596	0.774	5.2	0.0%	0.0%	#N/A	#N/A	0.116969
7	SOHR F7A	340	560	44.5	31	9	0.108	0.670	0.768	4.8	0.0%	0.0%	#N/A	#N/A	0.152
8	SOHR 18	0	500	53.4	43.6	11	0.301	0.116	0.325	0.1	0.0%	0.0%	#N/A	#N/A	n/a
22	SOHR 65	300	530	12.6	31	8	0.150	0.870	0.841	4.9	0.0%	0.0%	#N/A	#N/A	0.66032
22	SOHR 66	300	570	22.6	31	11	0.046	0.953	0.876	18.0	0.0%	0.0%	#N/A	#N/A	0.125299
23	SOHR F23A	380	530	27.8	31	6	0.075	0.567	0.759	5.8	0.0%	0.0%	#N/A	#N/A	0.276331
23	SOHR 23B	340	550	27.6	31	8	0.092	0.922	0.771	7.7	0.0%	0.0%	#N/A	#N/A	0.558519
24	SOHR 24B	450	530	58.1	31	4	0.371	0.120	0.648	0.2	0.0%	0.0%	#N/A	#N/A	0.87899
24	SOHR F24C	380	550	13.8	31	7	0.525	0.374	0.667	0.5	0.0%	0.0%	#N/A	#N/A	2.45337
26	SOHR F26A	340	550	15.0	31	8	0.103	0.450	0.800	3.5	0.0%	0.0%	#N/A	#N/A	0.32595
26	SOHR F26B	380	550	16.0	31	7	0.158	0.374	0.740	1.8	0.0%	0.0%	#N/A	#N/A	0.24223
26	SOHR F26C	380	530	21.2	31	6	0.078	0.476	0.725	4.4	0.0%	0.0%	#N/A	#N/A	0.335456
36	SOHR F36B	480	550	37.2	31	4	0.566	0.077	-1.128	0.2	0.0%	0.0%	#N/A	#N/A	0.30535
48	SOHR F48B	380	560	25.5	31	8	0.088	0.593	0.820	5.5	0.0%	0.0%	#N/A	#N/A	0.407005
48	SOHR F48.5	340	520	30.6	31	6	0.052	0.518	0.883	8.7	0.0%	0.0%	#N/A	#N/A	0.162173
48	SOHR F48.6	340	560	23.8	31	8	0.091	0.887	0.905	8.8	0.0%	0.0%	#N/A	#N/A	0.15448
176	SOHR 336	300	380	47.6	20.2	5	0.061	0.178	0.715	2.1	0.0%	0.0%	86.5	7.2	n/a
186	SOHR 348	400	575	258.0	19.97	14	0.343	1.051	0.297	0.9	0.0%	0.0%	#N/A	#N/A	n/a
189	SOHR 351	340	500	25.6	31	4	0.035	0.490	0.948	13.4	0.0%	0.0%	#N/A	#N/A	0.12809
193	SOHR 358	353	300	380	47.6	20.2	5	0.061	0.178	0.715	0.0%	0.0%	0.0%	86.5	0.0%
206	SOHR 382	300	560	26.2	31	10	0.069	0.514	0.786	5.9	0.0%	0.0%	#N/A	#N/A	0.12272
220	SOHR 414	300	550	33.8	31	9	0.072	0.997	0.878	12.1	0.0%	0.0%	#N/A	#N/A	0.296688
221	SOHR 423A	400	560	31.8	31	6	0.097	0.816	0.916	7.7	0.0%	0.0%	#N/A	#N/A	0.391106
221	SOHR 423B	400	560	23.9	31	7	0.094	0.645	0.620	4.3	0.0%	0.0%	#N/A	#N/A	0.82401
221	SOHR 425A	0	460	36.9	31	5	0.097	0.383	0.819	3.2	0.0%	0.0%	#N/A	#N/A	0.09923
221	SOHR 425B	520	560	40.2	31	4	0.027	0.354	0.586	7.8	0.0%	0.0%	#N/A	#N/A	0.140644
222	SOHR 428	300	460	58.1	42	9	0.489	0.063	0.605	0.1	0.0%	0.0%	#N/A	#N/A	n/a
237	SOHR 465A	340	520	10.4	31	6	0.045	0.500	0.658	7.4	0.0%	0.0%	#N/A	#N/A	0.130534
237	SOHR 465B	340	540	2.0	31	7	0.893	0.001	564.483	0.6	0.0%	0.0%	#N/A	#N/A	n/a

Table C9. Th-Perp Flow-level summary

Flow	Th-Perp (μT)	N_{pass}/ N_{tested}		Flow	Th-Perp (μT)	N_{pass}/ N_{tested}
2	29.4 ± 5.1	3/3		186		0/1
7	39.2	1/1		189	25.6	1/1
8		0/1		193		0/1
22	26.3	½		206	26.2	1/1
23	27.7 ± 0.1	2/2		220	33.8	1/1
24		0/2		221	39.5 ± 2.8	2/4
26	21.2	1/3		222		0/1
36		0/1		237	10.4	½
48	26.4 ± 4.1	3/3		Mean	27.8 ± 8.1	11/18
176		0/1				

Note: N_{pass} is the total number of specimens that passed the PI selection criteria. N_{tested} is the total number of specimens that were tested from a given flow with a given method. Empty cells indicate no experiments suceeded. For the mean row, N_{pass} and N_{tested} reference the number of flows.

Table C10. MW-Perp Arai plot fits

Flow	Sample	Low T	High T	PI estimate	H_{lab}	N	B	FRAC	G	Q	DRAT	CDRAT	Alpha	MAD (fixed)	K
8	SOHR 16 02	9	15	14.4	40	7	0.065	0.317	0.828	4.0	0.0%	0.0%	#N/A	#N/A	0.750124
8	SOHR 16 03	14	17	24.2	50	4	0.041	0.536	0.591	7.7	0.0%	0.0%	#N/A	#N/A	0.170187
8	SOHR 17 01	4	7	32.6	40	4	0.123	0.306	0.643	1.6	0.0%	0.0%	#N/A	#N/A	0.81945
8	SOHR 17 02	4	12	38.0	40	9	0.012	0.824	0.814	57.2	0.0%	0.0%	#N/A	#N/A	0.03073
87	SOHR 202 03	12	21	9.6	40	10	0.024	0.547	0.853	19.1	0.0%	0.0%	#N/A	#N/A	0.05257
87	SOHR 202 04	14	19	10.8	30	6	0.039	0.444	0.696	7.9	0.0%	0.0%	#N/A	#N/A	0.196703
91	SOHR F91 01	9	14	10.9	40	6	0.020	0.636	0.793	25.0	0.0%	0.0%	#N/A	#N/A	0.09249
95	SOHR 217 01	7	12	29.1	40	6	0.051	0.389	0.785	6.0	0.0%	0.0%	#N/A	#N/A	0.358938
95	SOHR 218 02	9	16	52.0	40	8	0.027	0.349	0.840	10.7	0.0%	0.0%	#N/A	#N/A	0.256626
193	SOHR 358 02	11	19	17.7	20	9	0.032	0.239	0.818	6.1	0.0%	0.0%	#N/A	#N/A	0.29811
196	SOHR 363 06	7	11	12.6	40	5	0.021	0.382	0.731	13.6	0.0%	0.0%	#N/A	#N/A	0.07986
220	SOHR 414 01	11	18	17.2	40	8	0.013	0.442	0.779	26.3	0.0%	0.0%	#N/A	#N/A	0.08057
220	SOHR 416 01	5	14	26.6	40	10	0.019	0.593	0.877	27.1	0.0%	0.0%	#N/A	#N/A	0.06536
220	SOHR 416 03	10	16	25.5	50	7	0.045	0.415	0.791	7.3	0.0%	0.0%	#N/A	#N/A	0.22377
220	SOHR 417 02	13	24	24.2	40	12	0.016	0.552	0.848	29.7	0.0%	0.0%	#N/A	#N/A	0.09147
220	SOHR 417 03	5	16	27.3	40	12	0.007	0.880	0.895	111.6	0.0%	0.0%	#N/A	#N/A	0.00197
220	SOHR 417 04	7	22	29.4	40	16	0.020	0.717	0.877	32.0	0.0%	0.0%	#N/A	#N/A	0.08885
220	SOHR 417 06	5	19	32.0	25	15	0.020	0.781	0.906	35.6	0.0%	0.0%	#N/A	#N/A	0.19065
223	SOHR 430 02	4	10	17.8	40	7	0.052	0.677	0.659	8.6	0.0%	0.0%	#N/A	#N/A	0.15759
223	SOHR 430 03	15	18	16.7	20	4	0.117	0.348	0.278	0.8	0.0%	0.0%	#N/A	#N/A	1.75208
237	SOHR 459 02	9	11	8.35	40	3	0.010	0.384	0.471	18.4	0.0%	0.0%	#N/A	#N/A	0.04441
237	SOHR 460 01	8	12	12.8	40	5	0.055	0.711	0.718	9.3	0.0%	0.0%	#N/A	#N/A	0.25318

Table C11. MW-Perp Flow-level summary, compared with the Gratton et al. (2005) data

Flow	MW-Perp (μT)	N_{pass}/ N_{tested}	Gratton et al. (2005) MW-Perp (μT)	N_{pass}/ N_{tested}
8	31.1 ± 9.8	2/4	38.3 ± 1.0	6/6
87	10.2 ± 0.8	2/2	14.6 ± 1.9	2/2
91	10.9	1/1	12.1 ± 0.8	3/3
95		0/2	8.3	1/4
193		0/1	15.0 ± 0.1	2/2
196	12.6	1/1		0/2
220	26.0 ± 4.7	7/7		0/5
223		0/2	22.6 ± 6.7	2/3
237		0/2	19.1 ± 0.2	2/2
Mean	18.2 ± 10	5/9	18.6 ± 9.8	7/9

Note: N_{pass} is the total number of specimens that passed the PI selection criteria. N_{tested} is the total number of specimens that were tested from a given flow with a given method. Empty cells indicate no experiments succeeded. For the mean row, N_{pass} and N_{tested} reference the number of flows.

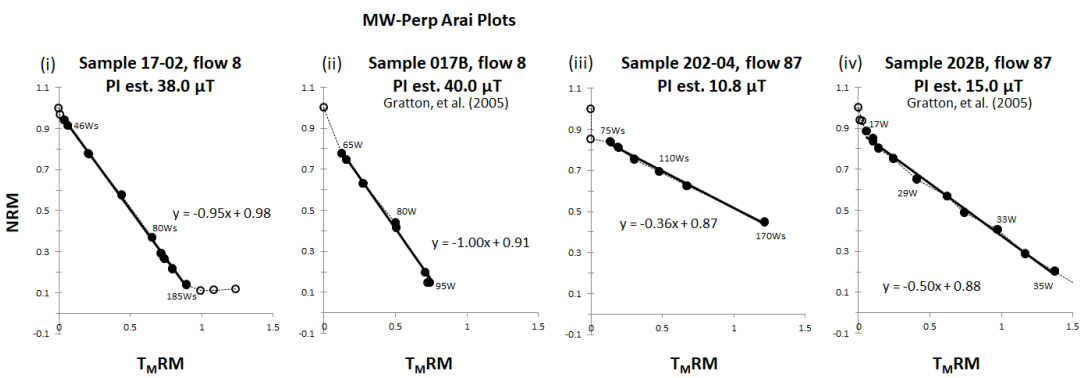

Figure 4 Normalized Arai plot examples for MW-Perp data. The data in (i) and (ii) are for flow 8. The data in (iii) and (iv) are for flow 87. The data in (i) and (iii) are newly obtained in this study and (ii) and (iv) are from Gratton et al (2005). The data are normalized by NRM_0. The filled circles are accepted data points, with the solid black line being the best-fit line. Open circles are rejected data points. All specimens presented pass their original

study's selection criteria. The powers given for the Gratton et al. (2005) MW data are power applied and the power integrals given in the new data are (inferred) energy absorbed.

C.4 New flow-level mean paleointensity estimates

In this section, new, flow-level averages are presented. The combined mean estimates are calculated by taking the means and standard deviations of all the accepted data from the Th-OT+ and MW-Perp datasets (the two largest datasets that also cover the range of values found). These data are therefore a combination of the new data from this study, the Teanby et al. (2002), and the Gratton et al. (2005) datasets. The mean estimate was calculated as the unweighted arithmetic mean of the Th-OT+ flow-level mean and the MW-Perp flow-level mean estimate. The standard deviation was calculated from the standard deviations of the flow-level data (without any weighting) from the total Th-OT+ and MW-Perp datasets. A mean flow-level paleointensity estimate of 29.2 ± 12 µT was found.

Table C12. Proposed averaging of flow-level Th-OT+ and MW-Perp datasets.

Flow	Th-OT+ estimate (µT)	SD	N	MW-Perp estimate (µT)	SD	N	Combined new estimate (µT)	SD	N
1	57.4	9.7	4	39.9	1.6	3	48.9	11	7
4	56.6	3.0	2	38.9	2.2	3	47.8	9.4	5
6	50.4	4.5	2	36.5	0.6	3	43.5	7.8	5
8	59.0	3.2	3	36.5	5.9	8	47.8	13	11
9	58.0	19	2	40.0	8.4	2	49.0	18	4
10	60.1	7.1	2	56.3	7.6	2	58.2	7.6	4
18	51.2	9.1	5	39.6	0.1	2	45.4	9.0	7
23	51.4	0.9	2	28.8	1.0	2	40.1	11	4
33	48.7	4.5	3	57.4	2.1	4	53.1	5.6	7
34	49.4	7.0	3	64.7	4.9	2	57.1	9.9	5
37	54.2	6.0	4	24.8	6.0	3	39.5	16	7
39	36.3	3.0	2	20.1	1.3	2	28.2	8.4	4
40	48.9	3.3	2	35.2	6.0	2	42.1	8.4	4
46	32.4	1.0	2	25.1	8.6	2	28.8	7.1	4
49	62.8	0.5	3	29.4	7.4	3	46.1	18	5
50	42.2	0.1	2	39.4	1.4	3	40.8	1.7	5
51	24.7	5.9	2	20.1	1.9	2	22.4	4.9	4
56	38.3	3.5	3	28.3	0.8	2	33.3	5.7	5
63	30.2	3.3	2	24.9	5.3	2	27.6	5.1	4
64	18.0	2.6	2	15.1	5.8	2	16.6	4.7	4
76	37.9	0.1	2	26.5	1.9	3	32.2	6.0	5
77	32.3	9.2	3	21.6	15.6	2	27.0	14	5
87	27.7	4.2	2	14.6	1.9	4	21.2	7.6	6
91	23.8	0.8	2	11.8	0.9	4	17.8	6.4	6
103	21.1	2.4	3	18.2	1.1	2	19.7	2.4	5
105	20.6	1.9	3	19.4	1.5	3	20.0	1.8	6
106	17.9	1.5	2	16.5	0.3	3	17.2	1.3	5
108	16.4	1.8	3	9.9	0.8	2	13.2	3.6	5
114	18.0	0	2	18.4	1.3	4	18.2	0.9	7

116	20.8	0.2	2	22.7	2.0	3	21.8	1.8	5
140	25.6	1.2	2	19.7	3.2	2	22.7	3.8	4
149	22.1	3.8	3	16.7	0.1	2	19.4	4.0	5
150	21.2	0.5	3	17.3	0.1	2	19.3	2.0	5
157	27.3	1.4	2	12.6	1.3	3	20.0	7.3	5
159	34.3	1.7	2	24.9	5.9	2	29.6	6.4	4
160	27.1	2	3	15.2	5.5	2	21.2	7.0	5
164	36.7	3.3	2	22.6	1	4	30.1	7.4	6
165	27.6	1.5	2	17.8	1.9	2	22.7	5.2	4
166	22.3	4.2	2	14.5	0.7	2	18.4	4.9	4
167	25.6	2.9	3	31.0	0.5	2	28.3	3.5	5
171	32.1	0.5	2	19.2	1.5	3	25.7	6.4	5
174	33.6	2.8	3	20.7	1.1	2	27.2	6.7	5
186	25.1	4.0	2	18.2	2.6	2	21.7	4.8	4
187	18.7	6.2	2	16.7	0.7	2	17.7	4.5	4
189	27.7	0.2	2	19.8	1	2	23.8	4.0	4
200	32.0	3.2	3	19.3	1.9	2	25.7	6.8	5
220	46.4	7.9	4	27.5	2.8	7	37.0	11	11
221	40.9	2.1	3	31.4	2.8	4	36.2	5.3	7
222	39.8	3.3	3	37.8	1.6	3	38.8	2.8	6
223	36.3	3.2	3	22.6	6.7	2	29.5	8.3	5
226	22.2	4.5	2	16.3	1.2	3	19.3	4.2	5
227	22.1	5.9	2	15.2	1.4	2	18.7	5.5	4
229	20.5	4.1	2	16.3	3.7	3	18.4	4.4	5
230	19.9	2.2	2	16.4	0.3	2	18.2	2.4	4
236	21.8	1.6	3	12.5	1.7	2	17.2	4.8	5
237	25.5	8.2	3	19.1	0.2	2	22.3	7.1	5
240	18.8	6.4	2	13.7	0.9	2	16.3	5.6	5
Mean	33.4	13		24.7	12		29.2	12	

Note. The MW-Perp data derive from both this study and Gratton et al. (2005). The Th-OT+ data derive from both this study and Teanby et al. (2002).

References

Cisowski, S., 1981, Interacting vs non-interacting single domain behavior in natural and synthetic samples: Physics of the Earth and Planetary Interiors, v. 26, no. 1-2, p. 56-62.

Gratton, M. N., Shaw, J., and Herrero-Bervera, E., 2005, An absolute palaeointensity record from SOH1 lava core, Hawaii using the microwave technique: Physics of the Earth and Planetary Interiors, v. 148, no. 2-4, p. 193-214.

Harrison, R. J., and Feinberg, J. M., 2008, FORCinel: An improved algorithm for calculating first-order reversal curve distributions using locally weighted regression smoothing: Geochemistry Geophysics Geosystems, v. 9.

Paterson, G. A., Muxworthy, A. R., Roberts, A. P., and Mac Niocaill, C., 2010, Assessment of the usefulness of lithic clasts from pyroclastic deposits for paleointensity determination: Journal of Geophysical Research-Solid Earth, v. 115.

Pike, C. R., Roberts, A. P., and Verosub, K. L., 2001, First-order reversal curve diagrams and thermal relaxation effects in magnetic particles: Geophysical Journal International, v. 145, no. 3, p. 721-730.

Roberts, A. P., Pike, C. R., and Verosub, K. L., 2000, First-order reversal curve diagrams: A new tool for characterizing the magnetic properties of natural samples: Journal of Geophysical Research-Solid Earth, v. 105, no. B12, p. 28461-28475.

Teanby, N., Laj, C., Gubbins, D., and Pringle, M., 2002, A detailed palaeointensity and inclination record from drill core SOH1 on Hawaii: Physics of the Earth and Planetary Interiors, v. 131, no. 2, p. 101-140.

SUPPLEMENTARY INFORMATION D: CHAPTER 8

In this section, the PI estimate is provided in μT. H_{lab} is the applied laboratory field (in μT). N is the number of data points on the Arai plot selected. B, or β, is a measure of scatter around the best-fit line. FRAC is a measure of the amount of NRM used for the fit. G is the gap factor. Q is the quality factor. DelCK refers to the individual pTRM checks' errors. DRAT is a normalized measure of alteration as defined by pTRM checks. CDRAT is a measure of the cumulative alteration. Alpha, or α, and MAD are measures of the goodness of the orthogonal vector plot fit. K, or |K'|, is the curvature criterion. The pass score refers to the number of selection criteria passed, with the format "A.B". A score of 7 is considered an A quality pass and a score of 6.1 is considered a B quality pass.

Table D1 Arai Plot fits for site 1

Sample	Low T	High T	PI estimate	H_{lab}	N	B	FRAC	G	Q	delCK	DRAT	CDRAT	Alpha	MAD (fixed)	DRATtail	Comment	K	Pass score	Th/MW	
KH1 1.1A	340	520	5.1	10	12	0.083	0.489	0.798	6.1	5.7%	8.1%	17.5%	13.7	8.2	0.0%		0.313	7	TH	IZZI+
KH1 1.1B	120	520	15.6	10	16	0.147	0.629	0.620	1.7	10.3%	14.0%	13.8%	13.8	5.2	0.0%	LTD	0.014	5.1	TH	LTD IZZI+
KH1 1.2A	310	505	5.6	10	12	0.088	0.499	0.866	6.5	10.3%	13.6%	32.6%	9.1	5.4	0.0%		0.722	5.1	TH	IZZI+
KH1 1.2B	370	505	5.1	10	10	0.086	0.374	0.856	7.4	7.5%	8.9%	9.6%	12.0	9.4	0.0%		0.663	6	TH	IZZI+
KH1 1.3C	370	475	4.4	10	8	0.109	0.359	0.808	5.5	7.9%	9.6%	19.9%	13.3	9.6	0.0%		0.733	5.1	TH	IZZI+
KH1 1.3D	385	505	4.3	10	9	0.089	0.401	0.826	5.3	5.2%	8.3%	26.9%	11.4	7.3	0.0%		0.055	7	TH	IZZI+
KH1 1.4A	120	520	14.3	10	16	0.140	0.764	0.792	4.0	22.0%	18.1%	23.0%	20.2	13.9	0.0%	LTD	0.917	3	TH	LTD IZZI+
KH1 1.4B	370	490	4.8	10	9	0.137	0.440	0.832	4.8	6.1%	7.0%	5.8%	8.2	5.8	0.0%		0.772	5	TH	IZZI+
KH1 1.4C	370	490	4.1	10	9	0.097	0.401	0.841	6.5	3.8%	4.7%	7.0%	12.5	9.4	0.0%		0.673	6	TH	IZZI+
KH1 1.4D	400	520	6.4	10	9	0.173	0.443	0.831	4.7	7.8%	6.7%	7.1%	3.4	5.2	0.0%	LTD	0.883	5	TH	LTD IZZI+
KH1 1.5B	370	490	4.5	10	9	0.126	0.425	0.817	5.1	3.6%	4.3%	6.6%	13.2	8.7	0.0%		0.835	5	TH	IZZI+
KH1 1.5C	370	505	3.4	10	10	0.107	0.407	0.840	6.9	5.7%	6.1%	10.6%	8.1	8.6	0.0%			6.1	TH	IZZI+
KH1 1.5C	280	475	10.7	10	11	0.075	0.379	0.788	6.5	7.0%	7.7%	7.7%	6.4	4.6	0.0%	LTD	0.395	7	TH	LTD IZZI+
KH1 1.5D	370	490	3.1	10	9	0.137	0.464	0.796	5.3	6.5%	6.8%	12.6%	9.4	11.9	0.0%		0.869	5	TH	IZZI+
KH1 1.5F	470	600	3.2	20	7	0.282	0.449	0.457	1.1	12.9%	19.4%	11.8%	7.4	8.8	0.0%	AF		5	TH	AF IZZI+
KH1 1A	3	8	4.6	10	6	0.057	0.467	0.702	10.3	23.4%	25.5%	21.3%	4.1	5.3	0.0%		0.262164	6	MW	IZZI+
KH1 1B	4	8	8.6	10	5	0.135	0.429	0.632	3.3	17.4%	18.6%	9.8%	7.8	6.3	0.0%		0.65391	5	MW	IZZI+
KH1 1C	3	8	6.4	10	6	0.105	0.378	0.728	4.6	14.0%	17.5%	18.5%	4.2	3.3	0.0%		0.324842	5.1	MW	IZZI+
KH1 1D	2	8	6.9	10	7	0.119	0.639	0.787	6.0	9.8%	8.8%	10.5%	5.1	4.7	0.0%		0.607272	5.1	MW	IZZI+
KH1 1E	3	8	5.5	10	6	0.070	0.628	0.577	7.4	29.3%	28.5%	29.8%	1.5	5.3	0.0%		0.398866	6	MW	IZZI+
KH1 1F	2	6	6.7	10	5	0.103	0.650	0.651	5.4	15.2%	14.7%	12.3%	4.5	4.0	0.0%		0.540139	4.2	MW	IZZI+
KH1 4T	500	600	1.3	20	6	0.327	0.354	0.355	0.9	17.9%	22.3%	17.9%	73.0	27.4	0.0%	AF		3	TH	AF IZZI+
KH1 H1T	540	600	3.6	20	4	0.143	0.366	0.588	3.2	16.3%	20.8%	13.2%	1.6	3.5	0.0%	AF		5	TH	AF IZZI+
KH1 H2L	440	600	6.4	20	8	0.097	0.524	0.648	3.8	8.7%	14.6%	11.6%	15.0	6.8	0.0%	AF	0.4064	6.1	TH	AF IZZI+
KH1 U.1B	400	580	7.1	20	8	0.092	0.664	0.678	5.5	19.2%	24.4%	24.1%	31.1	15.4	0.0%	AF		5	TH	AF IZZI+
KH1 U.1C	500	580	3.1	20	5	0.135	0.441	0.615	3.0	32.9%	49.3%	43.0%	18.0	10.5	0.0%	AF		4	TH	AF IZZI+
KH1 U.1D	400	560	8.3	20	7	0.145	0.484	0.593	1.9	5.4%	10.5%	9.2%	46.6	10.9	0.0%	AF		4.1	TH	AF IZZI+
KH1 U.1E	520	580	2.4	20	4	0.058	0.340	0.541	4.8	30.1%	58.7%	57.6%	27.5	10.3	0.0%	AF		4.1	TH	AF IZZI+
KH1 UA	0	8	0.0	0	7	0.135	0.915	0.692	4.3	13.4%	9.7%	0.9%	13.4	11.2	0.0%	LTD	999	5	MW	LTD IZZI+
KH1 UB	0	6	78.7	5	6	0.311	0.962	0.311	1.1	43.7%	2.6%	4.6%	5.5	5.3	0.0%	LTD	999	5	MW	LTD IZZI+
KH1 UC	0	7	7.8	5	7	0.083	0.951	0.769	9.4	24.9%	13.3%	17.2%	3.7	10.6	0.0%	LTD	0.38206	6.1	MW	LTD IZZI+
KH1 UD	2	7	3.0	5	6	0.084	0.350	0.579	6.0	54.1%	53.6%	55.1%	5.6	7.5	0.0%	LTD	999	5	MW	LTD IZZI+
KH1 UE	4	8	4.9	10	5	0.049	0.169	0.406	7.5	33.0%	33.0%	28.0%	4.4	6.0	0.0%	LTD	999	4	MW	LTD IZZI+
KH1 UF	2	5	3.1	10	4	0.181	0.304	0.532	1.2	2.0%	4.7%	4.7%	11.2	4.3	0.0%	LTD	999	4.1	MW	LTD IZZI+
KH1 UG	2	8	7.0	10	7	0.063	0.616	0.660	9.2	14.2%	13.2%	14.3%	6.3	8.3	0.0%	LTD	0.29732	6.1	MW	LTD IZZI+
KH1 UJ	2	8	6.9	5	7	0.049	0.779	0.655	12.5	8.5%	5.3%	11.9%	2.3	3.9	0.0%		0.020476	7	MW	IZZI+
KH1 UK	2	7	5.9	5	6	0.045	0.700	0.754	15.7	12.9%	9.0%	5.2%	3.3	4.0	0.0%		0.120495	7	MW	IZZI+
KH1 UN	1	5	3.4	5	5	0.094	0.758	0.653	6.7	1.3%	1.1%	0.3%	2.5	2.6	0.0%		0.361646	7	MW	IZZI+
KH1 UO	2	8	5.1	10	7	0.028	0.609	0.715	22.8	0.9%	0.9%	1.4%	3.9	6.2	0.0%		0.08228	7	MW	IZZI+
KH1 UP	2	8	6.6	5	7	0.071	0.762	0.724	9.5	20.1%	12.9%	8.0%	2.5	2.8	0.0%		0.11162	6.1	MW	IZZI+
KH1 UQ	4	8	5.0	10	5	0.050	0.677	0.706	12.3	12.9%	13.3%	9.6%	5.3	4.6	0.0%		0.08673	6.1	MW	IZZI+
KINGKH1H1A	5	12	4.0	5	8	0.062	0.515	0.816	12.2	6.7%	5.6%	8.8%	3.4	4.9	0.0%	Hawkins (2018)	0.310071	7	MW	IZZI+
KINGKH1H1B	4	12	7.0	5	9	0.075	0.354	0.811	10.5	16.4%	9.8%	11.4%	1.8	3.8	0.0%	Hawkins (2018)	0.446564	7	MW	IZZI+
KINGKH1H1C	4	10	5.1	5	7	0.045	0.399	0.745	13.7	22.8%	19.0%	19.1%	2.8	2.7	0.0%	Hawkins (2018)	0.00445	6	MW	IZZI+
KINGKH1H1D	4	9	19.5	5	6	0.170	0.348	0.738	2.9	26.7%	9.8%	17.1%	4.6	2.1	0.0%	Hawkins (2018)	1.06466	4.1	MW	IZZI+
KINGKH1H2A	4	13	6.9	5	10	0.045	0.510	0.853	13.1	3.4%	2.8%	2.2%	4.6	2.8	0.0%	Hawkins (2018)	0.348398	7	MW	IZZI+
KINGKH1H2B	2	8	6.6	5	7	0.076	0.580	0.827	9.1	12.6%	9.2%	13.8%	2.4	5.0	0.0%	Hawkins (2018)	0.357911	7	MW	IZZI+
KINGKH1H2C	3	9	7.1	5	7	0.092	0.473	0.779	4.8	4.7%	4.8%	2.3%	7.4	3.1	0.0%	Hawkins (2018)	0.343273	7	MW	IZZI+
KINGKH1H2D	3	11	9.4	5	9	0.073	0.536	0.763	6.3	3.9%	3.0%	2.3%	4.3	2.6	0.0%	Hawkins (2018)	0.278314	7	MW	IZZI+

Table D2 Arai Plot fits for site 2

Sample	Low T	High T	PI estimate	H_{ub}	N	B	FRAC	G	Q	delCK	DRAT	CDRAT	Alpha	MAD (fixed)	DRATtail	Comment	K	Pass score	Th/MW	
KH2-1	330	560	15.9	10	11	0.147	0.418	0.771	2.6	19.2%	20.7%	35.4%	24.3	12.5	0.0%		0.799	3	TH-	IZZI+
KH2-1A	1	7	4.0	10	7	0.047	0.399	0.681	9.5	5.7%	8.1%	6.5%	3.8	7.6	0.0%		0.328347	7	MW-	IZZI+
KH2-1B	1	7	0.9	10	7	0.329	0.400	0.250	0.1	0.9%	9.5%	5.6%	78.8	14.3	0.0%		1.593735	3	MW-	IZZI+
KH2-1C	6	10	1.7	20	5	0.055	0.434	0.650	8.8	12.5%	16.9%	29.3%	11.8	21.0	0.0%		0.04574	6	MW-	IZZI+
KH2-1D	2	6	3.9	10	5	0.021	0.641	0.645	25.6	1.3%	1.4%	1.6%	2.9	6.5	0.0%		0.033181	7	MW-	IZZI+
KH2-2	200	520	13.7	10	10	0.172	0.366	0.825	3.5	44.6%	36.0%	50.4%	17.9	8.2	0.0%		0.872	3	TH-	IZZI+
KH2-2J	400	580	6.5	20	8	0.316	0.310	0.758	0.5	7.0%	33.0%	51.3%	44.0	5.4	0.0%	AF		2.1	TH-	AF IZZI+
KH2-3	200	500	29.7	10	9	0.265	0.366	0.713	1.2	11.4%	8.2%	-2.0%	17.1	5.8	0.0%		0.539	5	TH-	IZZI+
KH2-4	280	520	17.3	10	9	0.152	0.358	0.769	3.2	24.7%	19.6%	20.2%	14.1	6.6	0.0%		0.700	4	TH-	IZZI+
KH2-5	0	550	27.9	10	18	0.118	0.854	0.837	6.6	20.7%	7.5%	7.6%	24.1	15.5	0.0%			5.1	TH-	IZZI+
KH2AB3	1	8	91.5	10	8	0.392	0.787	0.246	0.3	45.2%	11.2%	8.8%	1.1	2.3	0.0%	LTD		4.1	MW-	LTD IZZI+
KH2AB4	1	4	2.9	10	4	0.202	0.445	0.642	2.2	40.1%	54.6%	47.1%	28.1	17.4	0.0%	LTD		4	MW-	LTD IZZI+
KH2-H1.1	400	580	1.6	20	8	0.360	0.377	0.384	0.9	61.5%	69.0%	59.3%	168.8	34.5	0.0%	AF		3	TH-	AF IZZI+
KH2-H2A	300	470	7.3	20	5	0.513	0.181	0.716	0.4	15.9%	46.6%	32.3%	66.9	31.1	0.0%	AF		2	TH-	AF IZZI+
KH2-H2B	350	580	11.8	20	9	0.160	0.368	0.491	1.3	9.8%	20.7%	36.3%	21.3	3.6	0.0%	AF		4	TH-	AF IZZI+
KH2-H4.1	0	470	10.6	20	6	0.083	0.416	0.738	6.0	7.7%	10.0%	8.2%	13.8	6.7	0.0%	AF	0.428607	7	TH-	AF IZZI+
KH2L2A	3	8	94.6	10	6	0.199	0.581	0.651	1.7	36.7%	7.6%	-16.0%	1.0	4.3	0.0%	LTD		6	MW-	LTD IZZI+
KH2-L2A	0	535	31.9	10	17	0.140	0.628	0.800	3.7	10.7%	4.9%	8.9%	22.8	6.6	0.0%			5	TH-	IZZI+
KH2L2B	0	8	79.3	10	9	0.272	0.931	0.802	2.8	43.3%	5.6%	-6.7%	2.2	3.6	0.0%	LTD		6	MW-	LTD IZZI+
KH2-L2B	200	535	6.6	10	11	0.096	0.587	0.699	6.8	16.0%	14.3%	13.1%	2.7	5.3	0.0%		0.762	5.1	TH-	IZZI+
KH2L2C	1	8	6.3	10	8	0.097	0.677	0.754	4.9	10.7%	14.5%	20.6%	4.9	2.3	0.0%		0.62768	6.1	MW-	IZZI+
KH2-L2C	330	535	7.8	10	9	0.052	0.551	0.635	9.3	13.6%	14.1%	30.4%	2.1	6.6	0.0%		0.095	6.1	TH-	IZZI+
KH2L2D	3	8	8.2	10	6	0.065	0.518	0.682	7.9	23.8%	24.5%	33.2%	4.3	3.4	0.0%		0.083237	6	MW-	IZZI+
KH2-L2D	120	520	33.0	10	16	0.174	0.509	0.725	1.7	26.0%	18.5%	-4.7%	26.4	5.7	0.0%			4	TH-	IZZI+
KH2L2E	3	7	10.0	5	5	0.080	0.401	0.678	4.2	3.4%	3.1%	0.1%	0.9	1.8	0.0%		0.048196	7	MW-	IZZI+
KH2-L2E	120	520	107.2	10	16	0.346	0.436	0.963	0.9	31.3%	9.4%	22.0%	7.9	3.7	0.0%	LTD	4.183	4	TH-	LTD IZZI+
KH2L2F	4	8	6.2	10	5	0.084	0.506	0.711	6.8	8.9%	9.5%	14.4%	5.8	5.2	0.0%		0.300875	7	MW-	IZZI+
KH2-L2F	200	520	20.7	10	15	0.333	0.455	0.454	0.4	32.8%	47.8%	34.4%	41.0	6.6	0.0%		2.362	2	TH-	IZZI+
KH2L2G	2	8	6.2	5	6	0.051	0.620	0.723	13.1	21.2%	14.5%	17.6%	6.0	5.5	0.0%		0.048906	6.1	MW-	IZZI+
KH2-L2G	120	520	75.5	10	16	0.322	0.389	-1.376	-1.5	29.2%	11.2%	20.4%	4.8	3.1	0.0%	LTD	3.209	3.1	TH-	LTD IZZI+
KH2-UA	2	6	3.7	10	5	0.095	0.308	0.629	3.6	7.3%	12.7%	12.7%	16.7	6.3	0.0%		0.358592	4.2	MW-	IZZI+
KH2-UD	1	8	2.5	10	8	0.359	0.790	0.769	1.5	5.1%	7.3%	-1.4%	41.5	20.1	0.0%	LTD	2.033181	4	MW-	LTD IZZI+
KH2-UY	0	5	1.5	10	6	0.108	0.526	0.683	4.9	2.4%	3.1%	3.3%	16.3	12.4	0.0%		3.033181	4.1	MW-	IZZI+
KH2-UZ	1	8	3.0	10	7	0.115	0.788	0.683	4.1	13.7%	18.7%	23.4%	11.4	8.6	0.0%		1.033181	4.1	MW-	IZZI+
KINGKH2H1A	4	6	0.9	10	3	0.320	0.313	0.500	0.3	42.2%	215.2%	185.8%	88.5	33.9	0.0%	Hawkins (2018)	-1.83356	1.1	MW-	IZZI+
KINGKH2H2A	4	9	5.2	10	6	0.038	0.610	0.581	11.8	8.4%	9.6%	16.8%	4.9	3.6	0	Hawkins (2018)	0.30369	7	MW-	IZZI+
KINGKH2H2C	2	8	6.7	5	7	0.012	0.536	0.794	45.2	11.8%	10.6%	15.0%	3.8	2.6	0	Hawkins (2018)	0.04934	6.1	MW-	IZZI+
KINGKH2H2D	1	7	1.5	5	7	0.126	0.553	0.757	2.8	0.9%	1.9%	2.6%	36.2	13.5	0	Hawkins (2018)	0.076921	5	MW-	IZZI+

Table D3 Arai Plot fits for site A

Sample	Low T	High T	PI estimate	H_{lab}	N	B	FRAC	G	Q	delCK	DRAT	CDRAT	Alpha	MAD (fixed)	DRATtail	Comment	K	Pass score	Th/MW	
KHA 1.1A	370	500	2.1	10	6	0.121	0.413	0.704	4.5	3.8%	4.8%	1.6%	12.4	18.2	0.0%		0.319	6	TH	IZZI+
KHA 1.1B	330	500	2.3	10	7	0.090	0.477	0.753	6.9	2.0%	2.4%	3.5%	25.6	18.6	0.0%		0.204	6	TH	IZZI+
KHA 1.1C	430	560	2.1	10	9	0.105	0.444	0.701	4.2	7.6%	11.8%	36.4%	7.1	10.5	0.0%			5.2	TH	IZZI+
KHA 1.1C	280	460	4.4	10	10	0.116	0.526	0.743	2.4	12.5%	30.4%	81.5%	41.0	13.6	0.0%			4.1	TH	IZZI+
KHA 1.1E	340	505	4.1	10	11	0.137	0.417	0.796	2.1	16.7%	42.7%	5.6%	43.6	10.0	0.0%	LTD	0.173	4	TH	LTD IZZI+
KHA 1.1F	280	475	5.1	10	10	0.104	0.332	0.668	2.6	2.6%	5.8%	8.3%	32.5	8.3	0.0%	LTD	0.025	4.2	TH	LTD IZZI+
KHA 1.2A	400	500	2.2	10	5	0.177	0.377	0.605	1.9	3.0%	5.4%	1.3%	8.7	20.7	0.0%		0.023	6	TH	IZZI+
KHA 1.2B	415	560	2.1	10	10	0.087	0.503	0.787	7.0	4.8%	6.0%	14.3%	9.2	10.9	0.0%		0.555	6	TH	IZZI+
KHA 1.2E	340	520	4.5	10	12	0.138	0.859	0.860	4.9	9.3%	10.8%	13.0%	15.1	8.8	0.0%	LTD	0.989	3.1	TH	LTD IZZI+
KHA 1.3A	415	560	2.3	10	10	0.069	0.543	0.812	8.1	7.1%	10.0%	28.5%	4.8	10.8	0.0%		0.177	7	TH	IZZI+
KHA 1.3B	400	535	2.2	10	7	0.097	0.428	0.738	5.4	25.1%	34.7%	30.9%	1.9	21.8	0.0%		0.415	6	TH	IZZI+
KHA 1.3C	370	500	2.5	10	6	0.131	0.450	0.756	4.7	2.5%	3.0%	5.6%	15.0	18.2	0.0%		0.619	5	TH	IZZI+
KHA 1.3D	280	520	4.3	10	14	0.103	0.546	0.730	2.8	26.7%	61.5%	67.4%	43.5	13.0	0.0%	LTD	0.258	4.1	TH	LTD IZZI+
KHA 1.3E	300	470	3.5	20	5	0.161	0.166	0.430	1.1	2.3%	5.7%	0.7%	40.1	9.6	0.0%	AF		4	TH	AF IZZI+
KHA 1.4	340	490	5.9	10	10	0.144	0.487	0.808	4.9	16.2%	15.9%	35.4%	10.0	7.5	0.0%		0.837	4	TH	IZZI+
KHA 1.5A	200	475	6.0	10	12	0.101	0.408	0.855	6.2	14.5%	17.0%	33.8%	14.9	7.1	0.0%			5.1	TH	IZZI+
KHA 1.5B	310	490	6.3	10	11	0.118	0.564	0.756	4.8	20.9%	23.6%	63.7%	12.9	7.8	0.0%		0.555	4.1	TH	IZZI+
KHA 1A	4	10	4.3	10	7	0.063	0.461	0.732	9.1	16.8%	19.8%	7.8%	3.0	1.9	0		0.276911	6	MW	IZZI+
KHA 1B	4	10	4.0	10	7	0.076	0.358	0.652	5.7	10.1%	14.2%	16.1%	5.1	2.3	0.0%		0.01024	6.1	MW	IZZI+
KHA 1C	4	10	4.2	10	7	0.083	0.508	0.783	7.3	22.0%	26.1%	21.6%	3.8	5.8	0.0%		0.03906	6	MW	IZZI+
KHA 1D	3	9	4.8	10	7	0.094	0.613	0.538	5.1	40.1%	40.8%	30.1%	1.9	4.8	0.0%		0.50535	5	MW	IZZI+
KHA 1E	3	10	5.2	10	8	0.095	0.622	0.544	5.0	42.0%	42.2%	15.7%	1.9	3.5	0.0%	Hawkins (2018)	0.25837	6	MW	IZZI+
KHA 1F	4	10	3.2	10	7	0.060	0.474	0.682	10.0	7.4%	8.0%	5.0%	1.9	3.8	0.0%		0.009626	7	MW	IZZI+
KHA 1G	2	4	3.9	10	3	0.096	0.476	0.498	4.5	12.8%	13.8%	11.9%	6.9	6.3	0.0%		0.255067	5.1	MW	IZZI+
KHA 1Z	2	8	4.5	10	7	0.102	0.628	0.684	6.1	38.8%	38.7%	21.6%	1.8	3.3	0		0.0905	5.1	MW	IZZI+
KHA 2.1A	300	520	4.3	20	7	0.324	0.463	0.633	1.5	2.0%	2.5%	2.7%	4.0	6.1	0.0%	AF		6	TH	AF IZZI+
KHA 2.1C	300	540	5.8	20	8	0.704	0.578	112.181	6.1	19.6%	493.8%	666.5%	166.6	4.1	0.0%	AF		3	TH	AF IZZI+
KHA 2.1D	400	470	3.1	20	3	0.761	0.096	0.037	0.0	0.6%	2.7%	0.1%	7.7	2.2	0.0%	AF		3	TH	AF IZZI+
KHA 2.1E	300	540	5.9	20	8	0.720	0.627	156.411	7.0	26.4%	782.7%	1029.1%	165.6	4.5	0.0%	AF		3	TH	AF IZZI+
KHA 2.1G	300	470	2.1	20	5	0.332	0.148	0.157	0.1	0.5%	1.8%	1.0%	7.6	2.1	0.0%	AF		4	TH	AF IZZI+
KHA 2.1H	300	470	3.3	20	5	0.607	0.058	0.292	0.1	0.9%	4.2%	1.5%	2.9	1.8	0.0%	AF		4	TH	AF IZZI+

Table D4 Arai Plot fits for site B

Sample	Low T	High T	PI estimate	H_{ub}	N	B	FRAC	G	Q	delCK	DRAT	CDRAT	Alpha	MAD (fixed)	DRATtail	Comment	K	Pass score	Th/MW	
KHB 1.1	280	560	4.5	10	16	0.130	0.678	0.865	5.4	6.2%	7.0%	6.3%	15.7	9.1	0.0%			5	TH	IZZI+
KHB 1.2	200	550	6.0	10	16	0.098	0.678	0.886	6.4	6.1%	7.4%	-2.4%	16.6	6.7	0.0%			6	TH	IZZI+
KHB 1.2E	350	470	2.9	20	4	0.214	0.211	0.535	1.3	0.6%	1.2%	1.8%	19.8	7.5	0.0%	AF		4	TH	AF IZZI+
KHB 1.3	120	475	9.5	10	13	0.063	0.600	0.885	9.8	14.2%	14.7%	6.4%	13.7	7.4	0.0%		0.622	5.1	TH	IZZI+
KHB 1.3B	300	560	5.5	20	9	0.196	0.698	0.710	2.6	10.8%	14.5%	-13.5%	31.9	15.5	0.0%	AF		4.1	TH	AF IZZI+
KHB 1.3C	350	470	1.3	20	4	0.379	0.152	0.511	0.7	0.8%	1.5%	0.8%	5.1	2.6	0.0%	AF		4	TH	AF IZZI+
KHB 1.4	400	570	2.8	10	13	0.055	0.453	0.864	11.0	10.4%	14.2%	13.8%	1.8	6.2	0.0%		0.235	6.1	TH	IZZI+
KHB 1.5	200	460	7.0	10	7	0.081	0.432	0.762	6.2	3.4%	4.2%	-5.4%	14.4	7.6	0.0%		0.303	7	TH	IZZI+
KHB 1.6	280	460	7.4	10	6	0.098	0.395	0.748	5.3	16.0%	18.6%	23.9%	13.9	7.5	0.0%		0.485	5	TH	IZZI+
KHB 1.7	280	475	5.5	10	10	0.067	0.408	0.815	5.6	3.8%	7.2%	1.1%	5.4	3.9	0.0%	LTD	0.400	7	TH	LTD IZZI+
KHB 1.8	200	475	6.5	10	12	0.079	0.448	0.870	5.5	9.8%	16.6%	1.8%	21.5	6.2	0.0%	LTD	0.413	5	TH	LTD IZZI+
KHB 1A	3	9	6.9	10	7	0.133	0.541	0.685	4.3	37.5%	37.4%	36.2%	4.7	3.9	0.0%		0.36548	5	MW	IZZI+
KHB 1B	3	8	5.1	10	6	0.087	0.650	0.759	6.9	10.7%	12.0%	14.8%	8.7	8.4	0.0%		0.03288	6.1	MW	IZZI+
KHB 1C	0	10	8.3	10	11	0.079	0.994	0.800	10.6	19.6%	14.5%	7.1%	4.0	10.2	0.0%		0.396054	6.1	MW	IZZI+
KHB 1D	2	5	5.5	10	4	0.142	0.623	0.577	3.5	1.3%	1.3%	-2.7%	9.3	6.5	0.0%		0.568129	5	MW	IZZI+
KHB 1E	3	7	5.0	10	5	0.115	0.549	0.625	2.8	0.5%	0.8%	0.4%	32.2	11.4	0.0%		0.541185	4.1	MW	IZZI+
KHB 1F	3	10	6.5	10	8	0.074	0.302	0.780	6.5	10.7%	14.6%	25.1%	7.3	3.5	0.0%		0.057539	5.2	MW	IZZI+
KHB 1G	2	7	5.1	10	6	0.081	0.374	0.679	6.4	2.6%	3.1%	4.0%	2.7	7.1	0.0%		0.092821	7	MW	IZZI+
KHB 1Z	4	9	6.7	10	6	0.070	0.548	0.769	8.6	3.1%	3.3%	-1.4%	6.1	4.5	0.0%		0.38146	7	MW	IZZI+
KHB 2.1	200	475	6.7	10	12	0.095	0.480	0.860	4.6	10.3%	16.7%	14.0%	24.3	6.8	0.0%	LTD	0.060	5	TH	LTD IZZI+
KHB 2A	3	9	6.3	10	7	0.116	0.602	0.658	4.2	1.7%	1.9%	1.9%	5.9	4.6	0.0%		0.602925	5.1	MW	IZZI+
KHB 2B	3	9	5.4	10	7	0.070	0.508	0.738	7.3	4.3%	5.4%	3.4%	7.0	6.8	0.0%		0.251635	7	MW	IZZI+
KHB 2C	3	7	5.9	10	5	0.073	0.623	0.661	6.8	10.1%	11.5%	10.2%	6.7	7.2	0.0%		0.08994	6.1	MW	IZZI+
KHB 2D	2	7	5.6	10	6	0.087	0.620	0.713	6.0	3.0%	3.6%	2.5%	14.3	10.5	0.0%		0.066194	7	MW	IZZI+
KHB 2E	3	8	5.1	10	6	0.071	0.553	0.751	8.8	6.3%	6.7%	4.3%	0.2	4.0	0.0%		0.18801	7	MW	IZZI+
KHB 2V	350	520	5.6	20	6	0.097	0.469	0.604	3.5	17.0%	29.6%	22.4%	39.0	17.1	0	AF		5	TH	AF IZZI+
KHB 3A	300	560	8.0	20	9	0.211	0.635	0.704	2.1	9.4%	13.6%	13.7%	12.4	5.9	0.0%	AF		5.1	TH	AF IZZI+
KHB 3B	400	600	6.0	20	9	0.164	0.557	0.733	3.3	13.5%	17.4%	13.4%	5.4	4.6	0.0%	AF		5	TH	AF IZZI+
KHB 4A	350	470	2.8	20	4	0.031	0.239	0.589	8.6	8.4%	18.2%	21.1%	78.1	24.5	0.0%	AF		4	TH	AF IZZI+
KHB 4B	350	540	12.8	20	7	0.097	0.557	0.698	5.2	6.8%	7.9%	-1.5%	12.5	9.6	0.0%	AF		7	TH	AF IZZI+

Table D5 Arai Plot fits for site 4

Sample	Low T	High T	PI estimate	H_{lab}	N	B	FRAC	G	Q	delCK	DRAT	CDRAT	Alpha	MAD (fixed)	DRATtail	Comment	K	Pass score	Th/MW	
KH4 3CI	450	620	5.1	20	9	0.090	0.575	0.754	7.5	3.8%	4.2%	3.2%	3.9	6.5	0.0%	Hawkins (2018)	0.366291	7	TH	AF IZZI+
KH4 4CI	450	620	4.9	20	9	0.085	0.658	0.746	7.9	6.4%	6.9%	0.5%	3.6	7.2	0.0%	Hawkins (2018)	0.37737	7	TH	AF IZZI+
KH4 5CI	350	620	2.8	20	11	0.088	0.829	0.774	8.7	7.8%	7.8%	6.0%	6.1	10.8	0.0%	Hawkins (2018)	0.545249	6	TH	AF IZZI+
KH4 6BI	450	620	4.1	20	9	0.096	0.564	0.764	7.1	4.6%	5.0%	1.2%	5.8	10.2	0.0%	Hawkins (2018)	0.383042	7	TH	AF IZZI+
KH4 8BI	300	520	18.7	20	6	0.243	0.588	0.742	2.3	7.2%	6.8%	16.4%	9.0	5.1	0.0%	Hawkins (2018)	0.690448	5	TH	AF IZZI+
KH4 1C1	370	580	24.8	10	15	0.111	0.373	0.784	2.5	7.1%	7.7%	39.5%	3.9	1.2	0.0%		1.011863	5.1	TH	IZZI+
KH4 1C2	385	580	19.7	10	14	0.096	0.327	0.788	2.9	6.7%	8.6%	32.4%	2.5	1.0	0.0%		0.749845	5.1	TH	IZZI+
KH4 2A2	445	565	15.3	10	9	0.109	0.245	0.524	1.9	12.5%	17.6%	2.8%	8.7	2.2	0.0%		0.776896	3.1	TH	IZZI+
KH4 2AT	370	580	32.0	10	15	0.162	0.449	0.734	1.9	14.1%	9.9%	4.5%	3.6	1.6	0.0%		0.715866	5	TH	IZZI+
KH4 3C2	510	590	10.0	10	5	0.048	0.380	0.379	5.8	7.8%	7.5%	8.7%	8.7	3.9	0.0%	LTD	0.273568	7	TH	LTD IZZI+
KH4 4B	370	580	12.1	10	15	0.099	0.454	0.741	2.5	6.5%	12.4%	68.8%	8.3	2.0	0.0%		0.795099	5.1	TH	IZZI+
KH4 5B	310	565	6.4	10	16	0.073	0.496	0.409	1.7	4.4%	12.3%	62.2%	6.3	2.2	0.0%	B	0.09299	6.1	TH	IZZI+
KH4 5D2	390	530	8.4	10	8	0.122	0.431	0.440	1.2	5.5%	13.1%	41.7%	11.6	3.2	0.0%	LTD	0.242186	5.1	TH	LTD IZZI+
KH4 6B2	390	590	9.5	10	11	0.141	0.391	0.815	2.9	8.0%	11.4%	25.9%	8.3	3.2	0.0%	LTD	0.989564	4.1	TH	LTD IZZI+
KH4 8A2	370	580	13.9	10	15	0.110	0.411	0.769	2.5	7.1%	11.8%	66.9%	14.1	2.7	0.0%		1.044428	4.2	TH	IZZI+
KH4 8B2	430	590	7.1	10	9	0.104	0.250	0.700	2.7	12.6%	25.4%	74.7%	4.9	2.0	0.0%	LTD	0.68586	3.1	TH	LTD IZZI+
KINGKH4 3A	7	12	4.8	5	6	0.046	0.357	0.762	5.6	0.6%	1.2%	1.1%	10.8	2.8	0	Hawkins (2018)	0.25959	7	MW	IZZI+
KINGKH4 3B	5	12	6.4	5	8	0.025	0.697	0.814	21.6	6.8%	6.2%	12.5%	3.0	1.5	0	Hawkins (2018)	0.12473	7	MW	IZZI+
KINGKH4 4A	1	4	37.0	5	4	0.162	0.223	0.567	0.4	9.7%	10.4%	20.0%	72.8	10.9	0	Hawkins (2018)	1.009734	1.1	MW	IZZI+
KINGKH4 4B	4	14	5.7	5	11	0.037	0.701	0.789	18.1	7.6%	5.8%	10.1%	4.3	4.2	0.0%	Hawkins (2018)	0.20539	7	MW	IZZI+
KINGKH4 4C	6	17	6.0	5	12	0.039	0.845	0.872	17.7	10.4%	8.4%	7.2%	1.0	1.4	0.0%	Hawkins (2018)	0.26343	7	MW	IZZI+

Table D6 Arai Plot fits for site 6

Sample	Low T	High T	PI estimate	H_{lab}	N	B	FRAC	G	Q	delCK	DRAT	CDRAT	Alpha	MAD (fixed)	DRATtail	Comment	K	Pass score	Th/MW	
KH6 1.3	0	400	12.1	10	9	0.185	0.352	0.798	3.4	9.4%	7.6%	7.4%	46.2	25.9	0.0%			5	TH	IZZI+
KH6 1.4	330	400	1.8	10	3	0.169	0.129	0.398	1.7	4.3%	5.8%	0.3%	6.5	10.3	0.0%		0.649	3	TH	IZZI+
KH6 1.5	280	400	2.1	10	4	0.117	0.193	0.398	2.4	1.9%	2.6%	0.5%	50.9	24.4	0.0%		0.602	3.1	TH	IZZI+
KH6 1.7	330	460	1.3	10	4	0.254	0.162	0.316	0.8	4.4%	7.1%	7.4%	25.1	24.8	0.0%		1.064	2	TH	IZZI+
KH6 1AA	300	470	2.3	20	5	0.262	0.289	0.650	2.1	2.1%	2.4%	0.5%	14.7	19.1	0.0%	AF		5.1	TH	AF IZZI+
KH6 1AB	350	470	0.8	20	4	0.120	0.187	0.471	2.3	1.4%	2.5%	1.0%	72.4	26.2	0.0%	AF		4.1	TH	AF IZZI+
KH6 1AC	300	470	2.1	20	5	0.537	0.356	0.486	0.6	2.5%	3.9%	0.3%	75.9	35.1	0.0%	AF		4	TH	AF IZZI+
KH6 1AD	300	470	1.8	20	5	0.231	0.287	0.414	1.2	2.3%	3.4%	0.9%	57.6	21.8	0.0%	AF		4.1	TH	AF IZZI+
KH6 1AE	300	470	2.3	20	5	0.687	0.359	0.253	0.2	2.9%	4.9%	0.6%	106.5	32.8	0.0%	AF		4	TH	AF IZZI+
KH6 2.1A	400	535	5.3	10	8	0.099	0.357	0.834	3.9	7.2%	13.5%	27.7%	10.5	6.5	0.0%		0.641	5.1	TH	IZZI+
KH6 2.1D	310	520	9.7	10	13	0.154	0.411	0.839	2.1	19.5%	36.0%	15.8%	34.0	7.9	0.0%	LTD	0.414	4	TH	LTD IZZI+
KH6 2.1E	330	500	4.5	10	7	0.099	0.353	0.806	5.6	11.0%	14.7%	17.4%	16.7	10.4	0.0%		0.453	5.1	TH	IZZI+
KH6 2.2A	120	520	7.4	10	16	0.158	0.642	0.622	2.2	24.1%	33.9%	44.0%	36.4	14.6	0.0%	LTD	0.797	3	TH	LTD IZZI+
KH6 2.2B	370	535	7.6	10	8	0.067	0.517	0.842	9.6	14.1%	14.8%	12.0%	3.9	4.9	0.0%		0.355	6.1	TH	IZZI+
KH6 2.2C	120	520	26.1	10	16	0.263	0.598	0.244	0.3	26.0%	26.3%	40.8%	20.7	5.1	0.0%	LTD	1.711	2	TH	LTD IZZI+
KH6 2.2D	330	535	4.4	10	9	0.067	0.537	0.848	10.8	13.8%	14.8%	3.5%	10.2	9.8	0.0%		0.387	6.1	TH	IZZI+
KH6 2.3B	400	520	18.2	10	9	0.143	0.330	0.796	2.1	45.1%	57.4%	58.5%	7.1	4.0	0.0%			4.1	TH	IZZI+
KH6 2.3C	400	535	7.3	10	10	0.077	0.508	0.795	7.1	11.8%	13.8%	23.6%	3.7	3.9	0.0%		0.539	5.1	TH	IZZI+
KH6 2.3D	490	550	2.4	10	5	0.244	0.213	0.704	1.8	37.4%	58.2%	35.3%	15.9	10.1	0.0%			3	TH	IZZI+
KH6 2.4C	400	535	13.0	10	10	0.133	0.477	0.741	3.2	29.5%	30.8%	0.8%	6.1	6.3	0.0%		0.296	5	TH	IZZI+
KH6 2.4D	120	520	23.8	10	16	0.325	0.573	0.287	0.3	32.9%	38.9%	64.0%	27.5	5.7	0.0%	LTD	3.318	2	TH	LTD IZZI+
KH6 2A	1	7	10.1	10	7	0.037	0.355	0.585	6.8	3.1%	5.2%	5.2%	9.5	2.3	0.0%		0.175479	7	MW	IZZI+
KH6 2B	5	10	13.7	10	6	0.064	0.739	0.756	9.9	16.4%	11.5%	24.0%	3.6	2.6	0.0%		0.268511	6.1	MW	IZZI+
KH6 2C	4	12	13.3	10	9	0.030	0.646	0.838	23.6	16.6%	11.6%	18.9%	2.2	1.7	0.0%		0.074635	6.1	MW	IZZI+
KH6 2D	1	5	11.7	10	5	0.068	0.356	0.627	4.0	1.3%	1.9%	2.6%	3.5	3.2	0.0%		0.076	7	MW	IZZI+
KH6 2E	0	4	38.1	10	5	0.372	0.738	0.543	1.0	50.9%	19.4%	5.5%	22.8	11.0	0.0%	LTD		3	MW	LTD IZZI+
KH6 2E	300	520	5.5	20	7	0.166	0.511	0.655	1.6	11.0%	26.9%	32.8%	60.5	16.7	0.0%	AF		4	TH	AF IZZI+
KH6 2F	5	10	3.6	10	6	0.056	0.346	0.658	4.5	2.8%	6.8%	19.2%	14.5	5.4	0.0%		0.282948	6.1	MW	IZZI+
KH6 2F2	400	540	8.5	20	6	0.039	0.359	0.768	6.0	13.4%	40.6%	60.3%	48.3	10.5	0.0%	AF		5	TH	AF IZZI+
KH6 2G	6	16	7.7	10	11	0.066	0.509	0.849	10.2	6.9%	6.9%	3.1%	7.1	4.2	0.0%		0.244275	7	MW	IZZI+
KH6 2H	4	12	9.1	10	9	0.079	0.545	0.810	9.1	13.7%	11.4%	13.5%	4.5	3.5	0.0%		0.296175	6.1	MW	IZZI+
KH6 2I	120	520	8.6	10	16	0.165	0.683	0.803	2.6	17.7%	25.2%	23.7%	38.6	11.9	0.0%		1.391	3	TH	IZZI+
KH6 2L	5	9	11.1	10	5	0.141	0.155	0.678	0.9	35.4%	124.0%	92.2%	42.3	5.3	0.0%		0.584023	1	MW	IZZI+
KH6 2W	1	4	12.7	10	4	0.414	0.291	0.457	0.3	5.0%	10.4%	8.9%	61.6	17.6	0.0%	LTD		2.2	MW	LTD IZZI+
KH6 2X	4	8	1.7	10	5	0.211	0.344	0.658	2.1	19.2%	27.7%	24.2%	21.8	15.3	0.0%	LTD		3.1	MW	LTD IZZI+
KH6 2Y	2	7	1.3	10	6	0.442	0.397	0.091	0.1	6.0%	10.3%	12.4%	122.3	40.0	0.0%	LTD		3.1	MW	LTD IZZI+
KH6 2Z	4	7	1.0	10	4	0.245	0.320	0.570	1.8	1.8%	2.3%	2.3%	9.5	10.0	0.0%	LTD		5.1	MW	LTD IZZI+

Table D7 Arai Plot fits for site 7

Sample	Low T	High T	PI estimate	H_{lab}	N	B	FRAC	G	Q	delCK	DRAT	CDRAT	Alpha	MAD (fixed)	DRATtail	Comment	K	Pass score	Th/MW	
KH7 1CI	450	580	1.9	20	7	0.121	0.542	0.633	3.6	12.6%	18.3%	40.4%	0.6	12.7	0.0%	Hawkins (2018)	0.096608	5	TH	AF IZZI+
KH7 2CI	400	580	2.1	20	8	0.114	0.592	0.701	4.8	12.6%	16.1%	33.7%	9.3	13.6	0.0%	Hawkins (2018)	0.381124	5.1	TH	AF IZZI+
KH7 3CI	300	620	6.6	20	12	0.093	0.932	0.873	10.0	17.5%	15.6%	53.6%	2.2	3.2	0.0%	Hawkins (2018)	0.75853	5	TH	AF IZZI+
KH7 4CI	450	600	5.0	20	8	0.068	0.602	0.832	10.4	16.4%	18.5%	52.6%	3.1	4.0	0	Hawkins (2018)	0.121103	6	TH	AF IZZI+
KH7 5BI	500	600	9.7	20	7	0.056	0.405	0.824	9.6	5.2%	7.2%	26.9%	3.8	5.3	0	Hawkins (2018)	0.11159	7	TH	AF IZZI+
KH7 6BI	450	600	4.5	20	8	0.075	0.623	0.847	10.7	13.9%	14.4%	59.7%	2.6	4.1	0	Hawkins (2018)	0.332412	6.1	TH	AF IZZI+
KH7 7CI	450	600	5.0	20	8	0.079	0.642	0.844	10.3	13.0%	13.2%	52.8%	2.2	2.7	0	Hawkins (2018)	0.412842	6.1	TH	AF IZZI+
KH7 8CI	500	620	6.7	20	8	0.074	0.363	0.811	7.3	6.6%	9.4%	9.6%	4.5	4.8	0	Hawkins (2018)	0.000348	7	TH	AF IZZI+
KINGKH7 5A	5	12	15.4	5	8	0.027	0.602	0.834	20.1	8.4%	4.1%	11.8%	3.0	1.3	0.0%	Hawkins (2018)	0.140689	7	MW	IZZI+
KINGKH7 5B	4	17	13.9	5	14	0.016	0.816	0.883	45.6	8.1%	3.4%	8.2%	3.1	2.2	0.0%	Hawkins (2018)	0.013361	7	MW	IZZI+
KINGKH7 8A	5	14	8.5	5	10	0.036	0.601	0.874	18.3	7.3%	4.9%	10.9%	1.6	1.5	0.0%	Hawkins (2018)	0.307635	7	MW	IZZI+
KINGKH7 8B	7	14	9.6	20	8	0.029	0.478	0.840	17.2	6.0%	8.9%	24.3%	4.0	2.7	0.0%	Hawkins (2018)	0.022067	7	MW	IZZI+
KH7 1C2	120	580	13.1	10	20	0.147	0.667	0.878	4.5	17.4%	14.0%	16.9%	24.7	9.1	0.0%		1.564148	3.1	TH	IZZI+
KH7 2C2	310	565	13.0	10	16	0.173	0.427	0.830	2.6	10.1%	11.4%	20.3%	22.2	6.3	0.0%		1.866994	3.1	TH	IZZI+
KH7 2T	445	565	4.3	10	9	0.082	0.244	0.549	2.3	2.6%	7.2%	23.9%	5.1	3.6	0.0%		0.372855	6	TH	IZZI+
KH7 3B	340	580	25.3	10	15	0.066	0.559	0.853	7.1	26.0%	17.5%	3.0%	4.7	2.9	0.0%		0.301627	6	TH	IZZI+
KH7 3C2	385	580	20.6	10	14	0.069	0.485	0.846	6.2	22.6%	19.6%	9.1%	4.0	3.1	0.0%		0.530578	5	TH	IZZI+
KH7 7C1	385	565	14.3	10	13	0.092	0.405	0.652	2.6	9.1%	14.2%	72.4%	9.8	2.2	0.0%	B	0.160735	6.1	TH	IZZI+
KH7 4C	490	590	11.3	10	6	0.108	0.265	0.781	3.2	14.1%	21.2%	27.6%	4.3	2.9	0.0%	LTD	0.637553	3.2	TH	LTD IZZI+
KH7 7C1	0	570	18.6	10	17	0.114	0.613	0.850	3.9	10.7%	9.8%	28.7%	9.7	2.8	0.0%	LTD	0.657238	5.1	TH	LTD IZZI+
KH7 7C2	0	570	23.9	10	17	0.115	0.684	0.839	4.3	22.5%	14.6%	18.3%	8.9	3.3	0.0%	LTD	0.195306	5.2	TH	LTD IZZI+
KH7 6B2	410	570	13.8	10	9	0.086	0.308	0.839	4.2	19.1%	25.9%	20.4%	4.9	1.2	0.0%	LTD	0.676484	4.1	TH	LTD IZZI+

Table D8 Arai Plot fits for site 8

Sample	Low T	High T	PI estimate	H_{lab}	N	B	FRAC	G	Q	delCK	DRAT	CDRAT	Alpha	MAD (fixed)	DRATtail	Comment	K	Pass score	Th/MW	
KH8 1BI	350	600	3.7	20	10	0.095	0.631	0.835	8.4	8.5%	8.8%	18.7%	7.3	9.0	0	Hawkins (2018)	0.567371	6	TH	AF IZZI+
KH8 2BI	400	580	2.5	20	8	0.141	0.472	0.829	4.4	7.5%	9.9%	21.6%	10.7	9.9	0.0%	Hawkins (2018)	0.554893	5	TH	AF IZZI+
KH8 3BI	400	600	4.2	20	9	0.091	0.492	0.860	8.9	12.4%	12.8%	27.9%	1.5	2.5	0.0%	Hawkins (2018)	0.268617	6.1	TH	AF IZZI+
KH8 4BI	400	600	3.9	20	9	0.092	0.625	0.862	8.5	13.7%	14.9%	27.7%	2.3	3.2	0.0%	Hawkins (2018)	0.098272	6.1	TH	AF IZZI+
KH8 H1CI	500	620	6.7	20	7	0.131	0.437	0.761	4.7	9.0%	10.5%	16.4%	0.7	1.1	0.0%	Hawkins (2018)	0.694602	4.1	TH	AF IZZI+
KH8 H2AI	440	600	3.6	20	8	0.113	0.664	0.796	6.4	34.2%	36.9%	49.7%	2.0	3.4	0.0%	Hawkins (2018)	0.352606	5.1	TH	AF IZZI+
KINGKH8 1A	4	10	4.2	5	6	0.074	0.598	0.743	7.5	14.2%	14.6%	16.4%	1.4	2.7	0.0%	Hawkins (2018)	0.35279	6.1	MW	IZZI+
KINGKH8 1B	3	9	4.5	5	7	0.029	0.536	0.800	18.3	6.9%	7.8%	10.9%	9.6	4.5	0.0%	Hawkins (2018)	0.13672	7	MW	IZZI+
KINGKH8H1A	4	14	12.7	5	11	0.028	0.705	0.875	26.3	10.7%	4.7%	8.3%	1.4	1.1	0.0%	Hawkins (2018)	0.10444	7	MW	IZZI+
KH8 2A2	400	580	17.2	10	13	0.073	0.360	0.831	4.7	6.3%	7.7%	14.2%	2.1	0.8	0.0%		0.638258	6	TH	IZZI+
KH8 2B	445	565	5.2	10	9	0.054	0.243	0.565	2.6	2.3%	8.3%	8.6%	14.4	2.8	0.0%		0.175684	6	TH	IZZI+
KH8 H2T	310	580	22.1	10	17	0.096	0.595	0.870	5.4	12.2%	8.3%	8.0%	2.1	1.2	0.0%		0.729864	6	TH	IZZI+
KH8 3B2	310	565	6.7	10	16	0.063	0.411	0.700	4.5	4.9%	10.0%	1.2%	8.8	2.3	0.0%	A	0.154549	7	TH	IZZI+
KH8 3T	400	565	6.2	10	12	0.093	0.364	0.776	3.5	5.4%	10.8%	33.7%	1.9	2.7	0.0%	B	0.459753	6.1	TH	IZZI+
KH8 4B2	430	590	3.4	10	9	0.095	0.351	0.753	3.7	3.1%	6.3%	7.1%	7.3	2.8	0.0%	LTD	0.601405	6	TH	LTD IZZI+
KH8 2B2	470	590	2.4	10	6	0.097	0.321	0.625	3.2	2.9%	5.8%	2.9%	9.2	4.3	0.0%	LTD	0.429337	6.1	TH	LTD IZZI+
KH8 4T	120	450	101.5	10	2	#DIV/0!	0.449	#DIV/0!	#DIV/0!	41.2%	########	########	2.0	0.9	0.0%	LTD	'NA'	2	TH	LTD IZZI+

Table D9 Arai Plot fits for site 9

Sample	Low T	High T	PI estimate	H_{lab}	N	B	FRAC	G	Q	delCK	DRAT	CDRAT	Alpha	MAD (fixed)	DRATtail	Comment	K	Pass score	Th/MW	
KH9 1BII	500	580	1.8	20	5	0.065	0.397	0.710	5.6	16.6%	32.3%	40.1%	3.5	14.1	0.0%	Hawkins (2018)	0.28252	6	TH	AF IZZI+
KH9 2BII	500	580	1.9	20	5	0.161	0.353	0.719	2.3	16.1%	30.6%	39.5%	12.9	12.1	0.0%	Hawkins (2018)	0.277336	5	TH	AF IZZI+
KH9 3AII	500	580	2.2	20	5	0.197	0.341	0.707	1.8	14.1%	27.2%	33.1%	7.3	9.3	0.0%	Hawkins (2018)	0.526495	3.1	TH	AF IZZI+
KH9 4AII	520	620	10.8	20	6	0.145	0.390	0.769	3.1	13.1%	19.5%	28.5%	2.0	3.5	0.0%	Hawkins (2018)	0.38643	5	TH	AF IZZI+
KH9 5BII	470	600	2.3	20	7	0.218	0.603	0.802	2.9	26.1%	32.6%	43.3%	9.2	9.1	0.0%	Hawkins (2018)	0.594172	4	TH	AF IZZI+
KH9 1A2	120	530	14.9	10	14	0.141	0.497	0.791	2.8	16.3%	17.9%	7.9%	12.6	4.4	0.0%	LTD	1.014425	4	TH	LTD IZZI+
KH9 1B1	430	590	2.7	10	9	0.118	0.483	0.808	4.8	6.6%	9.2%	11.3%	9.7	5.0	0.0%	LTD	0.770272	5.1	TH	LTD IZZI+
KH9 1T	310	550	12.7	10	15	0.148	0.559	0.801	2.2	18.2%	27.8%	22.6%	16.9	5.8	0		1.34498	3	TH	IZZI+
KH9 2A2	390	530	8.6	10	8	0.168	0.239	0.767	1.6	4.1%	9.0%	8.7%	15.5	3.7	0.0%	LTD	0.90243	3	TH	LTD IZZI+
KH9 2B2	490	565	4.8	10	6	0.083	0.262	0.361	1.7	3.8%	8.8%	0.3%	10.9	4.0	0.0%		0.696584	5.1	TH	IZZI+
KH9 5A2	475	565	3.4	10	7	0.067	0.268	0.310	1.6	3.2%	8.7%	4.4%	9.0	2.9	0.0%	B	0.389229	6.1	TH	IZZI+
KH9 5B1	475	565	3.2	10	7	0.066	0.313	0.315	1.7	2.0%	5.1%	7.6%	6.2	3.5	0.0%	B	0.389496	6.1	TH	IZZI+
KINGKH9 1A	0	10	4.8	5	11	0.038	0.915	0.859	20.3	20.1%	15.9%	35.2%	3.3	3.4	0.0%	Hawkins (2018)	0.147604	6	MW	IZZI+
KINGKH9 1B	5	12	5.1	5	8	0.038	0.630	0.827	14.6	14.8%	15.3%	27.4%	1.9	3.4	0.0%	Hawkins (2018)	0.052134	6	MW	IZZI+
KINGKH9 3A	1	7	5.1	5	7	0.016	0.838	0.661	37.4	16.4%	12.9%	15.1%	2.0	5.5	0.0%	Hawkins (2018)	0.08337	6.1	MW	IZZI+
KINGKH9 3B	1	10	6.4	5	10	0.033	0.777	0.843	21.3	10.5%	7.8%	13.6%	2.6	1.8	0.0%	Hawkins (2018)	0.056624	7	MW	IZZI+
KINGKH9 3C	1	10	5.4	5	10	0.028	0.763	0.846	24.1	15.4%	13.0%	20.0%	4.9	3.2	0.0%	Hawkins (2018)	0.08522	6.1	MW	IZZI+
KINGKH9 4A	1	10	12.5	5	10	0.050	0.800	0.847	14.6	15.8%	6.9%	10.5%	1.2	0.8	0.0%	Hawkins (2018)	0.280907	7	MW	IZZI+
KINGKH9 4B	5	14	11.7	5	10	0.035	0.580	0.878	16.4	5.0%	3.0%	3.5%	1.7	2.0	0.0%	Hawkins (2018)	0.079516	7	MW	IZZI+
KINGKH9 4C	1	12	11.9	10	12	0.018	0.728	0.896	35.4	8.2%	7.3%	16.5%	1.7	0.8	0.0%	Hawkins (2018)	0.170131	7	MW	IZZI+
KINGKH9 5A	4	7	4.6	5	4	0.226	0.540	0.377	0.7	14.2%	25.8%	26.8%	6.3	6.2	0.0%	Hawkins (2018)	1.603797	3	MW	IZZI+

Table D10 Arai Plot fits for site 10

Sample	Low T	High T	PI estimate	H_{ub}	N	B	FRAC	G	Q	delCK	DRAT	CDRAT	Alpha	MAD (fixed)	DRATtail	Comment	K	Pass score	Th/MW	
KH10 1AI	500	620	1.4	20	7	0.101	0.178	0.745	4.7	30.6%	48.3%	102.3%	9.0	11.4	0.0%	Hawkins (2018)	0.50077	4.1	TH	AF IZZI+
KH10 2BI	500	620	1.6	20	7	0.070	0.213	0.742	6.9	32.1%	49.3%	103.6%	9.1	10.0	0.0%	Hawkins (2018)	0.19373	5	TH	AF IZZI+
KH10 3BI	500	620	1.1	20	7	0.050	0.150	0.746	9.4	33.1%	51.9%	120.4%	2.2	10.0	0.0%	Hawkins (2018)	0.052172	5	TH	AF IZZI+
KH10 4BI	470	620	1.1	20	8	0.090	0.199	0.796	7.1	37.4%	46.4%	106.9%	4.1	8.5	0.0%	Hawkins (2018)	0.48013	4	TH	AF IZZI+
KH10 5BI	470	620	1.1	20	8	0.096	0.221	0.741	5.5	39.5%	54.6%	119.3%	7.4	14.6	0.0%	Hawkins (2018)	0.492162	4	TH	AF IZZI+
KH10 6BI	440	620	1.2	20	9	0.108	0.297	0.788	6.2	35.0%	41.4%	104.7%	5.5	12.9	0.0%	Hawkins (2018)	0.684165	3.2	TH	AF IZZI+
KH10 7AI	470	620	1.2	20	8	0.042	0.180	0.777	13.3	34.5%	48.5%	129.7%	3.6	10.1	0.0%	Hawkins (2018)	0.16828	5	TH	AF IZZI+
KH10 8BI	0	440	5.6	20	5	0.056	0.753	0.223	2.6	24.8%	36.8%	36.7%	6.3	18.7	0.0%	Hawkins (2018)	0.21729	6	TH	AF IZZI+
KH10 9CI	500	620	1.3	20	7	0.041	0.109	0.703	9.8	29.2%	50.5%	155.5%	1.7	3.5	0.0%	Hawkins (2018)	0.246897	5	TH	AF IZZI+
KINGK10 2A	4	14	6.7	5	11	0.078	0.380	0.845	8.5	13.7%	10.4%	4.6%	13.3	8.8	0.0%	Hawkins (2018)	0.398854	6.1	MW	IZZI+
KINGK10 3A	3	10	7.1	5	8	0.084	0.296	0.762	6.0	14.9%	12.9%	-2.7%	5.4	3.8	0.0%	Hawkins (2018)	0.585467	4.2	MW	IZZI+
KINGK10 5A	0	10	3.0	5	11	0.096	0.798	0.869	5.7	10.6%	14.6%	-9.4%	32.5	14.1	0.0%	Hawkins (2018)	0.19174	5.1	MW	IZZI+
KINGKH108A	3	11	3.3	5	9	0.048	0.417	0.855	12.3	6.4%	7.8%	17.4%	4.8	8.7	0.0%	Hawkins (2018)	0.07988	7	MW	IZZI+
KINGKH108B	3	9	3.3	3	7	0.096	0.400	0.804	6.6	12.2%	10.4%	15.0%	9.1	7.2	0.0%	Hawkins (2018)	0.528724	5.1	MW	IZZI+
KINGKH109A	2	7	5.4	5	6	0.085	0.447	0.691	5.7	9.9%	9.5%	10.4%	4.5	3.6	0.0%	Hawkins (2018)	0.379138	7	MW	IZZI+
KINGKH109B	3	11	5.2	5	9	0.076	0.382	0.819	7.4	6.4%	6.5%	-1.4%	5.7	3.8	0.0%	Hawkins (2018)	0.339485	7	MW	IZZI+
KINGKH109C	2	10	6.4	5	9	0.098	0.478	0.826	6.4	16.8%	13.8%	1.1%	7.6	5.5	0.0%	Hawkins (2018)	0.629771	5.1	MW	IZZI+
KH10 2B1	310	565	3.6	10	16	0.065	0.450	0.896	10.2	9.9%	12.6%	1.8%	13.2	9.2	0	B	0.00706	6.1	TH	IZZI+
KH10 3B1	310	565	3.6	10	16	0.071	0.572	0.905	11.2	13.0%	13.9%	18.8%	6.6	10.7	0.0%	B	0.218815	6.1	TH	IZZI+
KH10 4A2	200	400	3.1	10	7	0.220	0.369	0.785	1.8	11.7%	22.4%	28.3%	36.8	10.5	0.0%		1.052862	3	TH	IZZI+
KH10 5A	200	400	3.4	10	7	0.033	0.300	0.728	9.9	5.1%	10.7%	19.0%	21.0	6.6	0.0%		0.10381	4.2	TH	IZZI+
KH10 5B1	200	385	3.0	10	6	0.054	0.281	0.729	5.6	3.2%	7.5%	3.3%	17.6	5.3	0.0%		0.36028	5.1	TH	IZZI+
KH10 8A2	200	385	3.0	10	6	0.055	0.357	0.681	8.5	6.7%	9.3%	12.1%	11.6	7.1	0.0%	A	0.36978	7	TH	IZZI+
KH10 8B1	120	370	2.4	10	6	0.111	0.474	0.504	2.8	8.8%	13.9%	16.9%	47.9	15.8	0.0%		0.23965	4.2	TH	IZZI+
KH10 9A3	200	370	2.6	10	5	0.069	0.373	0.462	3.8	10.7%	18.0%	25.6%	25.6	10.3	0.0%		0.39321	5	TH	IZZI+
KH10 4B1	280	430	3.0	10	4	0.044	0.194	0.601	7.3	15.8%	28.1%	30.1%	27.9	9.5	0.0%	LTD	0.082352	4	TH	LTD IZZI+
KH10 6B1	200	410	3.2	10	7	0.081	0.438	0.684	4.0	6.4%	12.9%	25.0%	18.9	7.4	0.0%	LTD	0.385251	5.1	TH	LTD IZZI+
KH10 2A2	390	410	2.1	10	2	#DIV/0!	0.053	0.000	#DIV/0!	8.7%	57.2%	54.6%	46.2	5.6	0.0%	LTD	'NA'	#DIV/0!	TH	LTD IZZI+
KH10 6A2	310	390	3.0	10	4	0.053	0.247	0.644	5.3	5.7%	12.5%	6.8%	2.3	4.9	0	LTD	0.124815	5.1	TH	LTD IZZI+
KH10 3A2	310	410	0.9	10	2	#DIV/0!	0.099	0.000	#DIV/0!	5.6%	33.5%	38.9%	59.8	9.5	0	LTD	'NA'	#DIV/0!	TH	LTD IZZI+

Table D11 Arai Plot fits for site C

Sample	Low T	High T	PI estimate	H_{lab}	N	B	FRAC	G	Q	delCK	DRAT	CDRAT	Alpha	MAD (fixed)	DRATtail	Comment	K	Pass score	Th/MW	
KHC 1.1A	330	400	2.0	10	3	0.486	0.158	0.492	0.6	3.6%	6.2%	4.9%	33.7	13.2	0.0%		1.335	1	TH	IZZI+
KHC 1.1B	350	470	1.8	20	4	0.141	0.328	0.482	2.6	2.1%	2.7%	1.1%	40.9	29.1	0	AF		4.1	TH	AF IZZI+
KHC 1.2A	120	445	3.1	10	11	0.258	0.752	0.727	3.1	5.2%	4.5%	3.5%	25.0	16.8	0.0%			5	TH	IZZI+
KHC 1.3B	340	400	1.9	10	4	0.149	0.268	0.596	2.0	3.5%	6.8%	4.9%	21.1	9.0	0.0%			4.1	TH	IZZI+
KHC 1.3E	300	540	3.8	20	7	0.454	0.655	0.241	0.3	44.7%	71.2%	74.6%	17.8	28.1	0	AF		3	TH	AF IZZI+
KHC 1.4A	350	470	1.3	20	4	0.434	0.411	0.359	0.6	1.5%	2.0%	1.3%	73.8	33.3	0	AF		4	TH	AF IZZI+
KHC 1.4B	120	370	10.2	10	6	0.244	0.234	0.760	1.3	7.2%	12.2%	16.2%	13.5	5.7	0.0%		0.895	3.1	TH	IZZI+
KHC 1A	3	11	25.8	10	9	0.078	0.324	0.401	2.0	11.7%	11.0%	28.3%	12.7	2.1	0.0%		0.59592	5.2	MW	IZZI+
KHC 1B	4	11	2.8	10	8	0.086	0.224	0.605	2.9	1.5%	3.6%	10.8%	19.8	3.5	0.0%		0.029663	5	MW	IZZI+
KHC 2.1A	330	520	6.4	10	8	0.136	0.469	0.773	4.7	22.5%	23.0%	24.9%	28.3	19.0	0		0.517	3	TH	IZZI+
KHC 2.1B	400	535	4.4	10	7	0.085	0.484	0.709	5.2	15.4%	22.6%	23.0%	17.8	19.0	0		0.316	5	TH	IZZI+
KHC 2.1C	330	535	3.9	10	9	0.085	0.522	0.792	7.3	15.5%	18.5%	19.9%	40.0	22.3	0		0.414	5	TH	IZZI+
KHC 2.1C	540	580	4.2	20	3	0.165	0.204	0.447	1.3	15.5%	32.3%	4.3%	6.2	3.3	0	AF		3	TH	AF IZZI+
KHC 2.1D	120	460	7.4	10	12	0.234	0.493	0.825	1.7	5.7%	9.6%	4.5%	56.8	17.4	0.0%			5	TH	IZZI+
KHC 2.1F	120	520	5.3	10	16	0.222	0.690	0.642	0.9	20.6%	59.7%	113.6%	68.0	21.6	0	LTD	2.279	2	TH	LTD IZZI+
KHC 2.2A	400	560	4.3	10	11	0.111	0.489	0.865	5.7	12.0%	14.9%	30.1%	19.9	11.9	0.0%			4.2	TH	IZZI+
KHC 2.2B	120	520	13.2	10	16	0.119	0.682	0.789	3.4	22.0%	25.9%	55.7%	19.8	6.8	0	LTD	0.787	3.1	TH	LTD IZZI+
KHC 2.3B	340	460	7.7	10	8	0.101	0.379	0.722	2.6	26.8%	57.5%	99.4%	22.0	8.8	0.0%			4.1	TH	IZZI+
KHC 2.3C	400	550	3.4	10	11	0.086	0.455	0.816	6.8	14.6%	19.3%	21.7%	10.8	14.4	0.0%		0.740	5	TH	IZZI+
KHC 2.3D	400	600	2.5	20	8	0.129	0.405	0.818	5.4	5.4%	6.3%	1.8%	36.4	21.4	0	AF		5	TH	AF IZZI+
KHC 2A	4	9	5.4	10	6	0.087	0.283	0.435	1.8	1.3%	3.2%	1.4%	14.1	2.6	0.0%		0.50741	5.1	MW	IZZI+
KHC 2B	2	9	6.4	10	8	0.120	0.549	0.699	5.3	2.5%	2.3%	1.0%	12.0	6.5	0.0%		0.686386	5.1	MW	IZZI+
KHC 2C	2	14	5.1	10	13	0.041	0.622	0.872	13.8	9.9%	13.9%	14.7%	4.9	3.8	0.0%		0.22961	6.1	MW	IZZI+
KHC 2D	0	4	34.9	10	5	0.275	0.123	0.585	0.2	5.9%	17.9%	16.1%	21.9	1.0	0.0%		0.06475	2	MW	IZZI+
KHC 2F	4	10	6.8	10	7	0.064	0.617	0.785	10.2	7.9%	7.9%	13.9%	6.4	4.5	0.0%		0.290062	7	MW	IZZI+
KHC 2G	1	7	7.6	10	7	0.026	0.419	0.602	9.5	11.6%	22.6%	19.3%	12.6	3.9	0.0%		0.15441	6	MW	IZZI+

Table D12 Arai Plot fits for site D

Sample	Low T	High T	PI estimate	H_{lab}	N	B	FRAC	G	Q	delCK	DRAT	CDRAT	Alpha	MAD (fixed)	DRATtail	Comment	K	Pass score	Th/MW	
KHD 2AB	400	520	6.1	20	5	0.323	0.252	0.558	0.5	6.5%	21.8%	35.3%	8.2	3.9	0	AF		3.1	TH	AF IZZI+
KHD 2.2F	400	520	6.0	20	5	0.279	0.256	0.598	0.7	6.5%	20.3%	28.5%	12.5	4.1	0	AF		3.1	TH	AF IZZI+
KHD 2AA	350	500	20.9	20	5	0.066	0.479	0.714	8.5	23.9%	20.9%	37.7%	9.0	5.9	0	AF		6	TH	AF IZZI+
KHD 2.2E	350	500	17.6	20	5	0.072	0.539	0.667	7.6	25.7%	23.4%	30.9%	7.4	5.9	0	AF		6	TH	AF IZZI+
KHD 2.4G	350	520	13.9	20	6	0.087	0.411	0.796	5.2	6.9%	9.9%	8.6%	11.6	5.2	0	AF	0.3349	7	TH	AF IZZI+
KHD 2.1A	370	520	10.6	10	10	0.096	0.456	0.865	7.3	11.4%	9.6%	4.0%	3.2	2.6	0.0%	B	0.643	6	TH	IZZI+
KHD 2.2A	370	520	8.6	10	10	0.099	0.438	0.863	7.8	11.7%	9.9%	13.0%	2.0	1.8	0.0%	B	0.675	6	TH	IZZI+
KHD 2.3A	340	535	9.1	10	12	0.130	0.547	0.878	6.1	12.0%	9.8%	14.3%	5.1	4.2	0.0%			6	TH	IZZI+
KHD 2.1B	330	500	9.2	10	7	0.198	0.432	0.816	3.3	12.7%	11.7%	22.5%	3.6	2.8	0		0.988	4.1	TH	IZZI+
KHD 2.1C	370	460	7.4	10	4	0.296	0.270	0.662	1.3	6.8%	9.2%	3.9%	7.1	3.8	0		1.066	4.1	TH	IZZI+
KHD 2.2B	330	430	15.8	10	4	0.129	0.244	0.618	2.4	18.5%	20.1%	28.7%	14.6	4.3	0		0.354	4	TH	IZZI+
KHD 2.2C	330	430	27.2	10	4	0.207	0.222	0.622	1.1	14.7%	13.5%	2.4%	7.9	1.7	0.0%		0.834	3.1	TH	IZZI+
KHD 2.3B	330	480	21.8	10	6	0.187	0.319	0.772	1.8	15.5%	14.5%	33.3%	6.8	2.6	0.0%		0.361	4.2	TH	IZZI+
KHD 2.4B	310	505	11.3	10	12	0.074	0.623	0.883	11.2	13.6%	9.6%	27.2%	7.5	7.6	0.0%	B	0.533	6	TH	IZZI+
KHD 2.4D	340	475	10.5	10	9	0.098	0.484	0.867	7.0	34.0%	29.6%	7.2%	8.6	6.3	0.0%			6	TH	IZZI+
KHD 2.4C	385	490	8.2	10	8	0.083	0.398	0.852	6.5	43.5%	53.5%	57.2%	1.9	5.6	0.0%		0.439	6	TH	IZZI+
KHD 2.5B	370	490	9.7	10	9	0.066	0.414	0.866	9.6	10.7%	10.6%	15.7%	6.5	5.2	0	B	0.340	6.1	TH	IZZI+
KHD 2A	9	13	22.9	10	5	0.091	0.762	0.630	6.1	22.0%	9.9%	9.0%	1.9	1.6	0.0%		0.420757	7	MW	IZZI+
KHD 2B	4	10	15.3	10	7	0.033	0.616	0.801	20.0	6.4%	4.3%	0.4%	1.7	2.0	0.0%		0.052286	7	MW	IZZI+
KHD 2C	4	12	15.4	10	9	0.059	0.643	0.838	12.6	6.9%	4.2%	3.2%	2.4	2.4	0.0%		0.146499	7	MW	IZZI+
KHD 2D	4	12	17.8	10	9	0.039	0.417	0.835	13.2	4.1%	3.2%	1.5%	1.6	0.7	0.0%		0.06349	7	MW	IZZI+
KHD 2E	4	10	17.9	10	7	0.073	0.491	0.739	6.5	8.7%	6.6%	15.7%	2.9	1.6	0		0.1008	7	MW	IZZI+
KHD 2F	3	10	17.8	10	8	0.070	0.553	0.796	7.6	13.3%	9.8%	1.6%	6.8	3.5	0		0.006735	7	MW	IZZI+
KHD 2G	4	12	14.7	10	9	0.050	0.533	0.828	11.7	4.2%	3.4%	3.3%	1.9	1.6	0		0.23517	7	MW	IZZI+
KHD 2H	4	11	13.4	10	8	0.071	0.602	0.825	10.2	10.6%	7.2%	4.3%	1.8	2.1	0		0.371354	7	MW	IZZI+
KHD 2.2D	400	520	10.5	10	9	0.095	0.411	0.867	7.4	17.5%	14.8%	22.6%	2.3	2.6	0.0%	LTD	0.113	6.1	TH	LTD IZZI+
KHD 2.4E	370	520	10.4	10	11	0.101	0.457	0.879	6.8	16.4%	14.5%	41.4%	2.9	4.5	0	LTD	0.676	4.2	TH	LTD IZZI+
KHD 2.4F	370	505	11.9	10	10	0.067	0.405	0.853	7.3	15.0%	16.8%	24.4%	3.9	4.7	0	LTD		6	TH	LTD IZZI+
KHD 2.5D	370	520	11.7	10	11	0.063	0.549	0.863	11.8	22.2%	16.8%	36.8%	6.4	6.0	0	LTD		6	TH	LTD IZZI+
KHD 2.5E	310	490	19.4	10	11	0.095	0.391	0.868	6.1	24.6%	16.8%	17.0%	7.6	4.7	0.0%	LTD		6	TH	LTD IZZI+

Table D13 Arai Plot fits for site E

Sample	Low T	High T	PI estimate	H_{ub}	N	B	FRAC	G	Q	delCK	DRAT	CDRAT	Alpha	MAD (fixed)	DRATtail	Comment	K	Pass score	Th/MW	
KHE 1.3A	500	580	7.3	20	5	0.589	0.372	0.214	0.1	4.8%	11.3%	22.9%	2.6	1.6	0	AF		4.1	TH	AF IZZI+
KHE 1.3D	500	580	7.4	20	5	0.629	0.381	0.234	0.1	9.5%	23.9%	32.3%	3.7	1.9	0.0%	AF		4	TH	AF IZZI+
KHE 1.4C	500	580	6.5	20	5	0.701	0.327	0.089	0.0	18.8%	49.3%	32.9%	7.7	5.4	0.0%	AF		3.1	TH	AF IZZI+
KHE 1.5B	500	580	7.5	20	5	0.373	0.336	0.645	0.9	28.6%	49.7%	37.0%	2.0	2.7	0.0%	AF		3.1	TH	AF IZZI+
KHE 1.3C	540	600	5.2	20	4	0.073	0.239	0.648	5.6	9.3%	14.2%	6.0%	1.1	1.0	0.0%	AF		5.1	TH	AF IZZI+
KHE 1.4B	540	600	4.3	20	4	0.040	0.211	0.646	11.4	11.9%	16.7%	21.9%	0.3	1.0	0.0%	AF		5	TH	AF IZZI+
KHE 1.5A	540	600	5.6	20	4	0.054	0.248	0.642	6.8	9.5%	15.9%	7.5%	1.8	2.3	0.0%	AF		5	TH	AF IZZI+
KHE 1.5C	540	580	5.8	20	3	0.026	0.160	0.410	7.0	14.2%	30.9%	33.4%	2.4	2.6	0.0%	AF		4	TH	AF IZZI+
KHE 1.1C	370	535	1.3	10	12	0.346	0.430	0.315	0.4	7.7%	17.6%	25.7%	47.3	13.0	0.0%			3	TH	IZZI+
KHE 1.1D	460	535	1.8	10	6	0.217	0.201	0.656	1.3	4.9%	10.7%	26.6%	26.4	7.7	0			3.1	TH	IZZI+
KHE 1.2G	340	570	2.3	10	16	0.062	0.420	0.883	11.6	8.0%	9.5%	2.4%	4.9	11.6	0		0.122	7	TH	IZZI+
KHE 1.2H	280	570	2.8	10	18	0.064	0.563	0.891	11.1	3.7%	4.5%	1.3%	2.6	10.4	0		0.315	7	TH	IZZI+
KHE 1.1E	340	535	2.0	10	13	0.122	0.365	0.844	4.7	12.7%	18.5%	30.3%	8.2	9.3	0.0%		0.322	5	TH	IZZI+
KHE 1.1F	310	535	2.7	10	14	0.120	0.382	0.877	4.9	11.2%	16.1%	24.3%	27.9	11.4	0		0.542	3	TH	IZZI+
KHE 1.2C	430	535	2.4	10	8	0.135	0.288	0.668	3.2	7.9%	12.1%	16.6%	14.5	7.9	0		0.516	3.2	TH	IZZI+
KHE 1.2D	280	535	2.3	10	15	0.126	0.548	0.813	5.8	13.9%	15.0%	10.9%	48.2	21.2	0		0.211	4.1	TH	IZZI+
KHE 1A	4	10	2.8	10	7	0.066	0.252	0.601	6.4	2.1%	2.9%	4.4%	9.5	5.8	0.0%		0.29516	6.1	MW	IZZI+
KHE 1B	6	12	7.1	10	7	0.129	0.368	0.735	2.9	36.9%	58.1%	68.6%	28.8	16.2	0.0%		0.02956	4	MW	IZZI+
KHE 1C	6	11	2.3	10	6	0.142	0.295	0.734	2.5	3.0%	6.0%	11.7%	26.9	8.7	0.0%		0.294205	4.1	MW	IZZI+
KHE 1D	6	10	1.9	5	5	0.202	0.183	0.638	1.4	8.1%	16.8%	31.7%	32.0	10.6	0.0%		1.184949	2	MW	IZZI+
KHE 1E	4	9	2.9	10	6	0.079	0.390	0.545	5.2	1.4%	1.8%	0.3%	9.2	8.1	0.0%		0.326925	7	MW	IZZI+
KHE 1F	6	13	3.3	10	8	0.064	0.200	0.739	5.1	6.7%	14.5%	34.1%	14.8	5.3	0.0%		0.506428	4.1	MW	IZZI+
KHE 1G	4	10	2.7	10	7	0.129	0.255	0.666	2.9	3.6%	6.3%	18.8%	22.8	8.7	0.0%		1.064235	3.1	MW	IZZI+
KHE 1H	6	14	3.1	10	9	0.091	0.404	0.820	6.5	6.1%	8.1%	6.5%	14.4	7.5	0.0%		0.453686	7	MW	IZZI+
KHE 1I	4	6	2.7	10	3	0.344	0.096	0.386	0.2	4.4%	22.4%	32.8%	54.6	8.7	0.0%		2.22942	0	MW	IZZI+
KHE 1J	4	8	3.0	10	5	0.113	0.217	0.604	2.8	4.6%	8.3%	16.2%	22.0	8.5	0.0%		0.6646	3.1	MW	IZZI+
KHE 1.1A	385	520	2.2	10	10	0.111	0.275	0.467	1.7	23.1%	55.8%	7.0%	144.3	14.3	0.0%	LTD	1.224	2.2	TH	LTD IZZI+
KHE 1.2E	385	520	1.8	10	10	0.204	0.267	0.492	1.5	32.0%	51.5%	12.7%	30.2	16.1	0.0%	LTD	1.811	2.1	TH	LTD IZZI+
KHE 1.2F	400	520	1.5	10	9	0.280	0.327	0.154	0.1	7.1%	36.1%	10.5%	65.9	10.5	0.0%	LTD	1.570	2.1	TH	LTD IZZI+
KHE 1.3B	310	490	2.2	10	9	0.350	0.180	0.793	2.1	42.7%	44.2%	37.3%	11.1	8.4	0	LTD	1.841424	3	TH	LTD IZZI+
KHE 1.5C	340	490	2.7	10	8	0.285	0.196	0.767	2.1	29.6%	36.4%	34.5%	9.8	4.7	0	LTD	1.828627	3	TH	LTD IZZI+

SUPPLEMENTARY INFORMATION E: CHAPTER 9

Table E1 Arai Plot fits for High Temperature Coe-Thellier (HiTeCT) experiments

Sample	Low T	High T	PI estimate	H_{lab}	N	B	FRAC	G	Q	delCK	DRAT	CDRAT	Alpha	MAD (fixed)	Net tail checks
H6 1 15D	490	520	38.0	36	11	0.168	0.173	0.644	1.4	6.4%	11.7%	26.0%	32.4	7.6	0.109
H6 1 16F	490	520	22.2	36	11	0.111	0.348	0.427	0.9	6.4%	23.5%	62.6%	7.7	2.0	0.074
H6 1 4A	0	490	36.5	36	2	#DIV/0!	0.461	0.000	#DIV/0!	0.0%	0.0%	0.0%	3.9	2.2	0.023
H6 1 9F	0	514	44.3	36	10	0.121	0.866	0.281	1.9	11.4%	8.7%	20.8%	4.9	5.0	0.095
H6 2 4E	490	520	58.3	36	11	0.237	0.246	11.756	1.2	23.6%	506.7%	595%	29.4	1.8	8.057
H6 2 5D	0	520	34.9	36	12	0.146	0.886	0.162	0.8	76.5%	72.6%	92.4%	14.0	12.2	0.790
KH10 1T	0	383	61.7	10	13	0.180	0.742	0.532	2.5	47.7%	8.9%	12.8%	17.1	7.6	0.077
KH10 3T	0	383	20.6	10	2	#DIV/0!	0.000	0.000	#DIV/0!	35.0%	23.6%	49.7%	19.5	10.9	0.094
KH10 4T	0	383	15.0	10	2	#DIV/0!	0.000	0.000	#DIV/0!	32.1%	29.5%	60.3%	25.9	14.6	0.078
KH10 4T2	350	383	3.3	10	12	0.110	0.470	0.685	1.6	7.8%	28.0%	56.5%	13.8	6.0	0.098
KH10 5T	350	383	8.5	10	12	0.186	0.357	0.567	0.5	11.5%	49.0%	90.4%	17.1	4.7	0.166
KH10 7T	350	383	10.4	10	12	0.342	0.357	0.111	0.0	13.9%	77.5%	148.7%	14.5	5.5	0.218
KH10 7T2	350	383	4.7	10	12	0.363	0.387	0.055	0.0	13.7%	83.5%	184.5%	55.3	11.2	0.237
KH4 1A	562	583	7.7	10	8	0.128	0.183	0.730	1.1	4.5%	17.7%	50.5%	3.9	1.0	0.197
KH4 5A	562	583	1.4	10	8	0.356	0.211	0.828	0.5	7.6%	33.1%	73.1%	68.8	8.1	0.330
KH4 5B	556	583	3.5	10	10	0.108	0.440	0.715	2.5	5.4%	13.7%	25.2%	6.4	2.6	0.108
KH4 7A	565	580	0.8	10	6	0.468	0.160	0.720	0.4	9.2%	33.8%	90.9%	61.1	12.0	0.460
KH4 9A	556	583	1.6	10	10	0.183	0.282	0.861	1.9	12.2%	30.4%	38.6%	39.2	12.9	0.250
SOH 101A	563	590	32.7	20	10	0.249	0.297	0.728	0.6	15%	36%	72%	14.4	3.8	#N/A
SOH 101B	563	584	21.5	20	8	0.123	0.169	0.831	1.0	4%	19%	8%	20.9	5.8	#N/A
SOH F120A.2	498	504	6.4	40	3	1.963	0.082	13.192	0.1	18%	1445%	1445%	9.5	1.3	#N/A
SOH1 292A	0	520	23.7	36	12	0.116	0.476	0.338	0.6	19.5%	76.9%	79.0%	13.4	2.6	0.784
SOH1 292B	0	520	30.1	36	12	0.130	0.496	0.388	0.9	23.7%	58.3%	65.1%	19.7	3.3	0.751
SOH1 294A	496	520	30.6	36	9	0.280	0.106	0.578	0.1	2.1%	21.8%	51.4%	2.9	0.9	0.541
SOH1 294B	496	520	27.2	36	9	0.304	0.100	0.518	0.1	2.3%	23.9%	61.7%	3.3	0.7	0.559
SOH1 296	490	517	23.9	36	10	0.100	0.440	0.717	2.1	13.7%	38.5%	7.5%	21.4	5.0	0.820
SOH1 454A	0	520	24.1	36	2	#DIV/0!	0.000	0.000	#DIV/0!	14.1%	16.2%	34.3%	12.3	7.6	0.070
SOH1 454C	0	520	23.9	36	2	#DIV/0!	0.000	0.000	#DIV/0!	14.6%	16.2%	32.2%	12.1	7.9	0.074
SOH 435A	563	590	25.7	20	10	0.227	0.189	0.793	0.9	14%	32%	49%	10.6	2.0	#N/A
SOH 435B	563	590	14.7	20	10	0.135	0.161	0.832	1.7	8%	25%	28%	168.9	6.6	#N/A
SOH 436A	572	590	2.1	20	7	0.474	0.081	0.314	0.1	6%	49%	128%	13.4	2.8	#N/A
SOH 436B	569	590	2.4	20	8	0.433	0.102	0.514	0.2	8%	41%	99%	4.5	1.6	#N/A
SOH 437A	560	590	21.1	20	11	0.072	0.380	0.869	6.4	7%	10%	10%	2.6	2.9	#N/A
SOH 437B	560	590	22.3	20	10	0.089	0.374	0.842	5.1	5%	6%	13%	2.0	3.4	#N/A
SOH 438A	563	590	6.0	20	9	0.263	0.137	0.839	1.0	16%	52%	55%	16.6	14.0	#N/A
SOH 438B	560	590	12.9	20	10	0.082	0.264	0.705	2.1	7%	25%	20%	0.8	3.1	#N/A
SOH 439	563	590	15.7	20	9	0.127	0.267	0.830	3.2	8%	14%	13%	1.0	1.5	#N/A
SOH 454B	0	520	24.2	36	2	#DIV/0!	0.000	0.000	#DIV/0!	13.9%	15.6%	32.6%	#NUM!	8.4	0.066
SOH 99A	560	590	12.6	20	11	0.049	0.185	0.886	6.1	13%	33%	110%	1.6	1.2	#N/A
SOH F123A.2	486	498	60.1	40	5	1.139	0.143	22.126	0.1	11%	1236%	1575%	28.4	2.8	#N/A
SOH F123C.1	492	501	1.6	40	4	1.235	0.081	n/a	5.5	0%	11808%	11808%	80.6	2.9	#N/A
SOH F126B.2	480	498	8.8	40	7	0.256	0.193	0.534	0.1	1%	21%	28%	105.8	6.5	#N/A
SOH F249	492	498	3.7	40	3	0.872	0.283	5.764	0.3	0%	9%	9%	43.9	32.4	#N/A
SOH F52B.2	480	498	23.7	40	7	0.031	0.148	0.656	6.5	6%	17%	23%	150.7	5.6	#N/A

Table E2 Arai Plot fits for Coe-Thellier experiments

Sample	Low T	High T	PI estimate	H_{lab}	N	B	FRAC	G	Q	delCK	DRAT	CDRAT	Alpha	MAD (fixed)	K'
Abridged															
F120B	460	600	23.3	30	8	0.177	0.328	0.781	2.9	9.4%	11.4%	20.8%	2.8	2.7	1.151
F120C.2	520	600	26.0	30	5	0.279	0.325	0.686	1.5	8.0%	10.1%	24.2%	2.0	2.9	1.379
F123A.2	400	580	27.2	30	9	0.051	0.718	0.736	11.0	2.1%	2.0%	5.1%	1.6	2.9	0.167
F123B.2	400	580	26.2	30	9	0.054	0.740	0.754	11.6	2.1%	1.9%	3.4%	0.7	2.7	0.303
F123C.2	400	580	26.0	30	9	0.073	0.694	0.788	9.2	4.2%	3.7%	8.6%	0.7	1.9	0.496
F147A.2	0	580	16.6	30	10	0.031	0.989	0.822	27.4	10.4%	8.9%	14.8%	3.2	4.8	0.145
F152B	0	560	39.7	30	7	0.101	0.699	0.709	5.1	8.8%	7.3%	13.4%	8.7	3.7	0.238
F152C	540	600	9.2	30	4	0.104	0.376	0.564	4.1	4.5%	5.7%	9.7%	2.2	3.3	0.504
F157C	460	600	27.1	30	8	0.049	0.716	0.747	10.9	9.5%	9.8%	21.5%	0.7	4.4	0.373
Full															
52A.1	0	400	37.4	40	5	0.210	0.424	3.919	9.5	44.3%	63.6%	63.6%	5.0	7.1	0.604
52C.2	0	350	44.7	40	4	0.120	0.274	0.622	2.9	27.8%	32.7%	32.7%	9.5	3.1	0.720
120A.1	0	570	56.5	40	11	0.048	0.367	0.864	11.7	5.4%	4.8%	5.2%	12.5	5.0	0.288
120C.1	0	350	471.1	40	4	0.692	0.363	0.287	0.1	9.4%	2.8%	2.8%	12.2	2.4	1.765
123A.1	0	555	42.7	40	10	0.034	0.527	0.871	12.3	0.0%	0.0%	0.0%	9.9	2.7	0.007
123B.1	0	555	51.5	40	10	0.023	0.511	0.874	18.4	0.0%	0.0%	0.0%	8.7	2.6	0.071
126A.1	200	555	48.8	40	9	0.062	0.247	0.853	5.5	0.0%	0.0%	0.0%	11.0	3.2	0.045
126B.1	200	555	23.1	40	9	0.077	0.327	0.845	5.7	0.0%	0.0%	0.0%	6.7	3.3	0.357
147A.1	200	555	19.2	40	9	0.080	0.227	0.844	5.0	0.0%	0.0%	0.0%	7.8	2.3	0.341
147B.1	200	555	19.1	40	9	0.093	0.121	0.829	4.5	0.0%	0.0%	0.0%	21.5	5.0	0.286
152A.1	200	555	43.0	40	9	0.044	0.163	0.853	8.2	0.0%	0.0%	0.0%	2.9	2.0	0.137
152C.2	200	555	44.8	40	9	0.056	0.270	0.839	7.2	0.0%	0.0%	0.0%	4.0	1.8	0.142
157A.1	200	555	31.3	40	9	0.037	0.612	0.839	12.7	0.0%	0.0%	0.0%	3.7	2.9	0.038
157B.1	0	555	29.8	40	10	0.058	0.750	0.848	11.1	0.0%	0.0%	0.0%	3.8	2.4	0.223

Table E3 Initial tail checks compared with initial Arai Plot data trend direction

Specimen	First tail check	Initial direction*
KH4-7A	-31	Reverse
KH4-5A	-20	Reverse
KH4-9A	-20	Reverse
H6-2-5D	-11	Reverse
H6-1-9F	-10	Reverse
SOH1-294A	-6	Normal
SOH1-294B	-6	Normal
KH10-1T	-5	Normal
KH10-7T2	-3	Normal
H6-1-15D	-2	Normal
SOH1-292B	-2	Normal
KH10-5T	-2	Normal
KH10-7T	-2	Normal
KH4-1A	-2	Normal
SOH1-296	-1	Normal
H6-2-4E	-1	Normal
KH10-3T	-1	Normal
SOH1-292A	0	Normal
KH10-4T	0	Normal
H6-1-16F	2	Normal
KH10-4T2	2	Normal
H6-1-4A	2	Positive
SOH1-454A	9	Positive
SOH1-454B	9	Positive
SOH1-454C	10	Positive
KH4-5B	12	Positive

* The possible initial trend directions are defined as Reverse (trending to TRM = NRM = 0), Normal (trending to TRM >> NRM), or Positive (trending to NRM >> TRM).

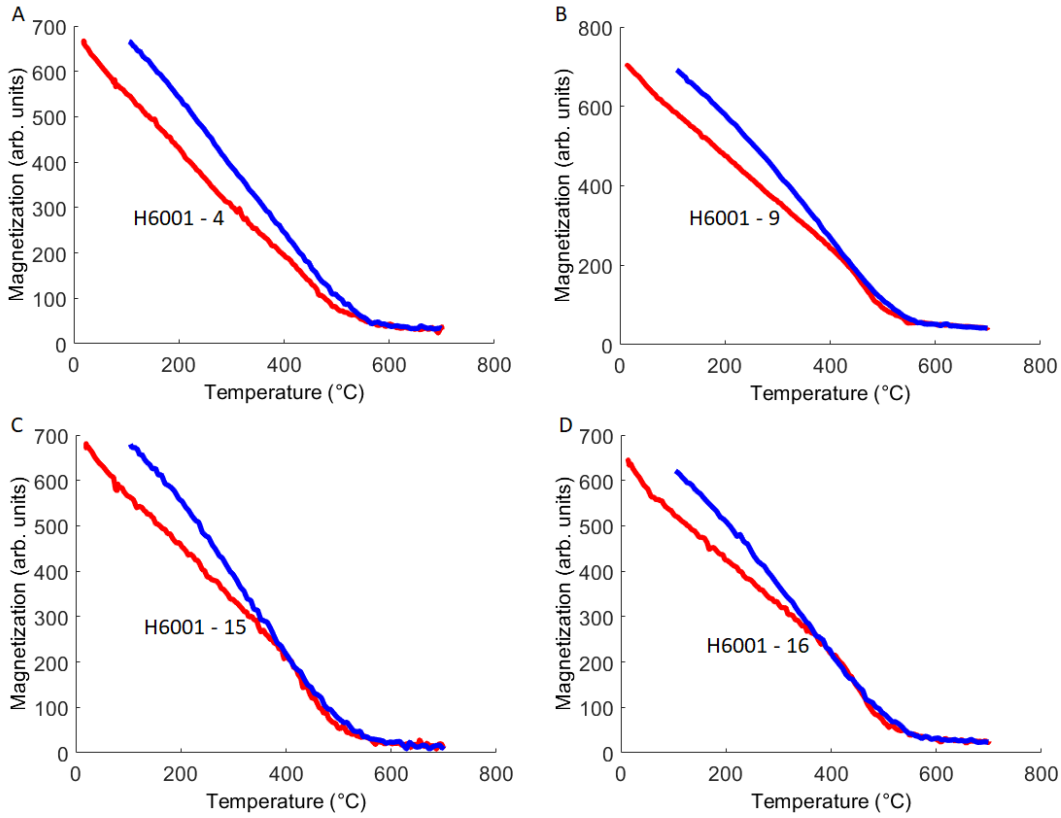

Figure E1 Curie curves for 1960 Kilauea lava flow

SUPPLEMENTARY INFORMATION F: PUBLISHED PAPERS

In this section, the typeset copies of published papers are presented. First, Grappone et al. (2019) is presented, which is the topic of Chapter 6.

Grappone, J. M., Biggin, A. J., and Hill, M. J., 2019, Solving the mystery of the 1960 Hawaiian lava flow: implications for estimating Earth's magnetic field: Geophysical Journal International, v. 218, no. 3, p. 1796-1806.

Second, Grappone et al. (2020) is presented, which is the topic of Chapter 7.

Grappone, J. M., Biggin, A. J., Barrett, T. J., Hill, M. J., & Sprain, C. J. (2020). Comparison of thermal and microwave paleointensity estimates in specimens displaying non-ideal behavior in Thellier-style paleointensity experiments. Journal of Geophysical Research: Solid Earth, 125, e2020JB019802.

Geophysical Journal International

Geophys. J. Int. (2019) **218,** 1796–1806
Advance Access publication 2019 May 31
GJI Geomagnetism, rock magnetism and palaeomagnetism

doi: 10.1093/gji/ggz252

Solving the mystery of the 1960 Hawaiian lava flow: implications for estimating Earth's magnetic field

J. Michael Grappone, Andrew J. Biggin and Mimi J. Hill

Geomagnetism Laboratory, School of Environmental Sciences, University of Liverpool, Liverpool L69 7ZE, UK. E-mail: jmgrappone@gmail.com

Accepted 2019 May 30. Received 2019 May 15; in original form 2018 September 26

SUMMARY

Studying historic lava flows provides a rare comparison between direct measurements of the Earth's magnetic field and the field information recorded in the rock record. Connecting direct and indirect measurements provides a way to bridge the gap between historic data in the last 50–100 yr to geologic data over kyr to Gyr. The field strength in Hawaii in 1960 was directly measured at the Honolulu observatory to be 36.47 μT, so our palaeointensity analysis of the 1960 flow is expected to give the same value. Two vertical sections of the 1960 flow (section 1 and section 2) were the focus of a previous microwave palaeointensity study. The microwave experiments were run using the non-standard, perpendicular modified Thellier-type protocol and produced either apparently good quality data that were biased to low values (section 1) or more scattered results averaging close to the expected value (section 2). The cause of the non-ideal behaviour observed in the data from the 1960 flow is a long-standing mystery that it is important to resolve to confirm the reliability of palaeointensity measurements in general, and the microwave demagnetization mechanism in particular. Here, we test the hypothesis that higher quality, unbiased (only random noise) measurements are possible using an improved Thellier-type protocol coupled to an updated microwave system. New palaeointensity experiments were performed primarily using the IZZI protocol (which allows alteration checks during the experiment) adapted for the microwave system. The specimens from section 1 produced more linear Arai plots and gave an estimate of 36.8 ± 3.4 μT, whereas those from section 2 gave an estimate of 39.1 ± 4.6 μT. Our new experiments demonstrate the microwave system's ability to produce accurate results and efficiently run any Thellier-style experiment. We investigate correcting perpendicular data for undetected alteration and find that using too strict selection criteria can be counterproductive to obtaining accurate and precise microwave palaeointensity results.

Key words: Palaeointensity; Palaeomagnetism; Remagnetization.

1 INTRODUCTION

Understanding the Earth's magnetic field is key to understanding the behaviour of the Earth's interior. Satellites give us extensive data on the geomagnetic field for the last 30–40 yr and ground-based observatories (such as the Honolulu observatory or the French Bureau Central de Magnétisme Terrestre) provide data for up to an additional 100 yr (Jackson *et al.* 2000). Palaeomagnetic techniques let us extend these data to Gyr timescales. Palaeomagnetic investigation of the rock record allows surface measurements that, given suitable rocks, can be used to provide insight into deep Earth processes at any point in geologic time.

Lavas contain magnetic field information stored in the magnetic grains of which the most common is (titano)magnetite. Palaeointensities (PIs) cannot be directly measured *in situ*, however. In order to extract PI estimates, we must subject specimens to extensive experiments, whose accuracies are the subject of some debate (Donadini *et al.* 2007; Biggin 2010; Cromwell *et al.* 2018). Data from historic lava flows, like those in Hawaii, therefore allow us to test various PI methods on many rock types, since the answer is already known. In addition, the data allow geomagnetic models to connect the modern, continuous data records with the discrete data sets that volcanic eruptions provide.

One of the most important places for palaeomagnetism is the Hawaiian Island chain. The island of Hawaii has active volcanoes and is located in the middle of the central Pacific, which covers 30 per cent of the Earth's surface. In 1960, Kilauea's east rift zone erupted. The proximity of this site to the Honolulu Observatory (370 km away) provides a close approximation (36.47 μT) of the magnetic field intensity at the eruption site (Tanaka & Kono 1991;

Böhnel *et al.* 2011). Coe & Gromme (1973) suggested that the local magnetic field at the volcano could deviate from the observatory data by up to ±2 μT. The International Geomagnetic Reference Field: 12th Edition (IGRF-12; Thebault *et al.* 2015) provides a second estimate of 36.2 μT, with the caveat that small-scale magnetic anomalies can go undetected (Coe & Gromme 1973).

Previous study-level average PI estimates (e.g. Hill & Shaw 2000; Böhnel *et al.* 2011; Cromwell *et al.* 2015; Yamamoto *et al.* 2003) range from 33.9 μT using the microwave-perpendicular (MW-Perp) method in Hill & Shaw (2000) to 49.0 μT using the Thellier–Coe method in Yamamoto *et al.* (2003). Detailed analyses of previous palaeodirection studies, which show a recorded modern field direction, and PI studies on the 1960 lava flow are given in Böhnel *et al.* (2011) and Cromwell *et al.* (2015). Herrero-Bervera & Valet (2009) extracted a highly accurate (<2 per cent error) PI estimate of 36.9 μT, using a (relatively large) set of 36 specimens. Cromwell *et al.* (2015) similarly obtained an accurate estimate of 36.0 μT, using very strict selection criteria, which resulted in a success rate of 38 per cent (7/18). In the previous MW study, Hill & Shaw (2000) used the non-standard perpendicular protocol out of necessity because the early 8.2 GHz MW system had poor power absorption reproducibility precluding both double treatments and alteration checks. For section 1, their data gave linear Arai plots, with a mean β (relative standard error) of 0.027, whose estimates were around 13 per cent lower than expected, at 31.6 ± 3.6 μT. At section 2, the Arai plots showed considerable nonlinear, two-slope behaviour, but an (accurate) estimate of 37.1 ± 6.4 μT was extracted by fitting the entire Arai plot, regardless of linearity. This result is unexpected, as more linear (less noisy) data would be expected to be more accurate than less ideal (noisier) data.

These previous studies found significant variations in magnetic properties throughout the 1960 lava flow both vertically and laterally. Previously reported scanning electron microscopy shows elongated primary low-Ti titanomagnetite, which forms during cooling and thus retains a thermoremanent magnetization (TRM; Dunlop & Ozdemir 2001; Böhnel *et al.* 2011). Yamamoto *et al.* (2003) determined that alterations leading to a thermochemical remanent magnetization (TCRM) can explain why many thermal studies give high PI estimates. Generally, studies that used more specimens had estimates closer to the expected value, which suggests that either the flow has significant heterogeneities across it (a point noted in Hill & Shaw 2000) or the PI methods used are inherently noisy. We note both of these explanations can be remedied by more extensive sampling of a given lava flow, since sparse sampling of heterogeneous flows can exaggerate the contribution of non-random (biased) noise in the data. Exaggerated non-single domain contributions can cause systematic differences in estimates for single- and double-treatment protocols (Biggin 2010). The cause of the non-ideal behaviour in these rocks, however, has been a mystery for over 20 yr.

Hill & Shaw (2000) undertook extensive reflected-light microscopy and obtained hysteresis properties, isothermal remanent magnetization acquisitions and Curie curves for sister samples to those used herein. Hill & Shaw (2000) found in both sections predominantly titanomagnetite with a Curie temperature of approximately 520 °C. They further found predominately linear Curie curves, which imply rapid cooling of the lava, preventing uniform iron oxide grain distribution. Fig. 3 in Hill & Shaw (2000) shows moderately low (broadly between the single- and multidomain ranges) hysteresis parameters, with section 2 having a larger range than section 1. Rapidly cooled pseudo-single-domain grains typical of basalts have been shown to have negligible cooling rate effects (Yu 2011; Biggin *et al.* 2013; Ferk *et al.* 2014); however, this has become the subject of some debate (Santos & Tauxe 2019). The previous MW data set from Hill & Shaw (2000) gave underestimates, which has the opposite sense to that expected if a cooling rate correction were needed. Cooling rate correction has, therefore, not been investigated in this study.

Advances in the MW technique now allow the use of the IZZI protocol (Yu *et al.* 2004), which allows $pT_{(M)}RM$ [partial (microwave-) thermoremanent magnetization] checks for alteration and contains a built-in check for multidomain behaviour, through the zigzagging of the Arai plots (Yu & Tauxe 2005). We need to understand if using the more modern IZZI protocol helps resolve the unexpected outcome from Hill & Shaw (2000) to solidify the utility of not only the MW system but also the IZZI protocol applied to the MW. Our goal herein is, therefore, to extract high-quality PI data that yield an estimate of 36.2–36.5 μT using Liverpool's most sophisticated MW system (Hill *et al.* 2008). We also aim, more generally, to determine the source of the non-ideal behaviour to confirm the reliability of PI measurements in general, and the MW system as a demagnetization mechanism in particular.

2 METHODS

The samples used are the archived samples remaining from Hill & Shaw (2000). In the original study, standard 25 mm diameter cores were taken from two sites, which were 16 m apart. At section 1, the flow was 1 m in height. At section 2, the flow was 75 cm in height. For full details, readers are referred to Hill & Shaw (2000). Due to the scarcity of material available, MW with a diameter of 5 mm and a height of 1–2 mm (instead of the more standard 5 mm height) were drilled from 21 individual 25 mm diameter cores to maximize the number of specimens.

The main protocol used in this study was the IZZI protocol (Yu *et al.* 2004), adapted for use on the MW system, which we ran on 59 specimens. To compare our data to the previous study, we also used the MW-Perp method (Hill & Shaw 2007) on 46 specimens of which 21 also included pT_MRM checks. All MW tests were run on the 14 GHz Tristan MW system at the University of Liverpool's Geomagnetism Laboratory (Hill *et al.* 2008). We used MW powers starting at 5 W for 5 s, up to the maximum of 40 W, for a maximum time of 20 s (normally 5–8 s maximum), generally until specimens have lost at least 90 per cent of their Natural Remanent Magnetization (NRM). We used an applied laboratory field of 36 μT, approximately the expected strength. The field was always applied perpendicular to the specimen's NRM. This can exaggerate Arai plot zigzagging (Yu & Tauxe 2005) from specimens that contain non-SD magnetic grains, according to Shaar *et al.* (2011), but it allows a more direct comparison with Hill & Shaw (2000).

The IZZI protocol is a double-treatment protocol that combines in-field (I) steps and zero-field (Z) steps in an enclosed couplet. At each MW power integral, both a Z and an I step are performed before being taken to a higher power integral and the treatments reversed. We used the variant ZIIZ, followed by a pT_MRM check step (P) with the same power integral as the last step in the previous couplet, which gives a complete pattern of 'ZIIZP'. The standard IZZI protocol includes pTRM checks (Yu *et al.* 2004), but it can, in theory, be run without them. Therefore, for consistency and clarity with the other protocols used, in this paper, we will refer to the MW version of IZZI with pT_MRM checks as MW-IZZI+.

The perpendicular protocol (Kono & Ueno 1977) uses only a single treatment at each temperature step, with the field applied perpendicular to the specimen's NRM. Variation from a perpendicularly applied field is represented by $\Delta\theta$ and is required to be small. For 21 specimens, we also included a Z step and a P step after every other I step. The Z step is necessary for the pT_MRM check to work. With the addition of the Z and P steps, this protocol can be written as 'IIZP'. We will refer to this protocol as MW-Perp++ to reflect the additional two steps. We note that Biggin (2010) predicted that the addition of Z and P steps to a perpendicular experiment would add considerable extra data point scatter on Arai plots if the remanence carriers do not behave as ideal single-domain grains.

In this paper, we use a primary, moderately strict, set of selection criteria, modelled after the MC-CRIT.C1 selection criteria (without tail checks) from Paterson *et al.* (2015). To test the influence of selection criteria on the PI estimates, we also tested two additional sets of selection criteria on the MW-IZZI+ data analysis: a loose set modelled after Bono *et al.* (2019) and a strict set modelled after Cromwell *et al.* (2015). These criteria can be found in Table 1. Paterson *et al.* (2015) details the statistics and showed that the moderately strict selection criteria have a median accuracy of 95.3 per cent in their experiments (with tail checks). In all cases, in order to try to minimize the impact of estimates made from lower power integral steps, we opted for the longest best-fit line that still passed the selection criteria.

First Order Reversal Curves (FORCs) were run on two specimens to assess their magnetic domain states. The data were gathered on a Princeton Instruments Vibrating Sample Magnetometer (VSM) at the Institute of Rock Magnetism (IRM) at the University of Minnesota. These data are available in Supporting Information Section A.

We were also interested in correlating changes in hysteresis parameters with pT_MRM check failures. To do this, we ran hysteresis loops on a Magnetic Measurements Variable Field Transition Balance to compare changes in hysteresis parameters with the failure of pT_MRM checks. We used sister specimens of those used in the PI experiments. We ran an initial hysteresis loop, then simulated an MW-IZZI+ experiment, completing the ZIIZP pattern at the same powers used on sister PI experiment specimens. Another hysteresis loop was measured, and then the specimen underwent another ZIIZP at the next power integral steps.

3 RESULTS

3.1 Palaeointensity estimates

We ran 70 specimens from 13 samples from section 1 and 35 specimens from 8 samples from section 2. Using our preferred selection criteria, the moderately strict set, 68 new PI estimates were accepted, for an overall success rate of 65 per cent. All new PI estimates and raw data will be available on the MagIC database. Arai plot fit data can be found in Supporting Information B. Some specimens showed an overprint removed at low power integrals, but the additional component generally disappeared by power integral applications of approximately 40–60 Ws. No systematic variation was observed over the available sampling of the section. We therefore report an arithmetic mean and one standard deviation of the successful specimens' PI estimates, in Table 2. Most specimens lost the majority of their magnetization by 1600 Ws. It was necessary, however, to treat some (usually in one or two large steps) to ~2400 Ws.

3.1.1 Section 1

Of the 41 specimens that underwent an MW-IZZI+ treatment, 70 per cent passed the loose selection criteria and averaged 37.3 ± 3.3 μT, 54 per cent passed the moderately strict selection criteria and averaged 36.8 ± 3.4 μT and 0 per cent passed the strict selection criteria. The loose and moderately strict estimates are not statistically distinct from the IGRF field estimate of 36.2 μT, with $p = 0.20$ and $p = 0.68$, respectively. The most common reason for failure for the MW-IZZI+ experiments were pT_MRM check failures. A set of four example Arai plots (Nagata *et al.* 1963) from these experiments that show the range of behaviour observed can be found in the top row of Fig. 1. Approximately half of the specimens that passed our selection criteria had a pT_MRM failure in the highest (not accepted) power integral ranges. Zigzag was visually observed in 14/41 (34 per cent) specimens (Fig. 1, top row), with the zigzag often increasing after a pT_MRM failure. In no case was the zigzag alone sufficient for the Arai plot data to have unacceptably high scatter (β).

We ran 17 specimens from section 1 using MW-Perp with an 88 per cent success rate. The two failures for the MW-Perp experiments were the result of the angle ($\theta_1 + \theta_2$) between the total vector and NRM (θ_1) and the total vector and B_{lab} (θ_2) (Hill & Shaw 2007) exceeding the tolerance allowed. This kind of failure can be attributed to anisotropy, alteration, or imperfect removal of any overprints (which results in a non-perpendicular field direction). We found an average PI of 31.2 ± 5.0 μT. The middle row of Fig. 1 demonstrates that although the plots are often very straight, the estimates are still biased to lower values.

As an intermediate between MW-IZZI+ and MW-Perp, we ran 12 specimens using MW-Perp++ , with a below average success rate of 50 per cent. Like the MW-IZZI+ specimens, the most common reason for failure was pT_MRM check failures. Like this section's MW-IZZI+ specimens, half of the specimens that passed the selection criteria had a pT_MRM failure in the highest (not accepted) power integrals. These specimens gave an estimate falling between that of the MW-IZZI+ and MW-Perp, at 33.5 ± 1.9 μT. The bottom row of Fig. 1 demonstrates that the MW-Perp++ also has Arai plots with data characteristics between those of MW-IZZI+ and MW-Perp.

3.1.2 Section 2

Section 2 gave higher estimates than section 1 and showed relatively consistent results from all three protocols. 18 specimens received an MW-IZZI+ treatment. 14 specimens (78 per cent) passed the loose selection criteria, 11 specimens (61 per cent) passed the moderately strict selection criteria and 3 specimens (17 per cent) passed the strict selection criteria. These gave the highest average PI estimates at 41.7 ± 6.5, 39.8 ± 4.6 and 43.9 ± 8.9 μT, respectively. The estimate givn by the loose selection criteria is statistically distinct from the expected value 36.2 μT ($p = 0.010$), but the moderately strict ($p = 0.090$) and strict estimates are not ($p = 0.29$). All the specimens that failed, did so because of pT_MRM check failures. Half of the specimens that passed had pT_MRM failures at higher (not-accepted) power integrals. The top row of Fig. 2 contains representative Arai plots from these data. Slight zigzag was observed in 5/18 (36 per cent) Arai plots, with minimal observed change after pT_MRM failures.

Of the eight specimens that received an MW-Perp treatment, five passed. The three failures were, like for specimens from section 1, the result of the $\theta_1 + \theta_2$ angle exceeding tolerance. The successful

Table 1. Selection criteria.

Type	N	FRAC	R^2	β	q	$\lvert\vec{K}'\rvert$	MAD_{ANC}[a]	α[a]	DRAT[b] (per cent)	$\Delta\theta$[c]
Loose[d]	≥4	–	≥0.9	–	–	–	≤10	–	≤10	–
Moderate	≥4	≥0.45	–	≤0.1	≥4	≤0.480	≤10	≤10	≤10	≤0.25°
Strict[d]	≥4	≥0.78	–	≤0.1	≥4	≤0.164	≤5	≤10	≤10	–

[a]For technical reasons, only IZZI+ data can use these criteria.
[b]Perpendicular data lack pT_MRM checks, so DRAT cannot be used for these data.
[c]Used only for perpendicular-style experiments.
[d]These criteria were only tested on MW-IZZI+ data.

Table 2. New palaeointensity estimates.

Method	Section 1 PI estimate (μT ± 1σ)	Median β (passed ± 1σ)	Success rate (per cent)	N	Section 2 PI estimate (μT)	Median β (passed ± 1σ)	Success rate (per cent)	N
MW-Perp	31.2 ± 5.0	0.0354 ± 0.015	88	15	37.7 ± 5.4	0.0395 ± 0.028	63	5
MW-Perp++	33.5 ± 1.9	0.0394 ± 0.0068	50	6	36.8 ± 5.7	0.0295 ± 0.016	89	8
MW-IZZI+ (loose)	37.3 ± 3.3	0.0615 ± 0.024	70	29	41.7 ± 6.5	0.0628 ± 0.028	78	14
MW-IZZI+ (moderate)	36.8 ± 3.4	0.0571 ± 0.022	54	22	39.1 ± 4.6	0.0692 ± 0.027	61	11
MW-IZZI+ (strict)	–	–	–	0	43.9 ± 8.9	0.0490 ± 0.036	17	3

experiments gave an average PI estimate of 37.7 ± 5.4 μT. The bottom row of Fig. 2 shows half of the accepted Arai plots from section 2's MW-Perp data set.

Like with section 1, the MW-Perp++ PI estimates for section 2 falls between that of the MW-IZZI+ and the MW-Perp. Only one specimen out of nine failed, as a result of its pT_MRM checks failing. Of the specimens that passed, two had pT_MRM failure at the highest (not accepted) power integrals. The successful specimens gave an average of 36.8 ± 5.7 μT. Representative Arai plots can be found in the middle row of Fig. 2.

3.2 Interpreting MW-IZZI+ as MW-Perp and MW-Perp++

The MW-IZZI+ experiments were run perpendicular to each specimen's NRM direction. For the derived MW-Perp++ (MW-derPerp++) test, we removed the first Z step data from each ZI-IZP couplet and treated the rest of the data as normal for MW-Perp++. For the derived MW-Perp (MW-derPerp) test, we removed all the Z and P steps from the raw data file. We then processed these data through the same plotting routine as the MW-Perp and MW-Perp++ data. Many specimens failed due to the angle changing, which was also observed in our real MW-Perp experiments.

From the MW-derPerp++ Arai plots (examples in Fig. 3), we found an average PI estimate of 33.2 ± 5.8 μT (28/41 passed) for section 1 and 39.9 ± 8.2 μT (10/18 passed) for section 2. These estimates are not statistically distinct from the (direct) MW-Perp++ estimates and are on average 10 per cent lower and 2 per cent higher than the respective MW-IZZI+ estimates. The MW-IZZI+ estimate for section 1 is statistically distinct from section 1 MW-derPerp++ estimate; section 2 estimates are not statistically distinct. Fig. 3 compares the specimen-level MW-derPerp++ PI estimates with the MW-IZZI+ data from which the MW-derPerp++ data are derived. Table 3 contains a comparison of the MW-derPerp++ mean with the MW-IZZI+ and MW-Perp++ means.

From the MW-derPerp Arai plots (examples in Fig. 4), we extracted an average PI estimate of 31.3 ± 4.6 μT (32/41 passed) for section 1 and 37.1 ± 9.9 μT (13/18 passed) for section 2. Using the MW-IZZI+ data without pT_MRM checks or Z steps gave PI estimates that are not statistically distinct from and are within 4 per cent our MW-Perp estimates of 31.2 and 37.7 μT, respectively (but are from each other). The estimates are 15 and 8.7 per cent lower than the respective MW-IZZI+ site-level estimates. Fig. 4 compares the specimen-level MW-derPerp PI estimates with the MW-IZZI+ data from which the MW-derPerp data are derived. Table 3 contains a comparison of the MW-derPerp mean with the MW-IZZI+ and MW-Perp means.

3.3 Using the MW-IZZI+ data to interpret the MW-Perp data

To try to remove the effects of alteration on the PI estimates, we repeated the analysis of the MW-Perp with the additional constraint that we only allowed data from power integrals below which pT_MRM checks in MW-IZZI+ sister specimens did not fail. We extracted PI estimates of 34.6 ± 4.7 μT (14/17 passed) for section 1 and 41.0 ± 7.0 (6/8 passed) for section 2. These estimates are not statistically different from their respective MW-IZZI+ , MW-Perp++ , or MW-Perp estimates. Assuming sister specimens had alterations occur at similar power integrals, this observation implies that undetected alterations caused a shallowing of the Arai plot, which caused PI estimates to be lower than expected.

3.4 pT_MRM checks versus hysteresis parameters

This experiment aims to test if changes observing hysteresis parameters are sufficient to identify alterations when pT_MRM checks are not present (Hill & Shaw 2000). We ran six specimens, three from section 1 and three from section 2 to compare the changes in the hysteresis parameters of the specimens with the results of pT_MRM checks measured during a series of treatments that mimicked a PI experiment. Fig. 5 contains the results of this experiment (the reader

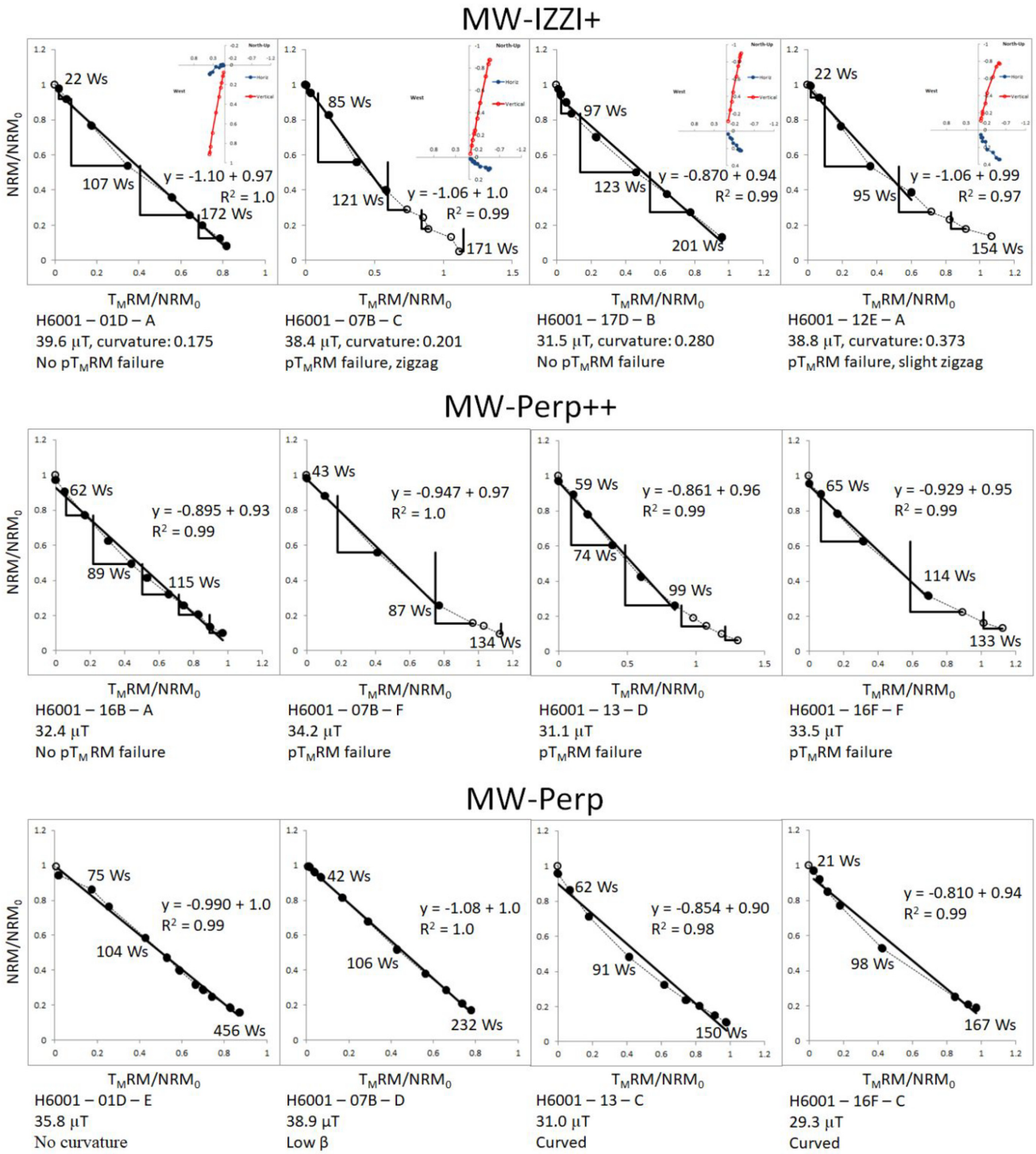

Figure 1. Section 1 Arai plot examples. Orthogonal projections are provided for MW-IZZI+ data. Black circles are accepted data points (with their line of best fit in black), open circles are rejected data points (using the moderately strict selection criteria). The black right-angled lines are pT_MRM checks, and $\boldsymbol{\beta}$ is a measure of data scatter around the best fit line. Evidence of alteration was found in approximately half of specimens that had pT_MRM checks. The MW-Perp specimens have some of the most linear Arai plots but on average also gave the lowest PI estimate.

is referred to Supporting Information Section A.2 for further discussion). All specimens exhibited a trend to move towards the single domain region as the applied power increased. The dotted lines correspond to failed pT_MRM checks and the solid lines correspond to positive pT_MRM checks for sister specimens. The largest changes in hysteresis parameters generally corresponded to pT_MRM check failures. The correlation, however, is insufficiently quantified to be used in place of pT_MRM checks.

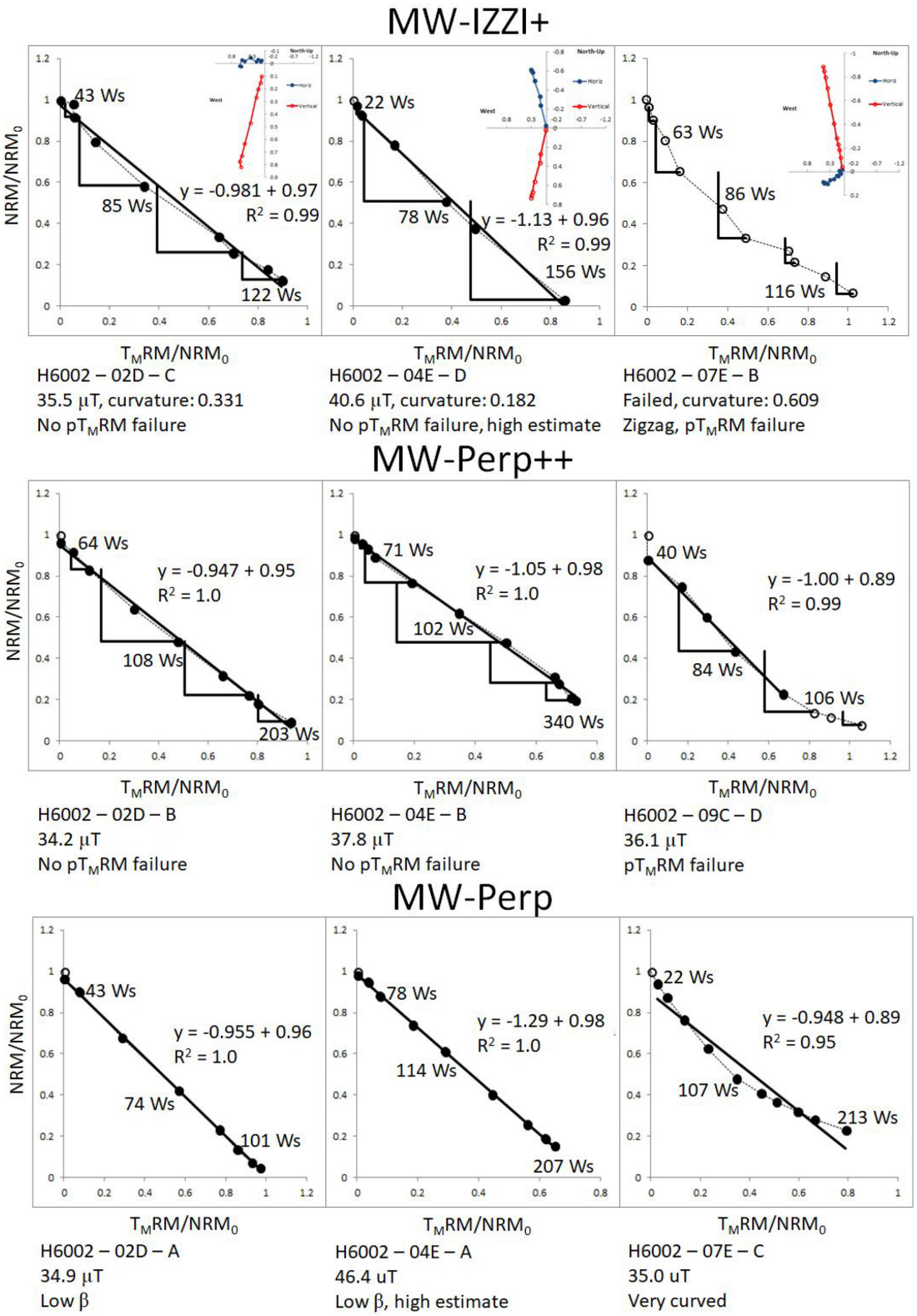

Figure 2. Section 2 Arai plot examples. Orthogonal projections are provided for MW-IZZI+ data. Black circles are accepted data points (with their line of best fit in black), open circles are rejected data points (using the moderately strict selection criteria). The black right-angled lines are pT_MRM checks, and $\boldsymbol{\beta}$ is a measure of data scatter around the best fit line. The Arai plots for specimens in section 2 had similar behaviour to those in section 1 in terms of pT_MRM failures and zigzagging MW-IZZI+ Arai plots.

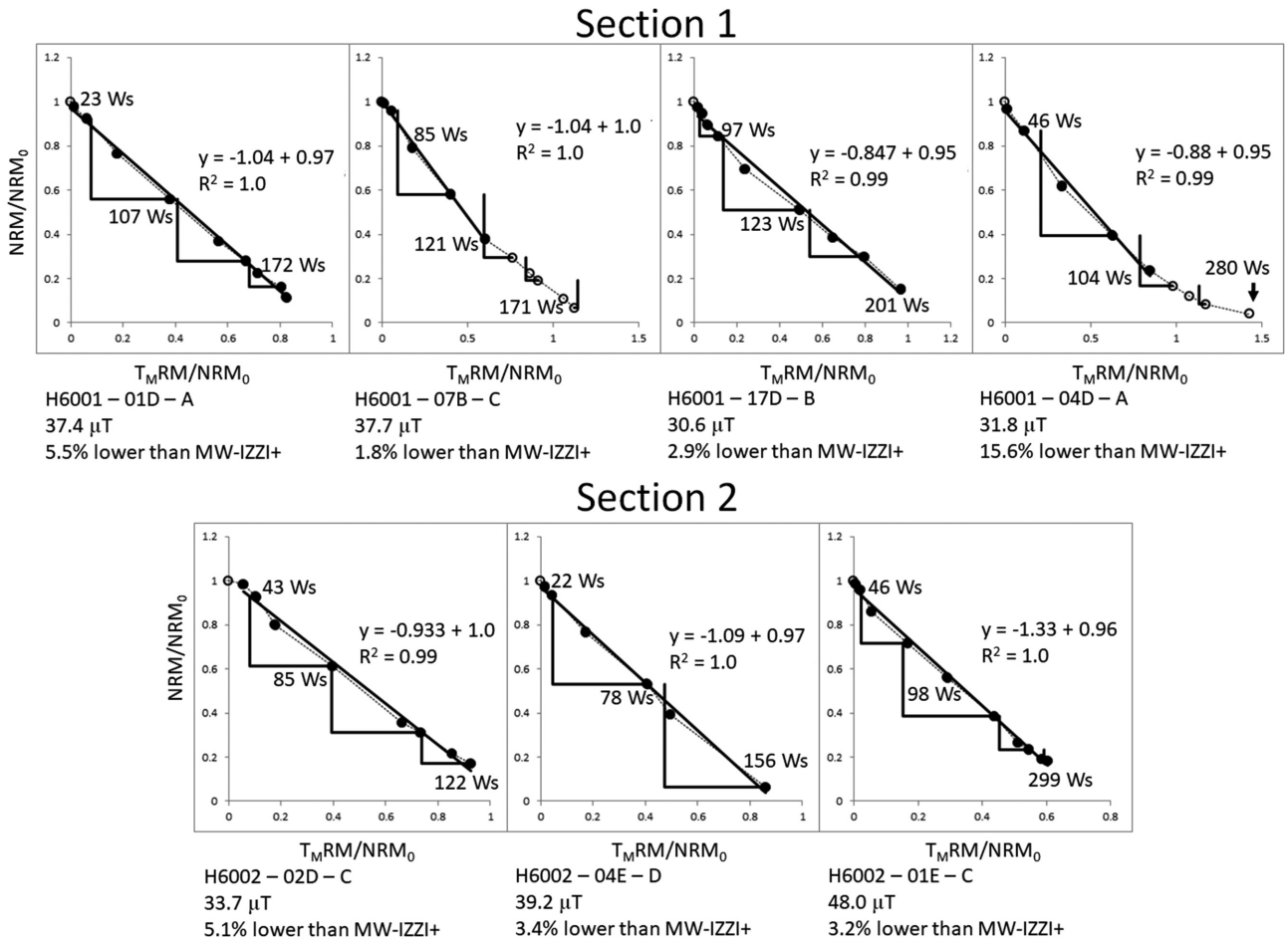

Figure 3. MW-IZZI+ data interpreted as MW-Perp++ (MW-derPerp++) data; appropriate Z steps were removed and then the raw data were replotted. Black circles are accepted data points (with their line of best fit in black), open circles are rejected data points. The black right-angled lines are pT_MRM checks. Top: section 1 (section average with this treatment: 33.2 ± 5.8 μT). Bottom: section 2 (section average with this treatment: 39.9 ± 8.2 μT).

Table 3. Estimates extracted by section and protocol.

Method	Section 1 PI estimate (μT)	IEF	N	Section 2 PI estimate (μT)	IEF	N
MW-Perp (new)	31.2 ± 5.0	0.16	15	37.7 ± 5.4	0.031	5
MW-Perp++ (new)	33.5 ± 1.9	0.081	6	36.8 ± 5.7	0.016	8
MW-IZZI+ (new, loose)	37.3 ± 3.3	0.030	29	41.7 ± 6.5	0.15	14
MW-IZZI+ (new, moderate)	36.8 ± 3.4	0.016	22	39.1 ± 4.6	0.074	11
MW-IZZI+ (new, strict)	–	–	0	43.9 ± 8.9	0.21	3
MW-IZZI+ (treated as MW-Perp in Section 3.2)	31.3 ± 4.6	0.016	32	37.1 ± 9.9	0.024	13
MW-IZZI+ (treated as MW-Perp++ in Section 3.2)	33.2 ± 5.8	0.090	28	39.9 ± 8.2	0.093	10
MW-Perp (treated as in Section 3.3)	34.6 ± 4.7	0.046	14	41.0 ± 7.0	0.12	6
MW-Perp	31.6 ± 3.6 (*all*)	0.15	40	37.1 ± 6.4 (*all*)	0.024	30
(Hill & Shaw 2000)	31.2 ± 3.4 (*sister*)	0.16	22	35.9 ± 5.5 (*sister*)	0.008	14
MW-Perp (treated as in Section 4.2)	33.4 ± 5.8	0.084	21	36.3 ± 6.4	0.003	14

Note: N is the number of specimens across all samples from the section. IEF is the intensity error fraction (Biggin *et al.* 2007).

4 DISCUSSION

4.1 Non-SD behaviour

The overall goal was to find estimates as close to 36.2–36.5 μT as possible, while minimizing the unnecessary rejection of measurement-level Arai plot data. Our closest estimate from section 1 was produced by MW-IZZI+ experiments and the closest estimate from section 2 came from its MW-Perp++ experiments (all estimates can be found in Table 3). Section 2 was previously shown in Hill & Shaw (2000) to exhibit two-slope behaviour in its Arai plots. We have found the inflection point for their two-sloped Arai plots to be correlated with pT_MRM check failures when present. The mean curvatures, $|\vec{K'}|$, for sections 1 and 2 are 0.283 and 0.261, respectively, which are relatively high. Curved Arai plots are the characteristic of specimens containing non-SD grains (Levi 1977; Shcherbakov & Shcherbakova 2001; Biggin

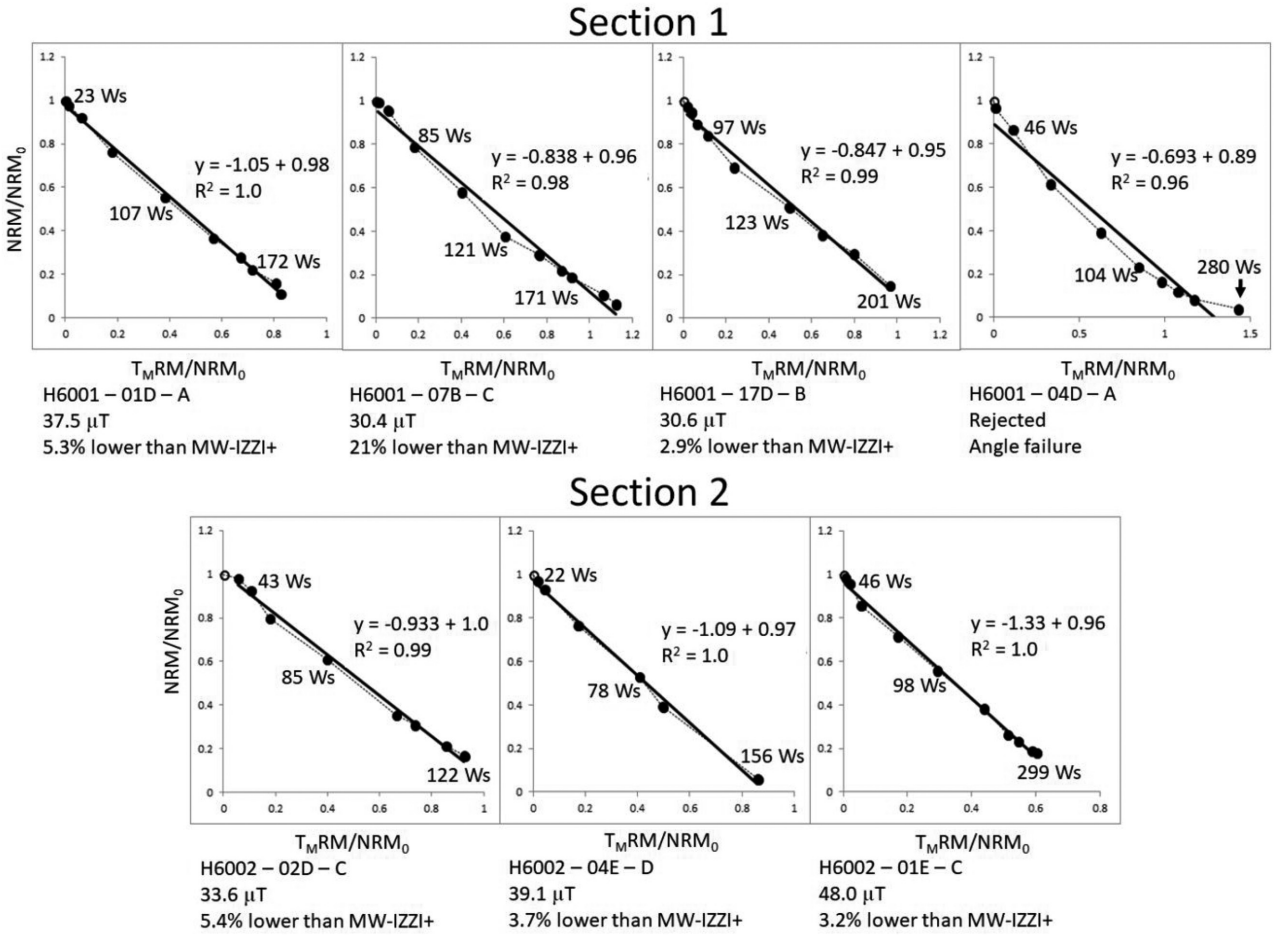

Figure 4. MW-IZZI+ data interpreted as derived MW-Perp (MW-derPerp) data; Z and P steps were removed and then the raw data were replotted. Black circles are accepted data points (with their line of best fit in black), open circles are rejected data points. The black right-angled lines are pT_MRM checks. Top: section 1 (section average with this treatment: 31.3 ± 4.6 μT). Bottom: section 2 (section average with this treatment: 37.1 ± 9.9 μT).

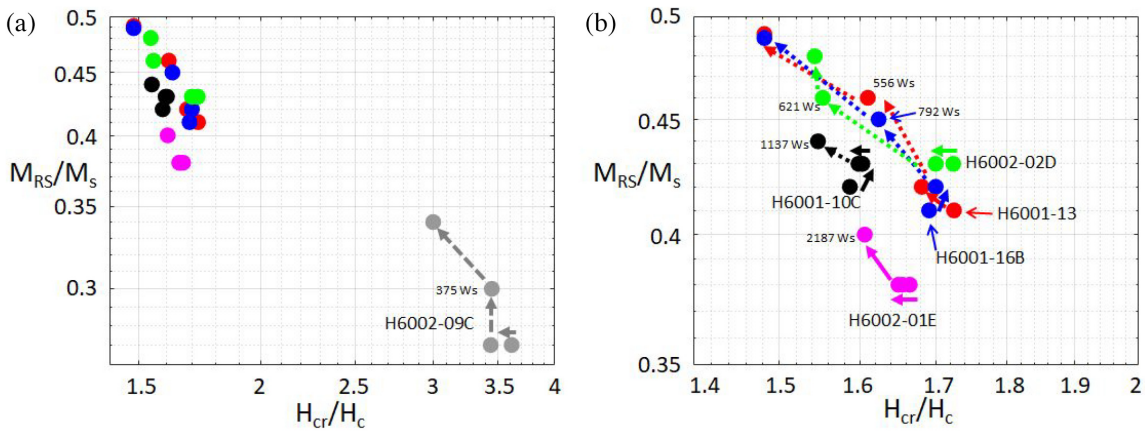

Figure 5. Hysteresis parameter plot showing movement over a simulated MW-IZZI+ experiment. (a) All data taken and (b) zoomed in near the S.D. section. Solid coloured arrows correspond to a passed pT_MRM check on sister specimens, whereas dotted coloured arrows correspond to a failed pT_MRM check on sister specimens. Power integrals are noted at the first failed pT_MRM check or highest power integral step.

2010; Hodgson *et al.* 2018). The pT_MRM check failures in the MW-Perp++ data are consistent with the findings in Biggin (2010), who found that pT_MRM checks can exaggerate non-SD behaviour. The MW-derPerp++ data have pT_MRM check failures at similar power integrals and NRM remaining to the MW-IZZI+ data. We interpret the pT_MRM check failures to be the result of irreversible thermo-chemical alteration, but the data also indicate non-SD behaviour as a potential source of error. The zigzagging Arai plots found in more than 1/3 of all new specimens given an IZZI+ treatment; this is also the characteristic of non-SD grains.

4.2 Comparison with previous microwave results

Our new MW-Perp estimates agree very closely with those from Hill & Shaw (2000). For section 1, we extracted an estimate of 31.2 ± 5.0 μT, compared to their overall estimate of 31.6 ± 3.6 μT. For section 2, we extracted an estimate of 37.7 ± 5.4, compared to their overall estimate of 37.1 ± 6.4. If we look only at estimates from the exact same core samples, Hill & Shaw (2000) extracted estimates of 31.2 ± 3.4 μT and 36.6 ± 7.1 μT, differences of <1 and 3 per cent, respectively. Like Hill & Shaw (2000), we found that specimens from section 1, on average, had straighter Arai plots than section 2. Even though we used a different MW system, the 14 GHz Tristan system, instead of the original 8 GHz system Hill & Shaw (2000) used, we still recovered the same MW-Perp estimates, so equipment effects appear to be negligible.

In section 3.3, we used our MW-IZZI+ power integrals and pT_MRM checks to select MW-Perp Arai plot points. Here we re-analyse the Hill & Shaw (2000) data to independently verify the results. Hill & Shaw (2000) used a different resonant cavity, so we cannot use the power integrals directly like in section 3.3. Instead, we can estimate the power integrals of the pT_MRM check failures on the Arai plots using the NRM remaining as a rough analogue. For example, if MW-IZZI+ specimen had a failed pT_MRM check when 40 per cent of the NRM remained, then we only accept MW-Perp data points from Hill & Shaw (2000) that have at least 40 per cent NRM remaining. Following this method, we extracted estimates of 33.4 ± 5.8 and 36.3 ± 6.4 μT for sections 1 and 2, respectively, which are < 2 per cent different from our new MW-Perp++ estimates of 33.5 ± 1.9 and 36.8 ± 5.7 μT, respectively. The lower estimates observed in MW-Perp compared to MW-Perp++ are, therefore, likely the result of undetected alterations in the MW-Perp data. In the original study of Hill & Shaw (2000), it appears that non-SD and alteration effects were cancelling one another out to a degree such that section 2 fortuitously recovered the PI accurately when the entire (curved) Arai plot was used.

MW-IZZI+ data, with moderately strict selection criteria, for both sections 1 and 2 produce PI estimates that are not statistically distinct ($p_1 = 0.417$; $p_2 = 0.063$) from the 36.2 μT value given by the IGRF (Thebault *et al.* 2015). The data with loose selection criteria give overestimates, which is broadly consistent with the findings of Herrero-Bervera & Valet (2009). The data with strict selection criteria give the smallest data set, which means the data likely do not sample the flow sufficiently (Biggin *et al.* 2003). The high scatter, with inaccurate values both above and below the expected value, is consistent with the findings of Paterson *et al.* (2012) that overly strict selection criteria can, in some cases, overly reject accurate data.

Both the new MW-Perp and MW-Perp++ data also give PI estimates that are not statistically different from 36.2 μT ($p_{\mathrm{perp}} = 0.85$; $p_{\mathrm{perp++}} = 0.77$). All new data have intensity error fractions (IEFs) of less than 0.1, except for the new MW-Perp data from section 1, which was expected to have the highest IEF. The new MW-Perp data have IEFs within 0.01 of the data from Hill & Shaw (2000).

The addition of alteration checks in the MW-Perp++ and the data treatment in section 3.3 decrease the IEF of the MW-Perp data in section 1 by 0.08 and 0.11, respectively. These same techniques increase the IEF of the MW-Perp data in section 2 by 0.01 and 0.08, respectively but the new estimates are within uncertainties of the former ones. The low estimates produced by the MW-Perp experiments appears, therefore, to be the result of undetected alterations in the MW-Perp data, rather than a systematic error caused by the MW radiation.

The MW-Perp++ data lack the zigzagging (Yu & Tauxe 2005) of the MW-IZZI+ data, which sometimes allowed more Arai plot data points to be selected. In the case of section 1, selecting additional Arai plot data produced a lower average PI estimate, which mirrors the behaviour seen in the MW-Perp data. For the generally less linear Arai plots in section 2, the different data caused a large increase of dispersion in the PI estimates because different specimens passed the selection criteria.

4.3 Implications for similar experiments

When compared to other, thermal studies on this lava flow (e.g. Böhnel *et al.* 2011), some of the MW data in Hill & Shaw (2000) appeared to be biased low. The large differences in properties between sections 1 and 2 further obfuscated their results. Cromwell *et al.* (2018) note this pattern to hold true for all non-thermal Thellier PI experiments for the 0–2 ka age range. We also note, however, that thermal studies from different, often sparsely sampled, sections of the 1960 Kilauea lava flow generally gave PI estimates higher than the 36.5 μT field strength observed at the Honolulu Observatory, which probably indicates that the data were affected by exaggerated non-single domain behaviour.

We have demonstrated that MW-IZZI+ experiments can produce results that are highly distinctive from those produced by MW-Perp experiments. With the newest MW system's ability to run any Thellier-style experiment, and the protocol-dependent PI estimates extracted in this paper, MW data should not be combined into a single 'MW method' data set. The new MW Thellier-style results are still lower than those reported in Böhnel *et al.* (2011) and Cromwell *et al.* (2018), but they are not statistically different from the expected values for this lava flow. A direct thermal—microwave comparison is therefore needed in the future on sister specimens.

The lower estimates observed herein for specimens receiving an MW-Perp treatment, compared to MW Thellier-style experiments, are broadly in agreement with Biggin (2010). Biggin (2010), found the largest discrepancies between MW and thermal studies where the MW demagnetization mechanism was coupled with the perpendicular protocol, but the thermal demagnetization mechanism was coupled with a double-heating Thellier-style protocol (see table 2 in Biggin 2010). We have expanded on these results and shown here that low MW-Perp estimates can potentially be the result of both undetected alterations because the Perp protocol lacks pT_MRM checks as well as the enhanced non-SD behaviour that can be observed in double-heating protocols (Biggin 2010; Hodgson *et al.* 2018).

Whenever relevant rock magnetic data are sparse, our data suggest that the IZZI+ protocol is preferred, as it contains a built-in check for non-SD behaviour and uses pT_MRM checks. However, as demonstrated in section 2, IZZI+ data can be prone to slight overestimations, so IZZI+, by itself (without any rock magnetism or other independent data), may not always be sufficient for high accuracy PI surveys on older, less well-behaved specimens. Using the MW-IZZI+ data to reinterpret the MW-Perp data gave a PI estimate that was not statistically different from the expected value. The Perp protocol only requires a single treatment at each step, which increases experimental speed and reduces chances for alteration. If the Perpendicular protocol is used, the data set can then be corrected using sister IZZI+ experiments.

A multitechnique approach is favoured when selection criteria have to be more relaxed, due to, for example, the age of the specimens and resulting poorer quality of the Arai plot data. The data

herein have showed that running IZZI+ with a perpendicular applied magnetic field allows the data to be interpreted as Perp or Perp++ to have an implicit second protocol to check robustness.

If a multitechnique approach is not possible for technical reasons, then maximizing the number of PI estimates another way is paramount. Multiple sampling sites—to maximize flow coverage, as suggested by Biggin *et al.* (2007)—and reduced-size cores (5 mm diameter × 1–2 mm height, in our case for microwave specimens), if possible, increase the amount of heterogeneity between specimens. We have seen with these specimens that averaging all these helps approach the correct mean strength of the Earth's magnetic field if previously unrecognized heterogeneities exist.

5 CONCLUSIONS

The modern, 14 GHz Tristan MW system, using the IZZI+ protocol, has yielded PI estimates that are not statistically distinct from the expected values. With the addition of pT_MRM checks, we have shown that undetected alterations are a primary cause of the lower estimates observed in the MW-Perp data, not a bias resulting from MW radiation or the older system. The MW-IZZI+ protocol has also showed that there is some non-single domain behaviour present in the data. Since the observed alteration mandates using lower 'temperature' (power integral) portions of (subtly) concave Arai plots, some of the PI data appear to be overestimated and often created large Arai plot data point scatter in the MW-Perp and MW-IZZI+ estimates. In addition, we have found that MW-IZZI+ and MW-Perp (with pT_MRM checks) are reliable protocols in samples with thermochemical alterations because their pT_MRM checks detect and therefore help mitigate the resulting effect on PI estimates. This non-ideal behaviour appears to be the primary cause of the high estimates and alterations appear to be the primary cause of the lower estimates. Our data herein, therefore, confirm the ability of the MW system to extract accurate PI estimates from samplings that exhibit thermochemical alterations and non-ideal behaviour. The data further demonstrate the utility of both a flexible IZZI protocol and a multiprotocol approach that can be applied to gather large and accurate data sets quickly from basalts that yield fewer ideal data.

ACKNOWLEDGEMENTS

This study was led by JMG as a portion of a University of Liverpool match-funded studentship, supported by the Duncan Norman Research Scholarship. JMG further acknowledges support from the NERC EAO Doctoral Training Partnership, grant NE/L002469/1 and NERC studentship 1793213. AJB acknowledges support from NERC standard grant NE/P00170X/1 and Leverhulme Research Leadership Award RL-2016-080. JMG thanks Louise Hawkins and the Institute for Rock Magnetism at the University of Minnesota for the use of their facilities to gather FORC data. MJH acknowledges the assistance of John Shaw, Emilio Herrero-Bevera and Don Tarling with the original collection of the examined lava samples. New raw data collected as part of this study will be available on MagIC at earthref.org/MagIC/16586.

REFERENCES

Biggin, A.J., 2010. Are systematic differences between thermal and microwave Thellier-type palaeointensity estimates a consequence of multidomain bias in the thermal results? *Phys. Earth planet. Inter.,* **180**(1–2), 16–40.

Biggin, A.J., Bohnel, H.N. & Zuniga, F.R., 2003. How many paleointensity determinations are required from a single lava flow to constitute a reliable average? *Geophys. Res. Lett.,* **30**(11).

Biggin, A.J., Perrin, M. & Dekkers, M.J., 2007. A reliable absolute palaeointensity determination obtained from a non-ideal recorder, *Earth planet. Sci. Lett.,* **257**(3–4), 545–563.

Biggin, A.J., Badejo, S., Hodgson, E., Muxworthy, A.R., Shaw, J. & Dekkers, M.J., 2013. The effect of cooling rate on the intensity of thermoremanent magnetization (TRM) acquired by assemblages of pseudo-single domain, multidomain and interacting single-domain grains, *Geophys. J. Int.,* **193**(3), 1239–1249.

Böhnel, H., Herrero-Bervera, E. & Dekkers, M.J., 2011, Paleointensities of the Hawaii 1955 and 1960 lava flows: further validation of the multispecimen method, in *The Earth's Magnetic Interior,* pp. 195–211, eds Petrovský, E., Ivers, D., Harinarayana, T. & Herrero-Bervera, E., Springer.

Bono, R.K., Tarduno, J.A., Nimmo, F. & Cottrell, R.D., 2019. Young inner core inferred from Ediacaran ultra-low geomagnetic field intensity, *Nat. Geosci.,* **12**(2), 143–147.

Coe, R.S. & Gromme, C.S., 1973. Comparison of 3 methods of determining geomagnetic paleointensities, *J. Geomagn. Geoelectr.,* **25**(4), 415–435.

Cromwell, G., Tauxe, L., Staudigel, H. & Ron, H., 2015. Paleointensity estimates from historic and modern Hawaiian lava flows using glassy basalt as a primary source material, *Phys. Earth planet. Inter.,* **241,** 44–56.

Cromwell, G., Trusdell, F., Tauxe, L., Staudigel, H. & Ron, H., 2018. Holocene paleointensity of the island of Hawai'i from glassy volcanics, *Geochem. Geophys. Geosyst.,* **19,** 3224–3245.

Donadini, F., Riisager, P., Korhonen, K., Kahma, K., Pesonen, L. & Snowball, I., 2007. Holocene geomagnetic paleointensities: a blind test of absolute paleointensity techniques and materials, *Phys. Earth planet. Inter.,* **161**(1–2), 19–35.

Dunlop, D.J. & Ozdemir, O., 2001. Beyond Neel's theories: thermal demagnetization of narrow-band partial thermoremanent magnetizations, *Phys. Earth planet. Inter.,* **126**(1–2), 43–57.

Ferk, A., Leonhardt, R., Hess, K.U., Koch, S., Egli, R., Krasa, D. & Dingwell, D.B., 2014. Influence of cooling rate on thermoremanence of magnetite grains: identifying the role of different magnetic domain states, *J. geophys. Res.,* **119**(3), 1599–1606.

Herrero-Bervera, E. & Valet, J.P., 2009. Testing determinations of absolute paleointensity from the 1955 and 1960 Hawaiian flows, *Earth planet. Sci. Lett.,* **287**(3–4), 420–433.

Hill, M.J. & Shaw, J., 2000. Magnetic field intensity study of the 1960 Kilauea lava flow, Hawaii, using the microwave palaeointensity technique, *Geophys. J. Int.,* **142**(2), 487–504.

Hill, M.J. & Shaw, J., 2007. The use of the 'Kono perpendicular applied field method' in microwave palaeointensity experiments, *Earth Planets Space,* **59**(7), 711–716.

Hill, M.J., Pan, Y.X. & Davies, C.J., 2008. An assessment of the reliability of palaeointensity results obtained from the Cretaceous aged Suhongtu section, Inner Mongolia, China, *Phys. Earth planet. Inter.,* **169**(1–4), 76–88.

Hodgson, E., Grappone, J.M., Biggin, A.J., Hill, M.J. & Dekkers, M.J., 2018. Thermoremanent behavior in synthetic samples containing natural oxyexsolved titanomagnetite, *Geochem. Geophys. Geosyst.,* **19**(6), 1751–1766.

Jackson, A., Jonkers, A.R.T. & Walker, M.R., 2000. Four centuries of geomagnetic secular variation from historical records, *Phil. Trans. R. Soc. Lond., A,* **358**(1768), 957–990.

Kono, M. & Ueno, N., 1977. Paleointensity determination by a modified Thellier method, *Phys. Earth planet. Inter.,* **13**(4), 305–314.

Levi, S., 1977. Effect of magnetite particle-size on paleointensity determinations of geomagnetic-field, *Phys. Earth planet. Inter.,* **13**(4), 245–259.

Nagata, T., Momose, K. & Arai, Y., 1963. Secular variation of geomagnetic total force during last 5000 years, *J. geophys. Res.,* **68**(18), 5277–5281.

Paterson, G.A., Biggin, A.J., Yamamoto, Y. & Pan, Y., 2012. Towards the robust selection of Thellier-type paleointensity data: the influence of experimental noise, *Geochem. Geophys. Geosyst.,* **13**(5), doi:10.1029/2012GC004046.

Paterson, G.A., Biggin, A.J., Hodgson, E. & Hill, M.J., 2015. Thellier-type paleointensity data from multidomain specimens, *Phys. Earth planet. Inter.,* **245,** 117–133.

Santos, C.N. & Tauxe, L., 2019. Investigating the accuracy, precision, and cooling rate dependence of laboratory-acquired thermal remanences during paleointensity experiments, *Geochem. Geophys. Geosyst.,* **20**(1), 383–397.

Shaar, R., Ron, N., Tauxe, L., Kessel, R. & Agnon, A., 2011. Paleomagnetic field intensity derived from non-SD: testing the Thellier IZZI technique on MD slag and a new bootstrap procedure, *Earth planet. Sci. Lett.,* **310**(3–4), 213–224.

Shcherbakov, V.P. & Shcherbakova, V.V., 2001. On the suitability of the Thellier method of palaeointensity determinations on pseudo-single-domain and multidomain grains, *Geophys. J. Int.,* **146**(1), 20–30.

Tanaka, H. & Kono, M., 1991. Preliminary-results and reliability of paleointensity studies on historical and C-14 dated Hawaiian lavas, *J. Geomagn. Geoelectr.,* **43**(5), 375–388.

Thebault, E. *et al.*, 2015. International geomagnetic reference field: the 12th generation, *Earth Planets Space,* **67,** 19, doi:10.1186/s40623-015-0228-9.

Yamamoto, Y., Tsunakawa, H. & Shibuya, H., 2003. Palaeointensity study of the Hawaiian 1960 lava: implications for possible causes of erroneously high intensities, *Geophys. J. Int.,* **153**(1), 263–276.

Yu, Y., 2011. Importance of cooling rate dependence of thermoremanence in paleointensity determination, *J. geophys. Res.,* **116,** doi:10.1029/2011JB008388.

Yu, Y.J. & Tauxe, L., 2005. Testing the IZZI protocol of geomagnetic field intensity determination, *Geochem. Geophys. Geosyst.,* **6,** doi:10.1029/2004GC000840.

Yu, Y.J., Tauxe, L. & Genevey, A., 2004. Toward an optimal geomagnetic field intensity determination technique, *Geochem. Geophys. Geosyst.,* **5,** 18.

SUPPORTING INFORMATION

Supplementary data are available at *GJI* online.

Figure A1. FORC diagrams for two specimens from section 1: (a) H6001–04A and (b) H6001–09D. Sister specimens of these gave lower than expected PI estimates from Arai plots with some pT_MRM check failures, so they appear to be characteristic of the specimens tested.

Table B1. MW-IZZI+
Table B2. MW-Perp++
Table B3. MW-Perp
Table B4. MW-Perp(using MW-IZZI+ pTmRM)
Table B5. MW-derPerp
Table B6. MW-derPerp++

Please note: Oxford University Press is not responsible for the content or functionality of any supporting materials supplied by the authors. Any queries (other than missing material) should be directed to the corresponding author for the paper.

JGR Solid Earth

RESEARCH ARTICLE
10.1029/2020JB019802

Key Points:
- Causes for significant inconsistencies in important paleointensity records over the 0–45 ka time period in Hawaii are investigated
- Disagreement is related to both the different demagnetization mechanisms and paleointensity protocols employed
- Both previous records are likely biased with the true values expected to lie intermediate between them

Supporting Information:
- Supporting Information S1

Correspondence to:
J. M. Grappone,
grappone@liverpool.ac.uk

Citation:
Grappone, J. M., Biggin, A. J., Barrett, T. J., Hill, M. J., & Sprain, C. J. (2020). Comparison of thermal and microwave paleointensity estimates in specimens displaying non-ideal behavior in Thellier-style paleointensity experiments. *Journal of Geophysical Research: Solid Earth*, *125*, e2020JB019802. https://doi.org/10.1029/2020JB019802

Received 18 MAR 2020
Accepted 2 JUL 2020
Accepted article online 7 JUL 2020

Comparison of Thermal and Microwave Paleointensity Estimates in Specimens Displaying Non-Ideal Behavior in Thellier-Style Paleointensity Experiments

J. Michael Grappone[1], Andrew J. Biggin[1], Thomas J. Barrett[1,2], Mimi J. Hill[1], and Courtney J. Sprain[1,3]

[1]Geomagnetism Laboratory, School of Environmental Sciences, University of Liverpool, Liverpool, UK, [2]School of Physical Sciences, The Open University, Milton Keynes, UK, [3]Department of Geological Sciences, The University of Florida, Gainesville, FL, USA

Abstract Determining the strength of the ancient geomagnetic field is vital to our understanding of the core and geodynamo, but obtaining reliable measurements of the paleointensity is fraught with difficulties. Over a quarter of magnetic field strength estimates within the global paleointensity database from 0 to 5 Ma come from Hawaii. Two previous studies on the SOH1 drill core gave inconsistent, apparently method-dependent paleointensity estimates, with an average difference of 30%. The paleointensity methods employed in the two studies differed both in demagnetization mechanism (thermal or microwave radiation) and Thellier-style protocol (perpendicular and original Thellier protocols)—both variables that could cause the strong differences in the estimates obtained. Paleointensity experiments have therefore been conducted on 79 specimens using the previously untested combinations of thermal-perpendicular and microwave-original Thellier methods to analyze the effects of demagnetization mechanism and protocol in isolation. We find that, individually, neither demagnetization mechanism nor protocol entirely explains the differences in paleointensity estimates. Specifically, we found that non-ideal multidomain-like effects are enhanced using the original Thellier protocol (independent of demagnetization mechanism), often resulting in paleointensity overestimation. However, we also find evidence, supporting recent findings from the 1960 Kilauea lava flow, that microwave-perpendicular experiments performed without partial thermal remanent magnetization checks can produce underestimates of the paleointensity due to unaccounted-for sample alteration at higher microwave powers. Together, these findings support that the true paleointensities fall between the estimates previously published and emphasize the need for future studies (thermal or microwave) to use protocols with both partial thermal remanent magnetization checks and a means of detecting non-ideal grain effects.

1. Motivation

The Pacific Ocean covers 30% of the Earth's surface but has few islands, with the Hawaiian Islands being some of the most easily accessed. Volcanic islands, like Hawaii, contain some of the best records of the temporal variation in Earth's magnetic field over the last few million years. Paleosecular variation timescales of this length are necessary to better understand long-term variations in geomagnetic behavior, as well as crust, mantle, and core interactions (e.g., McElhinny & Merrill, 1975). Accurate paleointensity (PI) data in the 0–5 Ma period are crucial because only in this interval is there enough spatial and temporal global coverage of data to characterize long-term (million years) variations. In order to obtain accurate PI data, an appropriate PI method for the mineral magnetic characteristics of any particular site must be used.

Many paleomagnetic studies over the last 60 years (e.g., Coe et al., 1978; Cromwell et al., 2018; de Groot et al., 2013; Doell & Cox, 1963, 1965; Teanby et al., 2002) have found the Hawaiian Islands ideal for studying magnetic field variations in the central Pacific Ocean over the past hundred to few million years. Hawaiian absolute PIs have substantial temporal coverage and comprise 28% of the global PI (PINT) database in this interval (Biggin et al., 2015) and are therefore important to study to understand long-term field behavior over this time interval. Numerous studies have taken advantage of the drill core from the Scientific Observation Hole (SOH) and Hawaii Scientific Drilling Project (HSDP) to extract the required PI data over the last 45 kyr

(e.g., Cai et al., 2017; Gratton et al., 2005; Teanby et al., 2002), but the data have proven to be inconsistent and thus of potentially limited use.

The paleomagnetism of the SOH1 core was studied twice previously—once by Teanby et al. (2002) using thermal PI experiments and again by Gratton et al. (2005) using microwave (MW) PI experiments and a different PI protocol. Teanby et al. (2002) and Gratton et al. (2005) each sampled the core independently and extracted PIs from 83 common flows. Teanby et al. (2002) additionally reported a new inclination record and dated the flows from 0 to 45 ka. The mean PIs reported by the two studies, 33.5 (Teanby et al., 2002) and 25.1 μT (Gratton et al., 2005), differ by approximately 33%. Both studies reported mean uncertainty estimates of approximately 10%, which implies the possibility for a resolvable difference between them.

At this stage, it is useful to introduce our nomenclature that a given PI "method" is composed of a combination of a specific "demagnetization mechanism" and a specific "protocol." Teanby et al. (2002) used the conventional thermal demagnetization mechanism paired with the original Thellier (OT) protocol (Thellier & Thellier, 1959), while Gratton et al. (2005) used the MW demagnetization mechanism paired (predominantly) with the perpendicular (Perp) protocol (Kono & Ueno, 1977). A third study, by Laj et al. (2011), used the raw data from Teanby et al. (2002) (reanalyzed with their updated selection criteria to give an SOH1 average of 29.7 μT) combined with additional (non-SOH1) data (acquired using the same method) from the SOH4 and HSDP1 drill cores, which cover additional flows, to create a more complete and statistically rigorous Hawaiian PI record. Even after the Laj et al. (2011) reassessment, there remains nearly a 20% discrepancy between the thermal mechanism OT protocol and the MW mechanism Perp protocol results.

To investigate discrepancies between PI results obtained using different demagnetization mechanisms (i.e., thermal and MW), a meta-analysis of 13 paired studies (including that of the SOH1 drill core) was undertaken by Biggin (2010). It is important to note that the studies assessed in the Biggin (2010) analysis differed not only in demagnetization mechanism but also in protocol. Biggin (2010) concluded, first, that systematic differences existed between PI estimates derived from thermal and MW experiments performed on the same rocks, with the former tending to be significantly higher than the latter (at the 95% confidence level). We carried out a further analysis (available in Supporting Information A), which showed this as well at the flow level. Second, Biggin (2010) suggested that the most plausible explanation for the bulk of these discrepancies resided in unrecognized biasing from multidomain-like effects being more prevalent in the thermal results. Importantly, it was suggested that the discrepancies were more or less entirely due to the difference in the *protocols* used rather than in the *demagnetization mechanism*. With respect to the SOH1 case, Biggin (2010) hypothesized that the thermal results being higher than the MW results was likely unrelated to the choice of thermal or MW energy for demagnetization. Rather, the discrepancy was due to Teanby et al. (2002) employing the OT protocol while Gratton et al. (2005) employed the Perp protocol.

Since our initial flow-level analysis of the SOH1 data confirmed the results of Biggin (2010), the aim of the present study is to test the hypothesis that the differences found in PI results from the SOH1 core are entirely due to protocol and not due to demagnetization mechanism. We hypothesize that if the demagnetization mechanism-protocol pairs are reversed, such that MW demagnetization is paired with the OT protocol and thermal demagnetization is paired with the Perp protocol, then the sense of the discrepancy between the MW and thermal results should reverse such that the former should give higher estimates than the latter. This study will explicitly test this hypothesis using new experiments performed on 24 of the same SOH1 flows as studied originally by both Teanby et al. (2002) and Gratton et al. (2005).

The results of this study are important on several levels. First, they provide improved insight into the strength of the magnetic field at the time of emplacement of the 241 flows sampled by the SOH1 drill core data set. Second, they have implications for how the swathes of PI estimates obtained by similar methods from rocks elsewhere in the world should be interpreted. As such, they expand the results of a recent restudy of the 1960 Kilauea lava flow by Grappone et al. (2019) to more Hawaiian lava flows. Lastly, they can provide guidance on how future PI experiments should be performed and analyzed in order to maximize their reliability.

2. Drill Core Geology and Sampling

The samples used in this study are from the SOH1 drill core, which was drilled from the Kilauea volcano on Hawaii Island between 1989 and 1991 at 19°29′N, 154°54′W, to a total depth of 1,685 m. The Hawaii Institute

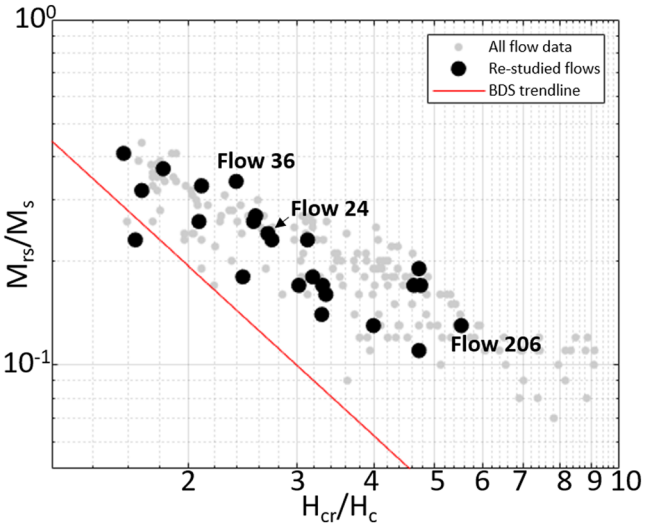

Figure 1. Hysteresis parameters plot for all the flows in the SOH1 borehole (as studied by Gratton et al., 2005), highlighting which flows were studied herein for new PI estimates. M_{rs}/M_s refers to the ratio of remanent saturation magnetization to the saturation magnetization and H_{CR}/H_C refers to the ratio of coercivity of remanence to coercivity. The bulk domain stability trendline derives from the results of Paterson et al. (2017). The three named flows have new PI estimates, as well as first-order reversal curves (FORCs) and scanning electron microscopy (SEM) analysis in Supporting Information B.

of Geophysics and Planetology and the Hawaii Natural Energy Institute drilled the borehole to assess the viability of using geothermal energy in the area (Quane et al., 2000). The core consists primarily of a′a (~66%) and pahoehoe (~22%) lavas from 241 aerial, subaerial, and submarine flows with thicknesses varying from 0.3 to 17.4 m (Gratton et al., 2005; Teanby et al., 2002). The remaining ~11% of the core consists of dyke intrusions. Samples were taken from 196 lava flows from the upper 779 m of the core to avoid the increasing number of dyke intrusions and apparent alteration at greater depths (Gratton et al., 2005). This portion of the core has been modeled with an age range of 0–45 ka (Teanby et al., 2002).

The portions of each drilled 2.5-cm diameter core that were saved by Gratton et al. (2005) from their SOH1 study were retrieved from the University of Liverpool archive and subsequently used in this study. We cut 120 new specimens for the restudy from the material remaining from 24 flows that span the range of flows sampled in Gratton et al. (2005). Although the specimens used in this study are sister specimens from Gratton et al. (2005), we cannot rule out the possibility that the flows may be inhomogeneous even on a centimeter scale. Flows were selected based on the degree of disagreement in PI estimates between the Gratton et al. (2005) and Teanby et al. (2002) studies, number of samples previously studied, and the availability of specimens. For the flows selected for this study, the Teanby et al. (2002) PI estimates, at the flow level, ranged from 21% lower to 53% higher (with a mean of 27% higher) than the Gratton et al. (2005) estimates.

3. Rock Magnetism

Gratton et al. (2005) undertook an extensive survey of the hysteresis loop parameters of the SOH1 borehole. The raw data from their rock magnetic survey were reanalyzed here using *HystLab's* automatic hysteresis loop processing program (Paterson et al., 2018) and are replotted in Figure 1, with the flows investigated herein highlighted. The bulk domain stability (BDS) trendline from Paterson et al. (2017) lies below the main sequence of hysteresis loop parameters for SOH1 flows, which indicates that the data have a mixture of magnetic domain types, potentially also including superparamagnetic grains. The specimens used in this study sample the main sequence of SOH1 data observed in Figure 1. The ratio of magnetic remanence to saturation magnetization (M_{rs}/M_s) values of the main sequence of SOH1 data lie consistently above the values that would be expected for multidomain grains of magnetite ($M_{rs}/M_s > 0.1$), which implies the presence of single domain and non-single domain grains. Gratton et al. (2005) also determined thermomagnetic behavior for all the flows in their study. They found highly reversible thermomagnetic curves with 98% of Curie temperatures falling in the range from 520°C to 600°C, with a mean of 561°C and median of 570°C. Twenty-two percent of flows also contained a secondary ferrimagnetic phase with Curie temperatures below 340°C.

The hysteresis and thermomagnetic parameters are typical of low-Ti magnetite-rich basaltic lavas found on Hawaii, and these have been the focus of other Hawaiian PI surveys (e.g., Cai et al., 2017; Cromwell et al., 2018; Hill & Shaw, 2000). Additional, new rock magnetic information (first-order reversal curve [FORC] and scanning electron microscopy [SEM] analysis) from the main sequence can be found in Supporting Information B.

4. Methods

All new thermal tests were carried out in air using a Magnetic Measurements MMTD-80 thermal demagnetizer, and specimens were cooled quickly using a built-in cooling fan. The specimens were then measured on the University of Liverpool Geomagnetism Laboratory's 2G SQUID Magnetometer and RAPID system. All MW tests were run on the 14-GHz Tristan Microwave System (Hill et al., 2008), also at the University of

Liverpool. The goal of this study was to replicate the experimental conditions of the previous studies as closely as possible to properly isolate each variable of interest.

In the OT protocol (Thellier & Thellier, 1959), each specimen is heated to a given temperature, T_N, in a known, non-zero intensity magnetic field and then cooled to room temperature and measured. The polarity of the magnetic field is then reversed, and the sample is taken to T_N again. The protocol can also be referred to as infield-infield, or "II." The process is then repeated at T_{N+1}. Partial thermal remanent magnetization (pTRM) checks were included after every second step (i.e., from T_{N+1} to T_{N-1}). For consistency with the PINT database (Biggin et al., 2009), when used with thermal energy, this protocol (with pTRM checks) will be referred to as Th-OT+, to acknowledge the pTRM check addition. The MW variant of the OT protocol simply replaces the heat with MW power integrals and will be referred to as MW-OT+. We used powers ranging from 5 to 40 W in 3 to 5 W steps, applied for 5 to 15 s and assumed that any power not reflected was absorbed by the specimen-cavity coupled system. For MW-OT+, we used a steady magnetic field applied parallel/antiparallel to the natural remanent magnetization (NRM), which Biggin (2010) predicted to be the least affected by non-ideal Arai plot behavior. For Th-OT+, we used an applied field with an inclination of ±90° in specimen coordinates.

The Perp protocol is a modification of the OT protocol that only requires a single thermal or MW treatment (Kono & Ueno, 1977). Samples first get stepwise demagnetized in a zero field to remove any soft magnetic overprints. Once the primary component of magnetization is identified as beginning at some T_P, the sample is then heated to T_{P+1} in a magnetic field applied in the direction perpendicular to the characteristic component (the remaining NRM). The process is then repeated for T_{P+2} and higher. Gratton et al. (2005) determined that many samples had a second ferrimagnetic phase with an unblocking temperature around 300°C, which they interpreted to be the result of oxyexsolution into Ti-rich and Ti-poor lamellae during extrusion. Therefore, samples undergoing Th-Perp were first stepwise demagnetized in 40–50°C steps from 100°C to 300–340°C to ensure that the perpendicular field was applied only to the high-temperature ferrimagnetic phase. After successfully finding the characteristic direction, the field in the oven was switched on. The steps continued to 590°C in 10–30°C increments. The process is the same using the MW system (MW-Perp), but with power integral steps instead of temperature steps until a consistent magnetic direction is obtained (Hill & Shaw, 2007). We did not include any pTRM checks in our new Perp experiments in order to replicate the methods used by Gratton et al. (2005). All data were analyzed using the methods described in Hill and Shaw (2007).

Laboratory field strengths were selected that were as close to the original analyses as possible. All experiments in Teanby et al. (2002) were carried out using an applied field of 40 μT, as were the new MW-OT+ experiments completed herein. MW studies are carried out one sample at a time, so the field strength often varied specimen to specimen within a flow in Gratton et al. (2005). For the specimens we selected, the mean applied field used in Gratton et al. (2005) for MW treatments was 31 ± 1.3 μT, so we used a field of 31 μT in our Th-Perp experiments.

A summary of the experiments carried out in this study is given in Table 1. We ran 79 specimens using either MW-OT+ or Th-Perp. Additionally, 19 specimens were tested using Th-OT+ and 22 were tested using MW-Perp, replicating the original studies in order to confirm the previous results. The median number of specimens tested from each of the 24 flows we examined was 3, with a range of 1–11.

Our selection criteria are based on the MC-CRIT.C1 selection criteria, without tail checks, from Paterson et al. (2015). These were also used successfully by Grappone et al. (2019) to study the 1960 Kilauea lava flow. We relaxed the FRAC/f criterion (Shaar & Tauxe, 2013) (a measure of the proportion of the NRM used to determine the result) from 0.45 (used in Grappone et al., 2019) to 0.35 because of extensive alteration observed at higher temperatures/power integrals and because of difficulties in demagnetizing the specimens using MWs. Relaxing this criterion yielded seven additional specimen-level estimates most notably from MW-Perp experiments, without changing any flow-level estimates in a statistically significant manner. The selection criteria are detailed in Table 2.

For our analysis, we use two statistical tests: the *t*-test and the Wilcoxon signed rank test (see, e.g., Klugh, 1986). For the study-level data, which are normally distributed (see the failure to reject the null hypothesis in Kolmogorov-Smirnov test in Supporting Information A), we use a two-sample, unpaired *t*-

Table 1
Summary Information of New Experiments Carried Out in This Study

Method	Number of specimens	Number of accepted estimates	Success rate (%)	Lab field (μT)
Microwave-OT+	48	33	69	40
Microwave-Perp	22	13	59	25–50
Thermal-OT+	19	10	52	40
Thermal-Perp	31	17	55	31
Total	120	73	61	25–50

Note. Number of specimens run for each method is given along with the number of specimens that gave acceptable results (number of passes) and the associated success rate. The final column gives the applied lab fields used during the experiment for each method.

test to test if the method-level means are equal. A paired difference test is more appropriate for the flow-level data, which have flow-level data pairings. The paired data do not visually appear to be normally distributed (a weak assumption required for a paired *t*-test), so we should choose a non-parametric test. Biggin (2010) used the Wilcoxon signed rank test in their analysis of the SOH1 data set, so for consistency, we also use that for flow-level data.

5. Paleomagnetic Results and Analysis

5.1. New Data

A summary of all experiments run herein is given in Supporting Information C, and these new experiments are described in this subsection. PI estimates that passed the selection criteria were obtained from experiments performed on 73 specimens from 20 flows. A pass rate of >50% at the specimen level was achieved for every experimental method tested. The most common reason for failure of the new MW-Perp and MW-OT+ experiments was low FRAC/f, as the MW often could not fully demagnetize each specimen. The most common reason for failure for the new Th-OT+ experiments was high DRAT (i.e., pTRM check failures), and for Th-Perp, it was high scatter around the best fit line (β). The only clear difference in Arai plot shape observed between the different methods is that the new Th-OT+ data often show two slopes where for some specimens, both slopes passed the selection criteria. In these cases, the low-temperature slope was selected, as they had the higher FRAC. These new Th-OT+ data additionally show the highest mean curvature values (as defined by $|\vec{K}'|$) at 0.30, compared with those of the Th-Perp (0.22), MW-OT+ (0.21), or MW-Perp (0.093). All new measurement data can be found on the MagIC database. Examples of passed MW-OT+ and Th-Perp data can be found in Figures 2a.ii, 2a.iii, 2b.ii, 2b.iii, 2c.ii, and 2c.iii. Examples of passed Th-OT+ and MW-Perp data can be found in Supporting Information C.

Flow mean results are detailed by PI method in Supporting Information C. The new Th-OT+ and MW-OT+ flow-level mean PI estimates tend to yield higher values with 44.0 ± 16 μT across five flows and 29.5 ± 9.2 μT, across 19 flows, respectively. New Th-Perp and MW-Perp experiments tend to yield lower mean PI estimates with estimates of 27.8 ± 8.1 μT, across 11 flows, and 18.5 ± 10 μT, across five flows, respectively. If we assume that our new PI estimates are normally distributed, which is noted (see Supporting Information A), we can use a two-sample *t*-test to determine whether observed differences between experiments are statistically significant. From the new data, the Th-OT+ mean estimate (44.0 μT) is higher than the MW-OT+ mean (29.5 μT), the Th-Perp mean (27.8 μT), and the MW-Perp mean (18.5 μT), at the 95% confidence level, with p values of 0.0147, 0.0176, and 0.0001, respectively. The new data's Th-Perp mean estimate is not statistically distinct from the new data's MW-OT+ mean estimate at the 95% confidence level ($p = 0.62$). The new data's MW-Perp flow-level mean PI estimate of 18.5 μT is lower than the new data's MW-OT+ mean estimate at the 95% confidence level, with a p value of 0.0015. The new data's Th-Perp and MW-Perp estimates are not statistically different at the 95% confidence interval, with a p value of 0.0676.

Table 2
Selection Criteria

N	FRAC/f[a]	β	q	$\lvert\vec{K}'\rvert$	MAD_{ANC}[b]	α[b]	DRAT[b]	$\Delta\theta$[c]
≥4	≥0.35	≤0.1	≥1	≤0.480	≤10	≤10	≤10%	≤1°

Note. N is the number of data points, FRAC/f are measures of the NRM used, β is a measure of scatter around the best fit line, q is a measure of the data quality, $|\vec{K}'|$ is a measure of Arai plot curvature, and MAD and α determine the scatter of the specimen's paleodirection. $\Delta\theta$ is the change in the $\theta_1 + \theta_2$ value, an indication of the perpendicularity between the NRM and TRM directions (Hill & Shaw, 2007) for the perpendicular experiment. For further details, the reader is referred to Paterson et al. (2015).
[a]FRAC is used for OT+ experiments and f for Perp experiments. [b]OT+ techniques use these criteria, but Perp does not, for technical reasons. [c]Used only for Perp experiments.

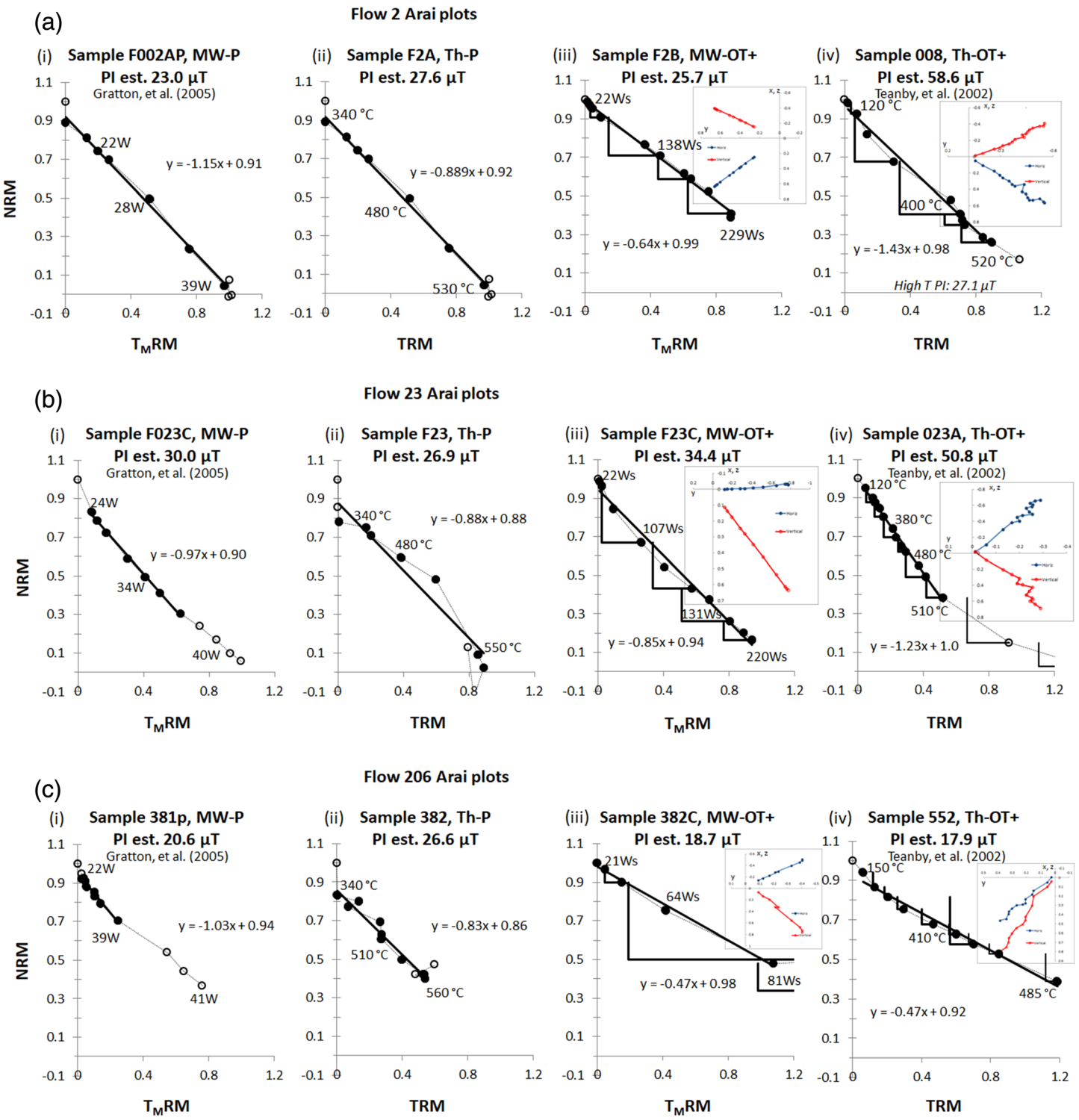

Figure 2. Normalized Arai plot examples comparing the different methods used. (a) Flow 2 (503-cm thickness), (b) Flow 23 (137-cm thickness), and (c) Flow 206 (290-cm thickness). The data are normalized by NRM_0. The filled circles are accepted data points, with the solid black line being the best fit line. Open circles are rejected data points. The black right angle lines are $pT_{(M)}RM$ checks, which are only present in OT+ data. Orthogonal vector plots are provided in core coordinates for the OT+ data. All specimens presented pass their original study's selection criteria. The microwave data are visually more linear than the thermal data, and the OT+ data are often two-sloped. The powers given for the Gratton et al. (2005) MW data are power applied and the power integrals given in the new data are (inferred) energy absorbed.

Table 3
Paleointensity Results, Broken Down by Flow and Method for the Combined Data Set, Consisting of New Data, Data From Teanby et al. (2002), and Data From Gratton et al. (2005)

Flow	Th-OT+ (μT)	N_{pass}/N_{tested}	MW-OT+ (μT)	N_{pass}/N_{tested}	Th-Perp (μT)	N_{pass}/N_{tested}	MW-Perp (μT)	N_{pass}/N_{tested}
2	58.6	1/2	22.5 ± 4.7	2/2	29.4 ± 5.1	3/3	21.3 ± 2.0	4/4
6	50.4 ± 4.5	2/3	45.1 ± 2.8	2/2			36.5 ± 0.6	3/3
7		0/1			39.2	1/1	35.8 ± 1.6	4/4
8	59.0 ± 3.2	3/3	43.7 ± 4.9	2/2		0/1	36.5 ± 5.9	8/10
22		0/1	37.2 ± 2.6	3/3	26.3	1/2	21.3 ± 9.5	2/2
23	51.4 ± 0.9	2/2	36.7 ± 2.2	3/5	27.7 ± 0.1	2/2	28.8 ± 1.0	2/2
24			25.9	1/2		0/2	18.5 ± 4.1	2/4
26		0/1	32.5	1/2	21.2	1/3	33.1 ± 2.0	5/5
36		0/1	32.7	1/1		0/1	34.8 ± 2.8	2/2
37	54.2 ± 6.0	4/5	33.4 ± 1.6	2/2			24.8 ± 6.0	3/4
48			29.4 ± 3.4	2/2	26.4 ± 4.1	3/3	28.0 ± 0.5	2/2
87	32.2 ± 2.3	2/4		0/1			14.6 ± 1.9	4/4
91	23.8 ± 0.8	2/3		0/1			11.8 ± 0.9	4/4
163	45.9 ± 11	3/3	25.7 ± 1.5	2/3			18.6	1/3
176	26.3 ± 13	3/4				0/1		
186	25.1 ± 4.0	2/6				0/1	18.2 ± 2.6	2/2
189	27.7 ± 0.2	2/3	22.1	1/1	25.6	1/1	19.8 ± 1.0	2/2
193	31.7	1/2	18.5	1/1		0/1	15.0 ± 0.1	2/3
196	24.7 ± 1.3	2/2	15	1/1			12.6	1/3
206	40.1 ± 29	2/5	18.7	1/3	26.2	1/1		0/3
220	46.4 ± 7.9	4/6	37.2 ± 6.1	2/3	33.8	1/1	26.0 ± 4.7	7/12
221	40.9 ± 2.1	3/3	36.7	1/4	39.5 ± 2.8	2/4	31.4 ± 2.8	4/5
222	39.8 ± 3.3	3/3	33.7	1/2		0/1	37.8 ± 1.6	3/3
237	25.5 ± 8.2	3/9	14.3 ± 8.5	4/5	10.4	1/2	19.1 ± 0.2	2/4
Mean	39.0 ± 12	18/22	29.5 ± 9.2	19/21	27.8 ± 8.1	11/18	24.8 ± 8.5	22/23

Note. N_{pass} is the combined number of specimens that passed the PI selection criteria. N_{tested} is the combined number of specimens that were tested from a given flow with a given method. Empty cells indicate that no experiments were attempted because of a lack of material. For the mean row, N_{pass} and N_{tested} reference the number of flows.

5.2. Incorporation of Existing Data Sets

The new Th-OT+ results reported here are broadly consistent with their original counterparts reported by Teanby et al. (2002) and Laj et al. (2011). Both have the same two-slope (concave up) behavior (see Figure 2 for Teanby et al., 2002, results and Supporting Information C for a direct comparison). When considering only the four flows tested in both the present study and by Teanby et al. (2002), the mean PI values (43.5 ± 19 and 30.8 ± 14 μT) have overlapping uncertainty bounds and are not statistically distinct from each other at the 95% confidence level ($p = 0.3232$).

The new MW-Perp data reported here also broadly replicate the lower estimates reported by Gratton et al. (2005). The Arai plots appear single sloped (see Figure 2 for Gratton et al., 2005, results and Supporting Information C for a direct comparison) and the mean PI values for the nine flows tested here and in Gratton et al. (2005) are 18.2 ± 10 and 18.6 ± 9.8 μT, respectively. These mean values are not statistically distinct at the 95% confidence level ($p = 0.9462$). This result supports Grappone et al.'s (2019) finding that the different generations of the MW systems give equivalent results.

The consistency of our newly obtained results with those from the previous studies enables us to conclude that we may reasonably combine our new Th-OT+ data with the Teanby et al. (2002) data and our new MW-Perp data with the Gratton et al. (2005) data. All the data are therefore combined to create one data set which forms the basis for discussion in the following section. The combined SOH1 data set, consisting of data from this study, Teanby et al. (2002), and Gratton et al. (2005), is summarized in Table 3.

5.3. Analysis of Combined Data Set

Figures 3–5 display a series of one-to-one comparisons of the PI data produced by different methods at the flow level, utilizing data from the combined data set, which allows the influence of demagnetization technique and PI protocol to be scrutinized. From visual inspection, the data do not appear to be symmetrically

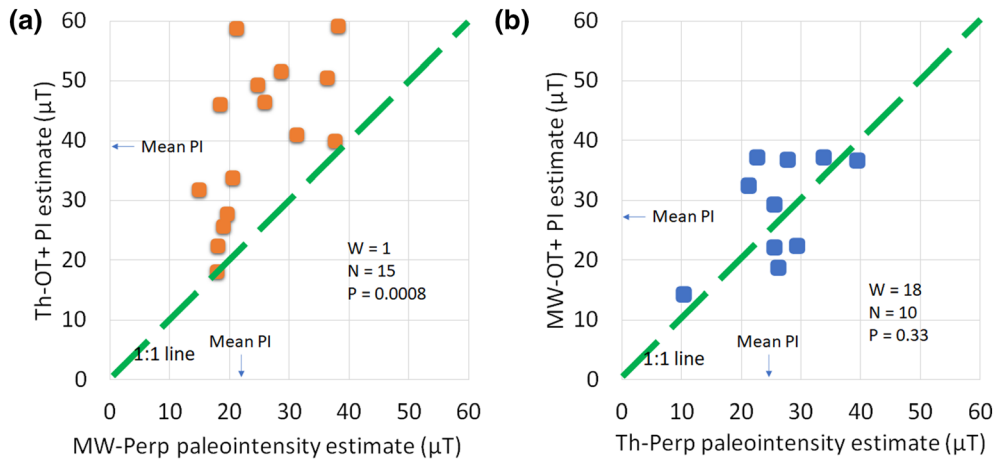

Figure 3. Testing Biggin's (2010) hypothesis that only paleointensity protocol affects PI estimate. Flow-level paleointensity estimates are plotted against each other for completely distinct PI methods (no shared protocol or demagnetization mechanism). (a) Confirming that the Th-OT+ data are higher than the MW-Perp data. (b) Checking if MW-OT+ data are higher than Th-Perp. The mean PIs listed are for the flows the methods have in common. N is the number of data points, and W and p are the statistics from the Wilcoxon signed rank test.

random about the 1:1 line nor cluster close to it. Thus, the PI estimate data pairs do not visually appear to be consistently normally distributed about the 1:1 line, which indicates that a two-sample t-test may be insufficient. We instead use the Wilcoxon signed rank test (see Biggin, 2010) to examine if the respective deviation of the data sets from the 1:1 line is significant at the 95% ($\alpha = 0.05$) confidence interval. The null hypothesis is that the data scatter about the 1:1 line is random.

In keeping with Biggin (2010), we first confirm that the Th-OT+ data are consistently higher than the MW-Perp data (Figure 3a). The Wilcoxon signed rank test gives $W = 1$, which corresponds to a p value of 0.0008 for 15 data points, so we can reject the null hypothesis that the deviation from the 1:1 line and hence the data scatter is random.

Next, we test the hypothesis of Biggin (2010) that the primary cause for the Th-OT+ data being consistently higher than the MW-Perp data is due to the differing PI protocol (OT+ vs. Perp) and not demagnetization mechanism (MW vs. thermal). We do this by comparing the MW-OT+ and Th-Perp data (i.e., the inverse combination) to see if the OT+ protocol continues to yield systematically higher values than the Perp protocol. It can be seen in Figure 3b that in fact, MW-OT+ data are not consistently higher than Th-Perp data; the paired results are significantly closer to and fall on either side of the 1:1 line. The Wilcoxon signed rank test gives $W = 18$, which corresponds to a p value of 0.33 for 10 data points, so we cannot reject the null hypothesis that the deviation from the 1:1 line is random. Having failed to support the simple hypothesis that the protocols are entirely responsible for the differences in PI results, we now examine demagnetization mechanisms and protocols in isolation to probe deeper into these specimens' behavior.

If the cause of the discrepancy between the Th-OT+ and MW-Perp data was purely the demagnetization mechanism, then we would expect that estimates from MW-OT+ and MW-Perp would be similar and would cluster around the 1:1 line. Similarly, estimates from Th-OT+ and Th-Perp would also be similar, clustering around their 1:1 line. These cases are plotted in Figure 4. For the flows they have in common (Figure 4a), the mean PI estimate for the MW-OT+ data is 30 ± 8.8 μT and 26.1 ± 7.7 μT for the MW-Perp data. The Wilcoxon signed rank test gives $W = 23$, which corresponds to a p value of 0.0065 for 18 data points, so we can reject the null hypothesis that the deviation from the 1:1 line is random. Next, we investigate the Th-OT+ and Th-Perp data (Figure 4b). For the flows they have in common, the mean PI estimate for the Th-OT+ data is 38.3 ± 14 μT and 27.5 ± 8.3 μT for the Th-Perp data. The Wilcoxon signed rank test for Th-OT+ versus Th-Perp gives $W = 3$, which gives a p value of 0.05 for seven data points, therefore also rejecting the null hypothesis that the deviation from the 1:1 line is random. Therefore, changing the protocol to OT+ from Perp does indeed cause higher PIs to be measured, but this is not the entire explanation for the discrepancy illustrated in Figure 3a.

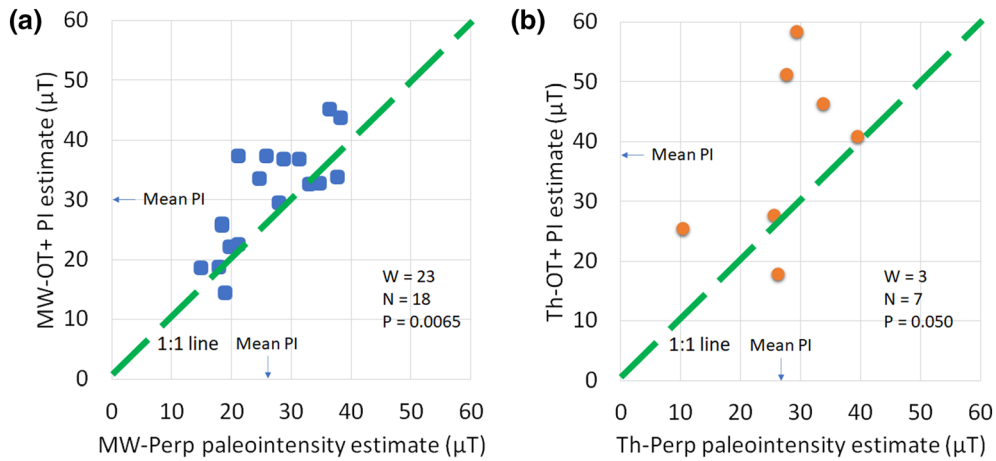

Figure 4. Testing the hypothesis that only paleointensity protocol affects PI estimate, control. Flow-level paleointensity estimates are plotted against each other for different PI protocols, separated by demagnetization mechanism. (a) Microwave data and (b) thermal data. The mean PIs listed are for the flows the methods have in common. N is the number of data points, and W and p are the statistics from the Wilcoxon signed rank test.

For the flows that have both Th-OT+ and MW-OT+ data (Figure 5a), we observe mean PI estimates of 40.7 ± 13 and 28.8 ± 10 μT, respectively. The Th-Perp and MW-Perp data give more similar estimates (Figure 5b). For the flows they have in common, the mean PI estimates are 28 ± 8.6 and 26.6 ± 5.9 μT, respectively. For Th-OT+ versus MW-OT+, the Wilcoxon signed rank test gives $W = 1$, which corresponds to a p value of 0.0012 for 14 data points. We can therefore reject the null hypothesis that the deviation from the 1:1 line is random, which indicates that Th-OT+ data are higher than the MW-OT+ data. For the Th-Perp and MW-Perp data, the Wilcoxon signed rank test gives $W = 25$, which corresponds to a p value of 0.24 for 11 data points. Thus, we cannot reject the null hypothesis that the Th-Perp and MW-Perp data's deviation is random, which suggests that the Th-Perp data are not higher than the MW-Perp data. This result agrees with the t-test in section 5.1.

We therefore observe that neither the demagnetization mechanism nor the protocol used can, in isolation, fully explain the differences in PI estimates observed. We additionally find that the Th-OT+ method yields results that are consistently (and statistically) higher than the other three methods used.

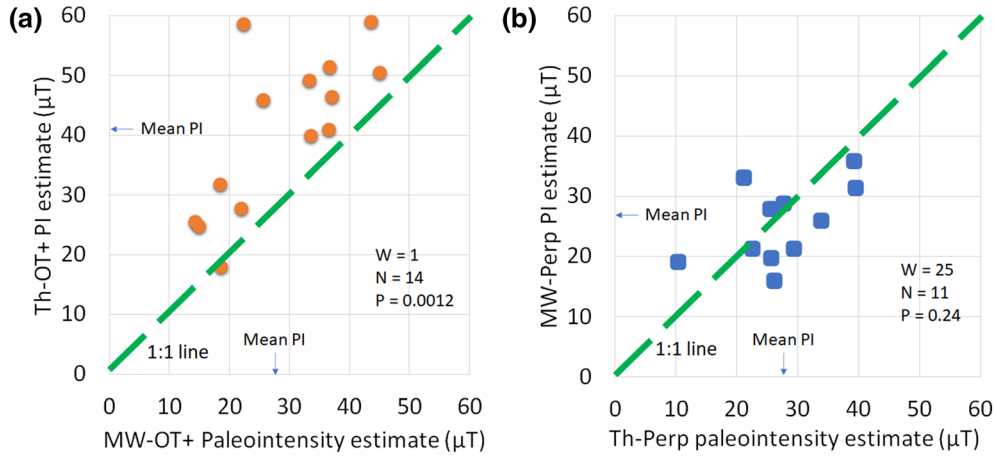

Figure 5. Testing the hypothesis that only demagnetization mechanism matters. Flow-level paleointensity estimates are plotted against each other for different PI methods, separated by protocol. (a) Original Thellier data and (b) perpendicular data. The mean PIs listed are for the flows the methods have in common. N is the number of data points, and W and p are the statistics from the Wilcoxon signed rank test.

6. Discussion

6.1. PI Methodology Differences

Double-heating Thellier protocols have long been known to have problems with multidomain components causing non-linear Arai plots (Levi, 1977). Hodgson et al. (2018) showed that this can apply to non-single domain oxyexsolved titanomagnetite grains as well, which are common in basaltic lavas such as the Hawaiian lavas of the SOH1 drill core. These non-single domain components can lead to concave up (two-slope) Arai plots. If the low blocking temperature (power integral) portion is used, the data give PI overestimates, and conversely, underestimates are obtained if the high blocking temperature (power integral) portion is used (Levi, 1977; Smirnov et al., 2017; Thomas, 1993; Xu & Dunlop, 2004). Grappone et al. (2019) studied samples from the 1960 Kilauea lava flow, another Hawaiian lava flow. They showed that the high estimates often found using thermal double-treatment methods (of which Th-OT is one) (e.g., Yamamoto et al., 2003) are not replicated when using the MW demagnetization mechanism. Our data here confirm this conclusion, as the Th-OT method yields the highest estimates, but the MW-OT data align much more closely with the Perp data sets obtained using either demagnetization mechanism.

A recent study by Cromwell et al. (2018) (using the thermal-IZZI method and strict selection criteria) reports PI estimates from 22 surface lava flows across the island of Hawaii. They found estimates consistent with geomagnetic field models in the 270–10,000 years range. However, the study was unable to reproduce the high estimates found in Teanby et al. (2002) and Laj et al. (2011). Cai et al. (2017) additionally found systematically lower estimates than Laj et al. (2011) using subaerial glassy basaltic margins on older flows from the HSDP2 core, using the same techniques as Cromwell et al. (2018). Based on the data herein and the other studies, the thermal OT method appears to give higher PI estimates than other PI methods and is likely an overestimate of the true palaeointensity due to exaggerated multidomain-like effects and the lack (in these experiments) of any mechanism to detect these.

The original MW study for the 1960 Kilauea lava flow, by Hill and Shaw (2000), gave site-level estimates up to 20% lower than the expected value of 36.5 μT. In both the Hill and Shaw (2000) and the Gratton et al. (2005) studies, an older MW system was used with the Perp protocol (Kono & Ueno, 1977), which uses only a single treatment per step and no pTRM checks. Grappone et al. (2019) showed that changing the MW experimental protocol to a more common double-treatment technique including alteration (pTRM) checks (in their case the IZZI protocol; Yu et al., 2004) gave the correct answer of 36.5 μT for the 1960 Kilauea lava flow. Although the OT protocol's additional treatments cause more thermochemical alteration than the Perp protocol, it is likely that the SOH1 samples behave in a similar way to the 1960 Kilauea flow and that the Perp data sets give low estimates due to undetected alteration.

The MW-Perp and the Th-Perp data sets are not statistically distinct, implying that it is not something inherent to the MW causing the differences between the original Teanby et al. (2002) and Gratton et al. (2005) data sets. It has been shown that for well-behaved (single-domain [SD]) grain-containing ceramics, there is a detectable difference in PI estimates due to differences in cooling rate (Poletti et al., 2013). Since the MW-Perp and the Th-Perp data sets are not statistically distinguishable, any cooling rate effect would be relatively minimal. Further, the MW-OT data have a faster cooling rate but give lower estimates than the Th-OT data, which is the opposite of the expected cooling rate effect (Poletti et al., 2013).

Additionally, the Perp protocol having less than half the number of treatments as in the OT protocol introduces another complication if these specimens undergo stress relaxation during the experiment. If even mild stress relaxation affects the specimens, the Perp data will appear too low because pTRMs would be gained more efficiently than NRM would be lost (Kosterov & Prevot, 1998).

That the MW-OT results are lower than their Th-OT counterparts suggests that something inherent to the MW demagnetization mechanism dampens the effects on the data from non-ideal vortex-state grains. If this finding was the result of the MW not causing the same magnitude of stress relaxation as in thermal experiments, the MW-Perp data would be expected to be even lower than the Th-Perp data (Kosterov & Prevot, 1998). This does appear to be the case here (Figure 5b), as the differences are not statistically significant.

Based on the above discussion, explanations therefore exist both for why the thermal OT experiments overestimate the true value (multidomain-like effects) and for why Perp experiments (both thermal and MW)

underestimate it (unrecognized alteration), which implies that the best estimate should fall between these two extremes.

The inherent uncertainty in the data and techniques used to obtain PI estimates can and should be expressed in the stated uncertainties associated with a flow-level mean (e.g., averaging the Th-OT+ and MW-Perp and providing the resulting large standard deviation). Until new, high-quality data exist for all the flows studied here from the SOH1 drill core, the authors propose that for each flow, the available flow-level Th-OT+ and MW-Perp data sets, which are the largest two, be averaged. Supporting Information D provides an example of this averaging for the flows containing at least two specimens in each Th-OT+ and MW-Perp data set (i.e., the flows studied in the meta-analysis described in Supporting Information A). This method gives a mean PI estimate of 29.2 ± 12 μT. This mean value is virtually identical to the mean MW-OT+ estimate of our newly collected data, 29.5 ± 9.2 μT, but higher than the equivalents measured by Gratton et al. (2005) and lower than those in Teanby et al. (2002). Flows characterized by data produced from only a single method (more than half; 97/181) across these studies (and the Laj et al., 2011, reanalysis) should not be considered accurate to within stated uncertainties.

6.2. Implications for Future Experiments

The Perp protocol has largely fallen out of use due to the lack of pTRM checks, but the OT protocol lives on as do the IZZI (Yu et al., 2004), Coe (ZI) (Coe, 1967), and Aitken (IZ) (Aitken et al., 1988) protocols. Modeling done in Biggin (2010) carries the implication that the OT protocol has the potential to exaggerate multidomain behavior compared with other Thellier-style double-treatment experiments, which is largely consistent with the study carried out here. We therefore suggest that any future experiments performed with the OT protocol (or indeed the Coe or Aitken protocols) should incorporate pTRM tail checks alongside pTRM checks such that multidomain-like effects may be detected. The IZZI protocol has the built-in advantage of allowing detection of non-ideal behavior via zig-zags in the Arai plot.

This study is consistent with previous studies (e.g., Grappone et al., 2019) that have shown that while different methods can give seemingly reliable data, non-ideal effects (multidomain behavior, stress relaxation, undetected alteration) can be a biasing influence. We therefore concur with the finding in Grappone et al. (2019) that at least pilot specimens should be run using at least two Thellier-style protocols (or the IZZI protocol) as a first order check for non-ideal PI behavior. Better still, different methods (e.g., thermal Thellier, MW Thellier, or multispecimen) should be employed to produce reliable multimethod PI estimates (de Groot et al., 2013), which, ideally, should be internally consistent. Biggin and Paterson (2014) provided a set of quantitative criteria for evaluating the reliability of PI estimates. Such PI estimates are required to satisfy the TECH QPI criterion of Biggin and Paterson (2014), which requires PI estimates to come from multiple techniques.

7. Conclusions

In this paper, we have sought to identify the cause for systematic discrepancies between previously published PI studies on the SOH1 drill core. New PI data confirm the systematic offset observed from previous studies when using the same methods, namely, Th-OT estimates were ~30% higher than MW- Perp estimates. For the first time, Th-Perp experiments and MW-OT experiments were undertaken on these rocks. Our results confirm that Th-OT data can be too high in the presence of magnetic carriers that do not behave as non-interacting SD grains. We further confirm that Perp data, which lack pTRM checks for alteration, can be too low due to undetected thermochemical alteration.

Until new measurements are made using reliable methods, results previously obtained from the SOH1 drill core using different methods should be combined at the flow level. The resulting enhanced standard deviation will accurately reflect the intrinsic uncertainty associated with the mean. The potential for biasing in those flows only represented by estimates produced by only one of the previously applied methods should be recognized.

Future studies undertaken using the thermal and/or MW demagnetization mechanisms should avoid any protocols which do not contain within them checks for both lab-induced alteration and non-ideal multidomain-like behavior. The IZZI protocol with pTRM checks satisfies both of these criteria.

Data Availability Statement

All new raw data collected in this study can be found on MagIC at earthref.org/MagIC/16664.

Acknowledgments

This study was carried out by J. Michael Grappone as part of a University of Liverpool match-funded studentship, with support from the Duncan Norman Research Scholarship. J. Michael Grappone acknowledges support from the NERC EAO Doctoral Training Partnership, grant NE/L002469/1 and NERC studentship 1793213. Andrew J. Biggin and Courtney J. Sprain acknowledge support from NERC standard grant NE/P00170X/1. Mimi J. Hill acknowledges NERC grant NE/I013873/1. Courtney J. Sprain thanks the Institute for Rock Magnetism at the University of Minnesota for use of their facilities to gather FORC data. The authors thank Nick Teanby for supplying the raw data from Teanby et al. (2002) and Martin Gratton for his systematic data archiving, from which we obtained the raw data from Gratton et al. (2005). The authors also acknowledge the extensive, helpful comments of the reviewers, associate editor, and editors of *JGR—Solid Earth*.

References

Aitken, M. J., Allsop, A. L., Bussell, G. D., & Winter, M. B. (1988). Determination of the intensity of the earths magnetic-field during archaeological times—Reliability of the Thellier technique. *Reviews of Geophysics*, *26*(1), 3–12.

Biggin, A. J. (2010). Are systematic differences between thermal and microwave Thellier-type palaeointensity estimates a consequence of multidomain bias in the thermal results? *Physics of the Earth and Planetary Interiors*, *180*(1-2), 16–40.

Biggin, A. J., & Paterson, G. A. (2014). A new set of qualitative reliability criteria to aid inferences on palaeomagnetic dipole moment variations through geological time. *Frontiers in Earth Science*, *2*(24).

Biggin, A. J., Piispa, E. J., Pesonen, L. J., Holme, R., Paterson, G. A., Veikkolainen, T., & Tauxe, L. (2015). Palaeomagnetic field intensity variations suggest Mesoproterozoic inner-core nucleation. *Nature*, *526*(7572), 245–248.

Biggin, A. J., Strik, G., & Langereis, C. G. (2009). The intensity of the geomagnetic field in the late-Archaean: New measurements and an analysis of the updated IAGA palaeointensity database. *Earth Planets and Space*, *61*(1), 9–22.

Cai, S., Tauxe, L., & Cromwell, G. (2017). Paleointensity from subaerial basaltic glasses from the second Hawaii Scientific Drilling Project (HSDP2) core and implications for possible bias in data from lava flow interiors. *Journal of Geophysical Research: Solid Earth*, *122*, 8664–8674. https://doi.org/10.1002/2017JB014683

Coe, R. S. (1967). Determination of paleo-intensities of earths magnetic field with emphasis on mechanisms which could cause non-ideal behavior in Thelliers method. *Journal of Geomagnetism and Geoelectricity*, *19*(3), 157–179.

Coe, R. S., Gromme, S., & Mankinen, E. A. (1978). Geomagnetic paleointensities from radiocarbon-dated lava flows on hawaii and question of pacific nondipole low. *Journal of Geophysical Research*, *83*, 1740–1756.

Cromwell, G., Trusdell, F., Tauxe, L., Staudigel, H., & Ron, H. (2018). Holocene paleointensity of the island of Hawai'i from glassy volcanics. *Geochemistry, Geophysics, Geosystems*, *19*, 3224–3245. https://doi.org/10.1002/2017GC006927

de Groot, L. V., Biggin, A. J., Dekkers, M. J., Langereis, C. G., & Herrero-Bervera, E. (2013). Rapid regional perturbations to the recent global geomagnetic decay revealed by a new Hawaiian record. *Nature Communications*, *4*.

Doell, R. R., & Cox, A. (1963). The accuracy of paleomagnetic method as evaluated from historic Hawaiian lava flows. *Journal of Geophysical Research*, *68*(7), 1997–2009.

Doell, R. R., & Cox, A. (1965). Paleomagnetism of Hawaiian lava flows. *Journal of Geophysical Research*, *70*(14), 3377–3405.

Grappone, J. M., Biggin, A. J., & Hill, M. J. (2019). Solving the mystery of the 1960 Hawaiian lava flow: Implications for estimating Earth's magnetic field. *Geophysical Journal International*, *218*(3), 1796–1806.

Gratton, M. N., Shaw, J., & Herrero-Bervera, E. (2005). An absolute palaeointensity record from SOH1 lava core, Hawaii using the microwave technique. *Physics of the Earth and Planetary Interiors*, *148*(2–4), 193–214.

Hill, M. J., Pan, Y. X., & Davies, C. J. (2008). An assessment of the reliability of palaeointensity results obtained from the Cretaceous aged Suhongtu section, Inner Mongolia, China. *Physics of the Earth and Planetary Interiors*, *169*(1–4), 76–88.

Hill, M. J., & Shaw, J. (2000). Magnetic field intensity study of the 1960 Kilauea lava flow Hawaii, using the microwave palaeointensity technique. *Geophysical Journal International*, *142*(2), 487–504.

Hill, M. J., & Shaw, J. (2007). The use of the 'Kono perpendicular applied field method' in microwave palaeointensity experiments. *Earth Planets and Space*, *59*(7), 711–716.

Hodgson, E., Grappone, J. M., Biggin, A. J., Hill, M. J., & Dekkers, M. J. (2018). Thermoremanent behavior in synthetic samples containing natural oxyexsolved titanomagnetite. *Geochemistry Geophysics Geosystems*, *19*, 1751–1766. https://doi.org/10.1029/2017GC007354

Klugh, H. E. (1986). *Statistics: The essentials for research*. London, UK: Taylor & Francis Group.

Kono, M., & Ueno, N. (1977). Paleointensity determination by a modified Thellier method. *Physics of the Earth and Planetary Interiors*, *13*(4), 305–314.

Kosterov, A. A., & Prevot, M. (1998). Possible mechanisms causing failure of Thellier palaeointensity experiments in some basalts. *Geophysical Journal International*, *134*(2), 554–572.

Laj, C., Kissel, C., Davies, C., & Gubbins, D. (2011). Geomagnetic field intensity and inclination records from Hawaii and the Reunion Island: Geomagnetic implications. *Physics of the Earth and Planetary Interiors*, *187*(3–4), 170–187.

Levi, S. (1977). Effect of magnetite particle-size on paleointensity determinations of geomagnetic-field. *Physics of the Earth and Planetary Interiors*, *13*(4), 245–259.

McElhinny, M. W., & Merrill, R. T. (1975). Geomagnetic secular variation over the past 5 m.y. *Reviews of Geophysics*, *13*(5), 687–708.

Paterson, G. A., Biggin, A. J., Hodgson, E., & Hill, M. J. (2015). Thellier-type paleointensity data from multidomain specimens. *Physics of the Earth and Planetary Interiors*, *245*, 117–133.

Paterson, G. A., Muxworthy, A. R., Yamamoto, Y., & Pan, Y. X. (2017). Bulk magnetic domain stability controls paleointensity fidelity. *Proceedings of the National Academy of Sciences of the United States of America*, *114*(50), 13120–13125.

Paterson, G. A., Zhao, X., Jackson, M., & Heslop, D. (2018). Measuring processing, and analyzing hysteresis data. *Geochemistry Geophysics Geosystems*, *19*, 1925–1945. https://doi.org/10.1029/2018GC007620

Poletti, W., Hartmann, G. A., Hill, M. J., Biggin, A. J., & Trindade, R. I. F. (2013). The cooling-rate effect on microwave archeointensity estimates. *Geophysical Research Letters*, *40*, 3847–3852. https://doi.org/10.1002/grl.50762

Quane, S. L., Garcia, M. O., Guillou, H., & Hulsebosch, T. P. (2000). Magmatic history of the East Rift Zone of Kilauea Volcano, Hawaii based on drill core from SOH 1. *Journal of Volcanology and Geothermal Research*, *102*(3–4), 319–338.

Shaar, R., & Tauxe, L. (2013). Thellier GUI: An integrated tool for analyzing paleointensity data from Thellier-type experiments. *Geochemistry Geophysics Geosystems*, *14*, 677–692. https://doi.org/10.1002/ggge.20062

Smirnov, A. V., Kulakov, E. V., Foucher, M. S., & Bristol, K. E. (2017). Intrinsic paleointensity bias and the long-term history of the geodynamo. *Science Advances*, *3*(2).

Teanby, N., Laj, C., Gubbins, D., & Pringle, M. (2002). A detailed palaeointensity and inclination record from drill core SOH1 on Hawaii. *Physics of the Earth and Planetary Interiors*, *131*(2), 101–140.

Thellier, E., & Thellier, O. (1959). Sur l'intensité du champ magnétique terrestre dans le passé historique et géologique. *Annals of Geophysics*, *15*, 285–376.

Thomas, N. (1993). An integrated rock magnetic approach to the selection or rejection of ancient basalt samples for paleointensity experiments. *Physics of the Earth and Planetary Interiors*, *75*(4), 329–342.

Xu, S., & Dunlop, D. J. (2004). Thellier paleointensity theory and experiments for multidomain grains. *Journal of Geophysical Research*, *109*, B07103. https://doi.org/10.1029/2004JB003024

Yamamoto, Y., Tsunakawa, H., & Shibuya, H. (2003). Palaeointensity study of the Hawaiian 1960 lava: Implications for possible causes of erroneously high intensities. *Geophysical Journal International*, *153*(1), 263–276.

Yu, Y. J., Tauxe, L., & Genevey, A. (2004). Toward an optimal geomagnetic field intensity determination technique. *Geochemistry Geophysics Geosystems*, *5*, Q02H07. https://doi.org/10.1029/2003GC000630

References From the Supporting Information

Cisowski, S. (1981). Interacting vs non-interacting single domain behavior in natural and synthetic samples. *Physics of the Earth and Planetary Interiors*, *26*(1–2), 56–62.

Harrison, R. J., & Feinberg, J. M. (2008). FORCinel: An improved algorithm for calculating first-order reversal curve distributions using locally weighted regression smoothing. *Geochemistry Geophysics Geosystems*, *9*, Q05016. https://doi.org/10.1029/2008GC001987

Paterson, G. A., Muxworthy, A. R., Roberts, A. P., & Mac Niocaill, C. (2010). Assessment of the usefulness of lithic clasts from pyroclastic deposits for paleointensity determination. *Journal of Geophysical Research*, *115*, B03104. https://doi.org/10.1029/2009JB006475

Pike, C. R., Roberts, A. P., & Verosub, K. L. (2001). First-order reversal curve diagrams and thermal relaxation effects in magnetic particles. *Geophysical Journal International*, *145*(3), 721–730.

Roberts, A. P., Pike, C. R., & Verosub, K. L. (2000). First-order reversal curve diagrams: A new tool for characterizing the magnetic properties of natural samples. *Journal of Geophysical Research*, *105*(B12), 28461–28475.